Université de Montréal

Mesure du rapport d'embranchement des désintégrations $B^0 \to \pi^- \ell^+ \nu$ et $B^+ \to \eta^{(\prime)} \ell^+ \nu$, du spectre des facteurs de forme des désintégrations $B^0 \to \pi^- \ell^+ \nu$ et $B^+ \to \eta \ell^+ \nu$, et extraction de $|V_{ub}|$ dans l'expérience BABAR

par
Martin Simard

Département de Physique
Faculté des arts et des sciences

Thèse présentée à la Faculté des études supérieures
en vue de l'obtention du grade de Philosophiæ Doctor (Ph.D.)
en Physique

Novembre, 2010

Université de Montréal
Faculté des études supérieures

Cette thèse intitulée:

Mesure du rapport d'embranchement des désintégrations $B^0 \to \pi^- \ell^+ \nu$ et $B^+ \to \eta^{(\prime)} \ell^+ \nu$, du spectre des facteurs de forme des désintégrations $B^0 \to \pi^- \ell^+ \nu$ et $B^+ \to \eta \ell^+ \nu$, et extraction de $|V_{ub}|$ dans l'expérience BABAR

présentée par:

Martin Simard

a été évaluée par un jury composé des personnes suivantes:

Victor Zacek,	président-rapporteur
Paul Taras,	directeur de recherche
Manu Paranjape,	membre du jury
François Corriveau,	examinateur externe

Thèse acceptée le: ....

RÉSUMÉ

Nous rapportons les résultats d'une étude des désintégrations semileptoniques non-charmées $B^+ \rightarrow \eta^{(\prime)}\ell^+\nu$ et $B^0 \rightarrow \pi^-\ell^+\nu$, mesurés par le détecteur BABAR avec une production d'environ 464 millions de paires de mésons $B\overline{B}$ issues des collisions e^+e^- à la résonance $\Upsilon(4S)$. L'analyse reconstruit les événements avec une technique relâchée des neutrinos. Nous obtenons les rapports d'embranchement partiels pour les désintégrations $B^+ \rightarrow \eta\ell^+\nu$ et $B^0 \rightarrow \pi^-\ell^+\nu$ en trois et douze intervalles de q^2, respectivement, à partir desquels nous extrayons les facteurs de forme $f_+(q^2)$ et les rapports d'embranchement totaux $\mathcal{B}(B^+ \rightarrow \eta\ell^+\nu)$ = $(3.39 \pm 0.46_{stat} \pm 0.47_{syst}) \times 10^{-5}$ et $\mathcal{B}(B^0 \rightarrow \pi^-\ell^+\nu)$ = $(1.42 \pm 0.05_{stat} \pm 0.08_{syst}) \times 10^{-4}$. Nous mesurons aussi $\mathcal{B}(B^+ \rightarrow \eta^{\prime}\ell^+\nu)$ = $(2.43 \pm 0.80_{stat} \pm 0.34_{syst}) \times 10^{-5}$. Nous obtenons les valeurs de la norme de l'élément $|V_{ub}|$ de la matrice CKM en utilisant trois calculs différents de la CDQ.

Mots clés : Semileptonique, exclusif, CKM, $|V_{ub}|$, chromodynamique, méson.

ABSTRACT

We report the results of a study of the exclusive charmless semileptonic decays, $B^+ \to \eta^{(\prime)}\ell^+\nu$ and $B^0 \to \pi^-\ell^+\nu$, undertaken with approximately 464 million $B\overline{B}$ pairs collected at the $\Upsilon(4S)$ resonance with the BABAR detector. The analysis uses events in which the signal B decays are reconstructed with a loose neutrino reconstruction technique. We obtain partial branching fractions for $B^+ \to \eta\ell^+\nu$ and $B^0 \to \pi^-\ell^+\nu$ decays in three and twelve bins of q^2, respectively, from which we extract the $f_+(q^2)$ form-factor shapes and the total branching fractions $\mathcal{B}(B^+ \to \eta\ell^+\nu) = (3.39 \pm 0.46_{stat} \pm 0.47_{syst}) \times 10^{-5}$ and $\mathcal{B}(B^0 \to \pi^-\ell^+\nu) = (1.42 \pm 0.05_{stat} \pm 0.08_{syst}) \times 10^{-4}$. We also measure $\mathcal{B}(B^+ \to \eta^{\prime}\ell^+\nu) = (2.43 \pm 0.80_{stat} \pm 0.34_{syst}) \times 10^{-5}$. We obtain values for the magnitude of the CKM matrix element $|V_{ub}|$ using three different QCD calculations.

Keywords : Semileptonic, exclusif, CKM, $|V_{ub}|$, chromodynamic, meson.

TABLE DES MATIÈRES

LISTE DES TABLEAUX

LISTE DES FIGURES

LISTE DES ANNEXES

LISTE DES SIGLES ET NOTATIONS

BAD	"BaBar Analysis document", document interne à la Collaboration BaBar.
BF	Rapport d'embranchement ("Branching Fraction").
BK	Paramétrisation "Becirevic Kaidalov" pour le facteur de forme $f_+(q^2)$.
CDQ	"ChromoDynamique Quantique", théorie de l'interaction forte.
CKM	Matrice "Cabibbo-Kobayashi-Maskawa", décrit le changement de saveur des quarks par l'interaction faible.
CPT	Produit des symétries C (conjuguaison de charge), P (parité) et T (temps).
DCH	Chambre à dérive ("Drift CHamber").
DCT	Système de déclenchement de la chambre à dérive ("Drift Chamber Trigger").
DIRC	Détecteur Čerenkov à réflexion interne ("Detector of Internally Reflected Čerenkov light").
EMC	Calorimètre électromagnétique ("ElectroMagnetic Calorimeter").
EMT	Système de déclenchement du calorimètre électromagmétique ("ElectroMagnetic calorimeter Trigger").
FF	Facteur de Forme ("Form Factor").
FSR	Photons de radiation finale ("Final State Radiation").
HER	Anneau de stockage de haute énergie ("High Energy Ring").
IFR	Retour de flux instrumenté ("Instrumented Flux Return").
IP	Point d'Interaction ("Interaction Point").
IR	Région d'interaction ("Interaction Region").
KEK	Laboratoire de recherche au Japon soutenant l'expérience Belle.
LCSR	Règle de Somme sur le Cône de Lumière ("Light Cone Sum Rules").
LER	Anneau de stockage de basse énergie ("Low Energy Ring").
Lissage	Terme utilisé pour traduire le mot anglais "fit".

MC	Simulation Monte Carlo.
MS	*Modèle Standard*.
PDF	Fonction de Densité de Probabilité (“Probability Density Function”).
PDG	“Particle Data Group”.
PEP-II	Colisionneur de Particules Electron-Positron (“Electron-Positron Project”).
PID	IDentification des Particules (“Particle IDentification”).
QCD	“Quantum ChromoDynamique”,voir CDQ.
RPC	Chambre à plaques résistives (“Resistive Plate Chamber”).
SF	Fonction de Forme (“Shape Function”).
SLAC	Laboratoire de recherche en Californie soutenant l’expérience *BABAR*.
SVT	Détecteur de vertex au silicium (“Silicon Vertex Detector”).

REMERCIEMENTS

Il ne fait aucun doute que sans l'implication et le soutien de nombreuses personnes, cette thèse n'aurait jamais vu le jour avec autant de détail et de précision. J'aimerais prendre le temps de remercier toutes ces personnes qui m'ont suivi tout le long de cette épanouissante aventure qu'est le doctorat.

Tout d'abord, j'aimerais remercier de tout coeur mon directeur de thèse, le professeur Paul Taras, de m'avoir donné l'opportunité de travailler dans l'expérience *BABAR* au SLAC, en Californie, pendant mes études de baccalauréat et ensuite de doctorat. Ce fut une expérience enrichissante tant au niveau social qu'intellectuel. Les nombreuses rencontres avec les experts présents dans la Collaboration *BABAR* ont certainement influencé mes capacités de recherche et mon esprit d'équipe et ont rendu cette expérience inoubliable. Merci également pour tes judicieux conseils et ton aide précieuse qui ont permi la publication des résultats présentés dans cette thèse. Votre aide fut indispensable ! Merci de m'avoir fait confiance et d'avoir investi de votre temps tout au long de ma thèse.

Je vous remercie chers parents, Marc et Francine, pour votre soutien, pour votre confiance et pour avoir toujours respecté mes choix. Merci de m'avoir donné cette liberté pour devenir la personne que je suis maintenant. Sans vos encouragements cette aventure aurait sans doute été plus difficile à vivre. Je remercie également mes frères François et Benoit pour leur soutien et pour les discussions intéressantes à propos de la physique. Merci grand-maman Denise, Lise et Carlos, Claire et Denis pour vos mots d'encouragement. Merci Benoit, Sophie, Kim, Maxime et Coryne, voir votre famille grandir est toujours une source de joie qui rend nos vies fascinantes. Merci André pour tes idées ingénieuses et ta créativité qui ont su m'inspirer. Pour toute ma famille qui a cru en moi et en ma réussite académique, un gros merci.

Je tiens à remercier mes amis et collègues David Côté, Sylvie Brunet, Benoît Viaud et Xuan Nguyen. Vos contributions pour le succès de cette thèse est sans équivoque.

David, j'ai bien aimé travailler à tes côtés et construire ensemble le logiciel *HistoMaker* ayant servi à ce présent ouvrage. Merci aussi d'avoir établi la nouvelle méthode du neutrino relâché qui est le sujet de ma présente thèse. Merci David et Sylvie de m'avoir accepté dans le groupe *BABAR* à l'Université de Montréal et pour votre hospitalité, votre générosité et votre amitié lors de nos séjours en Californie. Nos aventures californiennes resteront toujours dans mes pensées. Benoît, merci pour ton aide minutieuse pour l'analyse et l'interprétation des résultats. Sans toi, les résultats du lissage des données ne serait pas les mêmes. Merci pour ta compagnie en Californie, de ton humour et de m'avoir fait connaître la gastronomie et la culture française. Xuan, merci pour ta contribution inestimable pour les modes $B^+ \to \eta \ell^+ \nu$ et $B^+ \to \eta^{'} \ell^+ \nu$. Tes nouvelles idées et ton aide ont contibué grandement au progrès de l'analyse. Merci à vous tous de m'avoir supporté durant toutes ces années.

Merci aux professeurs de l'Université de Montréal, Louis Lessard, David London, Paul Taras, Richard MacKenzie, Victor Zacek, Manu Paranjape, Louis-André Hamel, Georges Azuelos, Sjoerd Roorda, François Schiettekatte et Claude Leroy pour la qualité de leurs enseignements et pour m'avoir donné le goût de poursuivre en physique des particules. Merci spécial pour l'enseignant en physique au secondaire, Louis Morettini, qui a su faire émerger en moi une passion pour la physique.

Je remercie également tous mes amis de l'Université de Montréal et du SLAC qui ont travaillé avec moi durant mes études. Merci pour votre aide et votre amitié. Je pense à Manuel, Joël, Marie-Élisabeth, Marie-Christine, Carsten, Swagato, Wells, Philippe, Mathieu, Martin, Jean-François, Jean-Philippe, Alexandre Alexi, Emmanuel, David, Ghyslain, Gaël, Guillaume, Haleh, Amir, Simon et Xavier. Merci spécial pour Bob Kowalewski, Jochen Dingfelder, Vera Lüth, David Lopes Pegna, Mike Kelsey, Concezio Bozzi, Walt Innes, Romulus Godang, John Walsh, Franco Simonetto et Marcello Rotondo, pour vos commentaires constructifs et votre aide à améliorer la qualité des résultats présentés dans cette thèse. J'apprécie l'effort et l'énergie que vous y avez mis.

Je ne veux pas oublier mes collègues de travail chez Vidéotron. Thomas Dufresne, merci pour m'avoir référé à cette compagnie. À tous les employés que j'ai eu la chance de cotoyer, merci beaucoup pour votre compréhension, pour votre support pour mes recherches, pour votre confiance et surtout pour votre bonne compagnie. La liste serait trop longue pour vous énumérer tous sans en oublier !

Je remercie Donald et Lauraine Gingras, pour m'avoir accompagné dans ma démarche et pour avoir approfondi ma foi chrétienne et mes connaissances bibliques. Merci du fond du coeur pour toutes les personnes qui ont prié pour ma réussite, notamment Dominico, Jean-Noël, Nicole, André, Michel, Louise, Lionel, Isabelle, Jérôme et Élysa. Je remercie mon ex-femme, Valérie Normand, et ses parents Marc et Hélène Normand pour m'avoir accompagné dans cette aventure pendant un certain temps. Vous resterez gravés dans mon coeur à tout jamais. Par-dessus tout, je ne peux pas m'empêcher de remercier la personne qui m'est la plus chère et qui m'a aidé á surmonter tous les obstacles de ma vie. Merci Seigneur Jésus. Je vous aime tous, autant que vous êtes ! Merci !

INTRODUCTION

Notre curiosité en tant qu'être humain, a permis de nous interroger sur la nature exacte de l'univers et les phénomènes physiques qui nous entourent. Si bien, qu'au fil du temps, l'homme est parvenu à découvrir les forces fondamentales de la nature qui expliquent les phénomènes observés. Par exemple, la force gravitationnelle a réussi à expliquer et à prédire le mouvement des corps célestes et terrestres. Cependant, même si la science explique ces événements avec précision, elle se base toujours sur des théories qui peuvent, un jour ou l'autre, être contredites par des observations expérimentales contraires à celles-ci. Ce fut notamment le cas pour la force d'*Isaac Newton* qui fut remplacée par celle de la relativité générale d'*Albert Einstein* pour expliquer la gravité. La physique subatomique, quant à elle, tente de répondre aux questions : "De quoi la matière est-elle constituée ?" et "Quelles sont les forces fondamentales qui maintiennent ces particules ensemble ?". Depuis 1972, le *Modèle Standard* est la théorie de la physique des particules pour décrire les particules élémentaires ainsi que leurs interactions. Cette description est vulgarisée en détail au Chapitre 1. Néanmoins, voyons ensemble un peu l'histoire qui a fait naître cette fameuse théorie qui n'a pas encore été contredite expérimentalement.

La physique des particules telle que nous la connaissons aujourd'hui, est le fruit de plus de 100 ans de recherche dans ce domaine. Bien avant notre ère, certains philosophes comme *Démocrite* avaient déjà postulé l'idée de particules élémentaires constituant la matière. Cette aventure a réellement débuté par la découverte de la première particule élémentaire par *Joseph Thomson* en 1897 par des rayons cathodiques déviés par un champ électrique. Cette particule est l'électron e^- et avait été postulée une trentaine d'années avant, afin d'expliquer les phénomènes électromagnétiques observés. Peu de temps après, en 1905, *Albert Einstein* démontra la nature corpusculaire de la lumière γ par l'effet photoélectrique. *Ernest Rutherford*, un étudiant de Thomson, a par la suite démontré en 1911 l'existence du noyau atomique massif chargé positivement et situé au centre de l'atome, expliquant les observations sur la diffusion alpha. Il prouva également, huit ans plus tard, l'existence du proton p en créant la première transmutation artificielle d'un élément du tableau périodique (azote) à un autre (oxygène). C'est un étudiant de Rutherford, *James Chadwick*, qui a découvert le neutron n en 1932 par des radiations neutres jusqu'alors inconnues. Par cette découverte, il fut notament possible de concevoir la première bombe atomique à l'aide d'isotopes radioactifs et la célèbre formule $E = mc^2$ d'Einstein. Ce sont ces trois particules, l'électron, le proton et le neutron, qui composent chaque atome de l'univers. À cette époque, nous savions qu'une force nucléaire devait exister pour maintenir les protons ensemble, pour contrer la répulsion coulombienne. C'est *Hideki Yukawa* qui proposa en 1935 que la force nucléaire était due à un échange de mésons massifs. Il faudra attendre jusqu'en 1973 pour décrire cette force "correctement" par l'échange de gluons neutres sans masse entre les particules nucléaires. Ce qui fut vérifié en 1979 par l'apparition d'un troisième jet de particules lors de collisions de particules électron-positron.

D'un autre coté, l'antimatière prédite par *Paul Dirac* fut découverte en 1932 par *Carl Anderson* en identifiant le positron e^+ par les mesures de traces chargées provenant des gerbes électromagnétiques produites par les rayons cosmiques. C'est également en utilisant cette méthode que lui et son assistant *Seth Neddermeyer* ont mis à l'évidence les particules de deuxième génération par la découverte du muon μ en 1936. L'antiproton $\bar{p}$, quant à lui, a été détecté pour la première fois en 1955 par *Owen Chamberlain* et *Emilio Segrè*. Cette particule a été produite à de hautes énergies à l'aide d'un accélérateur de particules en Californie. À partir de cet instant, la physique des particules fut désignée comme la physique des hautes énergies.

Dans les années 1960, des dizaines de particules ont été découvertes par les accélérateurs. Parmi ces particules, nous retrouvons en 1962 les neutrinos ν qui sont nécessaires pour expliquer l'énergie manquante dans les désintégrations β observées dès 1930. De plus, le nombre inquiétant de nouvelles particules suggérait une composition de particules plus fondamentale pour décrire les particules lourdes. Si bien qu'en 1964, *Murray Gell-Mann* postula l'existence des quarks u, d, s, et par la suite le c fut introduit, pour reconstruire toutes les particules découvertes incluant le proton et le neutron par ces quarks. Toutes les expériences confirmèrent l'existence de ces quarks et c'est seulement en 1967 que la théorie électrofaible fut postulée avec la prédiction de l'existence des bosons très massifs Z, W et le Higgs. Les bosons Z et W furent découvert en 1983 au CERN (*Organisation Européenne pour la Recherche Nucéaire*) et ayant exactement la masse prédite par la théorie. Des expériences en cours, notament le LHC (*Large Hadron Collider*) au CERN, tentent de détecter le Higgs pour la première fois. Mis à part le boson de Higgs, toutes les particules élémentaires prédites par le *Modèle Standard* ont été observées.

Après la confirmation de l'existence du quark c en 1974, nous avions à ce moment deux familles de quarks complètement vérifiées expérimentalement. Toutefois, nous savions qu'il manquait encore un ingrédient pour expliquer la violation CP observée. C'est *Makoto Kobayashi* et *Toshihide Maskawa* qui en 1972 proposèrent l'existence d'une troisième famille de particules pour expliquer cette violation CP donnant ainsi naissance à la théorie du *Modèle Standard*. Toutes ces nouvelle particules furent découvertes par la suite. Le lepton τ fut découvert par *Martin Perl* en 1976 au SLAC (*National Accelerator Laboratory*). Les quarks b et t ainsi que le ν_τ furent découverts au Fermilab (*Fermi National Accelerator Laboratory*) en 1977, 1995 et 2000, respectivement.

Malgré la réussite splendide de la théorie du *Modèle Standard*, elle pert un peu de son lustre par le nombre impressionnant de paramètres libres nécessaires à sa construction. Il y a en tout 19 paramètres, dont neuf pour les masses des fermions, quatre pour la matrice CKM, cinq pour les constantes de couplage et un dernier pour la CDQ (ChromoDynamique Quantique). Ces paramètres libres doivent absolument être obtenus expérimentalement. Comme nous allons le voir dans le Chapitre 1, les quatre paramètres de la matrice CKM sont décrits par trois angles et une phase. La mesure des éléments de cette matrice comme $|V_{ub}|$, qui représente la transition d'un quark b vers un quark u, permet de restreindre ces quatre paramètres. Nous verrons également que plusieurs méthodes existent pour extraire la valeur de $|V_{ub}|$. Il y a les méthodes *inclusives* qui regroupent l'ensemble des canaux de désintégration et *exclusives* qui consistent en l'étude d'un seul mode. Une tension existe entre ces deux techniques en obtenant des valeurs de $|V_{ub}|$ différentes de plus de deux fois l'erreur standard σ. C'est pourquoi une mesure plus précise de $|V_{ub}|$ provenant de ces deux méthodes permettrait de voir si de la physique nouvelle qui n'est pas décrite par le *Modèle Standard* peut expliquer cette différence ou si elle disparaît avec plus de précision.

Cette thèse présente les rapports d'embranchement des désintégrations semileptoniques $B^0 \to \pi^-\ell^+\nu$, $B^+ \to \eta\ell^+\nu$ et $B^+ \to \eta^{'}\ell^+\nu$. La mesure de $|V_{ub}|$ exclusive est ensuite extraite de la mesure des rapports d'embranchement partiels de $B^0 \to \pi^-\ell^+\nu$.

Le chapitre 1 discutera de la théorie fondamentale du *Modèle Standard*. De cette théorie découle la matrice de mélange des trois familles de quarks (matrice CKM) dont V_{ub} est un des éléments. Nous verrons le lien entre ce paramètre théorique et les mesures expérimentales.

Le chapitre 2 décrira le dispositif expérimental nécessaire pour l'expérience BABAR. Toutes les composantes du détecteur et des accélérateurs y seront expliquées en détails.

Les chapitre 3 et 4, sont les résultats expérimentaux de l'expérience BABAR. Le chapitre 3 contient les détails complets de l'analyse des désintégrations semileptoniques $B^0 \to \pi^-\ell^+\nu$, $B^+ \to \eta\ell^+\nu$ et $B^+ \to \eta^{'}\ell^+\nu$. Le chapitre 4, quant à lui, est une version condensée du chapitre 3 et qui a été publiée dans la revue PRD (*Physical Review D*). Ces deux chapitres ont déjà fait l'objet d'une révision complète et extrêmement minutieuse de plus de vingt experts, membres de la Collaboration BABAR.

Une discussion des résultats suivie d'une récapitulation sera faite à la toute fin de ce document.

CHAPITRE 1

ÉLÉMENTS DE THÉORIE DE LA PHYSIQUE DES PARTICULES

Les éléments théoriques discutés dans ce chapitre sont nécessaires pour comprendre l'importance des résultats expérimentaux présentés dans cette thèse.

1.1 Introduction au *Modèle Standard*

Le *Modèle Standard* introduit dans les années 1970, tente de décrire les constituants de la matière, c'est-à-dire les particules élémentaires et leurs interactions par des forces fondamentales : forte, faible et électromagnétique. Ce modèle est tellement précis qu'à ce jour aucune mesure expérimentale n'est venue contredire les prédictions faites par cette théorie. Pourtant, bien des questions restent sans réponse et ça implique que le *Modèle Standard* n'explique pas tous les phénomènes que nous pouvons observer en physique des particules, comme les récentes observations faites sur les oscillations de neutrino.

Le *Modèle Standard* est une théorie quantique des champs qui découle de la symétrie de jauge $SU(3)_C \otimes SU(2)_L \otimes U(1)_Y$, où $SU(3)_C$ est la symétrie de jauge de l'interaction forte et $SU(2)_L \otimes U(1)_Y$ est celle de l'interaction électrofaible, où la force électromagnétique et faible se combinent à haute énergie. Une description détaillée de la théorie des champs quantiques se trouve dans les références [1] et [2]. Il est primordial de comprendre que le concept de symétrie en physique est très important, car il permet notamment d'établir des lois de conservation. En effet, Emmy Noether a postulé dès 1918 son théorème qui stipule que toutes les lois de conservation de la nature sont les conséquences de symétries fondamentales. Par exemple, l'invariance par translation de l'espace-temps implique une conservation de l'énergie et de l'impulsion. Plus particulièrement pour le *Modèle Standard*, la symétrie de jauge $SU(3)_C \otimes SU(2)_L \otimes U(1)_Y$ implique une conservation de la couleur C, de l'isospin faible I et de l'hypercharge faible Y des particules. La couleur est la charge associée à la force forte, l'isospin faible est celle associée à la force faible et l'hypercharge faible est celle reliée à la charge électrique Q et à la composante longitudinale de l'isospin faible I_{3L} (aussi appelé chiralité gauche) de sorte que $Y = Q - I_{3L}$. La chiralité gauche implique que la composante longitudinale du spin de la particule est dans la même direction que son impulsion, tandis que la chiralté droite implique une direction opposée. Tout comme la masse et le spin, ces nombres quantiques sont des propriétés intrinsèques des particules. D'après ces nombres quantiques, nous pouvons regrouper les particules élémentaires du *Modèle Standard* en trois catégories : les *fermions*, les *bosons de jauge* et les *bosons scalaires*.

Les fermions sont des particules de spin 1/2 respectant donc la statistique de Fermi-Dirac. Cette statistique a comme particularité d'empêcher que des particules identiques se retrouvent avec le même niveau d'énergie quantique. Ils ont également un isospin faible $I = 1/2$ dont la composante longitudinale pour les fermions de type "up" et "down" est $I_{3L} = +1/2$ et $I_{3L} = -1/2$, respectivement. Pour les fermions de chiralité droite, cette composante de l'isospin est nulle $I_{3R} = 0$. Nous classons ces fermions en deux groupes : les *quarks* qui possèdent une des trois couleurs (rouge, bleu ou vert) et les *leptons* qui n'en ont pas et qui ne peuvent donc pas interagir avec la force forte. De plus, contrairement aux leptons ayant une charge électrique de $Q = 0$ ou $Q = -1$, les quarks se distinguent également par leur charge électrique fractionée de $Q = +2/3$ ou $Q = -1/3$, pour les fermions de type "up" ou "down", respectivement. Les leptons sans charge électrique sont les *neutrinos* et ils ne peuvent interagir que par la force faible. Au total on retrouve douze fermions divisés en trois générations comme illustrés sur le Tableau 1.1. Chacune des trois générations ne se diffère que par la masse des particules qui augmente selon la génération. Tous les autres nombres quantiques sont identiques.

Par ailleurs, il ne faut pas oublier qu'à chaque fermion il existe un anti-fermion de même masse, mais de nombres quantiques opposés. Par exemple, l'antiparticule de l'électron e^- est appelée positron e^+ et il possède exactement la même masse que l'électron mais avec la charge électrique opposée. De plus, les composantes de l'isospin

Tableau 1.1 – Les douze fermions et leurs caractéristiques.

	génération			isospin gauche	isospin droit	charge	couleur
	1	2	3	I_{3L}	I_{3R}	Q	C
Quarks	u	c	t	$+1/2$	0	$+2/3$	r,b,v
	d	s	b	$-1/2$	0	$-1/3$	
Leptons	ν_e	ν_μ	ν_τ	$+1/2$	-	0	-
	e	μ	τ	$-1/2$	0	-1	

gauche et droite sont inversées pour les antiparticules.

Les bosons de jauge sont les particules d'interaction de spin 1 respectant ainsi la statistique de Bose-Einstein. La force forte est véhiculée par huit bosons de masse et de charge électrique nulles qui sont nommés *gluons* (λ_a), où $a = 1, ..., 8$. Ils sont au nombre de huit, car il existe autant de générateurs pour le groupe de jauge $SU(3)_C$. Les gluons n'interagissent qu'avec les particules de couleur (les quarks) et entre eux, puisque ceux-ci contiennent également une charge de couleur. L'interaction entre les gluons impliquent une portée très réduite de la force forte. Les quarks ne pouvant être isolés sont confinés ensemble physiquement par les gluons formant ainsi les (*hadrons*). Ceux-ci sont formés de deux quarks (*mésons*) ou trois quarks (*baryons*). Dans un baryon, les couleurs des quarks sont tous différentes, tandis que les mésons contiennent un quark et un anti-quark, autrement dit une couleur et son anti-couleur. Le confinement des quarks vient du fait qu'en éloignant des quarks l'un de l'autre, l'interaction forte entre ces deux quarks augmente. En fournissant assez d'énergie pour vouloir isoler un quark, il y a automatiquement création de nouveaux quarks de sorte que les quarks ne se retrouvent jamais isolés. Toutefois, il est possible de créer un plasma quarks-gluons à de très hautes énergies, de sorte que les quarks ne sont plus confinés.

La force faible est responsable du changement de *saveur* des quarks. Ce changement de saveur consiste à changer le type de quark (“up” ou “down”) comme nous allons le voir plus loin. Il existe quatre bosons de jauge dûs au nombre de générateurs du groupe

$SU(2)_L \otimes U(1)_Y$: ce sont les bosons W^+, W^- et Z^0 pour l'interaction faible et le photon γ pour l'interaction électromagnétique. La portée de la force faible est également très courte puisque les bosons de cette interaction, très massifs et instables, interagissent entre eux. De plus, contrairement aux gluons, ces bosons interagissent avec tous les fermions, c'est-à-dire les quarks et les leptons. Fait intéressant, les bosons W^+ et W^- ne sont sensibles qu'à la chiralité gauche des fermions et droite des anti-fermions violant ainsi la symétrie P (*parité*). D'autres symétries comme C (conjugaison de charge) et T (renversement du temps) sont violées par l'interaction faible, mais toujours conservées par les interactions forte et électromagnétique. La parité consiste à inverser les coordonnées spatiales $\vec{r}$ à $-\vec{r}$. La conjugaison de charge consiste à remplacer les particules par leurs anti-particules. Par exemple, la parité et la conjugaison de charge sont violée par l'interaction $\pi^+ \rightarrow \mu^+\nu_\mu$. En effet, en changeant les coordonnées spatiales (P), le neutrino obtient une chiralité droite qui n'est pas observée expérimentalement. De plus, en substituant le neutrino par son antiparticule (C), nous obtenons un antineutrino gauche qui n'est également pas observé. Par contre, la symétrie CP est conservée, car nous obtenons un antineutrino droit et l'interaction $\pi^- \rightarrow \mu^-\bar{\nu}_\mu$ obtient le même taux de désintégration que l'interaction $\pi^+ \rightarrow \mu^+\nu_\mu$. Le renversement du temps consiste à mesurer l'amplitude de transition d'un état vers un autre et vice versa. Cependant, la symmétrie CPT est toujours conservée en théorie des champs pour toutes les interactions. Cette symétrie explique par ailleurs les masses et les temps de vie identiques pour les particules et leurs anti-particules. De notre côté, ce qui nous intéresse plus particulièrement, c'est la violation de la symétrie CP, le but principal de l'expérience BABAR et les résultats présentés dans cette thèse. Observée expérimentalement de façon directe pour la première fois dans le secteur des mésons K en 1999, elle fut observée de la même manière dans le secteur des mésons B en 2004 par les expériences BABAR et Belle.

De son côté, la force électromagnétique utilise le photon γ de masse et de charge électrique nulles. Le photon ne peut pas interagir avec lui-même comme le font les autres bosons de jauge. Ainsi, la portée de l'interaction électromagnétique est infinie. De plus, contrairement aux quarks contenant une charge de couleur qui ne peuvent être isolée, il est possible d'isoler un lepton possédant une charge électrique.

La force de gravité n'est malheureusement pas incluse dans le *Modèle Standard*. Néanmoins, dans tous les calculs il est possible d'ignorer cette force en physique des particules, car elle est $\sim 10^{39}$ fois moins intense que la force forte. Par comparaison, la force faible et electromagnétique est environ 10^5 et 10^2 fois moins intense que la force forte. Des expériences tentent toutefois de détecter une particule d'interaction pour la gravité nommée le *graviton*. Cette particule n'est pas décrite par le *Modèle Standard* et n'a jamais été détectée.

En terminant, il existe une troisième catégorie de particules qui sont les bosons scalaires. En fait, selon le *Modèle Standard* il existe au moins une particule élémentaire de spin 0 appelée *boson de Higgs*, souvent appelée la *particule de Dieu* [3]. Cette particule provient de la brisure spontanée de symétrie par le mécanisme de Higgs. C'est à ce mécanisme que l'on doit l'origine des différentes masses des fermions et des bosons de jauge. Le fait que les bosons W^+, W^- et Z^0 soient massifs implique que le groupe de jauge $SU(2)_L \otimes U(1)_Y$ n'est pas une symétrie du vide. En revanche, la masse nulle du photon implique que $U(1)_{em}$ est une symétrie du vide. La brisure spontanée est donc définie comme $SU(3)_C \otimes SU(2)_L \otimes U(1)_Y \to SU(3)_C \otimes U(1)_{em}$. Les bosons scalaires sont les seules particules du *Modèle Standard* à ce jour à ne pas avoir été observées expérimentalement. Des recherches pour les détecter sont présentement en cours avec le grand collisionneur de hadrons au CERN (*Organisation Européenne pour la Recherche Nucléaire*).

1.2 La matrice CKM et l'interaction faible

Comme nous venons de voir, seule la force faible permet un changement de saveur des quarks et une violation CP. Ce mélange des quarks peut être paramétrisé par la matrice CKM (Cabibbo-Kobayashi-Maskawa) [4]. Cette matrice décrit donc en détails la probabilité de changement de saveurs entres les différents quarks ainsi que l'importance de la violation CP dans l'interaction faible. Sans ce changement de saveurs, la désintégration semileptonique des mésons B ne serait pas possible. Par exemple, dans la désintégration semileptonique $B^0 \rightarrow \pi^- \ell^+ \nu$, le quark $\bar{b}$ doit se désintégrer en un quark $\bar{u}$ en émettant un boson W^- qui se désintègre en $\ell \nu_\ell$, où $\ell = e$, μ ou τ. Toutefois, même si la force forte ne joue aucun rôle dans la matrice CKM, il faut préciser tout de même qu'elle doit être prise en considération pour interpréter correctement les résultats expérimentaux. Cet effet de la force forte sur les quarks ne peut malheureusement être calculé de façon exacte puisque les calculs théoriques contiennent un nombre infini de termes. La valeur élevée de la constante de couplage de l'interaction forte g_s empêche l'utilisation de calculs perturbatifs. Comme nous allons le voir plus loin, il existe plusieurs calculs théoriques qui tentent d'obtenir le plus de précisions possibles sur l'effet de la force forte.

Dans le *Modèle Standard*, l'interaction faible étant décrite par le groupe $SU(2)_L \otimes U(1)_Y$, les chiralités *gauche* (L) et *droite* (R) des fermions sont exprimées par des doublets et des singulets, respectivement :

$$\begin{pmatrix} \nu_i \\ \ell_i \end{pmatrix}_L, \quad \begin{pmatrix} U_i \\ D_i \end{pmatrix}_L, \quad (\ell_i)_R, \quad (U_i)_R, \quad (D_i)_R, \tag{1.1}$$

où $i = 1, 2, 3$ est la génération. Seuls les neutrinos n'ont pas de chiralité droite. Autrement dit, leur spin est toujours en direction opposée à leur impulsion. Les leptons de type

(ℓ) et (ν), ainsi que les quarks (Q) de type “up” (U) et “down” (D) sont définis ainsi :

$$\begin{aligned}
D &\equiv \begin{pmatrix} d \\ s \\ b \end{pmatrix}, \quad \overline{D} \equiv \begin{pmatrix} \overline{d} & \overline{s} & \overline{b} \end{pmatrix}, \\
U &\equiv \begin{pmatrix} u \\ c \\ t \end{pmatrix}, \quad \overline{U} \equiv \begin{pmatrix} \overline{u} & \overline{c} & \overline{t} \end{pmatrix}, \\
\ell &\equiv \begin{pmatrix} e \\ \mu \\ \tau \end{pmatrix}, \quad \overline{\ell} \equiv \begin{pmatrix} \overline{e} & \overline{\mu} & \overline{\tau} \end{pmatrix}, \\
\nu &\equiv \begin{pmatrix} \nu_e \\ \nu_\mu \\ \nu_\tau \end{pmatrix}, \quad \overline{\nu} \equiv \begin{pmatrix} \overline{\nu}_e & \overline{\nu}_\mu & \overline{\nu}_\tau \end{pmatrix}, \\
Q &\equiv \begin{pmatrix} U \\ D \end{pmatrix}, \quad \overline{Q} \equiv \begin{pmatrix} \overline{U} & \overline{D} \end{pmatrix},
\end{aligned} \tag{1.2}$$

où $\overline{f} = f^\dagger\gamma^0$, f sont les douze fermions et γ^0 est une matrice de Dirac.

La description des interactions entre les différentes particules du *Modèle Standard* est définie par son Lagrangien [1, 2] :

$$\mathcal{L}_{MS} = \mathcal{L}_{CDQ} + \mathcal{L}_{EF}, \tag{1.3}$$

où $\mathcal{L}_{CDQ}$ décrit les interactions fortes et $\mathcal{L}_{EF}$ décrit les interactions électrofaibles.

Le terme $\mathcal{L}_{CDQ}$ représente donc les interactions quarks-gluons et les interactions gluons-gluons. Son Lagrangien s'écrit :

$$\begin{aligned}\mathcal{L}_{CDQ} &= \overline{Q}_i(iD_{ij} - m\delta_{ij})Q_j - \frac{1}{4}G^a_{\mu\nu}G^{\mu\nu}_a, & (1.4)\\ &= \overline{Q}_i(i\partial_\mu\gamma^\mu - m)Q_i + \overline{Q}_i\left(g_s\frac{\lambda^a_{ij}}{2}G^a_\mu\gamma^\mu\right)Q_j - \frac{1}{4}G^a_{\mu\nu}G^{\mu\nu}_a, & (1.5)\end{aligned}$$

où $D \equiv D_\mu\gamma^\mu$, dont la dérivée covariante pour l'interaction forte est :

$$D_\mu = \partial_\mu - ig_s\frac{\lambda^a}{2}G^a_\mu, \tag{1.6}$$

avec $\lambda^a,\ a = 1, ..., 8$, symbolisant les huits générateurs de $SU(3)_C$. Le symbole g_s est la constante de couplage de l'interaction forte, G^a_μ représente le champ des gluons et $G^a_{\mu\nu}$ est le tenseur gluonique définit comme :

$$G^a_{\mu\nu} = \partial_\mu G^a_\nu - \partial_\nu G^a_\mu - g_s f^{abc}G^b_\mu G^c_\nu, \tag{1.7}$$

où $f^{abc},\ a, b, c = 1, ..., 8$, sont les constantes de structure du groupe $SU(3)_C$. Ce qui nous intéresse plus particulièrement, c'est le deuxième terme du Lagrangien du *Modèle Standard*, celui qui représente la force électrofaible et qui permet un changement de saveur des quarks.

On peut décomposer le Lagrangien électrofaible $\mathcal{L}_{EF}$ en plusieurs Lagrangiens distincts pour décrire les interactions des différentes particules élémentaires comme suit :

$$\mathcal{L}_{EF} = \mathcal{L}_{Fermions} + \mathcal{L}_{Bosons} + \mathcal{L}_{Higgs} + \mathcal{L}_{Yukawa}. \tag{1.8}$$

Dans ce qui suit, nous allons voir en détail les caractéristiques et l'importance de chacun de ces termes.

Le Lagrangien $\mathcal{L}_{Fermions}$ est celui qui fait intervenir les interactions des fermions avec les bosons de jauge. C'est donc ce terme qui explique le changement de saveurs des quarks et il est défini ainsi :

$$\mathcal{L}_{Fermions} = \overline{f}_{Li}(iD_{ij})f_{Lj} + \overline{f}_{Ri}(iD_{ij})f_{Rj}, \tag{1.9}$$

où $D \equiv D_\mu \gamma^\mu$, dont la dérivée covariante pour l'interaction électrofaible est :

$$D_\mu = \partial_\mu - ig\frac{\tau^k}{2}W_\mu^k - ig'\frac{Y}{2}B_\mu, \tag{1.10}$$

où les constantes de couplage g et g', les générateurs $\tau^k,\ k = 1, 2, 3$ (matrices de Pauli) et Y, ainsi que les bosons électrofaibles W_μ^k et B_μ, sont caractéristiques des groupes de symétrie $SU(2)_L$ et $U(1)_Y$, respectivement. Ces bosons électrofaibles sont définis dans la base des états propres de l'interaction faible et ne sont pas obervables expérimentalement, contrairement aux bosons physiques $W_\mu^\pm$, Z_μ^0 et A_μ (le photon) qui sont définis dans la base des états propres de masse. Le passage d'une base à une autre s'obtient en utilisant des matrices de mélange de la façon suivante :

$$\begin{pmatrix} W_\mu^+ \\ W_\mu^- \end{pmatrix} = \frac{1}{\sqrt{2}}\begin{pmatrix} 1 & i \\ 1 & -i \end{pmatrix}\begin{pmatrix} W_\mu^1 \\ W_\mu^2 \end{pmatrix}, \tag{1.11}$$

$$\begin{pmatrix} A_\mu \\ Z_\mu^0 \end{pmatrix} = \begin{pmatrix} \cos\theta_W & \sin\theta_W \\ -\sin\theta_W & \cos\theta_W \end{pmatrix}\begin{pmatrix} B_\mu \\ W_\mu^0 \end{pmatrix}, \tag{1.12}$$

où $\theta_W \approx 28.74°$ est l'angle de Weinberg. Nous verrons plus loin que cet angle, relié aux constantes de couplage g et g' par les relations :

$$\frac{g}{\cos\theta_W} = \frac{g'}{\sin\theta_W} = \sqrt{g^2 + g'^2}, \tag{1.13}$$

est aussi relié aux masses des bosons de jauge obtenues après la brisure spontanée de symétrie par le mécanisme de Higgs. En développant le Lagrangien de l'équation 1.9 par les relations 1.10 à 1.12, nous retrouvons des termes d'interaction contenant des fermions de différentes saveurs (*Courant Chargé* CC) et des termes avec des fermions de même saveur (*Courant Neutre* CN), de sorte que :

$$\begin{aligned}
\mathcal{L}_{Fermions_{interaction}} &= \mathcal{L}_{CC} + \mathcal{L}_{CN}, & (1.14)\\
\mathcal{L}_{CC} &= \frac{g}{\sqrt{2}}(J^{\mu+}W_{\mu}^{+} + J^{\mu-}W_{\mu}^{-}), & (1.15)\\
\mathcal{L}_{CN} &= eJ_{em}^{\mu}A_{\mu} + \frac{g}{\cos\theta_W}(J_3^{\mu} - \sin^2\theta_W J_{em}^{\mu})Z_{\mu}, & (1.16)
\end{aligned}$$

où les courants chargés $J^{\mu+}$, $J^{\mu-}$ et neutres J_3^{μ}, J_{em}^{μ} sont :

$$\begin{aligned}
J^{\mu+} &= \overline{U}_{Li}\gamma^{\mu}D_{Lj} + \overline{\nu}_{Li}\gamma^{\mu}\ell_{Lj}, & (1.17)\\
J^{\mu-} &= \overline{D}_{Li}\gamma^{\mu}U_{Lj} + \overline{\ell}_{Li}\gamma^{\mu}\nu_{Lj}, & (1.18)\\
J_3^{\mu} &= I_{3L}(\overline{U}_{Li}\gamma^{\mu}U_{Lj} + \overline{D}_{Li}\gamma^{\mu}D_{Lj} + \overline{\ell}_{Li}\gamma^{\mu}\ell_{Lj} + \overline{\nu}_{Li}\gamma^{\mu}\nu_{Lj}), & (1.19)\\
J_{em}^{\mu} &= Q_U(\overline{U}_{L,Ri}\gamma^{\mu}U_{L,Rj}) + Q_D(\overline{D}_{L,Ri}\gamma^{\mu}D_{L,Rj}) + Q_{\ell}(\overline{\ell}_{L,Ri}\gamma^{\mu}\ell_{L,Rj}), & (1.20)
\end{aligned}$$

avec $i, j = 1, 2, 3$ représentant les générations, $I_{3L} = 1/2$ est la composante longitudiale de l'isospin faible de chiralité gauche et $Q_U = 2/3$, $Q_D = -1/3$, $Q_{\ell} = -1$ sont les charges électriques. Comme $I_{3R} = 0$, aucune composante droite ne se retrouve dans J_3^{μ} et similairement pour la charge électrique nulle du neutrino, aucun terme de neutrino n'est présent dans J_{em}^{μ}. Nous savons également que les constantes de couplage e et g peuvent être reliées par la relation $e = g\sin\theta_W \approx 0.5g$. Ainsi, la constante de couplage électrofaible g est environ deux fois plus grande que la constante de couplage électromagnétique e. Les courants chargés $J^{\mu+}$ et $J^{\mu-}$ contiennent des changements de saveurs pour les quarks et les leptons. Expérimentalement, on ne détecte des courants chargés que pour les quarks. Ceci indique donc que la base des états propres de l'interaction faible dans le secteur leptonique est également la base des états propres de masse. Ce n'est pas le cas pour les quarks comme nous allons le voir. Après la brisure spontanée de symétrie il faudra utiliser la matrice CKM pour passer d'une base à une autre.

Le Lagrangien $\mathcal{L}_{Bosons}$ est le terme du Lagrangien du *Modèle Standard* qui décrit les interactions des bosons de jauge entre eux. Ce terme important fait apparaître les tenseurs des bosons de l'interaction faible :

$$\mathcal{L}_{Bosons} = -\frac{1}{4}(W^i_{\mu\nu}W^{\mu\nu}_i + B_{\mu\nu}B^{\mu\nu}) + \mathcal{L}_{FP} + \mathcal{L}_{AJ}, \tag{1.21}$$

où les tenseurs sont :

$$W_{\mu\nu} = \partial_\mu W^i_\nu - \partial_\nu W^i_\mu + g\epsilon^{ijk}W^j_\mu W^k_\nu, \tag{1.22}$$

$$B_{\mu\nu} = \partial_\mu B_\nu - \partial_\nu B_\mu, \tag{1.23}$$

avec $i, j, k = 1, 2, 3$. Le Lagrangien $\mathcal{L}_{FP}$ est celui de Fadeev-Popov impliquant la virtualité de ces particules et le Lagrangien $\mathcal{L}_{AJ}$ est l'ajustement de jauge.

Le troisième terme du $\mathcal{L}_{EF}$ est $\mathcal{L}_{Higgs}$ et contient les interactions du Higgs avec lui-même et les bosons de jauge. Ce terme est très important, car il fait apparaître des termes de masses pour les bosons de jauge. Nous le définissons ainsi :

$$\mathcal{L}_{Higgs} = (D_\mu\phi)^\dagger(D^\mu\phi) - \lambda(\phi^\dagger\phi)^2 + \mu^2\phi^\dagger\phi, \tag{1.24}$$

où μ^2 et λ sont les paramètres réels du champ de Higgs ϕ qui est un doublet :

$$\phi = \begin{pmatrix} \phi^+ \\ \phi^0 \end{pmatrix} = \frac{1}{\sqrt{2}}\begin{pmatrix} \phi_1 + i\phi_2 \\ \phi_3 + i\phi_4 \end{pmatrix}. \tag{1.25}$$

C'est ici qu'intervient le mécanisme de Higgs et la brisure spontanée de symétrie. Ce mécanisme vient du fait qu'il existe une infinité de solutions pour les champs de Higgs ϕ_i, $i = 1, 2, 3, 4$, si la valeur du champs de Higgs dans le vide est non-nulle comme c'est le cas avec μ^2 et λ positif. Ainsi, pour définir le minimum du champ de Higgs, nous devons faire un choix :

$$\phi^\dagger\phi = \frac{\mu^2}{2\lambda} = \frac{v^2}{2}, \tag{1.26}$$

où v est la valeur moyenne du champ de Higgs dans le vide. Peu importe le choix, le résultat est le même et la symétrie $SU(2)_L \otimes U(1)_Y$ est brisée et devient $U(1)_{em}$. Après la brisure de symétrie, le doublet de Higgs devient :

$$\phi = \begin{pmatrix} \phi^+ \\ \phi^0 \end{pmatrix} = \frac{1}{\sqrt{2}} \begin{pmatrix} 0 \\ v+h \end{pmatrix}, \tag{1.27}$$

où h est le champ correspondant au boson de Higgs. En incorporant les équations 1.11, 1.12 et 1.27 dans le Lagrangien du Higgs, nous obtenons des termes qui définissent la masse des bosons de jauge et les termes sont :

$$\mathcal{L}_{masse} = \left(\frac{vg}{2}\right)^2 W_\mu^+ W^{\mu-} + \frac{1}{2}\left(\frac{v\sqrt{g^2+g'^2}}{2}\right)^2 Z_\mu Z^\mu. \tag{1.28}$$

L'absence de A_μ dans les termes de masse implique une masse nulle pour le photon. La masse des bosons W^+, W^-, et Z^0 sont définis par les constantes de couplages g et g' et sont :

$$m_{W^\pm} = \frac{vg}{2}, \tag{1.29}$$

$$m_{Z^0} = \frac{v\sqrt{g^2+g'^2}}{2}. \tag{1.30}$$

On peut définir le ratio de ces deux masses en utilisant l'angle de Weinberg :

$$m_{W^\pm}/m_{Z^0} = \cos\theta_W. \tag{1.31}$$

Finalement le dernier terme du Lagrangien du *Modèle Standard* $\mathcal{L}_{Yukawa}$ fait le couplage du champ de Higgs avec les fermions et s'écrit :

$$\begin{aligned}\mathcal{L}_{Yukawa} = & -(Y_{ij}^D(\overline{U}_{Li}\phi)D_{Rj} + Y_{ij}^D(\overline{D}_{Li}\phi)D_{Rj} + Y_{ij}^U(\overline{U}_{Li}\tilde{\phi})U_{Rj} + Y_{ij}^U(\overline{D}_{Li}\tilde{\phi})U_{Rj} \\ & +Y_{ij}^\ell(\overline{U}_{Li}\phi)\ell_{Rj} + Y_{ij}^\ell(\overline{D}_{Li}\phi)\ell_{Rj}) + \text{conjugué hermitien},\end{aligned} \tag{1.32}$$

où $i, j = 1, 2, 3$ sont les générations, Y sont des matrices 3x3 à déterminer et $\tilde{\phi} = i\tau_2\phi$.

Les matrices Y vont définir la matrice CKM et ils doivent être mesurées expérimentalement. L'absence de neutrinos droits dans $\mathcal{L}_{Yukawa}$ implique donc une masse nulle pour ces particules. De nos jours, nous savons que ce n'est pas le cas grâce aux oscillations de neutrinos observées expérimentalement dont l'amplitude d'oscillation d'une génération à une autre est proportionnelle à la différence des carrés de leur masse. De la même façon que les bosons de jauge, des termes de masse vont également apparaître après la brisure spontanée de symétrie pour donner une masse non-nulle aux fermions. En effet, en incorporant le champ de Higgs après la brisure spontanée de symétrie de l'équation 1.27 dans $\mathcal{L}_{Yukawa}$, il ne reste que les champs neutres et le Lagrangien devient :

$$\mathcal{L}_{Yukawa} = -(Y_{ij}^{D}\overline{D}_{Li}D_{Rj}+Y_{ij}^{U}\overline{U}_{Li}U_{Rj}+Y_{ij}^{\ell}\overline{\ell}_{Li}\ell_{Rj})\frac{v}{\sqrt{2}}\left(1+\frac{h}{v}\right)+\text{conjugué hermitien}, \tag{1.33}$$

où $i, j = 1, 2, 3$ sont les générations. Nous définissons les matrices $M_{ij}^{k} = Y_{ij}^{k}v/\sqrt{2}$, avec $k = D, U, \ell$. Si ces matrices sont diagonales, alors la base des états propres de l'interaction faible est la même que la base des états propres de masse et il n'y a pas de violation CP. Expérimentalement, on mesure la violation CP et des matrices non-diagonales dans le secteur des quarks. Ainsi, pour passer des quarks électrofaibles aux quarks physiques, il faut diagonaliser M_{ij} par des matrices unitaires, de sorte que :

$$M_{diag}^{k} = V_{Li}^{k}M_{ij}^{k}V_{Rj}^{k}, \tag{1.34}$$

où $V_{L,R}^{k}$ sont les matrices unitaires avec $k = D, U, \ell$ représentant les particules et $i, j = 1, 2, 3$ les générations. Nous obtenons finalement les quarks physiques U' et D' avec les matrices unitaires $V_{L,R}^{U}$ et $V_{L,R}^{D}$ à partir des quarks électrofaibles U et D avec :

$$U'_{L,Ri} = V_{L,Rij}^{U}U_{L,Rj}, \tag{1.35}$$

$$D'_{L,Ri} = V_{L,Rij}^{D}D_{L,Rj}, \tag{1.36}$$

où $i, j = 1, 2, 3$ sont les générations. En changeant la base des états propres de l'interaction faible par la base des états propres de masse dans le Lagrangien des fermions, seuls les termes des courants chargés impliquant les quarks de chiralité gauche et les bosons W_μ^+ sont modifiés :

$$\overline{U}_{Li}\gamma^\mu D_{Lk} = \overline{U}'_{Li}V^U_{Lij}\gamma^\mu V^{D\dagger}_{Ljk}D'_{Lk}. \tag{1.37}$$

On n'observe pas de mélange dans le secteur leptonique, à l'exception des oscillations de neutrinos. Les termes des courants neutres ne sont pas modifiés et sont invariants par cette transformation, car $VV^\dagger$ est la matrice identité. La définition de la matrice CKM est obtenue par la matrice de mélange des quarks électrofaibles et des quarks physiques pour passer d'une base à une autre et en utilisant l'équation 1.37 nous obtenons :

$$V_{CKM} \equiv V^U_L V^{D\dagger}_L = \begin{pmatrix} V_{ud} & V_{us} & V_{ub} \\ V_{cd} & V_{cs} & V_{cb} \\ V_{td} & V_{ts} & V_{tb} \end{pmatrix}. \tag{1.38}$$

Cette matrice doit être mesurée expérimentalement et c'est exactement ce que nous faisons dans cette thèse en mesurant la norme de l'élément V_{ub} de la matrice CKM.

1.2.1 Triangle d'unitarité

La matrice CKM contient donc neuf termes complexes faisant apparaître ainsi 18 paramètres réels. Toutefois, il est possible de démontrer [5] que le nombre de paramètres libres se réduit à seulement trois angles et une phase. En effet, la matrice CKM étant unitaire et orthogonale permet de construire neuf contraintes avec les relations :

$$\sum_{j=1}^{3} V_{ij}V^*_{kj} = \sum_{j=1}^{3} V_{ji}V^*_{jk} = \delta_{ik}, \tag{1.39}$$

où $i, j, k = 1, 2, 3$ sont les génerations, le premier indice de V correspond aux quarks U et le deuxième aux quarks D. Sur les neuf paramètres restants, cinq peuvent être éliminés par changement de convention de phase des champs de quarks. De sorte que seulement quatre paramètres dont trois angles et une phase sont des paramètres libres. C'est la phase qui est responsable de la violation CP dans le *Modèle Standard*. De manière générale, nous pouvons démontrer [5] que pour le nombre de génération n_g, il existe $n_g(n_g-1)/2$

angles et $(n_g - 1)(n_g - 2)/2$ phases. Ainsi, il est primordial d'avoir au minimum trois générations de quarks pour qu'une phase libre puisse exister.

Pour transformer les 18 paramètres de la matrice CKM en trois angles et une phase, nous pouvons utiliser la paramétrisation qui nous convient puisqu'il en existe une infinité. Toutefois, pour que les résultats soient tous cohérents entre eux, nous utilisons la paramétrisation standard pour toutes les analyses de la physique des particules et elle s'écrit :

$$\begin{aligned} V_{CKM} &= \begin{pmatrix} V_{ud} & V_{us} & V_{ub} \\ V_{cd} & V_{cs} & V_{cb} \\ V_{td} & V_{ts} & V_{tb} \end{pmatrix}, && (1.40) \\ &= \begin{pmatrix} c_{12}c_{13} & s_{12}c_{13} & s_{13}e^{-i\delta} \\ -s_{12}c_{23} - c_{12}s_{23}s_{13}e^{i\delta} & c_{12}c_{23} - s_{12}s_{23}s_{13}e^{i\delta} & s_{23}c_{13} \\ s_{12}s_{23} - c_{12}c_{23}s_{13}e^{i\delta} & -c_{12}s_{23} - s_{12}c_{23}s_{13}e^{i\delta} & c_{23}c_{13} \end{pmatrix} && (1.41) \end{aligned}$$

où $s_{ij} = \sin\theta_{ij}$, $c_{ij} = \cos\theta_{ij}$ et δ est la phase responsable de la violation CP. Il est pratique d'approximer cette paramétrisation par celle de *Wolfenstein* afin de connaître la hiérarchie des termes de la matrice CKM. Cette approximation découle du fait qu'expérimentalement on trouve $s_{13} \ll s_{23} \ll s_{12}$. Nous définissons ainsi l'approximation Wolfenstein [6] :

$$\begin{aligned} s_{12} &\equiv \lambda = \frac{|V_{us}|}{\sqrt{|V_{ud}|^2 + |V_{us}|^2}}, && (1.42) \\ s_{23} &\equiv A\lambda^2 = \frac{|V_{cb}|}{\sqrt{|V_{ud}|^2 + |V_{us}|^2}} = \lambda\frac{|V_{cb}|}{|V_{us}|}, && (1.43) \\ s_{13}e^{i\delta} &\equiv A\lambda^3(\rho + i\eta) = \frac{A\lambda^3(\bar{\rho} + i\bar{\eta})\sqrt{1 - A^2\lambda^4}}{\sqrt{1-\lambda^2}(1 - A^2\lambda^4(\bar{\rho} + i\bar{\eta}))} = V_{ub}^*, && (1.44) \end{aligned}$$

où

$$\bar{\rho} + i\bar{\eta} = -(V_{ud}V_{ub}^*)/(V_{cd}V_{cb}^*) = (\rho + i\eta)\left(1 - \frac{\lambda^2}{2} + \mathcal{O}(\lambda^4)\right). \qquad (1.45)$$

Ainsi, la matrice CKM s'écrit à l'ordre λ^3 :

$$V_{CKM} \approx \begin{pmatrix} 1-\lambda^2/2 & \lambda & A\lambda^3(\rho - i\eta) \\ -\lambda & 1-\lambda^2/2 & A\lambda^2 \\ A\lambda^3(1-\rho-i\eta) & -A\lambda^2 & 1 \end{pmatrix} + (\mathcal{O}\lambda^4). \tag{1.46}$$

Les relations d'orthogonalité de l'équation 1.39 peuvent être exprimées sous forme de triangles dans le plan complexe $\bar{\rho} - \bar{\eta}$. Il existe deux relations dont tous les termes sont de l'ordre $\mathcal{O}\lambda^3$, créant ainsi un triangle avec des angles et des côtés du même ordre de grandeur. Plus particulièrement, l'une d'entre elles est souvent définie comme étant *le* triangle d'unitarité de la matrice CKM, malgré le fait qu'il existe six relations orthogonales. Cette relation est la plus importante pour les mésons B et le sujet de cette thèse et c'est le produit des éléments de la première colonne de la matrice CKM avec le complexe conjugé des éléments de la troisième colonne :

$$\begin{aligned} V_{jd}V_{jb}^* &= V_{ud}V_{ub}^* + V_{cd}V_{cb}^* + V_{td}V_{tb}^* = 0, && (1.47) \\ &= \frac{V_{ud}V_{ub}^*}{V_{cd}V_{cb}^*} + 1 + \frac{V_{td}V_{tb}^*}{V_{cd}V_{cb}^*} = 0, && (1.48) \\ &= -(\bar{\rho} + i\bar{\eta}) + (1) - (1 - \bar{\rho} - i\bar{\eta}) = 0, && (1.49) \\ &= (\bar{\rho} + i\bar{\eta}) + (1 - \bar{\rho} - i\bar{\eta}) - (1) = 0, && (1.50) \end{aligned}$$

où $j = u, c, t$ les trois générations des quarks U. L'équation normalisée 1.48 est obtenue en divisant l'équation 1.47 par $V_{cd}V_{cb}^*$ qui est son terme le mieux connu. Avec ce choix de normalisation, le premier terme devient $-(\bar{\rho} + i\bar{\eta})$ par la définition 1.45. Nous exprimons finalement la relation 1.50 par un triangle dans le plan complexe $\bar{\rho} - \bar{\eta}$ illustré sur la Figure 1.1.

Nous pouvons surcontraindre le triangle en mesurant de plusieurs façons ses lon-

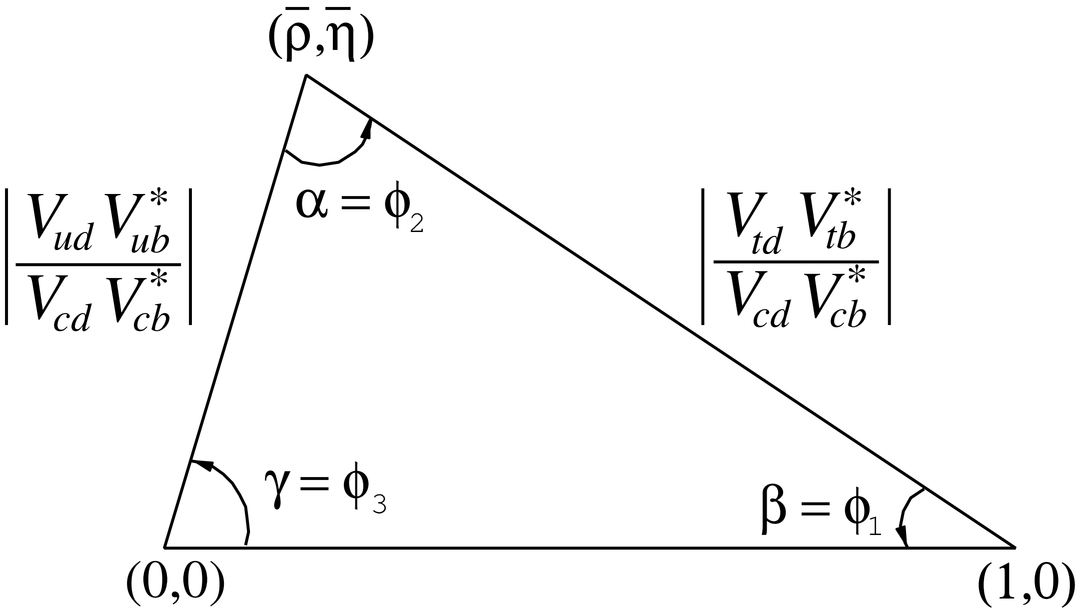

Figure 1.1 – Le triangle d'unitarité normalisé dans le plan complexe $\bar{\rho} - \bar{\eta}$.

gueurs (R_u, R_t, R_c) et ses angles (β, α, γ) qui sont donnés par les relations :

$$R_u = \left|\frac{V_{ud}V_{ub}^*}{V_{cd}V_{cb}^*}\right| = \sqrt{\bar{\rho}^2 + \bar{\eta}^2}, \tag{1.51}$$

$$R_t = \left|\frac{V_{td}V_{tb}^*}{V_{cd}V_{cb}^*}\right| = \sqrt{(1-\bar{\rho})^2 + \bar{\eta}^2}, \tag{1.52}$$

$$R_c = 1, \tag{1.53}$$

$$\beta = \phi_1 = arg\left(-\frac{V_{cd}V_{cb}^*}{V_{td}V_{tb}^*}\right), \tag{1.54}$$

$$\alpha = \phi_2 = arg\left(-\frac{V_{td}V_{tb}^*}{V_{ud}V_{ub}^*}\right), \tag{1.55}$$

$$\gamma = \phi_3 = arg\left(-\frac{V_{ud}V_{ub}^*}{V_{cd}V_{cb}^*}\right). \tag{1.56}$$

Il est primordial de mesurer ces paramètres avec la plus grande précision possible, car une déviation d'un seul de ces paramètres permettrait de mettre en évidence de la physique nouvelle qui n'est pas décrite par la théorie du *Modèle Standard*. Par exemple, la mesure de la norme de V_{ub} est utile pour mesurer le coté du triangle R_u dont l'incertitude est dominée par celle de $|V_{ub}|$. Il existe plusieurs méthodes pour extraire la valeur de $|V_{ub}|$ dont inclusives et exclusives. Les résultats de cette thèse offrent les plus grandes précisions des mesures exclusives de $|V_{ub}|$. Bien qu'une différence existe entre cette valeur et celle obtenue inclusivement, il n'en demeure pas moins que le *Modèle Standard* tient encore la route. En complétant un lissage sur toutes les valeurs expérimentales nous pouvons calculer les quatre paramètres de Wolfenstein et nous obtenons :

$$\lambda = 0.2253 \pm 0.0007, \tag{1.57}$$
$$A = 0.808^{+0.022}_{-0.015}, \tag{1.58}$$
$$\bar{\rho} = 0.132^{+0.022}_{-0.014}, \tag{1.59}$$
$$\bar{\eta} = 0.341 \pm 0.013. \tag{1.60}$$

Les normes des éléments de la matrice CKM obtenues après ce lissage des mesures expérimentales sont :

$$V_{CKM} = \begin{pmatrix} V_{ud} & V_{us} & V_{ub} \\ V_{cd} & V_{cs} & V_{cb} \\ V_{td} & V_{ts} & V_{tb} \end{pmatrix} \tag{1.61}$$
$$\approx \begin{pmatrix} 0.97428 \pm 0.00015 & 0.2253 \pm 0.0007 & 0.00347^{+0.00016}_{-0.00012} \\ 0.2252 \pm 0.0007 & 0.97345^{+0.00015}_{-0.00016} & 0.0410^{+0.0011}_{-0.0007} \\ 0.00862^{+0.00026}_{-0.00020} & 0.0403^{+0.0011}_{-0.0007} & 0.999152^{+0.000030}_{-0.000045} \end{pmatrix} \tag{1.62}$$

Une différence entre les mesures expérimentales de $|V_{ij}|$ et celles obtenues par des lissages globaux du triangle d'unitarité implique de la physique nouvelle ou une incompréhension des approximations de la force forte qui est nécessaire à l'extraction de $|V_{ij}|$. Finalement, les contraintes expérimentales des cotés et des angles du triangle d'unitarité sont représentées sur la Figure 1.2 qui montre l'emplacement possible du sommet du triangle d'unitarité [7].

Les mesures expérimentales principales pour extraire les paramètres du triangle d'unitatrité sont décrites dans le Tableau 1.2. Les valeurs de ces paramètres sont en accord

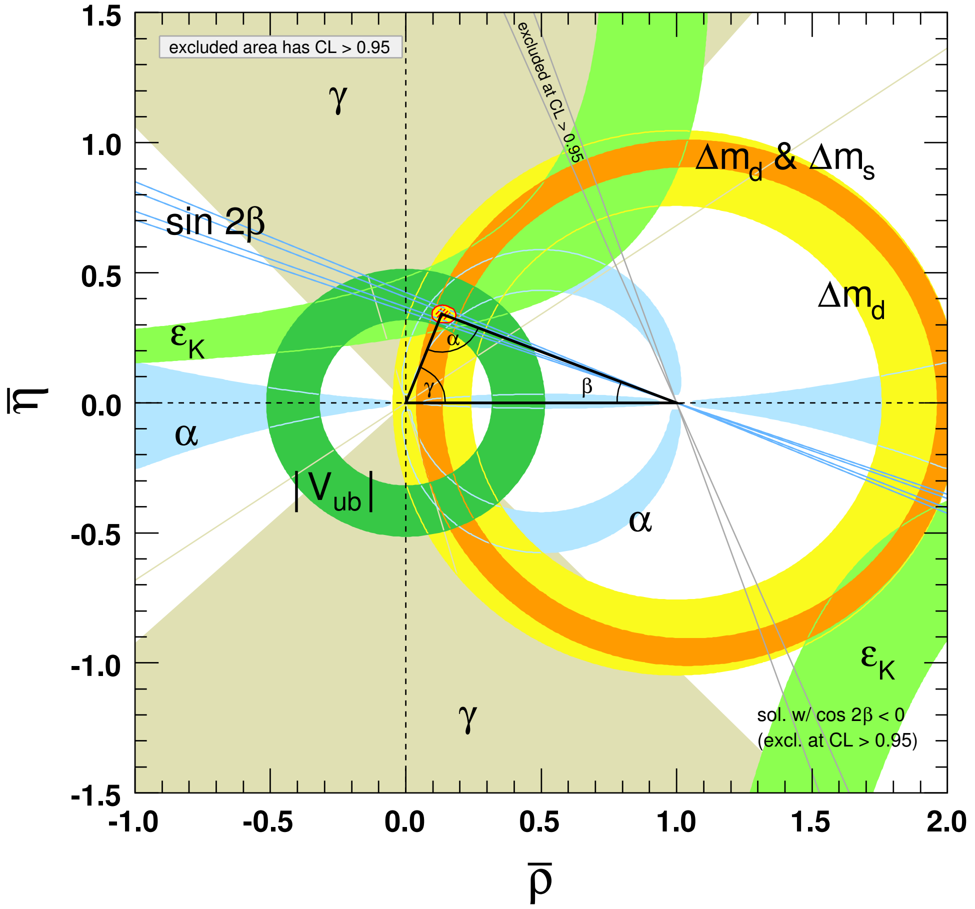

Figure 1.2 – Contraintes expérimentales sur les côtés et les angles du triangle d'unitarité.

Tableau 1.2 – Mesures expérimentales principales pour extraire les paramètres du triangle d'unitarité et leurs valeurs moyennes. [8]

Paramètres	Mesures expérimentales principales	Valeurs moyennes
$\lvert V_{ud}\rvert$	Désintégrations nucléaires β	0.97425 ± 0.00022
$\lvert V_{us}\rvert$	Désintégrations semileptoniques des mésons K	0.2252 ± 0.0009
$\lvert V_{cd}\rvert$	Désintégrations semileptoniques des mésons D et des interactions de neutrinos	0.230 ± 0.011
$\lvert V_{cs}\rvert$	Désintégrations leptoniques et semileptoniques des mésons D_s	1.023 ± 0.036
$\lvert V_{cb}\rvert$	Désintégrations semileptoniques inclusives et exclusives des mésons B en quark charmé	$(40.6 \pm 1.3) \times 10^{-3}$
$\lvert V_{ub}\rvert$	Désintégrations semileptoniques inclusives et exclusives des mésons B	$(3.89 \pm 0.44) \times 10^{-3}$
$\lvert V_{td}\rvert$	Différence de masse des mésons neutres $B^0 - \overline{B}^0$	$(8.4 \pm 0.6) \times 10^{-3}$
$\lvert V_{ts}\rvert$	Différence de masse des mésons neutres $B^0_s - \overline{B}^0_s$	$(38.7 \pm 2.1) \times 10^{-3}$
$\lvert V_{tb}\rvert$	Production singulière du qaurk t	0.88 ± 0.07
α	Désintégrations des mésons B ($B \to \pi\pi, \rho\pi, \rho\rho$)	$(89.0^{+4.4}_{-4.2})^\circ$
β	Désintégrations des mésons neutres B^0 en état charmonium $B^0 \to charmonium\ K^0_{S,L}$	$\sin 2\beta = 0.673 \pm 0.023$
γ	Désintégrations des mésons B chargés ($B \to D^0 K$)	$(73^{+22}_{-25})^\circ$

avec celles présentées dans l'équation 1.61, obtenues après un lissage global des résultats. Comme nous allons le voir, les désintégrations semileptoniques des mésons B sont les événements optimaux pour extraire une valeur précise de $|V_{ub}|$.

1.3 Détermination de $|V_{ub}|$ avec la désintégration semileptonique des mésons B

Les mésons B sont composés d'un quark de première génération et du quark b de troisième génération. Ainsi, nous reconstruisons les quatre mésons B^+ ($u\bar{b}$), B^- ($\bar{u}b$), B^0 ($d\bar{b}$) et $\overline{B}^0$ ($\bar{d}b$). Les désintégrations semileptoniques des mésons B qui se font par interaction faible consistent en un changement de saveur du quark b vers un quark u ou c par l'intermédiaire du boson de jauge W. Le boson W se désintègre par la suite en une paire $\ell - \nu_\ell$, où $\ell = e$ ou μ. L'autre quark est appelé quark *spectateur* puisqu'il

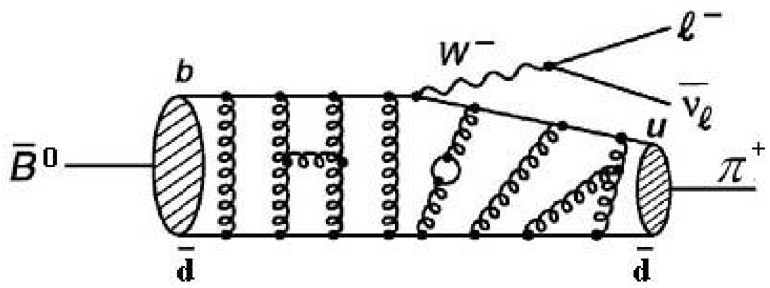

Figure 1.3 – Diagramme de Feynman de la désintégration $\overline{B}^0 \to \pi^+\ell^-\overline{\nu}$.

n'est pas modifié dans le processus de désintégration. La désintégration $\overline{B}^0 \to \pi^+\ell^-\overline{\nu}$ est représentée par le diagramme de Feynman de la Figure 1.3. Comme nous venons de voir, nous savons que les leptons n'interagissent pas avec les gluons, ce qui simplifie grandement les calculs théoriques de l'interaction forte pour ces désintégrations. Nous allons voir que le rapport d'embranchement de ces interactions est proportionnel à $|V_{ub}|^2$.

Afin d'extraire la valeur de $|V_{ub}|$ de ces désintégrations semileptoniques, nous devons établir le lien théorique entre cette valeur et ce que nous mesurons expérimentalement. Comme le montre le Tableau 1.2, nous pouvons extraire $|V_{ub}|$ inclusivement ou exclusivement. La méthode inclusive consiste à étudier la somme de tous les canaux possibles impliquant un quark u à l'état final, tandis que celle exclusive n'en étudie qu'un seul. Cette thèse présente la mesure exclusive de $|V_{ub}|$ via le canal $B^0 \to \pi^-\ell^+\nu$. Bien que les mesures inclusives permettent une plus grande précision sur $|V_{ub}|$, les mesures exclusives sont très importantes pour une meilleure compréhension des calculs théoriques de la force forte. Dans ce qui va suivre, nous expliquerons comment extraire $|V_{ub}|$ à l'aide d'une approche exclusive du canal $B^0 \to \pi^-\ell^+\nu$.

Nous définissons le rapport d'embranchement $\mathcal{B}$ comme étant le taux de désintégration Γ pour un canal en particulier divisé par le taux de désintégartion global de tous les canaux possibles. Ainsi, pour la désintégration $B^0 \to \pi^- \ell^+ \nu$ nous avons la relation :

$$\mathcal{B}(B^0 \to \pi^- \ell^+ \nu) = \frac{\Gamma(B^0 \to \pi^- \ell^+ \nu)}{\Gamma(B^0 \to X)} \tag{1.63}$$

$$= \Gamma(B^0 \to \pi^- \ell^+ \nu) \cdot \tau_{B^0}, \tag{1.64}$$

où τ_{B^0} est le temps de vie du méson B^0. Le taux de désintégration différentiel est défini ainsi :

$$d\Gamma(B^0 \to \pi^- \ell^+ \nu) = \frac{1}{2m_{B^0}} \left(\prod_f \frac{1}{2(2\pi)^3} \frac{d^3 p_f}{E_f} \right) |\mathcal{M}|^2 (2\pi)^4 \delta^{(4)} \left(P_{B^0} - \sum P_f \right), \tag{1.65}$$

où $f = \pi^-, \ell^+, \nu$ sont les particules à l'état final, m_{B^0} est la masse du méson B^0, E_i, p_i et P_i sont, respectivement, l'énergie, l'impulsion et le quadrivecteur de la particule i, $\delta^{(4)}$ est la fonction delta de Dirac et $\mathcal{M}$ est l'amplitude de probabilité de la désintégration $B^0 \to \pi^- \ell^+ \nu$. Il est important de constater que le taux de désintégration est proportionnel au carré de l'amplitude de probabilité $\mathcal{M}$ qui est definie [1, 9] de la façon suivante :

$$\mathcal{M}(B^0 \to \pi^- \ell^+ \nu) = -i \frac{G_F}{\sqrt{2}} V_{ub} L^\mu H_\mu, \tag{1.66}$$

où G_F est la constante de Fermi, L^μ et H_μ sont les courants leptonique et hadronique, respectivement :

$$L^\mu = \overline{u}_\ell \gamma^\mu (1 - \gamma^5) \nu_\nu, \tag{1.67}$$

$$H_\mu = \langle \pi^- | \bar{u} \gamma_\mu (1 - \gamma_5) \bar{b} | B^0 \rangle. \tag{1.68}$$

Il est possible de séparer ces deux courants l'un de l'autre, car les leptons n'interagissent pas avec la force forte. Le courant leptonique peut être calculé de façon précise par la méthode des perturbations, ce qui n'est pas le cas pour le courant hadronique où, comme nous l'avons mentionné, l'interaction des gluons crée une infinité de diagrammes de Feynman rendant ainsi les calculs infinis et non-perturbatifs. La théorie des perturbations ne peut donc pas être appliquée sur la force forte, car la constante de couplage g_s est trop grande. Il est commode d'exprimer l'équation 1.68 en terme de facteurs de forme hadroniques. Pour les mésons *pseudoscalaires* à l'état final (π, η ou η'), le terme $\gamma_\mu\gamma_5$ est nul ce qui ne sera pas le cas avec l'étude des mésons *vecteurs* (ρ ou ω). Ainsi, l'équation 1.68 devient :

$$H_\mu = \langle \pi^- | \bar{u}\gamma_\mu \bar{b} | B^0 \rangle. \tag{1.69}$$

$$= f_+(q^2)((P_{B^0} + P_{\pi^-})_\mu - AQ_\mu) + f_0(q^2)AQ_\mu, \tag{1.70}$$

où $A = (m_{B^0} - m_{\pi^-})/q^2$, $Q_\mu = P_{B^0} - P_{\pi^-}$, $f_+(q^2)$ et $f_0(q^2)$ sont les facteurs de forme qui dépendent de q^2 (le carré de la masse invariante du boson virtuel W donnant ainsi le carré de l'impulsion transférée à la paire $\ell - \nu$) :

$$q^2 = m_W^2 = (P_\ell + P_\nu)^2 = (P_B - P_\pi)^2. \tag{1.71}$$

Étant donné que la masse des leptons e et μ est faible comparativement à la masse du boson virtuel W, il est tout-à-fait correct de négliger les deux derniers termes de H_μ puisque $L^\mu Q_\mu \to 0$ et nous avons :

$$H_\mu = f_+(q^2)(P_{B^0} + P_{\pi^-})_\mu. \tag{1.72}$$

En combinant les équations 1.65 à 1.72, nous pouvons obtenir le taux de désintégration différentiel partiel en fonction de q^2 :

$$\frac{d\Gamma(B^0 \to \pi^-\ell^+\nu)}{dq^2} = \frac{G_F^2 |V_{ub}|^2}{24\pi^3} |\vec{p}_\pi|^3 |f_+(q^2)|^2, \tag{1.73}$$

où $|\vec{p}_\pi|$ peut être défini en fonction de q^2 :

$$|\vec{p}_\pi| = \sqrt{E_\pi^2 - m_\pi^2} \tag{1.74}$$

$$= \sqrt{\frac{(m_{B^0}^2 + m_\pi^2 - q^2)^2}{4m_{B^0}^2} - m_\pi^2}. \tag{1.75}$$

Ainsi, en intégrant en fonction de q^2 et en utilisant l'équation 1.64, nous retrouvons le rapport d'embranchement total :

$$\mathcal{B}(B^0 \to \pi^- \ell^+ \nu) = \tau_{B^0} \frac{G_F^2 |V_{ub}|^2}{24\pi^3} \int_{q^2_{min}}^{q^2_{max}} |\vec{p}_\pi|^3 |f_+(q^2)|^2 dq^2, \tag{1.76}$$

où $q^2_{min} = m_\ell^2 \approx 0 \;\; \text{GeV}^2$ et $q^2_{max} = (m_{B^0} - m_\pi)^2 \approx 26.4 \;\; \text{GeV}^2$. En posant :

$$\zeta = \frac{G_F^2}{24\pi^3} \int_{q^2_{min}}^{q^2_{max}} |\vec{p}_\pi|^3 |f_+(q^2)|^2 dq^2, \tag{1.77}$$

nous pouvons exprimer $|V_{ub}|$ en fonction des paramètres mesurables expérimentalement et du facteur théorique ζ :

$$|V_{ub}| = \sqrt{\frac{\mathcal{B}(B^0 \to \pi^- \ell^+ \nu)}{\tau_{B^0} \zeta}}. \tag{1.78}$$

Le terme ζ est la taux de désintégration normalisé qui est prédit par des calculs théoriques sur le facteur de forme $f_+(q^2)$. Normalement, les calculs théoriques font des approximations qui limitent la région de validité de ces calculs dans le spectre de q^2. C'est pour cette raison qu'il est parfois préférable d'intégrer les équations 1.76 et 1.77 pour une région limitée (q_i^2, q_j^2) du spectre de q^2 au lieu de (q^2_{min}, q^2_{max}) et nous avons :

$$|V_{ub}| = \sqrt{\frac{\Delta\mathcal{B}(q^2)}{\tau_{B^0} \Delta\zeta(q^2)}}. \tag{1.79}$$

Expérimentalement, nous mesurons $\mathcal{B}(B^0 \to \pi^- \ell^+ \nu)$ en mesurant le nombre de désintégrations $B^0 \to \pi^- \ell^+ \nu$ (N) sur une fraction (*efficacité* ϵ) du nombre total d'événements contenant un méson B^0 (n_{B^0}), de sorte que :

$$\mathcal{B}(B^0 \to \pi^- \ell^+ \nu) = \frac{N}{2\epsilon n_{B^0}}, \tag{1.80}$$

où le facteur 2 vient du fait que nous mesurons le lepton ℓ comme étant un e ou un

μ, mais que le rapport d'embranchement n'est donné que pour $\ell = e$ ou $\ell = \mu$. Nous verrons plus loin qu'un facteur 2 supplémentaire doit être inclus au dénominateur de l'équation 1.80, puisque les mésons B sont produits en paire dans l'expérience BABAR par la relation $e^+e^- \to \Upsilon(4S) \to B\overline{B}$. Toutefois, la rapport d'embranchement $\mathcal{B}(\Upsilon(4S) \to B^0\overline{B}^0) \approx 0.5$ annule ce facteur 2. Il est également possible de déterminer la forme du spectre de q^2 en mesurant $\Delta\mathcal{B}$ sur plusieurs intervalles de q^2. De cette manière, nous pouvons discriminer les spectres de q^2 obtenus théoriquement.

1.4 Calculs théoriques servant à l'extraction de $|V_{ub}|$

Il existe plusieurs prédictions théoriques du facteur de forme $f_+(q^2)$. Ces prédictions changent la forme et la normalisation du spectre de q^2 et les principales prédictions en sont illustrées sur la Figure 1.4. Dans cette thèse, nous utilisons deux techniques de calculs théoriques pour extraire la valeur de $|V_{ub}|$: les *Règles de Somme sur le Cône de Lumière* (LCSR) [10] et la *CDQ sur réseau* (LQCD) [11, 12]. Nous allons voir que ces deux approches sont complémentaires l'une à l'autre. En effet, la région de validité de ces calculs est à basse valeur de q^2 ($\lesssim$ 16 GeV) pour LCSR et à haute valeur de q^2 ($\gtrsim$ 16 GeV) pour LQCD. Ces deux méthodes rigoureuses permetent d'extraire de façon précise la valeur de $|V_{ub}|$.

1.4.1 Règles de Somme sur le Cône de Lumière (LCSR)

Cette technique s'applique pour des désintégrations de particules lourdes vers des particules légères ultra-relativistes, comme c'est la cas pour la désintégration $B^0 \to \pi^-\ell^+\nu$ pour les basses valeurs de q^2 ($\lesssim$ 16 GeV^2). En effet, plus la valeur de q^2 est basse, plus l'énergie du méson B est transférée au méson π.

Cette méthode utilise le même principe que la théorie des perturbations, mais elle est modifiée par des termes non-perturbatifs. Pour calculer $f_+(q^2)$, elle factorise une fonction de corrélation reliant le courant faible au courant hadronique en une série d'opéra-

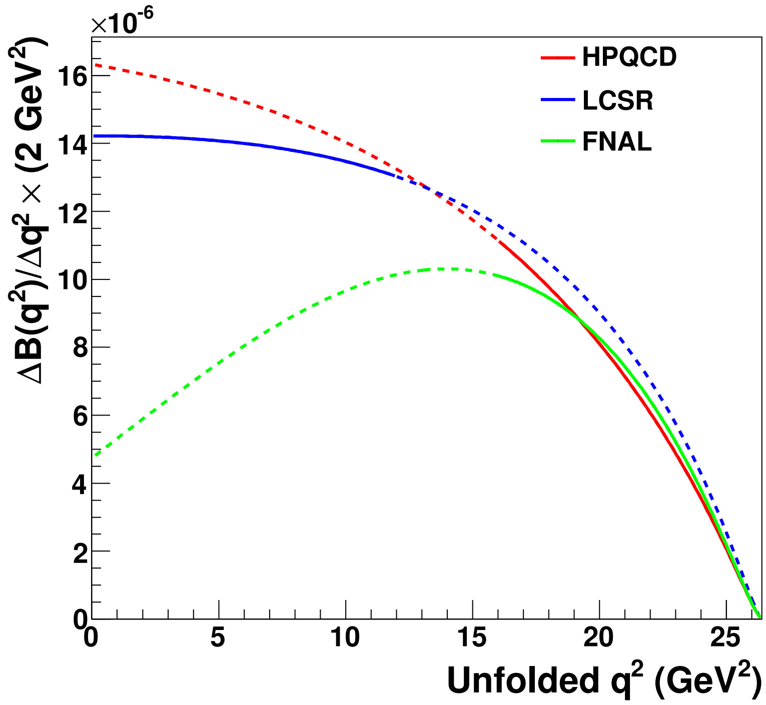

Figure 1.4 – Spectres de q^2 des trois principales prédictions théoriques. Les courbes sont normalisées en utilisant nos résultats expérimentaux dans leurs régions de validité (courbes continues).

teurs en puissance de γ_s et du *twist* $n = d - s$, où γ_s est la constante de couplage de l'interaction forte, d est la dimension de l'opérateur et s est le spin. Cette fonction est évaluée sur le cône de lumière à $q^2 = 0\ \text{GeV}^2$ et extrapolée jusqu'à $q^2 \approx 16\ \text{GeV}^2$ où les calculs LCSR perdent leur pertinence.

Les nouveaux calculs LCSR [10] se restreignent uniquement à la région $q^2 < 12\,\text{GeV}^2$ et obtiennent une incertitude théorique de $^{+14.6}_{-10.5}\%$ sur $|V_{ub}|$. Toutefois, il existe une incertitude irréductible de l'ordre de 10% qui empêche une amélioration de sa précision dans les années à venir. À long terme, la CDQ sur réseau est beaucoup plus prometteuse en terme de précision.

1.4.2 CDQ sur réseau (LQCD)

La CDQ sur réseau utilise une technique très simple. Il s'agit d'évaluer numériquement les intégrales de Feynman provenant du Lagrangien de la CDQ. Malgré son concept simple, plusieurs contraintes informatiques viennent compliquer les calculs. Inventée en 1974 par Kenneth G. Wilson, la CDQ sur réseau consiste à discrétiser l'espace-temps en un *réseau* (ou "latice") à quatre dimensions limitées. Cette limite se caractérise par une longueur L pour chaque dimension et se concrétise par un nombre fini de points espacés d'une distance a entre chaque point. Les paramètres observables sont calculés numériquement sur chaque point par de puissants ordinateurs utilisant des simulations Monte Carlo et sont extrapolés ensuite analytiquement sur l'ensemble du réseau par des relations nommées *actions de discrétisation*. Dans la limite où l'espace $a \to 0$ et que L est suffisamment grand, nous avons les résultats des intégrales de Feynman pour obtenir la fonction $f_+(q^2)$ parfaitement.

L'avantage de la technique de CDQ sur réseau est que théoriquement elle permet de calculer de façon exacte les effets de la CDQ. Cependant, le temps de calcul proportionnel à $(L/a)^n$, où $n > 5$ dépend du degré de discrétisation, est beaucoup trop long pour permettre des valeurs de a très petites ou de L très grandes. Cet effet oblige les théoriciens à augmenter les espacements a et à introduire des approximations sur les calculs de la CDQ. Plusieurs améliorations ont été faites ces dernières années et se feront dans les années à venir. Nous n'avons qu'à penser au bond phénoménal qu'a connu cette approche dans les années 2000 en utilisant des actions de discrétisation de 50 à 1000 fois plus rapides. Cette amélioration a permis de calculer les boucles des quarks u, d et s des quarks de la mer qui étaient négligées dans les calculs précédents. À partir de ce moment, les améliorations n'ont jamais cessé et les calculs de la CDQ sur réseau devinrent des calculs de haute précision.

Au cours des dernières années, deux groupes indépendants FNAL [11] et HPQCD [12] ont effectué des calculs de la CDQ sur réseau. Le groupe FNAL utilise des actions de discrétisation relativistes qui sont corrigées en simplifiant la CDQ par le fait que la masse du quark b est beaucoup plus grande que Λ_{CDQ}, où Λ_{CDQ} est l'énergie à partir de laquelle la CDQ devient non-perturbative. Ce sont donc des calculs perturbatifs en puissance de Λ_{CDQ}/m_b. De son côté, le groupe HPQCD utilise le Lagrangien de la CDQ non-relativiste.

Plusieurs façons permettront d'améliorer la précision des calculs de la CDQ sur réseau. Nous pouvons utiliser des ordinateurs plus puissants et plus rapides ce qui est potentiellement envisageable, puisque la vitesse des ordinateurs ne cesse d'augmenter année après année. Beaucoup de travaux se font également pour concevoir des actions de discrétisations plus rapides et plus précises. Ainsi, en utilisant ces nouveaux algorithmes et des ordinateurs ultra-rapides, il sera possible de diminuer davantage l'espacement a entre les points, diminuant du même coup l'incertitude reliée à l'impulsion maximale. En effet, cette espace limite l'impulsion maximale dans le réseau à $p_{max} = \pi/a$ ce qui entraîne des incertitudes de l'ordre de $(pa)^n$. Ces incertitudes restreignent la validité des calculs uniquement aux hautes valeurs de $q^2 \gtrsim 16\ \mathrm{GeV}^2$. D'autre part, pour diminuer le temps de calcul, la masse des quarks u et d est augmentée à $m_s/2$ et $m_s/8$, respectivement, où m_s est la masse du quark s. Cette manoeuvre est faite pour éviter le temps de calcul élevé qui est proportionnel à $1/m^2$. Une expansion perturbative est utilisée ensuite pour passer aux masses réelles des quarks u et d, ce qui génère des incertitudes supplémentaires aux calculs de la CDQ sur réseau. De cette manière, en utilisant directement les masses réelles des quarks u et d, nous augmentons la précision des calculs.

L'incertitude théorique sur $|V_{ub}|$ provenant des derniers calculs théoriques FNAL et HPQCD est de $^{+11.1}_{-9.2}\%$ et $^{+17.6}_{-11.4}\%$, respectivement. Ces incertitudes sont comparables à celles obtenues par la technique du LCSR, mais peuvent par contre être réduites davantage bien en-dessous de l'incertitude irréductible de 10% du LCSR. Cependant, la mesure de $|V_{ub}|$ obtenue par la technique du LCSR restera un résultat complémentaire important, étant donné que sa région de validité sur le spectre de q^2 est totalement différente de celle de la CDQ sur réseau. Il ne faut pas oublier qu'en diminuant l'espace a nous augmentons la région de validité des calculs de la CDQ sur réseau sur le spectre de q^2.

1.5 Paramétrisation de la forme du spectre de q^2

Nous avons vu dans les sections précédentes comment extraire la valeur de $|V_{ub}|$ expérimentalement par la désintégration semileptonique $B^0 \to \pi^-\ell^+\nu$ en utilisant le facteur de forme $f_+(q^2)$ décrit par des calculs théoriques de la CDQ. Une moyenne doit donc être faite sur toutes les valeurs de $|V_{ub}|$ obtenues par les différents calculs théoriques existants. Cette moyenne ajoute une incertitude théorique supplémentaire à la valeur de $|V_{ub}|$. Toutefois, comme le montre la Figure 1.4, chaque calcul théorique mène à une forme du spectre de q^2 différente. Cette forme est mesurable expérimentalement en mesurant les rapports d'embranchement partiels en fonction de q^2. En mesurant la forme de façon précise, il est possible en principe de discriminer entre les calculs théoriques pour trouver celui qui représente le mieux les données expérimentales. C'est notamment de cette manière qu'il fut possible d'éliminer le vieux modèle de quarks ISGW2 [13], puisque la forme théorique du spectre de q^2 ne concordait pas du tout avec la forme expérimentale.

Nous paramétrisons le spectre de q^2 par une fonction analytique, dont les paramètres sont déterminés par un lissage des rapports d'embranchement partiels expérimentaux en fonction de q^2. Dans cette thèse nous mesurons les rapports d'embranchement partiels sur 12 intervalles de q^2. Il existe plusieurs fonctions pouvant décrire la forme du spectre de q^2 et nous allons décrire trois de ces fonctions possibles que nous utilisons dans cette thèse : la fonction BK (Becirevic-Kaidalov) [14], Hill (Richard Hill) [15], et la fonction BGL (Boyd, Grinstein, Lebed) [16].

Pour la fonction Hill, le facteur de forme est donné par :

$$f_+(q^2) = \frac{(1-\alpha)\cdot(1-\delta q^2/m^2)}{(1-q^2/m^2_{B^*})\cdot(1-(\alpha+\delta(1-\alpha))q^2/m^2_{B^*})}, \tag{1.81}$$

où $m_{B^*} = 5.325$ GeV et les paramètres α et δ sont obtenus par un lissage des rapports d'embranchement partiels. Dans le cas où $\delta = 0$ nous définissons la fonction BK. Cette paramétrisation à l'avantage d'être simple et est définie à partir de l'existence du pôle B^* qui a une masse légèrement suérieure à celle du méson B limitant ainsi l'espace des phases pour les grandes valeurs de q^2. Les théoriciens ont laissé tomber cette paramétrisation depuis un certains temps jugeant qu'elle ne paramétrise pas très bien la forme du spectre de q^2.

La fonction BGL est une expansion de la fonction z qui décrit de façon plus précise la forme des spectres de q^2 tant au niveau théorique qu'expérimental. Le facteur de forme est défini comme suit :

$$f_+(t) = \frac{1}{P(t)\phi(t,t_0)} \sum_{k=0}^{\infty} a_k(t_0) z(t,t_0)^k, \tag{1.82}$$

où a_k sont les paramètres libres qui définissent la forme du spectre de q^2 et :

$$z(t,t_0) = \frac{\sqrt{t_+ - t} - \sqrt{t_+ - t_0}}{\sqrt{t_+ - t} + \sqrt{t_+ - t_0}}, \tag{1.83}$$

avec $t = q^2, t_+ = (m_B + m_{X_u})^2, t_- = (m_B - m_{X_u})^2$ et le paramètre libre t_0 que nous choisissons comme étant $t_0 = 0.65t_-$ pour diminuer l'incertitude théorique. Le facteur $Blaschke$ $P(t)$ tient en compte le pôle B^* et est donné par :

$$P(t) = z(q^2, m_{B^*}^2). \tag{1.84}$$

Le choix généralement utilisé dans la littérature [16] pour la fonction $\phi(t, t_0)$ est :

$$\phi(t,t_0) = \sqrt{\frac{3}{96\pi\chi_J^{(0)}}}\frac{(t_+ - t)(\sqrt{t_+ - t} + \sqrt{t_+ - t_0})(\sqrt{t_+ - t} + \sqrt{t_+ - t_-})^{3/2}}{(t_+ - t_0)^{1/4}(\sqrt{t_+ - t} + \sqrt{t_+})^5}, \tag{1.85}$$

où le facteur de normalisation $\chi_J^{(0)} = 0.000688919$. Les théoriciens de la CDQ paramétrisent de plus en plus leurs formes théoriques par la fonction BGL. En paramétrisant nos données expérimentales par la même formule, il est possible de faire une comparaison directe avec les paramètres théoriques. Bien que la somme de l'équation 1.82 soit infinie, on se contente généralement entre $k = 2$ et $k = 5$, étant donné que les termes d'ordre supérieur deviennent de plus en plus négligeables.

Dans le prochain chapitre, nous discuterons du dispositif expérimental utilisé à l'expérience BABAR et tout ce qui implique la production des mésons B pour mesurer les désintégrations semileptoniques $B^0 \to \pi^- \ell^+ \nu$, $B^+ \to \eta \ell^+ \nu$ et $B^+ \to \eta' \ell^+ \nu$.

BIBLIOGRAPHIE

[1] M. E. Peskin, D. V. Schroeder, *An Introduction to Quantum Field Theory*, Perseus Book (1995).

[2] G. Kane, *Modern Elementary Particle Physics*, Édition Addison-Whisley (1993).

[3] I. Sample, *Father of God Particle : Portrait of Peter Higgs Unveiled*, London : The Guardian (2009).

[4] M. Kobayashi and T. Maskawa, Prog. Theor. Phys. **49**, 652 (1973).

[5] M. Kobayashi, T. Maskawa, *CP-Violation in the Renormalizable Theory of Weak Interaction*, Prog. Theor. Phys., **49**, 652 (1973).

[6] L. Wolfenstein, *Parametrization of the Kobayashi-Maskawa Matrix*, Phys. Rev. Lett. **51**, 1945 (1983).

[7] CKMfitter Group (J. Charles *et al.*), Eur. Phys. J. **C41**, 1-131 (2005) [hep-ph/0406184], updated results and plots available at : http ://ckmfitter.in2p3.fr.

[8] K. Nakamura *et al.* (Particle Data Group), J. Phys. G **37**, 075021 (2010)

[9] P. R. Burchat, J. D. Richman, *Leptonic and semileptonic decays of charm and bottom hadrons*, Rev. Mod. Phys. **67**, 893 (1995).

[10] G. Duplancic *et al.*, JHEP **804**, 14 (2008) ;

[11] C. Bernard *et al.* (FNAL/MILC Collaboration), Phys. Rev. **D80**, 034026 (2009) ;

[12] E. Gulez *et al.* (HPQCD Collaboration), Phys. Rev. **D73**, 074502 (2006) ; Erratum ibid. **D75**, 119906 (2007).

[13] D. Scora and N. Isgur, Phys. Rev. **D52**, 2783 (1995).

[14] D. Becirevic and A. B. Kaidalov, Phys. Lett. **B478**, 417 (2000).

[15] R. Hill, *Heavy-to-light meson form-factors at large recoil*, Phys. Rev. **D73**, 014012 (2006) [hep-ph/0505129].

[16] C. G. Boyd and M. J. Savage, Phys. Rev. **D56**, 303 (1997).

CHAPITRE 2

LES ACCÉLÉRATEURS ET LE DÉTECTEUR BABAR

2.1 Introduction

L'idée de construire le détecteur BABAR [17–19] remonte en 1987. L'existence du méson B fut établie une dizaine d'années plus tôt en 1977. Toutefois, ce n'est qu'en 1987 qu'il fut découvert que la fréquence d'oscillations $B^0 - \bar{B}^0$ était relativement grande. Par conséquent, cette découverte combinée avec le temps de vie suffisament long du méson B démontrait pour la première fois que la violation CP dans le secteur des mésons B pouvait être mesurée expérimentalement. Il fut alors déterminé que la meilleure façon d'étudier et de comprendre cette violation CP serait de construire un collisionneur $e^+ - e^-$ d'énergie asymétrique pour produire les paires de mésons $B\overline{B}$. Ce n'est que sept ans plus tard en 1994, que la communauté scientifique a approuvé la construction d'un tel collisionneur. Cette expérience était tellement importante que ce type de collisionneur, aussi nommé *usine à mésons* B, fut construit simultanément en Californie (SLAC *National Accelerator Laboratory*) et au Japon (KEK *Kō Enerugī Kasokuki Kenkyū Kikō*). Naturellement, deux détecteurs furent également construits pour détecter les particules issues des désintégrations des mésons B instables. Les détecteurs BABAR au SLAC et Belle au KEK ont été principalement conçus pour étudier et comprendre la violation CP dans les désintégrations des mésons B et de mesurer avec précision différents paramètres du *Modèle Standard*.

Les résultats de ces expériences concordent extrêmement bien avec la théorie du *Modèle Standard*. Si bien qu'en novembre 2008, Makoto Kobayashi et Toshihide Maskawa furent récompensés en recevant le prestigieux *Prix Nobel de Physique*, 36 ans après avoir postulé leur théorie du *Modèle Standard* en 1972. Ces deux grands physiciens ont généreusement pris le temps de remercier les expérimentateurs de BABAR et Belle en ces mots : “Please accept our deepest respect and gratitude for the B factory achievements. In particular, the high-precision measurements of CP violation and the determination of the mixing parameters are great accomplishments, without which we would not have been able to earn the Prize." ce qui se traduit par : “S’il vous plaît, accepter nos plus profonds respects et notre gratitude pour les réalisations des usines à mésons B. En particulier, la haute précision des mesures de la violation CP et la détermination des paramètres de mélange sont de grands accomplissements, sans lesquelles nous n’aurions pas été en mesure de gagner le Prix.”. Les membres du groupe de l’*Université de Montréal* dans l’expérience BABAR, qui ont contribué directement à cet événement d’importance fondamentale en mesurant l’élément $|V_{ub}|$ de la matrice CKM, sont : Paul Taras (professeur), Benoit Viaud (attaché de recherches), Sylvie Brunet, David Côté et Martin Simard (étudiants).

2.2 Production de paires de mésons $B\overline{B}$ au *National Accelerator Laboratory*

La production de paires de mésons $B\overline{B}$ au SLAC consiste à faire entrer en collision des électrons e^- contre des positrons e^+ avec une énergie au centre de masse égale à 10.58 GeV, légèrement supérieure à la masse de la résonance $\Upsilon(4S)$ pour assurer sa production. De cette manière, il est alors possible de produire la réaction $e^+e^- \rightarrow \Upsilon(4S) \rightarrow B\overline{B}$. En effet, la particule $\Upsilon(4S)$ composée des quarks $b\bar{b}$ se désintègre presqu’exclusivement en paires de mésons $B\overline{B}$. C’est d’ailleurs pour cette dernière caractéristique et à la forte intensité des faisceaux d’électrons et de positrons que l’on nomme souvent l’expérience BABAR une *usine à mésons* B. Cependant, à cette énergie de collision, d’autres réactions se produisent régulièrement telles que $e^+e^- \rightarrow \ell^+\ell^-$ et $e^+e^- \rightarrow q\bar{q}$, où ℓ représente les leptons e, μ ou τ et q représente les quarks u, d, s ou c. Bien que ces types d’événements constituent du bruit de fond *continuum* à notre analyse, ils peuvent toutefois être utilisés pour étudier notamment les mésons D et les leptons τ. Les sections efficaces de production des différentes réactions avec une énergie au centre de masse égale à 10.58 GeV sont données dans le Tableau 2.1. Pour comparer les sections efficaces hadroniques des collisions e^+e^- à différentes énergies au centre de masse, la Figure 2.1 illustre la décroissance de production hadronique au fur et à mesure

Tableau 2.1 – Sections efficaces de production à une énergie au centre de masse égale à 10.58 GeV. La section efficace donnée pour $e^+e^- \rightarrow e^+e^-$ tient compte de l'acceptance du détecteur BABAR.

$e^+e^- \rightarrow$	section efficace (nb)
$b\bar{b}$	1.10
$c\bar{c}$	1.30
$s\bar{s}$	0.35
$u\bar{u}$	1.39
$d\bar{d}$	0.35
$\tau^+\tau^-$	0.92
$\mu^+\mu^-$	1.16
e^+e^-	~ 40

que l'énergie augmente. Bien entendu, seule la résonance $\Upsilon(4S)$ est assez massive pour permettre la création des mésons $B\overline{B}$.

Pour atteindre l'énergie de la résonance $\Upsilon(4S)$ lors des collisions e^+e^-, les électrons et les positrons doivent être accélérés par l'accélérateur linéaire *Linac* jusqu'aux énergies bien spécifiques de 9 GeV et 3.1 GeV, respectivement. Cette asymétrie des énergies est nécessaire afin de permettre de mesurer la distance parcourue par les mésons B. En effet, dans le référentiel du centre de masse les mésons B ont de très basses impulsions, car pratiquement toute l'énergie de la collision s'est transformée en masse. Combinée avec un temps de vie des mésons $B\overline{B}$ extrêmement faible, la distance parcourue par ceux-ci serait, par conséquent, trop courte pour être mesurable. Or, cette mesure de la distance est cruciale pour l'étude de la violation CP dépendante du temps. Les collisions asymétriques e^+e^- aux énergies mentionnées ci-haut, donnent une poussée relativiste ($\beta\gamma \simeq 0.56$) dans la direction du faisceau d'électrons permettant aux mésons B de parcourir en moyenne 260 μm avant de se désintégrer.

Une fois que les électrons et les positrons ont atteint leurs énergies respectives, le collisionneur circulaire PEP-II accumule les électrons et positrons, les accélère et les regroupe en paquets pour augmenter la luminosité du détecteur BABAR, soit le nombre de

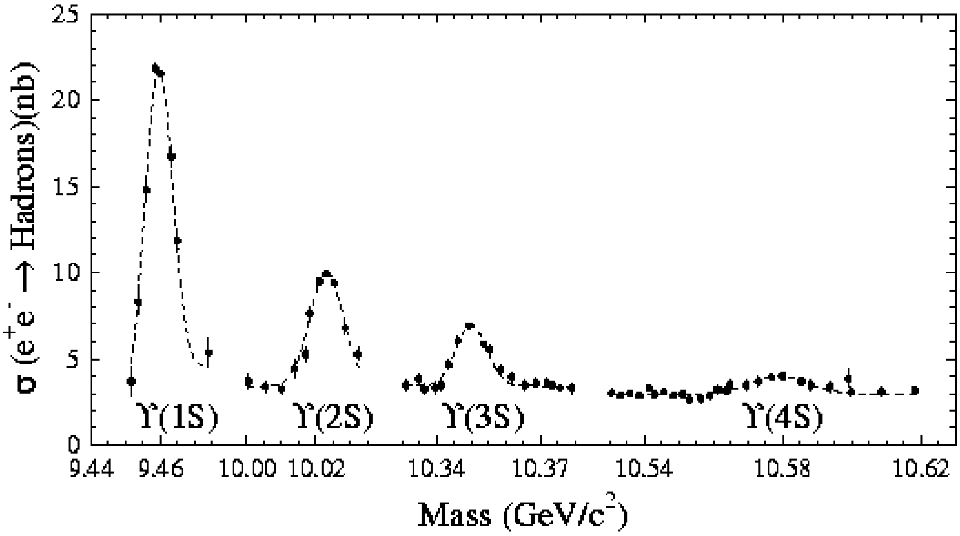

Figure 2.1 – Section efficace de production hadronique en fonction de l'énergie au centre de masse des collisions e^+e^- [20]. On distingue les résonances $\Upsilon(1S)$ à $\Upsilon(4S)$, formées des quark b et $\bar{b}$, au-dessus du continuum. La résonance $\Upsilon(4S)$ est cependant la seule qui soit suffisamment massive pour se désintégrer en une paire de mésons $B\overline{B}$.

collisions par unité de temps et de surface transversale.

Dans ce qui va suivre, nous allons décrire en détail comment les électrons et les positrons sont produits et accélérés par l'accélérateur *Linac* et accumulés et dirigés par le collisionneur circulaire PEP-II jusqu'à la collision à l'intérieur du détecteur BABAR. Une vue d'ensemble du Linac et du PEP-II est illustré sur la Figure 2.2.

2.2.1 L'accélérateur linéaire *Linac*

Avant d'accélérer les électrons et les positrons, il faut tout d'abord les produire en très grande quantité. On commence avant tout par produire les électrons avec ce qu'on appelle un *pistolet à électrons*. Cet instrument consiste à chauffer un filament métallique placé dans un champ électrique élevé. L'agitation thermique éjecte les électrons et le champ électrique les dirige vers un injecteur situé au début de l'accélérateur linéaire *Linac* avec une énergie d'environ 200 MeV. L'accélérateur linéaire du SLAC, long de 3.1 km, est le plus long au monde. Il permet notamment de donner une énergie aux électrons

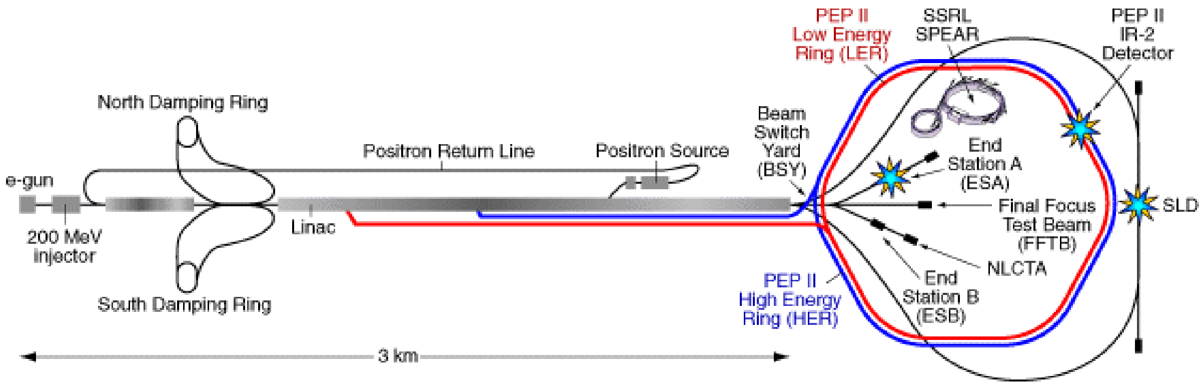

Figure 2.2 – Schéma de l'accélérateur linéaire *Linac* et du collisionneur PEP-II [21]. Les faisceaux d'électrons (*bleu*) et de positrons (*rouge*) du collisionneur PEP-II à droite se croisent dans le détecteur *BABAR* situé à IR-2. Les autres détecteurs présents sur cette figure ne sont pas utilisés pour l'expérience *BABAR*.

jusqu'à 50 GeV. Comme nous allons le voir, c'est amplement suffisant pour le 25 GeV nécessaire à la production des positrons.

L'accélération des électrons se fait grâce à des ondes électromagnétiques produites par des *klystrons*. Dans un klystron, les ondes électromagnétiques sont produites dans une cavité résonnante par le passage des électrons. Le klystron amplifie cette onde et la propage dans un guide d'onde jusqu'à l'un des 80 000 tubes de cuivre séparés par des espaces vides tout le long de l'accélérateur linéaire. Les ondes électromagnétiques provenant des klystrons produisent un courant alternatif à la surface de ces tubes créant ainsi un champ électrique dans l'axe de l'accélérateur et un champ magnétique tournant autour des tubes. Le courant alternatif, synchronisé par le passage des électrons, crée par conséquent un changement de polarisation à la surface des tubes faisant apparaître une différence de potentiel entre les tubes. Dans les espaces vides, les électrons sont accélérés du tube négatif au tube positif. À l'intérieur des tubes il n'y a pas d'accélération, car les tubes agissent come des cages isolantes de Faraday. Cependant, lorsque les électrons s'apprêtent à sortir d'un tuyau, il y a un changement de polarité des tuyaux. Ainsi, les électrons sont toujours accélérés entre les tuyaux dont la polarité est assurée par le synchronisme des klystrons. Le principe pour accélérer les positrons est le même,

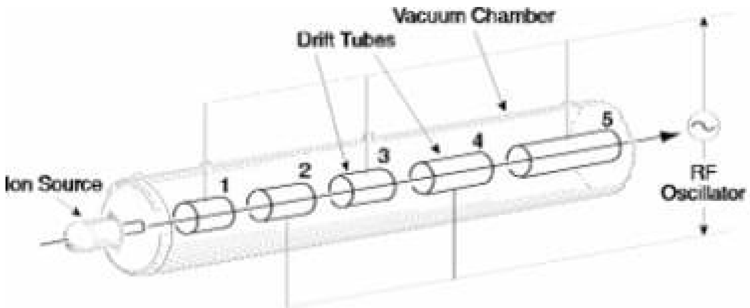

Figure 2.3 – Schéma d'un segment du Linac. La différence de potentielle entre les tubes de cuivre de polarité opposée accélère les électrons et positrons. La longueur des tubes est ajustée selon la vitesse de ceux-ci. Cependant, la vitesse des particules ultra-relativistes ne change pratiquement pas impliquant ainsi une longueur des tubes presque constante le long du Linac.

mais il est anti-synchronisé avec les électrons. Autrement dit, pendant que les électrons se déplacent dans les espaces vides les positrons se déplacent dans les tuyaux, et vice versa. La Figure 2.3 illustre un segment du Linac contenant les tubes.

Au total, ce sont 245 klystrons qui produisent les champs électromagnétiques de puissances croissantes au fur et à mesure que les électrons et les positrons avancent dans l'accélérateur linéaire. Les klystrons régularisent également la vitesse des électrons dans un même paquet, car les électrons plus rapides sont moins accélérés que les plus lents. Cet effet est simplement dû à la forme sinusoïdale du courant alternatif sur les tubes et il est illustré à la Figure 2.4. Par contre, l'impulsion transversale des électrons ne peut être régularisée par les klystrons. Cette régularisation est nécessaire pour augmenter la luminosité du collisionneur PEP-II.

Pour régulariser l'impulsion transversale des électrons et des positrons, deux *anneaux d'amortissement*, situés de chaque côté de l'accélérateur linéaire, sont utilisés. Lorsque les électrons et les positrons atteignent une énergie de 1.2 GeV, ils sont dirigés vers leurs anneaux d'amortissement respectifs. Le principe de fonctionnement de ces anneaux consiste à réduire l'impulsion des particules par radiation synchroton diminuant

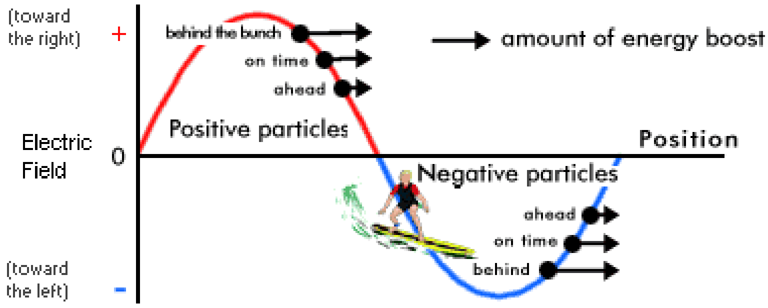

Figure 2.4 – Illustration de l'effet du champ électrique sur les électrons et positrons dans le Linac. La même onde électromagnétique accélére simultanément les électrons et les positrons de façon anti-synchronisée. La forme sinusoïdale du champ magnétique régularise leur vitesse longitudinale en donnant une poussée plus ou moins forte selon le cas, ce qui les regroupe en paquets.

ainsi l'impulsion dans toutes les directions. À l'aide d'un champ électrique, elles sont ensuite accélérées dans la direction voulue. Les électrons et les positrons tournent dans les anneaux d'amortissement jusqu'à ce que la composante tranversale de leurs impulsions soit réduite au maximum avant d'être retournés dans l'accélérateur Linac pour y être accélérés davantage.

Pour atteindre une énergie de 9 GeV, les électrons sont accélérés jusqu'au secteur 10 de l'accélérateur *Linac*, correspondant à un peu plus de la moitié de l'accélérateur, et sont par la suite dirigés vers l'anneau de stockage PEP-II de *haute énergie* (HER). Toutefois, une faible fraction de ces électrons servent à la production des positrons. Ces électrons sont accélérés jusqu'au secteur 19, correspondant au 3/4 de l'accélérateur, pour atteindre une énergie de 25 GeV et sont par la suite envoyés sur une cible de *tungstène*. La collision des électrons sur le tungstène crée des gerbes électromagnétiques contenant des paires e^+e^-. Les positrons sont ensuite extraits par un champ électrique et redirigés au début du Linac avec la même énergie de départ que les électrons, c'est-à-dire environ 200 MeV. Les positrons sont accélérés jusqu'au secteur 4, un peu moins de la moitié du Linac, de façon anti-synchronisée avec les électrons pour atteindre une énergie de 3.1 GeV. Les positrons sont par la suite dirigés vers l'anneau de stockage PEP-II de *basse* *énergie* (LER).

2.2.2 Le collisionneur *PEP-II*

Les deux anneaux de stockage PEP-II, un pour les électrons (HER) et un autre pour les positrons (LER), fonctionnent de la même façon que les anneaux d'amortissement utilisés par le Linac. En circulant dans les anneaux d'une circonférence de 2.2 km, les électrons et positrons émettent de la radiation synchroton. Le collisionneur PEP-II compense cette perte d'énergie en accélérant les électrons et les positrons de manière à ce que leur énergie de 9 GeV et de 3.1 GeV, respectivement, demeure toujours constante. Pour qu'il y ait une collision e^+e^-, le collisionneur croise les faisceaux d'électrons et de positrons dans le coeur du détecteur BABAR en utilisant une série d'aimants dipôles et quadrupôles situés à l'intérieur du détecteur près du point d'interaction, limitant ainsi l'angle d'acceptance du détecteur. Ce sont les dipôles qui changent la trajectoire des faisceaux, tandis que les quadrupôles les focalisent. Cette focalisation est également nécessaire pour augmenter la luminosité instantanée.

Au point d'interaction e^+e^- (IP), les électrons et les positrons entrent en collision avec une énergie au centre de masse de 10.58 GeV, juste assez pour produire une paire de mésons $B\overline{B}$ avec la réaction $e^+e^- \rightarrow \Upsilon(4S) \rightarrow B\overline{B}$. Toutefois, pour avoir une meilleure compréhension du bruit de fond continuum $e^+e^- \rightarrow q\bar{q}$, environ 10% des collisions frontales sont produites avec une énergie au centre de masse de 10.54 GeV (*hors-résonance*) rendant impossible la production de la résonance $\Upsilon(4S)$ et par conséquent les paires de mésons $B\overline{B}$.

La luminosité intégrée totale enregistrée par le détecteur BABAR est de 433 fb^{-1}, ce qui correspond à environ 476 millions de paires de mésons $B\overline{B}$. Le collisionneur PEP-II à également produit une luminosité intégrée totale de 44.1 fb^{-1} pour les événements hors-résonance afin de permettre l'analyse du bruit de fond provenant du continuum $e^+e^- \rightarrow q\bar{q}$. Par comparaison, la luminosité intégrée totale enregistrée par le détecteur Belle est de 711 fb^{-1}. Toutefois, les résultats présentés dans cette thèse ne tiennent

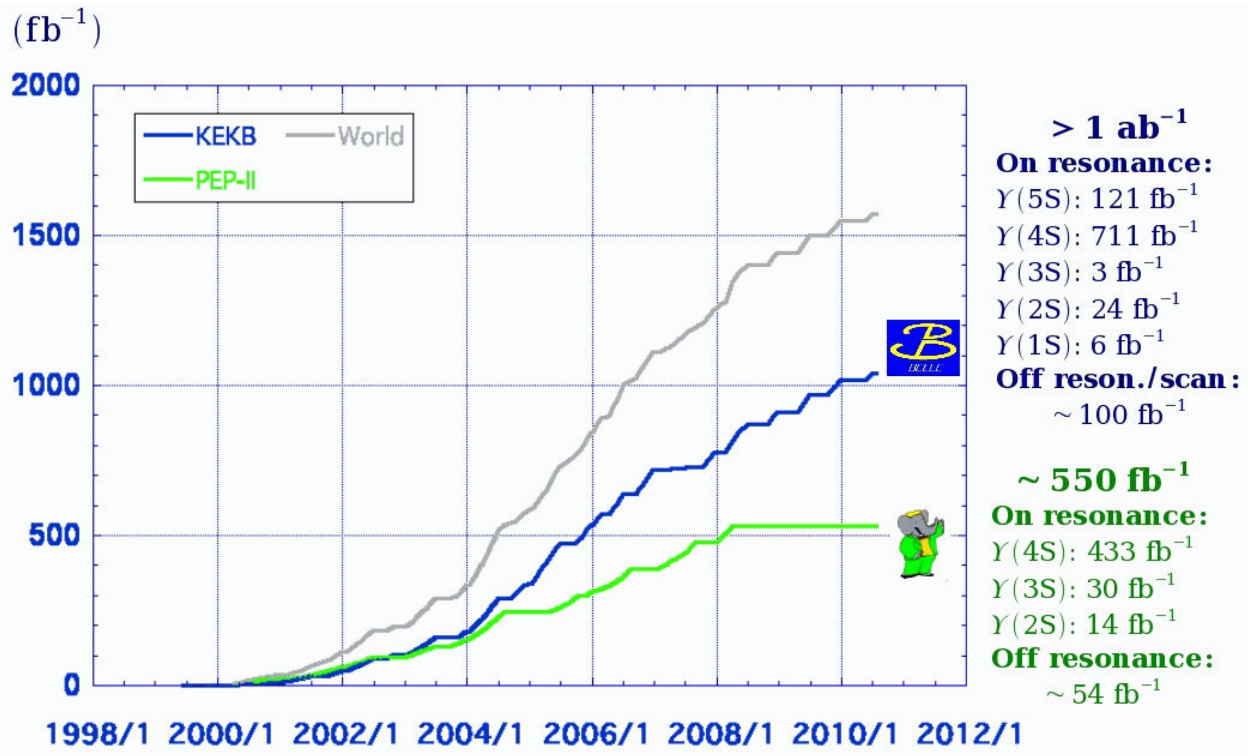

Figure 2.5 – Luminosité intégrée enregistrée par les usines à mésons B en fonction du temps (BABAR et Belle) [22].

compte que des événements enregistrés par le détecteur BABAR. Une représentation de la prise de données en fonction du temps est montrée sur la Figure 2.5.

2.3 Les composantes du détecteur BABAR

Le détecteur BABAR est un ensemble de plusieurs détecteurs de particules qui identifient et enregistrent les particules stables provenant des collisions e^+e^-. À l'expérience BABAR, les particules considérées *stables* sont les hadrons $\pi^\pm$, $K^\pm$, K^0, $p^\pm$, n, les leptons $e^\pm$, $\mu^\pm$, ν et le photon γ. Ce sont les seules particules dont le temps de vie est suffisamment long pour qu'elles puissent être détectées par le détecteur, à l'exception du ν qui n'interagit pratiquement pas avec la matière.

Les particules chargées sont détectées en se servant du détecteur de vertex au silicium entouré de la chambre à dérive de forme cylindrique. Les gerbes électromagnétiques provenant des électrons et des photons sont détectées par le calorimètre électromagnétique qui consiste en des rangées de cristaux d'iodure de césium (CsI) situés juste à l'intérieur d'une bobine solénoïdale d'un aimant supraconducteur de 1.5 T. Les muons et les hadrons neutres sont identifiés par des rangées de chambres à plaques résistives insérées dans les interstices du retour de flux d'acier de l'aimant. Les hadrons chargés sont identifiés par un détecteur de lumière Čerenkov entourant la chambre à dérive et par les mesures de perte d'*énergie différentielle* dE/dx (perte d'énergie par ionisation) dans le détecteur de vertex, la chambre à dérive et le calorimètre électromagnétique. Une coupe longitudinale et transversale du détecteur *BABAR* contenant tous les différents détecteurs sont illustrées sur la Figure 2.6.

Pour maximiser l'acceptance géométrique du détecteur en tenant compte de la poussée relativiste $\beta\gamma \simeq 0.56$ des collisions, le centre du détecteur est décalé de 0.37 m par rapport au point d'interaction (IP) dans la direction du faisceau des électrons. Avec ce décalage, l'acceptance géométriqe du détecteur, définie par rapport à la direction du faisceau délectron, s'étend de 20 degrés vers l'avant à 23 degrés vers l'arrière dans le référentiel du laboratoire. Cette limitation est principalement dûe au fait que les aimants nécessaires pour faire entrer en collision les électrons et les positrons doivent être placés très près du point d'interaction.

Mise à part l'acceptance géométrique du détecteur, il faut également considérer l'acceptance effective de chaque composante du détecteur. Dans ce qui va suivre, nous allons décrire en détails les fonctions et les caractéristiques de chacun de ces détecteurs utilisés à l'expérience *BABAR*.

2.3.1 Détecteur de vertex au silicium (SVT)

La principale fonction du SVT est de détecter et de mesurer avec une grande précision la direction et l'impulsion des particules chargées qui le traversent tout près du point

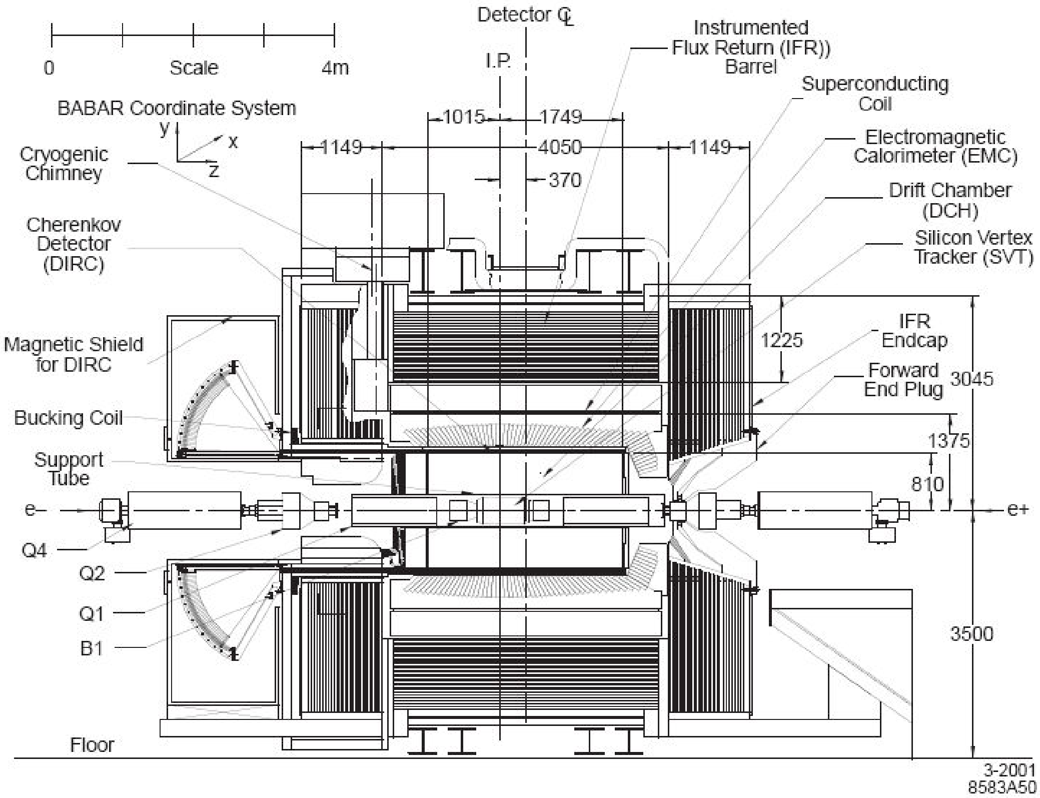

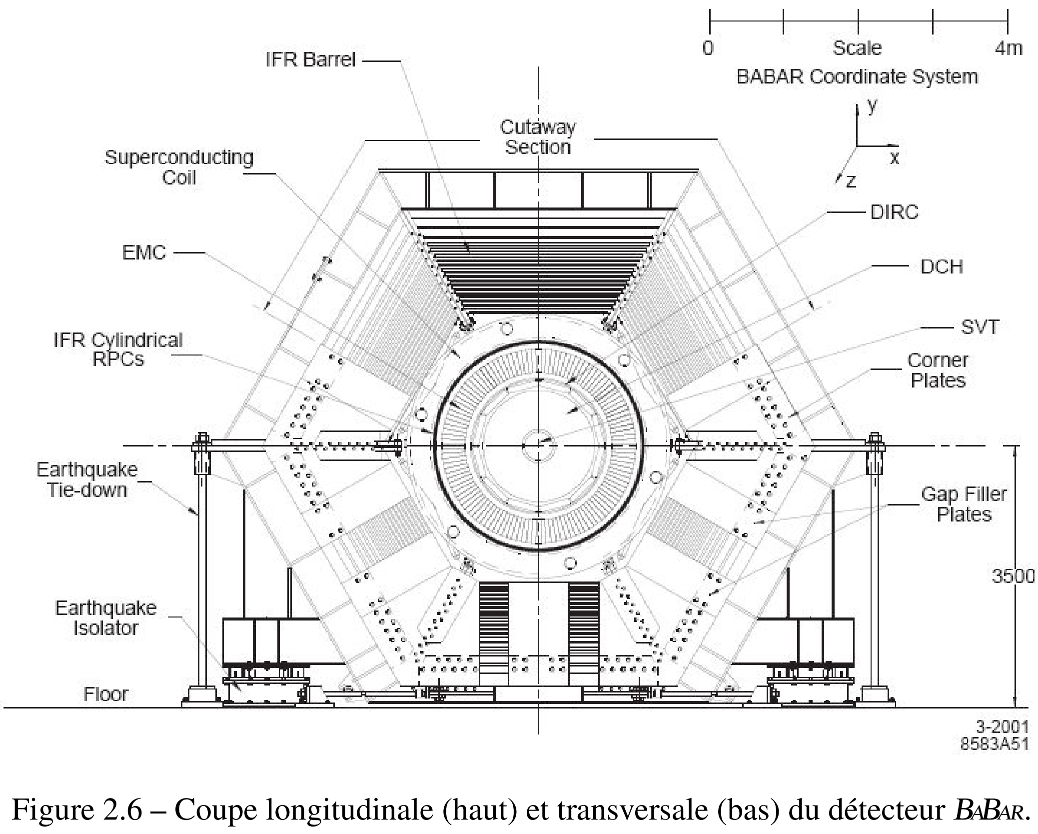

Figure 2.6 – Coupe longitudinale (haut) et transversale (bas) du détecteur *BABAR*.

d'interaction. Cette précision permet notamment de reconstruire la position du vertex de désintégration des mésons B, mesure cruciale pour l'étude de la violation CP dépendante du temps. Le SVT permet également d'identifier les particules en mesurant la perte d'énergie par ionisation dE/dx, une mesure caractéristique différente pour chaque particule.

Le SVT étant situé au centre du détecteur, il est donc inacessible durant le temps normal d'opération du détecteur. La robustesse et la fiabilité sont par conséquent des caractéristiques essentielles du détecteur. Le SVT à été conçu pour résister à une radiation intégrée de plus de 2 $MRad$, et reçoit en moyenne 1 $Rad/jour$.

Des coupes longitudinale et transversale du SVT sont illustrées sur les Figures 2.7 et 2.8, respectivement. Il est constitué de cinq couches doubles de bandes de silicium, un semiconducteur. Le passage des particules chargées crée des paires électrons-trous dans les semiconducteurs. En mettant sous tension les semiconducteurs, les électrons sont séparés des trous, permettant ainsi de mesurer la perte d'énergie des particules chargées. Les trois premières couches sont planes et sont situées tout près du point d'interaction pour permettre une meilleure résolution sur la position du vertex de désintégration des mésons B. Ces trois couches contiennent six modules chacune dans le plan transverse du détecteur. Les deux dernières couches sont en forme d'arche pour minimiser la quantité de silicium requise pour couvrir l'angle solide tout en augmentant l'angle de croisement des particules avec les bandes de silicium. Elles sont aussi situées un peu plus loin du point d'interaction permettant une meilleure extrapolation des trajectoires des particules avec les données recueillies par la chambre à dérive. Les quatrième et cinquième couches contiennent 16 et 18 modules dans le plan transverse du détecteur, respectivement. Au total, le SVT utilise une superficie de 0.96 m^2 de silicium avec approximativement 150 000 cannaux électroniques.

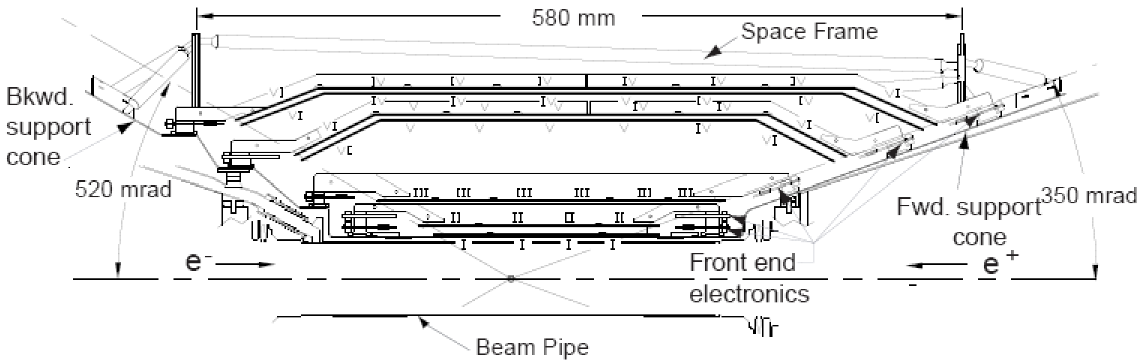

Figure 2.7 – Vue longitudinale du détecteur de vertex illustrant les cinq couches doubles de bandes de sillicium autour du point d’interaction.

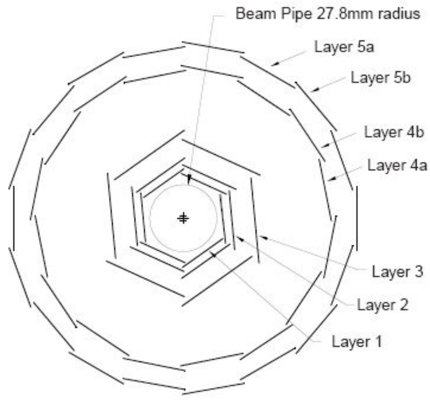

Figure 2.8 – Vue transversale schématique du détecteur de vertex illustrant les cinq couches doubles de bandes de sillicum autour du point d’interaction.

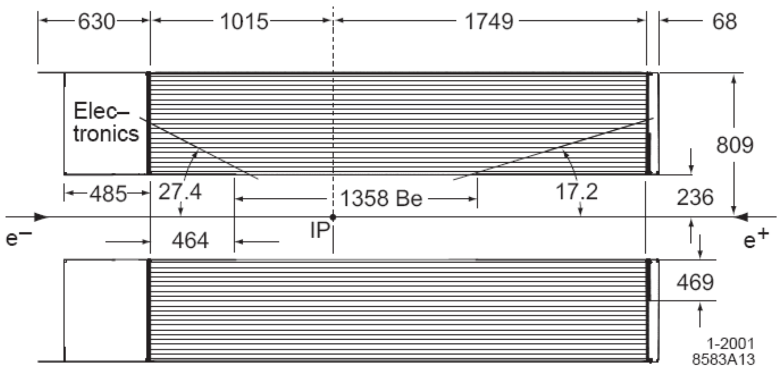

Figure 2.9 – Vue longitudinale de la chambre à dérive. Les longueurs sont données en millimètres et les angles en degrés.

2.3.2 Chambre à dérive (DCH)

Tel qu'illustré à la Figure 2.9, la DCH de forme cylindrique mesure 276.4 cm de long avec un rayon de 80.9 cm et englobe complètement le SVT avec son rayon de 23.6 cm. La DCH a principalement la même fonction que le SVT, mais ne peut mesurer la trajectoire et la perte d'énergie par ionisation dE/dx que pour les particules chargées avec une impulsion transverse supérieure à 120 MeV. Pour y arriver, la DCH est remplie de fils sous haute tension électrique (1930 V) et d'un gaz contenant 80% d'hélium et 20% d'isobutane.

Les particules chargées qui traversent la DCH ionisent le gaz en produisant des paires électrons-ions. Les électrons libres sont ensuite accélérés vers les fils conducteurs et ionisent davantage le gaz, créant ainsi des avalanches d'électrons. Il est par conséquent possible de reconstruire précisément la trajectoire des particules et leur dE/dx en étudiant les informations des cellules ayant reçues une avalanche d'électrons. La distance séparant les particules chargées et les fils est calculée à partir de la différence entre le temps de passage de la particule dans la cellule contenant le fil et le temps de détection de l'avalanche par celui-ci. En ajoutant le nombre d'électrons dans chaque avalanche comme information additionnelle, il devient possible de mesurer la perte d'energie par ionisation dE/dx. Ces mesures combinées avec celle du SVT permettent d'identifier

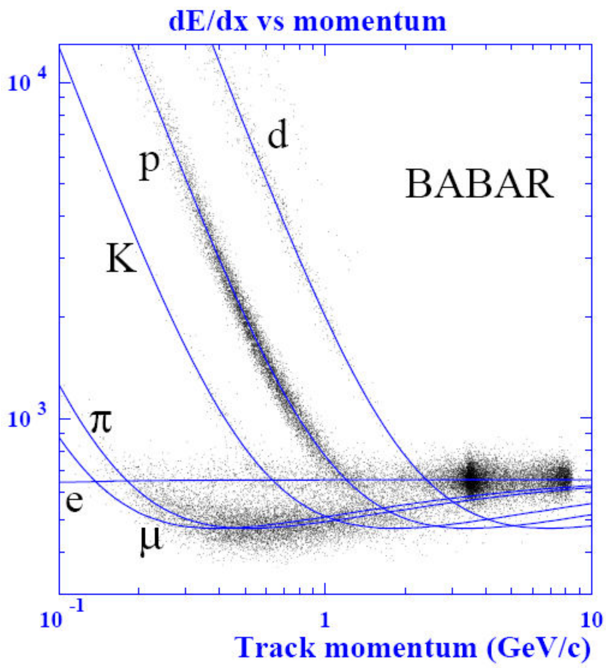

Figure 2.10 – Mesure de la perte d'énergie par ionisation dE/dx dans la chambre à dérive en fonction de l'impulsion. Les courbes représentent les prédictions de la formule de Bethe-Bloch pour divers types de particules.

précisément les particules de basses impulsions (< 700 MeV), comme illustré à la Figure 2.10.

Les fils de la DCH sont agencés en 40 couches cylindriques de celulles hexagonales et ces couches sont mises en groupe de quatre pour former dix supercouches placées dans l'orde AUVAUVAUVA. La Figure 2.11 montre les quatre premières supercouches intérieures AUVA de la DCH. Les supercouches de type A (axial) ont leurs fils parallèles aux faisceaux, tandis que les supercouches de types U et V (stéréo) ont leurs fils légèrement inclinés variant de 45 $mrad$ à 76 $mrad$ par rapport au faisceau des électrons, positivement pour U et négativement pour V, de l'intérieur à l'extérieur, respectivement. La concentration d'hélium et d'isobutane est optimisée pour augmenter l'efficacité de détection des avalanches. L'hélium a été choisi pour sa faible masse réduisant ainsi la probabilité d'une diffusion multiple. L'isobutane est nécessaire pour absorber les photons émis par les atomes excités provenant des avalanches. En revanche, une trop grande concentration d'isobutane augmenterait le taux de diffusions multiples. Ce mélange de gaz minimise aussi la détérioration des fils sous l'effet des radiations intenses lors des mesures ("*Aging effect*").

2.3.3 Détecteur de lumière Čerenkov à réflections internes (DIRC)

Le DIRC est une composante essentielle pour pouvoir identifier les particules chargées de haute impulsion ($0.7 < p < 4.2$ GeV). Son principe de fonctionnement consiste à mesurer l'angle du cône de lumière émis par le passage des particules dans les barres de verre de silice synthétique composant le DIRC. Lorsqu'une particule se déplace plus vite que la lumière dans un milieu, elle excite les atomes du milieu qui émettent de la lumière selon un certain angle caractéristique, appelé *angle Čerenkov* θ_C. Cette lumière forme ainsi un cône défini selon la direction de la particule. Cet angle est défini par la relation $cos\theta_C = 1/n\beta$, où $n = 1.473$ est l'indice de réfraction du silice et $\beta = v/c$. En mesurant l'angle Čerenkov, on permet d'extraire la vitesse v de la particule qui, combinée avec l'impulsion mesuré par le SVT et la DCH, permet d'en déduire sa masse. En effet, la Figure 2.12 montre l'angle Čerenkov mesuré en fonction de l'impulsion pour différentes particules.

Le DIRC utilise 144 barres de silice parallèles aux faisceaux et mesurent 4.9 m de longueur, 3.5 cm de largeur et 1.7 cm d'épaisseur. Les barres forment un polygone à 12 faces autour de la DCH, où chaque face contient 12 barres de silice comme illustré à la Figure 2.13. La lumière se propageant dans les barres par réflexion totale interne se rend jusqu'à un réservoir contenant 6000 litres d'eau purifiée situé à l'arrière du détecteur. Un miroir situé au bout avant de chaque barre réfléchit la lumière vers l'arrière. Une surface quasi-sphérique contenant 10752 *tubes photomultiplicateurs* (PMTs), chacun situé à 1.17 m des bouts des barres de silice, permet de déduire l'angle Čerenkov en connaissant la direction de la trajectoire de la particule dans le DIRC grâce à la reconstruction des traces chargées faite par le SVT et la DCH. La Figure 2.14 montre une coupe longitudinale d'une barre de silice synthétique avec la trajectoire lumineuse du

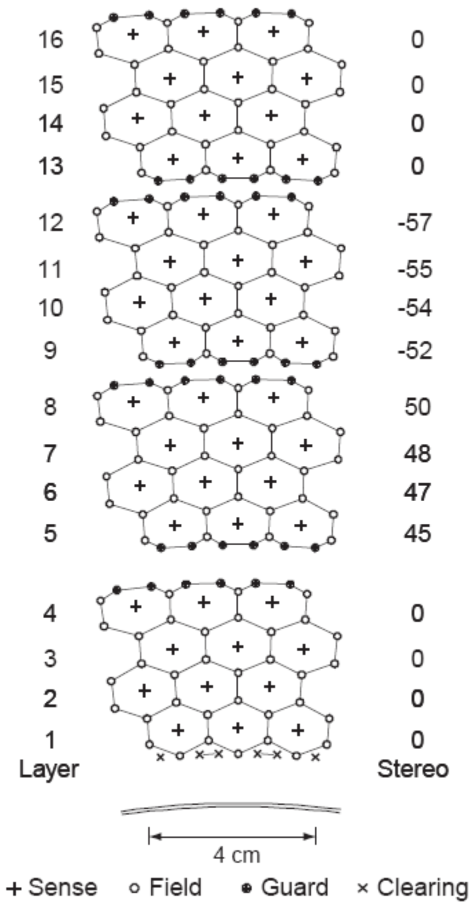

Figure 2.11 – Vue transversale des cellules hexagonales des quatre premières super-couches de la chambre à dérive. Des traits entre les fils représentant les cathodes sont dessinés pour mieux visualiser les cellules. Chaque cellule contient un fil sensible (anode) en son centre pour capter les électrons. Les nombres de la colonne de droite représentent les angles d'inclinaison des fils de chaque couche (en $mrad$).

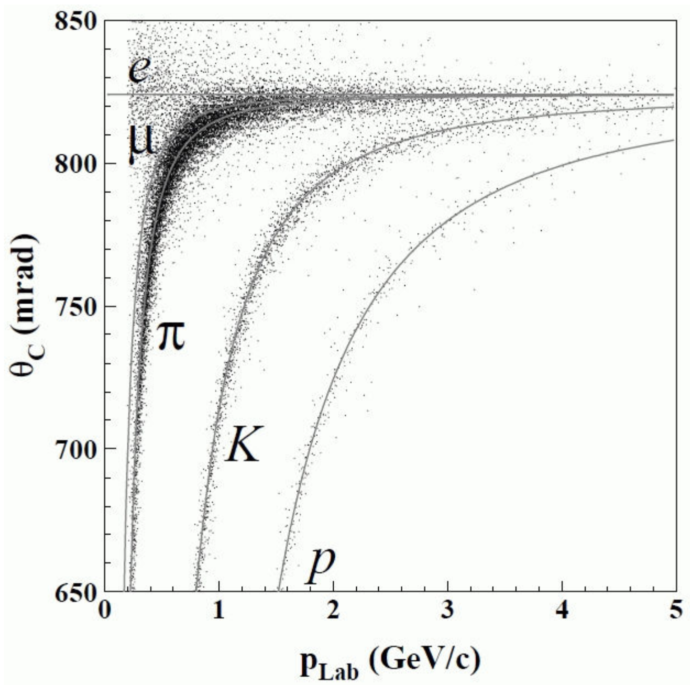

Figure 2.12 – Mesure de l'angle Čerenkov en fonction de l'impulsion. Les courbes représentent les prédictions pour différents types de particules.

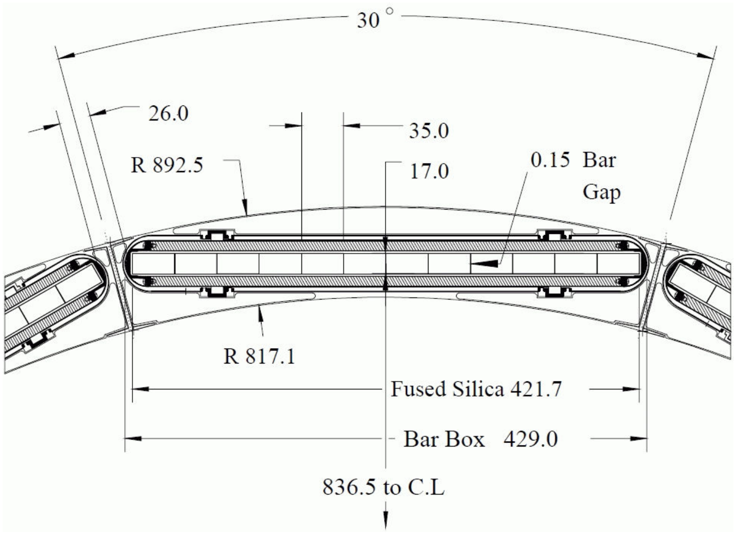

Figure 2.13 – Vue transversale d'une des 12 faces du DIRC contenant 12 barres de silice chacune. Toutes les dimensions sont en millimètres

cône de lumière focalisé sur les PMTs. L'eau purifiée a un indice de réfraction proche de celui du silice synthétique avec $n = 1.346$, limitant ainsi le changement d'angle de la lumière entre les deux milieux.

2.3.4 Calorimètre électromagnétique (EMC)

Le calorimètre EMC est indispensable pour mesurer l'énergie et la direction des photons ainsi que pour l'identification des électrons. Le EMC contient 6580 cristaux scintillateurs d'iodure de césium dopé avec 0.1% de thallium (CsI(Tl)) répartis sur 56 anneaux, comme illustré à la Figure 2.15 montrant une coupe longitudinale du EMC. La Figure 2.16 montre que ces cristaux sont de forme trapézoïdale ayant une aire de 22.1 cm^2 à l'intérieur et 36.6 cm^2 à l'extérieur permettant ainsi une résolution angulaire exceptionnelle de quelques $mrad$. La résolution angulaire est déterminée par la longueur transversale (4.7 cm) du cristal et la distance de celui-ci par rapport au point d'interaction (> 92 cm). Le rayon de Molière du CsI(Tl) est suffisamment petit (3.8 cm) et la longueur des cristaux suffisamment grande (> 16 longueurs de radiation) pour qu'un seul cristal puisse contenir toute une gerbe électromagnétique.

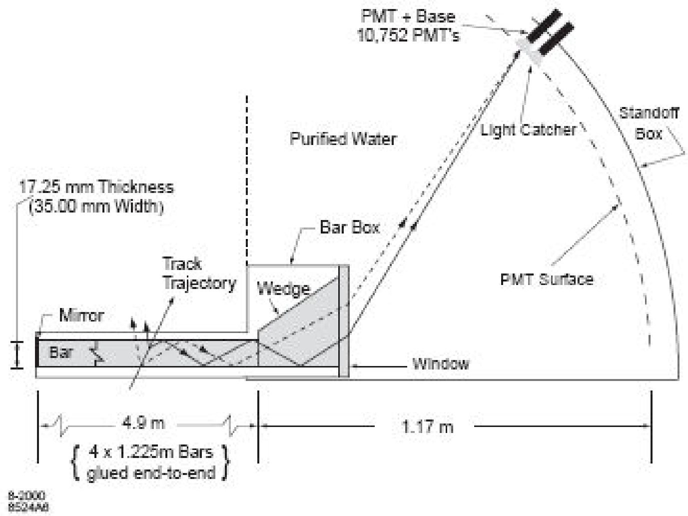

Figure 2.14 – Vue longitudinale d'une barre de silice et de la surface quasi-sphérique supportant les PMTs du DIRC.

Les scintillateurs absorbent l'énergie des photons et des électrons en produisant ce que l'on appelle des gerbes électromagnétiques. En effet, lorsque l'énergie le permet, les photons perdent leur énergie en créant une paire électron-positron $\gamma \to e^+e^-$. Les électrons et positrons quant à eux, émettent du rayonnement de freinage (*bremsstrahlung*) $e^\pm \to e^\pm\gamma$. Ce processus continue tant et aussi longtemps que l'énergie des photons est suffisante pour créer des pairesélectron-positron, $E_\gamma > 1.022$ MeV et que les électrons et positrons sont au-dessus de l'énergie critique où la perte d'énergie par ionisation est moins importante. Une illustration simple d'une gerbe électromagnétique est représentée sur la Figure 2.17.

À basse énergie, les photons perdent leur énergie par *diffusion Compton* ou par *effet photoélectrique* jusqu'à ce qu'ils puissent être absorbés par le scintillateur CsI(Tl). Une fois qu'un photon est absorbé par le scintillateur, des photons sont réémis avec une longueur d'onde caractéristique $\lambda = 565\ nm$ et leur nombre est proportionnel à l'énergie absorbée.

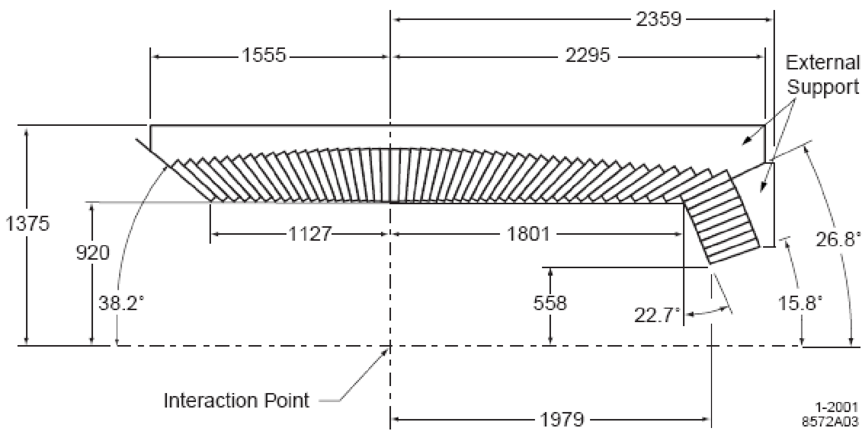

Figure 2.15 – Coupe longitudinale de la moitié supérieure du EMC. Toutes les dimensions sont en millimètres.

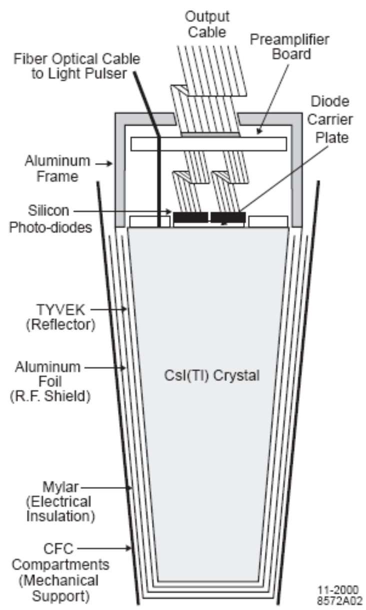

Figure 2.16 – Schéma d'un cristal de CsI(Tl) du EMC. Ce schéma n'est pas à l'échelle.

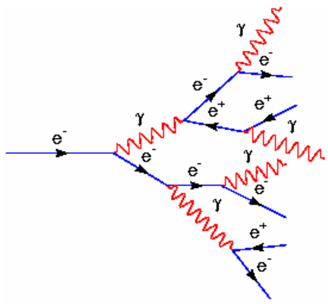

Figure 2.17 – Illustration d'une gerbe électromagnétique.

Les parois polies du cristal maintiennent les photons à l'intérieur par réflection interne. Une faible quantité de photons est toutefois transmise en dehors du cristal, mais la majorité est réfléchie par deux minces couches de 165 μm d'un matériau réflecteur situé autour des cristaux. Pour tenir compte de la distribution asymétrique en énergie des particules produites dans le détecteur, la longueur des cristaux passe de 29.6 cm à l'arrière du détecteur à 32.4 cm à l'avant du détecteur, ce qui correspond à 16 et 17.5 longueurs de radiation, respectivement. Pour capter le nombre de photons émis par le scintillateur, à l'arrière de chaque cristal se trouvent deux photodiodes qui redirigent le signal par fibre optique vers un amplificateur.

Par ailleurs, bien que le EMC à été conçu pour détecter les photons, les électrons et les positrons, d'autres particules interagissent faiblement avec le EMC et laissent ainsi des traces qui peuvent être utiles pour identifier les hadrons neutres comme les neutrons et les K^0_L.

2.3.5 Retour de flux instrumenté (IFR)

Le IFR est souvent appelé détecteur à muons, pour la simple et bonne raison que son objectif premier est d'identifier les muons. Les muons sont les seules particules chargées capable de traverser le détecteur et l'aimant pour se rendre au IFR. C'est le dernier détecteur de BABAR étant ainsi le plus éloigné du point d'interaction. Son principe de fonc-

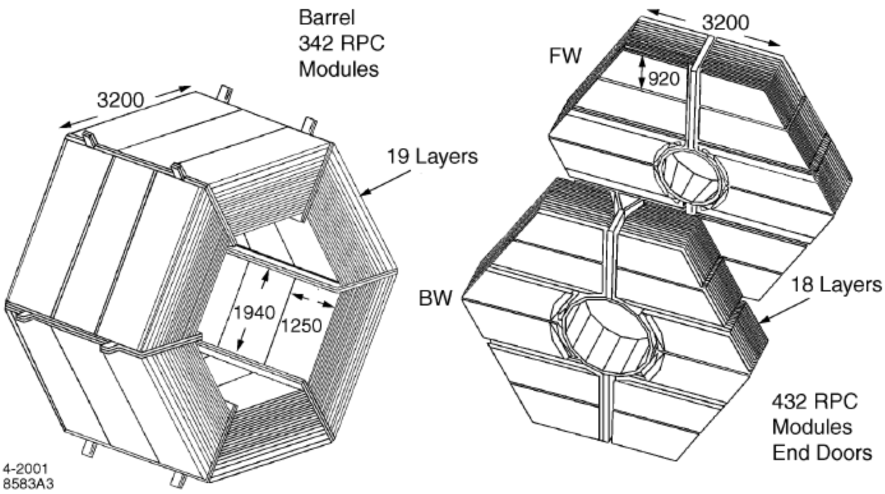

Figure 2.18 – Vue d'ensemble du IFR, incluant le barril et les extrémités avant (FW) et arrière (BW). Les dimensions sont indiquées en millimètres.

tionnement est similaire à la DCH en faisant ioniser un gaz par le passage des particules chargées.

Le IFR contient en tout 806 modules de matériel actif formant globalement un baril de forme hexagonale ainsi que deux extrémités hexagonales. Le baril contient 3 sections de 19 couches de matériel actif séparées par des plaques d'acier sur chacun des 6 côtés formant ainsi 342 modules. Les plaques d'acier ont une épaisseur variable allant de 2 cm à l'intérieur à 10 cm à l'extérieur et elles sont espacées de 3.5 cm à 3.2 cm, respectivement. Ce sont ces plaques qui permettent le retour de flux de l'aimant vers l'intérieur. Chacune des deux extrémités est découpée en 12 sections de 18 couches formant ainsi un total de 432 modules pour les deux extrémités. Nous avons également 32 modules situés sur deux couches cylindriques placées entre le EMC et le solénoïde servant principalement à détecter les particules qui passent à travers le EMC. Le solénoïde qui crée le champ magnétique uniforme de 1.5 T est donc situé entre ces deux couches et le reste du IFR. Il est composé de 46.5% de niobium et 53.5% de titanium. Une vue d'ensemble du IFR est illustrée sur la Figure 2.18.

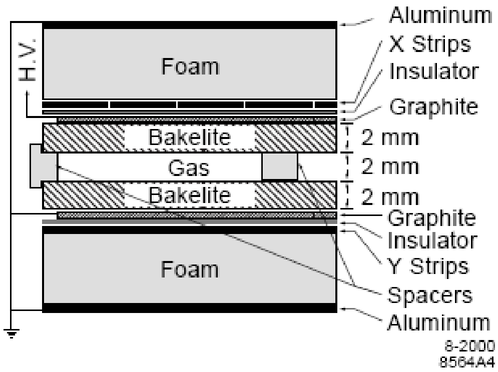

Figure 2.19 – Vue en coupe d'un RPC, incluant le schéma des connections électriques à haute tension.

Au départ, le matériel actif du IFR était constitué uniquement de *chambres à plaques résistives* (RPCs). Malheureusement, une défaillance des RPCs qui limitait l'efficacité de détection des muons oblige leur remplacement. En 2002, environ 200 RPCs situées aux extrémités furent remplacées par des RPCs plus performantes. Les RPCs sur les six côtés du baril quand à eux ont été remplacés par des *Limited Streamer Tubes* (LSTs) dont deux en 2004 et les quatres autres en 2006.

Les RPCs illustrées sur la Figure 2.19 contiennent une épaisseur de 2 mm de gaz, contenant 56.7% d'argon, 38.8% de fréon et 4.5% d'isobutane, qui est ionisé par le passage des muons, créant ainsi des paires électrons-ions. De la même façon que pour la DCH, les électrons sont accélérés par un fort champ électrique. Ce gaz est contenu entre deux plaques de *Bakelite* également de 2 mm d'épaisseur, un polymère très isolant. Le tout placé entre deux plaques de graphite avec une différence de potentiel entre les deux de 8000 V, beaucoup plus que celle de la DCH avec 1930 V. Ce fort champ électrique implique que les électrons ionisés produisent des *torrents* qui sont des *avalanches* d'électrons saturés. Contrairement à la DCH, il n'est donc pas possible de mesurer la quantité d'énergie déposée par les muons, puisque l'énergie mesurée y est saturée. Seulement la direction des muons peut être mesurée. L'avantage de la production des torrents c'est qu'elle augmente la charge mesurée par le IFR, simplifiant grandement la détection du

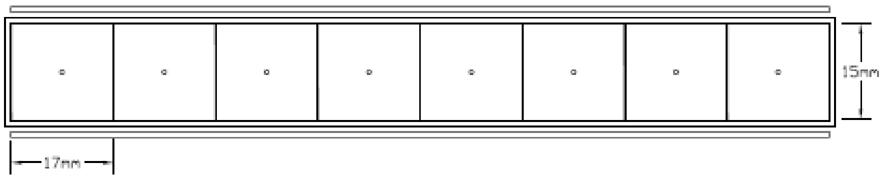

Figure 2.20 – Vue en coupe d'une plaque de LSTs.

passage des muons. Des bandes de lecture d'aluminium instalées parallèlement et perpendiculairement aux faisceaux viennent entourer les RPCs. Ces bandes mesurent les composantes z et ϕ des impacts, tandis que le rayon r est déterminé par la posistion du RPC.

Les LSTs illustrés à la Figure 2.20 forment des tubes carrés et fonctionnent avec le même principe que les RPCs en générant également des torrents par le passage des particules chargées. Le gaz contenu dans les LSTs, différent de celui des RPCs, contient 89% de CO^2, 8% d'isobutane et 3% d'argon. Chaque LST est rempli de ce gaz avec en son centre un fil sous haute-tension ayant une différence de potentiel de 5500 V avec les parois du LST. Les LSTs sont regroupés en groupe de huit, formant ainsi une plaque de LSTs. Des bandes de lecture métalliques sont également installées perpendiculairement aux plaques pour mesurer la composante z des impacts. Les composantes ϕ et r sont déterminées par la position des tubes.

Tout comme le EMC, le IFR peut aussi être utilisé pour détecter les K_L^0 et les n. Ces derniers peuvent se désintégrer dans le IFR ou interagir par interaction forte avec l'acier contenu dans le IFR produisant ainsi des particules chargées qui seront détectées par le IFR.

2.4 Système de déclenchement

Le détecteur ne détecte pas seulement les événements $e^+e^- \rightarrow \Upsilon(4S) \rightarrow B\overline{B}$, mais aussi tous les événements de bruits de fond provenant des faisceaux, des collisions de type $e^+e^- \rightarrow e^+e^-$ et bien d'autres. Malheureusement, le système d'acquisition de données ne peut pas enregistrer plus de 120 événements par seconde. Comme une collision se produit à environ toutes les 4.2 ns, il y a donc environ 238 millions de collisions par seconde. Ce qui implique que seulement 1 événement sur 2 millions peut être enregistré. Il est donc primordial que le système de déclenchement de BABAR (*trigger*) rejette le plus d'événements de bruits de fond possible tout en conservant les événements qui nous intéressent, c'est-à-dire ceux qui produisent les paires de mésons $B\overline{B}$, et ce de façon ultra-rapide. Le système de déclenchement de BABAR se fait en deux étapes distinctes, le niveau 1 (L1) (*algorithme d'appareillage* ou "*hardware*") et le niveau 3 (L3) (*algorithme informatique* ou "*software*").

Le L1 utilise trois microprocesseurs qui sont la DCT (*Drift Chamber Trigger*), le EMT (*ElectroMagnetic calorimeter Trigger*) et le GLT (*GLobal Trigger*). La DCT qui est le système de déclenchement de la DCH, utilise un algorithme de reconnaissance de forme pour reconstruire approximativement les traces chargées et estimer l'impulsion transverse de ces traces. Ces traces sont classées en trois catégories B, A et A', définies dans le Tableau 2.2. Le EMT quant à lui est le système de déclenchement du EMC et évalue l'énergie des *tours*. Les tours sont des groupes de 19 à 24 cristaux du EMC formant au total 280 tours. Dans chaque tour, seuls les cristaux accumulant une énergie de plus de 20 MeV sont pris en considération. Ces tours sont ensuite classées en cinq catégories M, G, E, X, et Y, définies dans le Tableau 2.2. Le GLT qui reçoit les informations de la DCT et du EMT est l'algorithme qui décide si un événement susceptible d'être un candidat intéressant doit être envoyé au L3. Cette décision se fait par une série de conditions logiques, comme par exemple ($B > 2$ & $A > 1$ & $M > 1$), où $B > 2$ signifie selon le Tableau 2.2 que plus de deux traces atteignent la cinquième supercouche de la DCH. Parmi les 238 millions de collisions par seconde, seulement 1000 d'entre eux, en moyenne, sont envoyés au L3, tout en éliminant plus de 99.9% du bruit de fond. Également, plus de 99.9% des événements $e^+e^- \rightarrow \Upsilon(4S) \rightarrow B\overline{B}$ se retrouvent parmi ces 1000 événements.

Tableau 2.2 – Principales caractéristiques des catégories de traces du DCT et de tours du EMT.

	Description	Origine	Seuil
B	Courte trace atteignant la supercouche 5	DCT	120 MeV
A	Longue trace atteignant la supercouche 10	DCT	180 MeV
A'	Trace de haute impulsion transverse	DCT	800 MeV
M	Tout θ, énergie d'ionisation minimale	EMT	100 MeV
G	Tout θ, énergie intermédiaire	EMT	250 MeV
E	Tout θ, énergie élevée	EMT	700 MeV
X	Bouchon avant, énergie d'ionisation minimale	EMT	100 MeV
Y	Arrière du barril, énergie élevée	EMT	1 GeV

Tableau 2.3 – Efficacité $(\%)$ du système de déclenchement pour divers processus physiques estimée par simulation Monte Carlo.

Algorithme L3	$\epsilon_{B\overline{B}}$	$\epsilon_{B\to\pi^0\pi^0}$	$\epsilon_{B\to\tau\nu}$	$\epsilon_{c\bar{c}}$	ϵ_{uds}	$\epsilon_{\tau\tau}$
DCH (toutes conditions)	99.4	89.1	96.6	97.1	95.4	95.5
EMC (toutes conditions)	93.5	95.7	62.3	87.4	85.6	46.3
DCH + EMC	>99.9	99.3	98.1	99.0	97.6	97.3
L1+L3 combinés	>99.9	99.1	97.8	98.9	95.8	92.0

Le L3 utilise des algorithmes informatiques plus précis permettant de faire un lissage sur la reconstruction des traces chargées et de considérer chaque cristal du EMC individuellement. Son principe de fonctionnement est similaire à celui du L1, mais permet d'éliminer davantage de bruits de fond provenant des faisceaux et d'événements de type Bhabha, $e^+e^- \to e^+e^-$. Ainsi, sur les 1000 événements par seconde envoyés au L3, moins que 120 sont sélectionnés par le L3. Les performances du L1 et du L3 sont décrites dans le Tableau 2.3 et conservent une efficacité de sélection de plus de 99.9% pour les événements $e^+e^- \to \Upsilon(4S) \to B\overline{B}$. Les événements acceptés par le L3 sont ensuite conservés dans une gigantesque base de données, tandis que les 238 millions restants par seconde sont perdus à jamais, d'où l'importance d'un système de déclenchement judicieux.

2.5 Reconstruction des traces chargées

Une fois les événements acceptés par le système de déclenchement L3, un lissage plus précis est fait sur la reconstruction des traces chargées afin d'avoir plus de précision sur le temps de départ t_0 ainsi que sur les cinq paramètres d_0, z_0, ϕ_0, ω et $tan(\lambda)$ qui sont mesurés au point d'approche maximale de la trace par rapport à l'axe z (l'axe des faisceaux). Le paramètre d_0 représente la distance de ce point par rapport à l'origine (point d'interaction) dans le plan $x - y$, z_0 représente cette distance par rapport à l'axe z, ϕ_0 est l'angle azimutal dans le plan $x - y$, $\omega = 1/p_t$ est l'inverse de l'impulsion transverse et $tan(\lambda)$ est la pente de la trace en ce point dans le plan $x - y$.

Cette reconstruction est essentielle pour déterminer le point de vertex d'origine de la trace de chaque particule et de reconstruire par le fait même les points de vertex de la désintégration des mésons B, qui rappelons-le est une mesure cruciale pour l'étude de la violation CP dépendante du temps. Pour ce faire, l'algorithme de reconstruction utilise les informations du SVT et de la DCH qui mesurent une série de points d'impacts au passage des particules chargées.

Les informations issues du lissage provenant du L3 sont utilisées pour améliorer la précision de t_0 par un lissage portant sur les paramètres d_0, ϕ_0 et t_0 en utilisant uniquement les traces trouvées par la DCH comportant des mesures dans au moins quatre de ses dix supercouches. Ensuite, une fonction hélicoïdale est utilisée (le champ magnétique est uniforme) pour ajouter aux traces reconstruites des points de mesures additionnels trouvés par le L3, améliorant encore plus la précision de t_0. Deux algorithmes sont ensuite utilisés pour reconstruire les traces qui ne franchissent pas la DCH au complet et les traces qui ne proviennent pas du point d'interaction. Un lissage qui tient compte du matériel et du champ magnétique du détecteur ainsi que de toutes les traces chargées trouvées est effectué pour améliorer encore une fois la précision sur les paramètres. Une extrapolation est ensuite faite jusqu'au SVT pour raccorder des segments de traces du SVT aux segments de la DCH. Le même lissage est répété en utilisant simultanément les traces du SVT et de la DCH. Un autre algorithme tente par la suite de reconstruire des traces dans le SVT qui ne sont pas associées à la DCH. Finalement, une tentative de relier avec la DCH ces segments trouvés uniquement dans le SVT est entreprise.

Au total, ce sont (96.4 $\pm$ 0.8)% des traces chargées qui sont détectées par cette procédure. Ces traces optimisées sont ensuite répertoriées dans différentes listes dépendamment de leur degré de qualité et de leurs caratéristiques. Ces traces chargées et leurs caractéristiques sont par la suite utilisées par des algorithmes d'identification des particules. Ce qui permet une sélection optimale pour chaque type d'analyse à l'expérience BABAR.

2.6 Identification des particules (PID)

Au départ, toutes les particules chargées sont considérées comme étant des pions, tandis que les maxima locaux du EMC sont considérés comme étant des photons. Ce sont les particules les plus plausibles et les plus abondantes produites dans les collisions e^+e^-. L'identification des particules chargées permet de calculer leur énergie connaissant leur impulsion par la formule $E = \sqrt{p^2 + m^2}$. L'identification des particules neutres permet de mettre en évidence les hadrons neutres dont l'énergie est mal mesurée par le EMC.

Plusieurs algorithmes informatiques se servent des informations reçues par les différents détecteurs qui constituent le détecteur BABAR pour identifier avec une certaine probabilité les particules stables décrites à la Section 2.3. Dans ce qui suit, nous allons décrire en détails les différents algorithmes utilisés dans cette thèse.

Pour identifier les électrons, l'algorithme choisi (*PidLHElectrons*) utilise une *fonction de vraisemblance (likelihood)* correspondant au produit des *Fonctions de Densité de Probabilité* (PDFs) de sept mesures qui sont :

– le rapport de l'énergie mesurée dans le EMC et de l'impulsion mesurée par le SVT et la DCH ($E/p \sim 1.0$ pour les électrons) ;

– le nombre de cristaux impliqués et la forme de la gerbe électromagnétique (longitudinale et transversale) dans le EMC ;
– la perte d'énergie par ionisation dE/dx dans la DCH ;
– le nombre de photons détectés par le EMC et l'angle de Čerenkov dans le DIRC.

Cet algorithme permet d'identifier les électrons avec un taux de plus de 90$\%$ d'efficacité et rejette par le fait même 99.9$\%$ des pions.

Pour identifier les muons, l'algorithme spécifique à notre analyse (*muNNTight*) utilise un *réseau de neurones* pour optimiser une combinaison de huit mesures qui sont :
– l'énergie mesurée par le EMC ;
– le nombre de longueurs de radiation mesurées jusqu'au dernier impact dans le IFR ;
– le nombre de longueurs de radiation prédites pour un muon qui aurait les paramètres de la trace chargée mesurée par le SVT et la DCH ;
– le χ^2 du lissage des impacts du IFR avec un polynôme de troisième degré ;
– le χ^2 de la reconstruction de la trace chargée en y ajoutant les impacts du IFR ;
– le nombre d'impacts moyen par couche du IFR ;
– la déviation standard du nombre d'impacts dans chaque couche du IFR ;
– la déviation standard de la trace dans le IFR par rapport à la prédiction obtenue par les mesures des impulsions de la trace dans le SVT et la DCH.

Cet algorithme de détection permet d'identifier environ 70$\%$ des muons en rejetant plus de 96$\%$ des pions.

Pour identifier les pions chargés, la particule chargée ne doit pas avoir été identifiée comme étant un électron et l'algorithme (*piLHLoose*) utilise une *fonction de vraisemblance (likelihood)* correspondant au produit des PDFs des six mesures suivantes :
– la mesure de l'énergie différentielle dE/dx dans le SVT et la DCH ;
– la derniére couche mesurant un impact dans la DCH ;
– le nombre de photons détectés et l'angle de Čerenkov dans le DIRC ;
– l'énergie captée par le EMC.

Cet algorithme permet une identification des pions de l'ordre de 95% et rejette de surcroît 80% des kaons chargés.

La liste des photons utilisée correspond tout simplement à tous les maxima locaux mesurés dans le EMC qui ne sont pas déjà associés à une particule chargée.

D'autres algorithmes sont utilisés pour identifier les $p^{\pm}$, $K^{\pm}$, K_L^0 et n ; cependant ils ne sont pas utilisés pour les résultats présentés dans cette thèse. Ces algorithmes utilisent principalement l'énergie différentielle dE/dx dans la DCH et le DIRC pour les particules chargées et utilisent pour les particules neutres la forme des amas mesurés par le EMC et les informations recueillies par le IFR qui ne sont pas déjà associées à une trace chargée.

Dans les deux prochains chapitres, nous allons discuter en détail de la méthode utilisée pour extraire les valeurs de $|V_{ub}|$ exclusives. Nous verrons qu'une sélection des données expérimentales sera nécessaire pour mesurer les rapports d'embranchement partiels et totaux des trois modes de désintégrations semileptoniques $B^0 \to \pi^- \ell^+ \nu$, $B^+ \to \eta \ell^+ \nu$ et $B^+ \to \eta^{'} \ell^+ \nu$. Par la suite, une étude sera faite pour évaluer minutieusement les incertitudes systématiques. Le nombre de paramètres de bruits de fond utilisé pour le lissage des rapports d'embranchement sera optimisé statistiquement. Finalement, les valeurs de $|V_{ub}|$ et des rapports d'embranchement seront présentés à la fin de ces chapitres.

[17] B. Aubert *et al.*, (*BaBar* Collaboration), Nucl. Instrum. Methods **A479**, 1 (2002).

[18] B. Aubert *et al.*, (*BaBar* Collaboration), *The BaBar Physics Book : Physics at an asymmetric B factory*, SLAC-R-504 (1998).

[19] B. Aubert *et al.*, (*BaBar* Collaboration), *BaBar Technical design report*, SLAC-R-95-457 (1995).

[20] *BaBar* Collaboration, *An Asymmetric B factory based on PEP : Conceptual design report*, SLAC-0372 (1991).

[21] SLAC Virtual Visitor Center, http ://www2.slac.stanford.edu/vvc/default.htm.

[22] Belle Collaboration home page, belle.kek.jp.

CHAPITRE 3

ARTICLE INTERNE À LA COLLABORATION BABAR (BAD1955) : MEASUREMENT OF THE $B^0 \to \pi^- \ell^+ \nu$ AND $B^+ \to \eta^{(\prime)} \ell^+ \nu$ BRANCHING FRACTIONS, THE $B^0 \to \pi^- \ell^+ \nu$ AND $B^+ \to \eta \ell^+ \nu$ FORM-FACTOR SHAPES, AND DETERMINATION OF $|V_{UB}|$

Martin Simard[1], **Xuan Nguyen**[1], **Paul Taras**[1]

Abstract

We report the results of a study of the exclusive charmless semileptonic decays, $B^+ \to \eta^{(\prime)} \ell^+ \nu$ and $B^0 \to \pi^- \ell^+ \nu$, undertaken with approximately 464 million $B\overline{B}$ pairs collected at the $\Upsilon(4S)$ resonance with the BABAR detector. The analysis uses events in which the signal B decays are reconstructed with a loose neutrino reconstruction technique. We obtain partial branching fractions for $B^+ \to \eta \ell^+ \nu$ and $B^0 \to \pi^- \ell^+ \nu$ decays in three and twelve bins of q^2, respectively, from which we extract the $f_+(q^2)$ form-factor shapes and the total branching fractions $\mathcal{B}(B^+ \to \eta \ell^+ \nu)$ = $(3.61 \pm 0.45_{stat} \pm 0.44_{syst}) \times 10^{-5}$ and $\mathcal{B}(B^0 \to \pi^- \ell^+ \nu)$ = $(1.42 \pm 0.05_{stat} \pm 0.08_{syst}) \times 10^{-4}$. We also measure $\mathcal{B}(B^+ \to \eta^{\prime} \ell^+ \nu)$ = $(2.43 \pm 0.80_{stat} \pm 0.34_{syst}) \times 10^{-5}$. We obtain values of the magnitude of the CKM element $|V_{ub}|$ using three different QCD calculations.

[1]Université de Montréal

3.1 Introduction

3.1.1 Physics motives

In the Standard Model, quark flavor changes can only occur through weak interactions, via the coupling of a W gauge boson. Such couplings are proportional to the relevant CKM matrix elements. In particular, the probability of a b quark to decay into a u quark is proportional to $|V_{ub}|^2$.

The requirement that the CKM matrix V be unitary and the freedom to arbitrarily choose the global phases of the quark fields reduce the initial nine unknown complex elements of V to three real numbers and one phase, where the latter gives rise to CP violation [23]. The values of the CKM matrix elements measured independently have to satisfy this unitarity condition if the Standard Model is correct. Since $|V_{ub}|$ is the second poorest known element of the matrix [24], its precise measurement would help constrain the description of the weak interactions and CP violation by the Standard Model. The known present range of $|V_{ub}|$ is given by the dark green band in Fig. 3.1.

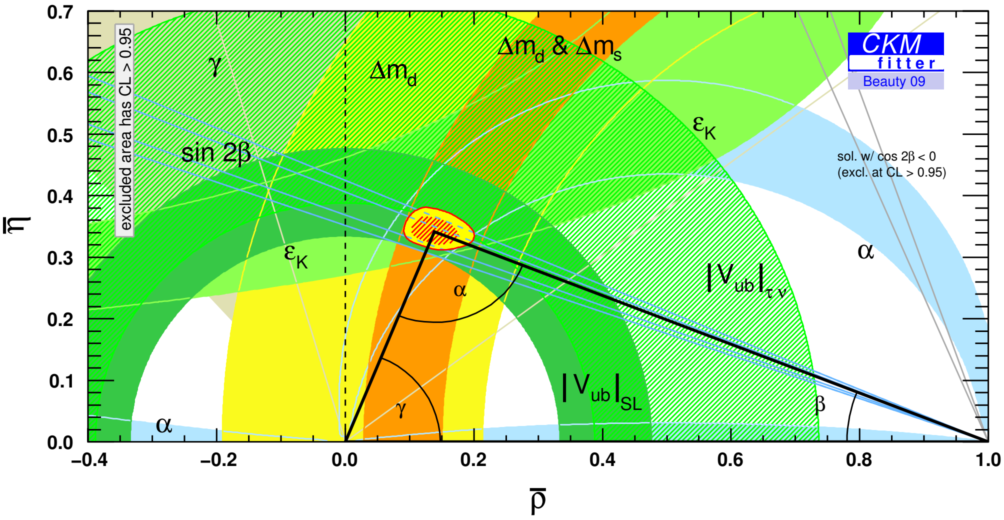

Figure 3.1 – Zoomed constraints in the $(\bar{\rho}, \bar{\eta})$ plane including the angle measurement of $\sin 2\beta$ (results as of Beauty 2009) [25].

Exclusive semileptonic B decays[2] such as $B^0 \to \pi^- \ell^+ \nu$ and $B^+ \to \eta^{(')} \ell^+ \nu$ transitions are interesting for many reasons. One of them is that they involve a $b \to u$ transition which is sensitive to the CKM matrix element $|V_{ub}|$. There is an abundant litterature on $|V_{ub}|$ and semileptonic B decays (for example [23, 24, 26]). In this section, we provide information on the link between the CKM matrix [27] element $|V_{ub}|$ and the exclusive semileptonic B decays, and on the main difficulty to extract $|V_{ub}|$ from the measurement of such decays. We also explain the importance to know the value of $|V_{ub}|$ as precisely as possible. The extraction of the value of $|V_{ub}|$ from different exclusive semileptonic decays could provide a possible clue as to why the value of $|V_{ub}|$ obtained in the $B^0 \to \pi^- \ell^+ \nu$ exclusive decay appears to be different from the one measured in inclusive semileptonic decays.

Another reason for the interest in $B^+ \to \eta^{(')} \ell^+ \nu$ decays is their sensitivity to $\eta - \eta'$ mixing and the effect of the $U(1)_A$ anomaly [28]. This anomaly is responsible for the large mass of the η' meson and induces potentially large flavour-singlet contributions. Fig. 3.2 shows a flavour-singlet contribution which is defined as the amplitude for producing either a pair of gluons or a quark-antiquark pair in a singlet state ($u\bar{u} + d\bar{d} + s\bar{s}$), followed by hadronization into an $\eta^{(')}$ meson.

For example, large branching fractions of inclusive $B \to \eta' X$ decays have been attributed to an enhanced flavour-singlet contribution [29].

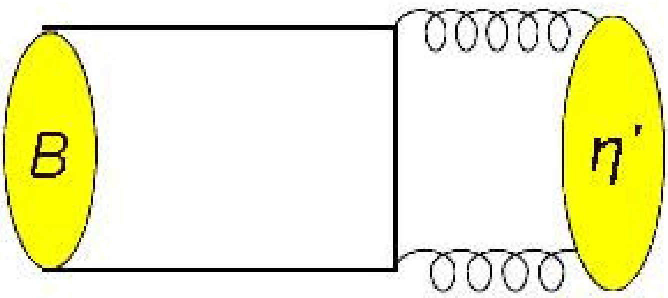

Figure 3.2 – Flavour-singlet contribution to a $B \to \eta^{'}$ transition.

The measurement of $|V_{ub}|$ requires the study of a $b \to u$ transition in a well-understood

[2]The charge conjugate decays are always implied throughout this document unless explicitly mentioned otherwise.

context. Semileptonic $b \to u\ell\nu$ decays are best for that purpose since they are much easier to understand than hadronic decays from a theoretical point of view, and much easier to study experimentally than purely leptonic decays because they are far more abundant. Fig. 3.3 shows the dominant Feynman diagram of electroweak interactions in the case of a $\overline{B}^0 \to \pi^+\ell^-\overline{\nu}$ decay. This figure also illustrates the strong interactions of the b and u quarks with the $\bar{d}$ quark of the B meson involved in the same decay. The non-perturbative QCD interactions between the quarks cannot be calculated from first principles.

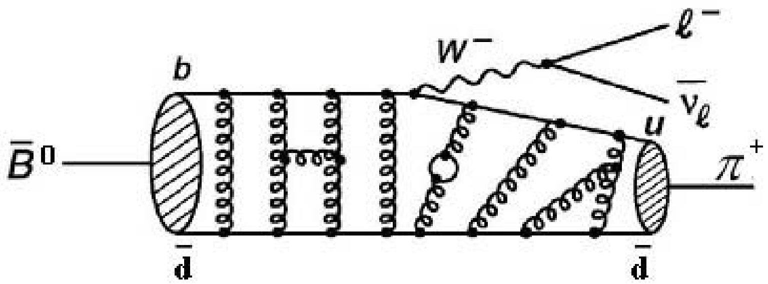

Figure 3.3 – Feynman diagram of electroweak and QCD interactions in a $\overline{B}^0 \to \pi^+\ell^-\overline{\nu}$ decay.

In exclusive analyses, there are important differences arising from the nature of the X_u meson produced in the decay of the B meson. If X_u is a vector meson (e.g. ρ, ω, ...), the decay of the B meson is expressed in terms of three QCD form factors[3], but if X_u is a pseudo-scalar meson (e.g. π, η, ...), the B meson decay is described by only one form factor[4] : $f_+(q^2)$, where q^2 is the momentum transfer squared.

Only the shape of $f_+(q^2)$ can be measured in a high statistics experiment. Its normalization needs to be given by theoretical calculations which suffer from relatively large uncertainties and, often, do not agree with each other. As a result, the normalization of the form factor(s) is the largest source of uncertainty in the extraction of $|V_{ub}|$ from the measurement of an exclusive $B \to X_u\ell\nu$ branching fraction. The theoretical predictions are currently more precise for $B^0 \to \pi^-\ell^+\nu$ decays than for any other exclusive $B \to X_u\ell\nu$ decays [24]. For $B^0 \to \pi^-\ell^+\nu$ decays, the most reliable calcu-

[3]In the limit of a massless lepton, a valid approximation for ℓ = e or even μ (see section 4.4 of [30]).
[4]Also in the limit of a massless lepton.

lation of $f_+(q^2)$ is obtained from unquenched lattice QCD [31, 32], but this technique can presently be used only at large q^2 ($> 16\ \mathrm{GeV}^2/c^4$). Experimentally, it is difficult to reconstruct a $B \to X_u \ell \nu$ decay at high q^2 where the hadron has very low momentum. The most reliable calculation of $f_+(q^2)$ for $B^+ \to \eta^{(')} \ell^+ \nu$ decays is currently provided by QCD sum rules on the light cone (LCSRs) including the gluonic singlet contributions (up to 20% for $B^+ \to \eta^{'} \ell^+ \nu$) [28], but this technique relies on approximations that are valid only at low q^2 ($< 16\ \mathrm{GeV}^2/c^4$). There is also a perturbative QCD approach [33] which finds that the flavour-singlet contribution is negligible for $B^+ \to \eta \ell^+ \nu$ but up to a few percent for $B^+ \to \eta^{'} \ell^+ \nu$.

Experimental data can be used to discriminate between various QCD calculations by measuring the $f_+(q^2)$ shape precisely. Such a measurement not only tests the approximations made in the calculations but it also leads to a smaller theoretical uncertainty on $|V_{ub}|$.

In this context, the present analysis of $B^0 \to \pi^- \ell^+ \nu$ and $B^+ \to \eta \ell^+ \nu$ decays will concentrate on obtaining an accurate measurement of the $f_+(q^2)$ shape in order to extract from the measurement of the partial $\mathcal{B}(B^0 \to \pi^- \ell^+ \nu)$ and partial $\mathcal{B}(B^+ \to \eta \ell^+ \nu)$ as precise a value of $|V_{ub}|$ as possible.

3.1.2 Physics observables measured in this analysis

The goal of this analysis is to measure the $f_+(q^2)$ shape in $B^0 \to \pi^- \ell^+ \nu$ and $B^+ \to \eta \ell^+ \nu$ decays as well as the total BFs $\mathcal{B}(B^0 \to \pi^- \ell^+ \nu)$ and $\mathcal{B}(B^+ \to \eta^{(')} \ell^+ \nu)$. The final q^2 spectrum is corrected for reconstruction effects by applying an unfolding algorithm on the raw $\tilde{q}^2$. The total BF is obtained from the sum of the partial BFs $\Delta\mathcal{B}(q^2)$, measured in twelve and three q^2 bins for the $B^0 \to \pi^- \ell^+ \nu$ and $B^+ \to \eta \ell^+ \nu$ decays, respectively. The q^2 shape of the signal is expressed as the spectrum of the partial branching fractions $\Delta\mathcal{B}(q^2)$, together with a covariance matrix giving the correlations between the values of the $\Delta\mathcal{B}(q^2)$. The measured $\Delta\mathcal{B}(q^2)$ spectra are also compared to the predictions of various QCD calculations, and fitted to model-dependent parametrizations of the $f_+(q^2)$ form factor. The values of the CKM matrix element $|V_{ub}|$ are then obtained from the fitted values of $\Delta\mathcal{B}(q^2)$. We extract the values of $|V_{ub} f_+(0)|$ from the $f_+(q^2)$ fit results, extrapolated to $q^2 = 0$.

3.1.3 Analysis strategy

3.1.3.1 Previous measurements

Values of $|V_{ub}|$ have already been extracted from the $\mathcal{B}(B^0 \to \pi^- \ell^+ \nu)$ by CLEO [34, 35], BABAR[36, 37] and BELLE [38]. The "loose neutrino reconstruction" used in our analysis has previously been used in a recent BABAR publication for $\mathcal{B}(B^0 \to \pi^- \ell^+ \nu)$ [39].

To reduce the uncertainty on the value of $|V_{ub}|$ contributed by the $f_+(q^2)$ dependence, our strategy has been to maximize the measured decay signal yields. This should lead to a better defined $f_+(q^2)$ shape and thus may allow us to discriminate between the various QCD models used to generate this shape. A precise experimental determination of the $f_+(q^2)$ shape also allows the extraction of $|V_{ub}|$ from only one well-calculated normalization point $f_+(0)$, with much reduced theoretical uncertainties.

The B tagging techniques on the other hand require cuts that result in a loss in detection efficiency and thus lead to signal yields that are too small to allow a precise measurement of the q^2 spectra of $B^0 \to \pi^- \ell^+ \nu$ and $B^+ \to \eta \ell^+ \nu$ decays with BABAR's runs 1-6 datasets [37, 38], even though they provide higher signal purity than with our approach. A large signal yield and thus small statistical uncertainties are the main motivations for implementing the loose neutrino reconstruction technique.

3.1.3.2 The loose neutrino reconstruction technique

The loose neutrino reconstruction [39] is largely inspired by the "traditional" neutrino reconstruction : both methods use the events' missing momentum as an approximation to the signal neutrino. The essential difference between the two approaches is that the tight neutrino quality cuts which ensure that the neutrino properties are well taken into account when computing $q^2 = (P_\ell + P_\nu)^2$ are avoided in the loose neutrino reconstruction technique. In this analysis, we calculate instead the momentum transfer as $q^2 = (P_B - P_{X_u})^2$, where X_u represents the hadron in the semi-leptonic decay. This difference may appear to be small, but results in a significantly increased signal efficiency. When using $q^2 = (P_\ell + P_\nu)^2$, the resolution of q^2 is completely dominated by the reconstructed neutrino : the higher the q^2 resolution, the more stringent the neutrino quality cuts. It turns out that the neutrino quality cuts depend as much on the signal B decay as on the other B decay (B mesons are always produced in pairs at B factories). As a consequence, many of the tight neutrino quality cuts are not good at discriminating signal from background. They do improve the $q^2 = (P_\ell + P_\nu)^2$ resolution but not the signal/background (S/B) ratio, and they lead to an important signal yield loss. Tight neutrino quality cuts have also resulted in relatively large systematic uncertainties in the past because of their sensitivity to many aspects of the full event simulation. In an analysis with a large number of q^2 bins, this effect becomes important. In the loose neutrino reconstruction, the reconstructed neutrino does not have to match the real signal neutrino with a good resolution because of the use of the relation $q^2 = (P_B - P_{X_u})^2$. Details on the reconstruction of $q^2 = (P_B - P_{X_u})^2$ are given in Sect. 3.3.3.

The process of reconstructing the neutrino can also be used to reject backgrounds quite efficiently. For example, the cuts on the quantities ΔE and $m_{\rm ES}$ [40] which require that the sum of the reconstructed neutrino, X_u and ℓ energies and momenta be compatible with $B \to X_u \ell \nu$ signal decays are among the most useful ones in rejecting the backgrounds in this analysis.

3.1.3.3 Signal extraction

As a result of its loose cuts, the loose neutrino reconstruction technique leads to high signal yields. These high signal yields are of course accompanied by high background yields. From a statistical point of view, high signal yields can compensate low S/B ratios to give small uncertainties. However, with a cut and count approach, these high background yields result in large systematic uncertainties because some of them are poorly known.

Consequently, the signal and background yields are extracted using a fit in the present analysis. In fact, the high background yields are useful since it makes it possible to fit them in separate categories and in several $\tilde{q}^2$ regions[5]. For example, the ΔE and m_{ES} shapes corresponding to the large number of continuum and $b \to u\ell\nu$ background events can easily be fitted separately. The high statistics provided by our technique also have the advantage that the off-resonance data control sample's yield can be known with a relatively good statistical precision. This is very useful to control the continuum-related systematic errors, and allows us to make a more precise comparison between data and simulation. For these reasons, the loose neutrino reconstruction technique results in high signal yields with small statistical uncertainties and relatively small systematic uncertainties, as shown in our previous publication [39]. It is thus ideally suited for a measurement of the $f_+(q^2)$ shapes as well as the BFs of the $B^0 \to \pi^-\ell^+\nu$ and $B^+ \to \eta^{(')}\ell^+\nu$ decays.

The signal η meson is reconstructed in its decay [24] to two photons $\mathcal{B}(\eta \to \gamma\gamma) = (39.30 \pm 0.20)\%$ and its decay to three pions $\mathcal{B}(\eta \to \pi^+\pi^-\pi^0) = (22.73 \pm 0.28)\%$. These two decay channels together contribute approximately 62% of the total decay rate of the η. The signal η' meson is reconstructed in its decay [24] $\mathcal{B}(\eta' \to \eta\pi^+\pi^-) = (44.6 \pm 1.4)\%$, where the η is reconstructed via the two decay channels described above. These two decays contribute about 28% of the total decay rate of the η'. An additionnal 29% from the $\eta' \to \rho^0\gamma$ could have been added, but this decay comes with a large background which is difficult to remove when using the loose neutrino reconstruction technique and it will not be considered in our analysis.

[5] $\tilde{q}^2$ defined in Sect. 3.1

3.2 Data samples

All our measurements were made with real and simulated data reconstructed with BABAR's Release 22 software, skimmed with the XSLBtoXulnuFilter software [41] and analyzed with the analysis-43 release. The simulation was done with BABAR's SP8 (Runs 1-5) and SP9 (Run 6) software releases. After the discovery of a muon strip multiplicity bug in Run 6 dataset, we reproduced a new dataset without the bug for Run 6.

The following samples are used in this analysis :

- Runs 1 - 6 on-resonance data ($\approx 422.6 fb^{-1}$ which corresponds, according to the B-counting algorithm [42], to 464 million $B\overline{B}$ decays) ;
- Runs 1 - 6 off-resonance data ($\approx 44.1 fb^{-1}$) taken at a center-of-mass energy approximately 40 MeV below the $\Upsilon(4S)$ resonance energy ;
- Signal SP8/SP9 FLATQ2 [30] $B^0 \rightarrow \pi^-\ell^+\nu$ and $B^+ \rightarrow \eta^{(\prime)}\ell^+\nu$ Monte Carlo (SP-4764 and SP-4759,(SP-4760), respectively) and $B^0 \rightarrow \pi^-\ell^+\nu$ Monte Carlo with PHOTOS turned off (SP-10106) :
  - 1954K $B^0 \rightarrow \pi^-\ell^+\nu$ / $\bar{B}^0 \rightarrow X$ (and its complex conjugate decays), where X stands for any possible final state of a $\bar{B}^0(B^0)$ decay ($\approx 6276.5 fb^{-1}$) ;
  - 1941K $B^+ \rightarrow \eta^{(\prime)}\ell^+\nu$ / $B^- \rightarrow X$ (and its complex conjugate decays), where X stands for any possible final state of a $B^-(B^+)$ decay ($\approx 23076.2 fb^{-1}$) ;
  - 2149K $B^0 \rightarrow \pi^-\ell^+\nu$ / $\bar{B}^0 \rightarrow X$ (and its complex conjugate decays) with PHOTOS turned off, where X stands for any possible final state of a $\bar{B}^0(B^0)$ decay ($\approx 6902.9 fb^{-1}$) ;
- SP8/SP9 MC backgrounds :
  - $\sim$711M generic $B^0\bar{B}^0$ decays[6] ($\approx 1336.1 fb^{-1}$) ;
  - $\sim$725M generic B^+B^- decays[7] ($\approx 1278.5 fb^{-1}$) ;
  - $\sim$17.1M non-resonant $b \rightarrow u\ell\nu$ decays ($\approx 2199.3 fb^{-1}$) ;
  - $\sim$1126M $c\bar{c}$ decays ($\approx 866.5 fb^{-1}$) ;
  - $\sim$932M $u\bar{u}/d\bar{d}/s\bar{s}$ decays ($\approx 446.0 fb^{-1}$) ;

[6] The $B^0 \rightarrow \pi^-\ell^+\nu$ signal events have been removed from the $B^0\bar{B}^0$ samples.

[7] The $B^+ \rightarrow \eta^{(\prime)}\ell^+\nu$ signal events have been removed from the B^+B^- samples.

– $\sim$394M $\tau^+\tau^-$ decays ($\approx 428.9 fb^{-1}$).

The following assumptions were made to obtain the integrated luminosities corresponding to the MC samples :

– We used the most recent values of the $\Upsilon(4S)$ branching fractions : $BF(\Upsilon(4S) \rightarrow B^0\bar{B}^0) = 48.4\%$ and $BF(\Upsilon(4S) \rightarrow B^+B^-) = 51.6\%$ [24] ;
– For the number of $B\bar{B}$ pairs, we used the values given by the B counting algorithm [42]. For each run, we obtain the number of $B\bar{B}$ pairs per fb^{-1} :
Run 1 : 1098151.6 $B\bar{B}$ pairs per fb^{-1}.
Run 2 : 1103455.1 $B\bar{B}$ pairs per fb^{-1}.
Run 3 : 1102246.6 $B\bar{B}$ pairs per fb^{-1}.
Run 4 : 1101391.2 $B\bar{B}$ pairs per fb^{-1}.
Run 5 : 1104514.5 $B\bar{B}$ pairs per fb^{-1}.
Run 6 : 1077016.8 $B\bar{B}$ pairs per fb^{-1}.

– For MC signal events, we assumed that $\mathcal{B}(B^0 \rightarrow \pi^-\ell^+\nu) = 1.46 \times 10^{-4}$ and $\mathcal{B}(B^+ \rightarrow \eta^{(\prime)}\ell^+\nu) = 3.01 \times 10^{-5}$;
– For non-resonant $b \rightarrow u\ell\nu$ decays, we subtract all the resonant $b \rightarrow u\ell\nu$ BFs from the total inclusive $B \rightarrow X_u\ell\nu$ BF $= 0.229 \times 10^{-2}$ [43] ;
– For $u\bar{u}/d\bar{d}/s\bar{s}$ and $c\bar{c}$, we used the cross-sections given in Ref. [44], yielding respectively 2.09M and 1.3M events per fb^{-1} ;
– For $\tau^+\tau^-$, we used the number given in Ref. [45] : 919k events per fb^{-1}.
– The values of the branching fractions of all processes relevant to the decays under study are listed in Table 3.25, both those used in the MC simulation and those used in our analysis.

3.3 Method

3.3.1 Overview of the analysis steps

Final results are obtained from a two-dimensional fit after performing an optimized event selection (Sect. 3.3.2). In each $\tilde{q}^2$ region, the two-dimensional ΔE-m_{ES} distribution is fitted to extract the signal yields as a function of $\tilde{q}^2$. The raw $\tilde{q}^2$ distributions are then unfolded to correct for the bias and resolution effects of the reconstruction. The unfolded q^2 yields are divided by the signal reconstruction efficiency in each q^2 bin to obtain the partial BFs $\Delta\mathcal{B}(q^2)$ in twelve and three q^2 regions for the $B^0 \to \pi^- \ell^+ \nu$ and $B^+ \to \eta \ell^+ \nu$ decays, respectively, and the total BF in one q^2 region for the $B^+ \to \eta^{'} \ell^+ \nu$ decay. The total BFs for the first two channels are obtained from the sums of the $\Delta\mathcal{B}(q^2)$. The fit also yields two covariance matrices for the $B^0 \to \pi^- \ell^+ \nu$ and $B^+ \to \eta \ell^+ \nu$ channels, one for the statistical uncertainties and the other one for the systematic uncertainties, which include the correlations between the values of the $\Delta\mathcal{B}(q^2)$ measured in the different q^2 bins.

3.3.2 Event selection

All the cuts attempt to extract the signal from background processes that look similar to the signal in $B^0 \rightarrow \pi^-\ell^+\nu$ as well as in $B^+ \rightarrow \eta^{(')}\ell^+\nu$ decays. The three main sources of background are semileptonic $b \rightarrow c\ell\nu$ decays with a D meson decaying semileptonically, semileptonic $b \rightarrow u\ell\nu$ decays and continuum events. The cuts can be subdivided in six classes : skim preselection, signal lepton and pion identification, kinematic consistency of the X_u meson and ℓ lepton momenta, continuum rejection, $b \rightarrow c\ell\nu$ rejection and neutrino reconstruction. When there are several signal candidates in an event after applying all the cuts for a given decay channel, we select only one candidate and reject the others (more details in Sect. 3.3.2.7).

As explained in Sect. 3.3.2.3, the signal X_u and ℓ tracks are fitted to a common vertex. This fit re-evaluates the X_u and ℓ track parameters by constraining both tracks to share a common origin in the three-dimensional space. Except for the skim preselection, we are always using the resulting X_u and ℓ refitted momenta.

An overview of all the cuts used in this analysis for $B^+ \rightarrow \eta^{'}\ell^+\nu$, $B^+ \rightarrow \eta\ell^+\nu$ and $B^0 \rightarrow \pi^-\ell^+\nu$ is given in Tables 3.1, 3.2 and 3.3, respectively. The definition of each cut is given in Subsects. 3.3.2.1 to 3.3.2.7. The procedure that leads to the particular choice of a value for each cut is described in Subsects. 3.3.2.8 and 3.3.2.9. The values of the $\tilde{q}^2$-dependent cuts for $B^+ \rightarrow \eta^{'}\ell^+\nu$, $B^+ \rightarrow \eta\ell^+\nu$ and $B^0 \rightarrow \pi^-\ell^+\nu$ are presented in Figs. 3.4, 3.5 and 3.6, respectively. The background reduction power of each cut is illustrated in Sect. I.1.5 of the appendix. The composition (according to MC simulation) of the final sample in the *fit region* is given in Tables 3.4 and 3.5 for $B^+ \rightarrow \eta^{'}\ell^+\nu$, Tables 3.6 and 3.7 for $B^+ \rightarrow \eta\ell^+\nu$ and Table 3.8 for $B^0 \rightarrow \pi^-\ell^+\nu$ decays, while the composition of the final sample in the *signal region* is given in Tables 3.9 and 3.10 for $B^+ \rightarrow \eta^{'}\ell^+\nu$, Tables 3.11 and 3.12 for $B^+ \rightarrow \eta\ell^+\nu$ and Table 3.13 for $B^0 \rightarrow \pi^-\ell^+\nu$ decays.

Tableau 3.1 – Summary of all $B^+ \to \eta^{'} \ell^+ \nu$ signal candidate selections.

XSLBToXulnuFilter skim
$-1.0 < \cos\theta_{BY} < 1.0$
$0.92 < m_{\eta'} < 0.98$ GeV/c^2
$0.51 < m_\eta < 0.57$ GeV/c^2
$Prob(\chi^2)\ Y > 0.01$
$0.41 < \theta_e, \theta_\pi < 2.46\ rad$
$0.45 < \theta_\mu < 2.36\ rad$
$-1.0 < \Delta E < 1.0$ GeV
$5.19 < m_{ES} < 5.29$ GeV/c^2
$\cos\theta_\ell < 0.85$ for all values of $\tilde{q}^2$
$0 < \tilde{q}^2 < 16$ GeV^2/c^4
(The three following cut variables are $\tilde{q}^2$-dependent, where $\tilde{q}^2$ is given in units of GeV^2/c^4)
$M^2_{miss}/2E_{miss} > -0.3$ GeV/c^4 for all values of $\tilde{q}^2$
$M^2_{miss}/2E_{miss} < 0.35 * \tilde{q}^2 + 0.325$ GeV/c^4, $\tilde{q}^2 < 2.5$ GeV^2/c^4
$M^2_{miss}/2E_{miss} < 1.2$ GeV/c^4, $2.5 < \tilde{q}^2 < 4.5$ GeV^2/c^4
$M^2_{miss}/2E_{miss} < -0.1 * \tilde{q}^2 + 1.65$ GeV/c^4, $\tilde{q}^2 > 4.5$ GeV^2/c^4
$\cos\theta_{thrust} < 0.05 * \tilde{q}^2 + 0.575$, $\tilde{q}^2 < 6.5$ GeV^2/c^4
$\cos\theta_{thrust} < 0.9$, $6.5 < \tilde{q}^2 < 12.5$ GeV^2/c^4
$\cos\theta_{thrust} < -0.05 * \tilde{q}^2 + 1.525$, $\tilde{q}^2 > 12.5$ GeV^2/c^4
$\theta_{miss} > -0.1 * \tilde{q}^2 + 0.45\ rad$, $\tilde{q}^2 < 2.5$ GeV^2/c^4
$\theta_{miss} > 0.2\ rad$, $2.5 < \tilde{q}^2 < 5.5$ GeV^2/c^4
$\theta_{miss} > 0.05 * \tilde{q}^2 - 0.075\ rad$, $\tilde{q}^2 > 5.5$ GeV^2/c^4
Best candidate : largest value of $\cos\theta_\ell$

Tableau 3.2 – Summary of all $B^+ \to \eta\ell^+\nu$ signal candidate selections.

XSLBToXulnuFilter skim
$-1.0 < \cos\theta_{BY} < 1.0$
$0.51 < m_\eta < 0.57$ GeV/c^2 for $\eta \to \gamma\gamma$
$0.52 < m_\eta < 0.57$ GeV/c^2 for $\eta \to \pi^+\pi^-\pi^0$
$Prob(\chi^2)\ Y > 0.01$
$0.41 < \theta_e, \theta_\pi < 2.46\, rad$
$0.45 < \theta_\mu < 2.36\, rad$
$-1.0 < \Delta E < 1.0$ GeV
$5.19 < m_{ES} < 5.29$ GeV/c^2
$\lvert\cos\theta_V\rvert < 0.95$
$0 < \tilde{q}^2 < 16$ GeV$^2/c^4$
(The four following cut variables are $\tilde{q}^2$-dependent, where $\tilde{q}^2$ is given in units of GeV$^2/c^4$)
$\cos\theta_\ell < 0.9$ for all values of $\tilde{q}^2$
$\cos\theta_\ell > 0.00629 * \tilde{q}^4 - 0.119 * \tilde{q}^2 - 0.252$
$M^2_{miss}/2E_{miss} < 0.8$ GeV/c^4, $\tilde{q}^2 < 7.5$ GeV$^2/c^4$
$M^2_{miss}/2E_{miss} < -0.05 * \tilde{q}^2 + 1.175$ GeV/c^4, $7.5 < \tilde{q}^2 < 16.0$ GeV$^2/c^4$
$\cos\theta_{thrust} < 0.05 * \tilde{q}^2 + 0.6$, $\tilde{q}^2 < 5.0$ GeV$^2/c^4$
$\cos\theta_{thrust} < 0.85$, $5.0 < \tilde{q}^2 < 16.0$ GeV$^2/c^4$
$\cos\theta_{miss} < 0.92$, $\tilde{q}^2 < 11.0$ GeV$^2/c^4$
$\cos\theta_{miss} < 0.88$, $11.0 < \tilde{q}^2 < 16.0$ GeV$^2/c^4$
Best candidate : largest value of $\cos\theta_\ell$

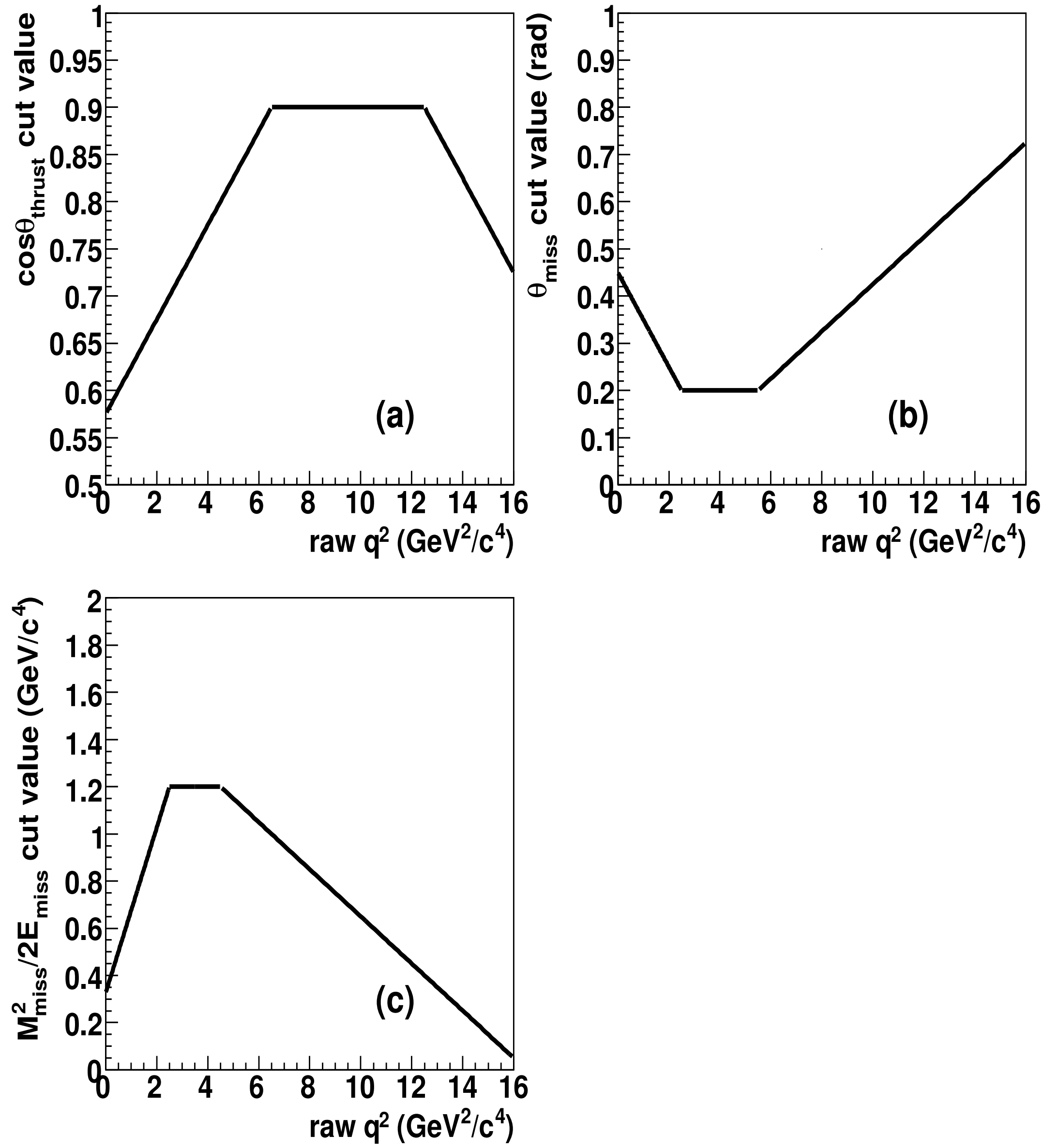

Figure 3.4 – Values of statistically optimal cuts of (a) $\cos\theta_{thrust}$, (b) θ_{miss} and (c) $M^2_{miss}/2E_{miss}$, based on the maximization of the quantity $S/\sqrt{(S+B)}$ in the $B^+ \rightarrow \eta^{'}\ell^+\nu$ signal region (see Sect. 3.3.2.9). The vertical axis represents the cut value for a given $\tilde{q}^2$ value. We cut an event if the values are above the curve for (a,c) and below the curve for (b).

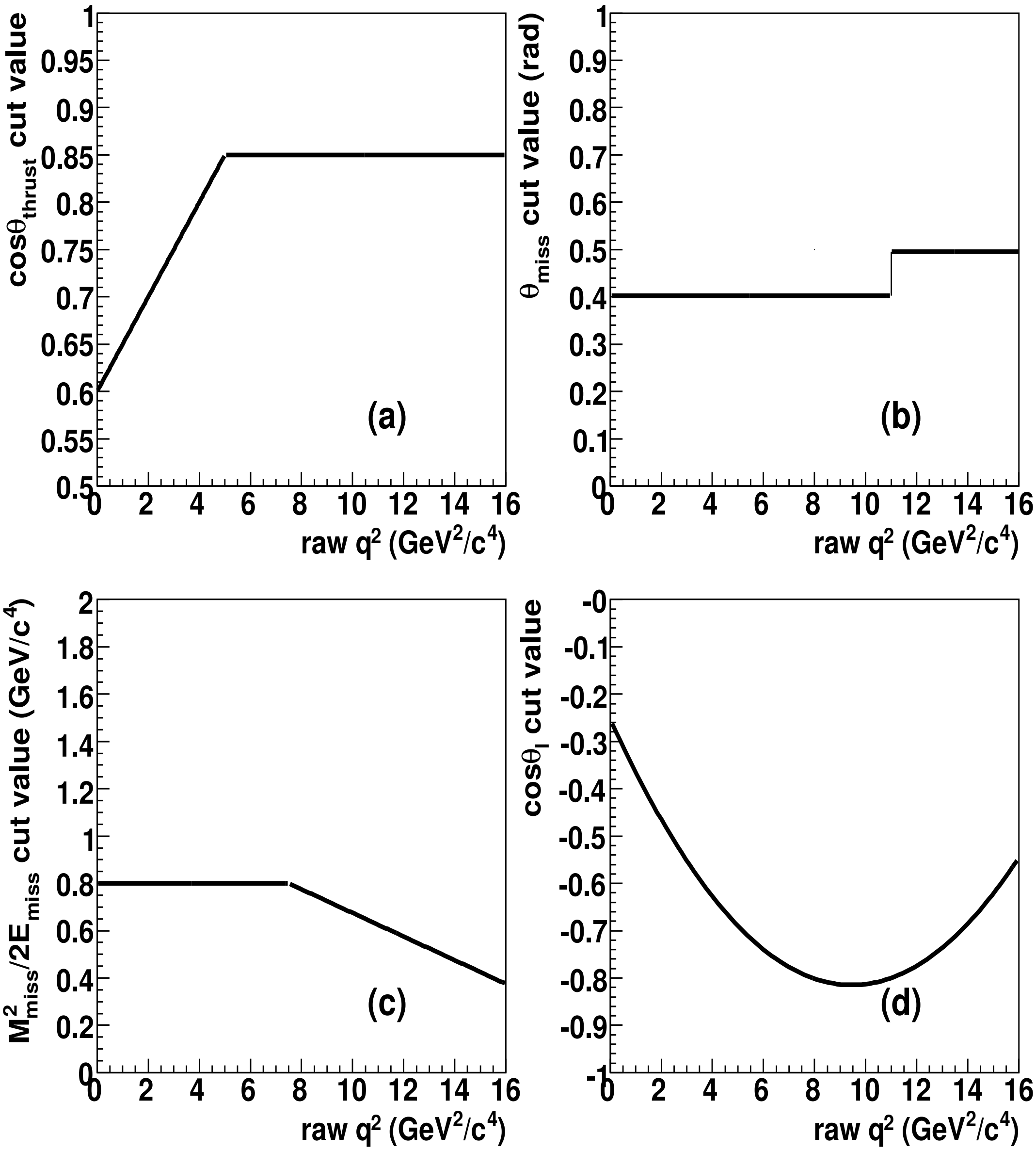

Figure 3.5 – Values of statistically optimal cuts of (a) $\cos\theta_{thrust}$, (b) θ_{miss}, (c) $M^2_{miss}/2E_{miss}$ and (d) $\cos\theta_l$, based on the maximization of the quantity $S/\sqrt{(S+B)}$ in the $B^+ \to \eta\ell^+\nu$ signal region (see Sect. 3.3.2.9). The vertical axis represents the cut value for a given $\tilde{q}^2$ value. We cut an event if the values are above the curve for (a,c) and below the curve for (b,d).

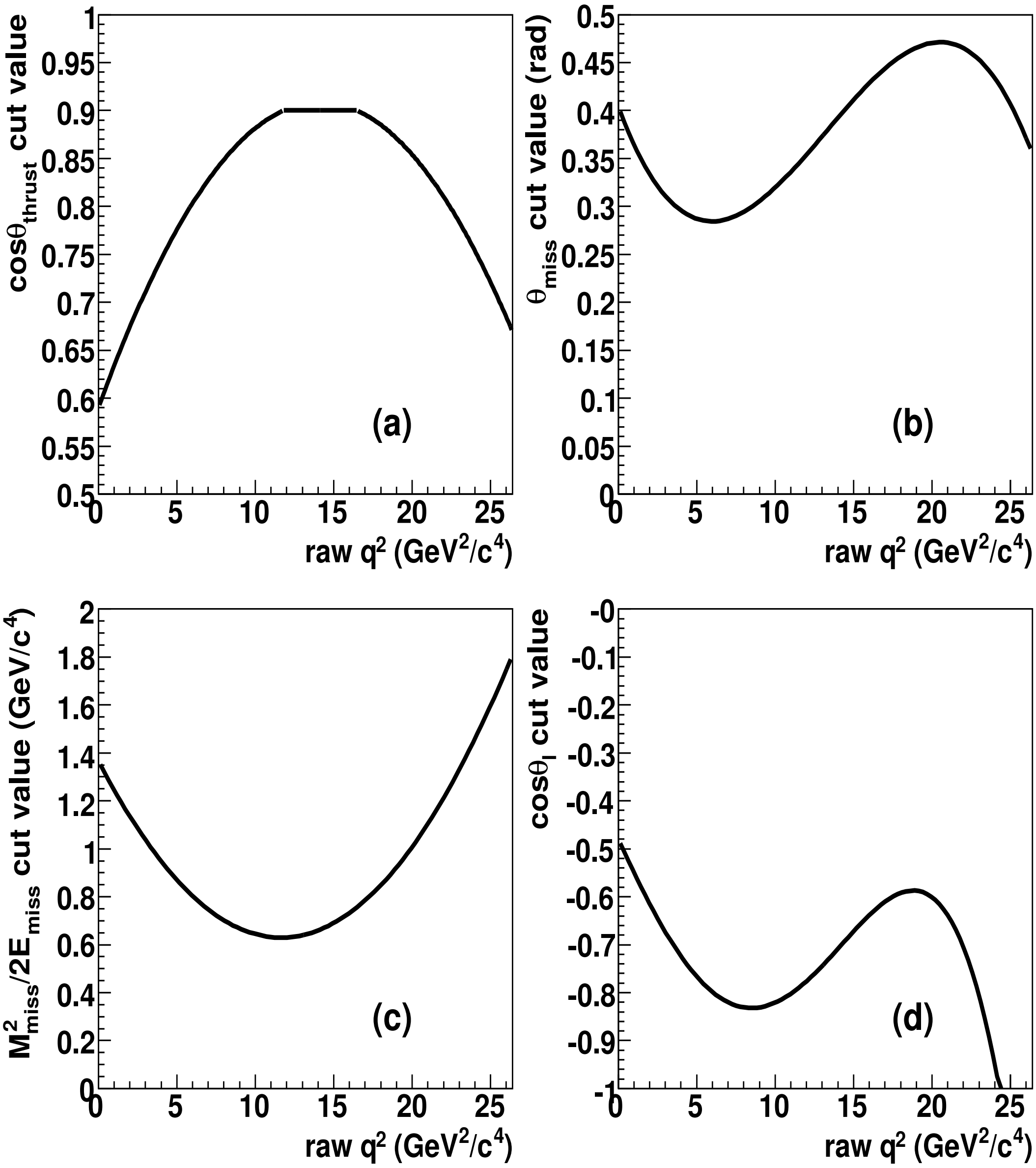

Figure 3.6 – Values of statistically optimal cuts of (a) $\cos\theta_{thrust}$, (b) θ_{miss}, (c) $M^2_{miss}/2E_{miss}$ and (d) $\cos\theta_l$, based on the maximization of the quantity $S/\sqrt{(S+B)}$ in the $B^0 \to \pi^-\ell^+\nu$ signal region (see Sect. 3.3.2.9). The vertical axis represents the cut value for a given $\tilde{q}^2$ value. We cut an event if the values are above the curve for (a,c) and below the curve for (b,d).

Tableau 3.3 – Summary of all $B^0 \rightarrow \pi^- \ell^+ \nu$ signal candidate selections.

XSLBToXulnuFilter skim
$-1.0 < \cos\theta_{BY} < 1.0$
$Prob(\chi^2)\ Y > 0.01$
$-1.0 < \Delta E < 1.0$ GeV
$5.19 < m_{ES} < 5.29$ GeV/c^2
$0.41 < \theta_e, \theta_\pi < 2.46\, rad$
$0.45 < \theta_\mu < 2.36\, rad$
BhaBhaVeto, J/PsiVeto and GammaConvVeto
(The four following cut variables are $\tilde{q}^2$-dependent, where $\tilde{q}^2$ is given in units of GeV$^2/c^4$)
$\cos\theta_\ell < 0.85$ for all values of $\tilde{q}^2$
$\cos\theta_\ell > -0.0000167 * \tilde{q}^8 + 0.000462 * \tilde{q}^6 + 0.000656 * \tilde{q}^4 - 0.0701 * \tilde{q}^2 - 0.48$
$M^2_{miss}/2E_{miss} > -0.5$ GeV/c^4 for all values of $\tilde{q}^2$
$M^2_{miss}/2E_{miss} < 0.00544 * \tilde{q}^4 - 0.127 * \tilde{q}^2 + 1.37$ GeV/c^4
$\cos\theta_{thrust} < 0.9$ for all values of $\tilde{q}^2$
$\cos\theta_{thrust} < -0.00159 * \tilde{q}^4 + 0.0451 * \tilde{q}^2 + 0.59$
$\theta_{miss} > -0.000122 * \tilde{q}^6 + 0.00483 * \tilde{q}^4 - 0.0446 * \tilde{q}^2 + 0.405\, rad$
Best candidate : largest value of $\cos\theta_\ell$

Tableau 3.4 – Sample composition of the ΔE-$m_{\rm ES}$ *fit region* for $B^+ \rightarrow \eta' \ell^+ \nu$ ($\eta' \rightarrow \eta\pi^+\pi^-$ and $\eta \rightarrow \gamma\gamma$) after all cuts. The ranges of the fit region are $-1.0 < \Delta E < 1.0$ GeV and $5.19 < m_{ES} < 5.29$ GeV/c^2.

Event type	Yields				Sample fraction (%)
	electrons		muons		
	real	fake	real	fake	
$B^+ \rightarrow \eta' \ell^+ \nu$	104.3	0.0	70.8	0.0	4.6
$B^+ \rightarrow \eta \ell^+ \nu$	1.6	0.0	1.3	0.0	0.1
non-res. $b \rightarrow u \ell \nu$	98.9	0.0	76.1	0.0	4.6
other $b \rightarrow u \ell \nu$	14.5	0.0	11.8	0.0	0.7
$B \rightarrow D \ell \nu$	276.8	1.3	206.3	2.6	12.7
$B \rightarrow D^* \ell \nu$	1047.5	0.4	824.6	1.9	48.8
other $b \rightarrow c \ell \nu$	177.4	0.0	124.2	0.7	7.9
$B \rightarrow hadrons$	191.5	9.1	34.2	45.4	7.3
continuum	226.3	13.2	116.7	160.9	13.5
total (MC)	2138.9	24.0	1465.9	211.5	100.0
on-res data	1960.0		1557.0		-
off-res data	239.5		277.8		-

Tableau 3.5 – Sample composition of the ΔE-$m_{\rm ES}$ *fit region* for $B^+ \to \eta^{'} \ell^+ \nu$ ($\eta' \to \eta\pi^+\pi^-$ and $\eta \to \pi^+\pi^-\pi^0$) after all cuts. The ranges of the fit region are $-1.0 < \Delta E < 1.0$ GeV and $5.19 < m_{ES} < 5.29$ GeV/c^2.

Event type	Yields				Sample fraction
	electrons		muons		
	real	fake	real	fake	(%)
$B^+ \to \eta^{'} \ell^+ \nu$	36.4	0.1	25.4	0.0	2.9
$B^+ \to \eta \ell^+ \nu$	0.3	0.0	0.2	0.0	0.0
non-res. $b \to u\ell\nu$	61.2	0.0	50.0	0.4	5.2
other $b \to u\ell\nu$	2.1	0.0	2.0	0.0	0.2
$B \to D\ell\nu$	108.2	0.0	74.2	0.0	8.5
$B \to D^*\ell\nu$	711.0	0.0	577.4	0.1	60.4
other $b \to c\ell\nu$	94.2	0.0	80.2	1.6	8.2
$B \to hadrons$	102.4	1.6	16.8	24.8	6.8
continuum	77.5	6.3	36.4	43.0	7.6
total (MC)	1193.3	7.9	862.5	69.8	100.0
on-res data	868.0		677.0		-
off-res data	86.2		86.2		-

Tableau 3.6 – Sample composition of the ΔE-$m_{\rm ES}$ *fit region* for $B^+ \to \eta \ell^+ \nu$ ($\eta \to \gamma\gamma$) after all cuts. The ranges of the fit region are $-1.0 < \Delta E < 1.0$ GeV and $5.19 < m_{ES} < 5.29$ GeV/c^2.

Event type	Yields				Sample fraction
	electrons		muons		
	real	fake	real	fake	(%)
$B^+ \to \eta \ell^+ \nu$	305.4	0.0	222.7	0.1	3.2
$B^+ \to \eta^{'} \ell^+ \nu$	3.3	0.0	4.0	0.0	0.0
non-res. $b \to u\ell\nu$	569.4	0.1	462.9	1.8	6.2
other $b \to u\ell\nu$	340.3	0.0	260.8	2.5	3.6
$B \to D\ell\nu$	1224.7	0.3	934.6	7.3	13.1
$B \to D^*\ell\nu$	3631.6	0.0	2954.1	6.0	39.8
other $b \to c\ell\nu$	492.5	0.2	387.0	7.8	5.4
$B \to hadrons$	494.0	7.8	146.7	215.6	5.2
continuum	1390.2	133.6	636.2	1713.1	23.4
total (MC)	8451.5	142.1	6009.0	1954.2	100.0
on-res data	7981.0		7510.0		-
off-res data	1523.1		2346.9		-

Tableau 3.7 – Sample composition of the ΔE-$m_{\rm ES}$ *fit region* for $B^+ \to \eta\ell^+\nu$ ($\eta \to \pi^+\pi^-\pi^0$) after all cuts. The ranges of the fit region are $-1.0 < \Delta E < 1.0$ GeV and $5.19 < m_{ES} < 5.29$ GeV/c^2.

Event type	Yields				Sample fraction
	electrons		muons		
	real	fake	real	fake	(%)
$B^+ \to \eta\ell^+\nu$	99.3	0.0	72.1	0.0	2.0
$B^+ \to \eta^{'}\ell^+\nu$	3.4	0.0	1.9	0.0	0.1
non-res. $b \to u\ell\nu$	285.5	0.0	209.1	0.2	5.7
other $b \to u\ell\nu$	42.0	0.0	36.9	0.0	0.9
$B \to D\ell\nu$	678.5	0.3	513.4	4.3	13.7
$B \to D^*\ell\nu$	2583.9	0.6	2053.4	5.4	53.1
other $b \to c\ell\nu$	431.3	0.0	301.6	5.0	8.4
$B \to hadrons$	275.8	2.4	58.9	99.8	5.0
continuum	277.5	18.5	174.6	515.9	11.3
total (MC)	4677.4	21.8	3421.9	630.6	100.0
on-res data	4655.0		3806.0		-
off-res data	297.0		689.7		-

Tableau 3.8 – Sample composition of the ΔE-m_{ES} *fit region* for $B^0 \to \pi^- \ell^+ \nu$ after all cuts. The ranges of the fit region are $-1.0 < \Delta E < 1.0$ GeV and $5.19 < m_{ES} < 5.29$ GeV/c^2.

Event type	Yields					Sample fraction (%)
	electrons		muons		total	
	real	fake	real	fake		
$B^0 \to \pi^- \ell^+ \nu$ same B	6465.6	2.9	4652.3	84.9	11205.7	7.1
$B^0 \to \pi^- \ell^+ \nu$ both B	635.7	0.7	513.5	17.0	1166.9	0.7
$B^+ \to \eta \ell^+ \nu$ same B	14.0	0.0	12.3	0.0	26.3	0.0
$B^+ \to \eta \ell^+ \nu$ both B	83.8	0.0	59.5	0.0	143.3	0.1
$B^+ \to \eta^{'} \ell^+ \nu$ same B	12.7	0.0	12.1	0.0	24.8	0.0
$B^+ \to \eta^{'} \ell^+ \nu$ both B	13.4	0.0	12.1	0.0	25.5	0.0
$B \to \rho \ell \nu$ same B	4918.7	0.4	3847.1	35.5	8801.7	5.6
$B \to \rho \ell \nu$ both B	1744.1	1.8	1461.4	6.5	3213.8	2.0
$B \to \omega \ell \nu$ same B	237.5	0.2	211.0	0.5	449.2	0.3
$B \to \omega \ell \nu$ both B	435.2	0.0	361.5	0.0	796.7	0.5
non-res. $b \to u \ell \nu$ same B	6211.1	5.3	4727.9	63.4	11007.7	7.0
non-res. $b \to u \ell \nu$ both B	3980.4	0.0	3181.8	7.8	7170.0	4.6
other $b \to u \ell \nu$ same B	66.3	0.0	52.6	0.4	119.3	0.1
other $b \to u \ell \nu$ both B	684.2	0.0	550.4	0.0	1234.6	0.8
$B \to D \ell \nu$ same B	5439.2	2.7	3817.9	124.9	9384.7	6.0
$B \to D \ell \nu$ both B	4459.9	3.4	3111.8	84.9	7660.0	4.9
$B \to D^* \ell \nu$ same B	6452.7	5.0	4860.6	74.9	11393.2	7.2
$B \to D^* \ell \nu$ both B	21101.9	4.1	15655.9	59.2	36821.1	23.4
$B \to D^{**} \ell \nu$ same B	347.0	0.5	262.7	20.0	630.2	0.4
$B \to D^{**} \ell \nu$ both B	3326.2	0.7	1930.3	39.1	5296.3	3.4
other $b \to c \ell \nu$ same B	0.0	0.3	0.0	0.5	0.8	0.0
other $b \to c \ell \nu$ both B	8.7	0.0	4.8	10.2	23.7	0.0
$B \to hadrons\ same\ B$	3859.8	57.0	2758.2	1489.3	8164.3	5.2
$B \to hadrons\ both\ B$	1032.9	65.1	580.0	1231.1	2909.1	1.8
total B decays same B	34024.6	74.3	25214.8	1894.2	61207.9	38.8
total B decays both B	37506.4	75.7	27423.0	1455.8	66460.9	42.2
continuum	10716.1	1066.3	4944.3	13160.2	29886.9	19.0
total (MC)	82247.3	1216.3	57582.1	16510.3	157556.0	100.0
on-resonance data	78001.0		69528.0		147529.0	-
off-resonance data	11782.3		18104.6		29886.9	-

Tableau 3.9 – Sample composition of the ΔE-m_{ES} *signal region* for $B^+ \to \eta^{'}\ell^+\nu$ ($\eta' \to \eta\pi^+\pi^-$ and $\eta \to \gamma\gamma$) after all cuts, where the signal region lies in the ranges $-0.16 < \Delta E < 0.20$ GeV and $m_{ES} > 5.2675$ GeV/c^2.

Event type	Yields				Sample fraction
	electrons		muons		
	real	fake	real	fake	(%)
$B^+ \to \eta^{'}\ell^+\nu$	32.0	0.0	21.4	0.0	21.3
$B^+ \to \eta\ell^+\nu$	0.8	0.0	0.1	0.0	0.4
non-res. $b \to u\ell\nu$	10.6	0.0	8.1	0.0	7.5
other $b \to u\ell\nu$	1.9	0.0	1.7	0.0	1.4
$B \to D\ell\nu$	12.9	0.0	12.1	0.0	10.0
$B \to D^*\ell\nu$	52.6	0.0	43.9	0.4	38.7
other $b \to c\ell\nu$	6.8	0.0	4.4	0.0	4.5
$B \to hadrons$	9.4	0.0	1.5	0.7	4.6
continuum	10.9	0.5	10.6	7.3	11.7
total (MC)	138.0	0.5	103.7	8.4	100.0
on-res data	141.0		103.0		-
off-res data	0.0		9.6		-

Tableau 3.10 – Sample composition of the ΔE-m_{ES} *signal region* for $B^+ \to \eta^{'}\ell^+\nu$ ($\eta' \to \eta\pi^+\pi^-$ and $\eta \to \pi^+\pi^-\pi^0$) after all cuts, where the signal region lies in the ranges $-0.16 < \Delta E < 0.20$ GeV and $m_{ES} > 5.2675$ GeV/c^2.

Event type	Yields				Sample fraction
	electrons		muons		
	real	fake	real	fake	(%)
$B^+ \to \eta^{'}\ell^+\nu$	11.5	0.0	7.6	0.0	14.1
$B^+ \to \eta\ell^+\nu$	0.0	0.0	0.0	0.0	0.0
non-res. $b \to u\ell\nu$	5.0	0.0	4.6	0.0	7.1
other $b \to u\ell\nu$	0.6	0.0	0.2	0.0	0.6
$B \to D\ell\nu$	10.4	0.0	4.2	0.0	10.8
$B \to D^*\ell\nu$	36.7	0.0	29.9	0.0	49.3
other $b \to c\ell\nu$	4.6	0.0	2.2	0.0	5.0
$B \to hadrons$	5.0	0.0	0.7	1.7	5.5
continuum	4.8	1.2	2.0	2.1	7.5
total (MC)	78.6	1.2	51.5	3.7	100.0
on-res data	48.0		49.0		-
off-res data	0.0		0.0		-

Tableau 3.11 – Sample composition of the ΔE-m_{ES} *signal region* for $B^+ \to \eta\ell^+\nu$ ($\eta \to \gamma\gamma$) after all cuts, where the signal region lies in the ranges $-0.16 < \Delta E < 0.20$ GeV and $m_{ES} > 5.2675$ GeV/c^2.

Event type	Yields: electrons real	electrons fake	muons real	muons fake	Sample fraction (%)
$B^+ \to \eta\ell^+\nu$	102.6	0.0	73.5	0.0	18.4
$B^+ \to \eta^{'}\ell^+\nu$	0.2	0.0	0.4	0.0	0.1
non-res. $b \to u\ell\nu$	53.8	0.0	41.7	0.2	10.0
other $b \to u\ell\nu$	56.8	0.0	44.6	0.0	10.6
$B \to D\ell\nu$	62.3	0.0	44.0	0.0	11.1
$B \to D^*\ell\nu$	141.0	0.0	110.8	0.5	26.4
other $b \to c\ell\nu$	20.7	0.0	9.7	0.2	3.2
$B \to hadrons$	23.0	0.4	7.9	10.2	4.3
continuum	56.3	0.0	37.4	57.3	15.8
total (MC)	516.8	0.4	370.1	68.4	100.0
on-res data	488.0		416.0		-
off-res data	105.4		124.5		-

Tableau 3.12 – Sample composition of the ΔE-m_{ES} *signal region* for $B^+ \to \eta\ell^+\nu$ ($\eta \to \pi^+\pi^-\pi^0$) after all cuts, where the signal region lies in the ranges $-0.16 < \Delta E < 0.20$ GeV and $m_{ES} > 5.2675$ GeV/c^2.

Event type	Yields: electrons real	electrons fake	muons real	muons fake	Sample fraction (%)
$B^+ \to \eta\ell^+\nu$	32.9	0.0	23.8	0.0	11.6
$B^+ \to \eta^{'}\ell^+\nu$	0.5	0.0	0.2	0.0	0.1
non-res. $b \to u\ell\nu$	24.8	0.0	21.5	0.0	9.4
other $b \to u\ell\nu$	6.4	0.0	2.9	0.0	1.9
$B \to D\ell\nu$	46.9	0.0	30.1	0.4	15.8
$B \to D^*\ell\nu$	111.7	0.0	95.2	0.2	42.2
other $b \to c\ell\nu$	21.1	0.0	12.7	1.5	7.2
$B \to hadrons$	15.6	0.0	2.0	3.2	4.3
continuum	14.9	0.0	4.2	17.6	7.5
total (MC)	274.9	0.0	192.7	22.9	100.0
on-res data	265.0		220.0		-
off-res data	9.6		19.2		-

Tableau 3.13 – Sample composition of the ΔE-m_{ES} *signal region* for $B^0 \to \pi^- \ell^+ \nu$ after all cuts, where the signal region lies in the ranges $-0.16 < \Delta E < 0.20$ GeV and $m_{ES} > 5.2675$ GeV/c^2.

Event type	Yields					Sample fraction (%)
	electrons		muons		total	
	real	fake	real	fake		
$B^0 \to \pi^- \ell^+ \nu$ same B	1976.1	1.7	1440.9	27.2	3445.9	29.6
$B^0 \to \pi^- \ell^+ \nu$ both B	63.8	0.0	54.1	1.9	119.8	1.0
$B^+ \to \eta \ell^+ \nu$ same B	0.0	0.0	0.2	0.0	0.2	0.0
$B^+ \to \eta \ell^+ \nu$ both B	6.2	0.0	5.4	0.0	11.6	0.1
$B^+ \to \eta^{'} \ell^+ \nu$ same B	0.8	0.0	0.9	0.0	1.7	0.0
$B^+ \to \eta^{'} \ell^+ \nu$ both B	0.3	0.0	0.8	0.0	1.1	0.0
$B \to \rho \ell \nu$ same B	572.1	0.0	439.1	4.7	1015.9	8.7
$B \to \rho \ell \nu$ both B	95.2	0.0	71.9	0.4	167.5	1.4
$B \to \omega \ell \nu$ same B	8.6	0.0	6.2	0.0	14.8	0.1
$B \to \omega \ell \nu$ both B	21.7	0.0	18.1	0.0	39.8	0.3
non-res. $b \to u \ell \nu$ same B	580.5	0.1	441.8	8.6	1031.0	8.9
non-res. $b \to u \ell \nu$ both B	234.9	0.0	179.9	1.0	415.8	3.6
other $b \to u \ell \nu$ same B	8.1	0.0	3.9	0.4	12.4	0.1
other $b \to u \ell \nu$ both B	72.9	0.0	45.6	0.0	118.5	1.0
$B \to D \ell \nu$ same B	329.4	0.4	208.3	7.1	545.2	4.7
$B \to D \ell \nu$ both B	176.6	0.0	122.1	3.4	302.1	2.6
$B \to D^{*} \ell \nu$ same B	227.9	1.2	164.3	4.8	398.2	3.4
$B \to D^{*} \ell \nu$ both B	815.2	0.0	586.6	3.2	1405.0	12.1
$B \to D^{**} \ell \nu$ same B	13.1	0.0	13.2	1.6	27.9	0.2
$B \to D^{**} \ell \nu$ both B	141.9	0.0	89.9	2.0	233.8	2.0
other $b \to c \ell \nu$ same B	0.0	0.0	0.0	0.0	0.0	0.0
other $b \to c \ell \nu$ both B	1.5	0.0	0.6	3.2	5.3	0.0
$B \to hadrons\ same\ B$	254.2	7.0	196.8	98.1	556.1	4.8
$B \to hadrons\ both\ B$	38.8	3.9	21.9	58.1	122.7	1.1
total B decays same B	3970.7	10.4	2915.5	152.5	7049.1	60.6
total B decays both B	1669.0	3.9	1196.9	73.3	2943.1	25.3
continuum	639.6	63.6	297.9	635.7	1636.8	14.1
total (MC)	6279.4	77.8	4410.4	861.5	11629.1	100.0
on-resonance data	5905.0		4802.0		10707.0	-
off-resonance data	718.4		881.3		1599.7	-

3.3.2.1 Skim preselection

As a first analysis step, we reject most of the background events with a special software tool named $XSLBtoXulnuFilter\ skim$. For the $B^+ \rightarrow \eta^{(\prime)}\ell^+\nu$ channel, this skim rejects about 99.925(99.975)% of the on-resonance data while keeping approximately 29.8(10.9)% of the signal events. For the $B^0 \rightarrow \pi^-\ell^+\nu$ channel, this skim rejects about 99.675% of the on-resonance data while keeping approximately 48.8% of the signal events. It is much more difficult to reconstruct the $B^+ \rightarrow \eta^{(\prime)}\ell^+\nu$ channels, because they involve more charged and neutral particles in their decays.

The $XSLBtoXulnuFilter$ preselections used in this analysis[8] are described in detail in Ref. [41], and are listed below :

– Event's ratio of the second to the zeroth Fox-Wolfram moments [46] smaller than 0.5 ;
– At least one lepton in the event ;
– Hadron momentum in the laboratory frame smaller than 10 GeV/c ;
– For π meson : $|p^*_{lep}| + |p^*_\pi| > 2.8$ GeV/c or $|p^*_{lep}| > 2.2$ GeV/c or $|p^*_\pi| > 1.3$ GeV/c, in the $\Upsilon(4S)$ frame, depending on the values of $|p^*_{lep}|$ and $|p^*_\pi|$;
– For η meson : $|p^*_{lep}|+|p^*_\eta| > 2.8$ GeV/c or $|p^*_{lep}| > 2.1$ GeV/c or $|p^*_\eta| > 1.3$ GeV/c, in the $\Upsilon(4S)$ frame, depending on the values of $|p^*_{lep}|$ and $|p^*_\eta|$;
– For η' meson : $0.69 \times\ |p^*_{lep}| + |p^*_{\eta'}| > 2.4$ GeV/c or $|p^*_{lep}| > 2.0$ GeV/c or $|p^*_{\eta'}| > 1.65$ GeV/c, in the $\Upsilon(4S)$ frame, depending on the values of $|p^*_{lep}|$ and $|p^*_{\eta'}|$;
– $-1.1 < \cos\theta_{BY} < 1.3$ (see Sect. 3.3.2.3) ;
– $\cos\theta_{thrust} < 0.9$ (see Sect. 3.3.2.4).

More stringent $\cos\theta_{BY}$ and $\cos\theta_{thrust}$ selection cuts are applied for the final event selection (Subsects : 3.3.2.2 to 3.3.2.9).

[8]The $XSLBtoXulnuFilter$ skim is a common tool also used by other research groups within the BABAR Collaboration.

3.3.2.2 Signal lepton, pion and photon selection

We ensure that the lepton and pion tracks are well reconstructed by requiring the BABAR's standard Good Tracks Loose (GTL) selection for all the leptons and the pions in the $B^0 \to \pi^- \ell^+ \nu$ signal decays, and the Good Tracks Very Loose (GTVL) selection for the pions in the $B^+ \to \eta^{(\prime)} \ell^+ \nu$ signal decays (see App. I.1). The angles of acceptance are normally given by the geometry of a given system. However, if we are too close to the edge of a system such as the EMC or the vertex chamber or the drift chamber, part of a given event may not be recorded thus distorting our observations. Our values are thus based on the range of agreement between data and MC shown in Fig. 3.7. We obtain : $0.41 < \theta_e, \theta_\pi < 2.46\, rad$ and $0.45 < \theta_\mu < 2.36\, rad$.

The detailed selection criteria for the electron, muon and pion associated with the signal B decay follow :

- electrons :
  - PidLHElectrons selections ;
  - GTL selections ;
  - Acceptance of SVT, DCH and EMC : $0.41 < \theta < 2.46\, rad$;
  - $p_{LAB} > 0.5$ GeV/c ;
  - BABAR's standard CompBremSelectors *Bremsstrahlung* recovery algorithm which uses the photons passing the GoodPhotonLoose selection (see App. I.1) ;
- muons :
  - muNNTight selections ;
  - GTL selections ;
  - Acceptance of SVT, DCH and EMC : $0.45 < \theta < 2.36\, rad$;
  - $p_{LAB} > 1.0$ GeV/c ;
- pions :
  - piLHLoose selections (corresponds to $p_{LAB} > 0.1$ GeV/c) ;
  - GTVL selections to reconstruct the $B^+ \to \eta^{(\prime)} \ell^+ \nu$ signal decays and GTL selections to reconstruct the $B^0 \to \pi^- \ell^+ \nu$ signal decays ;
  - Acceptance of SVT, DCH and EMC : $0.41 < \theta < 2.46\, rad$.

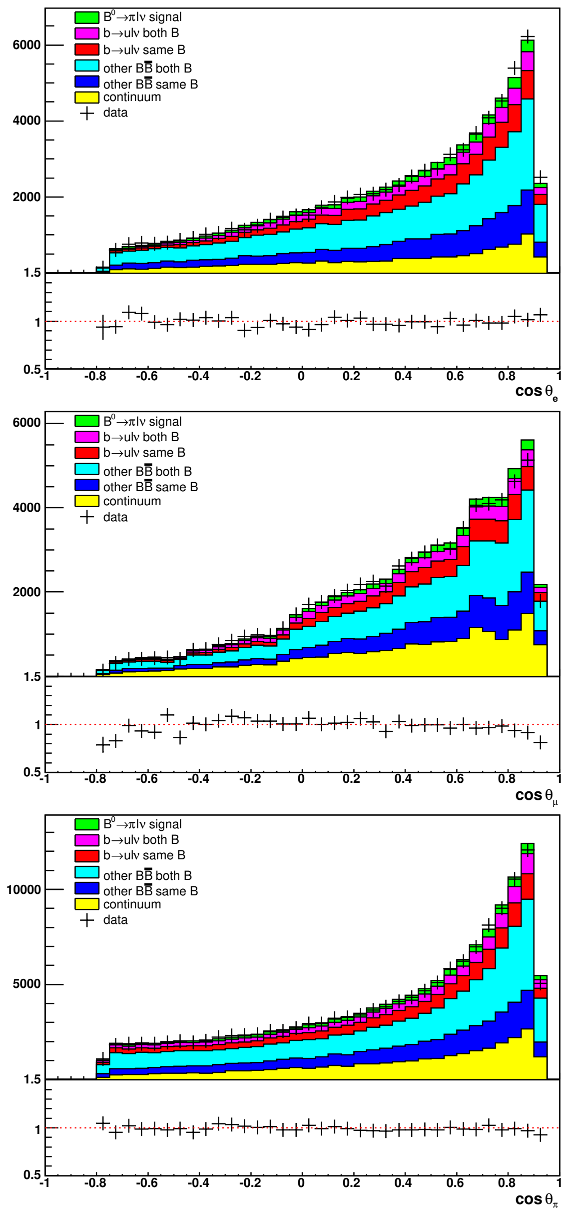

Figure 3.7 – Angles of acceptance based on the agreement between data and MC, for electrons (top), muons (middle) and pions (bottom).

– photons : All photons are given by the GoodPhotonLoose selection

3.3.2.3 Kinematic consistency of the signal

Leaving aside the neutrino for the moment, the kinematic compatibility of the lepton and X_u properties with a real $B \to X_u \ell \nu$ decay is constrained by two criteria :

- We require that the hadron and the lepton tracks be compatible with the same vertex by requiring that a geometrical fit performed with TreeFitter [47] gives a χ^2 probability greater than 0.01 for all three channels ;
- To ensure a good reconstruction of the $B^+ \to \eta^{(\prime)} \ell^+ \nu$ decays, we require that $0.92 < m_{\eta'} < 0.98$ GeV$^2/c^4$, $0.51 < m_\eta < 0.57$ GeV$^2/c^4$ for the $\eta \to \gamma\gamma$ channel and $0.52 < m_\eta < 0.57$ GeV$^2/c^4$ for the $\eta \to \pi^+\pi^-\pi^0$ channel. This is illustrated with the η invariant mass spectrum in Figs. 3.8 and 3.9, and the $\eta^{'}$ invariant mass spectrum in Fig. 3.10, where all cuts have been applied except for the χ^2 probability and the invariant mass ones. The abrupt drop in the yield at high mass values is due to a cut at the skim level. The mass range is more restricted in Fig. 3.9 compared to that of Fig. 3.8 because of the additional cuts on the pions. The signal in the lower plots is calculated in the framework of three different models. The signal in the upper plots is calculated according to the α parametrization.
- We also require that $-1.0 < \cos\theta_{BY} < 1.0$ for all three channels, where :

$$\cos\theta_{BY} = \frac{2f^2 \cdot E^*_Y \cdot E^*_{beam} - m_B^2 - f^2 \cdot m_Y^2}{2f \cdot |\vec{p}^*_B| \cdot |\vec{p}^*_Y|}. \tag{3.1}$$

In Eq. 3.1, θ_{BY} is the angle between the B and Y directions in the $\Upsilon(4S)$ frame where Y represents a fictive particle whose four-momentum is defined as the vectorial sum of the hadron and lepton four-momenta (see App. I.1) with m_Y as its invariant mass, and E^*_Y and p^*_Y as its energy and momentum, respectively, in the $\Upsilon(4S)$ frame[9] ; E^*_{beam} is the beam energy in the same frame, corresponding to half the center of mass energy of the colliding beam particles ; $p^*_B = \sqrt{f^2 \cdot E^{*2}_{beam} - m_B^2}$ where f is the off-

[9] All variables denoted with an asterisk (e.g. p^*) are given in the $\Upsilon(4S)$ rest frame ; all others are given in the laboratory frame.

resonance center of mass energy correction factor defined as $f \equiv 1.0$ for $E^*_{beam} \geq m_B$ and $f \equiv 5.2895/E^*_{beam}$ for $E^*_{beam} < m_B$ (5.2895 GeV is the mean center of mass energy of the on-resonance runs 1-6 real data)[10]. On resonance, $E^*_{beam} = E^*_B$, the B meson energy.

[10]The f factor only affects the off-resonance data, which are themselves only used to obtain corrections to the continuum MC (see Sect. 3.5.2.8).

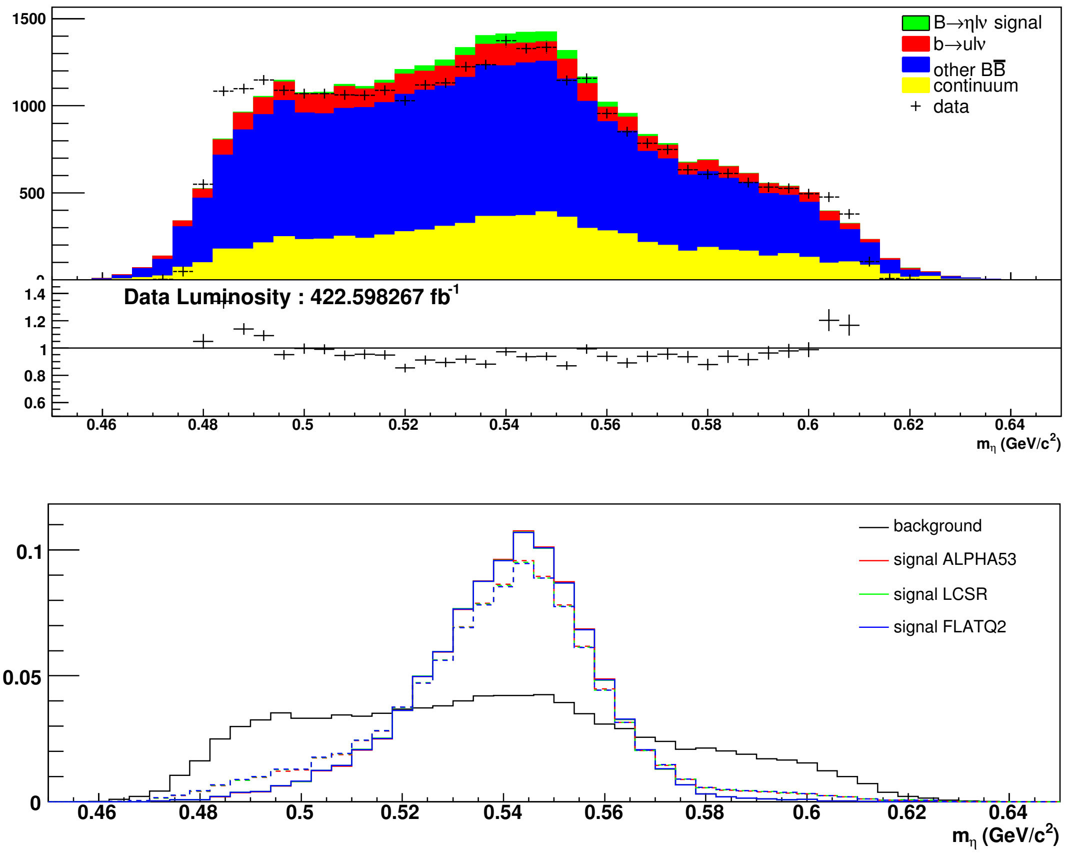

Figure 3.8 – η invariant mass spectrum in $B^+ \to \eta\ell^+\nu$ decays ($\gamma\gamma$ channel), illustrating the importance of the η invariant mass cut. Top figure is the data/MC comparison, while the bottom one is to compare signal MC with the total background MC shape. The full coloured lines describe the true signal only while the dashed lines also include the combinatorial signal. Only events where $0.51 < m_\eta < 0.57$ GeV/c^2 are considered.

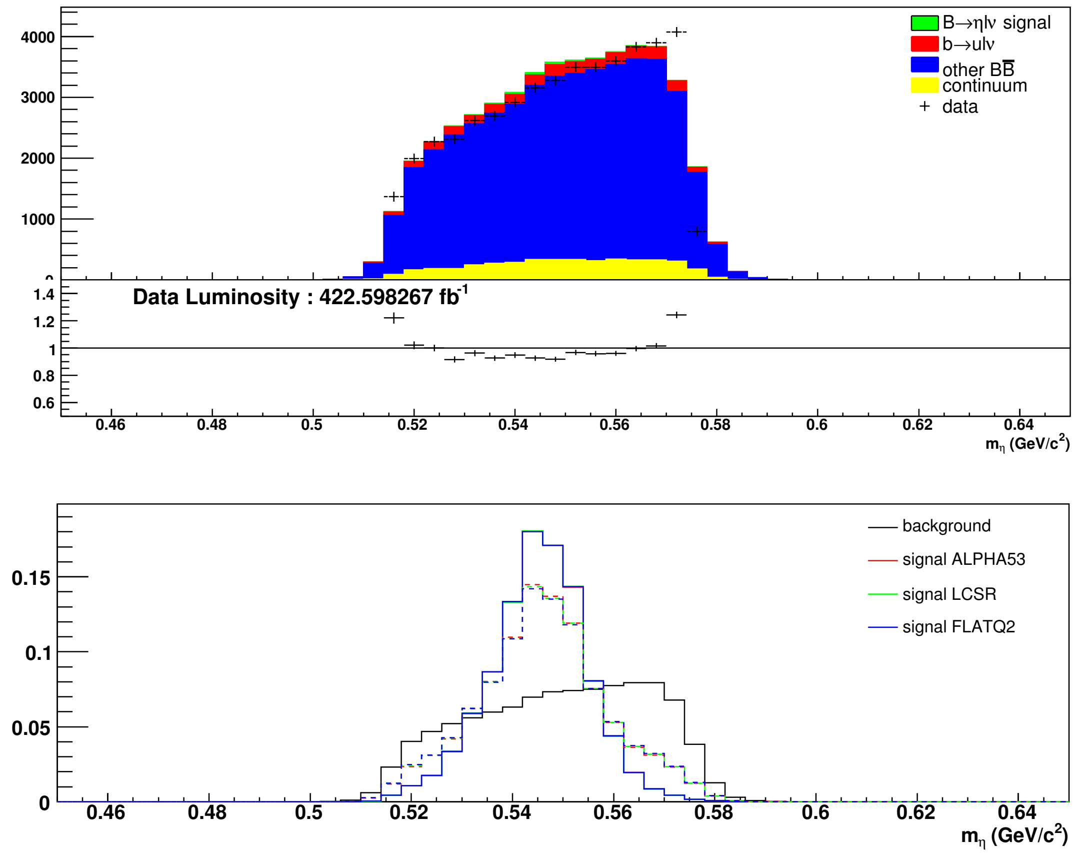

Figure 3.9 – η invariant mass spectrum in $B^+ \to \eta\ell^+\nu$ decays (3π channel), illustrating the importance of the η invariant mass cut. Top figure is the data/MC comparison, while the bottom one is to compare signal MC with the total background MC shape. The full coloured lines describe the true signal only while the dashed lines also include the combinatorial signal. Only events where $0.52 < m_\eta < 0.57\ \mathrm{GeV}/c^2$ are considered.

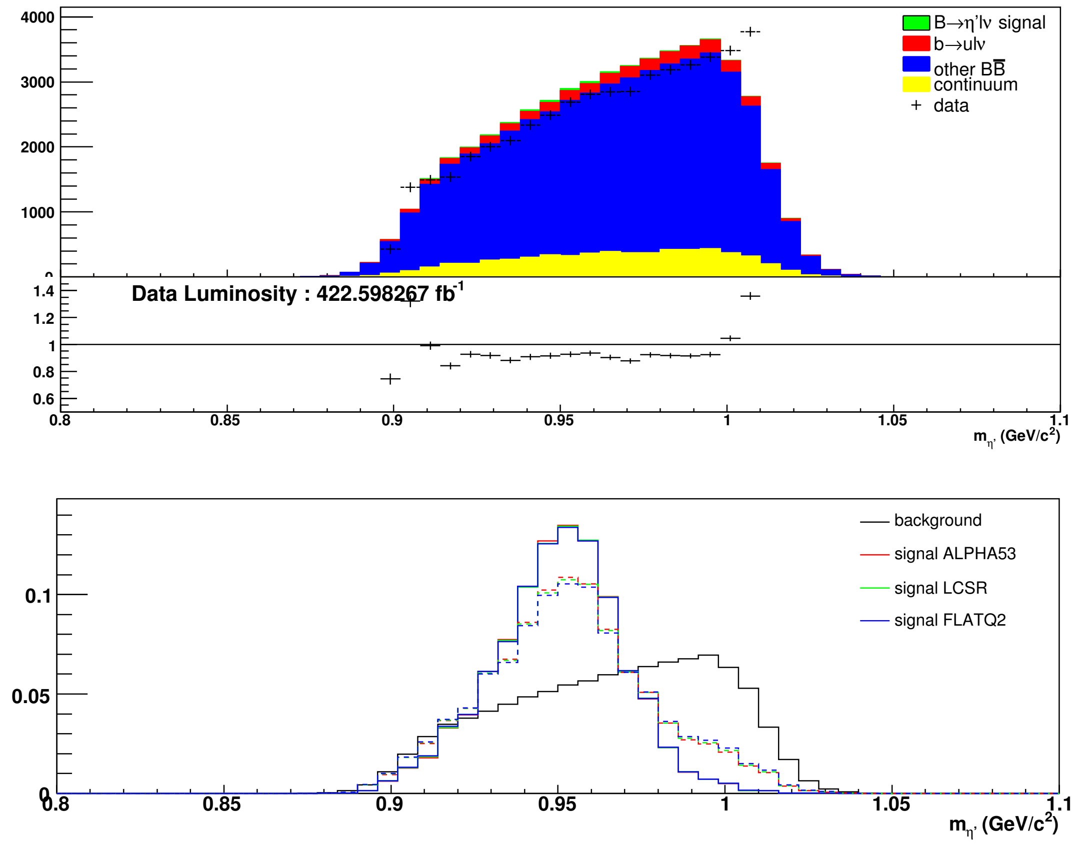

Figure 3.10 – $\eta^{'}$ invariant mass spectrum in $B^+ \to \eta^{'}\ell^+\nu$ decays ($\gamma\gamma$ channel), illustrating the importance of the $\eta^{'}$ invariant mass cut. Top figure is the data/MC comparison, while the bottom one is to compare signal MC with the total background MC shape. The full coloured lines describe the true signal only while the dashed lines also include the combinatorial signal. Only events where $0.92 < m_{\eta'} < 0.98\ \mathrm{GeV}/c^2$ are considered.

3.3.2.4 Continuum rejection

We rely on the event's topology to suppress this background ($B\bar{B}$ events tend to be more spherical while continuum events tend to be more jet-like in appearance).

To reduce the continuum background, we apply the following cuts :

– - For the $B^+ \to \eta^{'}\ell^+\nu$ channel :
 $\theta_{miss} > -0.1 * \tilde{q}^2 + 0.45\, rad$, $\tilde{q}^2 < 2.5$ GeV^2/c^4,
 $\theta_{miss} > 0.2\, rad$, $2.5 < \tilde{q}^2 < 5.5$ GeV^2/c^4,
 $\theta_{miss} > 0.05 * \tilde{q}^2 - 0.075\, rad$, $\tilde{q}^2 > 5.5$ GeV^2/c^4,
 - For the $B^+ \to \eta\ell^+\nu$ channel :
 $cos\theta_{miss} < 0.92$, $\tilde{q}^2 < 11.0$ GeV^2/c^4,
 $cos\theta_{miss} < 0.88$, $\tilde{q}^2 > 11.0$ GeV^2/c^4,
 - For the $B^0 \to \pi^-\ell^+\nu$ channel :
 $\theta_{miss} > -0.000122 * \tilde{q}^6 + 0.00483 * \tilde{q}^4 - 0.0446 * \tilde{q}^2 + 0.405\, rad$, where θ_{miss} is the polar angle associated with P_{miss} in the laboratory frame (see App. I.1.3) ;

– - For the $B^+ \to \eta^{'}\ell^+\nu$ channel :
 $\cos\theta_{thrust} < 0.05 * \tilde{q}^2 + 0.575$, $\tilde{q}^2 < 6.5$ GeV^2/c^4,
 $\cos\theta_{thrust} < 0.9$, $6.5 < \tilde{q}^2 < 12.5$ GeV^2/c^4,
 $\cos\theta_{thrust} < -0.05 * \tilde{q}^2 + 1.525$, $\tilde{q}^2 > 12.5$ GeV^2/c^4,
 - For the $B^+ \to \eta\ell^+\nu$ channel :
 $\cos\theta_{thrust} < 0.05 * \tilde{q}^2 + 0.6$, $\tilde{q}^2 < 5.0$ GeV^2/c^4,
 $\cos\theta_{thrust} < 0.85$, $\tilde{q}^2 > 5.0$ GeV^2/c^4,
 - For the $B^0 \to \pi^-\ell^+\nu$ channel :
 $\cos\theta_{thrust} < 0.9$, $\cos\theta_{thrust} < -0.00159 * \tilde{q}^4 + 0.0451 * \tilde{q}^2 + 0.59$, where $\cos\theta_{thrust}$ is the cosine of the angle between the Y's thrust axis and the rest of the event's thrust axis[11] ;

[11]The thrust axis $\vec{A}$ obtained from N particles is defined as the vector with unit length along which the maximum alignment is found according to the following formula :

$$thrust = max \left| \frac{\sum_{i=1}^{N} |\vec{A} \cdot \vec{p_i}|}{\sum_{i=1}^{N} p_i} \right|, \tag{3.2}$$

where $\vec{p_i}$ is the three momentum of the i^{th} particle.

– $\cos\theta_\ell < 0.85$ for $B^0 \to \pi^-\ell^+\nu$ and $B^+ \to \eta'\ell^+\nu$ decays, and $\cos\theta_\ell < 0.9$ for $B^+ \to \eta\ell^+\nu$ decays, where θ_ℓ is the helicity angle (Sect. 3.3.3) of the W boson [30], the angle between the direction of the virtual W boson boosted in the B rest frame and the direction of the lepton boosted in the rest frame of the W boson. The $b \to c\ell\nu$ background events peak at $\cos\theta_\ell \sim -1$, but they are far less prevalent at $\cos\theta_\ell \sim +1$, where continuum events predominate ;
– $|\cos\theta_V| < 0.95$ for the $B^+ \to \eta\ell^+\nu$ channel, where θ_V is the helicity angle of the η meson [30], the angle between the direction of the η meson boosted in the B rest frame and the direction of either γ boosted in the rest frame of the η for the $\eta \to \gamma\gamma$ channel, where the two γ are emitted back to back. For the $\eta \to \pi^+\pi^-\pi^0$ channel, we replace the direction of this γ by the direction of the vector resulting from the cross product of the two charged pions momenta evaluated in the $\Upsilon(4S)$ frame boosted in the rest frame of the η.

3.3.2.5 $b \to c\ell\nu$ rejection

Even though the $b \to c\ell\nu$ decays are our most abundant source of background, they do not represent a major challenge to the analysis because the shape of their ΔE-$m_{\rm ES}$ histogram is quite different from that of the signal and their abundance leads to a well-defined corresponding PDF.

We use the following cuts :

– Because of the relatively high fake rate of charged pions by muons, $J/\psi \to \mu^+\mu^-$ decays can often be mistaken for $B^0 \to \pi^-\mu^+\nu$ decays. We therefore combine any muon or any pion with any other muon or other pion of opposite charge and exclude the pair of particles whose mass is compatible with that of a J/ψ : $3.07 < m_Y < 3.13$ GeV/c^2. This veto is not applied to $B^0 \to \pi^-e^+\nu$ decays since the fake rate of charged pions by electrons is extremely low ;
– - For the $B^+ \to \eta\ell^+\nu$ channel :
$\cos\theta_\ell > 0.00629 * \tilde{q}^4 - 0.112 * \tilde{q}^2 - 0.252$,
- For the $B^0 \to \pi^-\ell^+\nu$ channel :
$\cos\theta_\ell > -0.0000167*\tilde{q}^8+0.000462*\tilde{q}^6+0.000656*\tilde{q}^4-0.0701*\tilde{q}^2-0.48$, where

$\tilde{q}^2$ is given in unit of GeV^2/c^4. We do not see an improvement in the $S/\sqrt{S+B}$ ratio for the $B^+ \to \eta^{'}\ell^+\nu$ signal region when cutting at low $\cos\theta_\ell$ values.

3.3.2.6 Neutrino reconstruction

Three neutrino reconstruction cut variables have been found to be useful to improve the $S/\sqrt{S+B}$ ratio. In each case, the signal neutrino four-momentum, $P_{miss} = (|\vec{p}_{miss}|, \vec{p}_{miss})$, is inferred from the difference between the momentum of the colliding-beam particles and the sum of the momenta of all the charged and neutral particles detected in a single event, see App. I.1.3. We use $|\vec{p}_{miss}|$ instead of E_{miss} for a better approximation of the massless neutrino energy since the missing energy resolution is worse than the missing momentum resolution (see App. I.1.3).

- - For the $B^+ \to \eta^{'}\ell^+\nu$ channel :
  $M^2_{miss}/2E_{miss} > -0.3\ \text{GeV}^2/c^4$ for all values of $\tilde{q}^2$,
  $M^2_{miss}/2E_{miss} < 0.35 * \tilde{q}^2 + 0.325\ \text{GeV}^2/c^4$, $\tilde{q}^2 < 2.5\ \text{GeV}^2/c^4$,
  $M^2_{miss}/2E_{miss} < 1.2\ \text{GeV}^2/c^4$, $2.5 < \tilde{q}^2 < 4.5\ \text{GeV}^2/c^4$,
  $M^2_{miss}/2E_{miss} < -0.1 * \tilde{q}^2 + 1.65\ \text{GeV}^2/c^4$, $\tilde{q}^2 > 4.5\ \text{GeV}^2/c^4$,
  - For the $B^+ \to \eta\ell^+\nu$ channel :
  $M^2_{miss}/2E_{miss} < 0.8\ \text{GeV}^2/c^4$, $\tilde{q}^2 < 7.5\ \text{GeV}^2/c^4$,
  $M^2_{miss}/2E_{miss} < -0.05 * \tilde{q}^2 + 1.175\ \text{GeV}^2/c^4$, $\tilde{q}^2 > 7.5\ \text{GeV}^2/c^4$,
  - For the $B^0 \to \pi^-\ell^+\nu$ channel :
  $M^2_{miss}/2E_{miss} > -0.5\ \text{GeV}^2/c^4$ for all values of $\tilde{q}^2$,
  $M^2_{miss}/2E_{miss} < 0.00544 * \tilde{q}^4 - 0.127 * \tilde{q}^2 + 1.37\ \text{GeV}^2/c^4$, where M^2_{miss} is the missing invariant mass squared ;
- $-1.0 < \Delta E < 1.0$ GeV for all three channels, where $\Delta E = (P_B \cdot P_{beams} - s/2)/\sqrt{s}$, where $\sqrt{s}$ is the center-of-mass energy of the colliding-beam particles, $\vec{p}_{beams}$ is the net momentum of those particles defining $P_{beams} = (E_{beams}, \vec{p}_{beams})$, E_{beams} is the beam energy E^*_{beams} in the $\Upsilon(4S)$ frame boosted in the laboratory frame and $P_B = (E_B, \vec{p}_B)$ is the B meson four-momentum, where $P_B = P_{meson} + P_\ell + P_{miss}$;
- $5.19 < m_{ES} < 5.29\ \text{GeV}/c^2$ for all three channels, where $m_{ES} = m'_{ES} -$

$(E^{*}_{beams} - 5.29)$ and $m'_{ES} = \sqrt{(s/2 + \vec{p}_B \cdot \vec{p}_{beams})^2/E^2_{beams} - \vec{p}^{\,2}_B}$. Without the $(E^{*}_{beams} - 5.29)$ offset, the maximum value of m'_{ES} is E^{*}_{beams}, while E^{*}_{beams} is not constant and can indeed vary significantly for off-resonance data. The effect of the offset is to set the maximum value of m_{ES} to exactly 5.29 GeV/c^2, independently of the value of E^{*}_{beams}.

The cut values (Figs. 3.4, 3.5 and 3.6) of $M^2_{miss}/2E_{miss}$ have been chosen to minimize the statistical uncertainty estimator $\sqrt{S+B}/S$. The cut values of ΔE and m_{ES} determine the boundaries of our fit region. We chose these boundaries to provide the best balance between the statistical precision and the systematic uncertainties related to the shape of the ΔE-m_{ES} distribution, according to a TOY MC study for which we repeated the analysis procedure in several configurations (see Sect. 3.8.1). The quantities ΔE and m_{ES} were first defined in Ref. [40]. They are expressed in terms of variables defined in the laboratory frame thereby avoiding inaccuracies resulting from CM frame boosts undertaken with potentially wrong mass hypotheses.

3.3.2.7 Choice of the best candidate

Since it is rare that an event results in candidates in both $B^+ \to \eta^{'}\ell^+\nu$ and $B^+ \to \eta\ell^+\nu$ decay channels (less than 0.1%), we keep all candidates for a given mode that have passed the $\cos\theta_\ell$ selection. When several candidates remain in that mode, we select the candidate with the largest value of $\cos\theta_\ell$ and reject the others. The variable $\cos\theta_\ell$ (defined in Sect. 3.3.2.5) has been chosen because it is uncorrelated with m_{ES}, ΔE and $\tilde{q}^2$, it discriminates signal against background, and its value is different for each $(X_u + \ell)$ candidate in an event. Selecting only one candidate per event improves the purity of the well-reconstructed signal. It also reduces the sensitivity of our analysis to the simulation of multiple candidates. In the signal region, 5.2%, 5.6% and 14.4% of the $B^+ \to \eta^{'}\ell^+\nu$, $B^+ \to \eta\ell^+\nu$ and $B^0 \to \pi^-\ell^+\nu$ decays, respectively, contain multiple candidates after all cuts. Unfortunately, 14.5%, 11.5% and 20.5%, respectively, of the events with multiple candidates have the good candidate already eliminated by the cuts. For the remaining events, the good candidate is selected 68%, 65% and 57% of the time, respectively, by our selection on the largest value of $\cos\theta_\ell$. The fraction of events containing multiple candidates is smaller in the whole data region, after all cuts, than the one observed in the signal region. For example, for the $B^0 \to \pi^- \ell^+ \nu$ decays, the fraction is 5.5% compared to 14.4%. This is due to the fact that, as expected, the backgrounds contain less multiple candidates than the signal region.

3.3.2.8 Procedure for the optimization of the cuts

Most cuts were chosen and optimized using BABAR's SP8/SP9 MC simulation to maximize the quantity $S/\sqrt{(S+B)}$ in the signal region that lies in the ranges $-0.16 < \Delta E < 0.20$ GeV and $m_{ES} > 5.2675$ GeV/c^2, and corresponds to the nine ΔE-m_{ES} bins that encompass the signal peak shown in Figs. 3.23 and 3.24 for $B^+ \to \eta^{(\prime)} \ell^+ \nu$ and $B^0 \to \pi^- \ell^+ \nu$ decays, respectively. The size of the ΔE vs m_{ES} plane was chosen to minimize both the statistical and systematic uncertainties on the $f_+(q^2)$ shape parameters as well as on the total $\mathcal{B}(B \to X_u \ell \nu)$, using the procedure described in Sect. 3.8.1. Most cuts are the same in all bins of $\tilde{q}^2$.

3.3.2.9 Procedure for $\tilde{q}^2$-dependent cuts

For each decay mode, four of the cuts were optimized as a function of $\tilde{q}^2$: θ_{miss}, $\cos\theta_{thrust}$, $\cos\theta_\ell$ defined in Sect. 3.3.2.4 and $M^2_{miss}/2E_{miss}$ defined in Sect. 3.3.2.6. One exception is that for $\cos\theta_\ell$ in the $B^+ \to \eta^{\prime} \ell^+ \nu$ channel, the cut value is the same for the whole $\tilde{q}^2$ range. The $\tilde{q}^2$-dependent cuts were optimized in the signal region. Four different cuts are considered because continuum and $b \to c\ell\nu$ events have different $\tilde{q}^2$ spectra and the cuts which reject the $b \to c\ell\nu$ background efficiently are inefficient for the continuum, and *vice versa*. As a result, the cuts are generally applied tighter at high and low $\tilde{q}^2$, as shown in Figs. 3.4, 3.5 and 3.6.

The $\tilde{q}^2$-dependence of the cuts was determined with the following procedure :

- Apply all the $\tilde{q}^2$-independent cuts ;
- Investigate each variable in bins of $\tilde{q}^2$, where the $\tilde{q}^2$ bins have a width of 1.0 GeV$^2/c^4$. The larger number of bins allows a better optimization of the cuts of each variable ;

– Obtain one by one the cut value of the cut variable in each of the $\tilde{q}^2$ bins that maximizes the value of the quantity $S/\sqrt{(S+B)}$ in one of the final bins of $\tilde{q}^2$ used by the fit (twelve bins for $B^0 \to \pi^- \ell^+ \nu$, three bins for $B^+ \to \eta \ell^+ \nu$ and one bin for $B^+ \to \eta^{'} \ell^+ \nu$).

– Do a linear or polynomial fit to the cut values obtained by the previous step and use the fitted function as the $\tilde{q}^2$-dependent cut.

– Carry out this procedure for the variables $M^2_{miss}/2E_{miss}$, θ_{miss}, $\cos\theta_{thrust}$ and $\cos\theta_{\ell}$.

3.3.3 Reconstruction of the variable $\tilde{q}^2$

We reconstruct $\tilde{q}^2$ in terms of two four-momenta : $\tilde{q}^2 = (P_B - P_{X_u})^2$ in a "Y-average frame" [48]. The difficulty with the reconstruction of $\tilde{q}^2$ is that even though the relation $q^2 = (P_B - P_{X_u})^2$ is strictly true and Lorentz-invariant, it cannot be used directly in the BABAR experiment because the value of P_B is not known outside its rest frame. Only the value of P_{X_u} (reconstructed in the lab frame) and that of the $\Upsilon(4S)$ four-momentum (obtained with high accuracy from the PEP-II parameters) are known. Nevertheless, since the B momentum is small in the $\Upsilon(4S)$ frame, a common approximation is to boost the X_u to the $\Upsilon(4S)$ frame and use the relation $q^2 = (P_B - P_{X_u})^2$ in that frame, where the B meson is assumed to be at rest.

However, a more accurate value of $\tilde{q}^2$ can be obtained in the so-called Y-average frame. This frame is defined below. It uses the fact that the B momentum magnitude is known in the $\Upsilon(4S)$ frame, it is $p_B^* = \sqrt{E_{beams}^{*2} - m_B^2}$ where $E_{beams}^* = \sqrt{s}/2$ is the center of mass beam energy. In addition, since the four-momentum of the fictive Y particle is given by $P_Y \equiv P_{X_u} + P_\ell$, the angle between the Y and B momenta in the $\Upsilon(4S)$ frame, θ_{BY}, can be determined by considering a fictive semileptonic $B \to Y\nu$ decay (see Sect. 3.3.2.3). Thus, in the $\Upsilon(4S)$ frame, the Y four-momentum, the B momentum and the angle θ_{BY} define a cone, illustrated in Fig. 3.11, where the true B four-momentum lies somewhere on the surface of the cone extending from the vertex to the base. The B rest frame is thus known up to an azimuthal angle ϕ defined with respect to the axis of the cone given by the Y momentum. The value of $\tilde{q}^2$ in the Y-average frame is computed as follows : it first assumes that the B rest frame is located at an arbitrary angle ϕ_0, and the value of q_0^2 is calculated in that particular frame position. The values of q_1^2, q_2^2 and q_3^2 are then calculated with the B rest frame at $\phi_1 = \phi_0 + 90°$, $\phi_2 = \phi_0 + 180°$ and $\phi_3 = \phi_0 + 270°$, respectively. The value of $\tilde{q}^2$ in the Y-average frame is then defined as the weighted average : $\tilde{q}^2 = \frac{q_0^2 \sin^2\theta_{B_0} + q_1^2 \sin^2\theta_{B_1} + q_2^2 \sin^2\theta_{B_2} + q_3^2 \sin^2\theta_{B_3}}{\sin^2\theta_{B_0} + \sin^2\theta_{B_1} + \sin^2\theta_{B_2} + \sin^2\theta_{B_3}}$, where θ_{B_i}, $i = 0,1,2,3$, is the angle between the B_i direction and the beam direction in the $\Upsilon(4S)$ frame. We note that $|\cos\theta_{BY}| \leq 1$ is required for the Y-average frame to be defined and that using more than four ϕ_i values in the definition of the Y-average frame does not significantly improve the $\tilde{q}^2$ resolution [49]. The cut variable $\cos\theta_\ell$ (see Sect. 3.3.2) is also defined in terms of the B meson four-momentum and computed in the Y-average frame.

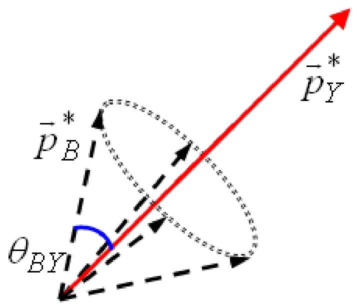

Figure 3.11 – Illustration of the Y-average frame approximation.

For completeness, we have to mention that the value of $\tilde{q}^2$ is also given by the relation $\tilde{q}^2 = (P_\ell + P_\nu)^2$ with P_ℓ and P_ν in the laboratory frame. It is however rather difficult to get a sufficiently good neutrino reconstruction resolution with this approach (see Sect. 3.1.3.2), so that we decided not to rely on the neutrino to reconstruct $\tilde{q}^2$.

The reconstructed values of $\tilde{q}^2$ are always computed in the Y-average frame in this analysis. Figs. 3.12, 3.13 and 3.14 show the improvement in q^2 resolution obtained after applying all the analysis cuts and MC corrections when using the Y-average frame instead of simply assuming that the B is at rest in the $\Upsilon(4S)$ frame. The improvement in q^2 resolution is 29.6%, 26.8% and 22.8%, for $B^+ \rightarrow \eta^{'}\ell^+\nu$, $B^+ \rightarrow \eta\ell^+\nu$ and $B^0 \rightarrow \pi^-\ell^+\nu$ decays, respectively. After all the analysis selections, we obtain a q^2 resolution of $\sigma = 0.570\ \mathrm{GeV}^2/c^4$, $\sigma = 0.611\ \mathrm{GeV}^2/c^4$ and $\sigma = 0.509\ \mathrm{GeV}^2/c^4$ when the selected X_u candidate and the lepton are known to come from a $B^+ \rightarrow \eta^{'}\ell^+\nu$, $B^+ \rightarrow \eta\ell^+\nu$ or $B^0 \rightarrow \pi^-\ell^+\nu$ decay (89.1%, 91.0% or 90.7% of our signal candidates), respectively. When a track coming from the other B is wrongly selected as the signal X_u, the q^2 resolution is very poor and biased. We correct our imperfect q^2 resolution with a q^2-unfolding algorithm performed at a later stage of the analysis (Sect. 3.3.5). The impact of the q^2-unfolding is relatively modest since our $\tilde{q}^2$ resolution is significantly smaller than our bin size of $16.0\ \mathrm{GeV}^2/c^4$ for $B^+ \rightarrow \eta^{'}\ell^+\nu$, 4.0 and 8.0 GeV^2/c^4

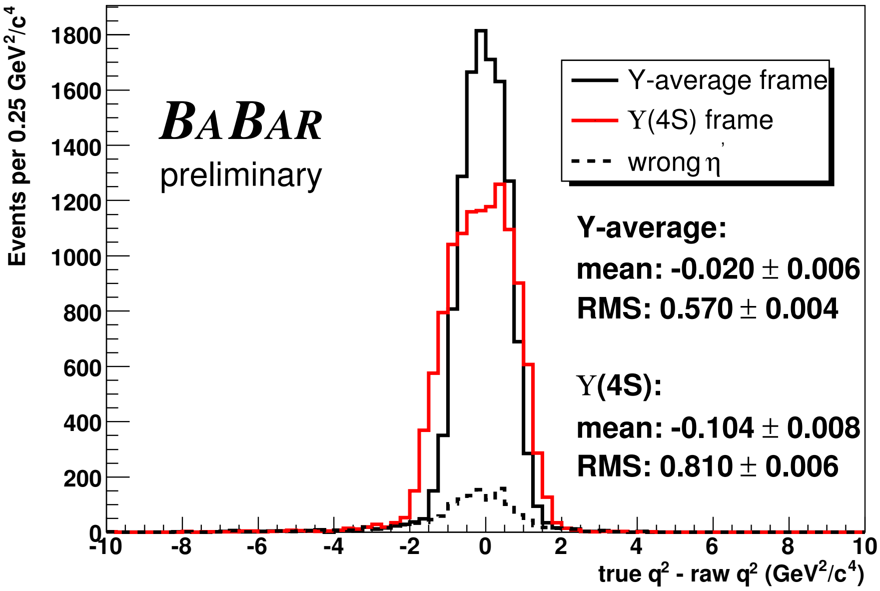

Figure 3.12 – q^2 resolution for the $B^+ \to \eta' \ell^+ \nu$ signal obtained in the Y-average and $\Upsilon(4S)$ frames after applying all analysis cuts and MC corrections. When the selected η' candidate is known to come from a $B^+ \to \eta' \ell^+ \nu$ decay, the q^2 resolution obtained with the Y-average frame approximation is unbiased and has a resolution $\sim 30\%$ better than when the B meson is assumed to be at rest in the $\Upsilon(4S)$ frame. The very wide tail is obtained when a track or photon coming from the other B is used to reconstruct the signal η' meson and accounts for 11.9% of the candidates.

for $B^+ \to \eta \ell^+ \nu$ and $2.0\ \mathrm{GeV}^2/c^4$ for $B^0 \to \pi^- \ell^+ \nu$ decays.

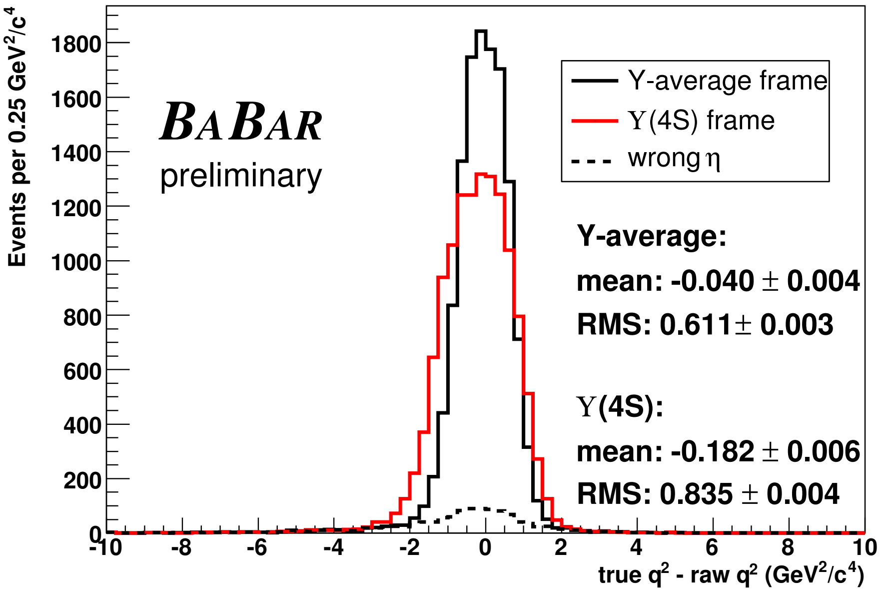

Figure 3.13 – q^2 resolution for the $B^+ \to \eta\ell^+\nu$ signal obtained in the Y-average and $\Upsilon(4S)$ frames after applying all analysis cuts and MC corrections. When the selected η candidate is known to come from a $B^+ \to \eta\ell^+\nu$ decay, the q^2 resolution obtained with the Y-average frame approximation is unbiased and has a resolution $\sim 27\%$ better than when the B meson is assumed to be at rest in the $\Upsilon(4S)$ frame. The very wide tail is obtained when a track or photon coming from the other B is used to reconstruct the signal η meson and accounts for 9.0% of the candidates.

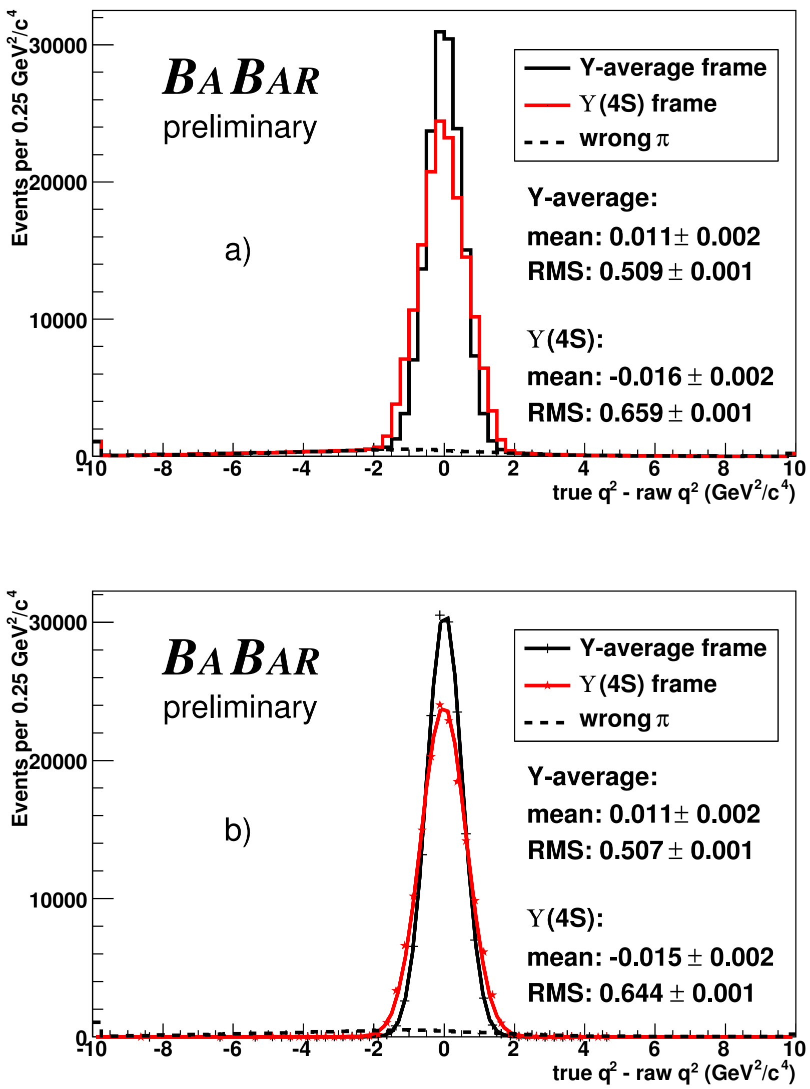

Figure 3.14 – Panel a) : q^2 resolution for the $B^0 \to \pi^-\ell^+\nu$ signal obtained in the Y-average and $\Upsilon(4S)$ frames after applying all analysis cuts and MC corrections. When the selected π candidate is known to come from a $B^0 \to \pi^-\ell^+\nu$ decay, the q^2 resolution obtained with the Y-average frame approximation is unbiased and has a resolution $\sim$ 23% better than when the B meson is assumed to be at rest in the $\Upsilon(4S)$ frame. The very wide tail is obtained when a track coming from the other B is wrongly selected as the signal π and accounts for 9.3% of the candidates ; Panel b) : Single gaussian fit to the data after removal of the tail.

3.3.4 Extraction of raw signal yields in $\tilde{q}^2$ bins

To obtain the signal yields in each of the reconstructed $\tilde{q}^2$ bins, we perform a 2+1 dimensional (ΔE-$m_{\rm ES}$, $\tilde{q}^2$) extended binned maximum likelihood fit based on a method developed in Ref. [50]. The fitted data samples in each $\tilde{q}^2$ bin are divided into four categories for $B^+ \to \eta^{'} \ell^+ \nu$ and $B^+ \to \eta \ell^+ \nu$ decays : $B \to X_u \ell \nu$ signal and three backgrounds, $b \to u \ell \nu$, other $B\bar{B}$ and continuum. For $B^0 \to \pi^- \ell^+ \nu$ decays, we considered six categories : $B \to X_u \ell \nu$ signal and five backgrounds, $b \to u \ell \nu$ same B, $b \to u \ell \nu$ both B, other $B\bar{B}$ same B, other $B\bar{B}$ both B and continuum. The phrase "other $B\bar{B}$" means resonant and non-resonant events other than $b \to u \ell \nu$, mostly $b \to c \ell \nu$. The phrase "same B" means that both reconstructed particles (pion and lepton) come from the same B while the phrase "both B" means that the pion comes from one B and the lepton from the other B of the $B^0 \bar{B}^0$ pair . The distinctive structures of these categories in the two-dimensional ΔE-$m_{\rm ES}$ plane are illustrated in Figs. 3.20, 3.21 and 3.22, for the $B^+ \to \eta^{'} \ell^+ \nu$, $B^+ \to \eta \ell^+ \nu$ and $B^0 \to \pi^- \ell^+ \nu$ channels, respectively. Since the correlation between ΔE and $m_{\rm ES}$ cannot be neglected and is difficult to parametrize, we use the ΔE-$m_{\rm ES}$ histograms obtained from the full MC simulation as two-dimensional PDFs. For the $B^0 \to \pi^- \ell^+ \nu$ decays, the fit of the MC PDFs to the experimental data gives the values of 24 parameters (Table 3.24) : twelve signal parameters (one for each $\tilde{q}^2$ bin), three for the other $B\bar{B}$ same B background, two for the other $B\bar{B}$ both B background, two for the $b \to u \ell \nu$ same B background, two for the $b \to u \ell \nu$ both B background and three for the continuum background. The signal extraction fitting algorithm is described in more detail in Sect. 3.4. For the $B^+ \to \eta \ell^+ \nu$ decays ($\gamma\gamma$ decay channel), we fix the $b \to u \ell \nu$ background in the 2+1 dimensional (ΔE-$m_{\rm ES}$, $\tilde{q}^2$) fit and the fit gives the values of 5 parameters : three signal parameters (one for each $\tilde{q}^2$ bin), one for the other $B\bar{B}$ background and one for the continuum. For the $B^+ \to \eta \ell^+ \nu$ decays ($\pi^+\pi^-\pi^0$ decay channel) and for the $B^+ \to \eta^{'} \ell^+ \nu$ decays, we have to fix both continuum and $b \to u \ell \nu$ backgrounds and the fit gives the values of 2 parameters : one for the signal and one for the other $B\bar{B}$ background parameter. The $\tilde{q}^2$ continuum spectra are adjusted to match the off-resonance data control sample (see Sect. 3.5.2.8).

3.3.5 q^2-unfolding

The $B \to X_u \ell\nu$ signal yields extracted in bins of raw $\tilde{q}^2$ are used to obtain the values of the partial $\Delta\mathcal{B}(q^2)$ and the $f_+(q^2)$ shape as a function of the *true* q^2. For this, the raw $\tilde{q}^2$ distribution must be unfolded into the true q^2 one, and the unfolded yields must be divided by the respective signal efficiencies in each bin of true q^2. This gives the partial $\Delta\mathcal{B}(q^2)$ distribution in bins of true q^2, and thus, the total $\mathcal{B}(B \to X_u \ell\nu)$ and $f_+(q^2)$ shape information. The main reason to unfold the values of $\tilde{q}^2$ is to be model independent when extracting $f_+(q^2)$. Our signal MC is generated with a specific form-factor model. The unfolding algorithm allows us to be model-independent since it yields the true spectrum of our signal which, by definition, does not depend on any model.

The q^2-unfolding is carried out using the information given in Figs. 3.15, 3.16 and 3.17 for the $B^+ \to \eta' \ell^+\nu$, $B^+ \to \eta\ell^+\nu$ and $B^0 \to \pi^-\ell^+\nu$ decays, respectively. However, the fact that the $B^+ \to \eta' \ell^+\nu$ decay signal is evaluated in only one $\tilde{q}^2$ bin means that we cannot extract an unfolding matrix for this channel. As can be seen, each raw $\tilde{q}^2$ bin contributes a certain fraction of events to each true q^2 bin. These fractions form a signal detector response matrix D whose elements D_{rt} are :

$$D_{rt} = \frac{N_{rt}}{\sum_{r=1}^{n} N_{rt}} \tag{3.3}$$

where N_{rt} is the signal yield obtained in a 2D ("raw" $\tilde{q}^2_r$, "true" q^2_t) bin[12] from the signal MC sample after all cuts, and :

$$\sum_{r=1}^{n} D_{rt} \equiv 1. \tag{3.4}$$

The fractions D_{rt} are independent of the actual $\tilde{q}^2$ yields observed in data. The signal yields in bins of the unfolded q^2 are obtained by using the inverted detector response matrix D^{-1} :

$$T = D^{-1}\, R \tag{3.5}$$

where R is the vector of fitted signal yields in bins of raw $\tilde{q}^2$ and T is the vector of signal

[12]Note that N_{rt} is defined without using truth-matching or fitting.

yields in bins of unfolded (true) q^2.

We invert the signal detector response matrix using the method $TMatrixD :: Invert()$ provided by the $root$ software [51] developed at CERN[13]. The values of the elements of the signal detector response matrix and of its inverse matrix are given in Tables 3.14 and 3.16 for $B^+ \to \eta\ell^+\nu$ and Tables 3.15 and 3.17 for $B^0 \to \pi^-\ell^+\nu$ decays. The q^2-unfolding algorithm was validated with statistically independent signal MC samples. Half of the signal events were used to produce the raw $\tilde{q}^2$ and true q^2 histograms. The remaining signal events were used to build two unfolding matrices, with the Becirevic-Kaidalov (BK) form-factor parametrization [52] ($\alpha_{BK} = 0.53$ or $\alpha_{BK} = 0.70$). Two values of α_{BK} are used simply to validate the unfolding procedure to show that, as expected, the unfolded shape of q^2 is model independent. As shown in Fig. 3.18, the true and raw yield distributions can differ slightly for some values of q^2. However, the unfolded values of q^2 match all the true values very well, independently of the values of α_{BK} used to compute the detector response matrix. Hence, we conclude that the q^2-unfolding procedure works properly.

The total yield is left unchanged by the unfolding process. In the individual q^2 bins, the process of unfolding significantly increases the statistical uncertainties of the raw yields, as can be seen in Tables 3.18 and 3.19 for $B^+ \to \eta\ell^+\nu$ and $B^0 \to \pi^-\ell^+\nu$ decays, respectively. However, the q^2-unfolding also introduces anti-correlations between the q^2 bins, such that there is no net increase in uncertainty for the total BF. Systematic uncertainties arising from the unfolding process are fully taken into account, as explained in Sect. 3.6.

For true $B \to X_u\ell\nu$ signal events, the deterioration in q^2 resolution has two different sources. First, a track issued from the decay of the non-signal B can be wrongly identified as that of a signal X_u candidate. These candidates account for 11.9%, 9.0% and 9.3% of all the selected signal candidates (according to the MC simulation with $\alpha_{BK} = 0.53$) for $B^+ \to \eta'\ell^+\nu$, $B^+ \to \eta\ell^+\nu$ and $B^0 \to \pi^-\ell^+\nu$ decays, respectively, and tend to show up more frequently at higher q^2 values, where the hadron momentum is small. In Figs. 3.15, 3.16 and 3.17, these candidates correspond to the off-diagonal

[13] A matrix whose determinant is zero would not be (easily) invertable.

points with little correlation between true and raw q^2 values. All the signal candidates truth-matched to the correct hadron lie along the diagonal region of these figures. Second, an uncertainty results from the boost due to the fact that the true B frame is not precisely known. In the B frame, $q^2 = (P_B - P_{X_u})^2 = m_B^2 + m_{X_u}^2 - 2m_B E_{X_u}$ where E_{X_u} is the only variable term. There is thus an increase in the uncertainty of the hadron boost towards lower q^2 values because the value of E_{X_u} increases for those values of q^2. As a result, the resolution in Figs. 3.15, 3.16 and 3.17 also gets worse towards lower q^2 values. As shown in Fig. 3.18, a maximum in yield is expected at low values of q^2. This is indeed what is observed in Figs. 3.16 and 3.17. Furthermore, this maximum is indeed quite pronounced because of two additional effects. First, the events are scattered within a percentage of the q^2 value and thus wihtin a narrower range for low q^2 values. Second, the scatter at very low q^2, around 0.5 GeV, is restricted to the positive regions from that value of q^2.

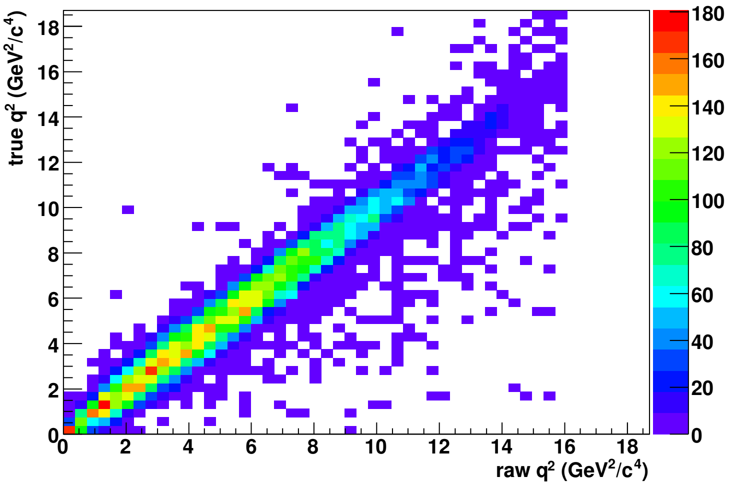

Figure 3.15 – True q^2 vs raw $\tilde{q}^2$ for signal $B^+ \to \eta' \ell^+ \nu$ MC ($\gamma\gamma$ channel).

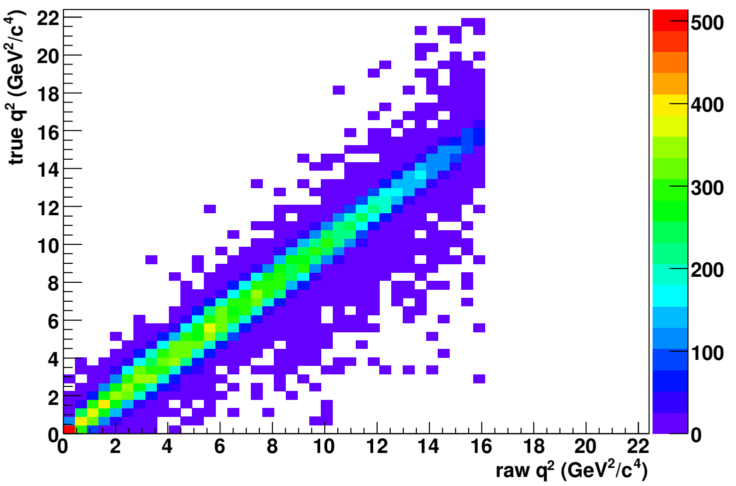

Figure 3.16 – True q^2 vs raw $\tilde{q}^2$ for signal $B^+ \to \eta\ell^+\nu$ MC ($\gamma\gamma$ channel).

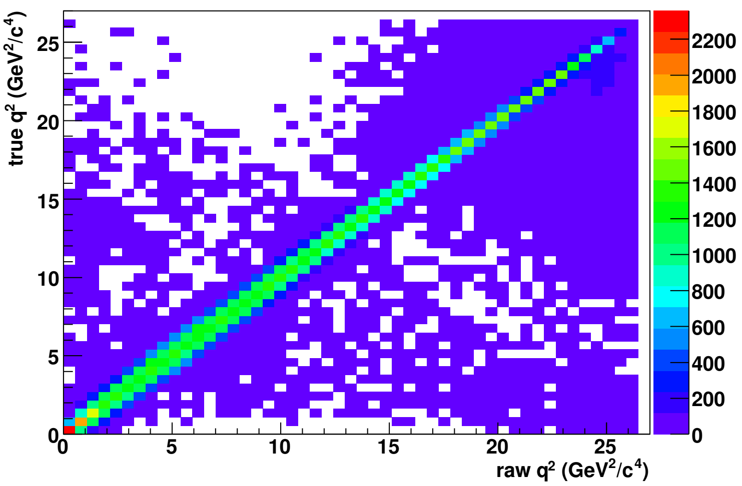

Figure 3.17 – True q^2 vs raw $\tilde{q}^2$ for signal $B^0 \to \pi^-\ell^+\nu$ MC.

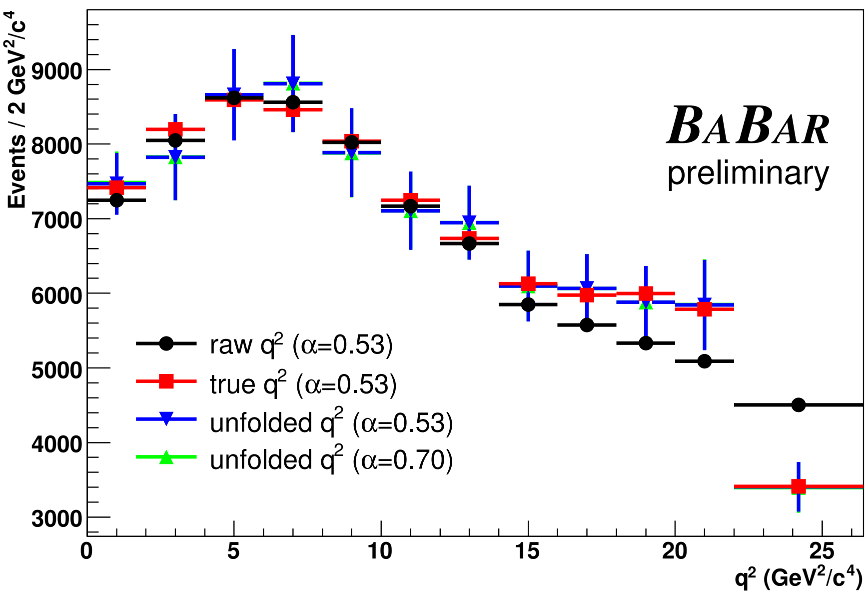

Figure 3.18 – Validation of the q^2-unfolding procedure with statistically independent $B^0 \rightarrow \pi^- \ell^+ \nu$ signal MC samples. The blue and green points mostly overlap.

Tableau 3.14 – Values of the detector response matrix elements for the $B^+ \to \eta\ell^+\nu$ signal. Each column corresponds to a true q^2 bin and contains the fraction of events (%) belonging to each raw $\tilde{q}^2$ bin. The sum of each column is identically 100%, such that the q^2-unfolding process changes the shape of the q^2 spectrum but conserves the total number of events.

$\tilde{q}^2 \setminus q^2$ (GeV^2/c^4)	0-4	4-8	8-16
0-4	89	6.3	0.0017
4-8	11	85	4.8
8-16	0.36	8.9	95

Tableau 3.15 – Values of the detector response matrix elements for the $B^0 \to \pi^-\ell^+\nu$ signal. Each column corresponds to a true q^2 bin and contains the fraction of events (%) belonging to each raw $\tilde{q}^2$ bin. The sum of each column is identically 100%, such that the q^2-unfolding process changes the shape of the q^2 spectrum but conserves the total number of events.

$\tilde{q}^2 \setminus q^2$ (GeV^2/c^4)	0-2	2-4	4-6	6-8	8-10	10-12	12-14	14-16	16-18	18-20	20-22	22-26.4
0-2	85.6	10.6	0.048	0.039	0.036	0.089	0.084	0.065	0.045	0.043	0.057	0.013
2-4	12.9	73.1	13.3	0.11	0.057	0.072	0.19	0.14	0.087	0.11	0.014	0.015
4-6	0.043	14.0	72.4	14.7	0.11	0.068	0.15	0.12	0.13	0.062	0.014	0.018
6-8	0.068	0.2	12.9	72.3	14.0	0.082	0.053	0.055	0.05	0.051	0	0
8-10	0.029	0.28	0.24	11.8	74.4	13.0	0.19	0.16	0.061	0.0098	0.0063	0
10-12	0.038	0.2	0.21	0.17	10.4	76.0	12.0	0.07	0.031	0.049	0.023	0.0032
12-14	0.077	0.13	0.19	0.2	0.16	9.5	75.9	10.5	0.097	0.069	0.023	0.022
14-16	0.083	0.23	0.18	0.17	0.15	0.15	8.6	75.5	8.1	0.25	0.22	0.075
16-18	0.091	0.2	0.18	0.17	0.055	0.11	0.31	8.0	75.4	7.3	0.75	0.39
18-20	0.23	0.19	0.11	0.1	0.088	0.15	0.34	0.76	6.9	70.8	6.7	1.7
20-22	0.12	0.23	0.078	0.031	0.076	0.13	0.4	0.89	1.5	7.1	66.2	7.0
22-26.4	0.69	0.65	0.18	0.19	0.41	0.66	1.8	3.7	7.6	14.2	26.0	90.7

Tableau 3.16 – Values of the inverse detector response matrix elements used to unfold the $\tilde{q}^2$ distribution of the $B^+ \to \eta\ell^+\nu$ signal.

$\tilde{q}^2 \setminus q^2$ (GeV^2/c^4)	0-4	4-8	8-16
0-4	1.1	-0.085	0.0043
4-8	-0.14	1.2	-0.061
8-16	0.0088	-0.11	1.1

Tableau 3.17 – Values of the inverse detector response matrix elements used to unfold the $\tilde{q}^2$ distribution of the $B^0 \to \pi^-\ell^+\nu$ signal.

$\tilde{q}^2 \setminus q^2$ (GeV^2/c^4)	0-2	2-4	4-6	6-8	8-10	10-12	12-14	14-16	16-18	18-20	20-22	22-26.4
0-2	1.19	-0.18	0.033	-0.0073	0.0011	-0.0013	-0.00065	-0.00058	-0.00045	-0.00032	-0.00093	-6.7e-05
2-4	-0.22	1.45	-0.28	0.056	-0.011	0.0014	-0.0029	-0.0016	-0.00074	-0.0017	0.00018	-0.00014
4-6	0.043	-0.29	1.49	-0.31	0.058	-0.011	-0.0003	-0.0016	-0.0019	-0.00041	-0.00013	-0.00022
6-8	-0.0085	0.05	-0.27	1.48	-0.29	0.049	-0.0077	0.00095	-0.00036	-0.00087	0.00013	5.3e-05
8-10	0.0016	-0.012	0.041	-0.24	1.42	-0.25	0.037	-0.0077	-0.00019	0.00014	-5.7e-05	2.9e-06
10-12	-0.00023	-0.0011	-0.0082	0.032	-0.2	1.38	-0.22	0.03	-0.0033	-0.00045	-0.00041	3.5e-05
12-14	-0.00081	-0.0012	-0.0013	-0.0065	0.023	-0.17	1.37	-0.19	0.019	-0.0025	0.00035	-0.00022
14-16	-0.00057	-0.0031	-0.002	-0.0012	-0.0046	0.018	-0.16	1.36	-0.15	0.011	-0.0038	-0.00037
16-18	-0.00055	-0.0024	-0.0018	-0.0024	0.00033	-0.003	0.012	-0.14	1.36	-0.14	0.00029	-0.0031
18-20	-0.003	-0.0022	-0.0011	-0.0013	-0.00093	-0.0015	-0.0049	0.0021	-0.13	1.44	-0.14	-0.016
20-22	-0.00038	-0.0033	-0.00056	0.0001	-0.00066	-0.00089	-0.0036	-0.01	-0.0066	-0.13	1.57	-0.12
22-26.4	-0.0069	-0.0068	-0.00015	-0.0014	-0.0044	-0.0055	-0.018	-0.038	-0.086	-0.18	-0.43	1.14

Tableau 3.18 – Relative statistical uncertainty (%) of the raw and unfolded signal yields in each q^2 bin for $B^+ \to \eta\ell^+\nu$.

q^2 (GeV^2/c^4)	0-4	4-8	8-16	total
raw yield	28.0	21.0	30.1	16.7
unfolded yield	30.6	24.6	32.5	16.7

Tableau 3.19 – Relative statistical uncertainty (%) of the raw and unfolded signal yields in each q^2 bin for $B^0 \to \pi^-\ell^+\nu$.

q^2 (GeV^2/c^4)	0-2	2-4	4-6	6-8	8-10	10-12	12-14	14-16	16-18	18-20	20-22	22-26.4	total
raw yield	8.9	6.9	5.9	6.6	7.0	7.6	8.1	9.8	9.7	9.9	9.6	6.8	2.4
unfolded yield	10.5	10.1	9.2	9.9	10.3	10.6	10.8	12.5	12.3	12.9	14.1	11.9	2.4

3.3.6 Partial $\Delta\mathcal{B}(q^2)$

3.3.6.1 Measured partial BFs

After the signal yields have been obtained as a function of the unfolded values of q^2, the partial branching fractions are calculated in each bin by using the total number of N_B mesons (B^+ mesons for $B^+ \to \eta^{'}\ell^+\nu$ and $B^+ \to \eta\ell^+\nu$ decays or B^0 mesons for $B^0 \to \pi^-\ell^+\nu$ decays) in the dataset and the corresponding $B^+ \to \eta^{'}\ell^+\nu$, $B^+ \to \eta\ell^+\nu$ ($\gamma\gamma$ and $\pi^+\pi^-\pi^0$ channels) and $B^0 \to \pi^-\ell^+\nu$ signal reconstruction efficiencies given in Tables 3.20, 3.21, 3.22 and 3.23, respectively. Thus, for each t^{th} q^2 bin, the partial branching fraction $\Delta\mathcal{B}(q^2)$ is given by :

$$\Delta\mathcal{B}(q_t^2) = \left(\frac{E^{-1}\,T}{2N_B}\right)_{q_t^2} \tag{3.6}$$

where T is given by Eq. 3.5 and E^{-1} is the inverse diagonal efficiency matrix whose elements E_{rt}^{-1} are the inverse of the signal efficiency :

$$E_{rt}^{-1} = \begin{cases} \frac{N_t^0}{N_t} & r = t \\ 0 & r \neq t \end{cases} \tag{3.7}$$

where N_t is the signal yield obtained from the signal MC sample, after all cuts, in the t^{th} q^2 bin and N_t^0 is the total number of $B \to X_u\ell\nu$ decays in the t^{th} q^2 bin, before any cut.

In Eq. 3.6, there is a factor of 2 in the denominator because the signal yields and efficiencies are obtained from the sum of electrons and muons in this analysis, while the ℓ in the $B \to X_u\ell\nu$ decay stands for only one lepton flavor, electron or muon. The total number of B^+ and B^0 are :

$$N_{B^+} = 2N_{BB} \times \mathcal{B}(\Upsilon(4S) \to B^+B^-) \tag{3.8}$$

$$N_{B^0} = 2N_{BB} \times \mathcal{B}(\Upsilon(4S) \to B^0\bar{B}^0) \tag{3.9}$$

where N_{BB} is the total number of $B\bar{B}$ pairs given by the B counting algorithm [42]. We have to introduce a factor 2 in Eq. 3.8 because we also consider the charge conjugate modes in our analysis. We use the most recent $\Upsilon(4S)$ BF values, $\mathcal{B}(\Upsilon(4S) \to B^0\bar{B}^0) = 0.484 \pm 0.006$ and $\mathcal{B}(\Upsilon(4S) \to B^+B^-) = 0.516 \pm 0.006$, to obtain the central values of our results.

Tableau 3.20 – Signal $B^+ \to \eta^{'}\ell^+\nu$ ($\gamma\gamma$ channel) efficiency. The values labelled "Without FSR" correspond to the case where FSR effects are removed.

true q^2 bin	signal efficiency (%)	
(GeV^2/c^4)	With FSR	Without FSR
0-16	0.61 ± 0.01	0.61 ± 0.01

Tableau 3.21 – Signal $B^+ \to \eta\ell^+\nu$ ($\gamma\gamma$ channel) efficiency for each bin of true q^2. The values labelled "Without FSR" correspond to the case where FSR effects are removed.

true q^2 bin	signal efficiency (%)	
(GeV^2/c^4)	With FSR	Without FSR
0-4	2.01 ± 0.03	2.01 ± 0.03
4-8	2.55 ± 0.03	2.57 ± 0.03
8-16	1.42 ± 0.01	1.42 ± 0.01

Tableau 3.22 – Signal $B^+ \to \eta\ell^+\nu$ ($\pi^+\pi^-\pi^0$ channel) efficiency. The values labelled "Without FSR" correspond to the case where FSR effects are removed.

true q^2 bin	signal efficiency (%)	
(GeV^2/c^4)	With FSR	Without FSR
0-16	0.59 ± 0.01	0.59 ± 0.01

It has been shown in Appendix C. of Ref. [30] that the signal efficiency has very little dependence on the underlying theoretical model used as the generator as long as the signal efficiency is computed in a large number of q^2 bins or varies smoothly with q^2 (see Fig. 3.19 for $B^0 \to \pi^-\ell^+\nu$ decays).

Tableau 3.23 – Signal $B^0 \to \pi^- \ell^+ \nu$ efficiency for each bin of true q^2. The values labelled "Without FSR" correspond to the case where FSR effects are removed.

true q^2 bin	signal efficiency (%)	
(GeV^2/c^4)	With FSR	Without FSR
0-2	8.34 ± 0.09	8.00 ± 0.09
2-4	9.10 ± 0.10	8.97 ± 0.09
4-6	9.22 ± 0.09	9.15 ± 0.09
6-8	9.09 ± 0.09	9.18 ± 0.09
8-10	8.59 ± 0.09	8.63 ± 0.09
10-12	8.46 ± 0.09	8.53 ± 0.09
12-14	8.53 ± 0.09	8.58 ± 0.09
14-16	8.50 ± 0.09	8.61 ± 0.09
16-18	9.40 ± 0.10	9.45 ± 0.10
18-20	10.52 ± 0.10	10.66 ± 0.10
20-22	11.61 ± 0.11	11.71 ± 0.11
22-26.4	14.59 ± 0.09	14.70 ± 0.09

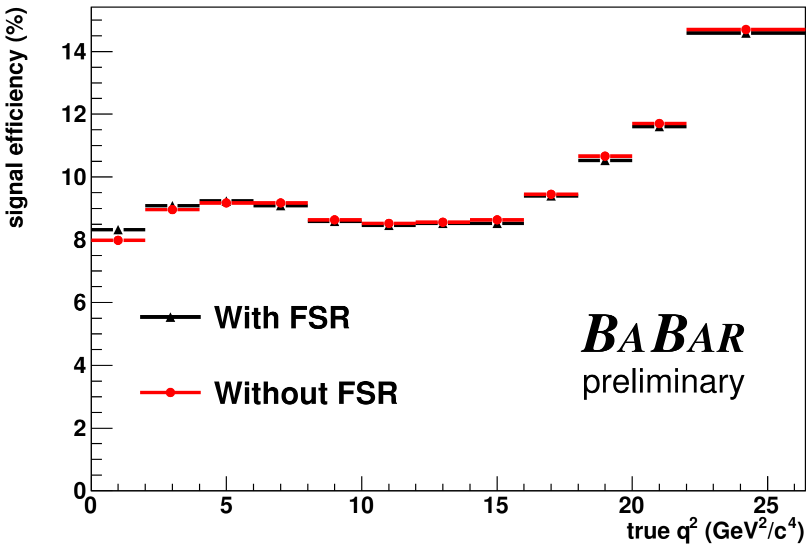

Figure 3.19 – Signal efficiency as a function of true q^2 for $B^0 \to \pi^- \ell^+ \nu$ (including FSR effects).

3.3.6.2 Partial BFs without FSR

As described in Sect. 3.6.2.4, there are radiative processes associated with $B \to X_u \ell \nu$ decays. Such decays arise via a QED process named *Final State Radiation* (FSR). While these processes undoubtedly exist and have to be taken into account to model the signal yields and the total $\mathcal{B}(B \to X_u \ell \nu)$ that we measure, they are not taken into account in the QCD calculations that we use to extract $|V_{ub}|$ or the $f_+(q^2)$ shape. It is thus important to obtain a $\Delta\mathcal{B}(q^2)$ distribution that is modified to remove the FSR effects in order to fit the $f_+(q^2)$ shape that can then be compared directly to QCD predictions, and then extract $|V_{ub}|$ (Sect. 3.3.8 to 3.3.10). To get such a distribution, we recall that the signal efficiency for each bin of q^2 is given by Eq. 3.7, $\epsilon = N_t/N_t^0$. The value of ϵ is normally obtained in MC calculations incorporating the FSR effects. To remove the FSR effects, we calculate N_t^0, the total number of $B \to X_u \ell \nu$ decays in a q^2 bin before any cut, with the PHOTOS package turned ON (with FSR) and OFF (without FSR), using the GeneratorsQA(EvtGen) software. The effect of FSR is constrained to the value of N_t^0. Modifying both, N_t and N_t^0, will not affect the value of ϵ. The values of the signal efficiciency to be used to generate $\Delta\mathcal{B}(q^2)$ without FSR are then given by :

$$\epsilon(withoutFSR) = \epsilon(withFSR) \times \frac{N_t^0(withFSR)}{N_t^0(withoutFSR)}$$

Since the events with FSR (emission of $n\gamma$) result in a lower value of P_π for a given value of P_B and thus a higher value of q^2, we expect to have more events (a larger value of N_t^0) at higher values of q^2 due to the FSR effects. As a consequence, we expect, as observed in Table 3.23, a signal efficiency without FSR to be larger at high q^2 and smaller at low q^2, respectively, than the signal efficiency with FSR.

3.3.7 Total $\mathcal{B}(B^+ \to \eta^{(\prime)} \ell^+ \nu)$ and $\mathcal{B}(B^0 \to \pi^- \ell^+ \nu)$

The total BF for each $B \to X_u \ell \nu$ decay channel is simply obtained by summing up the partial $\Delta\mathcal{B}(q^2)$ in the n q^2 bins, where n=3(1) for the $B^+ \to \eta^{(\prime)} \ell^+ \nu$ channels and n=12 for the $B^0 \to \pi^- \ell^+ \nu$ channel :

$$\mathcal{B}(B \to X_u \ell \nu) = \sum_{t=1}^{n} \Delta\mathcal{B}(B \to X_u \ell \nu, q_t^2), \tag{3.10}$$

To estimate the statistical uncertainty on this branching ratio, we use the covariance matrix V_Y of the fitted yields. The covariance matrix V of the partial branching fractions is given by the relation :

$$V = B\, V_Y\, B^T \tag{3.11}$$

where $B = \frac{E^{-1}\ T}{2N_B}$ (from Eq. 3.6). Then, the standard formula for uncertainty propagation is used :

$$\sigma_{BF}^2 = \sum_{i,j=1}^{n} V_{ij}. \tag{3.12}$$

In addition to the fit errors, covariance matrices are computed for each systematic uncertainty in the measurement of $\Delta\mathcal{B}(q^2)$ as described in Sect. 3.6. We have verified that these systematic uncertainties are compatible with the direct variation of the total BF value when the analysis is repeated using modified MC samples (see Sect. 3.6). The total covariance matrix is given by the sum of the individual matrices, such that the statistical and systematic uncertainties are added in quadrature to obtain the total uncertainty.

The error propagation formula and the total covariance matrices V of our measured partial $\Delta\mathcal{B}(q^2)$ spectra are also used to obtain the q^2 spectra shape uncertainties and to relate the measured $\Delta\mathcal{B}(q^2)$ spectra to the theoretical $f_+(q^2)$ shapes. With these uncertainties and their correlations, the q^2 spectrum shape measurements are particularly useful because they are model-independent due to the unfolding process (see Sect. 3.3.5). These data can then be used to extract the $f_+(q^2)$ shape parameters using *any* theoretical parametrization.

3.3.8 Fits of $|V_{ub} f_+(0)|$ and the $f_+(q^2)$ shape parameters

The measured $\Delta\mathcal{B}(q^2)$ spectra shapes together with their statistical and systematic covariance matrices are the most important results of this analysis. It is however interesting to go one step further and represent this shape information in the form of an $f_+(q^2)$

function. This can be done by fitting either the Becirevic-Kaidalov (BK) [52] parametrization or Hill [53] parametrization or the Boyd, Grinstein, Lebed (BGL) [54] expansion to our data.

We perform a binned χ^2 fit using the standard differential decay rate formula for a semileptonic B decay to a pseudo-scalar meson (X_u) as the PDF :

$$F(q^2) = |\vec{p}_{X_u}|^3 \cdot |f_+(q^2, c_B, \alpha)|^2 \tag{3.13}$$

$$= \frac{24\pi^3}{|V_{ub}|^2 G_F^2} \frac{d\Gamma(B \to X_u \, \ell^+ \nu_\ell)}{dq^2}, \tag{3.14}$$

where :

$$|\vec{p}_{X_u}| = \sqrt{\frac{(m_B^2 + m_{X_u}^2 - q^2)^2}{4m_B^2} - m_{X_u}^2}, \tag{3.15}$$

In the case of the Hill parametrization the $f_+(q^2)$ function is given by :

$$f_+(q^2) = \frac{c_B(1-\alpha) \cdot (1 - \delta q^2/m^2)}{(1 - q^2/m_{B^*}^2) \cdot (1 - (\alpha + \delta(1-\alpha))q^2/m_{B^*}^2)}. \tag{3.16}$$

The parameters α, δ and c_B are allowed to vary to minimize χ^2. In the case of the BK parametrization we set δ to zero in the fit. For the BGL expansion, the $f_+(q^2)$ function is given by :

$$f_+(t) = \frac{1}{P(t)\phi(t, t_0)} \sum_{k=0}^{\infty} a_k(t_0) z(t, t_0)^k, \tag{3.17}$$

where :

$$z(t, t_0) = \frac{\sqrt{t_+ - t} - \sqrt{t_+ - t_0}}{\sqrt{t_+ - t} + \sqrt{t_+ - t_0}}, \tag{3.18}$$

and $t = q^2, t_+ = (m_B + m_{X_u})^2, t_- = (m_B - m_{X_u})^2$. The *Blaschke* factor $P(t)$ accounts for the B^* pole and is given by :

$$P(t) = z(q^2, m_{B^*}^2). \tag{3.19}$$

The usual choice for the function $\phi(t,t_0)$ is :

$$\phi(t,t_0) = \sqrt{\frac{3}{96\pi\chi_J^{(0)}}} \frac{(t_+ - t)(\sqrt{t_+ - t} + \sqrt{t_+ - t_0})(\sqrt{t_+ - t} + \sqrt{t_+ - t_-})^{3/2}}{(t_+ - t_0)^{1/4}(\sqrt{t_+ - t} + \sqrt{t_+})^5}. \tag{3.20}$$

$t_0 = q_0^2$ is a parameter whose value varies according to the decay under study [54]. We have : t_0=10.85 GeV^2/c^4 for $B^+ \to \eta' \ell^+ \nu$ decays and 14.14 GeV^2/c^4 for $B^+ \to \eta\ell^+\nu$ decays [28], and 17.17 GeV^2/c^4 for $B^0 \to \pi^-\ell^+\nu$ decays [32]. The series in Eq. (3.17) provides a systematic expansion in terms of a_k coefficients with the value k_{max} given by the value of k for which there is no significant improvement in χ^2. In our analysis, $k_{max} = 2$.

The expression for χ^2 minimized in the fit uses the total covariance matrix V to take into account the correlations between the measurements in the n q^2 bins, where n=3 for the $B^+ \to \eta\ell^+\nu$ channel and n=12 for the $B^0 \to \pi^-\ell^+\nu$ channel :

$$\chi^2 = \sum_{i,j=1}^{n} \left(\Delta\mathcal{B}(q_i^2) - b\int F(q_i^2)dq^2\right) V_{ij}^{-1} \left(\Delta\mathcal{B}(q_j^2) - b\int F(q_j^2)dq^2\right), \tag{3.21}$$

where $\int F(q_i^2)dq^2$ denotes the integral of Eq. 3.13 over the range of the ith q^2 bin and $b = |V_{ub}|^2 G_F^2/24\pi^3 = \sum_{i=1}^{n} \Delta\mathcal{B}(q_i^2)/\sum_{i=1}^{n}\int F(q_i^2)dq^2$.

The central values of the $f_+(q^2)$ shape parameters, and their total uncertainties, are obtained using the total covariance matrix in Eq. 3.21. In the present case, using either the statistical or the systematic covariance matrix in Eq. 3.21 yields the statistical or the systematic uncertainty, respectively. Their quadratic sum is in fact consistent with the total uncertainty.

We also obtain the values of the product $|V_{ub}f_+(0)|$ from our $\Delta\mathcal{B}(q^2)$ spectra extrapolated to $q^2 = 0$, using our fitted $f_+(q^2)$ function. The uncertainties on these values are obtained using the statistical and systematic covariance matrices of the fit parameters, hence taking into account the correlation between them. The values of $f_+(0)$ cannot be obtained from these products since the value of $|V_{ub}|$ is not known at this stage.

3.3.9 Tests of QCD calculations

Once the $\Delta\mathcal{B}(q^2)$ spectrum and its covariance matrices are obtained, they can be used to test various QCD calculations. We are doing so by comparing our measured q^2 spectrum shapes with the theoretical predictions over their q^2 ranges of validity. Because of limited statistics in the $B^+ \to \eta^{(')}\ell^+\nu$ channels, we can carry out these tests only with the $B^0 \to \pi^-\ell^+\nu$ decay data. We do not use the normalization of the form factor to test the calculations because that would require a knowledge of the value of $|V_{ub}|$.

We use the following procedure to compare the predicted q^2 spectra with our data :

1. We modify our measured $\Delta\mathcal{B}(q^2)$ spectra to remove FSR effects, as described in Sect. 3.3.6.2. Even though the FSR removal does not have a big impact (less than 1%), it is more precise to do so since FSR effects have not been included in the QCD calculations to date. We call these modified $\Delta\mathcal{B}(q^2)$ histograms H_{meas}.

2. For a given QCD model, we calculate a histogram H_{th} with the predicted q^2 spectrum shape, scaled to the BF values that we have measured over the q^2 range of validity of the model under consideration, and with the same binning as H_{meas}. This histogram, constructed with the FLATQ2 generator, is reweighted to match the q^2 spectrum of the QCD calculation being investigated, using the method described in Ref. [30]. H_{th} contains one million entries, so that its statistical fluctuations are negligible.

3. Comparison of the measured and predicted histograms H_{meas} and H_{th}, bin by bin, for n bins over the q^2 range for which the theoretical calculation is valid, yields a value of χ^2. The χ^2 is computed as :

$$\chi^2 = \sum_{i,j=1}^{n} \left(H_{meas}(q_i^2) - H_{th}(q_i^2)\right)\ V_{ij}^{-1}\ \left(H_{meas}(q_j^2) - H_{th}(q_j^2)\right), \qquad (3.22)$$

   where the covariance matrix V includes all the statistical and systematic experimental uncertainties, but neglects the theoretical uncertainties.

4. The probability that the QCD calculation under investigation describes our measured spectra is obtained from the value of χ^2 determined above, using the standard

procedure for n degrees of freedom, where n is the number of q^2 bins.

We tested three different QCD calculations : two recent unquenched lattice QCD calculations [31, 32] and one recent Light Cone Sum Rule calculation [55]. We provide sufficient information so that any future calculation can be tested against our results. These are the measured $\Delta\mathcal{B}(q^2)$ distributions, and those "without FSR", and their associated covariance matrices.

3.3.10 Extraction of $|V_{ub}|$

The final step of our analysis consists in extracting the value of $|V_{ub}|$ for the exclusive $B \to X_u \ell\nu$ decays. We simply compute the values of $|V_{ub}|$ corresponding to each semileptonic model investigated in Sect. 3.3.9, with the uncertainty calculated by error propagation. Doing so, we obtain several values of $|V_{ub}|$. In the abstract and summary, we quote the $|V_{ub}|$ value associated with the published lattice QCD calculation [31] of the form factor for the $B^0 \to \pi^-\ell^+\nu$ decays that gives the best fit to our data.

To extract a value of $|V_{ub}|$ from a given model, using our measured $\Delta\mathcal{B}(q^2)$ spectra, we consider the standard relation :

$$\Delta\mathcal{B} = \frac{\tau_{B^0}|V_{ub}|^2 G_F^2}{24\pi^3} \int_{q^2_{min}}^{q^2_{max}} |\vec{p}_{X_u}|^3 f_+(q^2)^2 dq^2, \tag{3.23}$$

in which $|\vec{p}_{X_u}|$ is a function of q^2 defined by Eq. 3.15. Eq. 3.23 is often written as :

$$|V_{ub}| = \sqrt{\Delta\mathcal{B}/(\tau_{B^0}\Delta\zeta)} \tag{3.24}$$

where $\tau_{B^0} = 1.530 \pm 0.009$ ps [24] is the B^0 lifetime and

$$\Delta\zeta = \frac{G_F^2}{24\pi^3} \int_{q^2_{min}}^{q^2_{max}} |\vec{p}_{X_u}|^3 f_+(q^2)^2 dq^2. \tag{3.25}$$

is the normalized theoretical partial decay rate. As can be seen in Eq. 3.25, $\Delta\zeta$ depends only on well-known quantities, except for the values of the $f_+(q^2)$ form factor and its uncertainty that are provided by a QCD calculation in a given q^2 range. Since the lattice QCD model applies only for $q^2 > 16\ \mathrm{GeV}^2/c^4$, and our experimental values for $B^+ \to \eta\ell^+\nu$ are obtained for $q^2 < 16\ \mathrm{GeV}^2/c^4$ only, our discussion for the $B^+ \to \eta\ell^+\nu$ channel will be restricted to the LCSR calculation valid for this lower range of q^2. For the $B^0 \to \pi^-\ell^+\nu$ channel, we can use both lattice QCD and LCSR calculations to extract a value of $|V_{ub}|$. The corresponding partial BFs, $\Delta\mathcal{B}$, and their uncertainties are obtained by summing over the relevant q^2 bins in Eqs. 3.10 and 3.12. At this stage, we have everything we need to extract $|V_{ub}|$ using Eq. 3.24. We follow the procedure used by HFAG [43] to propagate the uncertainties of the input quantities $\Delta\mathcal{B}$, τ_{B^0} and $\Delta\zeta$ to $|V_{ub}|$. We first compute $|V_{ub}|$ with the central values of these quantities, then we compute it again with each quantity plus and minus its uncertainty. The ensuing variations of $|V_{ub}|$ are considered to be its uncertainties.

3.4 Signal extraction fit technique

Many other analyses in BaBar also use fits to the ΔE and m_{ES} distributions. Indeed, for signal events, this distribution has a typical shape, which differs greatly from the shape observed for background events. For most of these analyses, analytical probability density functions (PDFs) that provide a satisfactory description of the observed distributions are available.

Analyses of semileptonic decays can also use similar ΔE-m_{ES} distributions. However, the presence of a neutrino results in a less precise reconstruction of these two quantities. This is specially the case in the present analysis due to the fact that we use loose neutrino quality cuts. This leads to a ΔE-m_{ES} distribution (Figures 3.20 ($B^+ \rightarrow \eta^{'} \ell^+ \nu$), 3.21 ($B^+ \rightarrow \eta \ell^+ \nu$) and 3.22 ($B^0 \rightarrow \pi^- \ell^+ \nu$)) whose shape is difficult to model precisely with an analytic PDF. This difficulty comes mostly from the fact that a correlation is introduced between these two quantities by the missing momentum of the neutrino. For this reason, it is more optimal to fit the data distribution to the signal and background ΔE-m_{ES} histogrammed distributions obtained from the Monte Carlo samples described in Sect. 3.5. The parameters determined by the fit are the scaling factors applied to the yields predicted by the Monte Carlo simulation to infer the true yields in the data. The fit[14] is based on a generalized binned likelihood fit method first developed by R. Barlow and C. Beeston [50].

The Barlow and Beeston technique is of interest to us since it takes into account not only the statistical fluctuations affecting the data distribution, but also those affecting the Monte Carlo distributions that we fit to these data. This feature of the fit is important because, as will be explained in Sects. 3.5.2.8 and 3.8.1.1, the statistics available for the Monte Carlo continuum events are relatively small, specially when they are spread over three bins of $\tilde{q}^2$ for $B^+ \rightarrow \eta \ell^+ \nu$ decays and twelve bins of $\tilde{q}^2$ for $B^0 \rightarrow \pi^- \ell^+ \nu$ decays.

As stated in Sects. 3.1.2 and 3.3.4, we perform a fit to the ΔE-m_{ES} distributions to extract the signal and background yields in n q^2 bins, where n=1 for $B^+ \rightarrow \eta^{'} \ell^+ \nu$ decays, n=1 for $B^+ \rightarrow \eta \ell^+ \nu$ decays (3π channel), n=3 for $B^+ \rightarrow \eta \ell^+ \nu$ decays ($\gamma\gamma$

[14] We use a package named BToXulnuFitter which incorporates the same core fitter as the EcsFitter package, used in Ref. [36], but with a different user interface adapted to our analysis code.

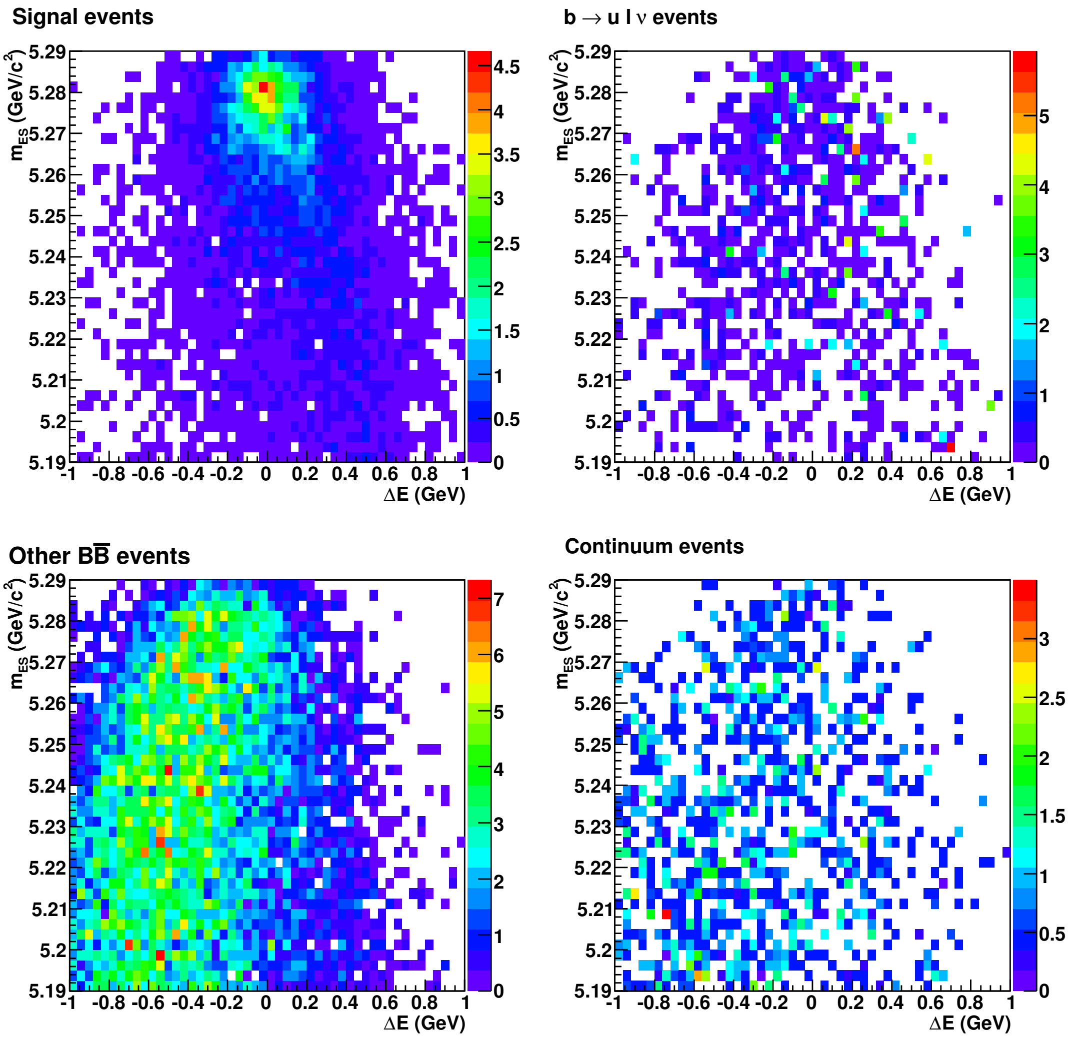

Figure 3.20 – ΔE-m_{ES} $B^+ \to \eta' \ell^+ \nu$ distributions ($\gamma\gamma$ channel) for the four categories of events used in the signal extraction fit after all selections.

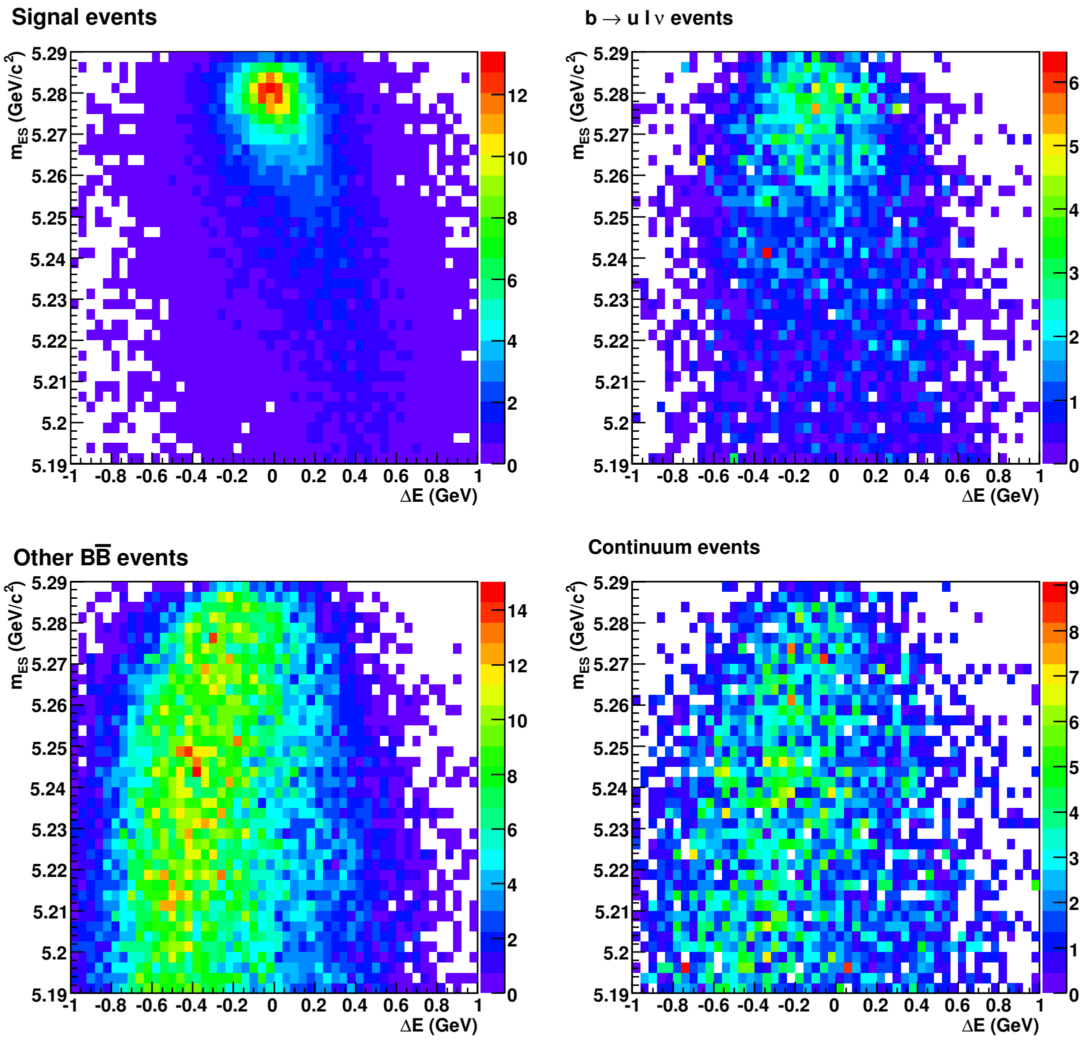

Figure 3.21 – ΔE-m_{ES} $B^+ \to \eta\ell^+\nu$ distributions ($\gamma\gamma$ channel) for the four categories of events used in the signal extraction fit after all selections.

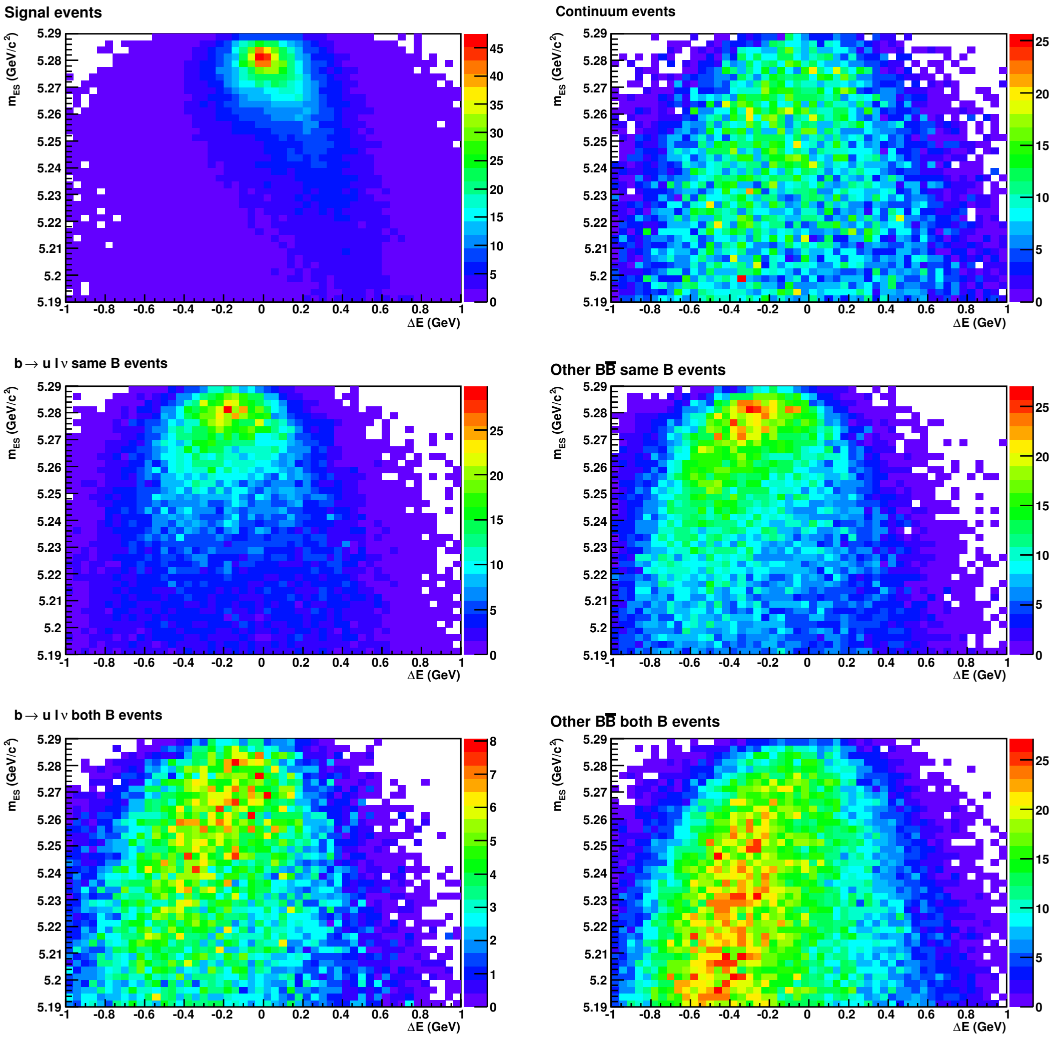

Figure 3.22 – ΔE-m_{ES} $B^0 \rightarrow \pi^- \ell^+ \nu$ distributions for the six categories of events used in the signal extraction fit after all selections.

channel), and n=12 for $B^0 \rightarrow \pi^- \ell^+ \nu$ decays. The simplest way is to perform the fit in each q^2 bin separately, determining for each q^2 bin the signal yield, as well as the $b \rightarrow u\ell\nu$, other $B\bar{B}$ and continuum background yields. However, we found that for $B^0 \rightarrow \pi^- \ell^+ \nu$ decays, the $b \rightarrow u\ell\nu$ and other $B\bar{B}$ backgrounds where the pion and lepton are coming from the same B have ΔE-m_{ES} distributions that differ from those of the $b \rightarrow u\ell\nu$ and other $B\bar{B}$ backgrounds coming from both B. To take this into account, we now have five background categories for these decays : $b \rightarrow u\ell\nu$ same B, $b \rightarrow u\ell\nu$ both B, other $B\bar{B}$ same B, other $B\bar{B}$ both B and continuum. The number of categories and fit parameters were chosen to provide a good balance between reliance on simulation predictions, complexity of the fit and total uncertainty, as discussed in Sect. 3.9.2. They are shown in Table 3.24. The q^2 range of the background binning for the $B^0 \rightarrow \pi^- \ell^+ \nu$ decay is 0-18-26.4 GeV^2/c^4 for the $b \rightarrow u\ell\nu$ same B category, 0-22-26.4 GeV^2/c^4 for the $b \rightarrow u\ell\nu$ both B category, 0-10-26.4 GeV^2/c^4 for the other $B\bar{B}$ same B category, 0-14-26.4 GeV^2/c^4 for the other $B\bar{B}$ both B category and 0-22-26.4 GeV^2/c^4 for the continuum category. These bin widths have been adjusted to have about the same number of events in each bin.

Tableau 3.24 – Categories and number of fit parameters for each decay mode.

Categories	Decay mode				
	$\pi\ell\nu$	$\eta\ell\nu$ ($\gamma\gamma$ & 3π)	$\eta\ell\nu$ ($\gamma\gamma$)	$\eta\ell\nu$ (3π)	$\eta'\ell\nu$ ($\gamma\gamma$)
Signal	12	3	3	1	1
$b \rightarrow u\ell\nu$ same B	2	fixed	fixed	fixed	fixed
$b \rightarrow u\ell\nu$ both B	2	-	-	-	-
other $B\bar{B}$ same B	2	1	1	1	1
other $B\bar{B}$ both B	2	-	-	-	-
Continuum	2	1	1	fixed	fixed

For $B^0 \rightarrow \pi^- \ell^+ \nu$ decays, we find that the fit is optimal when we use two parameters for the $b \rightarrow u\ell\nu$ same B, for the $b \rightarrow u\ell\nu$ both B and for the other $B\bar{B}$ both B backgrounds, while we use three parameters for the other $B\bar{B}$ same B and for the continuum backgrounds. For $B^+ \rightarrow \eta^{(\prime)} \ell^+ \nu$ decays, we find that the ΔE-m_{ES} distributions are similar, within statistics, for the $b \rightarrow u\ell\nu$ same B and $b \rightarrow u\ell\nu$ both B, and other $B\bar{B}$

same B and other $B\bar{B}$ both B backgrounds. For $B^+ \to \eta\ell^+\nu$ decays, we then find that the fit is optimal when we fix one $b \to u\ell\nu$ background while we use only one parameter for the other $B\bar{B}$ background and one parameter for the continuum in the $\gamma\gamma$ channel but a fixed continuum for the 3π channel. For $B^+ \to \eta^{'}\ell^+\nu$ decays, we find that the fit is optimal when we fix both the $b \to u\ell\nu$ and the continuum backgrounds and allow only one parameter for the other $B\bar{B}$ background category.

The initial total yield and shape of the continuum are adjusted using the off-resonance data control sample.

3.4.1 Brief description of the fit technique

To extract the signal and background yields by maximizing a generalized binned likelihood, the ΔE-m_{ES} distributions are subdivided into n bins : 19 bins for $B^+ \to \eta^{(\prime)}\ell^+\nu$ decays (Fig. 3.23) and 34 bins for $B^0 \to \pi^-\ell^+\nu$ decays (Fig. 3.24), both in the data and Monte Carlo samples. Note that this n number of bins does not have the same meaning as the n number of q^2 bins. The total number of events, in the data and Monte Carlo samples are :

$$N_D = \sum_{i=1}^{n} d_i, \quad and \quad N_{MC} = \sum_{j=1}^{m} N_j = \sum_{i=1}^{n}\sum_{j=1}^{m} a_{ji}, \tag{3.26}$$

respectively, where d_i is the number of data events in the i^{th} bin. In the present analysis, the samples selected for the fit are assumed to contain six categories of events for $B^0 \to \pi^-\ell^+\nu$ decays : signal and continuum, $b \to u\ell\nu$ same B, $b \to u\ell\nu$ both B, other $B\bar{B}$ same B and other $B\bar{B}$ both B backgrounds, and four categories of events for $B^+ \to \eta^{(\prime)}\ell^+\nu$ decays : signal and continuum, $b \to u\ell\nu$ and other $B\bar{B}$ backgrounds. The number of Monte Carlo events of category j in the i^{th} bin is a_{ji} and N_j is the total number of events of this category. The index m represents the number of categories of events in our sample.

If we could neglect the statistical fluctuations affecting the Monte Carlo distributions we fit to the data, this likelihood would simply be the probability to observe in the data a given set $\{d_i\}$:

$$ln\mathcal{L} = \sum_{i=1}^{n} d_i ln f_i - f_i, \tag{3.27}$$

where f_i is the **predicted** number of events in the i^{th} bin. Since what we fit to the data distribution are the distributions observed in the Monte Carlo simulation, f_i can be written as :

$$f_i = N_D \sum_{j=1}^{m} P_j w_{ji} a_{ji}/N_j = \sum_{j=1}^{m} p_j w_{ji} a_{ji} \tag{3.28}$$

where P_j is the fraction of the data sample containing events from type j, and w_{ji} is a weight taking into account the ratio between the luminosity of the data sample and the luminosity of the Monte Carlo sample, as well as any other correction, like those described in Sect. 3.5.2. The scaling factors to be determined by the fit are $p_j = N_D P_j/N_j$.

As can be seen from Eq. 3.28, statistical fluctuations can affect f_i through the yields a_{ji} and N_j. Thus, f_i is closer to its true value when it can be written in terms of A_{ji}, the $true$ value around which a_{ji} fluctuates :

$$f_i = \sum_{j=1}^{m} p_j w_{ji} A_{ji} \tag{3.29}$$

To minimize the effect of the limited Monte Carlo statistics in the fit procedure, we do not maximize the likelihood given by Eq. 3.27, but rather maximize a generalized version of this likelihood, based on the combined probability to observe a given set $\{d_i\}$ in the data and a given set $\{a_{ji}\}$ in the Monte Carlo distributions :

$$ln\mathcal{L} = \sum_{i=1}^{n} d_i ln f_i - f_i + \sum_{i=1}^{n} \sum_{j=1}^{m} a_{ji} ln A_{ji} - A_{ji}. \tag{3.30}$$

Since the yields A_{ji} are unknown, in addition to the m scaling factors p_j, we now have $m \times n$ unknown parameters to be determined from the maximization of the likelihood. Despite its apparent complexity, Barlow and Beeston [50] have shown that this maximization could be handled in a simple way. This maximization requires that the derivative of $ln\mathcal{L}$ (Eq. 3.30) with respect to A_{ji} be zero, from which :

$$A_{ji} = \frac{a_{ji}}{1 + p_j w_{ji} t_i}, \tag{3.31}$$

where $t_i = 1 - d_i/f_i$. Thus, the likelihood is maximized with respect to A_{ji} when the values of t_i are the solutions of the set of n equations defined by :

$$\frac{d_i}{1 - t_i} = f_i = \sum_{j=1}^{m} \frac{p_j w_{ji} a_{ji}}{1 + p_j w_{ji} t_i}. \tag{3.32}$$

These equations can be solved numerically. Finally, the value of $ln\mathcal{L}$ is maximized with respect to the $m = 6(4)$ scaling factors p_j using an iterative procedure. At each iteration, the most appropriate value of A_{ji} is obtained from Eqs. 3.31 and 3.32. Only $(m + n)$ equations have to be solved (a great simplification compared to the $(n + 1) \times m$ coupled and non-linear equations required to be solved with a standard approach) to find the best estimate of p_j, as well as the best estimate of A_{ji}.

The procedure described above applies to the fit to a single distribution. We need to fit six(four) such distributions to extract the signal yield as a function of q^2. This is done by finding the maximum of

$$ln\mathcal{L} = \sum_{k=1}^{n} ln\mathcal{L}^k \tag{3.33}$$

where each value of $ln\mathcal{L}^k$ is given by Eq. 3.30, for the ΔE-m_{ES} distribution of the events found in the k^{th} q^2 bin. In the present analysis, 2 scaling factors are determined in the fit to $B^+ \rightarrow \eta^{'} \ell^+ \nu$ decays and $B^+ \rightarrow \eta \ell^+ \nu$ decays in the 3π channel : 1 for the signal and 1 for the other $B\bar{B}$ background ; 5 scaling factors for $B^+ \rightarrow \eta \ell^+ \nu$ decays in the $\gamma\gamma$ channel : 3 for the signal, 1 for the other $B\bar{B}$ background and 1 for the continuum ; 24 scaling factors for $B^0 \rightarrow \pi^- \ell^+ \nu$ decays : 12 for the signal, 2 for the $b \rightarrow u \ell \nu$ same B, 2 for the $b \rightarrow u \ell \nu$ both B, 3 for the other $B\bar{B}$ same B, 2 for the other $B\bar{B}$ both B and 3 for the continuum.

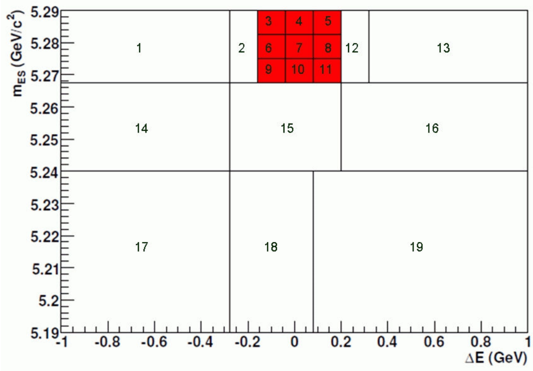

Figure 3.23 – ΔE-m_{ES} 2D binning used in the nominal fit for $B^+ \to \eta^{(\prime)}\ell^+\nu$ decays. The signal region (in red), $-0.16 < \Delta E < 0.2$ GeV and $m_{\mathrm{ES}} > 5.2675$ GeV$/c^2$, is covered by 9 bins. The entire fit region contains 19 bins.

3.4.2 Optimization of the fit performance

The optimization of the fit performance entails essentially the selection cuts and the choice of the Monte Carlo fit categories. Because of the possible correlations between the cut variables and ΔE and m_{ES}, the choice of the value of the cuts can have a major impact on the shape of the ΔE-m_{ES} distribution. With the procedure described in Sect. 3.3.2.8 and 3.3.2.9, the search for optimal cuts was dictated partly by the fact that the larger the difference in shape between the signal and background ΔE-m_{ES} distributions, the easier is the fit.

Other choices have an impact on the performance of the fit, in particular the range of the fit region and the binning chosen inside this region. The choices found to be optimal in our case are shown in Figs. 3.23 and 3.24, for $B^+ \to \eta^{(\prime)}\ell^+\nu$ and $B^0 \to \pi^-\ell^+\nu$ decays, respectively. The range of m_{ES} varies from 5.19 to 5.29 GeV$/c^2$ while that of ΔE varies from -1 to +1 GeV for each $B \to X_u\ell\nu$ channel. The ΔE-m_{ES} binning has been chosen to balance the need for small statistical uncertainties and large number of bins.

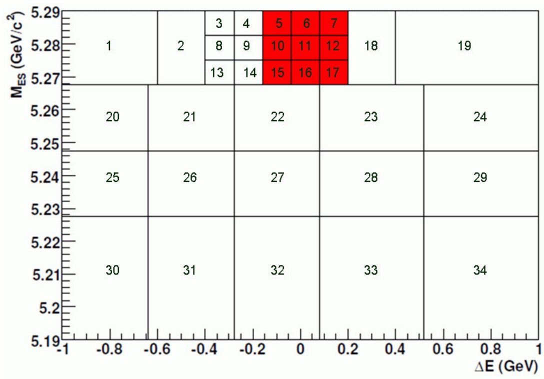

Figure 3.24 – ΔE-m_{ES} 2D binning used in the nominal fit for $B^0 \to \pi^- \ell^+ \nu$ decays. The signal region (in red), $-0.16 < \Delta E < 0.2$ GeV and $m_{\mathrm{ES}} > 5.2675$ GeV$/c^2$, is covered by 9 bins. The entire fit region contains 34 bins.

3.5 Simulation of the data

The $B\bar{B}$ background is simulated with BABAR's standard SP8 (Runs 1 - 5) and SP9 (Run 6) simulation packages to generate $B^0\bar{B}^0$ and B^+B^- events. The $B \to X_u\ell\nu$ signal is also produced with the same packages. In that case, the events with a generic decay are assigned to the decay of one B while the $B \to X_u\ell\nu$ decay signal is generated with the FLATQ2 generator [30] for the decay of the other B. The continuum background is simulated with BABAR's standard SP8/SP9 generic $u\bar{u}/d\bar{d}/s\bar{s}/c\bar{c}$ and $\tau^+\tau^-$ events. The number of events of each type in each sample are given in Sect. 3.2. All the simulated events are scaled to the on-resonance data luminosity. They are corrected as described in Sect. 3.5.2.

3.5.1 Use of the simulation in this analysis

The Monte Carlo simulation plays an essential role in this analysis. It is used to obtain the cut boundaries, the fit biases, the ΔE-m_{ES} histograms used as fit PDFs, the signal efficiency and the signal q^2-unfolding matrix. It is also used to obtain the q^2 shape of the backgrounds. All these quantities are needed to analyze the real data and extract our final results as well as their systematic uncertainties given in Sect. 3.8.4.

With the central values of all the parameters, the histograms obtained from the full MC simulation are also used to generate new distributions by varying randomly only the parameter of interest over a full ($> 3\sigma$) gaussian distribution whose standard deviation is given by the uncertainty in that specific parameter. Such distributions will be referred to as "MC event samples". Each MC event sample is then analyzed the same way as the real data to estimate the contribution of that parameter to the systematic uncertainty in the BF under study, as described in Sect. 3.8.1. This allows the optimization of several parameters of the analysis such as the cut values, the number of $\tilde{q}^2$ bins, the ranges of the ΔE-m_{ES} fit region and the ΔE-m_{ES} and $\tilde{q}^2$ binning, while keeping the analysis blind to the real data. The MC event samples are also used to determine the systematic uncertainties arising from a potential bias in the fits of the central values of the $\mathcal{B}(B \to X_u\ell\nu)$ and $f_+(q^2)$ shape parameters, as described in Sect. 3.6.4.

Once the values of the cuts and other analysis parameters are determined, we perform various Data/MC comparisons described mainly in Sect. 3.9.1 to verify that the agreement between the two is reasonable.

3.5.2 Corrections applied to the MC simulation

While BABAR's MC simulation is based on many parameters which are not all well known, our knowledge of several of these parameters has improved since the start of the original SP8/SP9 MC production. We use this knowledge by reweighting these parameters to their most recent values or by applying corrections in the form of tracks or neutrals killing[15]. The central values of our final results are obtained with the fully corrected and most up to date MC simulation, denoted thereafter as the "central configuration". The remaining uncertainties in the simulation parameters are taken into account when estimating the systematic uncertainties (Sect. 3.6).

The corrections applied to the MC simulation are listed below.

3.5.2.1 Branching Fractions

For each candidate in a simulated $B\bar{B}$ sample (including signal events), we examine the generator-level information to find out the true decays of the $\Upsilon(4S)$, of the two B and of potential D mesons. Since the SP8/SP9 branching fractions of such decays do not always correspond to the most recent value, we apply a weight to them :

$$w_{BF} = w_{\Upsilon(4S)} \times w_{B1} \times w_{B2} \times w_D \tag{3.34}$$

where $w_{\Upsilon(4S)}$, w_{B1}, w_{B2} and w_D are each defined as $w \equiv \frac{most\ recent\ BF}{SP8/SP9\ BF}$. To preserve the value of the total $B \to X$ branching fraction when the branching fractions of some of

[15] In this context, the term "killing" means that a fraction of the simulated tracks and/or neutral candidates are not considered in the analysis to correct for the fact that the reconstruction efficiency is higher in the MC simulation than in data. The candidates which are excluded are chosen randomly.

its decays are modified, its remaining decays are given a weight :

$$w_{remaining} = \frac{1 - (sum\ of\ the\ modified\ BFs)}{sum\ of\ the\ unmodified\ BFs}. \tag{3.35}$$

The same procedure is applied to preserve the total $\Upsilon(4S)$ and D mesons' branching fractions. All the branching fractions modified in the present analysis are listed in Table 3.25.

3.5.2.2 $\Upsilon(4S)$ center-of-mass energy correction

The $\Upsilon(4S)$ center-of-mass energy value used in MC is not the same as the value found in the data. Since the resolution of the $\Upsilon(4S)$ energy is less than 5 MeV, it is possible to correct the MC center-of-mass energy by an energy-dependent weight function $WF(E)$:

$$WF(E) = \psi exp(-\frac{(E_{data} - E_{MC})(E_{data} + E_{MC} - 2E)}{2\sigma_E^2}, \tag{3.36}$$

where $\sigma_E = 4.95\,\mathrm{MeV}$ is the $\Upsilon(4S)$ energy resolution, E the $\Upsilon(4S)$ energy for a given event, E_{data} and E_{MC} are the $\Upsilon(4S)$ mean energies and ψ is a normalization factor given by the ratio of the integrals of the initial and reweighted energy spectra. The values of the parameters to be used in eq. 36 are given in Table 3.26 for each Run. As can be seen, the correction is more important for Runs 5 and 6 where the mean energy difference between data and MC is larger than in Runs 1-4.

3.5.2.3 Form factors

Our knowledge of the $B^+ \to \eta^{(\prime)}\ell^+\nu$, $B^0 \to \pi^-\ell^+\nu$, $B \to \rho\ell\nu$, $B \to \omega\ell\nu$, $B \to D\ell\nu$ and $B \to D^*\ell\nu$ form factors has improved since the initial SP8/SP9 MC production. We are using the form factor reweighting procedure described in Ref. [30] to change these form factors to their most recent values without running the full simulation again.

The values used are :

Branching Fractions (%)	SP8/SP9	this analysis	uncertainty
$\mathcal{B}(\Upsilon(4S) \to B^0 B^0)$	0.5000	0.4840	$\pm$ 0.0060
$\mathcal{B}(\Upsilon(4S) \to B^+ B^-)$	0.5000	0.5160	$\pm$ 0.0060
$\mathcal{B}(B^0 \to D\ell\nu)$	0.0207	0.0217	$\pm$ 0.0009
$\mathcal{B}(B^0 \to D^*\ell\nu)$	0.0570	0.0511	$\pm$ 0.0019
$\mathcal{B}(B^0 \to D_1^*\ell\nu)$	0.0052	0.0069	$\pm$ 0.0014
$\mathcal{B}(B^0 \to D_2^*\ell\nu)$	0.0023	0.0056	$\pm$ 0.0011
$\mathcal{B}(B^0 \to D_0^*\ell\nu)$	0.0045	0.0081	$\pm$ 0.0024
$\mathcal{B}(B^0 \to D_1'\ell\nu)$	0.0083	0.0076	$\pm$ 0.0022
$\mathcal{B}(B^0 \to non-res\ c\ell\nu)$	0.0040	0.0000	$\pm$ 0.0030
$\mathcal{B}(B^0 \to \pi\ell\nu)$	0.000133	0.000139	$\pm$ 0.000009
$\mathcal{B}(B^0 \to \rho\ell\nu)$	0.000269	0.000238	$\pm$ 0.000038
$\mathcal{B}(B^0 \to non-res\ u\ell\nu)$	0.001948	0.001833	$\pm$ 0.001833
$\mathcal{B}(B^+ \to D\ell\nu)$	0.0224	0.0232	$\pm$ 0.0008
$\mathcal{B}(B^+ \to D^*\ell\nu)$	0.0617	0.0548	$\pm$ 0.0027
$\mathcal{B}(B^+ \to D_1^*\ell\nu)$	0.0056	0.0077	$\pm$ 0.0015
$\mathcal{B}(B^+ \to D_2^*\ell\nu)$	0.0030	0.0059	$\pm$ 0.0012
$\mathcal{B}(B^+ \to D_0^*\ell\nu)$	0.0049	0.0088	$\pm$ 0.0026
$\mathcal{B}(B^+ \to D_1'\ell\nu)$	0.0090	0.0082	$\pm$ 0.0025
$\mathcal{B}(B^+ \to non-res\ c\ell\nu)$	0.0038	0.0000	$\pm$ 0.0030
$\mathcal{B}(B^+ \to \pi\ell\nu)$	0.000072	0.000075	$\pm$ 0.000005
$\mathcal{B}(B^+ \to \eta\ell\nu)$	0.000084	0.0000301	$\pm$ 0.0000064
$\mathcal{B}(B^+ \to \eta'\ell\nu)$	0.000084	0.0000301	$\pm$ 0.0000064
$\mathcal{B}(B^+ \to \rho\ell\nu)$	0.000145	0.000129	$\pm$ 0.000020
$\mathcal{B}(B^+ \to \omega\ell\nu)$	0.000145	0.000130	$\pm$ 0.000054
$\mathcal{B}(B^+ \to non-res\ u\ell\nu)$	0.001892	0.0019758	$\pm$ 0.0019758
$\mathcal{B}(D^+ \to Xe)$	0.1699	0.1600	$\pm$ 0.0040
$\mathcal{B}(D^+ \to X\mu)$	0.1656	0.1760	$\pm$ 0.0320
$\mathcal{B}(D^0 \to Xe)$	0.0677	0.0653	$\pm$ 0.0017
$\mathcal{B}(D^0 \to X\mu)$	0.0656	0.0670	$\pm$ 0.0060
$\mathcal{B}(D^s \to Xe)$	0.0692	0.0800	$\pm$ 0.0550
$\mathcal{B}(D^s \to X\mu)$	0.07536	0.0800	$\pm$ 0.0550
$\mathcal{B}(\tau \to Xe)$	0.1778	0.1785	$\pm$ 0.0005
$\mathcal{B}(\tau \to X\mu)$	0.1731	0.1736	$\pm$ 0.0005
$\mathcal{B}(J/\psi \to Xe)$	0.0593	0.0594	$\pm$ 0.0006
$\mathcal{B}(J/\psi \to X\mu)$	0.0588	0.0593	$\pm$ 0.0006

Tableau 3.25 – Branching fractions (%) used in the SP8/SP9 MC simulation and in this analysis. These latter values and uncertainties were taken from Ref. [56] and Ref. [24], The quoted uncertainties were used to estimate the systematic uncertainties (see. Sect. 3.6.2.1).

Run	E_{data} (GeV)	E_{MC} (GeV)	ψ
1	10.57756	10.57730	0.99714
2	10.57869	10.57783	0.99219
3	10.57843	10.57773	0.99457
4	10.57771	10.57727	0.99574
5	10.57811	10.57670	0.98919
6	10.57960	10.57616	0.98654

Tableau 3.26 – $\Upsilon(4S)$ center-of-mass energy correction parameters for each run cycle.

- $B^+ \to \eta^{(\prime)}\ell^+\nu$ and $B^0 \to \pi^-\ell^+\nu$: $\alpha_{BK} = 0.52$, the central value of our previous result[39] using the Becirevic-Kaidalov $f_+(q^2)$ parametrization [52], instead of the ISGW2 quark model [57] used in SP8/SP9 MC ;
- $B \to \rho\ell\nu$ and $B \to \omega\ell\nu$: the Light Cone Sum Rules calculation by Ball & Zwicky [58] instead of the ISGW2 quark model [57] used in SP8/SP9 MC ;
- $B \to D\ell\nu$: $\rho^2 = 1.18$, the World Average value of the ρ^2 parameter [43] using the Caprini, Lellouch, Neubert (CLN) parametrization [59] instead of the ISGW2 quark model [57] used in SP8/SP9 MC ;
- $B \to D^*\ell\nu$: $R1 = 1.429$, $R2 = 0.827$ and $\rho^2 = 1.191$, the central values measured by BABAR [60] using the CLN parametrization instead of the SP8/SP9 MC values of $R1 = 1.18$, $R2 = 0.72$ and $\rho^2 = 0.92$.

3.5.2.4 Non-resonant $b \to u\ell\nu$ decays

The description of non-resonant $B \to X_u\ell\nu$ decays has improved since the initial SP8/SP9 MC production. Instead of the one dimensional m_{X_u} probability function used in SP8/SP9, we use the so-called "Hybrid MC" three dimensional weights : $w(m_{X_u}, q^2, E_\ell)$ where E_ℓ is the lepton energy measured in the $\Upsilon(4S)$ frame [61]. We apply a correction to our MC simulation to benefit from this improvement.

Our central Hybrid MC weights are calculated based on the BF values given in Table 3.25 and on the inclusive $b \to u$ Shape Function parameters : a=1.33 and m_b=4.6586 GeV/c^2 [62, 63]. The parameters (a, m_b) used by the HybridMC weighting tool are obtained from the Kagan-Neubert scheme parameters $(\bar{\Lambda}, \lambda_1)$ given in Ref. [63] by the relations :

$$a = -\frac{3\bar{\Lambda}^2}{\lambda_1} - 1; \tag{3.37}$$

$$m_b = m_B - \bar{\Lambda}. \tag{3.38}$$

3.5.2.5 Particle identification

As mentioned in Sect. 3.3.2.2, we are using BABAR's standard PidLHElectrons, muNN-Tight and piLHLoose selections to identify the signal's lepton and pion. We take into account the fact that PID efficiencies and fake rates are different in data and MC by applying the standard PID-weighting procedure described in Ref. [64]. Following that procedure, the appropriate weights and their statistical uncertainties are taken from the conditions database while producing ntuples with the BABAR Framework latest release. After a random variation of the individual weights, track by track, with a gaussian standard deviation delimited by their statistical uncertainties, we apply the weight $w \equiv w_{lepton\_PID} \cdot w_{pion\_PID}$ to the signal candidate yields.

3.5.2.6 Tracking reconstruction efficiency

This analysis depends on the tracking reconstruction efficiency in two ways. First, the probability of finding the signal's lepton and hadron depends directly on the tracking reconstruction efficiency. Second, we are using several full-event reconstruction quantities, namely : ΔE, m_{ES}, θ_{miss}, $M^2_{miss}/2E_{miss}$ and $\cos\theta_{thrust}$ (see Sect. 3.3.2) which require summing over all charged tracks in an event and thus depend on the tracking reconstruction efficiency.

To reconstruct the signal lepton and hadron, we use BABAR's standard Good Tracks Loose and standard Good Tracks Very Loose selections, respectively (see Sect. 3.3.2.2). For the full-event reconstruction quantities, we use BABAR's standard Good Tracks Very Loose selections. In release 22 [65], the tracking efficiency is taken to have the value given by the simulation. It is no longer corrected by applying a level of killing.

K_L^0 momentum (GeV/c)	Probability ($\%$)	σ_{stat} ($\%$)	σ_{tot} ($\%$)
$0-0.4$	22	3.5	6.7
$0.4-1.4$	1	1.6	6.0
>1.4	9	5.0	7.6

Tableau 3.27 – EMC clusters transformation probabilities and their uncertainties.

3.5.2.7 Production and reconstruction of neutral candidates

The neutral candidates (EMC bumps not associated with a charged track) are directly used in the reconstruction of the signal when the η meson decays into gammas. They are also used for the reconstruction of full-event quantities, namely : ΔE, m_{ES}, θ_{miss}, $M^2_{miss}/2E_{miss}$ and $\cos\theta_{thrust}$, Bhabha veto and γ conversion veto (see Sect. 3.3.2).

If the neutral candidate's truth-matching does not point to a K_L^0 or to a neutron, it is considered to be a photon. In this case, the reconstruction efficiency of the photon is obtained by applying a killing of 0.7% to candidates with reconstructed momentum greater than 1 GeV/c, and no killing to candidates with momentum lower than 1 GeV/c, as described in Ref. [66]. No correction is applied to the reconstruction efficiency of the neutrons.

The K_L^0 production rate needs to be corrected. For this purpose, we use the results of a study of K_S^0 production documented in BAD 1642 [67]. The correction cannot be done by removing clusters but instead by randomly transforming clusters associated with K_L^0 into "pseudo-photons" and thus effectively reducing the number of K_L^0. This is done by rescaling the measured momentum of the K_L^0 cluster to the true K_L^0 momentum and by rescaling its energy assuming zero mass for the pseudo-photons. The probabilities for the transformation and their uncertainties are taken from Ref. [67] and are reproduced in Table 3.27.

Following the procedure described in Ref. [68], the K_L^0 reconstrution efficiency is corrected by applying a level of killing to the EMC clusters truth-matched to a K_L^0. The level of killing varies between 0% and 27%, depending on the true K_L^0 momentum. In addition, the energy deposited by a K_L^0 in the EMC is corrected with scale factors varying between 1.014 and 1.223, depending on the true K_L^0 momentum.

3.5.2.8 Continuum data

We are using the off-resonance data to compute corrections to the simulated continuum events. The corrections for $B^+ \to \eta' \ell^+ \nu$, $B^+ \to \eta \ell^+ \nu$ ($\gamma\gamma$ channel), $B^+ \to \eta \ell^+ \nu$ (3π channel) and $B^0 \to \pi^- \ell^+ \nu$ decays to the yields and $\tilde{q}^2$ spectra of the simulated continuum events described below are obtained from the distributions shown in Figs. 3.25, 3.26, 3.27 and 3.28, respectively. As can be seen, there is fair agreement, within statistics, between data and MC for the ΔE, $m_{\rm ES}$ and $\tilde{q}^2$ shapes in both lepton channels in most cases. There is some discrepancy in the electron channel for $B^0 \to \pi^- \ell^+ \nu$ decays. As explained below, this is taken care of by reweighting the total MC continuum yield, the result is shown in Fig. 3.29, and by reweighting the MC continuum $\tilde{q}^2$ spectrum shape, with the result shown in Fig. 3.30.

After all the analysis selections, the off-resonance data yields are only 54, 404, 103 and 3120 events for $B^+ \to \eta' \ell^+ \nu$, $B^+ \to \eta \ell^+ \nu$ ($\gamma\gamma$ channel), $B^+ \to \eta \ell^+ \nu$ (3π channel) and $B^0 \to \pi^- \ell^+ \nu$ decays, respectively, (electrons and muons combined). These are not large numbers when distributed over $19 \times\ 1 = 19$ (ΔE,$m_{\rm ES}$,$\tilde{q}^2$) 3D bins used in the nominal fit for $B^+ \to \eta' \ell^+ \nu$ decays, $19 \times\ 3 = 57$ 3D bins for $B^+ \to \eta \ell^+ \nu$ decays and $34 \times\ 12 = 408$ 3D bins for $B^0 \to \pi^- \ell^+ \nu$ decays. The continuum MC yields are respectively 936.7, 5776.7, 1156.9 and 30522.2 events, more than 10 times the off-resonance data yields. Therefore, it is preferable to use the continuum MC rather than the off-resonance data to get the fit PDF of the continuum.

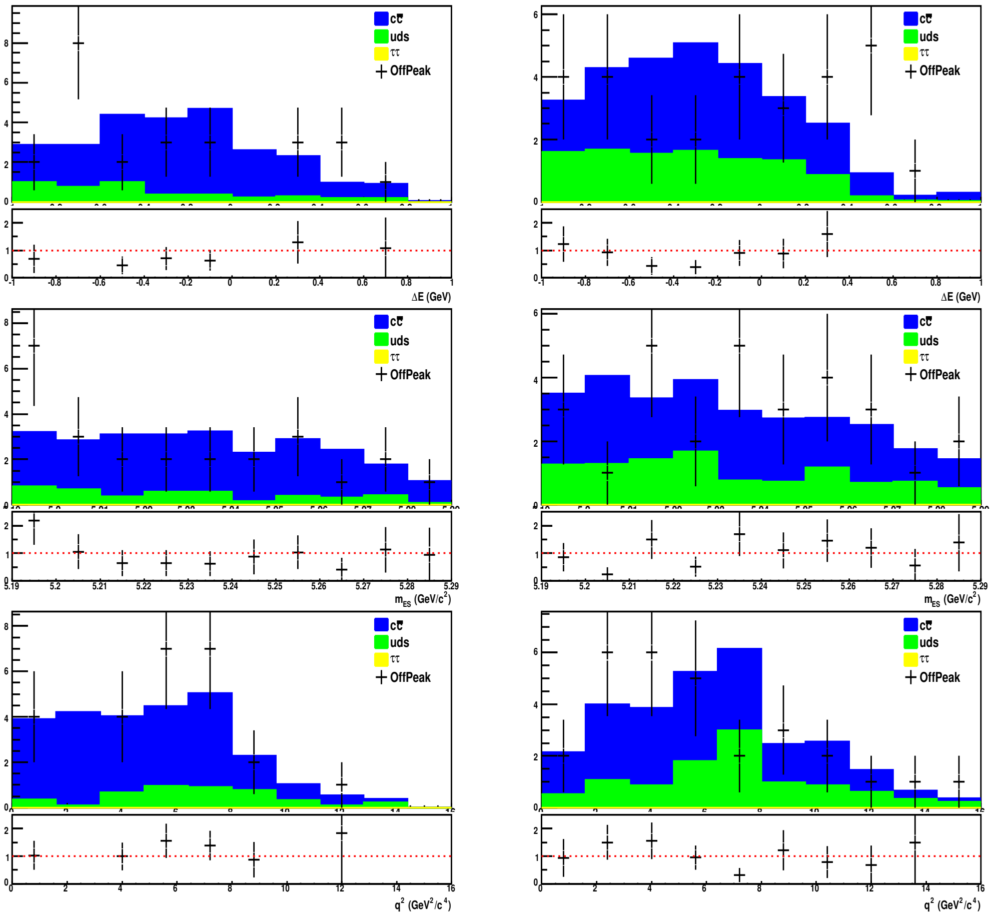

Figure 3.25 – Comparison of the ΔE, m_{ES} and $\tilde{q}^2$ distributions obtained in the off-resonance data and simulated continuum for $B^+ \to \eta^{\prime} \ell^+ \nu$, separately for electrons (left) and muons (right). All the analysis cuts and MC corrections have been applied except for the correction for the continuum yields.

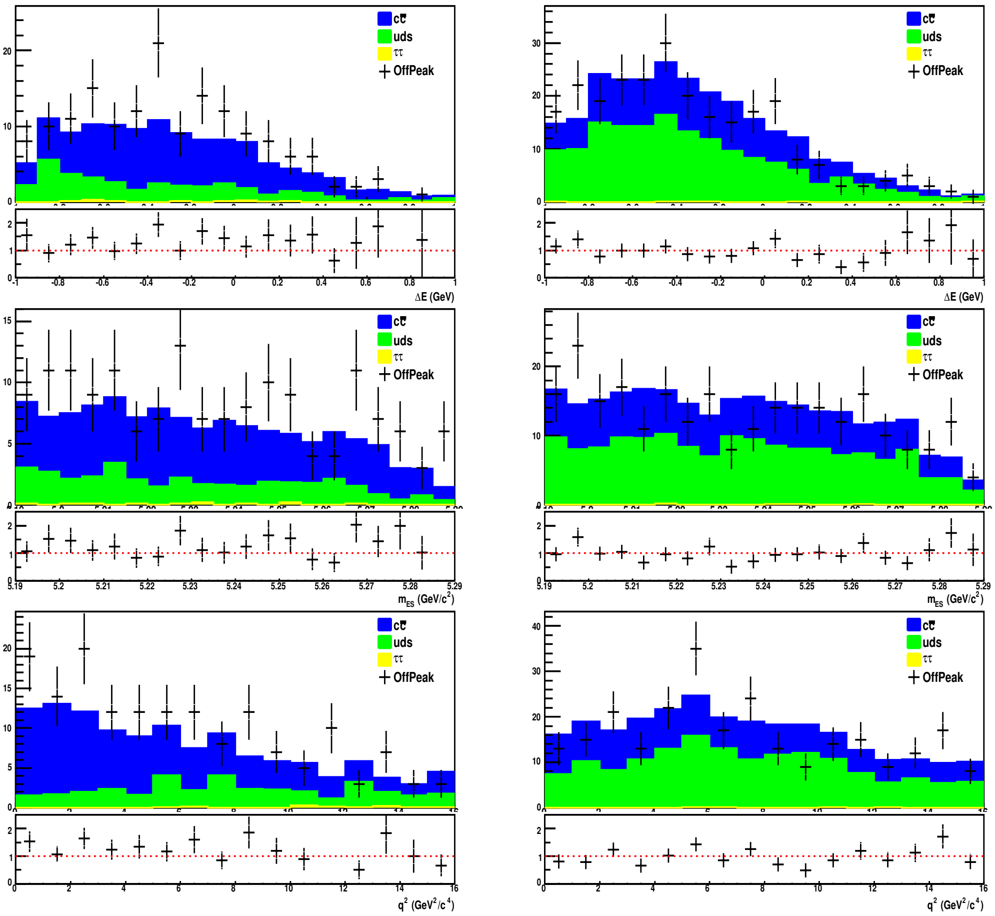

Figure 3.26 – Comparison of the ΔE, m_{ES} and $\tilde{q}^2$ distributions obtained in the off-resonance data and simulated continuum for $B^+ \to \eta\ell^+\nu$ ($\gamma\gamma$ channel), separately for electrons (left) and muons (right). All the analysis cuts and MC corrections have been applied except for the correction for the continuum yields.

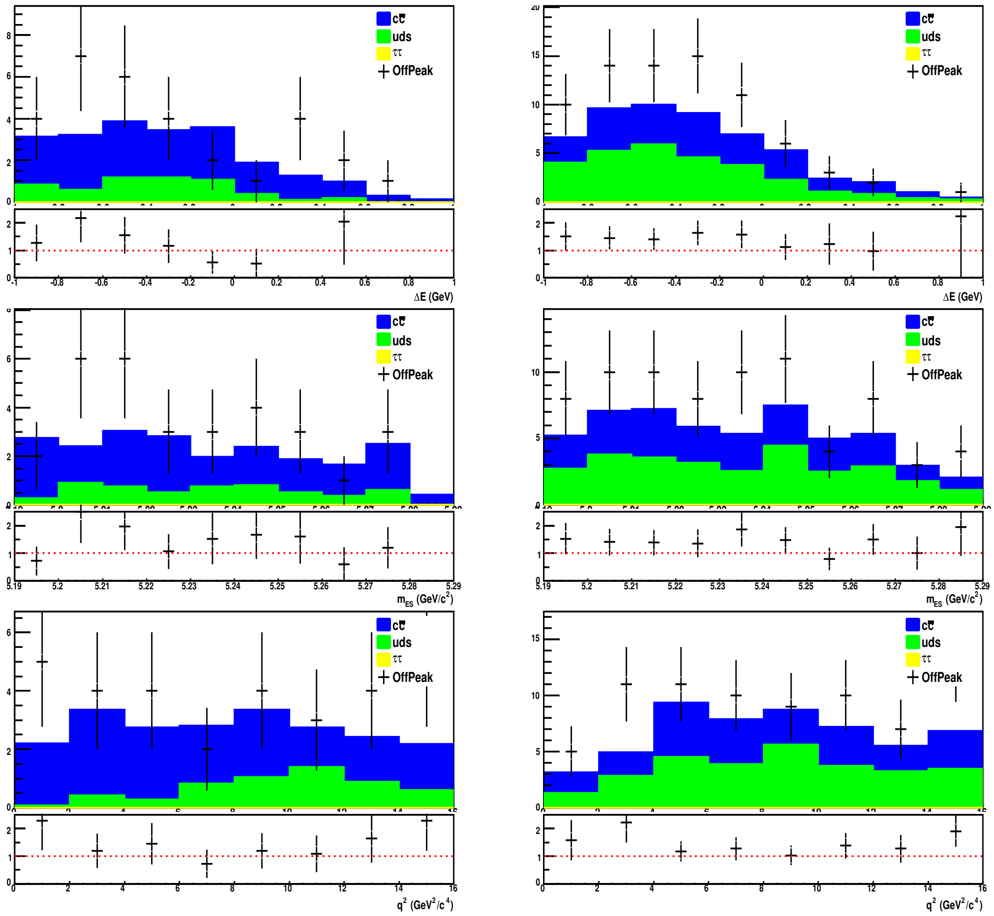

Figure 3.27 – Comparison of the ΔE, $m_{\rm ES}$ and $\tilde{q}^2$ distributions obtained in the off-resonance data and simulated continuum for $B^+ \to \eta\ell^+\nu$ (3π channel), separately for electrons (left) and muons (right). All the analysis cuts and MC corrections have been applied except for the correction for the continuum yields.

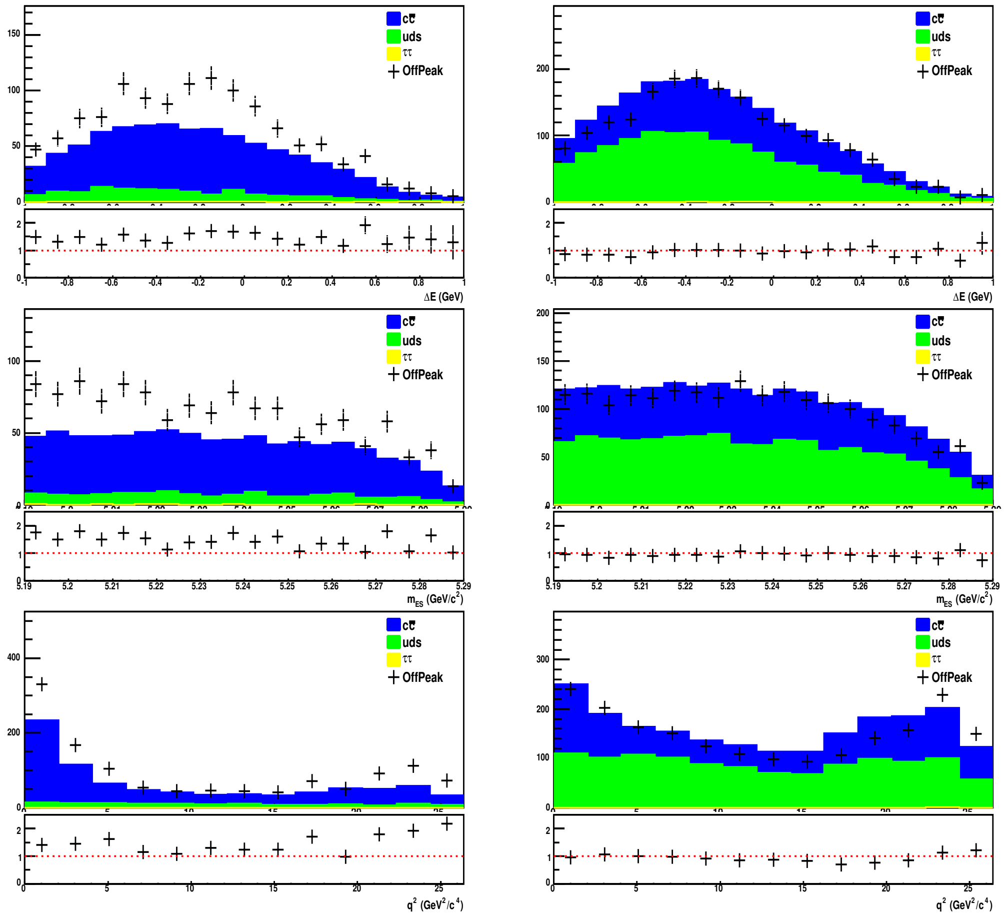

Figure 3.28 – Comparison of the ΔE, m_{ES} and $\tilde{q}^2$ distributions obtained in the off-resonance data and simulated continuum for $B^0 \to \pi^- \ell^+ \nu$, separately for electrons (left) and muons (right). All the analysis cuts and MC corrections have been applied except for the correction for the continuum yields.

Total MC continuum yield corrections

The total yields of the continuum MC are corrected separately for the electron and muon channels, using the off-resonance data control samples.

In the electron channel, the off-resonance total data yields after all the analysis selections are 25.0 ± 5.0, 159.0 ± 12.6, 31 ± 5.6 and 1230.0 ± 35.1 while they are 23.7 ± 1.1, 123.7 ± 2.7, 21.8 ± 1.1 and 835.9 ± 7.1 in the continuum MC (scaled to the luminosity of the off-resonance data), for $B^+ \to \eta^{'} \ell^+ \nu$, $B^+ \to \eta \ell^+ \nu$ $(\gamma\gamma)$, $B^+ \to \eta \ell^+ \nu$ (3π) and $B^0 \to \pi^- \ell^+ \nu$ decays, respectively. Thus, we apply a constant weight :

- For $B^+ \to \eta^{'} \ell^+ \nu$ decays : $w_{e\_cont} = \frac{25.0 \pm 5.0}{23.7 \pm 1.1} = 1.054 \pm 0.211$
- For $B^+ \to \eta \ell^+ \nu$ $(\gamma\gamma)$ decays : $w_{e\_cont} = \frac{159.0 \pm 12.6}{123.7 \pm 2.7} = 1.285 \pm 0.106$
- For $B^+ \to \eta \ell^+ \nu$ (3π) decays : $w_{e\_cont} = \frac{31.0 \pm 5.6}{21.8 \pm 1.1} = 1.419 \pm 0.265$
- For $B^0 \to \pi^- \ell^+ \nu$ decays : $w_{e\_cont} = \frac{1230.0 \pm 35.1}{835.9 \pm 7.1} = 1.471 \pm 0.042$

to all the electron candidates of the continuum MC.

In the muon channel, the off-resonance total data yields after all the analysis selections are 29.0 ± 5.4, 245.0 ± 15.7, 72.0 ± 8.5 and 1890.0 ± 43.5 while they are 23.9 ± 1.2, 252.7 ± 4.2, 51.1 ± 1.9 and 1971.6 ± 12.2 in the continuum MC (scaled to the luminosity of the off-resonance data), for $B^+ \to \eta^{'} \ell^+ \nu$, $B^+ \to \eta \ell^+ \nu$ $(\gamma\gamma)$, $B^+ \to \eta \ell^+ \nu$ (3π) and $B^0 \to \pi^- \ell^+ \nu$ decays, respectively. Thus, we apply a constant weight :

- For $B^+ \to \eta^{'} \ell^+ \nu$ decays : $w_{\mu\_cont} = \frac{29.0 \pm 5.4}{23.9 \pm 1.2} = 1.211 \pm 0.225$
- For $B^+ \to \eta \ell^+ \nu$ $(\gamma\gamma)$ decays : $w_{\mu\_cont} = \frac{245.0 \pm 15.7}{252.7 \pm 4.2} = 0.969 \pm 0.064$
- For $B^+ \to \eta \ell^+ \nu$ (3π) decays : $w_{\mu\_cont} = \frac{72.0 \pm 8.5}{51.1 \pm 1.9} = 1.410 \pm 0.174$
- For $B^0 \to \pi^- \ell^+ \nu$ decays : $w_{\mu\_cont} = \frac{1890.0 \pm 43.5}{1971.6 \pm 12.2} = 0.959 \pm 0.022$

to all the muon candidates of the continuum MC.

The results of the correction for the MC continuum yields are displayed in Fig. 3.29 for the $B^0 \to \pi^- \ell^+ \nu$ decays. Only the central values of w_{e_cont} and w_{μ_cont} are used for the central configuration of the simulation.

MC continuum $\tilde{q}^2$ spectrum shape

The $\tilde{q}^2$ shape of the MC continuum is adjusted to be closer to that of the off-resonance data by applying a correction given by the functions shown in Figs. 3.32, 3.33, 3.34 and 3.35 to the MC continuum yields. These functions are listed below[16] :

– For $B^+ \to \eta^{'}\ell^+\nu$ decays : $w_{q^2\_cont} = 1.096 - 0.0398 \cdot \tilde{q}^2$

– For $B^+ \to \eta\ell^+\nu$ decays ($\gamma\gamma$ channel) : $w_{q^2\_cont} = 1.024 - 0.00555 \cdot \tilde{q}^2$

– For $B^+ \to \eta\ell^+\nu$ decays (3π channel) : $w_{q^2\_cont} = 0.908 + 0.00492 \cdot \tilde{q}^2$

– For $B^0 \to \pi^-\ell^+\nu$ decays : $w_{q^2\_cont} = 0.952 + 0.0470 \cdot \tilde{q}^2 - 0.00742 \cdot \tilde{q}^4 + 0.000249 \cdot \tilde{q}^6$

The $w_{q^2\_cont}$ weight functions are obtained from a fit to the ratios of off-resonance data to continuum MC yields where the events from the electron and muon channels have been added to form a single data set. It follows that the same weight function is applied to both lepton channels. This procedure is justified since the data/MC ratios of $\tilde{q}^2$ are similar in both channels, within statistics, after the total yield correction (see Fig. 3.29 for $B^0 \to \pi^-\ell^+\nu$ decays). As displayed in Fig. 3.30 for $B^0 \to \pi^-\ell^+\nu$ decays, there is now an excellent agreement between data and MC for both electron and muon channels, once the MC continuum yields have been corrected and the $w_{q^2\_cont}$ weight functions applied.

We note that we apply 1D corrections only to the continuum $\tilde{q}^2$ shape. No correction is applied to ΔE and m_{ES} in the central configuration since they would need to be corrected by 2D functions.

[16] In these equations, $\tilde{q}^2$ is given in units of GeV^2/c^4.

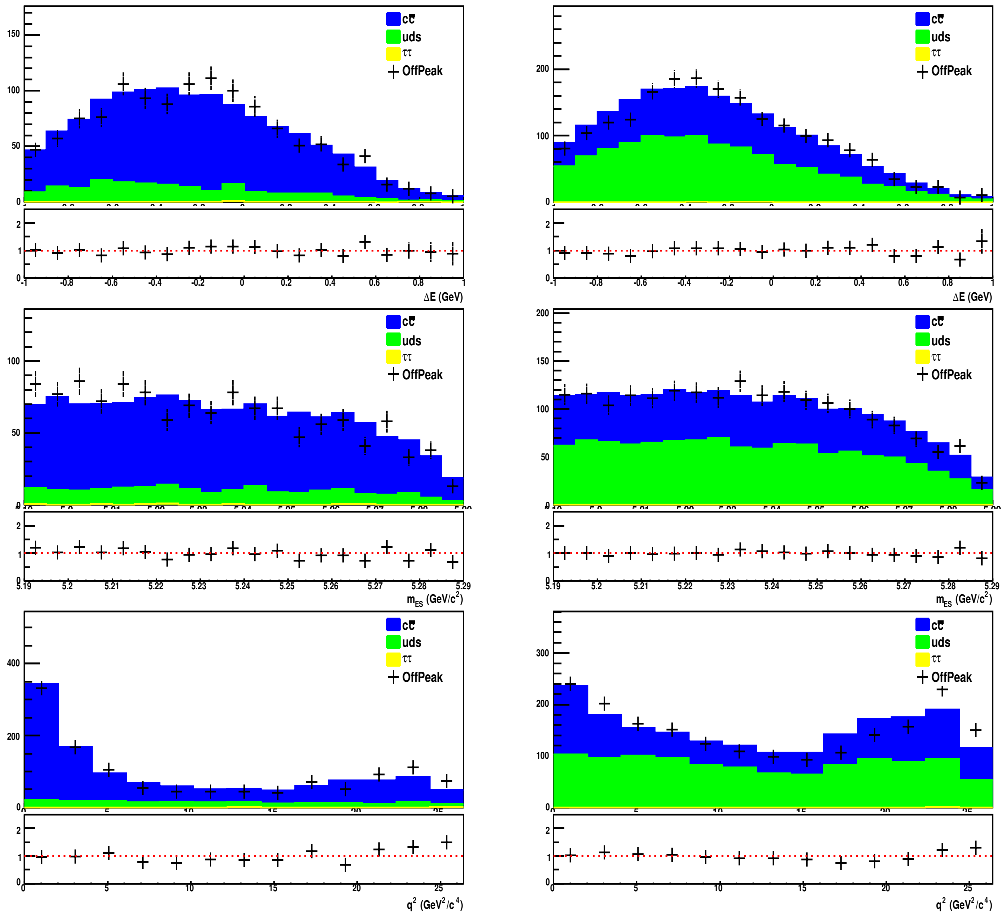

Figure 3.29 – Comparison of the ΔE, m_{ES} and $\tilde{q}^2$ distributions obtained in the off-resonance data and simulated continuum for $B^0 \to \pi^- \ell^+ \nu$, separately for electrons (left) and muons (right). The MC continuum yields for all distributions have been corrected, as explained in the text.

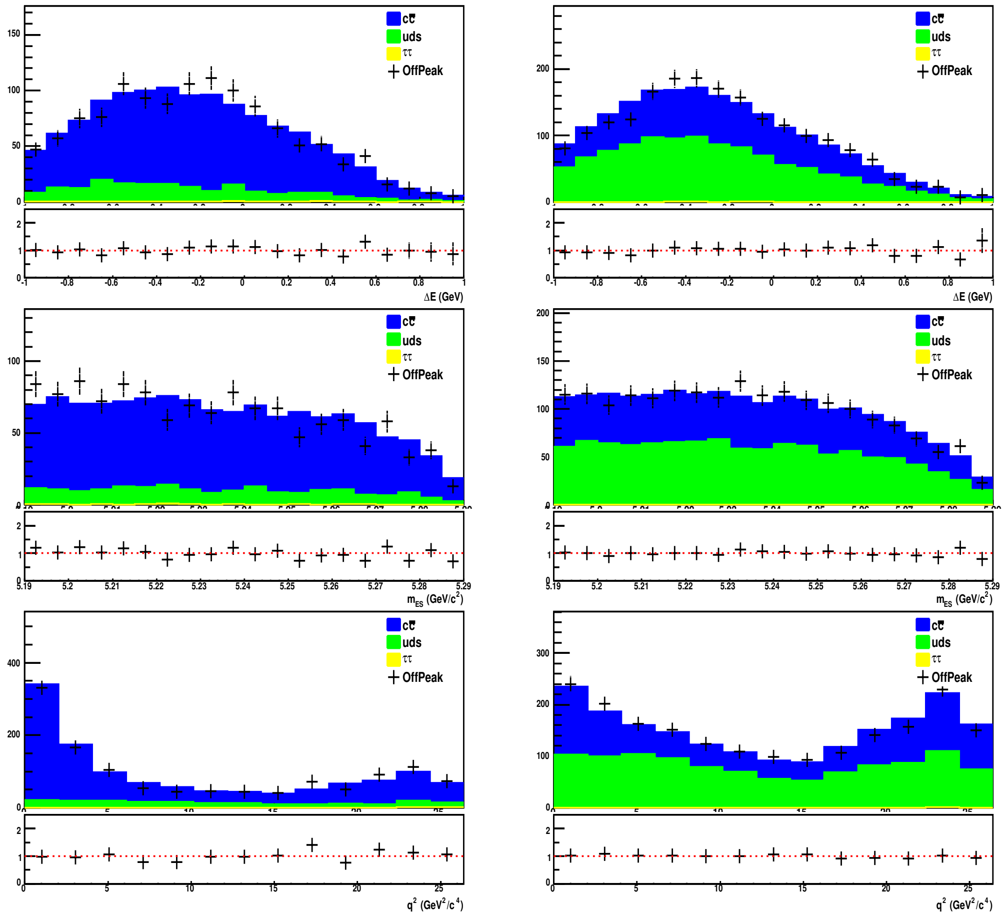

Figure 3.30 – Comparison of the ΔE, $m_{\rm ES}$ and $\tilde{q}^2$ distributions obtained in the off-resonance data and simulated continuum for $B^0 \to \pi^- \ell^+ \nu$, separately for electrons (left) and muons (right). The continuum yields have been corrected and the $w_{q^2\_cont}$ weight function has been applied to the q^2 distribution only.

3.6 Systematic uncertainties

There are various sources of systematic uncertainties in this analysis. Most of them arise from differences between the data and the MC simulation since the analysis relies on their comparison to obtain the signal efficiency of the cuts, the signal q^2-unfolding matrix, as well as the shape of the ΔE-$m_{\rm ES}$ PDFs used in the signal extraction fit. These uncertainties are estimated from the variations of the resulting partial BF values when the data are re-analyzed with different simulation parameters. For each parameter[17], we use the full MC data set obtained after the skim to generate at least one hundred additional MC event samples (see Sect. 3.5). When the procedure involves modified tracks or neutrals killing, only cuts on variables not affected by the killing such as $\cos\theta_{BY}$, invariant mass, ... are used to generate the reduced ntuples. When only the weights are varied, the generation of MC samples is carried out from ntuples where all the analysis cuts are pre-applied. To account for all possible effects, the entire analysis is repeated for each MC event sample with resulting signal efficiencies, q^2-unfolding matrices, ΔE-$m_{\rm ES}$ PDFs, and $B \to X_u \ell\nu$ signal yields extracted from the fits in each selected bin of q^2. For exemple, in the case of $B^0 \to \pi^-\ell^+\nu$ decays, each one of the 100 MC event samples yields 12 values of $\Delta\mathcal{B}$ and one value for the total BF. The distribution of the $\Delta\mathcal{B}$ values in each bin of q^2 gives the uncertainty σ_i (RMS value) for each $\Delta\mathcal{B}(q_i^2)$ value, while the distribution of the values of the total BFs gives the uncertainty σ for the total BF for the specific parameter under investigation.

To obtain the correlation and covariance matrices from these repeated measurements, we also build two-dimensional $\Delta\mathcal{B}(q_i^2)$ vs. $\Delta\mathcal{B}(q_j^2)$ distributions for each $q_i^2 - q_j^2$ combination. For each source of systematic uncertainty, each one of the 100 MC samples results in one point in such a histogram that will contain a total of 100 points for a given $q_i^2 - q_j^2$ combination e.g. the value of $\Delta\mathcal{B}$ in the first q^2 bin associated with the value of $\Delta\mathcal{B}$ in the second q^2 bin. For any such histogram, the correlation factor $C_{i,j}$ is calculated according to the TH2D function in ROOT. The elements of the covariance matrices are given by the relation $V_{i,j} = \sigma_i\sigma_j C_{i,j}$ where σ_i and σ_j are the uncertainties in the i^{th}

[17]Exceptions are the FSR and bremsstrahlung processes where only one sample has been generated (see Sect. 3.6.2.4) and B counting whose systematic uncertainty has been evaluated to be 1.1% in each q^2 bin.

and j^{th} bins of $\tilde{q}^2$. We obtain the total covariance matrix by summing all the individual covariance matrices for each source of systematic uncertainty.

In what follows, we explain *how* each systematic uncertainty is estimated. Their numerical values are presented in Sect. 3.8.

3.6.1 Detector simulation

The interactions of charged and neutral particles with the BABAR detector are very carefully simulated with Geant4 [69] in BABAR's standard simulation productions. However, the simulation of the detector is not perfect. The effects of modifying the detector simulation within the range recommended by the experts were carefully investigated.

3.6.1.1 PID of Y candidates

The PIDs used in the reconstruction of a $(X_u + \ell)$ candidate are corrected with weights in the MC simulation, as described in Sects. 3.5.2.5. These weights have systematic uncertainties that arise from the differences between the PID control samples and the sample used in this analysis. These systematic uncertainties are assumed to be fully correlated between all tracks. Their values are given in Table 3.28 [70]. For both, electrons and muons, the systematic uncertainty of the weights is larger for fake candidates.

	weights' systematic uncertainties
electron ID	0.8% / 50%
muon ID	2.2% / 5%
charged pion ID	0.2%

Tableau 3.28 – Systematic uncertainties of the PID weights. For electron and muon ID, the first number applies to real electrons and muons and the second one to fake ones.

The effects of wrong PID have been evaluated by generating MC event samples, one hundred for the leptons and one hundred for the pions, in which the mean values of the PID weights, determined using the procedure described in Sect. 3.5.2.5, were varied from sample to sample with a gaussian standard deviation given by the systematic uncertainties quoted in Table 3.28. The full analysis was performed on each set of hundred samples. The RMS of the resulting BFs distributions yields the contribution to the systematic uncertainty of the BFs due to the uncertainties on the identification of the leptons and the pions, respectively.

3.6.1.2 Full-event reconstruction

The corrections to the simulation of the neutral reconstruction efficiencies take the form of neutrals "killing" (described in Sect. 3.5.2.7) when the full-event quantities ΔE, m_{ES}, $\cos\theta_{miss}$, $M^2_{miss}/2E_{miss}$, $\cos\theta_{thrust}$, Bhabha veta and γ conversion veto are involved. These corrections have associated systematic uncertainties, but their impact on the final results cannot be evaluated with the method described in Sect. 3.6.1.1 since it would sometimes lead to a *negative* level of killing. This is rather difficult to take into account since it requires adding a new neutral whose properties are ill-defined. The full-event reconstruction's systematic uncertainties due to the neutrals reconstruction efficiency are thus evaluated by generating at least one hundred MC event samples[18] in which the level of killing (given in Table 3.29) is randomly *increased*, sample by sample, according to a one-sided gaussian standard deviation. The full analysis is performed for each sample. The results thus obtained with each sample are symmetrized to account for the fact that the level of killing is always increased but never decreased. Considering that the results R_s obtained with each sample differ from their central value by $\Delta R_s = R_s - R_{ref}$ (such that $R_s = R_{ref} + \Delta R_s$), the results are symmetrized by adding both R_s and a mirror entry $R'_s = R_{ref} - \Delta R_s$ to the distribution, for each sample. The RMS of the resulting BFs distribution yield the systematic uncertainties. This procedure is done separately for photons and K^0_L reconstruction. Even though we do not use killing to correct the tracking reconstruction efficiency, this procedure is also used to estimate the systematic uncertainties due to the tracking reconstruction efficiencies. It was deemed advisable not to take into account any systematic uncertainty due to the neutron reconstruction efficiency since this process has not yet been studied.

There are two more contributions to the systematic uncertainties to take into account

[18]We use 150 event samples for the track killing procedure, 250 event samples for the photon killing procedure and 100 event samples for the K^0_L and neutron killing procedure.

due to the detector simulation. The uncertainty due to the K_L^0 production rate is evaluated by generating one hundred MC event samples in which the transformation probabilities are varied randomly, sample by sample, over a full gaussian distribution whose standard deviation is given by their uncertainties (Sect. 3.5.2.7). To estimate the uncertainties due to the energy deposit of the K_L^0, we generate one hundred MC event samples in which the energy scale factors (Sect. 3.5.2.7) are varied randomly, sample by sample, over a full gaussian distribution with a standard deviation determined by their uncertainties given in Ref. [68]. In both cases, the full analysis is performed on each sample. The RMS of the resulting BFs distributions, obtained for the K_L^0 production rate and for the K_L^0 energy deposit, yield the systematic uncertainties due to each.

	default level of killing (%)	systematic uncertainty (%)
K_L^0	0 to 27	± 2 to ± 25
$\gamma, p < 1.0 \text{ GeV}/c$	0	± 1.8
$\gamma, p > 1.0 \text{ GeV}/c$	0.7	± 0.7
charged tracks $p_t > 0.180 \text{ GeV}/c$		
GTL, Run-1	0	± 0.677
GTL, Run-2	0	± 0.377
GTL, Run-3	0	± 0.477
GTL, Run-4	0	± 0.672
GTL, Run-5	0	± 0.776
GTL, Run-6	0	± 0.435
GTVL, Run-1	0	± 0.701
GTVL, Run-2	0	± 0.351
GTVL, Run-3	0	± 0.455
GTVL, Run-4	0	± 0.709
GTVL, Run-5	0	± 0.771
GTVL, Run-6	0	± 0.448
$p_t < 0.180 \text{ GeV}/c$	0	± 2.0

Tableau 3.29 – Levels of tracks/neutrals killing and associated uncertainties. The level of K_L^0 killing and its associated uncertainty varies with the value of the true K_L^0 momentum. For charged tracks and $p_t > 0.180 \text{ GeV}/c$, the level of killing varies with Run number (GTL and GTVL). For charged tracks and $p_t < 0.180 \text{ GeV}/c$, the level of killing is the same for all runs.

3.6.2 Physical properties of B and D mesons

The generator-level input to the simulation also contains imprecisions which can lead to systematic uncertainties. We have estimated these uncertainties by varying the values of several branching fractions and form factors of the B and D meson decays.

3.6.2.1 Branching fractions

We investigated the branching fractions of semileptonic B mesons decays, as well as those of the inclusive $D, J/\psi, \tau \to X\ell$ (secondary lepton decays) and $\Upsilon(4S) \to B\bar{B}$ decays.

The effects of possibly unrealistic $B \to X_u\ell\nu$ branching fractions have been evaluated by generating one hundred MC event samples for each individual exclusive $B \to X_u\ell\nu$ branching fraction whose values were varied randomly[19], sample by sample, according to a full gaussian distribution with standard deviation and mean values taken from Table 3.25 (Sect. 3.5.2.1), with the constraint that the total $b \to u\ell\nu$ branching fraction remains within one standard deviation of its known value. To preserve the value of the total $B \to X$ branching fraction in spite of the fact that the total $B \to X_u\ell\nu$ branching fraction is modified, all the non-$b \to u\ell\nu$ events are given a weight of $w = (1 - Modified\,\mathcal{B}(B \to X_u\ell\nu))/(1 - Original\,\mathcal{B}(B \to X_u\ell\nu))$. The full analysis was performed on each sample. The RMS of the resulting BF distribution yields the systematic uncertainty due to each specific BF under study. The same procedure was repeated for the $B \to X_c\ell\nu$, secondary lepton decays and $\Upsilon(4S) \to B\bar{B}$ branching fractions, always using the mean values and standard deviations of Table 3.25.

3.6.2.2 Form factors

We estimated the systematic uncertainties on the partial and total BFs and $f_+(q^2)$ shape parameters due to the form factor hypotheses of the $B^+ \to \eta^{(\prime)}\ell^+\nu$, $B^0 \to \pi^-\ell^+\nu$, $B \to \rho\ell\nu$, $B \to \omega\ell\nu$, $B \to D^*\ell\nu$ and $B \to D\ell\nu$ decays used in the simulation.

---

[19]The $B^+ \to \eta^{(\prime)}\ell^+\nu$ and $B^0 \to \pi^-\ell^+\nu$ BFs were also modified. The signal efficiency is however recomputed for each MC sample.

$B^+ \to \eta^{(\prime)}\ell^+\nu$ and $B^0 \to \pi^-\ell^+\nu$ scalar form factors

For the $f_+(q^2)$ shape, the central results were obtained using the Becirevic-Kaidalov parametrization[52] and the value of its parameter $\alpha = 0.520 \pm 0.058$ taken from Ref. [39]. We generated one hundred MC event samples in which the values of the α parameter was determined randomly, sample by sample, according to a full gaussian distribution with a mean of 0.520 and a standard deviation of 0.058. This procedure is justified since the uncertainty quoted in Ref. [39] for α includes rigorously estimated statistical and systematic errors. The full analysis was performed on each sample. The RMS of the resulting BF distribution yields the systematic uncertainty.

$B \to \rho\ell\nu$ and $B \to \omega\ell\nu$ vector form factors

For these form factors, we only considered the latest Light Cone Sum Rules calculation by Ball & Zwicky [58], and ignored older and less reliable calculations. We generated one hundred MC event samples in which the values of the three form factors $A1(q^2)$, $A2(q^2)$ and $V(q^2)$ were determined randomly, sample by sample, using the square-root method. This method varies the parameters taking into account the correlations among them (see method RooFitResult : :randomizePars() of the RooFit software [71]). The mean values of the form factors were taken from Ref. [58]. Their uncertainties[72] were 10% at $q^2 = 0$, with a linear increase towards higher q^2 values : $error = 0.1 + \frac{0.03}{14} \cdot q^2$. The full analysis was performed on each sample. The RMS of the resulting BF distribution yields the systematic uncertainty.

$B \to D^*\ell\nu$ form factors

In the central configuration, we used the central values of the $B \to D^*\ell\nu$ form factor parameters given in Ref. [60] : $R1 = 1.429 \pm 0.075$, $R2 = 0.827 \pm 0.044$ and $\rho^2 = 1.191 \pm 0.056$. To estimate the systematic uncertainty due to the $B \to D^*\ell\nu$

form factors, we used the $R1$, $R2$ and ρ^2 uncertainties and correlations given in Ref. [60] : $\sigma_{R1} = 0.075$, $\sigma_{R2} = 0.044$, $\sigma_{\rho^2} = 0.056$, $\eta_{R1-R2} = -0.84$, $\eta_{R1-\rho^2} = +0.71$ and $\eta_{R2-\rho^2} = -0.83$, and generated one hundred MC event samples in which the values of the $R1$, $R2$ and ρ^2 parameters were determined randomly, sample by sample, using the square-root method. The full analysis was performed on each sample. The RMS of the resulting BF distribution yields the systematic uncertainty.

$B \to D\ell\nu$ form factors

In the central configuration, we used the World Average value of the ρ^2 parameter [43] obtained with the CLN parametrization [59] : $\rho^2 = 1.18 \pm 0.18$. We generated one hundred MC event samples in which the values of the ρ^2 parameter were determined randomly, sample by sample, according to a full gaussian distribution with a mean of 1.18 and a standard deviation of 0.18. The full analysis was performed on all hundred samples. The RMS of the resulting BF distribution yields the systematic uncertainty.

3.6.2.3 Non-resonant $b \to u\ell\nu$ decays

The Hybrid MC weights used for the simulation of non-resonant $b \to u\ell\nu$ events in our central configuration were computed according to the central BF values given in Table 3.25 and the shape function parameters : a=1.33 and m_b=4.6586 GeV/c^2 taken from Refs. [62, 63]. To estimate the systematic uncertainty due to these heavy quark parameters, we generated one hundred MC event samples in which the values of the a and m_b parameters were determined randomly, sample by sample, according to a two-dimensional gaussian distribution with standard deviation and mean values taken from Ref. [63], illustrated in Fig. 3.31. The full analysis was performed on each sample. The RMS of the resulting BF distribution yields the systematic uncertainty due to the shape function parameters.

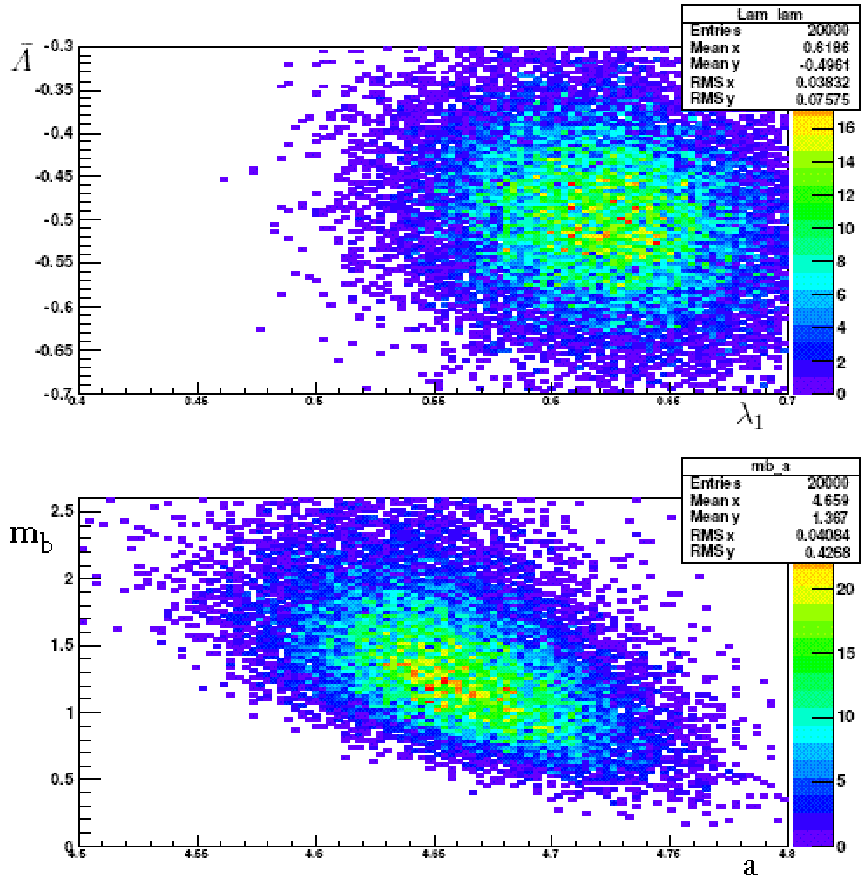

Figure 3.31 – Two-dimensional gaussian distributions used to vary the heavy quark parameters used in the simulation of the non-resonant $b \to u\ell\nu$ decays. The (a, m_b) parameters (lower panel) used by the HybridMC weighting tool are obtained from the $(\bar{\Lambda}, \lambda_1)$ parameters (upper panel) given in Ref. [63] by the relations given in Sect. 3.5.2.4.

3.6.2.4 Final State Radiation

A fraction of the $B \to X_u \ell \nu$ decays subsequently emits Final State Radiation (FSR). This effect is simulated by the PHOTOS package[73, 74], with a conservative uncertainty of 20% attributed to its radiative corrections. FSR affects the kinematic of the $B \to X_u \ell \nu$ decay, including its q^2 spectrum, and generally lowers the signal selection efficiency. To estimate the systematic uncertainty due to FSR, we used a MC signal sample simulated with Moose where PHOTOS is turned off (see Sect. 3.2). This No PHOTOS sample has been skimmed and analyzed with the full event reconstruction and selection. The entire analysis has then been repeated. We take 20% of the difference in the BFs when PHOTOS is turned on and off to be the systematic uncertainty due to FSR.

3.6.2.5 Bremsstrahlung corrections

The uncertainty due to the bremsstrahlung correction is determined by the uncertainty in the thickness of the detector material[75] of $4.5 \pm 0.15\% X_0$. It is estimated from the difference in the BF values with, and without, the additional $0.15\% X_0$ layer of material. To take into account this extra layer of material, we randomly reduce the electron momentum p_e in the laboratory frame by the quantity $p_{brem} = p_{min}\text{exp}(x\text{ln}(p_e/p_{min}))$, where $p_{min} = 10^{-9}$ GeV and x is a random number uniformly distributed between 0 and 1. We reduce the electron momemtum by p_{brem} only for the fraction $0.0015\text{ln}(p_e/p_{min})$ of the events randomly selected.

3.6.3 Modelling of the continuum data

We dispose of a control sample for the continuum, the off-resonance data, from which we are able to estimate the systematic uncertainties with an empirical approach. The systematic uncertainties described below are derived from the distributions shown in Figs. 3.25, 3.26, 3.27 and 3.28 (Sect. 3.5.2.8) for $B^+ \to \eta' \ell^+ \nu$, $B^+ \to \eta \ell^+ \nu$ ($\gamma\gamma$ channel), $B^+ \to \eta \ell^+ \nu$ (3π channel) and $B^0 \to \pi^- \ell^+ \nu$ decays, respectively.

3.6.3.1 Continuum yield

As explained in Sect. 5.2.8, the yields of the continuum MC are corrected by applying weights to the continuum events. These weights are given by the ratios of the off-resonance data and the continuum MC yields after all selections, separately in the electron and muon channels. They are : $w_e = 1.054 \pm 0.211$ and $w_\mu = 1.211 \pm 0.225$ for $B^+ \to \eta^{'} \ell^+ \nu$ decays, $w_e = 1.285 \pm 0.106$ and $w_\mu = 0.969 \pm 0.064$ for $B^+ \to \eta \ell^+ \nu$ ($\gamma\gamma$ channel) decays, $w_e = 1.419 \pm 0.265$ and $w_\mu = 1.410 \pm 0.174$ for $B^+ \to \eta \ell^+ \nu$ (3π channel) decays and $w_e = 1.471 \pm 0.042$ and $w_\mu = 0.959 \pm 0.022$ for $B^0 \to \pi^- \ell^+ \nu$ decays (see Sect. 3.5.2.8). In the central configuration, the central values of w_e and w_μ are used. To evaluate the systematic uncertainty due to the continuum yields, we generate one hundred MC event samples in which w_e and w_μ are determined randomly, sample by sample, according to a full gaussian distribution. The full analysis is performed on each sample. The RMS of the resulting BF distributions yield the systematic uncertainties due to the continuum yield. For $B^0 \to \pi^- \ell^+ \nu$ and $B^+ \to \eta \ell^+ \nu$ ($\gamma\gamma$ and combined channels), there is no systematic uncertainty due to the continuum yield, because the continuum yield is not fixed.

3.6.3.2 $\tilde{q}^2$ distributions

As explained in Sect. 3.5.2.8, the $\tilde{q}^2$ distributions of the continuum MC are corrected by applying weights to the continuum events. These weights, $w_{\tilde{q}^2}$, are given by linear functions for $B^+ \to \eta^{(')} \ell^+ \nu$ decays and a third order polynomial for $B^0 \to \pi^- \ell^+ \nu$ decays. For each decay mode, the values of the parameters of these functions are determined by a fit to the ratios of the off-resonance data to the continuum MC yields, after all selections and corrections. Only the central values of the $w_{\tilde{q}^2}$ weight functions are used in our results. To evaluate the systematic uncertainty due to the shape of the $\tilde{q}^2$ distribution of the continuum, we generate one hundred MC event samples in which the parameters of the given function are determined randomly, sample by sample, using the square-root method and the covariance matrix given by the fit of the data/MC ratios. The full analysis is performed on each sample. Each sample is renormalized to ensure that the number of continuum events does not change. The RMS of the resulting BF distribution yields the systematic uncertainty. The same procedure is repeated for each of the four weight functions. The data/MC ratios used as well as some of the $w_{\tilde{q}^2}$ functions are illustrated in Fig. 3.32 for $B^+ \to \eta^{'}\ell^+\nu$, Fig. 3.33 for $B^+ \to \eta\ell^+\nu$ ($\gamma\gamma$ channel), Fig. 3.34 for $B^+ \to \eta\ell^+\nu$ ($\pi^+\pi^-\pi^0$ channel) and Fig. 3.35 for $B^0 \to \pi^-\ell^+\nu$, respectively.

3.6.3.3 ΔE-$m_{\rm ES}$ distributions

No weights are applied to correct the ΔE -$m_{\rm ES}$ distributions of the continuum events in the central configuration. Because of low statistics for the $B^+ \to \eta\ell^+\nu$ and $B^+ \to \eta^{'}\ell^+\nu$ decays, we estimate the systematic uncertainty due to the shape of the ΔE -$m_{\rm ES}$ distribution of the continuum only for the $B^0 \to \pi^-\ell^+\nu$ decay. The procedure is similar to that used to obtain the systematic uncertainty due to the shape of the $\tilde{q}^2$ distribution of the continuum. The data/MC ratios used as well as some of the $w_{\Delta E}$ and $w_{m_{ES}}$ linear weight functions are illustrated in Figs. 3.36 and 3.37.

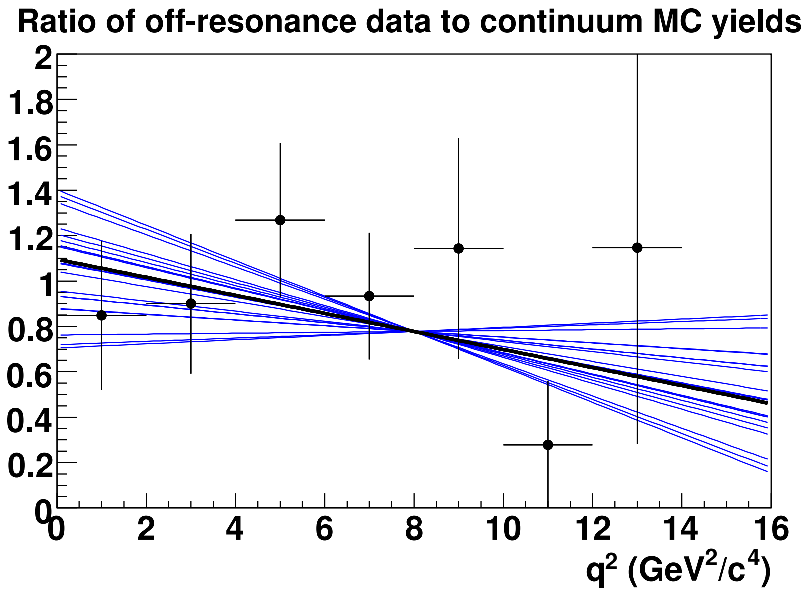

Figure 3.32 – Ratios of off-resonance data to MC continuum yields as a function of $\tilde{q}^2$ for $B^+ \to \eta^{'} \ell^+ \nu$ ($\gamma\gamma$ decay channel) once the data and MC yields (sum of electron and muon channels data) have each been normalized to an area of one. The heavy black curve is a linear function fitted to the central values of the ratios. The blue curves are 20 of the 100 curves randomly generated from the fitted parameters to estimate the systematic uncertainty resulting from the $\tilde{q}^2$ shape of the continuum. All the curves have the same integral. The data and MC distributions from which the ratios are taken are shown in Fig. 3.25 (Sect. 3.5.2.8).

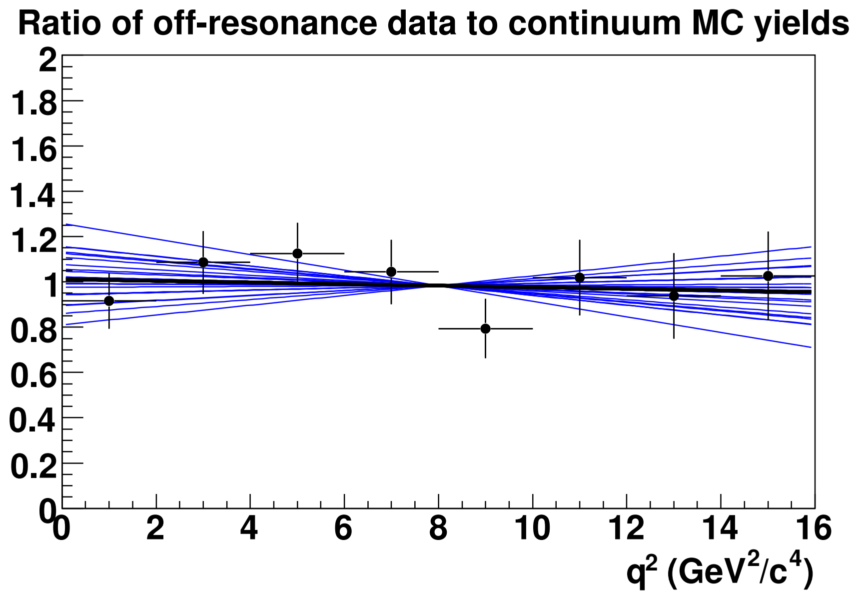

Figure 3.33 – Ratios of off-resonance data to MC continuum yields as a function of $\tilde{q}^2$ for $B^+ \to \eta\ell^+\nu$ ($\gamma\gamma$ decay channel) once the data and MC yields (sum of electron and muon channels data) have each been normalized to an area of one. The heavy black curve is a linear function fitted to the central values of the ratios. The blue curves are 20 of the 100 curves randomly generated from the fitted parameters to estimate the systematic uncertainty resulting from the $\tilde{q}^2$ shape of the continuum. All the curves have the same integral. The data and MC distributions from which the ratios are taken are shown in Fig. 3.26 (Sect. 3.5.2.8).

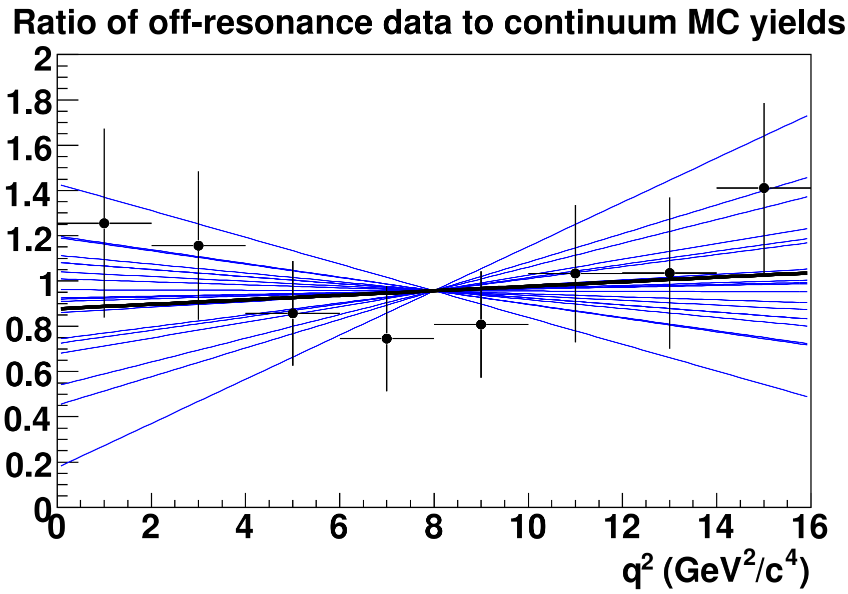

Figure 3.34 – Ratios of off-resonance data to MC continuum yields as a function of $\tilde{q}^2$ for $B^+ \to \eta\ell^+\nu$ ($\pi^+\pi^-\pi^0$ decay channel) once the data and MC yields (sum of electron and muon channels data) have each been normalized to an area of one . The heavy black curve is a linear function fitted to the central values of the ratios. The blue curves are 20 of the 100 curves randomly generated from the fitted parameters to estimate the systematic uncertainty resulting from the $\tilde{q}^2$ shape of the continuum. All the curves have the same integral. The data and MC distributions from which the ratios are taken are shown in Fig. 3.27 (Sect. 3.5.2.8).

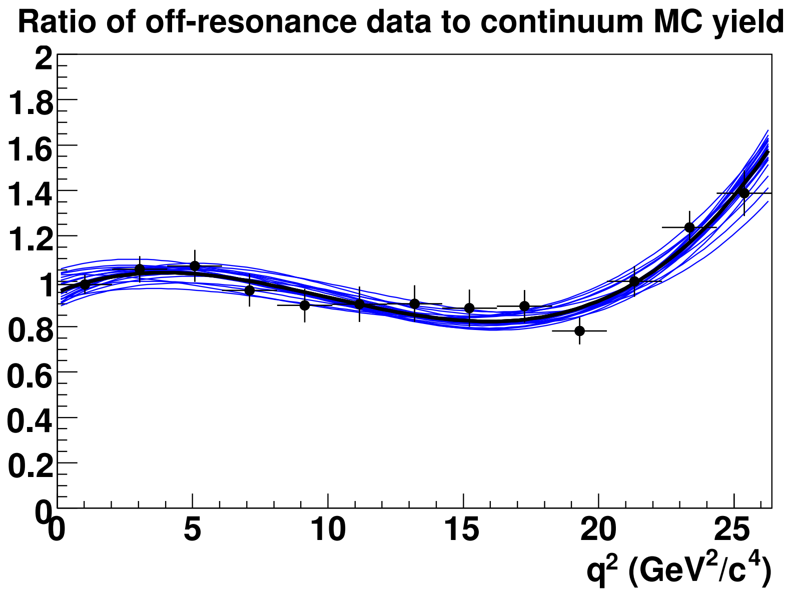

Figure 3.35 – Ratios of off-resonance data to MC continuum yields as a function of $\tilde{q}^2$ for $B^0 \to \pi^- \ell^+ \nu$ once the data and MC yields (sum of electron and muon channels data) have each been normalized to an area of one. The heavy black curve is a third order polynomial function fitted to the central values of the ratios. The blue curves are 20 of the 100 curves randomly generated from the fitted parameters to estimate the systematic uncertainty resulting from the $\tilde{q}^2$ shape of the continuum. All the curves have the same integral. The data and MC distributions from which the ratios are taken are shown in Fig. 3.28 (Sect. 3.5.2.8).

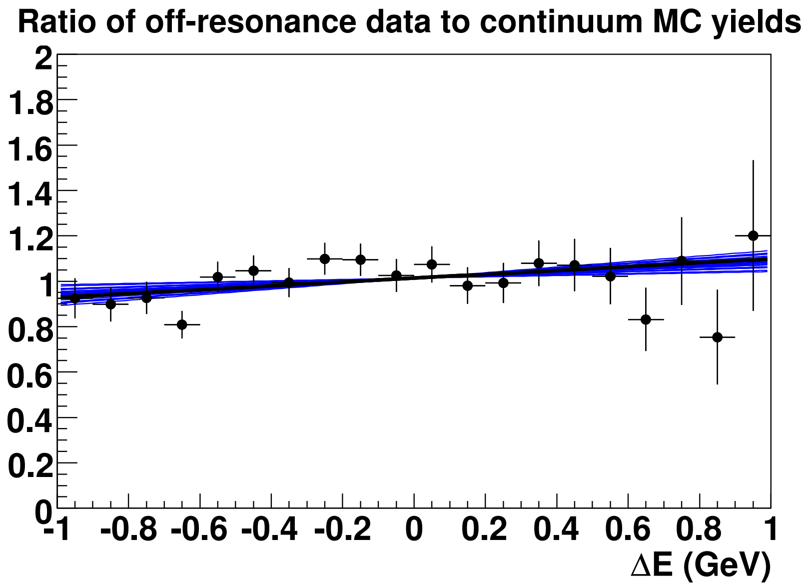

Figure 3.36 – Ratios of off-resonance data to MC continuum yields as a function of ΔE for $B^0 \to \pi^- \ell^+ \nu$ once the data and MC yields (sum of electron and muon channels data) have each been normalized to an area of one. The heavy black curve is a linear function fitted to the central values of the ratios. The blue curves are 20 of the 100 curves randomly generated from the fitted parameters to estimate the systematic uncertainty resulting from the ΔE shape of the continuum. All the curves have the same integral. The data and MC distributions from which the ratios are taken are shown in Fig. 3.28 (Sect. 3.5.2.8).

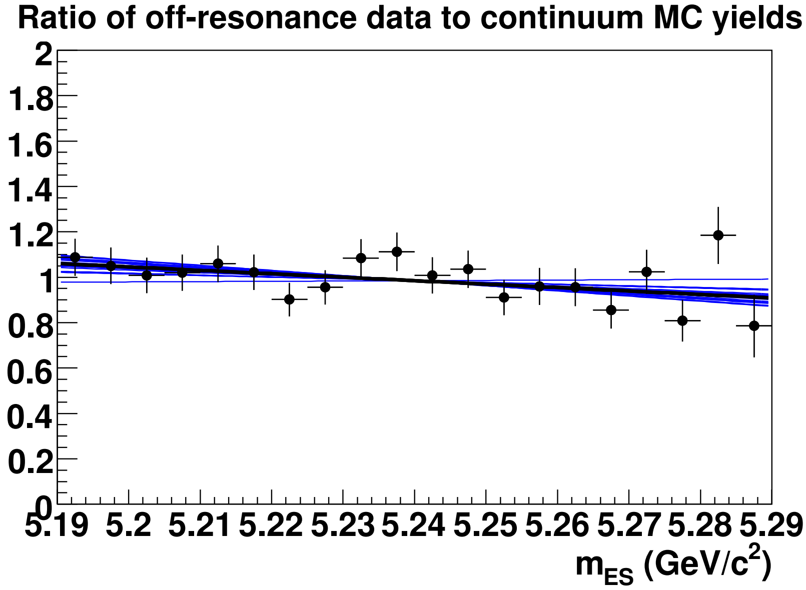

Figure 3.37 – Ratios of off-resonance data to MC continuum yields as a function of $m_{\rm ES}$ for $B^0 \to \pi^-\ell^+\nu$ once the data and MC yields (sum of electron and muon channels data) have each been normalized to an area of one. The heavy black curve is a linear function fitted to the central values of the ratios. The blue curves are 20 of the 100 curves randomly generated from the fitted parameters to estimate the systematic uncertainty resulting from the $m_{\rm ES}$ shape of the continuum. All the curves have the same integral. The data and MC distributions from which the ratios are taken are shown in Fig. 3.28 (Sect. 3.5.2.8).

3.6.4 Fit bias

The procedure described in Sect. 3.8.1.2 was used to obtain, separately for $B^+ \to \eta^{'}\ell^+\nu$, $B^+ \to \eta\ell^+\nu$ and $B^0 \to \pi^-\ell^+\nu$ decays, 1000 statistically independent TOY MC data samples. These MC samples were used to extract, separately for each decay mode, 1000 values of the total BFs, 1000 values of the total yields and 1000 values of the yields in each bin of q^2. We use for the TOY MC data the luminosity measured for the real data. To generate the pull distributions of interest, we use the yields instead of the BFs to avoid possible efficiency or q^2-unfolding problems.

The values of the total $\mathcal{B}(B^+ \to \eta^{'}\ell^+\nu)$, $\mathcal{B}(B^+ \to \eta\ell^+\nu)$ ($\gamma\gamma$ channel), $\mathcal{B}(B^+ \to \eta\ell^+\nu)$ (3π channel), $\mathcal{B}(B^+ \to \eta\ell^+\nu)$ (combined channels) and $\mathcal{B}(B^0 \to \pi^-\ell^+\nu)$ are shown in Figs. 3.38, 3.39, 3.40, 3.41 and 3.42, respectively. To take into account the very small observed bias, we use the relation :

$$BF_f = BF_i + (BF_G - BF_{fit}) \times BF_i/BF_{fit} \tag{3.39}$$

where BF_i is the value of the total BF before any correction for any possible fit bias, BF_G is the value used in the MC generator, BF_{fit} is the fitted value and BF_f is the value of the total BF after the correction for any fit bias. The uncertainty due to the fit bias is given by ($BF_{fit} - BF_G$) added in quadrature to the error of the fit. The corresponding pull distributions of the total $B^+ \to \eta^{'}\ell^+\nu$, $B^+ \to \eta\ell^+\nu$ ($\gamma\gamma$ channel), $B^+ \to \eta\ell^+\nu$ (3π channel), $B^+ \to \eta\ell^+\nu$ (combined channels) and $B^0 \to \pi^-\ell^+\nu$ decay yields are shown in Figs. 3.43, 3.44, 3.45, 3.46 and 3.47, respectively.

The pull distributions of the $B^+ \to \eta^{'}\ell^+\nu$, $B^+ \to \eta\ell^+\nu$ ($\gamma\gamma$ channel), $B^+ \to \eta\ell^+\nu$ (3π channel), $B^+ \to \eta\ell^+\nu$ (combined channels) and $B^0 \to \pi^-\ell^+\nu$ signal and background yields as a function of q^2 are shown in Figs. 3.43, 3.48, 3.45, 3.49 and 3.50, respectively. To take into account the small bias shown by the pull distributions, the uncertainty on each yield is corrected according to the relation :

$$corrected\ uncertainty = fitted\ uncertainty/standard\ deviation\ \sigma.$$

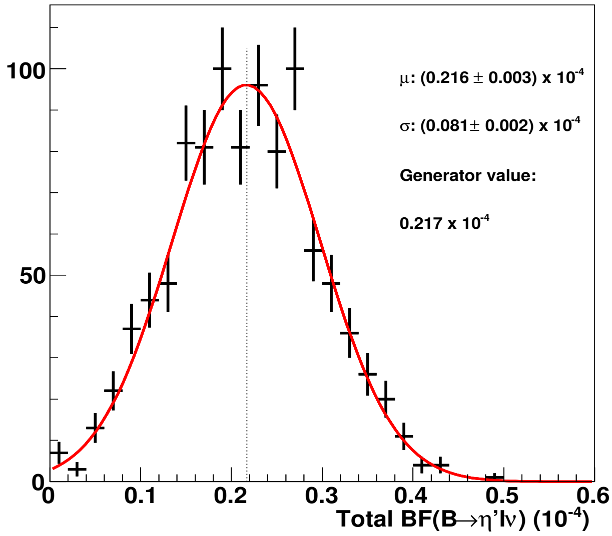

Figure 3.38 – Values of the total $\mathcal{B}(B^+ \to \eta' \ell^+ \nu)$ obtained from 1000 statistically independent TOY MC data samples.

while we also add a systematic uncertainty to each yield due to the fit bias :

$$systematic\, uncertainty = fitted\, yield - corrected\, yield = mean\, \mu \times fitted\, uncertainty$$

where the fitted uncertainty is the one provided by the fit to our data. The corrections for possible fit biases are sufficiently small that they do not change the final total systematic uncertainty on any of our BFs.

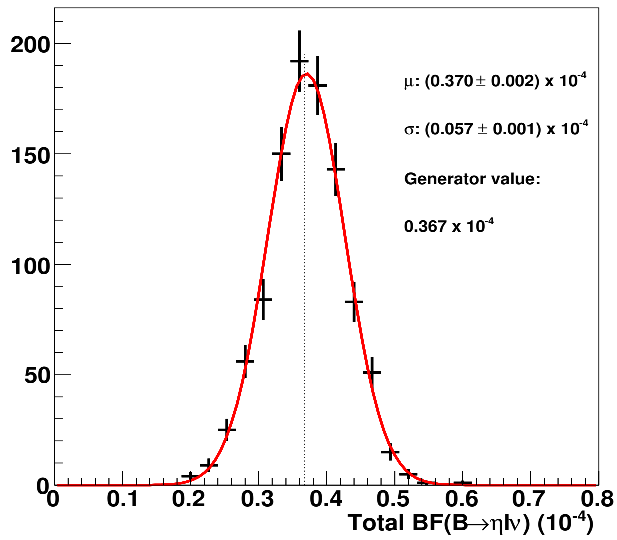

Figure 3.39 – Values of the total $\mathcal{B}(B^+ \to \eta\ell^+\nu)$ ($\gamma\gamma$ channel) obtained from 1000 statistically independent TOY MC data samples.

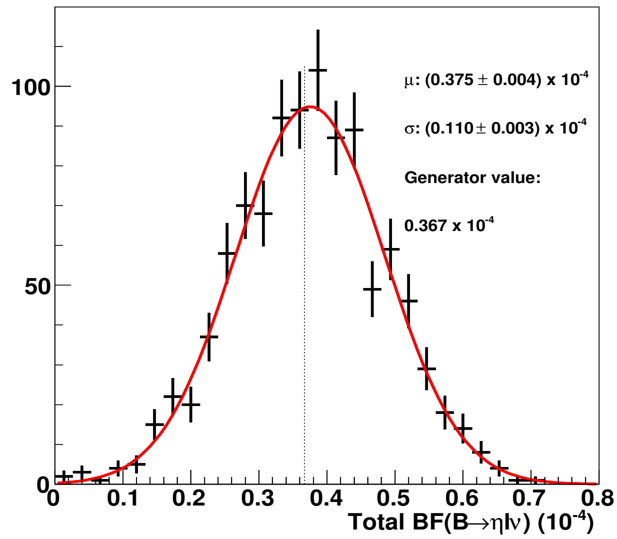

Figure 3.40 – Values of the total $\mathcal{B}(B^+ \to \eta\ell^+\nu)$ (3π channel) obtained from 1000 statistically independent TOY MC data samples.

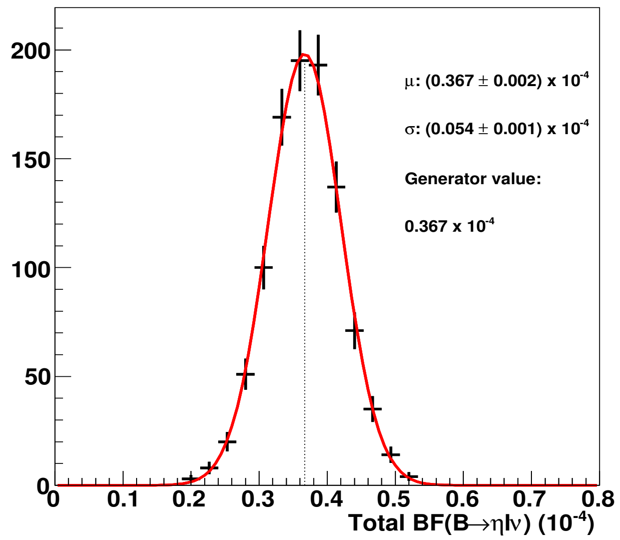

Figure 3.41 – Values of the total $\mathcal{B}(B^+ \to \eta\ell^+\nu)$ ($\gamma\gamma$ and 3π channels combined) obtained from 1000 statistically independent TOY MC data samples.

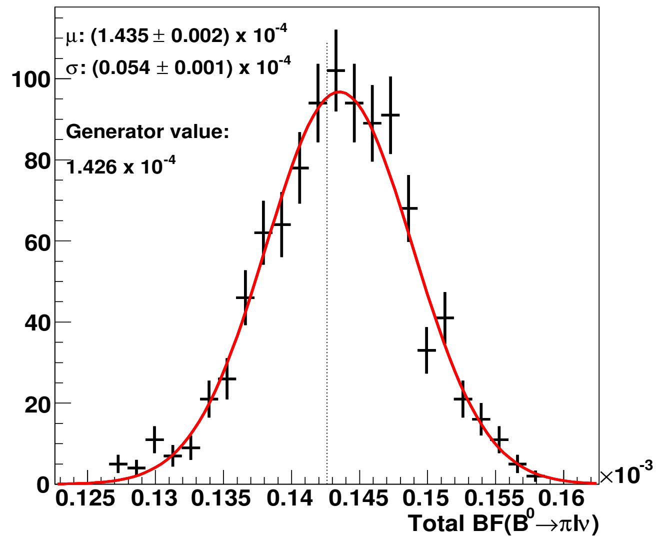

Figure 3.42 – Values of the total $\mathcal{B}(B^0 \to \pi^-\ell^+\nu)$ obtained from 1000 statistically independent TOY MC data samples.

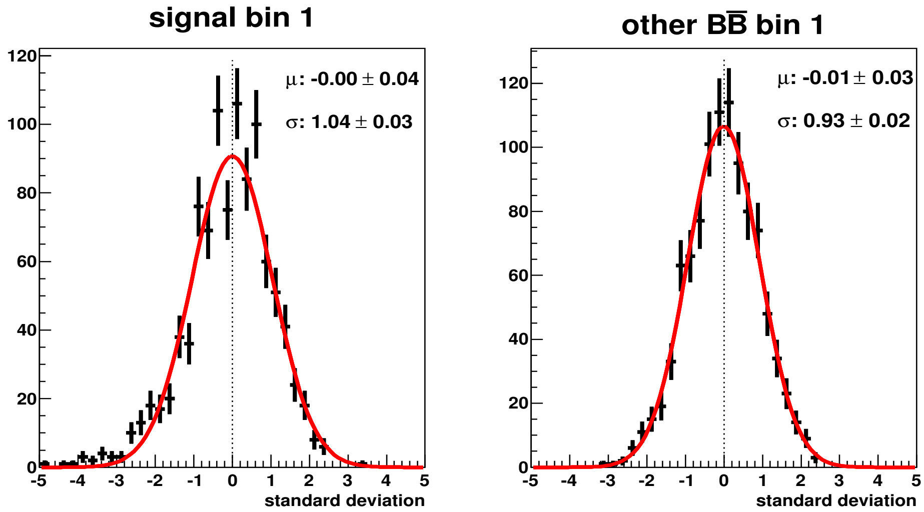

Figure 3.43 – Pull distributions of all the fitted yields obtained from 1000 statistically independent TOY MC data samples for $B^+ \to \eta' \ell^+ \nu$ decays ($\gamma\gamma$ channel). The continuum and $B \to X_u \ell \nu$ yields are fixed in the fit.

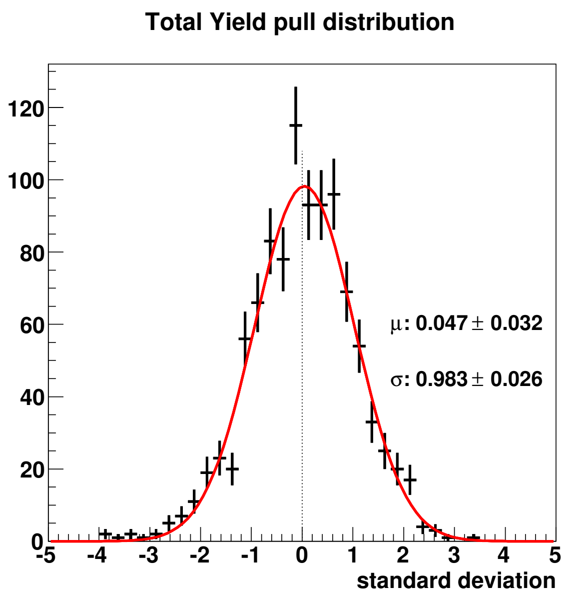

Figure 3.44 – Pull distributions of the total $B^+ \to \eta \ell^+ \nu$ ($\gamma\gamma$ channel) yield obtained from 1000 statistically independent TOY MC data samples. The $B \to X_u \ell \nu$ yields are fixed in the fit.

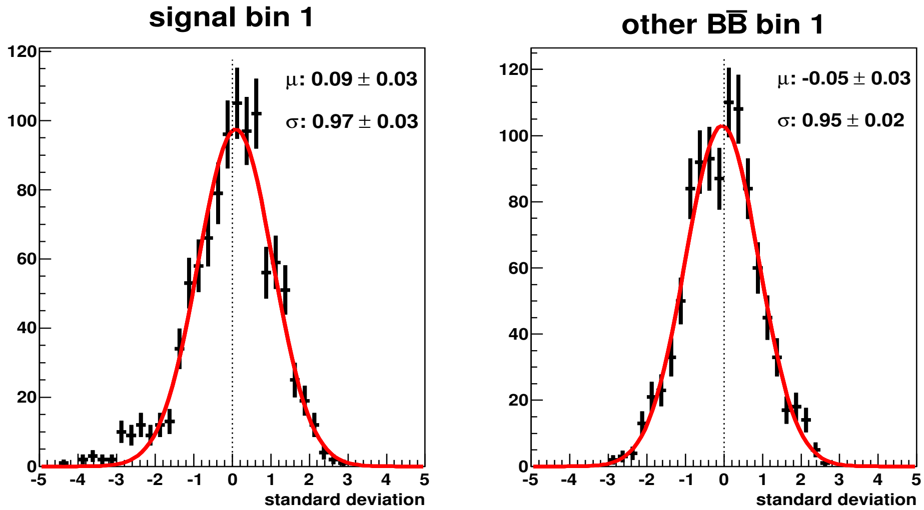

Figure 3.45 – Pull distributions of all the fitted yields obtained from 1000 statistically independent TOY MC data samples for $B^+ \to \eta \ell^+ \nu$ (3π channel) decays. The continuum and the $B \to X_u \ell \nu$ yields are fixed in the fit.

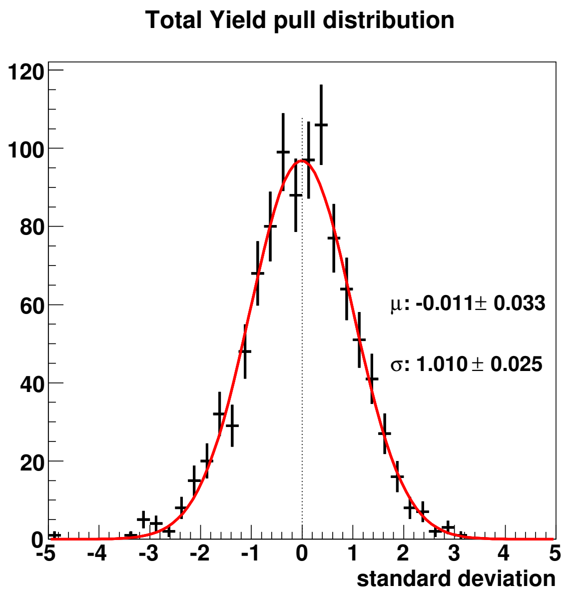

Figure 3.46 – Pull distributions of the total $B^+ \to \eta \ell^+ \nu$ ($\gamma\gamma$ and 3π channels combined) yield obtained from 1000 statistically independent TOY MC data samples. The $B \to X_u \ell \nu$ yields are fixed in the fit.

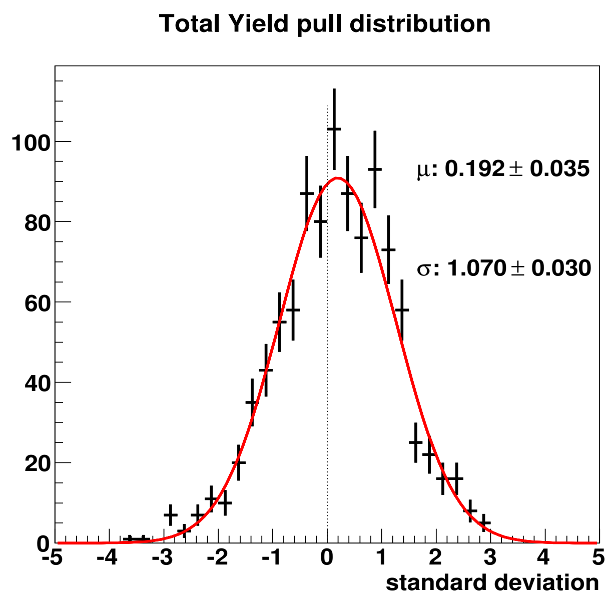

Figure 3.47 – Pull distributions of the total $B^0 \rightarrow \pi^- \ell^+ \nu$ yield obtained from 1000 statistically independent TOY MC data samples.

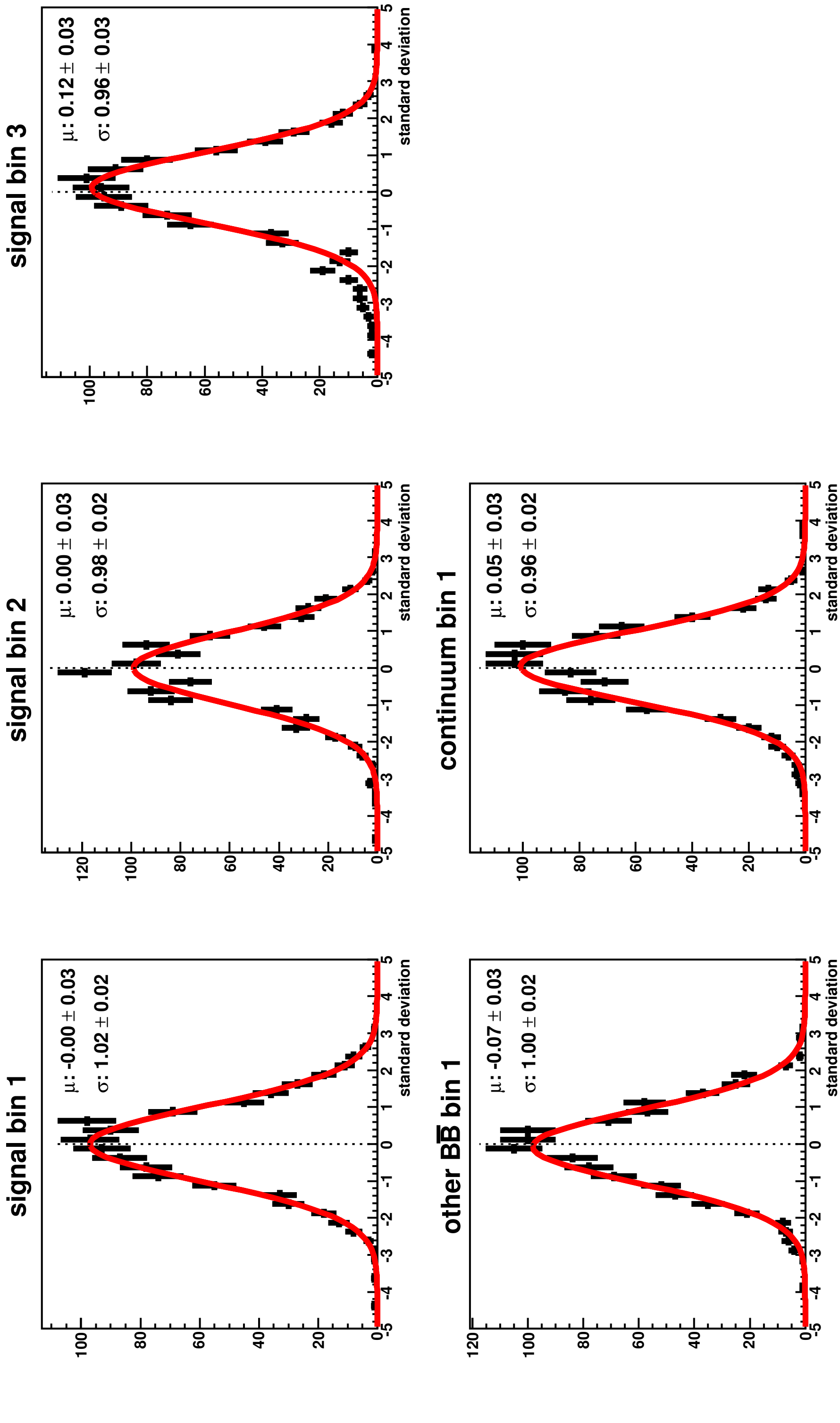

Figure 3.48 – Pull distributions of all the fitted yields obtained from 1000 statistically independent TOY MC data samples for $B^+ \to \eta\ell^+\nu$ ($\gamma\gamma$ channel) decays. The $B \to X_u\ell\nu$ yields are fixed in the fit.

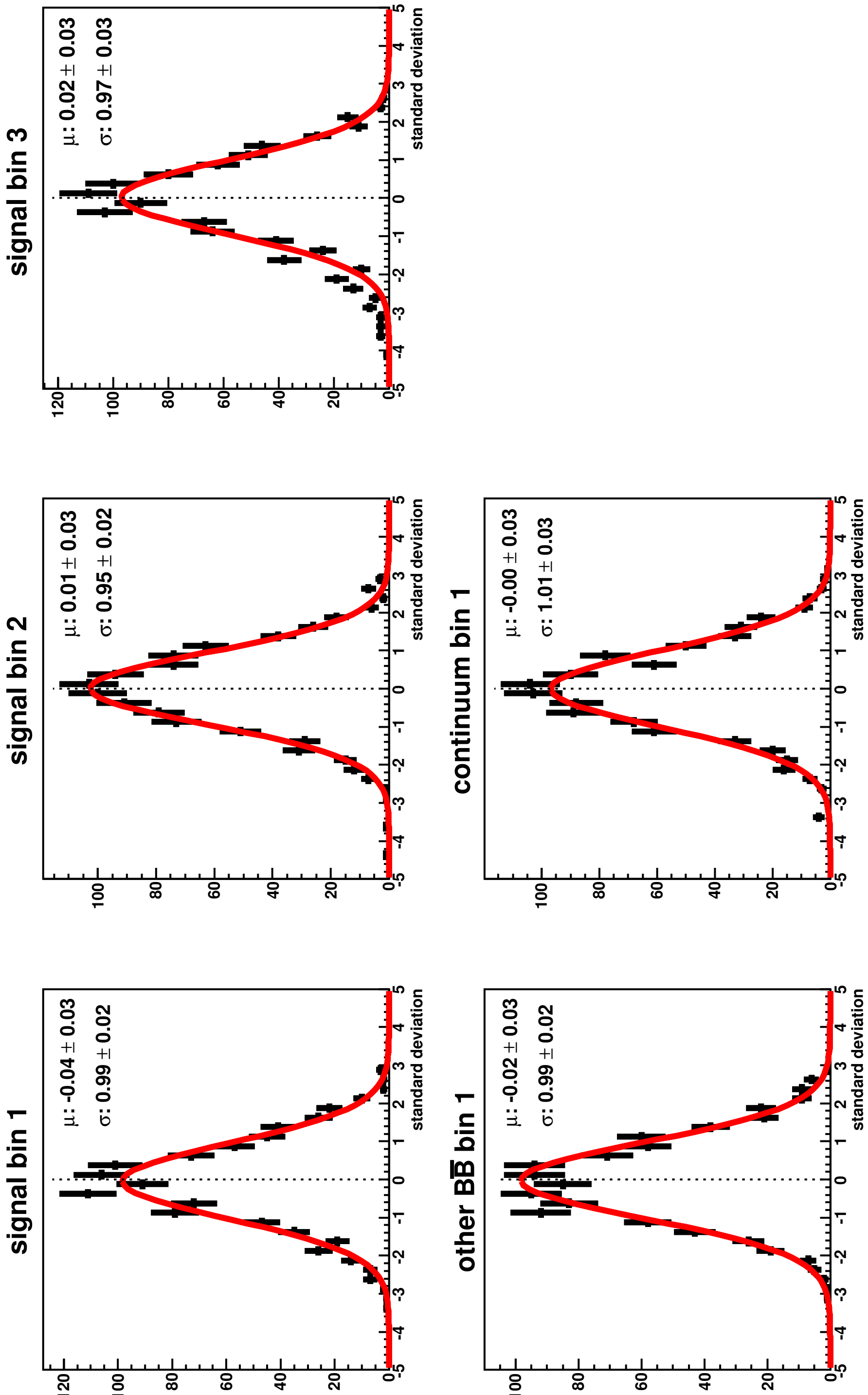

Figure 3.49 – Pull distributions of all the fitted yields obtained from 1000 statistically independent TOY MC data samples for $B^+ \to \eta\ell^+\nu$ ($\gamma\gamma$ and 3π channels combined) decays. The $B \to X_u\ell\nu$ yields are fixed in the fit.

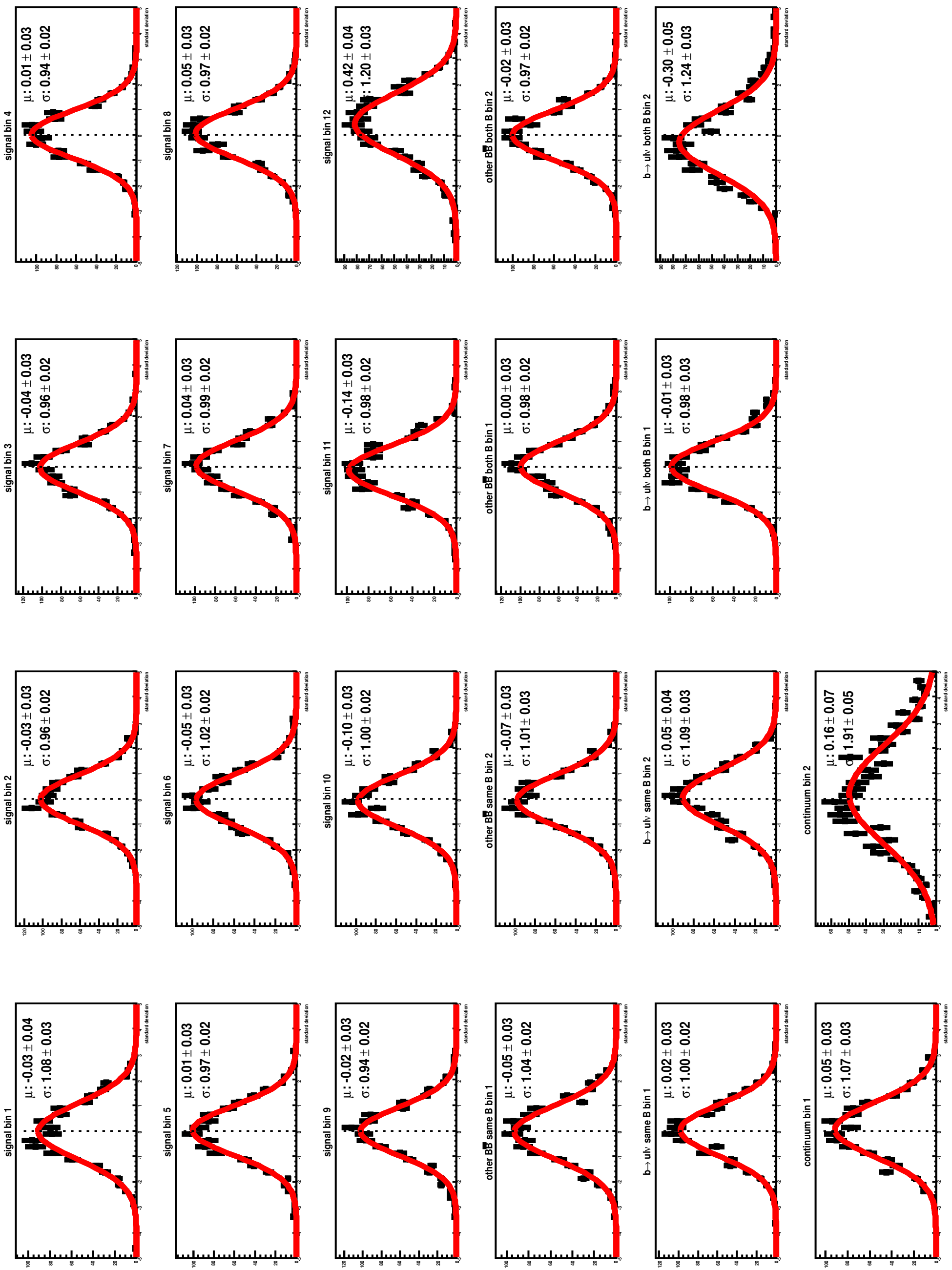

Figure 3.50 – Pull distributions of all the fitted yields obtained from 1000 statistically independent TOY MC data samples for $B^0 \to \pi^- \ell^+ \nu$ decays.

3.7 Combination of the two η decay channels

As previously explained in sect. 3.1.3.3, we reconstruct the $B^+ \to \eta\ell^+\nu$ decays in two different channels. We reconstruct the signal η meson in the channels $\eta \to \gamma\gamma$ and $\eta \to \pi^+\pi^-\pi^0$. These two channels together contribute approximately 62% of the total decay rate of the η. Statistics are not sufficient to reconstruct the $\eta \to \pi^+\pi^-\pi^0$ channel in the $B^+ \to \eta^{'}\ell^+\nu$ mode.

For the $B^+ \to \eta\ell^+\nu$ decay mode, we first construct the PDF distributions for each of the $\eta \to \gamma\gamma$ and $\eta \to \pi^+\pi^-\pi^0$ decay channels. We can then use the sum of these two PDFs in our fit procedure. This yields a single fit result for the combined decay channels for the $B^+ \to \eta\ell^+\nu$ mode. As shown in Sect. 3.8, the result of the fit is in excellent agreement with the weighted average of the results for each decay channel.

No attempt has been made to combine the $B^+ \to \eta^{'}\ell^+\nu$, $B^+ \to \eta\ell^+\nu$ and $B^0 \to \pi^-\ell^+\nu$ decay modes for a simultaneous fit.

3.8 Results

The results of the analysis are presented in this section : the total $\mathcal{B}(B^+ \to \eta^{(\prime)}\ell^+\nu)$ and $\mathcal{B}(B^0 \to \pi^-\ell^+\nu)$, and for the $B^+ \to \eta\ell^+\nu$ and $B^0 \to \pi^-\ell^+\nu$ decays, the unfolded $\Delta\mathcal{B}(q^2)$ spectra and their statistical and systematic covariance matrices, as well as their corresponding values of the $f_+(q^2)$ shape parameters. Because of low statistics in the $B^+ \to \eta\ell^+\nu$ decay mode, the values of $|V_{ub}f_+(0)|$ and $|V_{ub}|$ are only extracted from the $B^0 \to \pi^-\ell^+\nu$ decay mode.

To check our procedure, to optimize our cuts and to obtain unbiased results, we first kept the analysis blind and extracted all the desired results using only the simulation. The procedure used to extract these MC-based results is described in Sect. 3.8.1. These MC-based results are given in Sect. 3.8.2. The results with the actual data are given in Sect. 3.8.4.

All results are obtained using the general analysis method described in Sects. 3.3 and 3.4 with analysis-43 packages and release 22. The central values of all the results are obtained by fitting the data with the PDFs established with the central configuration of the simulation parameters described in Sect. 3.5.2. The systematic uncertainties are then derived from the variation of the results obtained by re-analyzing the same data with modified PDFs, as described in Sect. 3.6.

3.8.1 Special procedure for MC-based results

The relatively high yields and low signal purity resulting from the use of the loose neutrino reconstruction technique mean that the systematic uncertainties are not expected to be small compared to the statistical uncertainties. Thus, both the statistical and the systematic uncertainties need to be minimized when the parameters of the analysis such as the values of the cuts, the numbers of free parameters in the fit, the boundaries of the fit region, and the numbers of $\tilde{q}^2$ and ΔE-$m_{\rm ES}$ bins are optimized. A detailed MC-based study was thus performed to evaluate the statistical and systematic uncertainties before unblinding the analysis. This study requires the generation of TOY Monte Carlo data samples on which the entire analysis is performed as it would be with the real data, following the procedure described in Sect. 3.8.1.1 to 3.8.1.3. The final results and uncertainties obtained by the analysis of the TOY MC data samples with optimized parameters are presented in Sect. 3.8.2. These results can then be used to establish whether the final results obtained with the same analysis of the unblinded data are reasonable.

3.8.1.1 Generation of TOY MC data samples

Realistic PDFs are needed to generate realistic TOY MC data samples. This is not straightforward for this analysis since analytic PDFs that can describe the data are not available (see Sect. 3.4). In our case, the realistic PDFs are the ΔE-m_{ES} histogrammed distributions extracted from the full Monte Carlo simulation for the different $\tilde{q}^2$ intervals. These generated distributions need to be sufficiently smooth to meet the requirements of the fitting algorithm. They were used to generate 1000 realistic TOY MC data samples in three(one) $\tilde{q}^2$ intervals for $B^+ \to \eta^{(\prime)}\ell^+\nu$ decays and twelve intervals for $B^0 \to \pi^-\ell^+\nu$ decays. Technically, this was done by generating a Poissonian random number of entries in each (ΔE, m_{ES}, $\tilde{q}^2$) bin according to the data statistics and ΔE-m_{ES} probability distribution of each event type : signal as well as $b \to u\ell\nu$, other $B\bar{B}$ (decay from same and both B for the $B^0 \to \pi^-\ell^+\nu$ mode) and continuum backgrounds.

3.8.1.2 Central values and statistical uncertainties

To obtain the central values of our MC-based results, we fitted the above 1000 TOY MC data samples and determined the total BFs for the three decay channels. For $B^+ \to \eta\ell^+\nu$ and $B^0 \to \pi^-\ell^+\nu$ decays, we also obtained the partial $\Delta\mathcal{B}(q^2)$ as well as the $f_+(q^2)$ parameters for each sample. The mean values of the resulting distributions are the central values of our MC-based results, and their RMS give the statistical uncertainties. Deviation of the mean values from their input central values indicates a systematic bias of the fit and requires a corresponding systematic uncertainty (see Sect. 3.6.4). As a cross-check, the statistical uncertainties given by the RMS of the distributions were found to be consistent with the statistical uncertainties given by the covariance matrix of the fits.

The central values of the total BFs as well as the pull distributions of the yields obtained with the 1000 TOY MC samples are shown in Figs. 3.38 and 3.43, 3.39 and 3.48, 3.40 and 3.45, 3.41 and 3.49, and 3.42 and 3.50 (Sect. 3.6.4), for $B^+ \to \eta^{'} \ell^+ \nu$, $B^+ \to \eta \ell^+ \nu$ ($\gamma\gamma$ channel), $B^+ \to \eta \ell^+ \nu$ (3π channel), $B^+ \to \eta \ell^+ \nu$ ($\gamma\gamma$ and 3π channels combined) and $B^0 \to \pi^- \ell^+ \nu$ decays, respectively.

3.8.1.3 Systematic uncertainties in MC simulation

To estimate the MC-based systematic uncertainties, we follow exactly the procedure described in Sect. 3.6, using the MC event samples described in Sect. 3.5 instead of the real data. To prevent our results from being affected by statistical fluctuations, we estimate the systematic uncertainties independently for 10 statistically independent sets of 100 MC event samples each. We quote the mean value of the 10 uncertainties as the MC-based systematic uncertainty. In this case, the elements of the covariance matrix of each systematic uncertainty are defined as :

$$V_{i,j} = \bar{\sigma}_i \bar{\sigma}_j \bar{C}_{i,j} \tag{3.40}$$

where $\bar{\sigma}_i$ and $\bar{\sigma}_j$ are the mean uncertainties obtained in the ith and j^{th} bin of $\tilde{q}^2$, and $\bar{C}_{i,j}$ is the mean correlation factor obtained from the 10 MC event sets.

3.8.2 Results and uncertainties based on MC simulation

3.8.2.1 Signal yields, statistical and systematic uncertainties in MC simulation

The MC-based values of the raw signal yields and their statistical and systematic uncertainties are obtained with the methods described in Sect. 3.3.4 and Sect. 3.6, respectively. They are given in Tables 3.30, 3.31, 3.32 and 3.33 for $B^+ \to \eta^{'} \ell^+ \nu$, $B^+ \to \eta \ell^+ \nu$ ($\gamma\gamma$ channel), $B^+ \to \eta \ell^+ \nu$ (3π channel) and $B^+ \to \eta \ell^+ \nu$ ($\gamma\gamma$ and 3π channels combined) respectively, assuming BFs of $\mathcal{B}(B^+ \to \eta^{(')} \ell^+ \nu) = 0.301 \times 10^{-4}$. Similar calculations for the $B^0 \to \pi^- \ell^+ \nu$ decays were not carried out since they were deemed not to be necessary by the review committee, given that the methods had been tested in our previous analysis [76] for this particular case. For $B^+ \to \eta^{'} \ell^+ \nu$ and $B^+ \to \eta \ell^+ \nu$

decays, the statistical uncertainty (fit error) is larger than the systematic one while for $B^0 \to \pi^- \ell^+ \nu$ decays, the systematic uncertainty is larger than the statistical one.

For illustrative purposes, the ΔE and m_{ES} fit projections obtained in each signal q^2 bin are displayed in Figs. 3.51 and 3.52 for $B^+ \to \eta^{'} \ell^+ \nu$, Figs. 3.53 and 3.54 for $B^+ \to \eta \ell^+ \nu$ ($\gamma\gamma$ channel), Figs. 3.55 and 3.56 for $B^+ \to \eta \ell^+ \nu$ (3π channel), Figs. 3.57 and 3.58 for $B^+ \to \eta \ell^+ \nu$ ($\gamma\gamma$ and 3π channels combined) and Figs. 3.59 and 3.60 for $B^0 \to \pi^- \ell^+ \nu$. The ΔE distributions correspond to a cut of $m_{\mathrm{ES}} >$ 5.2675 GeV/c^2 and the m_{ES} distributions to a cut of $-0.16 < \Delta E < 0.2$ GeV. These distributions are the results of one of the fits described in Sect. 3.8.1.2, selected at random[20]. They are in good agreement with the Toy MC data generated with PDFs established in Sect. 3.8.1

[20]The same sample was used to make Figs. 3.51 to 3.60

Tableau 3.30 – Raw fitted yields of $B^+ \to \eta^{'}\ell^+\nu$ ($\gamma\gamma$ channel) decays and their statistical (fit error) and systematic (all the others) uncertainties from all sources, obtained from MC simulation. The BF is assumed to be 0.301×10^{-4}. The errors are given as % (relative errors).

$\tilde{q}^2$ bins (GeV^2/c^4)	Total
fitted yield	152.7
tracking efficiency	3.9
photon efficiency	4.9
K_L^0 efficiency	2.0
ℓ/π identification	1.3
continuum yield	4.4
$\tilde{q}^2$ continuum shape	4.3
$\mathcal{B}(B \to X_u\ell\nu)$	1.9
η BF	0.0
shape function parameters	3.1
$B \to \rho\ell\nu$ FF	0.1
$B^+ \to \eta^{'}\ell^+\nu$ FF	0.1
other scalar FF	2.5
$B \to \omega\ell\nu$ FF	0.9
$\mathcal{B}(B \to X_c\ell\nu)$	1.8
$B \to D\ell\nu$ FF	0.3
$B \to D^*\ell\nu$ FF	0.5
$\mathcal{B}(D \to X\ell\nu)$	2.7
$\mathcal{B}(\Upsilon(4S) \to B^0\bar{B}^0)$	0.3
$D \to K_L^0$ BF	8.5
total syst error	13.6
fit error	29.3
total error	32.3

Tableau 3.31 – Raw fitted yields of $B^+ \to \eta\ell^+\nu$ ($\gamma\gamma$ channel) decays and their statistical (fit error) and systematic (all the others) uncertainties from all sources, obtained from MC simulation. The BF is assumed to be 0.301×10^{-4}. The errors are given as % (relative errors).

$\tilde{q}^2$ bins (GeV^2/c^4)	0-4	4-8	8-16	Total
fitted yield	130.1	167.7	213.2	511.0
tracking efficiency	4.2	2.9	3.4	3.1
photon efficiency	3.3	2.6	2.1	1.5
K_L^0 efficiency	2.5	1.5	1.9	1.3
ℓ/π identification	3.3	1.1	1.4	0.2
$\tilde{q}^2$ continuum shape	5.8	1.7	4.4	0.2
$\mathcal{B}(B \to X_u\ell\nu)$	0.7	1.9	7.6	3.9
η BF	0.2	0.2	0.3	0.2
shape function parameters	1.7	3.0	9.9	5.5
$B \to \rho\ell\nu$ FF	0.2	1.6	1.1	0.9
$B^+ \to \eta\ell^+\nu$ FF	0.2	0.1	0.3	0.2
other scalar FF	1.0	0.0	0.0	0.3
$B \to \omega\ell\nu$ FF	0.2	0.4	1.6	0.6
$\mathcal{B}(B \to X_c\ell\nu)$	1.4	1.7	1.8	0.8
$B \to D\ell\nu$ FF	0.2	0.1	0.3	0.2
$B \to D^*\ell\nu$ FF	0.8	0.7	0.7	0.3
$\mathcal{B}(D \to X\ell\nu)$	0.5	0.3	3.3	1.4
$\mathcal{B}(\Upsilon(4S) \to B^0B^0)$	0.3	0.1	0.3	0.2
$D \to K_L^0$ BF	1.4	1.8	8.8	3.9
signal MC stat error	0.7	0.8	0.4	0.0
total syst error	12.5	7.1	17.3	8.9
fit error	29.3	20.5	31.6	17.7
total error	31.8	21.7	36.0	19.8

Tableau 3.32 – Raw fitted yields of $B^+ \to \eta\ell^+\nu$ (3π channel) decay and their statistical (fit error) and systematic (all the others) uncertainties from all sources, obtained from MC simulation. The BF is assumed to be 0.301×10^{-4}. The errors are given as % (relative errors).

$\tilde{q}^2$ bins (GeV^2/c^4)	Total
fitted yield	152.6
tracking efficiency	11.4
photon efficiency	4.8
K_L^0 efficiency	5.3
ℓ/π identification	1.2
continuum yield	1.5
$\tilde{q}^2$ continuum shape	4.4
$\mathcal{B}(B \to X_u\ell\nu)$	5.2
η BF	0.1
shape function parameters	9.8
$B \to \rho\ell\nu$ FF	1.0
$B^+ \to \eta\ell^+\nu$ FF	0.2
other scalar FF	6.4
$B \to \omega\ell\nu$ FF	3.3
$\mathcal{B}(B \to X_c\ell\nu)$	3.2
$B \to D\ell\nu$ FF	0.5
$B \to D^*\ell\nu$ FF	1.1
$\mathcal{B}(D \to X\ell\nu)$	4.2
$\mathcal{B}(\Upsilon(4S) \to B^0B^0)$	0.2
$D \to K_L^0$ BF	7.8
total syst error	21.7
fit error	39.6
total error	45.1

Tableau 3.33 – Raw fitted yields of $B^+ \to \eta\ell^+\nu$ ($\gamma\gamma$ and 3π channels combined) decays and their statistical (fit error) and systematic (all the others) uncertainties from all sources, obtained from MC simulation. The BF is assumed to be 0.301×10^{-4}. The errors are given as % (relative errors).

$\tilde{q}^2$ bins (GeV^2/c^4)	0-4	4-8	8-16	Total
fitted yield	160.9	225.1	294.3	680.2
tracking efficiency	4.6	2.9	5.8	4.4
photon efficiency	3.8	3.6	3.1	2.0
K_L^0 efficiency	2.0	2.0	2.8	2.0
ℓ/π identification	2.5	0.6	1.6	0.4
$\tilde{q}^2$ continuum shape	5.2	0.8	3.1	0.5
$\mathcal{B}(B \to X_u\ell\nu)$	0.7	1.6	7.3	3.8
η BF	0.3	0.2	0.3	0.3
shape function parameters	1.8	3.5	10.7	6.2
$B \to \rho\ell\nu$ FF	0.3	1.3	0.7	0.6
$B^+ \to \eta\ell^+\nu$ FF	0.3	0.2	0.4	0.3
other scalar FF	0.9	0.0	0.0	0.2
$B \to \omega\ell\nu$ FF	0.3	0.3	2.8	1.2
$\mathcal{B}(B \to X_c\ell\nu)$	1.6	2.1	1.8	0.9
$B \to D\ell\nu$ FF	0.3	0.2	0.6	0.3
$B \to D^*\ell\nu$ FF	0.8	1.2	0.9	0.5
$\mathcal{B}(D \to X\ell\nu)$	0.4	0.2	4.8	2.0
$\mathcal{B}(\Upsilon(4S) \to B^0\bar{B}^0)$	0.4	0.2	0.4	0.2
$D \to K_L^0$ BF	1.6	2.3	9.6	4.6
signal MC stat error	0.7	0.3	0.3	0.0
total syst error	11.7	7.6	19.0	10.4
fit error	25.0	20.0	27.3	15.6
total error	27.6	21.4	33.2	18.7

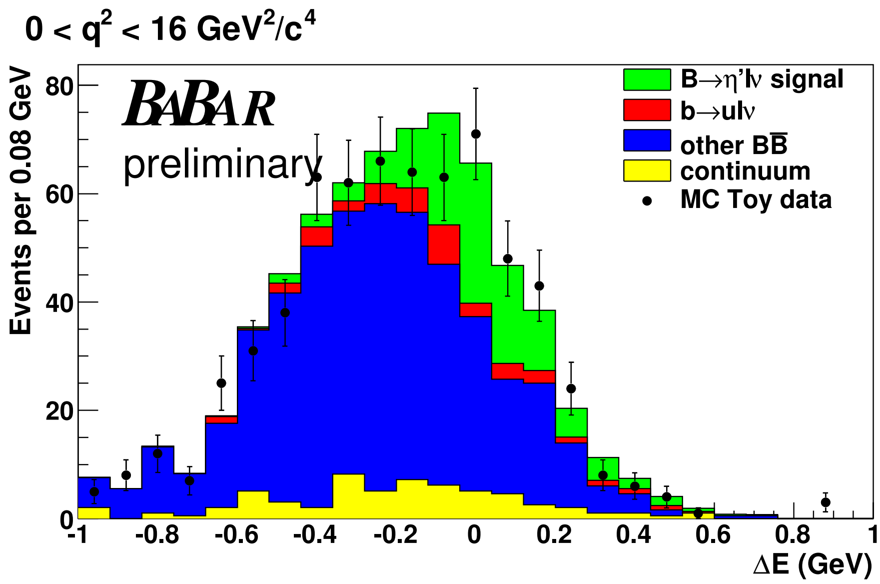

Figure 3.51 – MC ΔE yield fit projections with $m_{\mathrm{ES}} > 5.2675\ \mathrm{GeV}/c^2$ obtained in one $\tilde{q}^2$ bin from one of the fits described in Sect. 3.8.1.2, selected at random for $B^+ \to \eta^{'}\ell^+\nu$ ($\gamma\gamma$ channel) decays. The fit was done using the full ΔE-m_{ES} fit region.

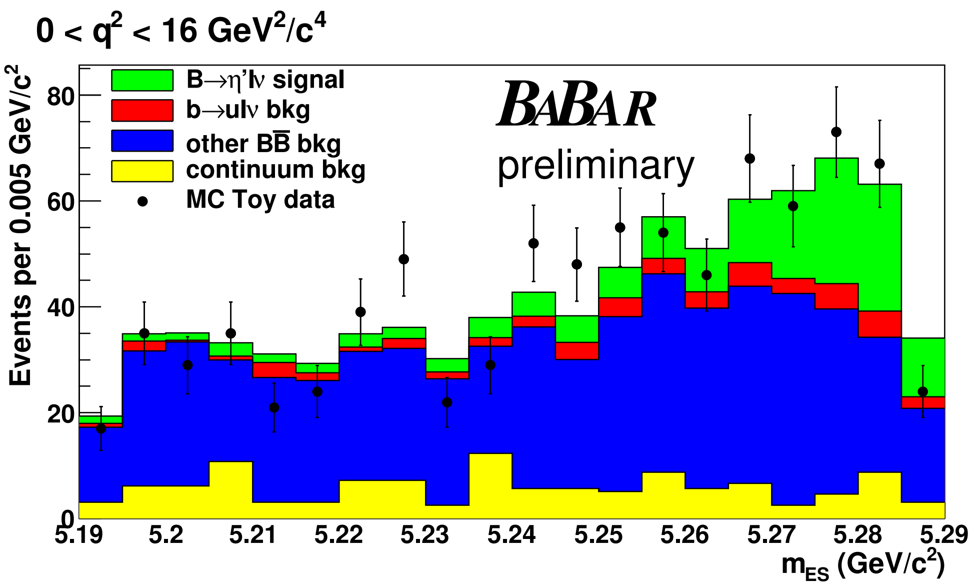

Figure 3.52 – MC m_{ES} yield fit projections with $-0.16 < \Delta E < 0.2$ GeV obtained in one $\tilde{q}^2$ bin from one of the fits described in Sect. 3.8.1.2, selected at random for $B^+ \to \eta^{'}\ell^+\nu$ ($\gamma\gamma$ channel) decays. The fit was done using the full ΔE-m_{ES} fit region.

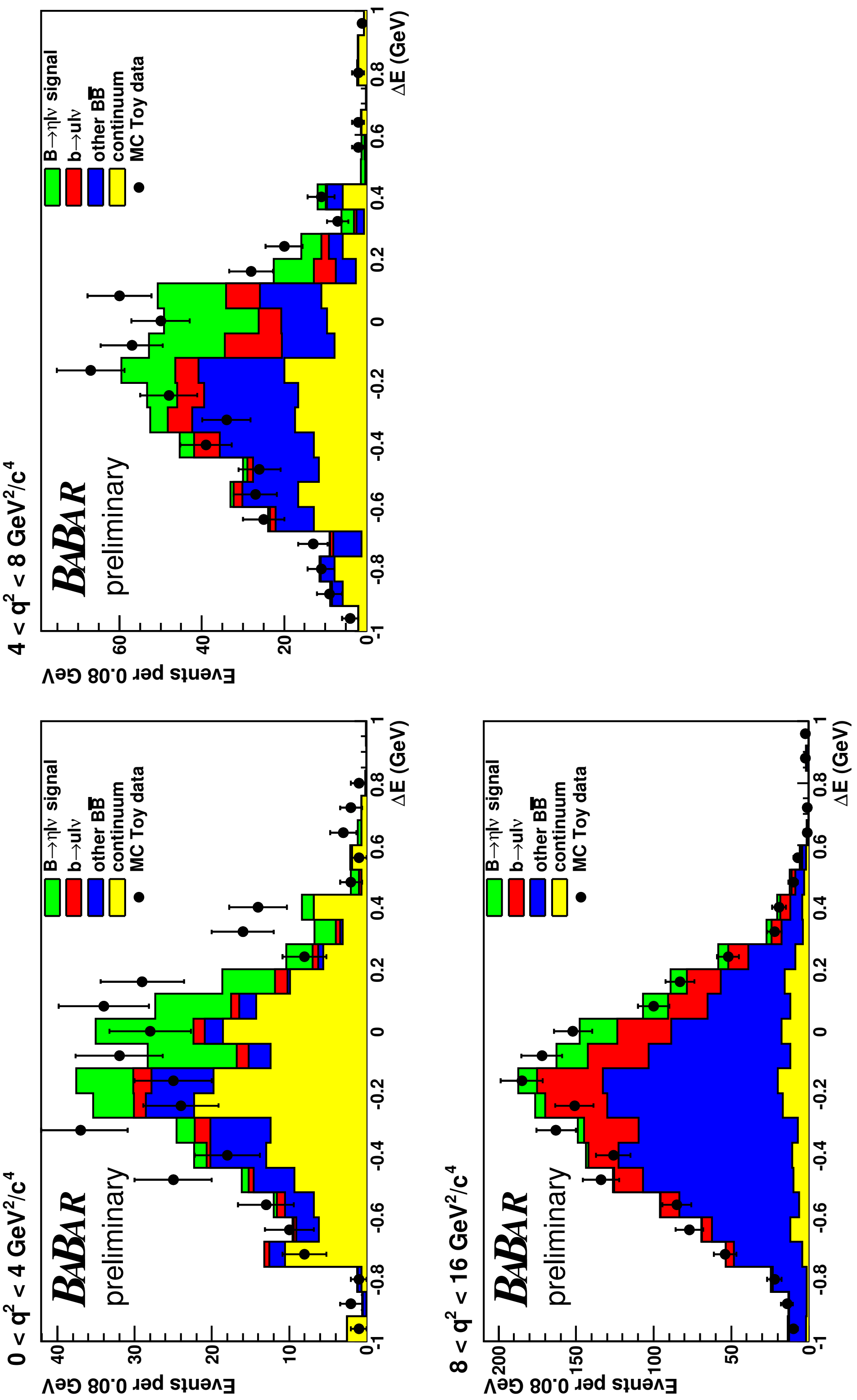

Figure 3.53 – MC ΔE yield fit projections with $m_{\text{ES}} > 5.2675\ \text{GeV}/c^2$ obtained in three $\tilde{q}^2$ bins from one of the fits described in Sect. 3.8.1.2, selected at random for $B^+ \to \eta\ell^+\nu$ decays in the $\gamma\gamma$ channel. The fit was done using the full ΔE-m_{ES} fit region.

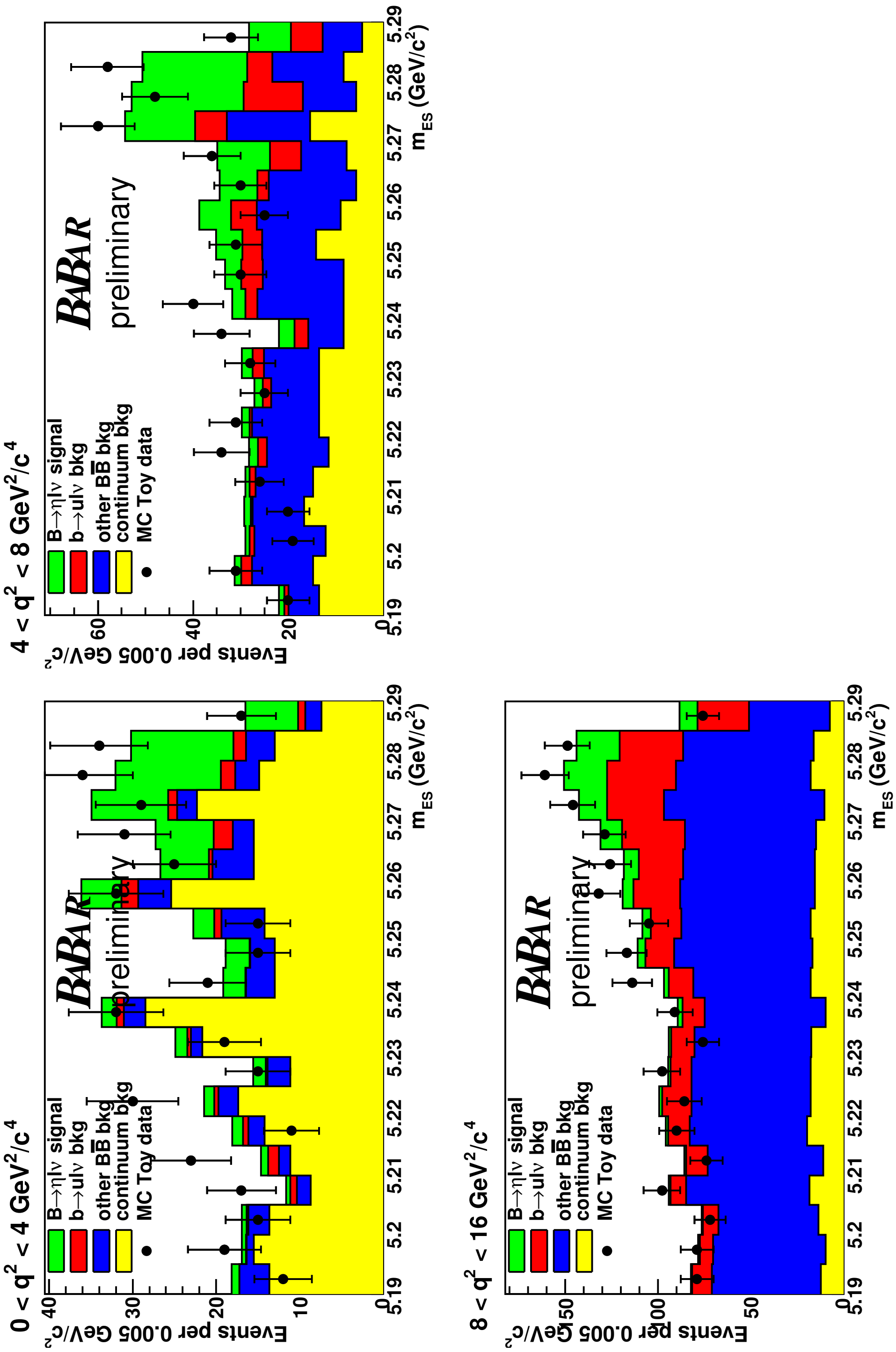

Figure 3.54 – MC m_{ES} yield fit projections with $-0.16 < \Delta E < 0.2$ GeV obtained in three $\tilde{q}^2$ bins from one of the fits described in Sect. 3.8.1.2, selected at random for $B^+ \to \eta \ell^+ \nu$ decays in the $\gamma\gamma$ channel. The fit was done using the full ΔE-m_{ES} fit region.

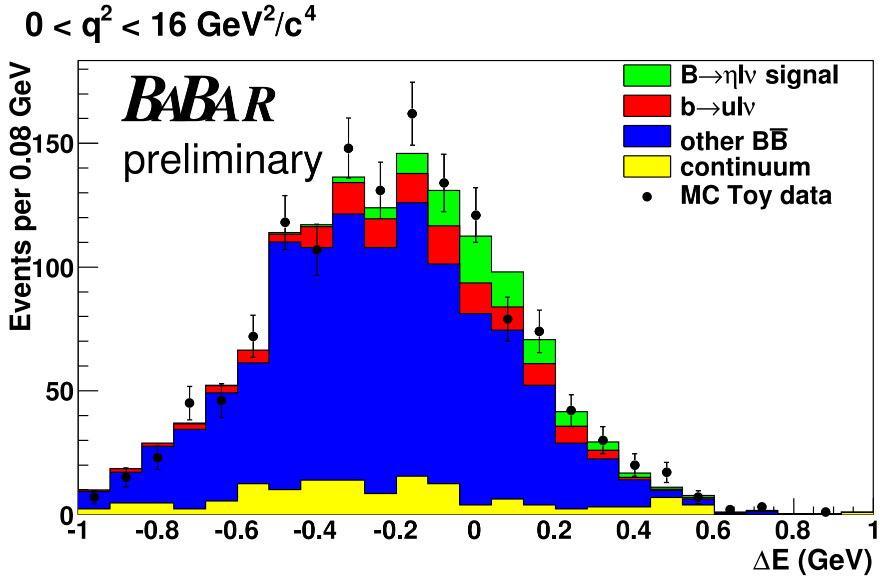

Figure 3.55 – MC ΔE yield fit projections with $m_{\text{ES}} > 5.2675\ \text{GeV}/c^2$ obtained in one $\tilde{q}^2$ bin from one of the fits described in Sect. 3.8.1.2, selected at random for $B^+ \to \eta\ell^+\nu$ decays in the 3π channel. The fit was done using the full ΔE-m_{ES} fit region.

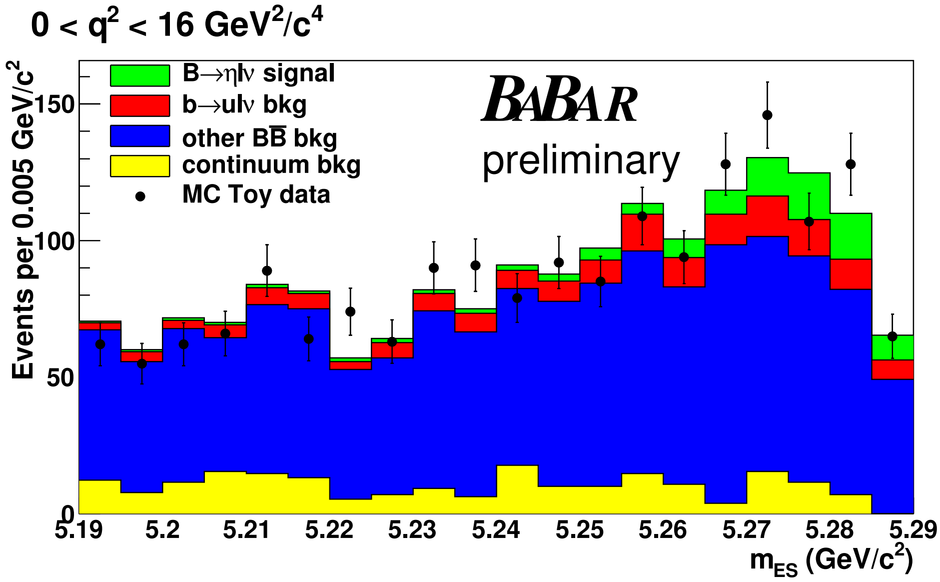

Figure 3.56 – MC m_{ES} yield fit projections with $-0.16 < \Delta E < 0.2\ \text{GeV}$ obtained in one $\tilde{q}^2$ bin from one of the fits described in Sect. 3.8.1.2, selected at random for $B^+ \to \eta\ell^+\nu$ decays in the 3π channel. The fit was done using the full ΔE-m_{ES} fit region.

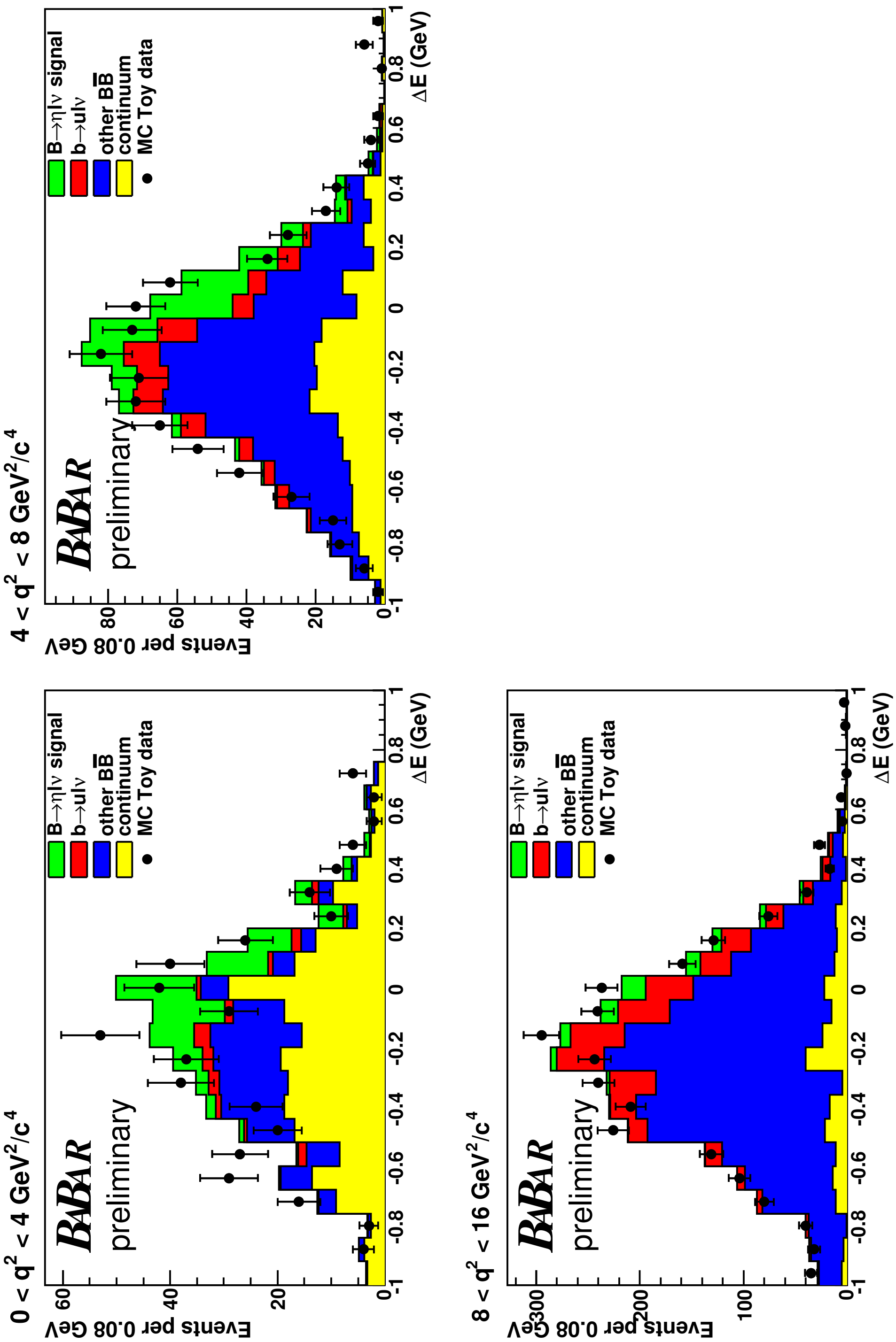

Figure 3.57 – MC ΔE yield fit projections with $m_{\mathrm{ES}} > 5.2675\ \mathrm{GeV}/c^2$ obtained in three $\tilde{q}^2$ bins from one of the fits described in Sect. 3.8.1.2, selected at random for $B^+ \to \eta\ell^+\nu$ ($\gamma\gamma$ and 3π channels combined) decays. The fit was done using the full ΔE-m_{ES} fit region.

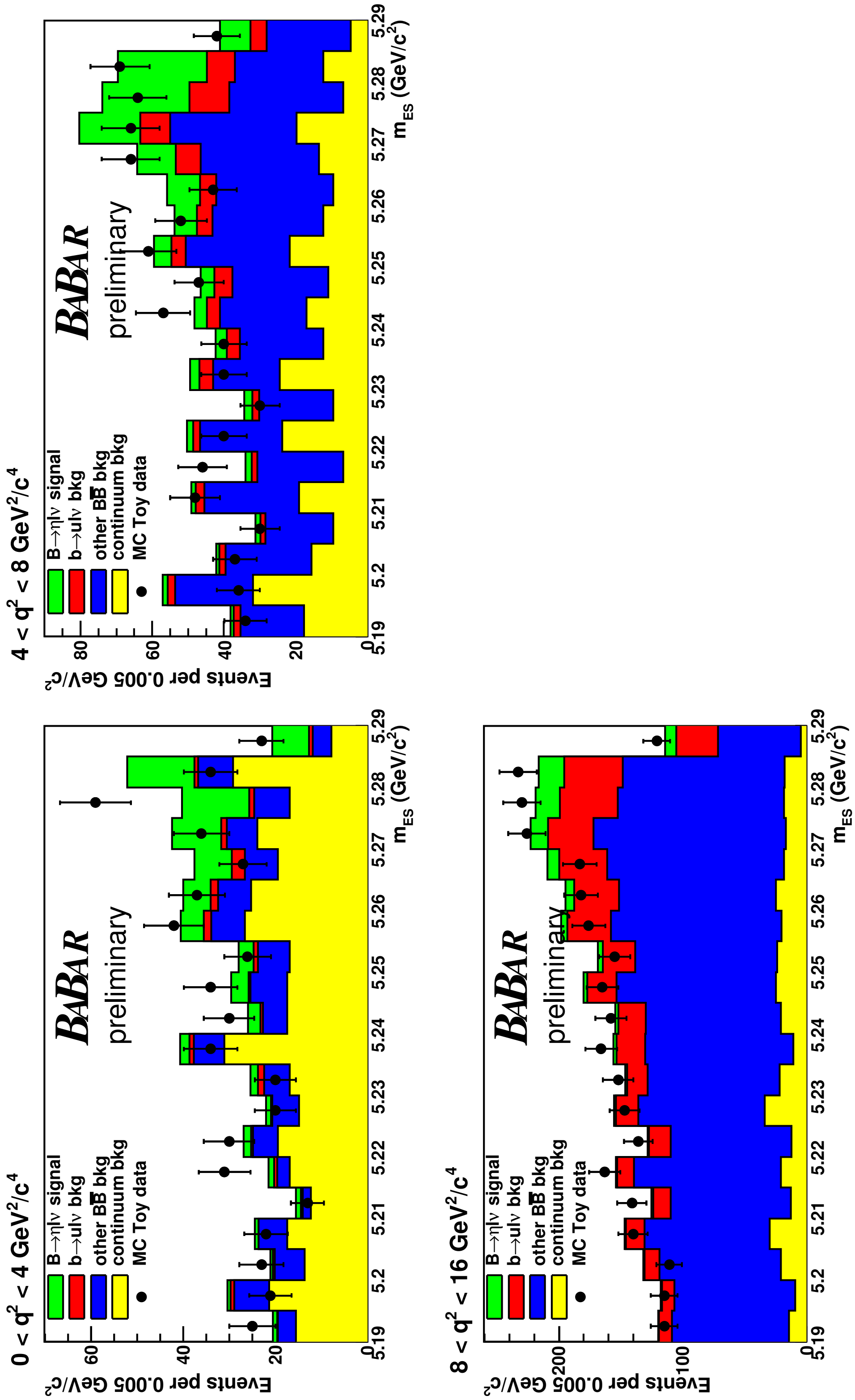

Figure 3.58 – MC m_{ES} yield fit projections with $-0.16 < \Delta E < 0.2$ GeV obtained in three $\tilde{q}^2$ bins from one of the fits described in Sect. 3.8.1.2, selected at random for $B^+ \to \eta\ell^+\nu$ ($\gamma\gamma$ and 3π channels combined) decays. The fit was done using the full ΔE-m_{ES} fit region.

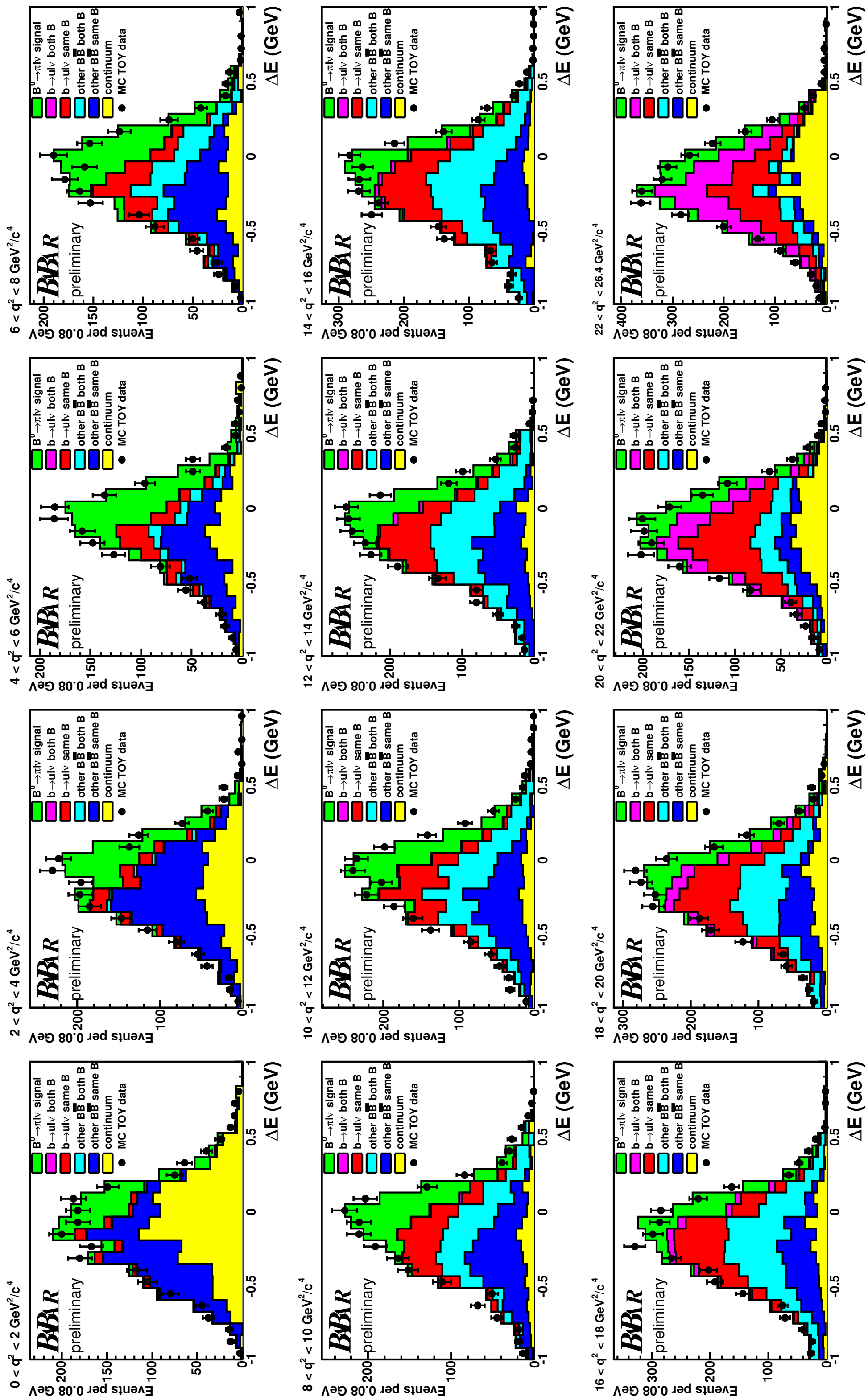

Figure 3.59 – MC ΔE yield fit projections with $m_{\mathrm{ES}} > 5.2675\ \mathrm{GeV}/c^2$ obtained in twelve $\tilde{q}^2$ bins from one of the fits described in Sect. 3.8.1.2, selected at random for $B^0 \to \pi^- \ell^+ \nu$ decays. The fit was done using the full ΔE-m_{ES} fit region.

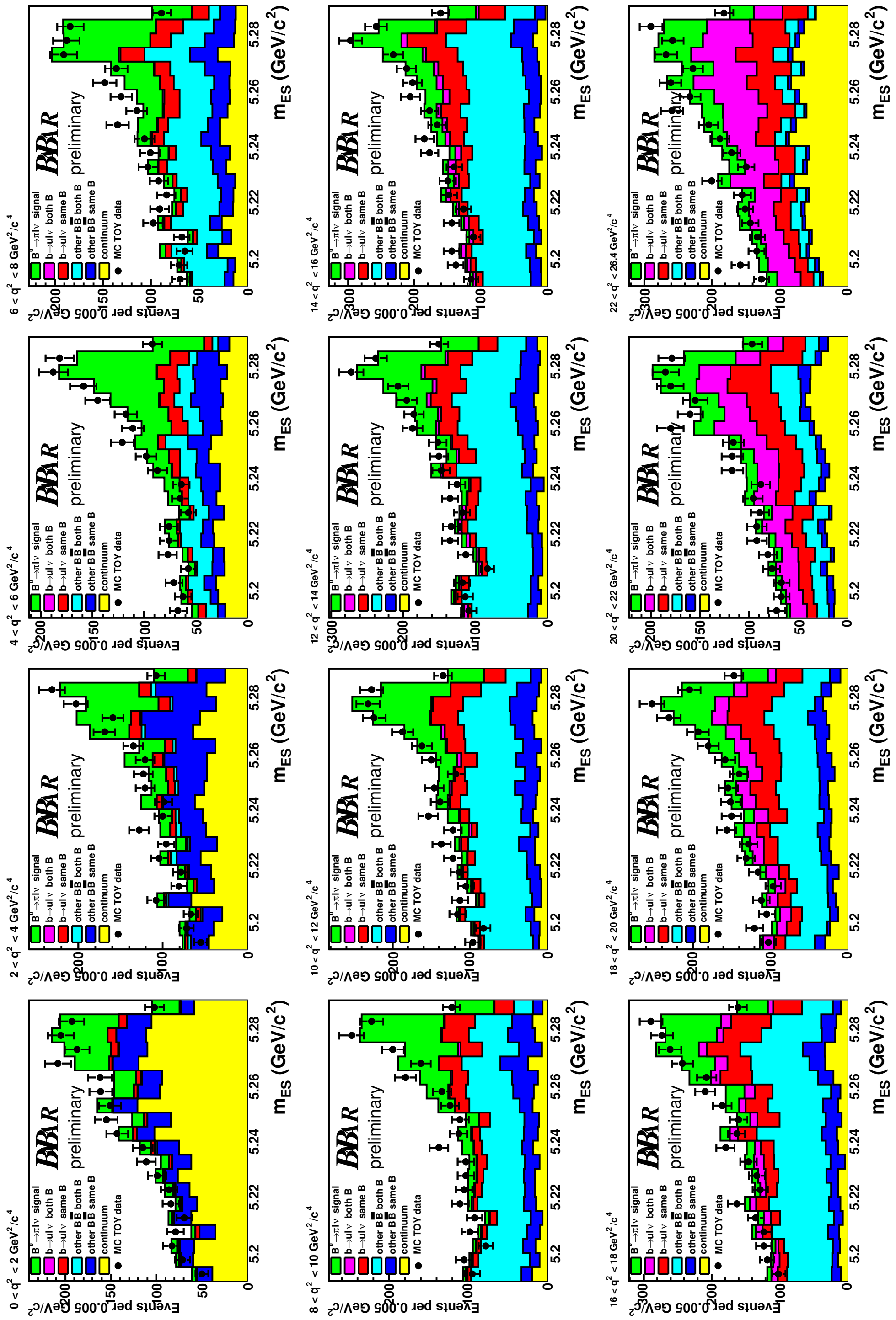

Figure 3.60 – MC $m_{\rm ES}$ yield fit projections with $-0.16 < \Delta E < 0.2$ GeV obtained in twelve $\tilde{q}^2$ bins from one of the fits described in Sect. 3.8.1.2, selected at random for $B^0 \to \pi^- \ell^+ \nu$ decays. The fit was done using the full ΔE-$m_{\rm ES}$ fit region.

3.8.2.2 Goodness of fit in MC simulation

The goodness of the signal extraction fit is evaluated by comparing the data from the full MC simulation to those obtained from the TOY MC data samples described in Sect. 3.8.1.1 where the underlying probability distributions are identical in both. We use a special χ^2 function which takes into account the statistical uncertainties of the data distribution in the TOY MC data samples as well as those of the histogrammed PDFs used in this analysis in the full MC simulation [77]. The results of this study are shown in Fig. 3.61. As expected, we obtain a mean $\chi^2/ndof$ close to 1.0. Hence, the value of the χ^2 we obtain can be used to estimate the probability that the fitted results describe the real data.

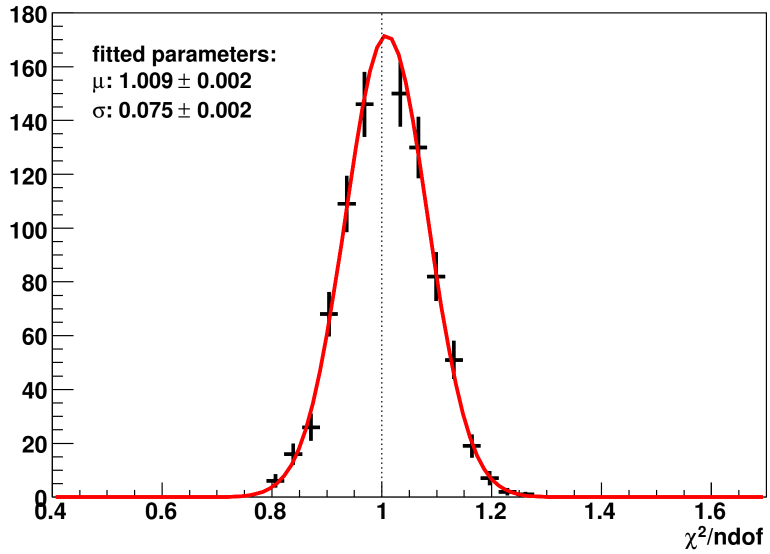

Figure 3.61 – $\chi^2/ndof$ obtained from fits to 1000 statistically independent TOY MC data samples generated with PDF histograms as described in Sect. 3.8.1.1 for $B^0 \to \pi^- \ell^+ \nu$ decays.

3.8.2.3 Partial $\Delta\mathcal{B}(q^2)$ and total $\mathcal{B}(B^+ \to \eta^{(\prime)}\ell^+\nu)$and $\mathcal{B}(B^0 \to \pi^-\ell^+\nu)$ from MC simulation

The MC-based values of the partial and total $\mathcal{B}(B^+ \to \eta^{'}\ell^+\nu)$, $\mathcal{B}(B^+ \to \eta\ell^+\nu)$ ($\gamma\gamma$ channel), $\mathcal{B}(B^+ \to \eta\ell^+\nu)$ (3π channel) and $\mathcal{B}(B^+ \to \eta\ell^+\nu)$ ($\gamma\gamma$ and 3π channels combined) and their uncertainties obtained with the methods described in Sects. 3.3.6 and 3.3.7 are given in Tables 3.34, 3.35, 3.36 and 3.37, respectively. We also give the associated statistical and systematic correlation matrices in Tables 3.38 and 3.39, and the corresponding statistical and systematic covariance matrices in Tables 3.40 and 3.41 for the $B^+ \to \eta\ell^+\nu$ ($\gamma\gamma$ channel) decays. We give similar matrices in Tables 3.42, 3.43, 3.44 and 3.45 for the $B^+ \to \eta\ell^+\nu$ ($\gamma\gamma$ and 3π channels combined). As explained earlier, it was deemed not necessary to carry out similar calculations for the $B^0 \to \pi^-\ell^+\nu$ decays. Compared to the raw yields uncertainties, we note that the q^2-unfolding process increases the relative statistical and systematic uncertainties of the partial $\Delta\mathcal{B}(q^2)$. On the other hand, the uncertainties on the total BFs are smaller than those on the partial BFs because of correlation effects.

Tableau 3.34 – Total $\mathcal{B}(B^+ \to \eta^{'} \ell^+ \nu)$ in the $\gamma\gamma$ decay channel and its statistical (fit error) and systematic (all the others) uncertainties from all sources, obtained from MC simulation. The BF is assumed to be 0.301×10^{-4}. The errors are given as % (relative errors).

$\tilde{q}^2$ bins (GeV^2/c^4)	Total
$BF \times 10^7$	270.6
tracking efficiency	2.4
photon efficiency	3.2
K_L^0 efficiency	1.7
ℓ/π identification	2.3
continuum yield	4.4
$\tilde{q}^2$ continuum shape	4.3
$\mathcal{B}(B \to X_u \ell \nu)$	1.9
η BF	0.0
shape function parameters	3.1
$B \to \rho \ell \nu$ FF	0.1
$B^+ \to \eta^{'} \ell^+ \nu$ FF	0.8
other scalar FF	2.5
$B \to \omega \ell \nu$ FF	0.9
$\mathcal{B}(B \to X_c \ell \nu)$	1.8
$B \to D \ell \nu$ FF	0.3
$B \to D^* \ell \nu$ FF	0.5
$\mathcal{B}(D \to X \ell \nu)$	2.5
$\mathcal{B}(\Upsilon(4S) \to B^0 B^0)$	1.2
$D \to K_L^0$ BF	7.7
B counting	1.1
signal MC stat error	0.9
total syst error	12.5
fit error	29.3
total error	31.8

Tableau 3.35 – Partial $\Delta\mathcal{B}(q^2)$ and total $\mathcal{B}(B^+ \to \eta\ell^+\nu)$ in the $\gamma\gamma$ decay channel and their statistical (fit error) and systematic (all the others) uncertainties from all sources, obtained from MC simulation. The BF is assumed to be 0.301×10^{-4}. The errors are given as % (relative errors).

$\tilde{q}^2$ bins (GeV^2/c^4)	0-4	4-8	8-16	Total
$\Delta\mathcal{B}(q^2)$ $\times 10^7$	70.8	70.0	155.7	296.5
tracking efficiency	3.1	2.1	2.8	2.0
photon efficiency	5.9	2.2	5.9	4.4
K_L^0 efficiency	3.0	1.5	1.6	1.2
ℓ/π identification	2.8	2.5	2.4	1.2
$\tilde{q}^2$ continuum shape	6.6	2.3	4.6	1.4
$\mathcal{B}(B \to X_u\ell\nu)$	0.6	1.6	8.1	4.7
$/eta$ BF	0.5	0.7	0.6	0.6
shape function parameters	1.6	2.6	10.4	6.5
$B \to \rho\ell\nu$ FF	0.2	1.9	1.1	0.9
$B^+ \to \eta\ell^+\nu$ FF	0.2	0.1	1.4	0.8
other scalar FF	1.1	0.1	0.0	0.2
$B \to \omega\ell\nu$ FF	0.2	0.6	1.7	0.8
$\mathcal{B}(B \to X_c\ell\nu)$	1.7	2.3	2.0	1.0
$B \to D\ell\nu$ FF	0.2	0.1	0.3	0.2
$B \to D^*\ell\nu$ FF	1.0	0.9	0.7	0.4
$\mathcal{B}(D \to X\ell\nu)$	0.8	0.4	3.3	1.5
$\mathcal{B}(\Upsilon(4S) \to B^0B^0)$	1.5	1.0	1.1	1.2
$D \to K_L^0$ BF	3.1	1.4	8.3	3.9
B counting	1.1	1.1	1.1	1.1
signal MC stat error	1.4	1.5	1.0	0.6
total syst error	14.6	7.9	18.6	10.8
fit error	32.0	24.1	34.1	20.1
total error	35.1	25.3	38.9	22.9

Tableau 3.36 – Total $\mathcal{B}(B^+ \rightarrow \eta\ell^+\nu)$ in the 3π decay channel and its statistical (fit error) and systematic (all the others) uncertainties from all sources, obtained from MC simulation. The BF is assumed to be 0.301×10^{-4}. The errors are given as % (relative errors).

$\tilde{q}^2$ bins (GeV^2/c^4)	Total
$BF \times 10^7$	274.2
tracking efficiency	7.9
photon efficiency	5.5
K_L^0 efficiency	4.9
ℓ/π identification	2.5
continuum yield	1.5
$\tilde{q}^2$ continuum shape	4.4
$\mathcal{B}(B \rightarrow X_u\ell\nu)$	5.0
η BF	1.2
shape function parameters	9.6
$B \rightarrow \rho\ell\nu$ FF	1.0
$B^+ \rightarrow \eta\ell^+\nu$ FF	1.1
other scalar FF	6.3
$B \rightarrow \omega\ell\nu$ FF	3.2
$\mathcal{B}(B \rightarrow X_c\ell\nu)$	3.1
$B \rightarrow D\ell\nu$ FF	0.5
$B \rightarrow D^*\ell\nu$ FF	1.1
$\mathcal{B}(D \rightarrow X\ell\nu)$	3.7
$\mathcal{B}(\Upsilon(4S) \rightarrow B^0B^0)$	1.3
$D \rightarrow K_L^0$ BF	5.9
B counting	1.1
signal MC stat error	1.3
total syst error	19.5
fit error	39.6
total error	44.1

Tableau 3.37 – Partial $\Delta\mathcal{B}(q^2)$ and total $\mathcal{B}(B^+ \to \eta\ell^+\nu)$ in the $\gamma\gamma$ and 3π decay channels combined and their statistical (fit error) and systematic (all the others) uncertainties from all sources, obtained from MC simulation. The BF is assumed to be 0.301×10^{-4}. The errors are given as % (relative errors).

$\tilde{q}^2$ bins (GeV^2/c^4)	0-4	4-8	8-16	Total
$\Delta\mathcal{B}(q^2)\ \times 10^7$	69.6	70.1	159.2	298.9
tracking efficiency	3.3	1.8	4.2	2.9
photon efficiency	8.1	2.0	4.0	3.6
K_L^0 efficiency	2.3	2.0	2.6	1.8
ℓ/π identification	1.9	1.9	2.7	1.5
$\tilde{q}^2$ continuum shape	5.8	1.3	3.3	0.7
$\mathcal{B}(B \to X_u\ell\nu)$	0.7	1.3	7.7	4.5
η BF	0.5	0.6	0.5	0.5
shape function parameters	1.7	3.1	11.2	7.1
$B \to \rho\ell\nu$ FF	0.3	1.5	0.8	0.5
$B^+ \to \eta\ell^+\nu$ FF	0.3	0.2	1.4	0.8
other scalar FF	1.0	0.1	0.0	0.2
$B \to \omega\ell\nu$ FF	0.3	0.5	3.1	1.5
$\mathcal{B}(B \to X_c\ell\nu)$	1.9	2.6	1.9	1.1
$B \to D\ell\nu$ FF	0.3	0.1	0.6	0.4
$B \to D^*\ell\nu$ FF	1.0	1.5	0.9	0.5
$\mathcal{B}(D \to X\ell\nu)$	0.6	0.6	4.8	2.3
$\mathcal{B}(\Upsilon(4S) \to B^0B^0)$	1.4	1.2	1.0	1.1
$D \to K_L^0$ BF	3.0	1.7	8.9	4.4
B counting	1.1	1.1	1.1	1.1
signal MC stat error	1.5	1.2	0.9	0.6
total syst error	14.5	7.4	19.2	11.4
fit error	27.3	23.3	29.2	17.3
total error	30.9	24.5	35.0	20.7

Tableau 3.38 – Correlation matrix of the partial $\Delta\mathcal{B}(q^2)$ statistical uncertainties for $B^+ \to \eta\ell^+\nu$ ($\gamma\gamma$ channel) decays obtained from the MC simulation.

q^2 bins (GeV^2/c^4)	0-4	4-8	8-16
0-4	1.00	-0.08	0.01
4-8	-0.08	1.00	-0.10
8-16	0.01	-0.10	1.00

Tableau 3.39 – Correlation matrix of the partial $\Delta\mathcal{B}(q^2)$ systematic uncertainties for $B^+ \rightarrow \eta\ell^+\nu$ ($\gamma\gamma$ channel) decays obtained from the MC simulation.

q^2 bins (GeV^2/c^4)	0-4	4-8	8-16
0-4	1.00	-0.11	0.04
4-8	-0.11	1.00	0.43
8-16	0.04	0.43	1.00

Tableau 3.40 – Covariance matrix of the partial $\Delta\mathcal{B}(q^2)$ statistical uncertainties for $B^+ \rightarrow \eta\ell^+\nu$ ($\gamma\gamma$ channel) decays obtained from the MC simulation.

q^2 bins (GeV^2/c^4)	0-4	4-8	8-16
0-4	919.7	-61.3	10.6
4-8	-61.3	606.9	-71.9
8-16	10.6	-71.9	934.1

Tableau 3.41 – Covariance matrix of the partial $\Delta\mathcal{B}(q^2)$ systematic uncertainties for $B^+ \rightarrow \eta\ell^+\nu$ ($\gamma\gamma$ channel) decays obtained from the MC simulation.

q^2 bins (GeV^2/c^4)	0-4	4-8	8-16
0-4	142.3	-9.9	9.2
4-8	-9.9	62.1	62.2
8-16	9.2	62.2	333.6

Tableau 3.42 – Correlation matrix of the partial $\Delta\mathcal{B}(q^2)$ statistical uncertainties for $B^+ \rightarrow \eta\ell^+\nu$ ($\gamma\gamma$ and 3π channels combined) decays obtained from the MC simulation.

q^2 bins (GeV^2/c^4)	0-4	4-8	8-16
0-4	1.00	-0.09	0.01
4-8	-0.09	1.00	-0.08
8-16	0.01	-0.08	1.00

Tableau 3.43 – Correlation matrix of the partial $\Delta\mathcal{B}(q^2)$ systematic uncertainties for $B^+ \rightarrow \eta\ell^+\nu$ ($\gamma\gamma$ and 3π channels combined) decays obtained from the MC simulation.

q^2 bins (GeV^2/c^4)	0-4	4-8	8-16
0-4	1.00	-0.33	0.04
4-8	-0.33	1.00	0.36
8-16	0.04	0.36	1.00

Tableau 3.44 – Covariance matrix of the partial $\Delta\mathcal{B}(q^2)$ statistical uncertainties for $B^+ \to \eta\ell^+\nu$ ($\gamma\gamma$ and 3π channels combined) decays obtained from the MC simulation.

q^2 bins (GeV^2/c^4)	0-4	4-8	8-16
0-4	779.4	-56.4	5.5
4-8	-56.4	534.7	-53.5
8-16	5.5	-53.5	762.5

Tableau 3.45 – Covariance matrix of the partial $\Delta\mathcal{B}(q^2)$ systematic uncertainties for $B^+ \to \eta\ell^+\nu$ ($\gamma\gamma$ and 3π channels combined) decays obtained from the MC simulation.

q^2 bins (GeV^2/c^4)	0-4	4-8	8-16
0-4	208.9	-35.6	10.1
4-8	-35.6	55.2	51.7
8-16	10.1	51.7	368.1

3.8.2.4 Fit of the $f_+(q^2)$ shape parameters in MC simulation

Fig. 3.62 shows one of the TOY MC data samples for $B^0 \to \pi^-\ell^+\nu$ decays, selected at random[21] from a set of samples generated with the BK $f_+(q^2)$ parametrization (see Sect. 3.3.8) parameter α_{BK} having a central value of 0.53. The fitting algorithm used to mimimize the χ^2 value yields the input value of α_{BK} for this particular data sample. In this particular case, α_{BK} = 0.56 ± 0.04. This shows that our procedure to evaluate the $f_+(q^2)$ shape parameters is correct. Only statistical errors are used in this test.

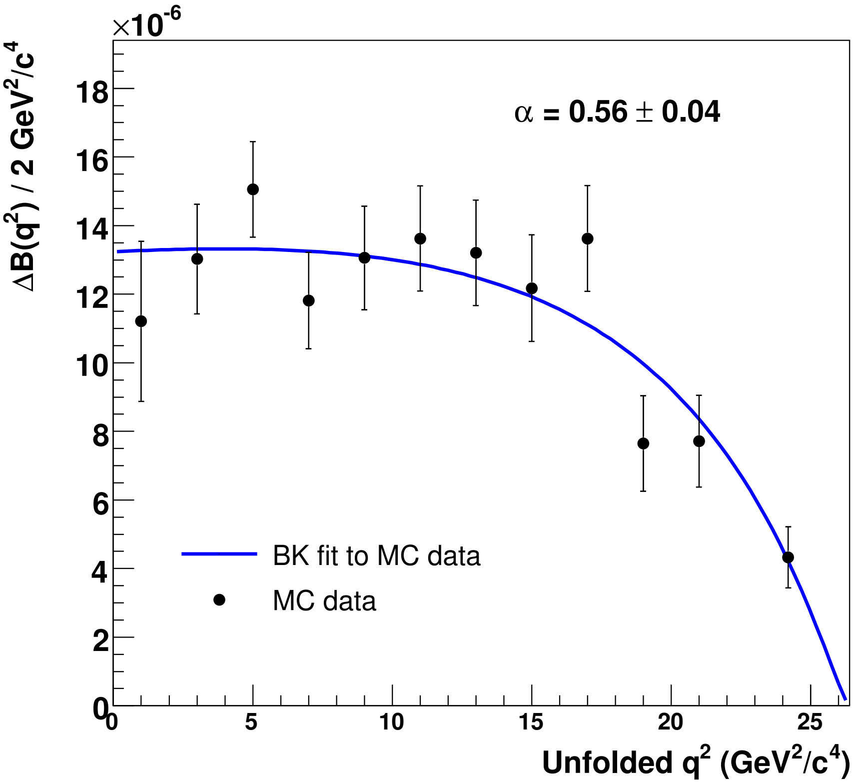

Figure 3.62 – Differential decay rate formula (Eq. 3.13) with the BK parametrization fitted to the partial $\Delta\mathcal{B}(q^2)$ spectrum. The data points correspond to the $\Delta\mathcal{B}(q^2)$ values generated for a particular TOY MC data sample

Note that these MC-based results were not necessarily obtained with the final configurations and central values in all cases. Thus, there may be minor variations in the

[21]The same sample was used to make Figs. 3.59, 3.60 and 3.62.

actual numbers but our conclusions remain.

3.8.3 Procedure for real data results - blind analysis

With real data, there is only one dataset. The procedure is then relatively simple : the dataset is analyzed using the method described in Sects. 3.3 to 3.6. The only complication in this procedure could arise from the measured values which would be systematically biased because of a problem with the analysis method. This possibility cannot be studied with only one dataset, but it can be studied with TOY MC data samples. We performed such a study with the result that there is no significant bias in our analysis, as shown in Sect. 3.6.4.

The analysis was kept completely blind to the signal events of the real on-resonance data until the detailed analysis method was approved by the reviewers of the BABAR Semileptonic Analysis Working Group. We followed this procedure to prevent our measurement from being biased towards any specific value.

Finally, as presented in Sects. 3.8.1 and 3.8.2, the entire analysis was performed on simulated samples treated like real data. We note that after the unblinding, we have results very similar to these predictions. This is not only true of the central values, but also of the relative error sizes and of the covariance matrices. Considering our blind analysis procedure, this gives confidence that our precise results are indeed correct.

3.8.4 Results and uncertainties obtained with the real data

The results presented in this section are obtained with the full data set (Runs 1-6) and for electrons and muons combined. The raw fit parameters and signal yields are presented in Sect. 3.8.4.1 and the values of the partial and total BFs are given in Sect. 3.8.4.2. In Sect. 3.8.4.3, the $\Delta\mathcal{B}(q^2)$ distributions are displayed in Figs. 3.73 and 3.74 for the $B^0 \to \pi^-\ell^+\nu$ and $B^+ \to \eta\ell^+\nu$ ($\gamma\gamma$ and 3π channels combined) decays, respectively, together with the results of a $f_+(q^2)$ shape fit using the parametrizations presented in Sect. 3.3.8. Our measured $\Delta\mathcal{B}(q^2)$ distributions are also compared to theoretical predictions in Sect. 3.8.4.4. Values of $|V_{ub}f_+(0)|$ and $|V_{ub}|$ are extracted in Sect. 3.8.4.5.

3.8.4.1 Extraction of raw signal yields in $\tilde{q}^2$ bins from the real data

The fit of the MC PDFs to the data worked as expected, with a χ^2 value of 19.2 for 17 degrees of freedom, 59.0 for 52 degrees of freedom, 16.2 for 17 degrees of freedom, 56.2 for 52 degrees of freedom and 411 for 386 degrees of freedom for $B^+ \to \eta^{'}\ell^+\nu$, $B^+ \to \eta\ell^+\nu$ ($\gamma\gamma$ channel), $B^+ \to \eta\ell^+\nu$ (3π channel), $B^+ \to \eta\ell^+\nu$ ($\gamma\gamma$ and 3π channels combined) and $B^0 \to \pi^-\ell^+\nu$ decays, respectively. They are summarized in Table 3.46. This is compatible with the MC predictions for the goodness of fit shown in Fig. 3.61.

Tableau 3.46 – χ^2 values of the fit of the MC PDFs to the data for the different decay modes.

decay mode	$\chi^2/ndof$	Prob. (%)
$B^0 \to \pi^-\ell^+\nu$	411/386	18.7
$B^+ \to \eta\ell^+\nu$ ($\gamma\gamma$)	59.0/52	23.5
$B^+ \to \eta\ell^+\nu$ (3π)	16.2/17	51.0
$B^+ \to \eta\ell^+\nu$ ($\gamma\gamma$ and 3π combined)	56.2/52	32.1
$B^+ \to \eta^{'}\ell^+\nu$	19.2/17	31.7

The signal yields and their various uncertainties in each $\tilde{q}^2$ bin are given in Tables 3.47, 3.48, 3.49, 3.50 and 3.51 for $B^+ \to \eta^{'}\ell^+\nu$, $B^+ \to \eta\ell^+\nu$ ($\gamma\gamma$ channel), $B^+ \to \eta\ell^+\nu$ (3π channel), $B^+ \to \eta\ell^+\nu$ ($\gamma\gamma$ and 3π channels combined) and $B^0 \to \pi^-\ell^+\nu$ decays, respectively.

The $\Delta E(m_{\rm ES})$ fit projections are displayed in Figs. 3.63(3.64) in one q^2 bin for $B^+ \to \eta^{'}\ell^+\nu$ decays, in Figs. 3.65(3.66) in three q^2 bins for $B^+ \to \eta\ell^+\nu$ ($\gamma\gamma$ channel) decays, in Figs. 3.67(3.68) in one q^2 bin for $B^+ \to \eta\ell^+\nu$ (3π channel) decays, in Figs. 3.69(3.70) in three q^2 bins for $B^+ \to \eta\ell^+\nu$ ($\gamma\gamma$ and 3π channels combined) decays and in Figs. 3.71(3.72) in twelve q^2 bins for $B^0 \to \pi^-\ell^+\nu$ decays. The ΔE distributions correspond to a cut of $m_{ES} > 5.2675$ GeV/c^2 and the $m_{\rm ES}$ distributions to a cut of $-0.16 < \Delta E < 0.2$ GeV.

Tableau 3.47 – Raw fitted yields and their relative uncertainties (%) from all sources for $B^+ \to \eta^{'} \ell^+ \nu$ decays ($\gamma\gamma$ channel), obtained from the real data.

$\tilde{q}^2$ bins (GeV^2/c^4)	Total
fitted yield	141.0
tracking efficiency	7.6
photon efficiency	4.0
K_L^0 efficiency	2.8
K_L^0 production rate	2.7
K_L^0 energy	1.0
ℓ identification	1.2
π identification	0.3
bremsstrahlung	1.9
continuum yield	5.2
$\tilde{q}^2$ continuum shape	5.3
$\mathcal{B}(B^0 \to \pi^- \ell^+ \nu)$	0.0
$\mathcal{B}(B^+ \to \pi^0 \ell^+ \nu)$	0.2
$\mathcal{B}(B^+ \to \eta \ell^+ \nu)$	0.5
$\mathcal{B}(B^0 \to \rho^- \ell^+ \nu)$	0.4
$\mathcal{B}(B^+ \to \rho^0 \ell^+ \nu)$	0.0
$\mathcal{B}(B^+ \to \omega \ell^+ \nu)$	0.9
non resonant $b \to u \ell \nu$ BF	2.3
η BF	0.3
SF parameters	4.3
$B \to \rho \ell \nu$ FF	0.1
$B^+ \to \eta^{'} \ell^+ \nu$ FF	0.1
other scalar FF	3.2
$B \to \omega \ell \nu$ FF	1.3
$\mathcal{B}(B \to D \ell \nu)$	0.7
$\mathcal{B}(B \to D^* \ell \nu)$	0.3
$\mathcal{B}(B \to D^{**} \ell \nu)$	1.4
non resonant $b \to c \ell \nu$ BF	0.2
$B \to D \ell \nu$	0.1
$B \to D^* \ell \nu$ FF	0.7
$\mathcal{B}(\Upsilon(4S) \to B^0 B^0)$	0.2
secondary lepton	4.7
Total systematic error	14.6
Fit error	32.8
Total error	35.9

Tableau 3.48 – Raw fitted yields and their relative uncertainties (%) from all sources for $B^+ \to \eta\ell^+\nu$ ($\gamma\gamma$ channel) decays, obtained from the real data.

$\tilde{q}^2$ bins (GeV^2/c^4)	0-4	4-8	8-16	Total
fitted yield	279.9	216.8	146.7	643.4
tracking efficiency	1.7	2.0	13.3	4.2
photon efficiency	1.8	1.3	4.8	1.4
K_L^0 efficiency	0.8	0.7	2.7	0.6
K_L^0 production rate	0.8	0.5	2.8	0.8
K_L^0 energy	0.7	0.3	1.7	0.6
ℓ identification	1.5	1.1	2.1	0.2
bremsstrahlung	1.6	1.8	22.7	5.2
$\tilde{q}^2$ continuum shape	3.0	1.4	6.3	0.6
$\mathcal{B}(B^0 \to \pi^-\ell^+\nu)$	0.0	0.0	0.1	0.0
$\mathcal{B}(B^+ \to \pi^0\ell^+\nu)$	0.3	0.9	4.4	1.5
$\mathcal{B}(B^+ \to \eta^{'}\ell^+\nu)$	0.1	0.1	0.7	0.2
$\mathcal{B}(B^0 \to \rho^-\ell^+\nu)$	0.1	1.2	6.0	1.8
$\mathcal{B}(B^+ \to \rho^0\ell^+\nu)$	0.0	0.1	0.4	0.1
$\mathcal{B}(B^+ \to \omega\ell^+\nu)$	0.1	0.3	2.1	0.6
non resonant $b \to u\ell\nu$ BF	0.5	1.1	8.4	2.5
η BF	0.1	0.1	0.4	0.1
SF parameters	1.5	2.9	14.9	5.0
$B \to \rho\ell\nu$ FF	0.1	2.1	1.7	1.0
$B^+ \to \eta\ell^+\nu$ FF	0.1	0.1	0.5	0.2
other scalar FF	0.8	0.0	0.0	0.3
$B \to \omega\ell\nu$ FF	0.1	0.4	2.2	0.4
$\mathcal{B}(B \to D\ell\nu)$	0.1	0.7	0.6	0.3
$\mathcal{B}(B \to D^*\ell\nu)$	0.1	0.5	0.9	0.2
$\mathcal{B}(B \to D^{**}\ell\nu)$	0.4	0.9	2.0	0.5
non resonant $b \to c\ell\nu$ BF	0.1	0.1	0.6	0.1
$B \to D\ell\nu$ FF	0.1	0.1	0.4	0.1
$B \to D^*\ell\nu$ FF	0.4	0.6	1.1	0.3
$\mathcal{B}(\Upsilon(4S) \to B^0\bar{B}^0)$	0.2	0.1	0.4	0.1
secondary lepton	0.6	0.8	8.5	1.9
Total systematic error	5.1	5.8	34.9	9.6
Fit error	13.9	17.2	33.9	12.0
Total error	14.8	18.1	48.7	15.3

Tableau 3.49 – Raw fitted yields and their relative uncertainties (%) from all sources for $B^+ \to \eta\ell^+\nu$ (3π channel) decays, obtained from the real data.

$\tilde{q}^2$ bins (GeV^2/c^4)	Total
fitted yield	244.8
tracking efficiency	7.2
photon efficiency	5.0
K_L^0 efficiency	1.1
K_L^0 production rate	1.3
K_L^0 energy	1.6
ℓ identification	0.9
π identification	0.2
bremsstrahlung	0.3
continuum yield	1.3
$\tilde{q}^2$ continuum shape	2.3
$\mathcal{B}(B^0 \to \pi^-\ell^+\nu)$	0.1
$\mathcal{B}(B^+ \to \pi^0\ell^+\nu)$	0.1
$\mathcal{B}(B^+ \to \eta^{'}\ell^+\nu)$	0.4
$\mathcal{B}(B^0 \to \rho^-\ell^+\nu)$	0.5
$\mathcal{B}(B^+ \to \rho^0\ell^+\nu)$	0.3
$\mathcal{B}(B^+ \to \omega\ell^+\nu)$	1.1
non resonant $b \to u\ell\nu$ BF	3.5
η BF	0.1
SF parameters	6.3
$B \to \rho\ell\nu$ FF	0.7
$B^+ \to \eta\ell^+\nu$ FF	0.2
other scalar FF	3.9
$B \to \omega\ell\nu$ FF	2.1
$\mathcal{B}(B \to D\ell\nu)$	0.9
$\mathcal{B}(B \to D^*\ell\nu)$	0.2
$\mathcal{B}(B \to D^{**}\ell\nu)$	1.4
non resonant $b \to c\ell\nu$ BF	0.1
$B \to D\ell\nu$	0.3
$B \to D^*\ell\nu$ FF	0.9
$\mathcal{B}(\Upsilon(4S) \to B^0B^0)$	0.1
secondary lepton	6.1
Total systematic error	14.3
Fit error	25.6
Total error	29.3

Tableau 3.50 – Raw fitted yields and their relative uncertainties ($\%$) from all sources for $B^+ \to \eta\ell^+\nu$ ($\gamma\gamma$ and 3π channels combined) decays, obtained from the real data.

$\tilde{q}^2$ bins (GeV^2/c^4)	0-4	4-8	8-16	Total
fitted yield	303.9	331.5	252.5	887.9
tracking efficiency	2.5	2.6	13.1	5.4
photon efficiency	3.5	4.3	8.8	4.0
K_L^0 efficiency	0.6	0.5	2.5	0.8
K_L^0 production rate	0.7	0.4	1.7	0.7
K_L^0 energy	0.5	0.3	2.0	0.7
ℓ identification	1.3	0.4	1.9	0.3
π identification	0.1	0.1	0.5	0.2
bremsstrahlung	0.6	0.9	12.9	3.5
$\tilde{q}^2$ continuum shape	2.9	0.4	3.6	0.2
$\mathcal{B}(B^0 \to \pi^-\ell^+\nu)$	0.0	0.0	0.1	0.0
$\mathcal{B}(B^+ \to \pi^0\ell^+\nu)$	0.3	0.6	2.6	1.1
$\mathcal{B}(B^+ \to \eta^{'}\ell^+\nu)$	0.1	0.1	0.8	0.3
$\mathcal{B}(B^0 \to \rho^-\ell^+\nu)$	0.1	0.7	3.9	1.4
$\mathcal{B}(B^+ \to \rho^0\ell^+\nu)$	0.0	0.0	0.5	0.1
$\mathcal{B}(B^+ \to \omega\ell^+\nu)$	0.1	0.8	0.7	0.5
non resonant $b \to u\ell\nu$ BF	0.4	0.8	7.4	2.6
η BF	0.1	0.1	0.4	0.2
SF parameters	1.6	2.7	12.8	5.2
$B \to \rho\ell\nu$ FF	0.1	1.3	0.7	0.6
$B^+ \to \eta\ell^+\nu$ FF	0.1	0.1	0.3	0.1
other scalar FF	0.7	0.0	0.0	0.2
$B \to \omega\ell\nu$ FF	0.1	0.2	3.3	0.9
$\mathcal{B}(B \to D\ell\nu)$	0.1	0.8	0.7	0.5
$\mathcal{B}(B \to D^*\ell\nu)$	0.2	0.5	0.9	0.3
$\mathcal{B}(B \to D^{**}\ell\nu)$	0.4	0.6	2.4	0.7
non resonant $b \to c\ell\nu$ BF	0.2	0.1	0.6	0.2
$B \to D\ell\nu$ FF	0.1	0.1	0.8	0.3
$B \to D^*\ell\nu$ FF	0.4	1.0	1.1	0.4
$\mathcal{B}(\Upsilon(4S) \to B^0B^0)$	0.2	0.1	0.5	0.2
secondary lepton	0.4	1.7	8.7	2.8
Total systematic error	5.8	6.6	28.1	10.3
Fit error	14.1	14.2	26.6	11.0
Total error	15.3	15.6	38.7	15.1

Tableau 3.51 – Raw fitted yields and their relative uncertainties (%) from all sources for $B^0 \to \pi^-\ell^+\nu$ decays, obtained from the real data.

$\tilde{q}^2$ bins (GeV$^2/c^4$)	0-2	2-4	4-6	6-8	8-10	10-12	12-14	14-16	16-18	18-20	20-22	22-26.4	$\tilde{q}^2$<16	$\tilde{q}^2$>16	Total
fitted yield	894.7	987.8	1177.1	1181.3	1178.6	1122.1	996.1	884.5	904.3	847.5	729.9	873.9	8422.1	3355.4	11777.6
tracking efficiency	1.4	2.9	0.8	0.8	1.2	0.5	1.0	0.6	1.1	1.6	1.2	4.0	0.9	1.1	0.7
photon efficiency	3.9	2.2	0.4	0.6	0.5	0.4	0.8	0.9	2.4	1.8	3.4	10.4	0.4	3.6	1.3
K_L^0 efficiency	0.9	0.5	0.3	0.4	0.2	0.7	0.4	0.4	0.3	0.5	1.2	2.9	0.4	1.0	0.4
K_L^0 production rate	0.8	0.6	0.5	0.4	0.6	0.6	0.4	1.9	1.3	0.9	1.7	3.9	0.5	1.8	0.9
K_L^0 energy	0.9	0.5	0.2	0.2	0.2	0.2	0.2	0.3	0.4	0.7	0.8	2.9	0.2	1.0	0.4
ℓ identification	4.5	0.7	0.2	0.2	0.5	0.4	0.3	0.2	0.3	0.4	0.6	2.2	0.6	0.8	0.6
π identification	0.5	0.2	0.1	0.1	0.1	0.1	0.2	0.3	0.3	0.3	0.4	2.3	0.2	0.8	0.4
bremsstrahlung	0.5	0.2	0.1	0.2	0.1	0.2	0.2	0.3	0.3	0.3	0.4	2.2	0.2	0.8	0.4
$\tilde{q}^2$ continuum shape	6.8	0.4	0.9	0.3	0.5	0.4	0.9	0.3	0.7	1.0	1.0	2.3	0.8	1.0	0.7
$m_{\rm ES}$ continuum shape	8.2	1.7	1.0	0.6	0.2	0.5	0.6	0.6	1.1	1.1	2.4	11.7	1.5	4.1	2.3
ΔE continuum shape	3.4	2.5	0.7	0.5	0.4	0.2	0.2	0.3	0.4	1.4	2.1	4.3	0.9	2.0	1.2
$\mathcal{B}(B^+ \to \pi^0\ell^+\nu)$	0.5	0.2	0.1	0.1	0.1	0.1	0.2	0.3	0.3	0.3	0.6	2.9	0.2	1.0	0.4
$\mathcal{B}(B^0 \to \rho^-\ell^+\nu)$	0.5	0.3	0.1	0.1	0.2	0.1	0.2	0.3	0.3	0.3	0.4	3.9	0.2	1.1	0.4
$\mathcal{B}(B^+ \to \rho^0\ell^+\nu)$	0.6	0.2	0.1	0.1	0.2	0.2	0.2	0.3	0.3	0.3	0.5	3.0	0.2	1.0	0.4
$\mathcal{B}(B^+ \to \omega\ell^+\nu)$	0.5	0.2	0.1	0.1	0.1	0.1	0.2	0.3	0.3	0.4	0.6	3.4	0.2	1.1	0.4
$\mathcal{B}(B^+ \to \eta\ell^+\nu)$	0.5	0.2	0.1	0.1	0.1	0.1	0.2	0.2	0.3	0.3	0.4	2.3	0.2	0.8	0.4
$\mathcal{B}(B^+ \to \eta^{'}\ell^+\nu)$	0.5	0.2	0.1	0.1	0.1	0.1	0.2	0.3	0.3	0.3	0.5	2.3	0.2	0.8	0.4
non resonant $b \to u\ell\nu$ BF	0.6	0.3	0.1	0.1	0.2	0.2	0.2	0.4	0.4	0.3	0.5	3.0	0.2	0.9	0.4
SF parameters	0.9	0.6	0.8	0.5	0.3	0.4	0.4	0.3	0.5	1.5	3.9	9.8	0.4	3.0	1.1
$B \to \rho\ell\nu$ FF	2.2	1.6	1.9	1.6	1.8	1.5	0.8	0.6	1.7	2.4	1.5	7.0	1.5	2.4	1.7
$B^0 \to \pi^-\ell^+\nu$ FF	0.5	0.2	0.1	0.1	0.1	0.1	0.2	0.3	0.3	0.3	0.5	3.0	0.2	1.0	0.4
other scalar FF	1.1	0.4	0.3	0.4	0.4	0.2	0.4	0.9	1.5	1.5	1.6	2.2	0.4	0.6	0.4
$B \to \omega\ell\nu$ FF	0.5	0.2	0.1	0.1	0.1	0.1	0.2	0.2	0.4	0.7	1.2	7.3	0.2	2.3	0.7
$\mathcal{B}(B \to D\ell\nu)$	0.5	0.4	0.2	0.2	0.1	0.1	0.3	0.3	0.3	0.5	0.5	2.3	0.2	0.8	0.4
$\mathcal{B}(B \to D^*\ell\nu)$	0.5	0.2	0.1	0.3	0.3	0.3	0.3	0.5	0.5	0.4	0.5	2.4	0.3	0.9	0.4
$\mathcal{B}(B \to D^{**}\ell\nu)$	0.6	0.3	0.2	0.3	0.3	0.2	0.6	0.6	1.0	0.7	0.7	2.4	0.2	0.9	0.4
non resonant $b \to c\ell\nu$ BF	0.6	0.2	0.2	0.1	0.1	0.2	0.2	0.4	0.3	0.4	0.5	2.3	0.2	0.9	0.4
$B \to D\ell\nu$ FF	0.5	0.2	0.2	0.1	0.2	0.1	0.2	0.3	0.3	0.4	0.5	2.4	0.2	0.9	0.4
$B \to D^*\ell\nu$ FF	0.6	0.2	0.2	0.3	0.2	0.8	0.5	1.6	0.5	0.7	1.2	3.0	0.3	1.2	0.6
$\Upsilon(4S) \to B^0B^0$ BF	0.5	0.4	0.1	0.1	0.1	0.1	0.2	0.3	0.3	0.3	0.6	2.6	0.2	0.9	0.4
secondary lepton	3.2	2.4	0.6	0.6	0.3	1.0	1.3	0.8	1.2	1.0	2.2	2.5	0.5	1.0	0.5
final state radiation	0.8	0.3	0.5	0.4	0.0	0.4	0.3	0.5	0.7	0.3	0.2	0.8	0.4	0.5	0.4
Total systematic error	13.7	5.9	3.1	2.7	2.8	2.7	2.9	3.6	4.7	5.3	7.9	25.6	3.0	8.9	4.3
Fit error	12.8	8.1	6.0	6.4	6.7	7.0	8.2	9.8	10.3	10.5	14.0	21.0	3.6	7.9	3.7
Total error	20.2	10.5	7.2	7.2	7.5	7.7	9.1	10.6	11.7	12.2	15.8	32.2	5.2	11.5	5.8

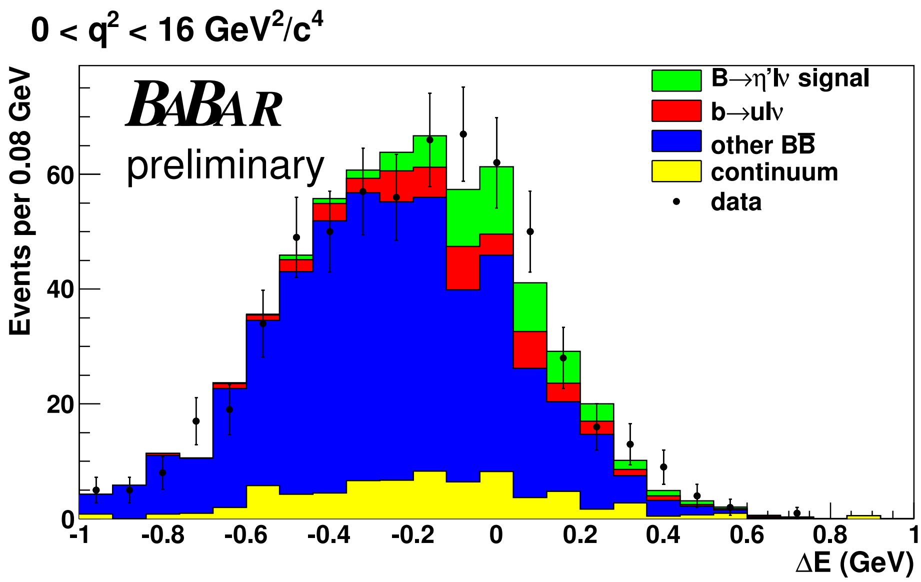

Figure 3.63 – ΔE yield fit projections with $m_{\mathrm{ES}} > 5.2675\ \mathrm{GeV}/c^2$ obtained in one $\tilde{q}^2$ bin from the fit to the real data for $B^+ \to \eta^{\prime} \ell^+ \nu$ decays. The fit was done using the full ΔE-m_{ES} fit region.

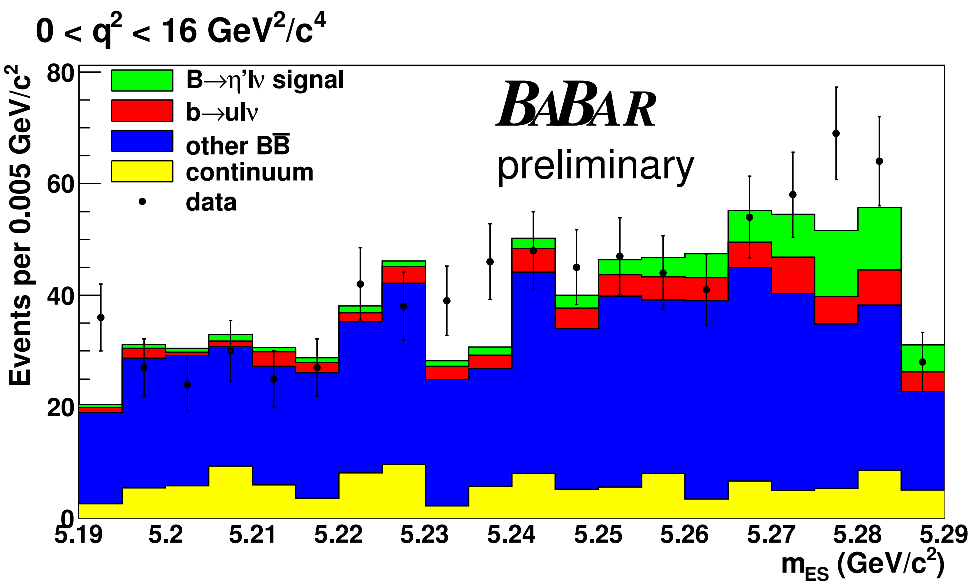

Figure 3.64 – m_{ES} yield fit projections with $-0.16 < \Delta E < 0.2$ GeV obtained in one $\tilde{q}^2$ bin from the fit to the real data for $B^+ \to \eta^{\prime} \ell^+ \nu$ decays. The fit was done using the full ΔE-m_{ES} fit region.

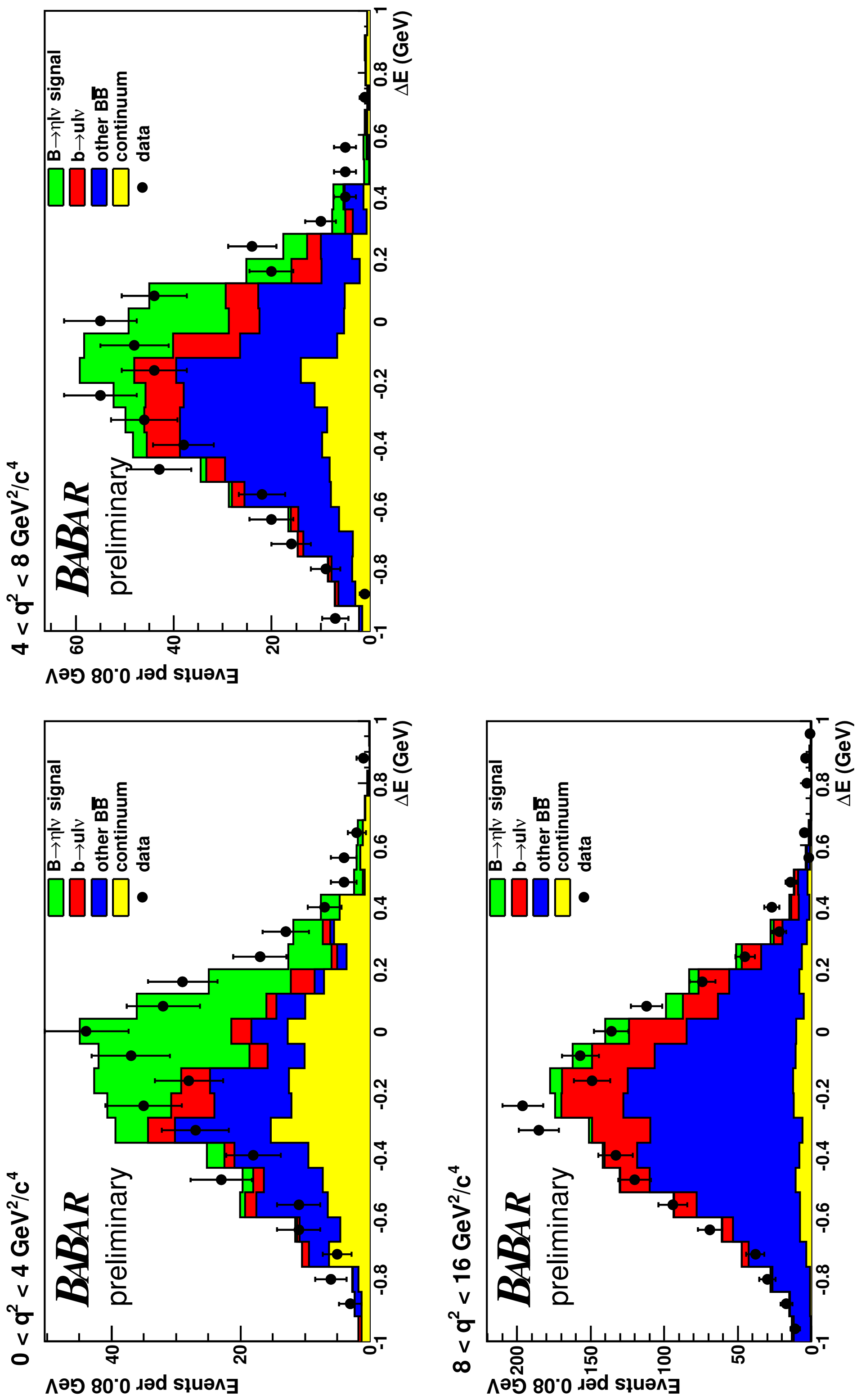

Figure 3.65 – ΔE yield fit projections with $m_{\rm ES} > 5.2675$ GeV/c^2 obtained in three $\tilde{q}^2$ bins from the fit to the real data for $B^+ \to \eta\ell^+\nu$ ($\gamma\gamma$ channel) decays. The fit was done using the full ΔE-$m_{\rm ES}$ fit region.

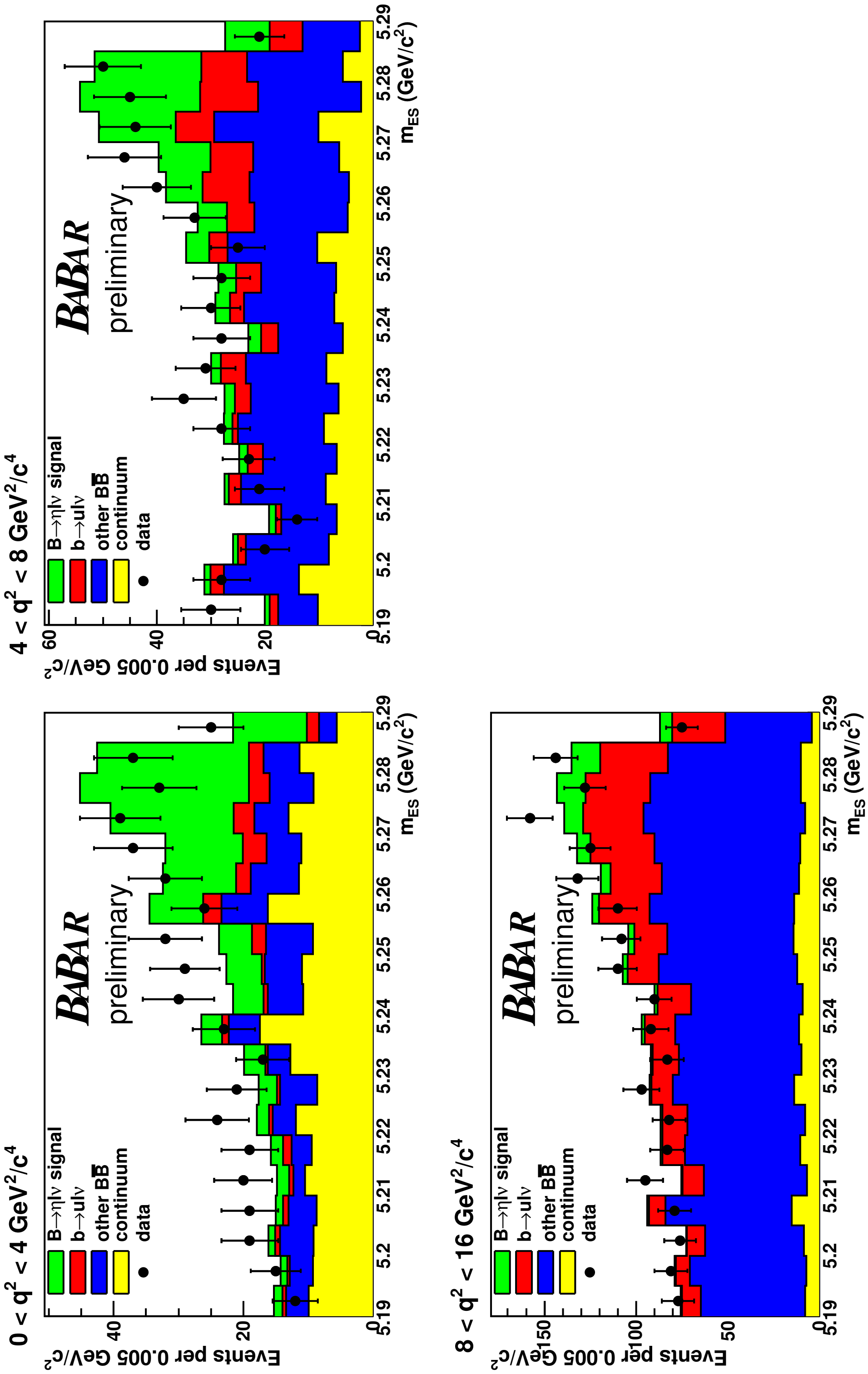

Figure 3.66 – m_{ES} yield fit projections with $-0.16 < \Delta E < 0.2$ GeV obtained in three $\tilde{q}^2$ bins from the fit to the real data for $B^+ \to \eta\ell^+\nu$ ($\gamma\gamma$ channel) decays. The fit was done using the full ΔE-m_{ES} fit region.

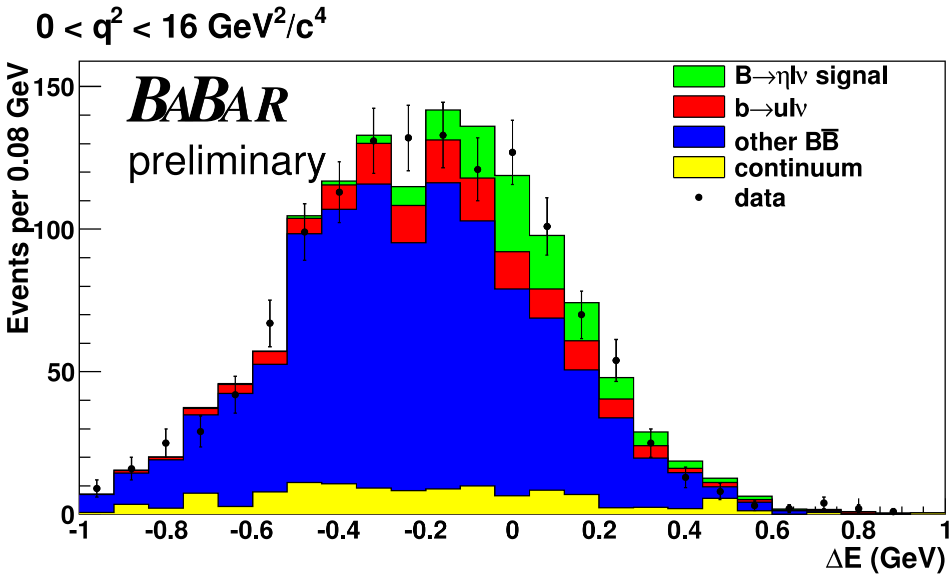

Figure 3.67 – ΔE yield fit projections with $m_{\mathrm{ES}} > 5.2675\ \mathrm{GeV}/c^2$ obtained in one $\tilde{q}^2$ bin from the fit to the real data for $B^+ \to \eta\ell^+\nu$ (3π channel) decays. The fit was done using the full ΔE-m_{ES} fit region.

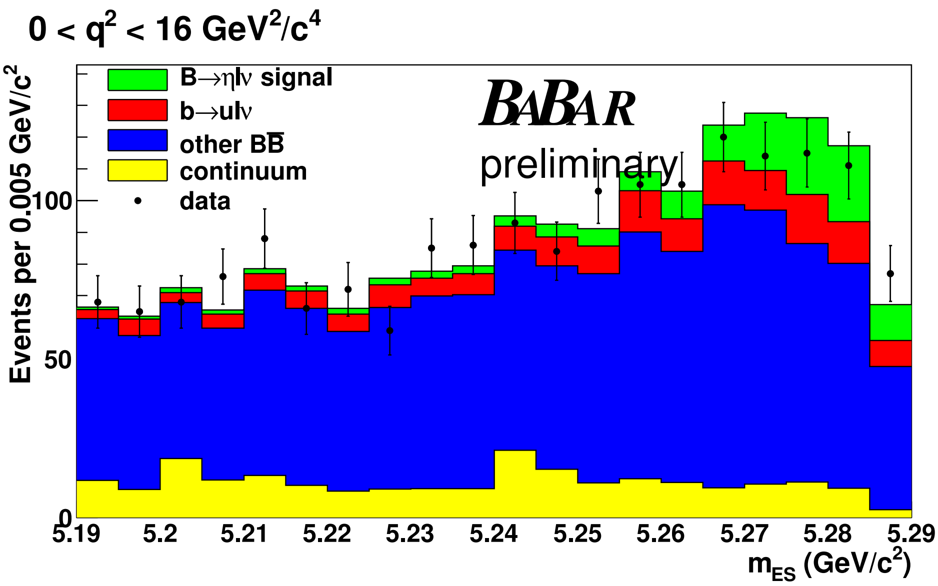

Figure 3.68 – m_{ES} yield fit projections with $-0.16 < \Delta E < 0.2\ \mathrm{GeV}$ obtained in one $\tilde{q}^2$ bin from the fit to the real data for $B^+ \to \eta\ell^+\nu$ (3π channel) decays. The fit was done using the full ΔE-m_{ES} fit region.

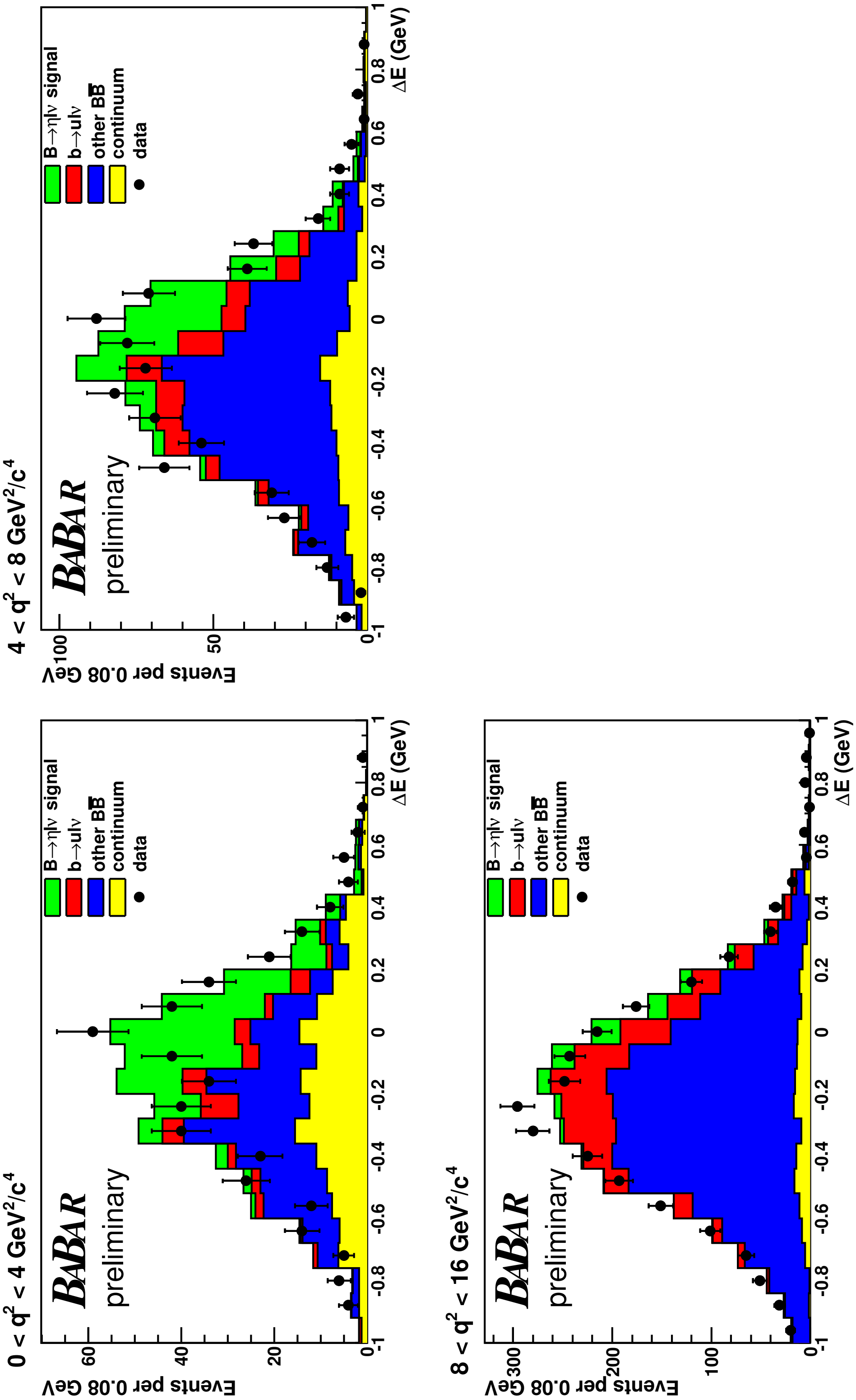

Figure 3.69 – ΔE yield fit projections with $m_{\mathrm{ES}} > 5.2675$ GeV/c^2 obtained in three $\tilde{q}^2$ bins from the fit to the real data for $B^+ \to \eta\ell^+\nu$ ($\gamma\gamma$ and 3π channels combined) decays. The fit was done using the full ΔE-m_{ES} fit region.

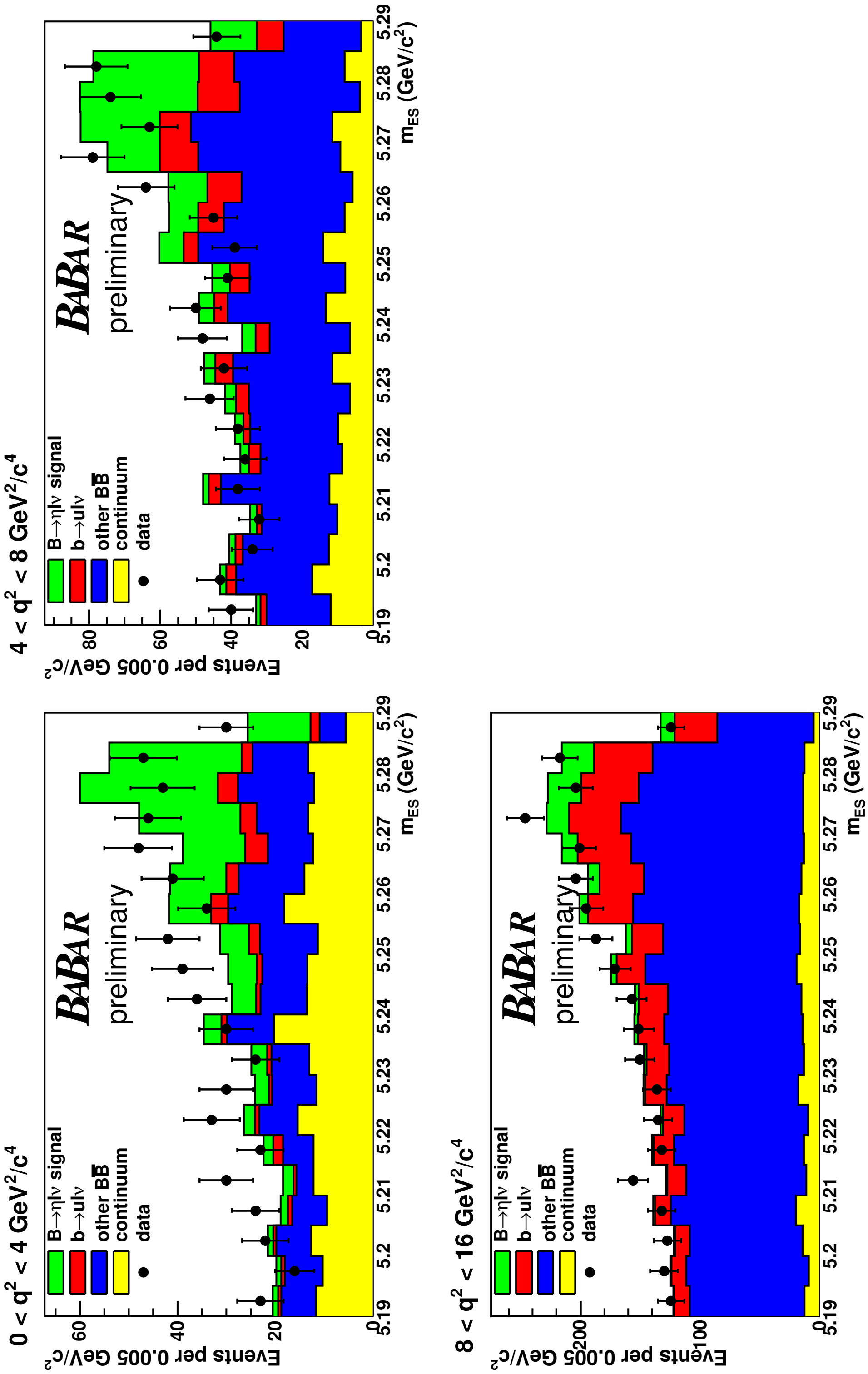

Figure 3.70 – $m_{\rm ES}$ yield fit projections with $-0.16 < \Delta E < 0.2$ GeV obtained in three $\tilde{q}^2$ bins from the fit to the real data for $B^+ \to \eta\ell^+\nu$ ($\gamma\gamma$ and 3π channels combined) decays. The fit was done using the full ΔE-$m_{\rm ES}$ fit region.

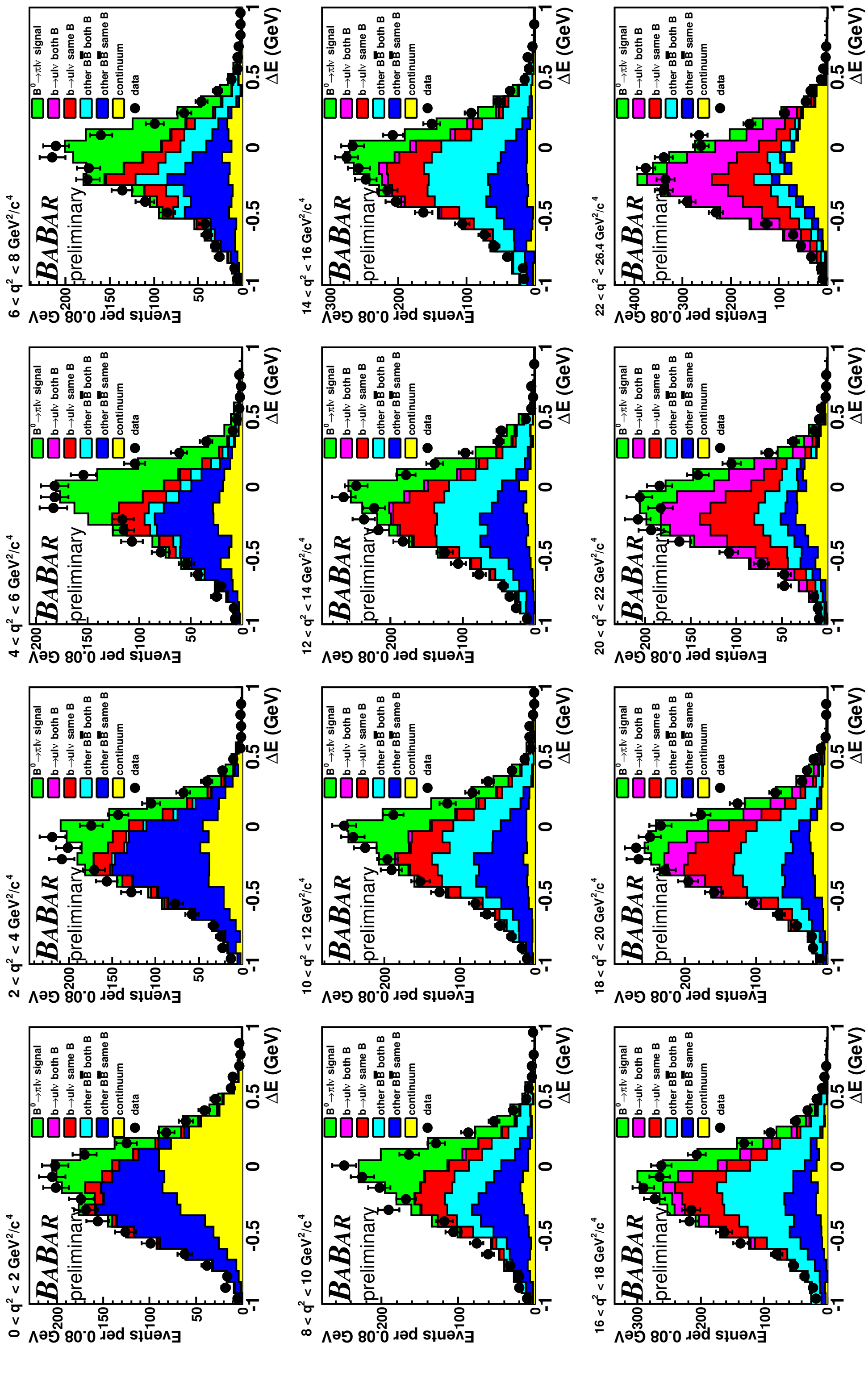

Figure 3.71 – ΔE yield fit projections with $m_{\mathrm{ES}} > 5.2675\ \mathrm{GeV}/c^2$ obtained in 12 $\tilde{q}^2$ bins from the fit to the real data for $B^0 \to \pi^- \ell^+ \nu$ decays. The fit was done using the full ΔE-m_{ES} fit region.

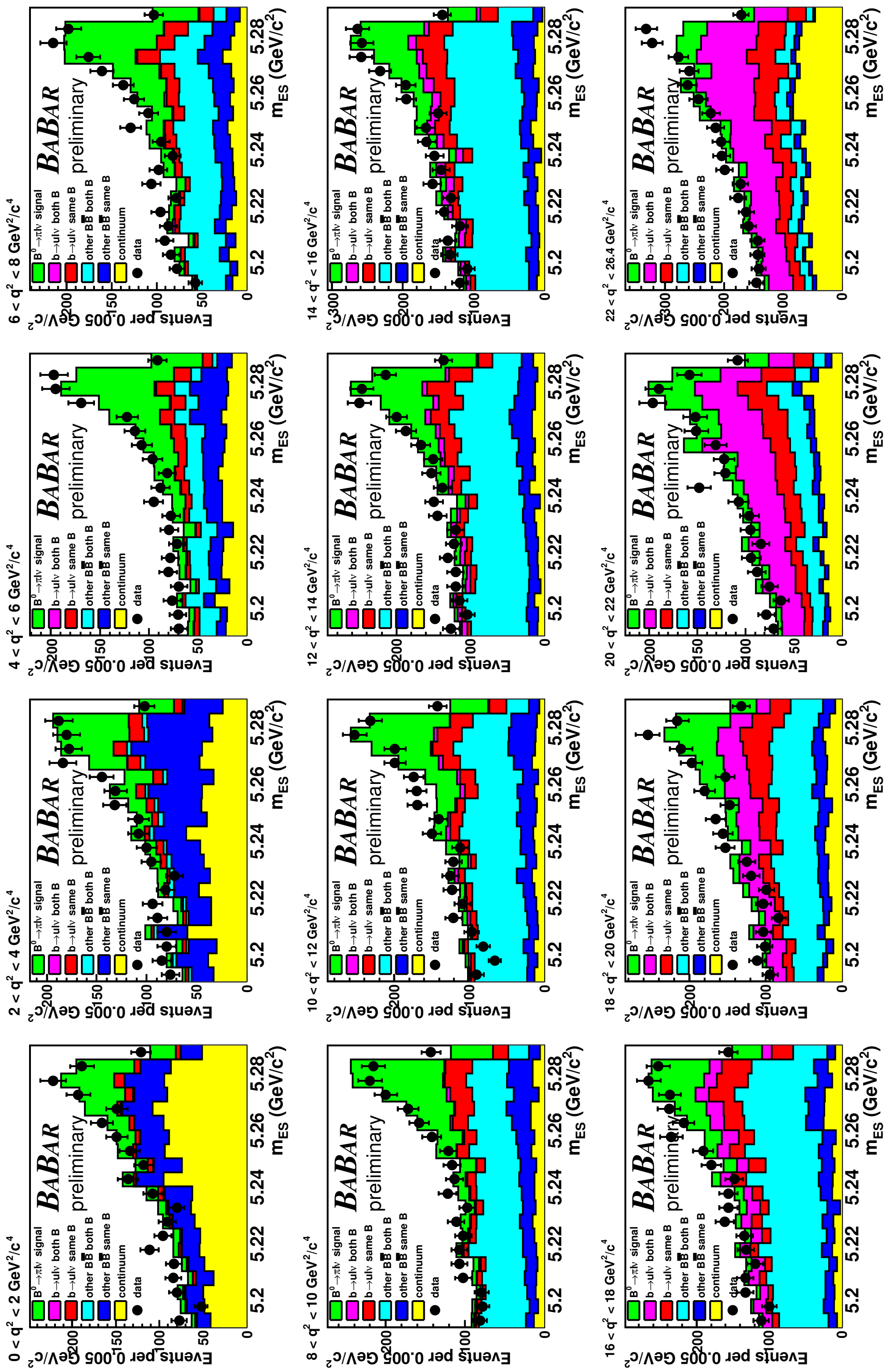

Figure 3.72 – $m_{\rm ES}$ yield fit projections with $-0.16 < \Delta E < 0.2$ GeV obtained in 12 $\tilde{q}^2$ bins from the fit to the real data for $B^0 \to \pi^- \ell^+ \nu$ decays. The fit was done using the full ΔE-$m_{\rm ES}$ fit region.

Tableau 3.52 – Scaling factors and raw yields given by the fit results obtained with real data for $B^+ \to \eta^{'} \ell^+ \nu$ ($\gamma\gamma$ channel) decays.

Event Types	Scaling Factors	Yields
signal bin1	1.116 $\pm$ 0.366	141.0 $\pm$ 46.3
$b \to u\ell\nu$ bin1	1.000 (fixed)	203.6 (fixed)
other $B\bar{B}$ bin1	0.902 $\pm$ 0.028	2660.3 $\pm$ 81.7
continuum bin1	1.000 (fixed)	517.3 (fixed)

Tableau 3.53 – Scaling factors and raw yields given by the fit results obtained with real data for $B^+ \to \eta \ell^+ \nu$ ($\gamma\gamma$ channel) decays.

Event Types	Scaling Factors	Yields
signal bin1	1.705 $\pm$ 0.237	279.9 $\pm$ 38.9
signal bin2	1.041 $\pm$ 0.179	216.8 $\pm$ 37.3
signal bin3	0.541 $\pm$ 0.183	146.7 $\pm$ 49.7
$b \to u\ell\nu$ bin1	1.000 (fixed)	1627.7 (fixed)
other $B\bar{B}$ bin1	0.998 $\pm$ 0.018	10485.1 $\pm$ 189.9
continuum bin1	0.710 $\pm$ 0.040	2735.7 $\pm$ 156.9

In each fit, we adjust the scaling factor of the signal and, where possible, that of each of the backgrounds. Depending on the channel under investigation, this is done in one or more $\tilde{q}^2$ bin. The scaling factors are given in Tables 3.52, 3.53, 3.54, 3.55 and 3.56 for $B^+ \to \eta^{'} \ell^+ \nu$ ($\gamma\gamma$ channel), $B^+ \to \eta \ell^+ \nu$ ($\gamma\gamma$ channel), $B^+ \to \eta \ell^+ \nu$ (3π channel), $B^+ \to \eta \ell^+ \nu$ ($\gamma\gamma$ and 3π channels combined) and $B^0 \to \pi^- \ell^+ \nu$ decays, respectively.

A fitted scaling factor value of 1.0 means that the fitted value of the yield is equal to the MC prediction, a value < 1.0 means that the fitted value is lower than the MC prediction. We observe that the fitted $b \to u\ell\nu$ backgrounds are lower (higher) than their MC

Tableau 3.54 – Scaling factors and raw yields given by the fit results obtained with real data for $B^+ \to \eta \ell^+ \nu$ (3π channel) decays.

Event Types	Scaling Factors	Yields
signal bin1	1.173 $\pm$ 0.300	244.8 $\pm$ 62.7
$b \to u\ell\nu$ bin1	1.000 (fixed)	573.0 (fixed)
other $B\bar{B}$ bin1	0.950 $\pm$ 0.018	6658.3 $\pm$ 125.2
continuum bin1	1.000 (fixed)	986.7 (fixed)

Tableau 3.55 – Scaling factors and raw yields given by the fit results obtained with real data for $B^+ \to \eta\ell^+\nu$ ($\gamma\gamma$ and 3π channels combined) decays.

Event Types	Scaling Factors	Yields
signal bin1	1.475 $\pm$ 0.208	303.9 $\pm$ 42.8
signal bin2	1.186 $\pm$ 0.168	331.5 $\pm$ 47.0
signal bin3	0.688 $\pm$ 0.183	252.5 $\pm$ 67.3
$b \to u\ell\nu$ bin1	1.000 (fixed)	2200.7 (fixed)
other $B\bar{B}$ bin1	0.995 $\pm$ 0.014	17428.8 $\pm$ 246.7
continuum bin1	0.707 $\pm$ 0.040	3435.1 $\pm$ 194.9

Tableau 3.56 – Scaling factors and raw yields given by the fit results obtained with real data for $B^0 \to \pi^-\ell^+\nu$ decays.

Event Types	Scaling Factors	Yields
signal bin1	0.924 $\pm$ 0.119	894.7 $\pm$ 114.8
signal bin2	0.899 $\pm$ 0.072	987.8 $\pm$ 79.5
signal bin3	1.022 $\pm$ 0.062	1177.1 $\pm$ 70.8
signal bin4	1.066 $\pm$ 0.068	1181.3 $\pm$ 75.3
signal bin5	1.127 $\pm$ 0.076	1178.6 $\pm$ 79.5
signal bin6	1.135 $\pm$ 0.080	1122.1 $\pm$ 79.0
signal bin7	1.064 $\pm$ 0.088	996.1 $\pm$ 82.1
signal bin8	1.015 $\pm$ 0.100	884.5 $\pm$ 87.0
signal bin9	1.048 $\pm$ 0.108	904.3 $\pm$ 93.6
signal bin10	1.040 $\pm$ 0.109	847.5 $\pm$ 89.0
signal bin11	0.989 $\pm$ 0.139	729.9 $\pm$ 102.4
signal bin12	0.582 $\pm$ 0.122	873.9 $\pm$ 183.1
$b \to u\ell\nu$ same B bin1	0.672 $\pm$ 0.060	7551.9 $\pm$ 672.8
$b \to u\ell\nu$ same B bin2	0.733 $\pm$ 0.066	6674.8 $\pm$ 603.7
other $B\bar{B}$ same B bin1	0.889 $\pm$ 0.030	12675.3 $\pm$ 432.6
other $B\bar{B}$ same B bin2	0.918 $\pm$ 0.043	14045.2 $\pm$ 661.4
$b \to u\ell\nu$ both B bin1	1.327 $\pm$ 0.111	7408.5 $\pm$ 618.7
$b \to u\ell\nu$ both B bin2	0.888 $\pm$ 0.051	6157.4 $\pm$ 352.7
other $B\bar{B}$ both B bin1	0.931 $\pm$ 0.017	21824.4 $\pm$ 406.7
other $B\bar{B}$ both B bin2	1.080 $\pm$ 0.018	31640.2 $\pm$ 519.0
continuum bin1	0.905 $\pm$ 0.032	21989.2 $\pm$ 777.5
continuum bin2	1.040 $\pm$ 0.043	5800.7 $\pm$ 239.4

predictions for same (both) B processes in $B^0 \to \pi^- \ell^+ \nu$ decays. The other $B\bar{B}$ fit parameters indicate that the fitted yields are close to the MC predictions for all decay modes. In $B^0 \to \pi^- \ell^+ \nu$ decays, the fitted signal yields are lower than their MC predictions at low q^2, while they are comparable or higher at mid and high q^2 values, except for the highest q^2 bin. These results are compatible with our Data/MC comparison cross-check done in the sideband region (Sect. 3.9.1.2).

The full correlation matrix (elements in %) of the fitted scaling factors for the $B^+ \to \eta^{'} \ell^+ \nu$ ($\gamma\gamma$ channel) decay is :

```
signal bin1:        100 -56
otherBB_bkg bin1:       100
```

The full correlation matrix (elements in %) of the fitted scaling factors for the $B^+ \to \eta \ell^+ \nu$ ($\gamma\gamma$ channel) decay is :

```
signal bin1:        100  23 -50  12   0
otherBB_bkg bin1:       100 -56  -2 -39
continuum bin1:             100 -20   6
signal bin2:                    100   7
signal bin3:                        100
```

The full correlation matrix (elements in %) of the fitted scaling factors for the $B^+ \to \eta \ell^+ \nu$ ($\pi^+\pi^-\pi^0$ channel) decay is :

```
signal bin1:        100 -52
otherBB_bkg bin1:       100
```

The full correlation matrix (elements in $\%$) of the fitted scaling factors for the $B^+ \to \eta \ell^+ \nu$ ($\gamma\gamma$ and 3π channels combined) decay is :

```
signal bin1:        100  23 -48  11   0
otherBB_bkg bin1:        100 -58  -5 -41
continuum bin1:              100 -17   7
signal bin2:                     100   8
signal bin3:                         100
```

The full correlation matrix (elements in $\%$) of the fitted scaling factors for the $B^0 \to \pi^- \ell^+ \nu$ decay is :

```
signal bin1: 100 -13  18  39  22 -65  18  14   5   0   3   8   2   6  10   6   3  -3   4   2   0   0
ulnu_bkg bin1:   100 -15 -44  -9 -18  -9 -28 -30 -31 -27 -51 -33 -34  -8 -38  -3  32  -4  -9  -9  -2
ulnu_bothB_bkg bin1: 100  27 -15 -27   5   8   6   4   1  21  -1   2 -41 -14  -4 -69 -44  15  41  13
otherBB_bkg bin1:        100   4 -73  -3  12   8   4  16  37  17  16   3  18   5 -17   5   6   5   2
otherBB_bothB_bkg bin1:      100 -25  12   0 -15 -23 -11 -47 -15   5  50   9   0  21  11  -3 -11  -3
continuum bin1:                  100 -17 -16  -3   5  -4 -14  -3  -6 -10  -7  -4   7  -5  -2   0   0
signal bin2:                         100  10   6   4   2   2   2   4   5   4   1  -1   2   1   0   0
signal bin3:                             100  12  12   9  19  11  10   1  11   2  -9   2   3   3   1
signal bin4:                                 100  17  12  27  15  11  -5  12   2 -12   1   4   5   1
signal bin5:                                     100  13  31  17  11  -8  12   2 -12   1   4   5   2
signal bin6:                                         100  10  18  10   7  12   1  -5   3   2   1   0
otherBB_bkg bin2:                                        100  17  18 -48  19   7 -34   1   9  14   5
signal bin7:                                                 100  12   6  15   2  -5   5   2   0   0
signal bin8:                                                     100 -12  22   2  -1   1   0   1   0
otherBB_bothB_bkg bin2:                                              100  -2   0  21  28   0 -18  -6
signal bin9:                                                             100   3   8  11  -1  -5  -1
signal bin10:                                                                100 -25  24   6  13   4
ulnu_bkg bin2:                                                                   100   3 -23 -51 -16
signal bin11:                                                                        100   1  -4  -1
signal bin12:                                                                            100 -46 -19
ulnu_bothB_bkg bin2:                                                                         100  -8
continuum bin2:                                                                                  100
```

3.8.4.2 Partial $\Delta\mathcal{B}(q^2)$ and total $\mathcal{B}(B^+ \to \eta^{(\prime)}\ell^+\nu)$ and $\mathcal{B}(B^0 \to \pi^-\ell^+\nu)$ from the real data

The partial and total BFs and their various uncertainties are given in Tables 3.57, 3.58, 3.59, 3.60 and 3.61 for $B^+ \to \eta^{'}\ell^+\nu$ ($\gamma\gamma$ channel), $B^+ \to \eta\ell^+\nu$ ($\gamma\gamma$ channel), $B^+ \to \eta\ell^+\nu$ (3π channel), $B^+ \to \eta\ell^+\nu$ ($\gamma\gamma$ and 3π channels combined) and $B^0 \to \pi^-\ell^+\nu$ decays, respectively. To take into account the correlations among the measurements in the various $\tilde{q}^2$ bins, we need the correlation and covariance matrices presented in Tables 3.62, 3.63, 3.64 and 3.65 for the $B^+ \to \eta\ell^+\nu$ ($\gamma\gamma$ channel) decays, in Tables 3.66, 3.67, 3.68 and 3.69 for the $B^+ \to \eta\ell^+\nu$ ($\gamma\gamma$ and 3π channels combined) decays and in Tables 3.70, 3.71, 3.72, and 3.73 for the $B^0 \to \pi^-\ell^+\nu$ decays. Our value of the total BF for $B^+ \to \eta^{'}\ell^+\nu$, $(2.43 \pm 0.80_{stat} \pm 0.34_{syst}) \times 10^{-5}$ with a significance of 2.67σ, is an order of magnitude smaller than the most recent CLEO result [24] : $(2.66 \pm 0.80_{stat} \pm 0.56_{syst}) \times 10^{-4}$. Our value of the total BF for $B^+ \to \eta\ell^+\nu$ from the combined fit, $(3.61 \pm 0.45_{stat} \pm 0.44_{syst}) \times 10^{-5}$, is the most precise measurement to date and is compatible with a previous BABAR result [24] : $(0.37 \pm 0.06_{stat} \pm 0.07_{syst}) \times 10^{-4}$. It is in excellent agreement with the weighted average, $(3.59 \pm 0.42_{stat} \pm 0.40_{syst}) \times 10^{-5}$, of the total BFs $(3.39 \pm 0.46_{stat} \pm 0.47_{syst}) \times 10^{-5}$ and $(4.31 \pm 1.10_{stat} \pm 0.55_{syst}) \times 10^{-5}$ obtained for the $\gamma\gamma$ and 3π channels, separately. The $\mathcal{B}(B^+ \to \eta^{'}\ell^+\nu)/\mathcal{B}(B^+ \to \eta\ell^+\nu)$ ratio value of 0.67 ± 0.27 allows an important gluonic singlet contribution to the η' form factor [28]. Our value of the total BF for $B^0 \to \pi^-\ell^+\nu$, $(1.424 \pm 0.050_{stat} \pm 0.079_{syst}) \times 10^{-4}$ rounded off to $(1.42 \pm 0.05_{stat} \pm 0.08_{syst}) \times 10^{-4}$, is in very good agreement with the previous BABAR result [24], $1.46 \pm 0.07 \pm 0.11$ and has comparable precision to the present world average [24] : $(1.36 \pm 0.05_{stat} \pm 0.05_{syst}) \times 10^{-4}$. There is a significant decrease in the statistical uncertainty compared to the previous BABAR analysis because of higher statistics. The systematic uncertainty is also reduced in spite of the fact that additional systematic uncertainties arising from the form factors in $\omega, \pi^0, \eta, \eta'\ell\nu$ decays and the bremsstrahlung process are now taken into account. This reduction is due to many improvements. In particular, the systematic uncertainties arising from the branching fractions and form factors of the backgrounds have now been significantly reduced.

Tableau 3.57 – Total $\mathcal{B}(B^+ \to \eta^{'} \ell^+ \nu)$ ($\gamma\gamma$ channel) ($\times 10^7$) and its statistical (fit error) and systematic (all the others) uncertainties from all sources, obtained from the real data. The errors are given as % (relative errors).

$\tilde{q}^2$ bins (GeV^2/c^4)	Total
$BF \times 10^7$	242.5
tracking efficiency	5.2
photon efficiency	5.6
K_L^0 efficiency	2.5
K_L^0 production rate	2.7
K_L^0 energy	1.1
ℓ identification	2.0
π identification	0.6
bremsstrahlung	0.5
continuum yield	4.9
$\tilde{q}^2$ continuum shape	5.2
$\mathcal{B}(B^0 \to \pi^- \ell^+ \nu)$	0.0
$\mathcal{B}(B^+ \to \pi^0 \ell^+ \nu)$	0.2
$\mathcal{B}(B^+ \to \eta \ell^+ \nu)$	0.4
$\mathcal{B}(B^0 \to \rho^- \ell^+ \nu)$	0.3
$\mathcal{B}(B^+ \to \rho^0 \ell^+ \nu)$	0.0
$\mathcal{B}(B^+ \to \omega \ell^+ \nu)$	0.8
non resonant $b \to u \ell \nu$ BF	2.3
η BF	3.1
SF parameters	4.3
$B \to \rho \ell \nu$ FF	0.1
$B^+ \to \eta^{'} \ell^+ \nu$ FF	1.1
other scalar FF	2.9
$B \to \omega \ell \nu$ FF	1.2
$\mathcal{B}(B \to D \ell \nu)$	1.6
$\mathcal{B}(B \to D^* \ell \nu)$	0.3
$\mathcal{B}(B \to D^{**} \ell \nu)$	2.0
non resonant $b \to c \ell \nu$ BF	0.1
$B \to D \ell \nu$ FF	0.1
$B \to D^* \ell \nu$ FF	0.6
$\mathcal{B}(\Upsilon(4S) \to B^0 B^0)$	1.1
secondary lepton	4.2
B counting	1.1
signal MC stat error	1.2
Total systematic error	14.3
Fit error	32.8
Total error	35.8

Tableau 3.58 – Partial $\Delta\mathcal{B}(q^2)$ and total $\mathcal{B}(B^+ \to \eta\ell^+\nu)$ ($\gamma\gamma$ channel) ($\times 10^7$) and their statistical (fit error) and systematic (all the others) uncertainties from all sources, obtained from the real data. The errors are given as % (relative errors).

$\tilde{q}^2$ bins (GeV^2/c^4)	0-4	4-8	8-16	Total
unfolded yield	299.1	210.9	133.3	643.4
$\Delta\mathcal{B}(q^2)$ $\times 10^7$	155.3	86.3	97.7	339.3
tracking efficiency	3.2	2.4	14.6	2.6
photon efficiency	10.1	4.3	27.4	7.0
K_L^0 efficiency	8.6	2.9	27.2	3.2
K_L^0 production rate	4.7	1.5	16.2	2.5
K_L^0 energy	0.6	0.5	2.5	0.9
ℓ identification	0.1	2.7	3.9	1.8
bremsstrahlung	1.6	2.7	22.2	8.0
$\tilde{q}^2$ continuum shape	2.6	1.5	4.5	0.5
$\mathcal{B}(B^0 \to \pi^-\ell^+\nu)$	0.0	0.0	0.1	0.0
$\mathcal{B}(B^+ \to \pi^0\ell^+\nu)$	0.4	0.9	5.2	1.9
$\mathcal{B}(B^+ \to \eta'\ell^+\nu)$	0.0	0.1	0.8	0.2
$\mathcal{B}(B^0 \to \rho^-\ell^+\nu)$	0.1	1.1	6.9	2.3
$\mathcal{B}(B^+ \to \rho^0\ell^+\nu)$	0.1	0.1	0.5	0.1
$\mathcal{B}(B^+ \to \omega\ell^+\nu)$	0.1	0.2	2.6	0.8
non resonant $b \to u\ell\nu$ BF	0.4	0.9	9.5	3.1
η BF	0.5	0.7	0.7	0.6
SF parameters	1.4	2.7	16.8	6.1
$B \to \rho\ell\nu$ FF	0.1	2.3	1.7	0.9
$B^+ \to \eta\ell^+\nu$ FF	0.1	0.1	1.4	0.4
other scalar FF	7.7	1.4	0.1	3.2
$B \to \omega\ell\nu$ FF	0.1	0.5	2.8	0.7
$\mathcal{B}(B \to D\ell\nu)$	0.3	0.7	0.6	0.3
$\mathcal{B}(B \to D^*\ell\nu)$	0.1	0.8	1.2	0.4
$\mathcal{B}(B \to D^{**}\ell\nu)$	0.6	0.9	2.5	0.7
non resonant $b \to c\ell\nu$ BF	0.2	0.1	0.8	0.2
$B \to D\ell\nu$ FF	0.1	0.1	0.5	0.2
$B \to D^*\ell\nu$ FF	0.5	0.9	1.3	0.4
$\mathcal{B}(\Upsilon(4S) \to B^0 B^0)$	1.4	1.1	0.9	1.2
secondary lepton	1.3	0.7	9.1	2.1
B counting	1.1	1.1	1.1	1.1
signal MC stat error	1.4	1.6	1.2	0.7
Total systematic error	17.0	8.7	55.4	14.1
Fit error	14.6	21.0	39.3	13.7
Total error	22.4	22.7	67.9	19.6

Tableau 3.59 – Total $\mathcal{B}(B^+ \to \eta\ell^+\nu)$ (3π channel) ($\times 10^7$) and its statistical (fit error) and systematic (all the others) uncertainties from all sources, obtained from the real data. The errors are given as % (relative errors).

$\tilde{q}^2$ bins (GeV^2/c^4)	Total
$BF \times 10^7$	431.5
tracking efficiency	4.1
photon efficiency	3.1
K_L^0 efficiency	0.7
K_L^0 production rate	1.4
K_L^0 energy	1.4
ℓ identification	1.8
π identification	0.5
bremsstrahlung	0.2
continuum yield	1.1
$\tilde{q}^2$ continuum shape	2.6
$\mathcal{B}(B^0 \to \pi^-\ell^+\nu)$	0.1
$\mathcal{B}(B^+ \to \pi^0\ell^+\nu)$	0.0
$\mathcal{B}(B^+ \to \eta^{'}\ell^+\nu)$	0.4
$\mathcal{B}(B^0 \to \rho^-\ell^+\nu)$	0.5
$\mathcal{B}(B^+ \to \rho^0\ell^+\nu)$	0.3
$\mathcal{B}(B^+ \to \omega\ell^+\nu)$	1.1
non resonant $b \to u\ell\nu$ BF	3.5
η BF	1.2
SF parameters	6.3
$B \to \rho\ell\nu$ FF	0.7
$B^+ \to \eta\ell^+\nu$ FF	1.0
other scalar FF	4.2
$B \to \omega\ell\nu$ FF	2.1
$\mathcal{B}(B \to D\ell\nu)$	0.7
$\mathcal{B}(B \to D^*\ell\nu)$	0.4
$\mathcal{B}(B \to D^{**}\ell\nu)$	1.2
non resonant $b \to c\ell\nu$ BF	0.1
$B \to D\ell\nu$ FF	0.3
$B \to D^*\ell\nu$ FF	0.9
$\mathcal{B}(\Upsilon(4S) \to B^0B^0)$	1.2
secondary lepton	5.0
B counting	1.1
signal MC stat error	1.1
Total systematic error	12.4
Fit error	25.6
Total error	28.4

Tableau 3.60 – Partial $\mathcal{B}(B^+ \to \eta\ell^+\nu)$ ($\gamma\gamma$ and 3π channels combined) ($\times 10^7$) and their statistical (fit error) and systematic (all the others) uncertainties from all sources, obtained from the real data. The errors are given as % (relative errors).

$\tilde{q}^2$ bins (GeV^2/c^4)	0-4	4-8	8-16	Total
unfolded yield	319.3	334.8	233.9	887.9
$\Delta\mathcal{B}(q^2)$ $\times 10^7$	131.8	102.6	126.2	360.6
Tracking efficiency	2.1	2.0	11.1	2.8
Photon efficiency	8.0	3.8	9.0	5.7
K_L^0 efficiency	1.0	0.5	2.2	0.6
K_L^0 production spectrum	0.8	0.5	2.3	1.0
K_L^0 energy	0.6	0.4	2.3	1.0
ℓ identification	0.2	1.9	3.4	1.8
π identification	0.1	0.2	0.5	0.3
Bremsstrahlung	0.3	0.7	12.3	4.2
Continuum yield	-	-	-	-
$\tilde{q}^2$ continuum shape	2.4	0.7	2.8	0.3
$\mathcal{B}(B^0 \to \pi^-\ell^+\nu)$	0.0	0.0	0.1	0.0
$\mathcal{B}(B^+ \to \pi^0\ell^+\nu)$	0.3	0.6	2.9	1.3
$\mathcal{B}(B^+ \to \eta^{(\prime)}\ell^+\nu)$	0.1	0.1	1.0	0.4
$\mathcal{B}(B^0 \to \rho^-\ell^+\nu)$	0.1	0.6	4.2	1.7
$\mathcal{B}(B^+ \to \rho^0\ell^+\nu)$	0.0	0.1	0.8	0.2
$\mathcal{B}(B^+ \to \omega\ell^+\nu)$	0.1	0.1	2.6	0.9
Non resonant $b \to u\ell\nu$ BF	0.5	0.6	8.6	3.4
η BF	0.5	0.6	0.7	0.5
SF parameters	1.5	2.5	14.3	6.2
$B \to \rho\ell\nu$ FF	0.1	1.5	0.9	0.5
$B^+ \to \eta^{(\prime)}\ell^+\nu$ FF	0.1	0.1	1.5	0.6
Other scalar FF	0.7	0.1	0.0	0.2
$B \to \omega\ell\nu$ FF	0.1	0.4	3.9	1.3
$\mathcal{B}(B \to D\ell\nu)$	0.3	0.7	0.7	0.4
$\mathcal{B}(B \to D^*\ell\nu)$	0.1	0.7	1.0	0.4
$\mathcal{B}(B \to D^{**}\ell\nu)$	0.6	0.7	2.6	0.9
Non resonant $b \to c\ell\nu$ BF	0.3	0.1	0.4	0.2
$B \to D\ell\nu$ FF	0.1	0.1	0.7	0.3
$B \to D^*\ell\nu$ FF	0.5	1.2	1.2	0.4
$\mathcal{B}(\Upsilon(4S) \to B^0B^0)$	1.4	1.2	1.0	1.2
Secondary lepton	1.2	1.6	9.3	3.0
B counting	1.1	1.1	1.1	1.1
Signal MC stat error	1.3	1.3	1.0	0.5
Total systematic error	9.3	6.6	28.7	11.6
Fit error	15.2	16.6	30.3	12.5
Total error	17.8	17.8	41.8	17.0

Tableau 3.61 – Partial $\Delta\mathcal{B}(q^2)$ and total $\mathcal{B}(B^0 \to \pi^-\ell^+\nu)$ $(\times 10^7)$ and their statistical (fit error) and systematic (all the others) uncertainties from all sources, obtained from the real data. The errors are given as % (relative errors). The $\Delta\mathcal{B}(q^2)$ values labelled "Without FSR" are modified to remove Final State Radiation effects.

q^2 bins (GeV^2/c^4)	0-2	2-4	4-6	6-8	8-10	10-12	12-14	14-16	16-18	18-20	20-22	22-26.4	q^2<12	q^2<16	q^2>16	Total
Unfolded yield	919.9	960.7	1189.6	1184.5	1182.9	1141.5	1027.3	929.2	979.5	979.9	905.8	376.7	6579.1	8535.7	3241.9	11777.6
$\Delta\mathcal{B}(q^2)$	122.7	117.6	143.6	145.0	153.4	150.2	134.1	121.7	116.0	103.7	86.8	28.7	832.5	1088.3	335.3	1423.5
$\Delta\mathcal{B}(q^2)$ (Without FSR)	128.0	119.2	144.6	143.7	152.5	149.0	133.3	120.1	115.3	102.3	86.1	28.5	837.0	1090.5	332.3	1422.8
Tracking efficiency	3.1	1.9	3.1	2.3	2.3	3.9	2.6	4.1	3.5	1.3	4.1	9.4	2.3	2.5	2.9	2.6
Photon efficiency	5.8	3.3	2.6	1.3	2.2	2.5	3.1	3.0	5.0	1.4	5.2	24.4	1.9	2.2	4.7	2.7
K_L^0 efficiency	0.8	0.3	0.6	0.3	0.5	0.4	0.5	0.8	0.6	0.5	1.7	6.9	0.3	0.3	1.0	0.4
K_L^0 production spectrum	0.9	0.6	1.0	0.6	1.1	1.0	0.6	2.8	1.7	1.0	2.0	8.3	0.7	0.9	1.9	1.1
K_L^0 energy	1.0	0.6	0.3	0.2	0.2	0.3	0.2	0.4	0.6	0.7	0.8	7.1	0.2	0.3	0.8	0.3
ℓ identification	3.8	1.0	1.2	1.3	0.6	0.6	1.6	1.0	0.9	1.6	0.7	4.9	0.3	0.5	1.1	0.6
π identification	0.5	0.2	0.2	0.2	0.2	0.2	0.2	0.3	0.3	0.3	0.3	5.6	0.2	0.2	0.7	0.3
Bremsstrahlung	0.5	0.3	0.1	0.2	0.2	0.2	0.2	0.3	0.3	0.3	0.3	5.3	0.2	0.2	0.7	0.3
$\tilde{q}^2$ continuum shape	7.6	1.6	0.9	0.3	0.7	0.3	1.1	0.3	0.7	1.2	1.2	5.5	0.9	0.8	1.0	0.7
m_{ES} continuum shape	8.8	0.6	1.1	0.6	0.1	0.5	0.7	0.5	1.1	0.8	1.6	28.3	1.8	1.5	3.4	2.0
ΔE continuum shape	3.4	2.7	0.4	0.5	0.5	0.1	0.2	0.3	0.3	1.4	2.1	9.0	1.2	0.9	1.8	1.1
$\mathcal{B}(B^+ \to \pi^0\ell^+\nu)$	0.5	0.1	0.1	0.1	0.1	0.1	0.2	0.3	0.3	0.3	0.4	7.2	0.2	0.2	0.8	0.3
$\mathcal{B}(B^0 \to \rho^-\ell^+\nu)$	0.5	0.3	0.1	0.1	0.2	0.1	0.2	0.3	0.3	0.4	0.5	10.2	0.2	0.2	0.9	0.3
$\mathcal{B}(B^+ \to \rho^0\ell^+\nu)$	0.6	0.2	0.1	0.1	0.2	0.2	0.2	0.3	0.4	0.3	0.3	7.4	0.2	0.2	0.9	0.3
$\mathcal{B}(B^+ \to \omega\ell^+\nu)$	0.5	0.1	0.1	0.1	0.1	0.1	0.2	0.3	0.3	0.4	0.3	8.3	0.2	0.2	1.0	0.3
$\mathcal{B}(B^+ \to \eta\ell^+\nu)$	0.5	0.1	0.1	0.1	0.1	0.1	0.2	0.3	0.3	0.3	0.2	5.6	0.2	0.2	0.7	0.3
$\mathcal{B}(B^+ \to \eta^{'}\ell^+\nu)$	0.5	0.1	0.1	0.1	0.1	0.1	0.2	0.3	0.3	0.3	0.3	5.4	0.2	0.2	0.7	0.3
Non resonant $b \to u\ell\nu$ BF	0.6	0.3	0.1	0.1	0.2	0.2	0.2	0.4	0.5	0.3	0.6	7.9	0.2	0.2	0.7	0.3
SF parameters	0.9	0.5	0.9	0.4	0.3	0.5	0.6	0.3	0.5	2.3	4.1	23.5	0.6	0.4	2.3	0.8
$B \to \rho\ell\nu$ FF	2.3	1.4	2.0	1.4	1.9	1.6	0.8	0.7	2.4	3.0	1.1	16.7	1.8	1.5	1.8	1.5
$B^0 \to \pi^-\ell^+\nu$ FF	0.5	0.1	0.1	0.1	0.1	0.1	0.2	0.3	0.3	0.3	0.3	7.5	0.2	0.2	0.9	0.3
Other scalar FF	1.0	0.3	0.5	0.5	0.4	0.3	0.3	0.7	1.7	2.1	2.1	8.7	0.4	0.3	0.6	0.3
$B \to \omega\ell\nu$ FF	0.5	0.1	0.1	0.1	0.1	0.1	0.2	0.3	0.5	0.6	0.6	18.2	0.2	0.2	1.8	0.5
$\mathcal{B}(B \to D\ell\nu)$	0.5	0.6	0.2	0.1	0.3	0.2	0.5	0.3	0.4	0.4	0.4	5.7	0.2	0.3	0.7	0.4
$\mathcal{B}(B \to D^*\ell\nu)$	0.6	0.3	0.2	0.3	0.4	0.3	0.3	0.5	0.4	0.3	0.5	5.7	0.3	0.3	0.7	0.4
$\mathcal{B}(B \to D^{**}\ell\nu)$	0.7	0.3	0.3	0.5	0.5	0.3	0.8	0.6	1.1	0.7	0.7	5.9	0.3	0.3	0.9	0.4
Non resonant $b \to c\ell\nu$ BF	0.6	0.2	0.2	0.1	0.2	0.2	0.2	0.5	0.3	0.3	0.3	5.6	0.2	0.2	0.7	0.3
$B \to D\ell\nu$ FF	0.5	0.2	0.3	0.1	0.2	0.1	0.2	0.4	0.4	0.3	0.4	5.7	0.2	0.2	0.7	0.3
$B \to D^*\ell\nu$ FF	0.6	0.2	0.2	0.4	0.2	1.0	0.6	2.0	0.4	0.7	1.2	7.0	0.2	0.3	1.0	0.5
$\Upsilon(4S) \to B^0B^0$ BF	1.4	1.7	1.2	1.3	1.3	1.3	1.5	1.2	1.4	1.4	1.0	5.9	1.3	1.4	1.2	1.3
Secondary lepton	4.1	3.1	2.1	1.2	1.7	0.5	1.2	0.5	0.5	0.9	3.7	5.9	1.0	0.9	1.2	0.9
Final state radiation	0.3	1.3	0.8	2.2	0.3	1.4	1.2	1.3	1.4	1.6	0.8	3.4	1.0	1.1	1.5	1.2
B counting	1.1	1.1	1.1	1.1	1.1	1.1	1.1	1.1	1.1	1.1	1.1	1.1	1.1	1.1	1.1	1.1
Fit bias	0.1	0.3	0.4	0.1	0.1	0.4	0.4	0.7	0.1	1.0	2.0	30.8	0.2	0.0	1.8	0.4
Signal MC stat error	1.3	1.5	1.3	1.6	1.4	1.5	1.4	1.4	1.3	1.5	1.2	2.5	0.6	0.4	0.6	0.3
Total systematic error	15.5	6.9	6.0	5.0	5.0	5.9	5.7	7.1	7.9	6.6	10.4	68.8	5.0	4.9	9.2	5.7
Fit error	14.7	11.9	9.0	9.3	9.4	9.4	10.8	12.5	12.8	12.8	17.6	56.7	3.9	3.7	7.6	3.5
Total error	21.4	13.8	10.8	10.6	10.7	11.1	12.2	14.3	15.0	14.4	20.5	89.2	6.3	6.2	12.0	6.7

Tableau 3.62 – Correlation matrix of the partial $\Delta\mathcal{B}(q^2)$ statistical uncertainties for $B^+ \to \eta\ell^+\nu$ ($\gamma\gamma$ channel) obtained from the real data.

q^2 bins (GeV^2/c^4)	0-4	4-8	8-16
0-4	1.00	-0.08	0.00
4-8	-0.08	1.00	-0.08
8-16	0.00	-0.08	1.00

Tableau 3.63 – Correlation matrix of the partial $\Delta\mathcal{B}(q^2)$ systematic uncertainties for $B^+ \to \eta\ell^+\nu$ ($\gamma\gamma$ channel) obtained from the real data.

q^2 bins (GeV^2/c^4)	0-4	4-8	8-16
0-4	1.00	-0.01	0.40
4-8	-0.01	1.00	0.05
8-16	0.40	0.05	1.00

Tableau 3.64 – Covariance matrix of the partial $\Delta\mathcal{B}(q^2)$ statistical uncertainties for $B^+ \to \eta\ell^+\nu$ ($\gamma\gamma$ channel) obtained from the real data.

q^2 bins (GeV^2/c^4)	0-4	4-8	8-16
0-4	1034.4	-64.6	1.8
4-8	-64.6	654.4	-108.2
8-16	1.8	-108.2	2948.3

Tableau 3.65 – Covariance matrix of the partial $\Delta\mathcal{B}(q^2)$ systematic uncertainties for $B^+ \to \eta\ell^+\nu$ ($\gamma\gamma$ channel) obtained from the real data.

q^2 bins (GeV^2/c^4)	0-4	4-8	8-16
0-4	119.5	-0.6	182.1
4-8	-0.6	46.2	12.9
8-16	182.1	12.9	1695.1

Tableau 3.66 – Correlation matrix of the partial $\Delta\mathcal{B}(q^2)$ statistical uncertainties for $B^+ \to \eta\ell^+\nu$ ($\gamma\gamma$ and 3π channels combined) obtained from the real data.

q^2 bins (GeV^2/c^4)	0-4	4-8	8-16
0-4	1.00	-0.08	0.00
4-8	-0.08	1.00	-0.06
8-16	0.00	-0.06	1.00

Tableau 3.67 – Correlation matrix of the partial $\Delta\mathcal{B}(q^2)$ systematic uncertainties for $B^+ \to \eta\ell^+\nu$ ($\gamma\gamma$ and 3π channels combined) obtained from the real data.

q^2 bins (GeV^2/c^4)	0-4	4-8	8-16
0-4	1.00	0.36	0.05
4-8	0.36	1.00	0.29
8-16	0.05	0.29	1.00

Tableau 3.68 – Covariance matrix of the partial $\Delta\mathcal{B}(q^2)$ statistical uncertainties for $B^+ \to \eta\ell^+\nu$ ($\gamma\gamma$ and 3π channels combined) obtained from the real data.

q^2 bins (GeV^2/c^4)	0-4	4-8	8-16
0-4	799.4	-57.0	4.8
4-8	-57.0	578.1	-84.3
8-16	4.8	-84.3	2927.5

Tableau 3.69 – Covariance matrix of the partial $\Delta\mathcal{B}(q^2)$ systematic uncertainties for $B^+ \to \eta\ell^+\nu$ ($\gamma\gamma$ and 3π channels combined) obtained from the real data.

q^2 bins (GeV^2/c^4)	0-4	4-8	8-16
0-4	151.3	29.6	22.2
4-8	29.6	45.9	72.3
8-16	22.2	72.3	1311.8

Tableau 3.70 – Correlation matrix of the partial $\Delta\mathcal{B}(q^2)$ statistical uncertainties obtained from the real data for $B^0 \to \pi^- \ell^+ \nu$ decays. The correlations have the same values for the "Without FSR" case as for the one "with FSR", within the quoted precision.

q^2 bins (GeV^2/c^4)	0-2	2-4	4-6	6-8	8-10	10-12	12-14	14-16	16-18	18-20	20-22	22-26.4
0-2	1.00	-0.16	0.17	0.02	-0.02	0.03	0.01	0.04	0.05	0.02	0.04	-0.00
2-4	-0.16	1.00	-0.32	0.11	0.00	-0.00	-0.01	0.01	0.01	-0.00	0.00	-0.00
4-6	0.17	-0.32	1.00	-0.30	0.15	0.02	0.06	0.06	0.07	0.00	0.01	0.01
6-8	0.02	0.11	-0.30	1.00	-0.22	0.13	0.07	0.06	0.07	0.00	0.00	0.02
8-10	-0.02	0.00	0.15	-0.22	1.00	-0.22	0.16	0.05	0.08	0.01	-0.00	0.02
10-12	0.03	-0.00	0.02	0.13	-0.22	1.00	-0.15	0.10	0.07	-0.01	0.02	0.00
12-14	0.01	-0.01	0.06	0.07	0.16	-0.15	1.00	-0.16	0.13	-0.01	0.05	-0.00
14-16	0.04	0.01	0.06	0.06	0.05	0.10	-0.16	1.00	-0.01	0.01	-0.02	-0.02
16-18	0.05	0.01	0.07	0.07	0.08	0.07	0.13	-0.01	1.00	-0.17	0.09	-0.08
18-20	0.02	-0.00	0.00	0.00	0.01	-0.01	-0.01	0.01	-0.17	1.00	0.05	-0.05
20-22	0.04	0.00	0.01	0.00	-0.00	0.02	0.05	-0.02	0.09	0.05	1.00	-0.35
22-26.4	-0.00	-0.00	0.01	0.02	0.02	0.00	-0.00	-0.02	-0.08	-0.05	-0.35	1.00

Tableau 3.71 – Correlation matrix of the partial $\Delta\mathcal{B}(q^2)$ systematic uncertainties obtained from the real data for $B^0 \to \pi^- \ell^+ \nu$ decays. The correlations have the same values for the "Without FSR" case as for the one "with FSR", within the quoted precision.

q^2 bins (GeV^2/c^4)	0-2	2-4	4-6	6-8	8-10	10-12	12-14	14-16	16-18	18-20	20-22	22-26.4
0-2	1.00	-0.19	0.41	0.33	0.49	0.42	0.49	0.35	0.39	0.13	0.46	0.50
2-4	-0.19	1.00	-0.17	0.08	-0.20	-0.07	-0.15	-0.16	-0.31	0.41	-0.24	0.06
4-6	0.41	-0.17	1.00	0.78	0.82	0.76	0.67	0.68	0.53	0.33	0.72	0.45
6-8	0.33	0.08	0.78	1.00	0.71	0.74	0.65	0.63	0.47	0.49	0.55	0.35
8-10	0.49	-0.20	0.82	0.71	1.00	0.74	0.71	0.70	0.49	0.36	0.65	0.35
10-12	0.42	-0.07	0.76	0.74	0.74	1.00	0.74	0.80	0.62	0.36	0.60	0.38
12-14	0.49	-0.15	0.67	0.65	0.71	0.74	1.00	0.69	0.73	0.29	0.55	0.35
14-16	0.35	-0.16	0.68	0.63	0.70	0.80	0.69	1.00	0.71	0.35	0.64	0.36
16-18	0.39	-0.31	0.53	0.47	0.49	0.62	0.73	0.71	1.00	-0.01	0.62	0.26
18-20	0.13	0.41	0.33	0.49	0.36	0.36	0.29	0.35	-0.01	1.00	0.04	0.23
20-22	0.46	-0.24	0.72	0.55	0.65	0.60	0.55	0.64	0.62	0.04	1.00	0.54
22-26.4	0.50	0.06	0.45	0.35	0.35	0.38	0.35	0.36	0.26	0.23	0.54	1.00

Tableau 3.72 – Covariance matrix of the partial $\Delta\mathcal{B}(q^2)$ statistical uncertainties obtained from the real data for $B^0 \to \pi^-\ell^+\nu$ decays. The elements have the same values for the "Without FSR" case as for the one "with FSR", within the quoted precision.

q^2 bins (GeV^2/c^4)	0-2	2-4	4-6	6-8	8-10	10-12	12-14	14-16	16-18	18-20	20-22	22-26.4
0-2	327.6	-41.5	38.9	3.7	-6.2	7.7	2.7	12.2	14.0	4.1	10.1	-0.4
2-4	-41.5	195.4	-57.8	21.7	0.6	-0.4	-1.3	1.6	2.3	-0.9	0.5	-0.7
4-6	38.9	-57.8	165.9	-51.7	27.6	4.4	11.4	11.2	14.0	0.6	2.0	2.5
6-8	3.7	21.7	-51.7	182.9	-43.8	24.4	13.4	11.3	13.9	0.5	0.2	3.4
8-10	-6.2	0.6	27.6	-43.8	209.1	-44.8	33.1	10.9	18.1	1.0	-0.0	4.2
10-12	7.7	-0.4	4.4	24.4	-44.8	198.4	-29.5	20.8	14.6	-1.1	3.3	0.4
12-14	2.7	-1.3	11.4	13.4	33.1	-29.5	208.0	-35.0	28.2	-1.2	9.9	-1.1
14-16	12.2	1.6	11.2	11.3	10.9	20.8	-35.0	229.5	-2.8	2.7	-3.7	-3.9
16-18	14.0	2.3	14.0	13.9	18.1	14.6	28.2	-2.8	219.1	-33.6	20.6	-19.5
18-20	4.1	-0.9	0.6	0.5	1.0	-1.1	-1.2	2.7	-33.6	177.5	9.5	-11.8
20-22	10.1	0.5	2.0	0.2	-0.0	3.3	9.9	-3.7	20.6	9.5	234.4	-87.2
22-26.4	-0.4	-0.7	2.5	3.4	4.2	0.4	-1.1	-3.9	-19.5	-11.8	-87.2	265.7

Tableau 3.73 – Covariance matrix of the partial $\Delta\mathcal{B}(q^2)$ systematic uncertainties obtained from the real data for $B^0 \to \pi^-\ell^+\nu$ decays. The elements have the same values for the "Without FSR" case as for the one "with FSR", within the quoted precision.

q^2 bins (GeV^2/c^4)	0-2	2-4	4-6	6-8	8-10	10-12	12-14	14-16	16-18	18-20	20-22	22-26.4
0-2	395.9	-31.7	71.1	47.2	74.0	73.9	73.4	59.1	70.2	18.1	82.8	196.6
2-4	-31.7	68.3	-12.4	4.5	-12.8	-5.1	-9.2	-11.3	-23.7	23.0	-17.6	9.2
4-6	71.1	-12.4	76.5	49.0	54.8	58.6	44.4	51.0	42.7	19.6	56.1	77.6
6-8	47.2	4.5	49.0	51.5	39.0	46.8	35.7	38.9	30.8	23.8	35.3	48.9
8-10	74.0	-12.8	54.8	39.0	58.4	50.0	40.9	45.7	34.6	18.5	44.8	53.2
10-12	73.9	-5.1	58.6	46.8	50.0	78.4	50.0	60.4	50.0	21.6	48.0	65.7
12-14	73.4	-9.2	44.4	35.7	40.9	50.0	57.7	44.8	51.0	14.8	37.5	52.0
14-16	59.1	-11.3	51.0	38.9	45.7	60.4	44.8	72.8	55.9	20.0	49.1	60.5
16-18	70.2	-23.7	42.7	30.8	34.6	50.0	51.0	55.9	84.0	-0.6	50.9	46.7
18-20	18.1	23.0	19.6	23.8	18.5	21.6	14.8	20.0	-0.6	45.7	2.4	30.1
20-22	82.8	-17.6	56.1	35.3	44.8	48.0	37.5	49.1	50.9	2.4	80.5	94.3
22-26.4	196.6	9.2	77.6	48.9	53.2	65.7	52.0	60.5	46.7	30.1	94.3	385.1

3.8.4.3 Fits of $|V_{ub}f_+(0)|$ and the $f_+(q^2)$ shape parameters in real data

The $\Delta\mathcal{B}(q^2)$ distribution is displayed in Fig. 3.73 for the $B^0 \to \pi^-\ell^+\nu$ decays together with theoretical predictions. The $\Delta\mathcal{B}(q^2)$ distribution for $B^+ \to \eta\ell^+\nu$ ($\gamma\gamma$ and 3π channels combined) decays is displayed in Fig. 3.74 together with a LCSR theoretical prediction [28]. As described in Sect. 3.3.8, the measured q^2 distributions shown in these figures have had the FSR effects removed in order to allow a direct comparison with the theoretical predictions which do not include such effects. We obtain the $f_+(q^2)$ shape from a fit to these distributions. The χ^2 function minimized in the $f_+(q^2)$ fits uses a PDF based on the three parametrizations presented in Sect. 3.3.8. It is defined in terms of the $\Delta\mathcal{B}(q^2)$ covariance matrix to take into account the correlations among the measurements in the various q^2 bins. The results of the fits are given in Table 3.74. The value of α_{BK} = 0.50 ± 0.05 is in good agreement with our previous measurement, α_{BK} = 0.52 ± 0.06 [39]. However, the values of χ^2 obtained in the fits of the three parametrizations to the $B^0 \to \pi^-\ell^+\nu$ decay data clearly indicate that the Hill [53] and BGL [54] parametrizations represent the data better than the BK [52] parametrization. Because of low statistics, the data for the $B^+ \to \eta\ell^+\nu$ decays cannot differentiate between the three parametrizations with, however, again a preference for the BGL parametrization. We then use the BGL expansion to obtain, from the $B^0 \to \pi^-\ell^+\nu$ decays data, a value of $|V_{ub}f_+(0)|$ from the fit extrapolated to $q^2 = 0$, of $(8.6 \pm 0.3_{stat} \pm 0.3_{syst}) \times 10^{-4}$ compared to our previous value of $(9.6 \pm 0.3_{stat} \pm 0.2_{syst}) \times 10^{-4}$ obtained [39] with the BK parametrization. This value of $|V_{ub}f_+(0)|$ can be used to predict [53] rates of other decays such as $B \to \pi\pi$.

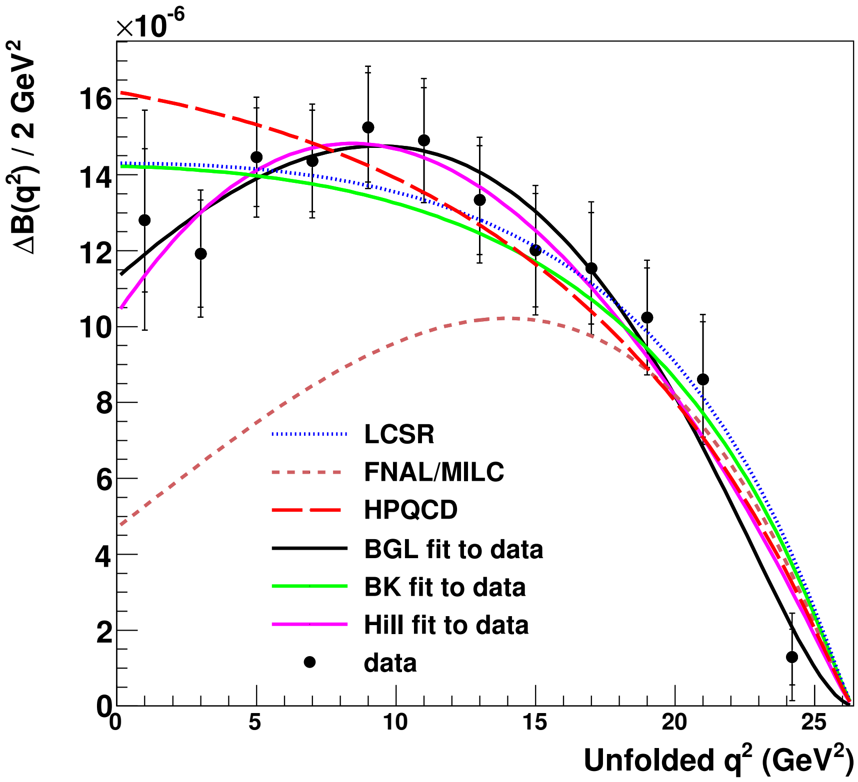

Figure 3.73 – Partial $\Delta\mathcal{B}(q^2)$ spectrum in 12 bins of q^2 for $B^0 \to \pi^- \ell^+ \nu$ decays. The smaller error bars are statistical only while the larger ones include systematic uncertainties. The solid black, green and pink curves show the results of the fit of the BGL, BK and Hill parametrizations to the data, respectively. The data are also compared to unquenched LQCD calculations (HPQCD and FNAL/MILC) [31, 32] and a LCSR calculation [55].

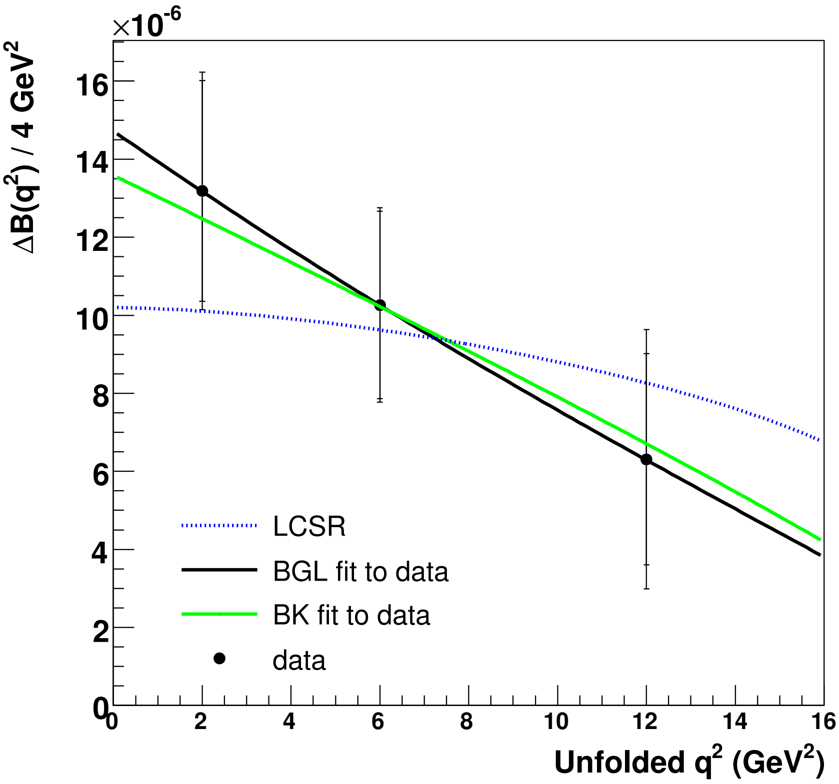

Figure 3.74 – Partial $\Delta\mathcal{B}(q^2)$ spectrum in 3 bins of q^2 for $B^+ \rightarrow \eta\ell^+\nu$ ($\gamma\gamma$ and 3π channels combined) decays. The smaller error bars are statistical only while the larger ones include systematic uncertainties. The solid black and green curves show the results of the fit of the BGL and BK parametrizations to the data, respectively. The data are also compared to a LCSR calculation [28].

Tableau 3.74 – Fitted parameter values of different parametrizations for $B^0 \to \pi^-\ell^+\nu$ and $B^+ \to \eta\ell^+\nu$ ($\gamma\gamma$ and 3π channels combined) decays.

Function Ref.	Fit Parameter	$B^+ \to \eta\ell^+\nu$ value	χ^2/ndf	Prob.	$B^0 \to \pi^-\ell^+\nu$ value	χ^2/ndf	Prob.
BK [52]	α_{BK}	0.0 ± 1.49	0.07/1	79.0%	0.51 ± 0.04	10.5/10	39.6%
Hill [53]	α_{Hill}				0.48 ± 0.05	5.0/9	83.5%
	δ_{Hill}				-3.2 ± 2.3		
BGL [54]	a_1/a_0	0.08 ± 1.23	0.0/1	99.9%	-1.58 ± 0.13	19.3/10	3.7%
BGL [54]	a_1/a_0				-0.64 ± 0.30	3.8/9	92.2%
	a_2/a_0				-6.8 ± 1.8		
BGL [54]	a_1/a_0				-0.69 ± 0.38	3.8/8	87.5%
	a_2/a_0				-7.9 ± 2.7		
	a_3/a_0				6.7 ± 15.2		

3.8.4.4 Tests of QCD calculations

Tableau 3.75 – χ^2 values and associated probabilities for various QCD calculations compared to our measured $B^0 \to \pi^- \ell^+ \nu$ decays q^2 spectrum.

QCD model	q^2 range (GeV^2/c^4)	stat error only χ^2/ndf	$Prob(\chi^2)$	stat+syst errors χ^2/ndf	$Prob(\chi^2)$
LCSR [55]	< 12	7.5/6	27.4%	5.6/6	47.0%
HPQCD [31]	> 16	7.6/4	10.7%	4.9/4	30.1%
FNAL [32]	> 16	10.0/4	4.0%	6.2/4	18.4%

Three different models are compared to the $B^0 \to \pi^- \ell^+ \nu$ decay data in Fig. 3.73. We give the values of χ^2 and their associated probabilities in Table 3.75 for the three models, taking into account the experimental (statistical and systematic) uncertainties, but not the theoretical ones, as explained in Sect. 3.3.9. All three calculations, valid over different q^2 ranges, are compatible with the data. A LCSR calculation [28] is also available for the $B^+ \to \eta \ell^+ \nu$ decays. As shown in Fig. 3.74, its predictions are compatible with our data.

3.8.4.5 Extraction of $|V_{ub}|$

We extract $|V_{ub}|$ from the partial $\Delta\mathcal{B}(q^2)$ measured in the $B^0 \to \pi^- \ell^+ \nu$ decays using the relation : $|V_{ub}| = \sqrt{\Delta\mathcal{B}(q^2)/(\tau_{B^0}\Delta\zeta)}$, where $\tau_{B^0} = 1.525 \pm 0.009$ ps [24] is the B^0 lifetime and $\Delta\zeta = \Gamma/|V_{ub}|^2$ is the normalized partial decay rate predicted by the form-factor calculations [31, 32, 55] ($q^2 < 12$ or $q^2 > 16\ \mathrm{GeV}^2/c^4$ depending on the model used, see Sect. 3.3.10). The values of $|V_{ub}|$ thus obtained are given in Table 3.76. They range from $(3.14 - 3.70) \times 10^{-3}$. The three values are all acceptable acording to our data and are consistent with the value measured in inclusive semileptonic $B \to X_u \ell \nu$ decays. We note that the inclusive results are very sensitive to the mass of the b quark whose extraction depends on higher-order QCD corrections. A value of $|V_{ub}|$ cannot be obtained from $B^+ \to \eta \ell^+ \nu$ decays because the required theoretical input is missing.

Tableau 3.76 – Values of $|V_{ub}|$ derived from the form-factor calculations applied to the $B^0 \to \pi^- \ell^+ \nu$ decay data. The first two uncertainties arise from the statistical and systematic uncertainties of the partial BFs, respectively. The third uncertainty comes from the uncertainties on $\Delta\zeta$ due to the calculations.

	q^2 (GeV^2/c^4)	$\Delta\mathcal{B}$ (10^{-4})	$\Delta\zeta$ (ps^{-1})	$\|V_{ub}\|$ (10^{-3})
LCSR [55]	< 12	$0.84 \pm 0.03 \pm 0.04$	$4.00^{+1.01}_{-0.95}$	$3.70 \pm 0.07 \pm 0.09^{+0.54}_{-0.39}$
HPQCD [31]	> 16	$0.33 \pm 0.03 \pm 0.03$	2.07 ± 0.57	$3.24 \pm 0.13 \pm 0.16^{+0.57}_{-0.37}$
FNAL [32]	> 16	$0.33 \pm 0.03 \pm 0.03$	$2.21^{+0.47}_{-0.42}$	$3.14 \pm 0.12 \pm 0.16^{+0.35}_{-0.29}$

3.9 Cross-checks

We have performed various cross-checks to make sure that the results and their uncertainties are self-coherent. There is good agreement between data and simulation for the variables used in our analysis. Consistent results are obtained when dividing the final dataset into sub-samples as well as using modified binnings and modified event selections. These cross-checks are not intended to estimate the systematic uncertainties.

3.9.1 Data/MC comparisons

We compare the data and MC distributions of key quantities of the analysis after all selections and corrections are applied. Note that the MC histograms in this chapter have been adjusted with the values of the scaling factors obtained in the fit to the ΔE and m_{ES} data.

3.9.1.1 Comparison of off-resonance data with continuum MC

In Figs. 3.25, 3.26, 3.27 and 3.28, Sect. 3.5.2.8, we compare distributions obtained with the central configuration of the continuum MC simulation with those of the off-resonance data control sample in the entire ΔE-m_{ES} fit region, and separately for electrons and muons for $B^+ \to \eta' \ell^+ \nu$, $B^+ \to \eta \ell^+ \nu$ and $B^0 \to \pi^- \ell^+ \nu$ decays, respectively. The agreement between data and MC is reasonable. As discussed in Sect. 3.5.2.8, this agreement becomes excellent when the MC continuum yields are corrected and the weight functions applied (see, for example, Fig. 3.30).

3.9.1.2 Comparison of on-resonance data with full MC simulation in the sidebands of ΔE and m_{ES}

In Figs. 3.75-3.77, 3.78-3.79 and 3.80-3.81, we compare Y signal candidates related distributions obtained with the central configuration of the simulation with those of the on-resonance data, both generated from the ΔE-m_{ES} sidebands[22] where the signal

[22]The ΔE-m_{ES} sidebands are the entire fit region outside the signal region (see Figs. 3.23 and 3.24 for $B^+ \to \eta^{(\prime)} \ell^+ \nu$ and $B^0 \to \pi^- \ell^+ \nu$ decays, respectively). They are defined for $\Delta E < -0.16$ GeV *or*

contribution is depleted, for $B^+ \to \eta^{'}\ell^+\nu$, $B^+ \to \eta\ell^+\nu$ ($\gamma\gamma$ channel) and $B^0 \to \pi^-\ell^+\nu$ decays, respectively. In Figs. 3.82-3.83, 3.84-3.85 and 3.86-3.87, we compare similar distributions for event variables that are of interest since they can affect the neutrino reconstruction with consequences on the ΔE and m_{ES} distributions, for $B^+ \to \eta^{'}\ell^+\nu$, $B^+ \to \eta\ell^+\nu$ ($\gamma\gamma$ channel) and $B^0 \to \pi^-\ell^+\nu$ decays, respectively. There is a very good agreement between data and MC in all cases.

$\Delta E > 0.20$ GeV *or* $m_{ES} < 5.2675$ GeV/c^2.

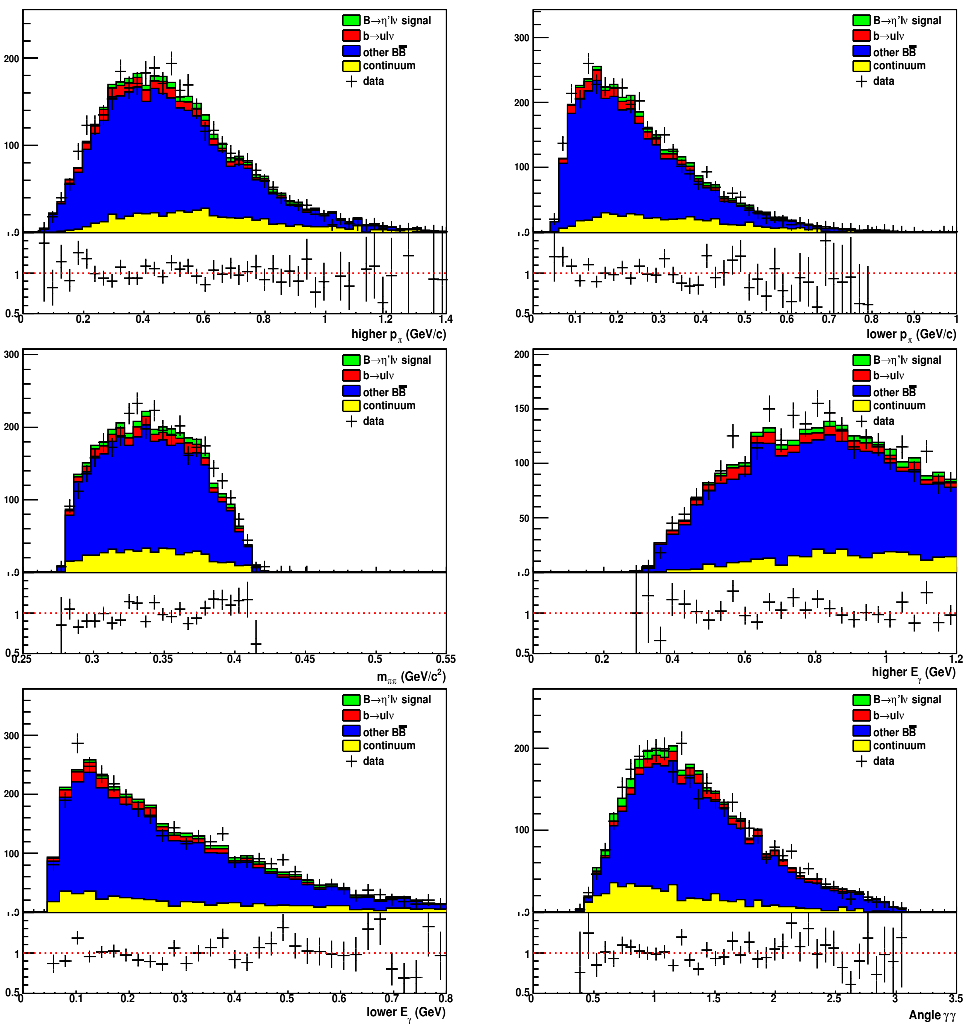

Figure 3.75 – Comparison of Y signal candidates related distributions obtained from the on-resonance data and MC simulation, both generated from the sidebands of ΔE and m_{ES}, for $B^+ \to \eta^{'} \ell^+ \nu$ ($\gamma\gamma$ decay channel only), after applying all analysis cuts and MC simulation corrections.

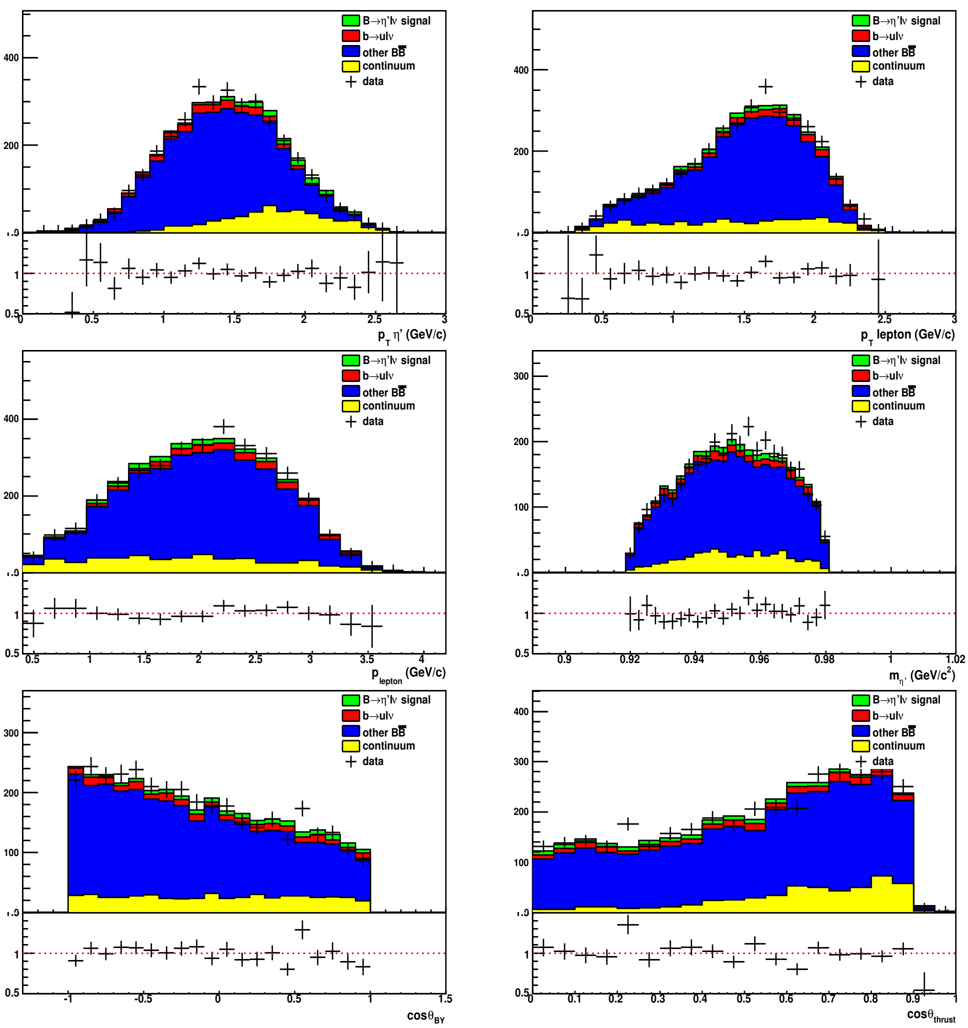

Figure 3.76 – Comparison of additional Y signal candidates related distributions obtained from the on-resonance data and MC simulation, both generated from the sidebands of ΔE and m_{ES}, for $B^+ \to \eta^{\prime} \ell^+ \nu$ ($\gamma\gamma$ decay channel only), after applying all analysis cuts and MC simulation corrections.

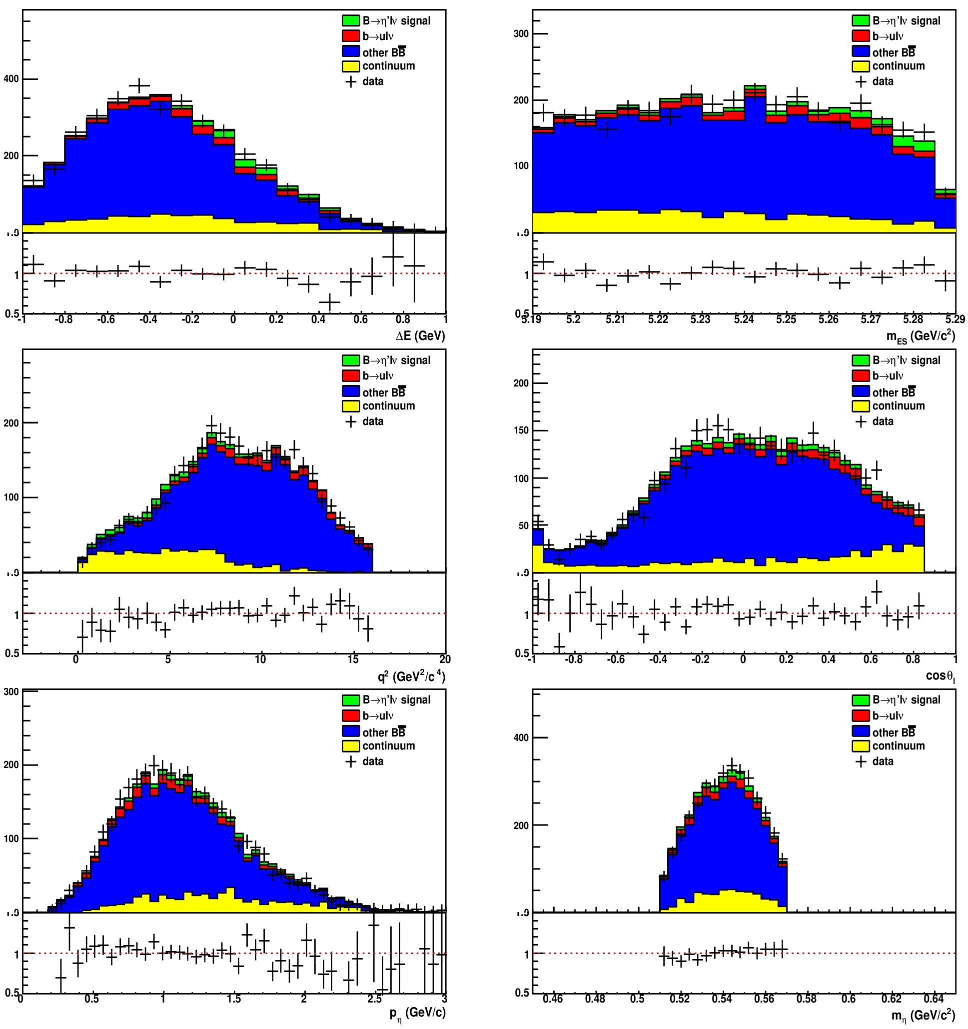

Figure 3.77 – Comparison of additional Y signal candidates related distributions obtained from the on-resonance data and MC simulation, both generated from the sidebands of ΔE and m_{ES}, for $B^+ \to \eta' \ell^+ \nu$ ($\gamma\gamma$ decay channel only), after applying all analysis cuts and MC simulation corrections.

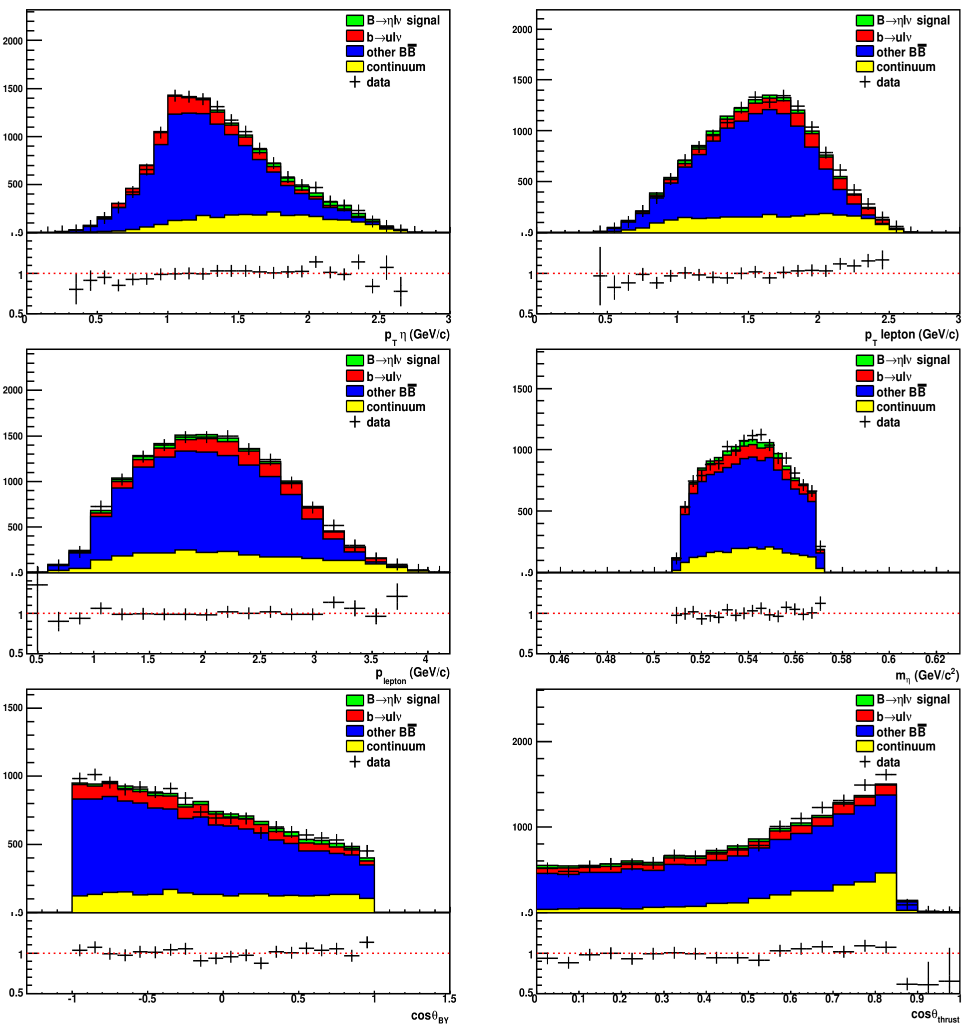

Figure 3.78 – Comparison of Y signal candidates related distributions obtained from the on-resonance data and MC simulation, both generated from the sidebands of ΔE and m_{ES}, for $B^+ \to \eta\ell^+\nu(\gamma\gamma$ decay channel only), after applying all analysis cuts and MC simulation corrections.

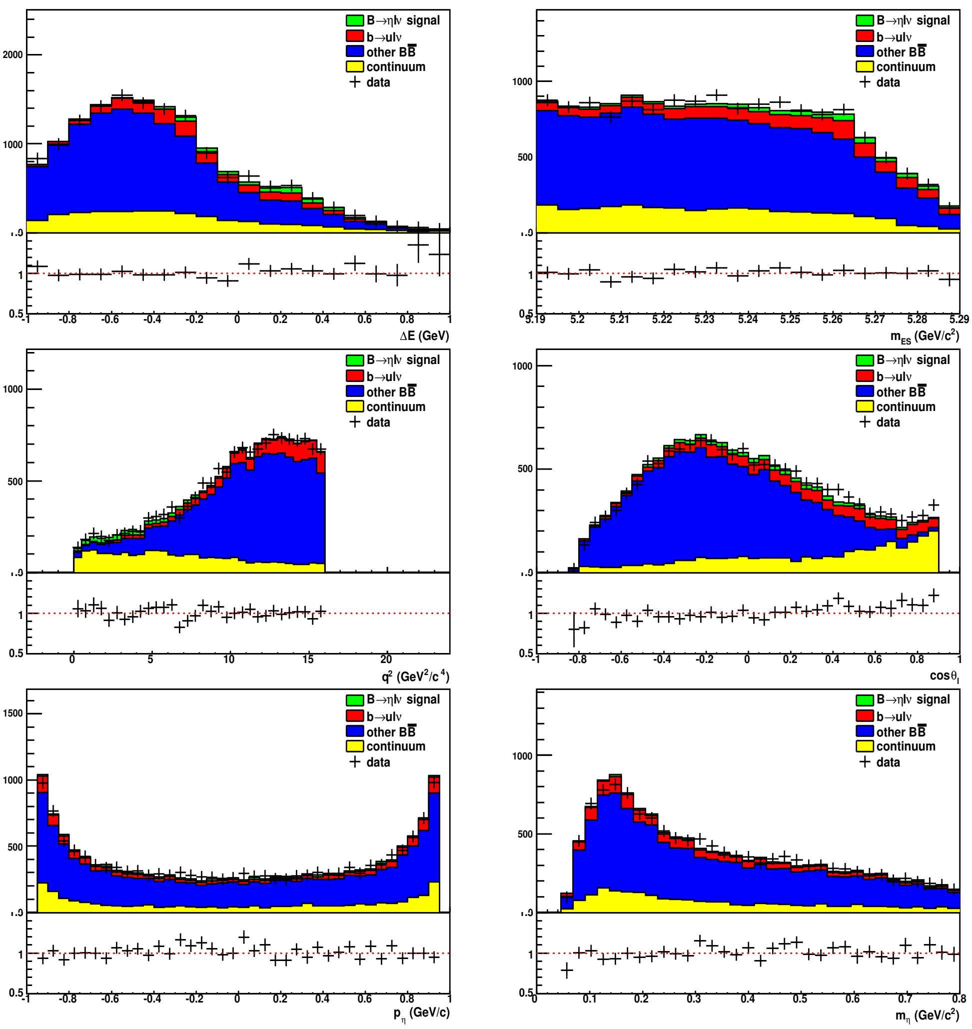

Figure 3.79 – Comparison of additional Y signal candidates related distributions obtained from the on-resonance data and MC simulation, both generated from the sidebands of ΔE and m_{ES}, for $B^+ \to \eta\ell^+\nu$ ($\gamma\gamma$ decay channel only), after applying all analysis cuts and MC simulation corrections.

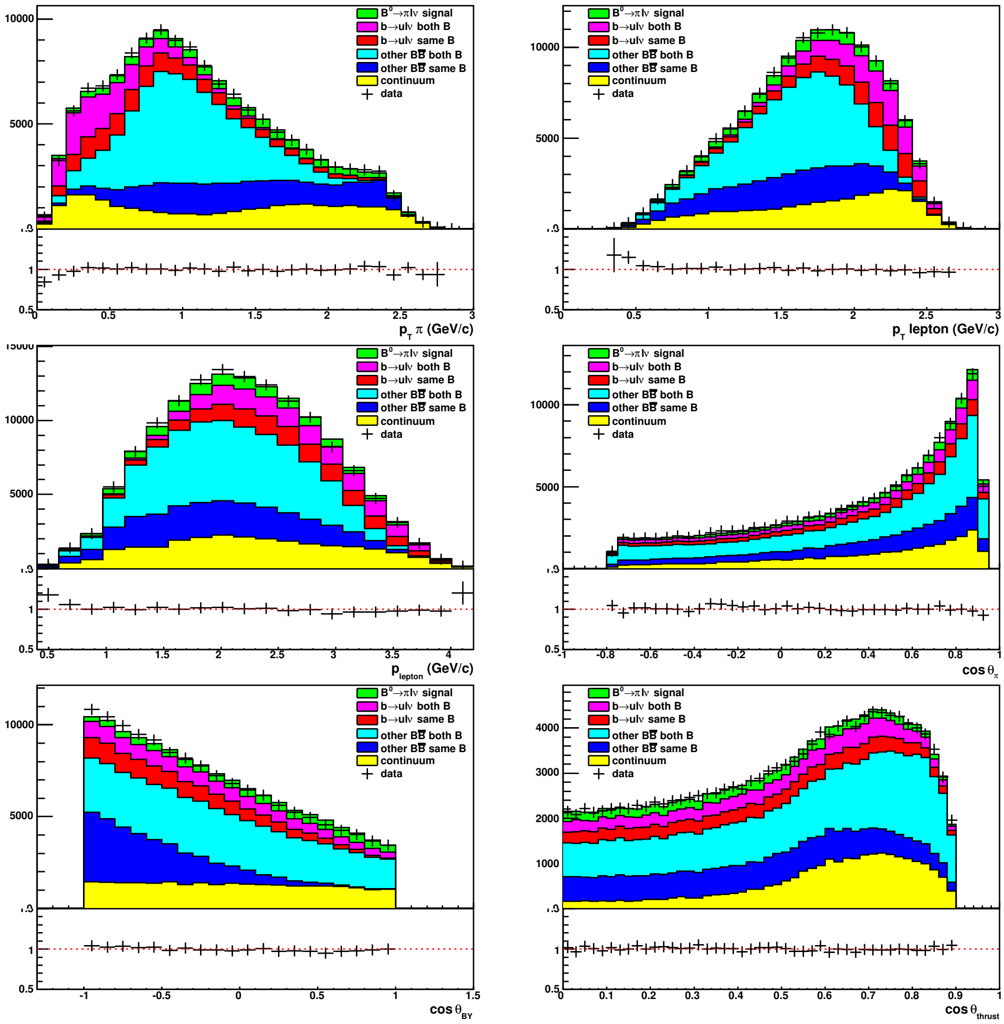

Figure 3.80 – Comparison of Υ signal candidates related distributions obtained from the on-resonance data and MC simulation, both generated from the sidebands of ΔE and m_{ES}, for $B^0 \to \pi^- \ell^+ \nu$, after applying all analysis cuts and MC simulation corrections.

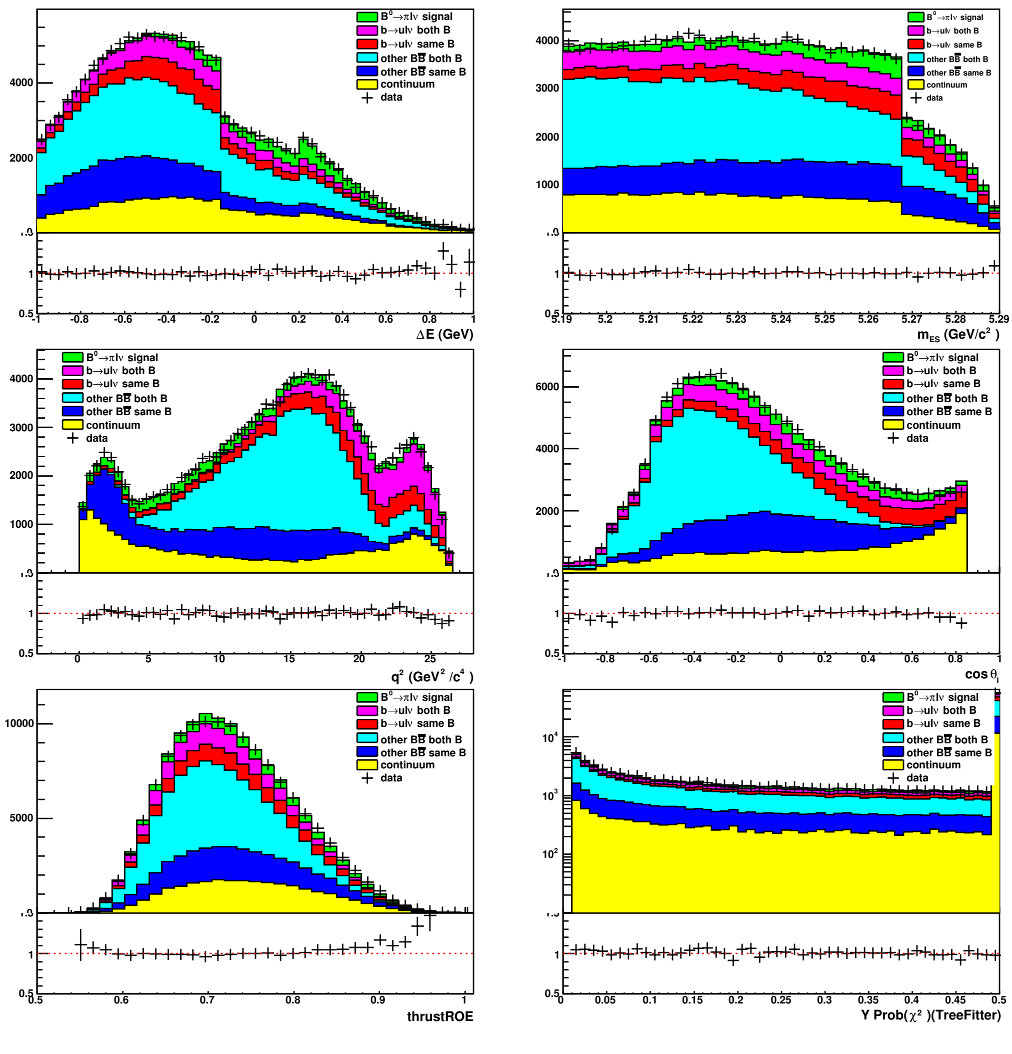

Figure 3.81 – Comparison of additional Y signal candidates related distributions obtained from the on-resonance data and MC simulation, both generated from the sidebands of ΔE and m_{ES}, for $B^0 \to \pi^- \ell^+ \nu$, after applying all analysis cuts and MC simulation corrections.

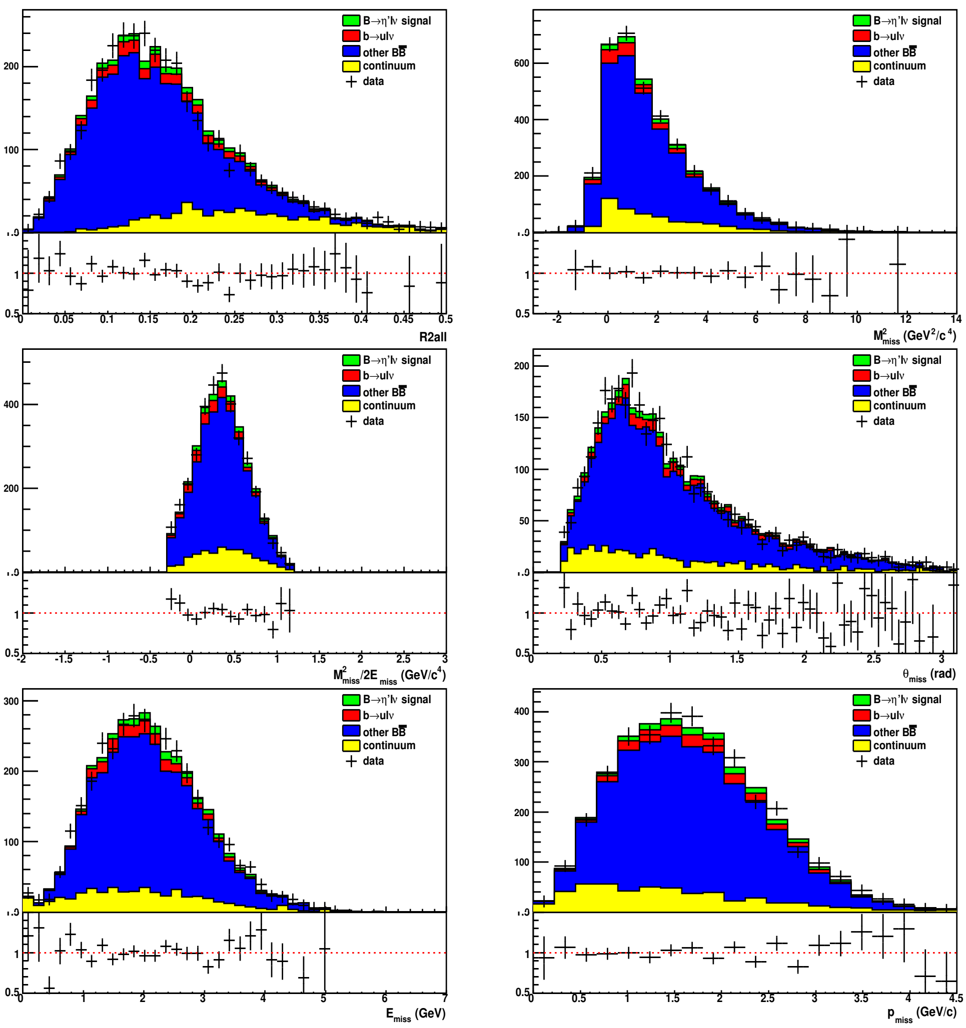

Figure 3.82 – Comparison of event variables' distributions obtained from the on-resonance data and MC simulation, both generated from the sidebands of ΔE and m_{ES}, for $B^+ \to \eta' \ell^+ \nu$ ($\gamma\gamma$ decay channel only), after applying all analysis cuts and MC simulation corrections.

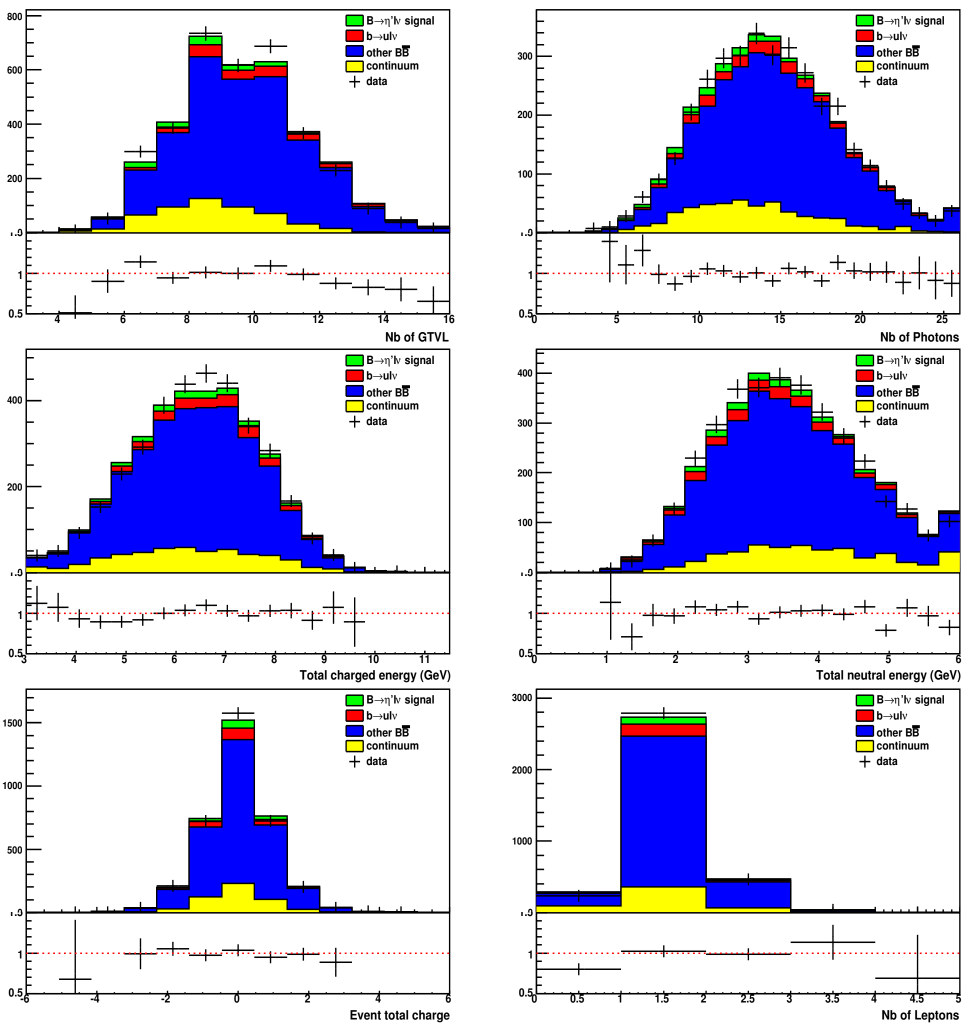

Figure 3.83 – Comparison of additional event variables' distributions obtained from the on-resonance data and MC simulation, both generated from the sidebands of ΔE and m_{ES}, for $B^+ \to \eta^{'} \ell^+ \nu$ ($\gamma\gamma$ decay channel only), after applying all analysis cuts and MC simulation corrections.

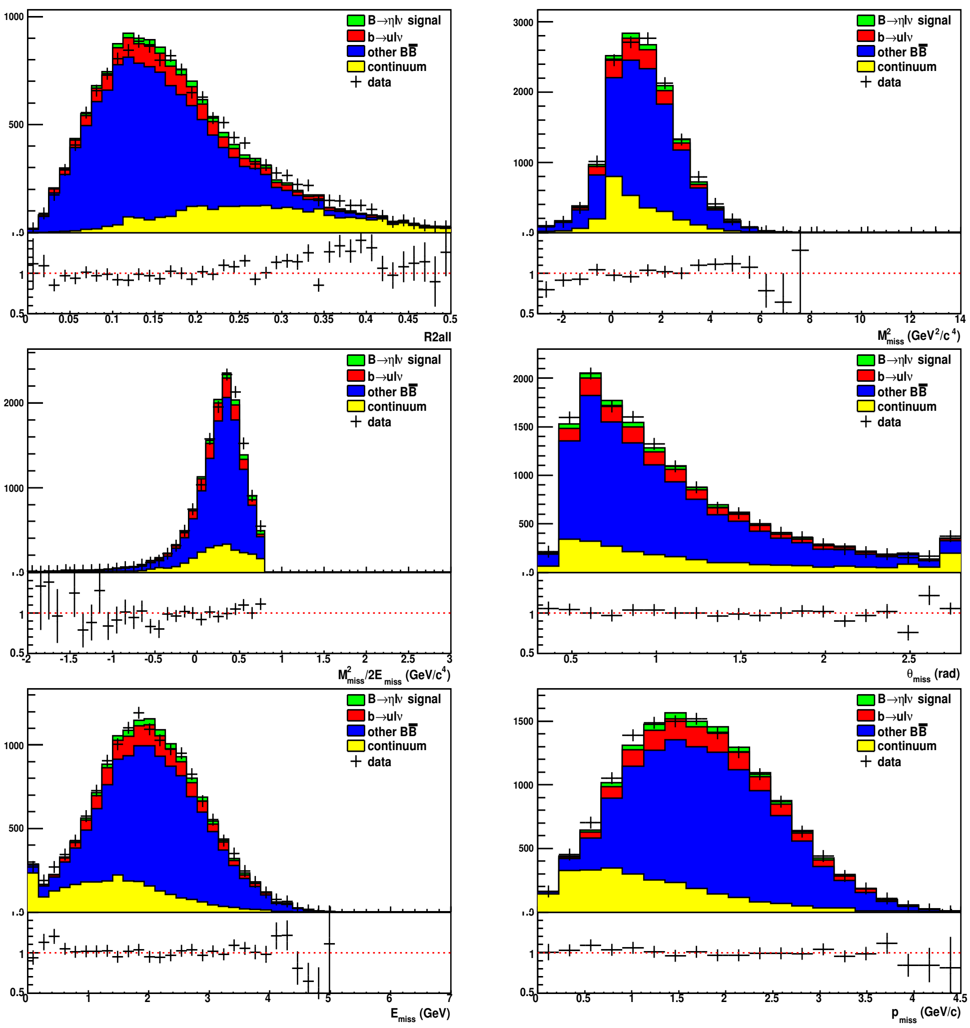

Figure 3.84 – Comparison of event variables' distributions obtained from the on-resonance data and MC simulation, both generated from the sidebands of ΔE and $m_{\rm ES}$, for $B^+ \to \eta\ell^+\nu$ ($\gamma\gamma$ decay channel only), after applying all analysis cuts and MC simulation corrections.

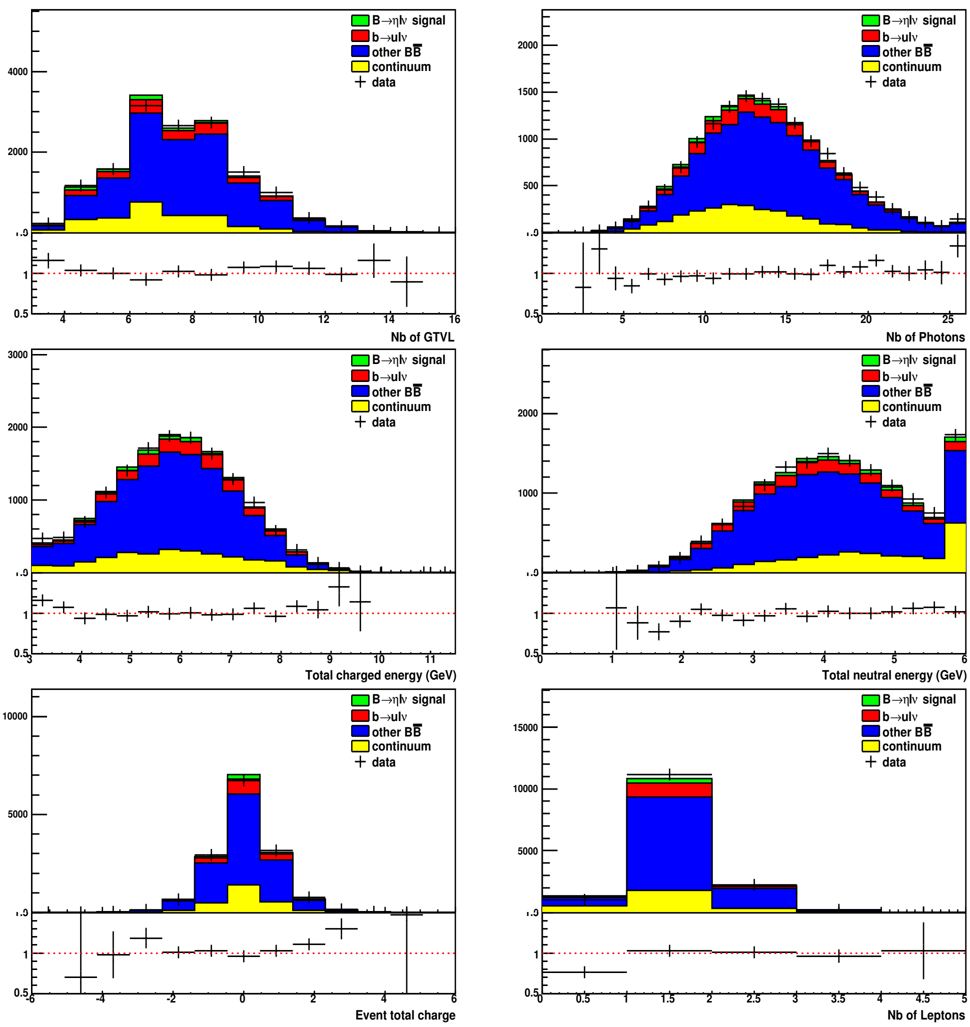

Figure 3.85 – Comparison of additional event variables' distributions obtained from the on-resonance data and MC simulation, both generated from the sidebands of ΔE and $m_{\rm ES}$, for $B^+ \to \eta \ell^+ \nu$ ($\gamma\gamma$ decay channel only), after applying all analysis cuts and MC simulation corrections.

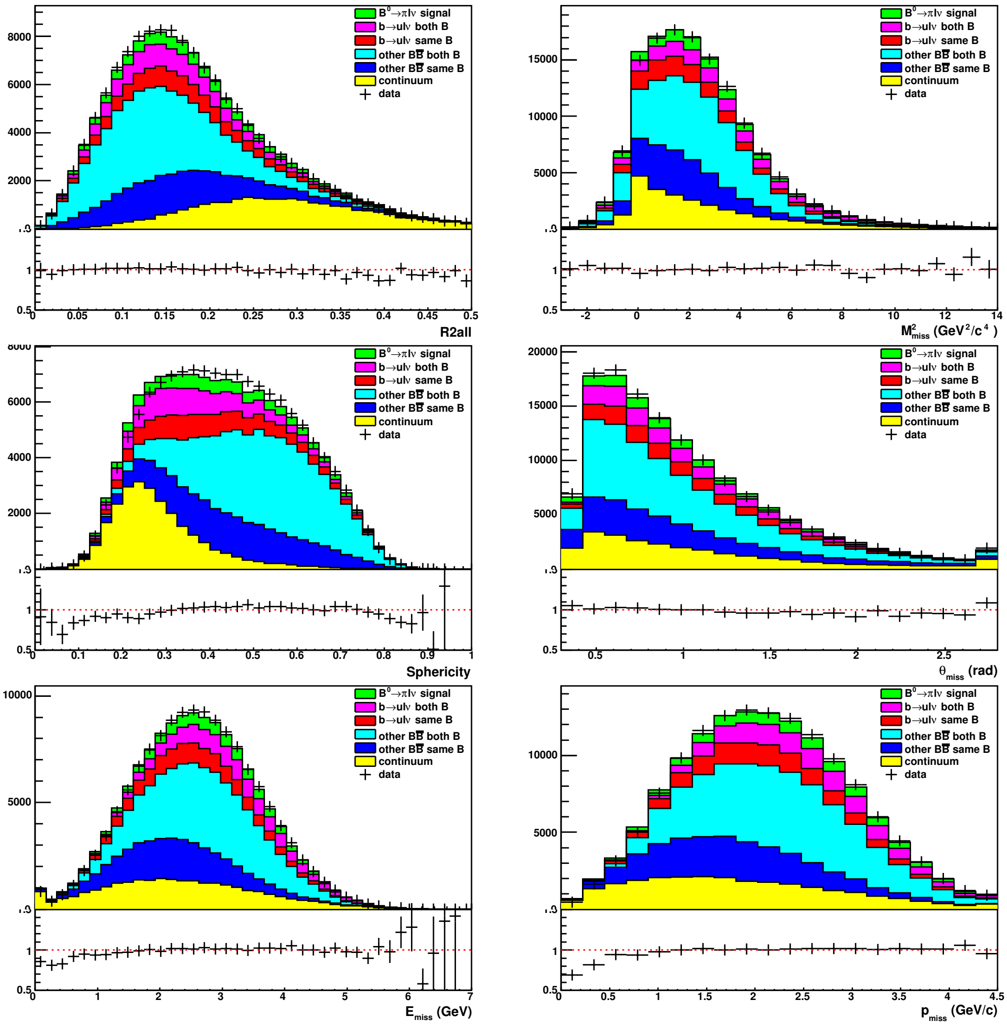

Figure 3.86 – Comparison of event variables' distributions obtained from the on-resonance data and MC simulation, both generated from the sidebands of ΔE and m_{ES}, for $B^0 \to \pi^- \ell^+ \nu$, after applying all analysis cuts and MC simulation corrections.

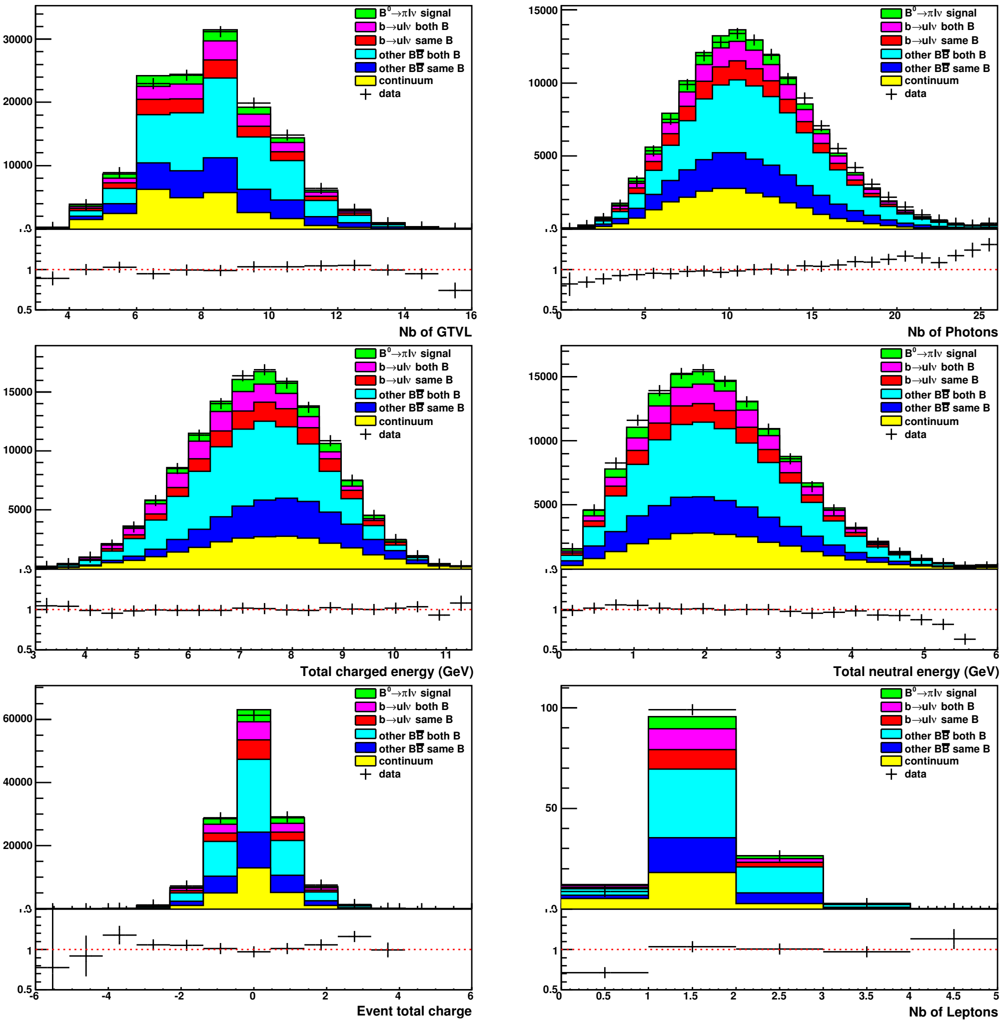

Figure 3.87 – Comparison of additional event variables' distributions obtained from the on-resonance data and MC simulation, both generated from the sidebands of ΔE and $m_{\rm ES}$, for $B^0 \to \pi^- \ell^+ \nu$, after applying all analysis cuts and MC simulation corrections.

3.9.1.3 Comparison of on-resonance data with full MC simulation in the signal region of ΔE and $m_{\rm ES}$

In Figs. 3.88-3.90, 3.91-3.92 and 3.93-3.94, we compare Y signal candidates related distributions obtained with the central configuration of the simulation with those of the on-resonance data, both generated from the ΔE-$m_{\rm ES}$ signal region[23] where the signal contribution is enhanced, for $B^+ \to \eta^{'}\ell^+\nu$, $B^+ \to \eta\ell^+\nu$ ($\gamma\gamma$ channel) and $B^0 \to \pi^-\ell^+\nu$ decays, respectively. In Figs. 3.95-3.96, 3.97-3.98 and 3.99-3.100, we compare similar distributions for event variables that are of interest since they can affect the neutrino reconstruction with consequences on the ΔE and $m_{\rm ES}$ distributions, for $B^+ \to \eta^{'}\ell^+\nu$, $B^+ \to \eta\ell^+\nu$ ($\gamma\gamma$ channel) and $B^0 \to \pi^-\ell^+\nu$ decays, respectively. We note that there is a good agreement between data and MC whenever we have a large number of events.

[23]The ΔE-$m_{\rm ES}$ signal region (see Figs. 3.23 and 3.24 for $B^+ \to \eta^{(')}\ell^+\nu$ and $B^0 \to \pi^-\ell^+\nu$ decays, respectively), is defined for $\Delta E > -0.16$ GeV *and* $\Delta E < 0.20$ GeV *and* $m_{ES} > 5.2675$ GeV/c^2.

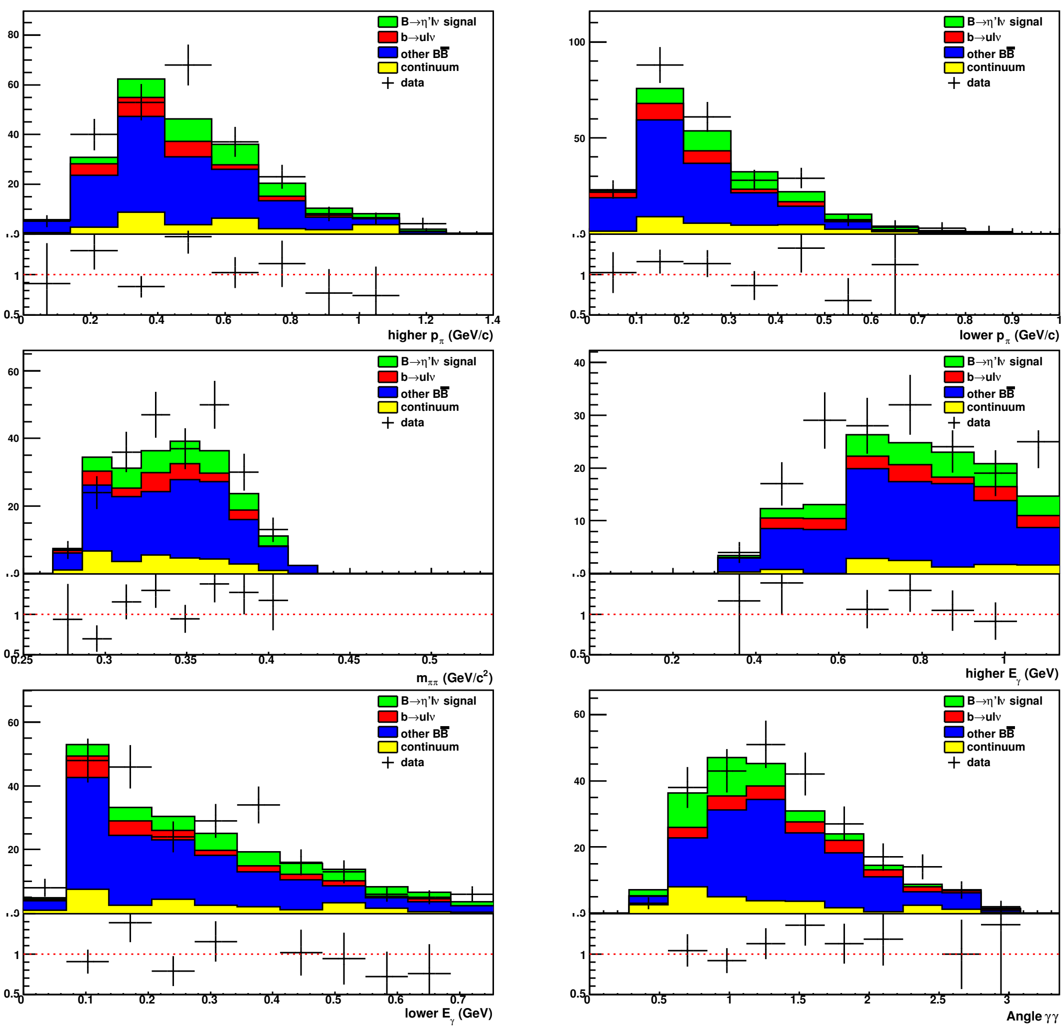

Figure 3.88 – Comparison of Y signal candidates related distributions obtained from the on-resonance data and MC simulation, both generated from the signal region of ΔE and $m_{\rm ES}$, for $B^+ \to \eta' \ell^+ \nu$ ($\gamma\gamma$ decay channel only), after applying all analysis cuts and MC simulation corrections.

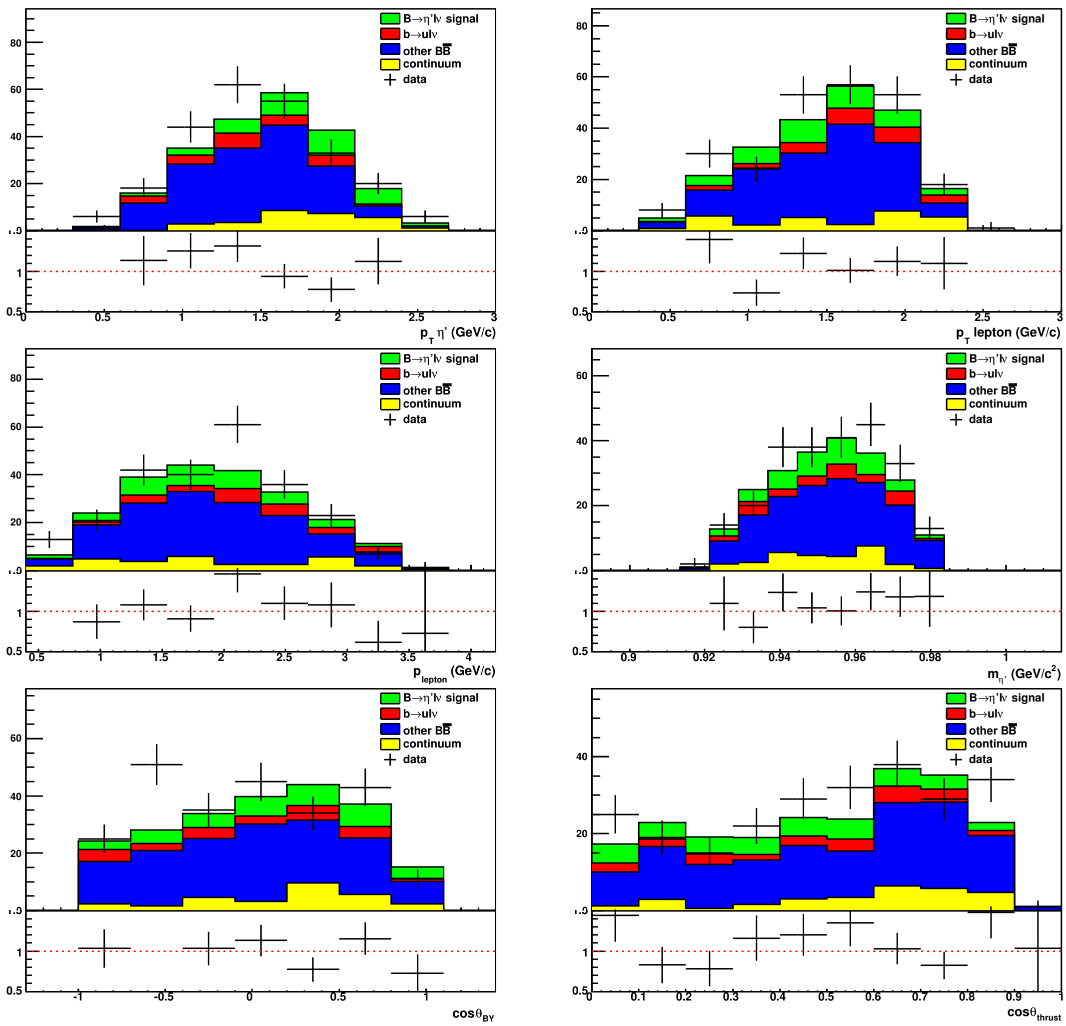

Figure 3.89 – Comparison of additional Y signal candidates related distributions obtained from the on-resonance data and MC simulation, both generated from the signal region of ΔE and m_{ES}, for $B^+ \to \eta' \ell^+ \nu$ ($\gamma\gamma$ decay channel only), after applying all analysis cuts and MC simulation corrections.

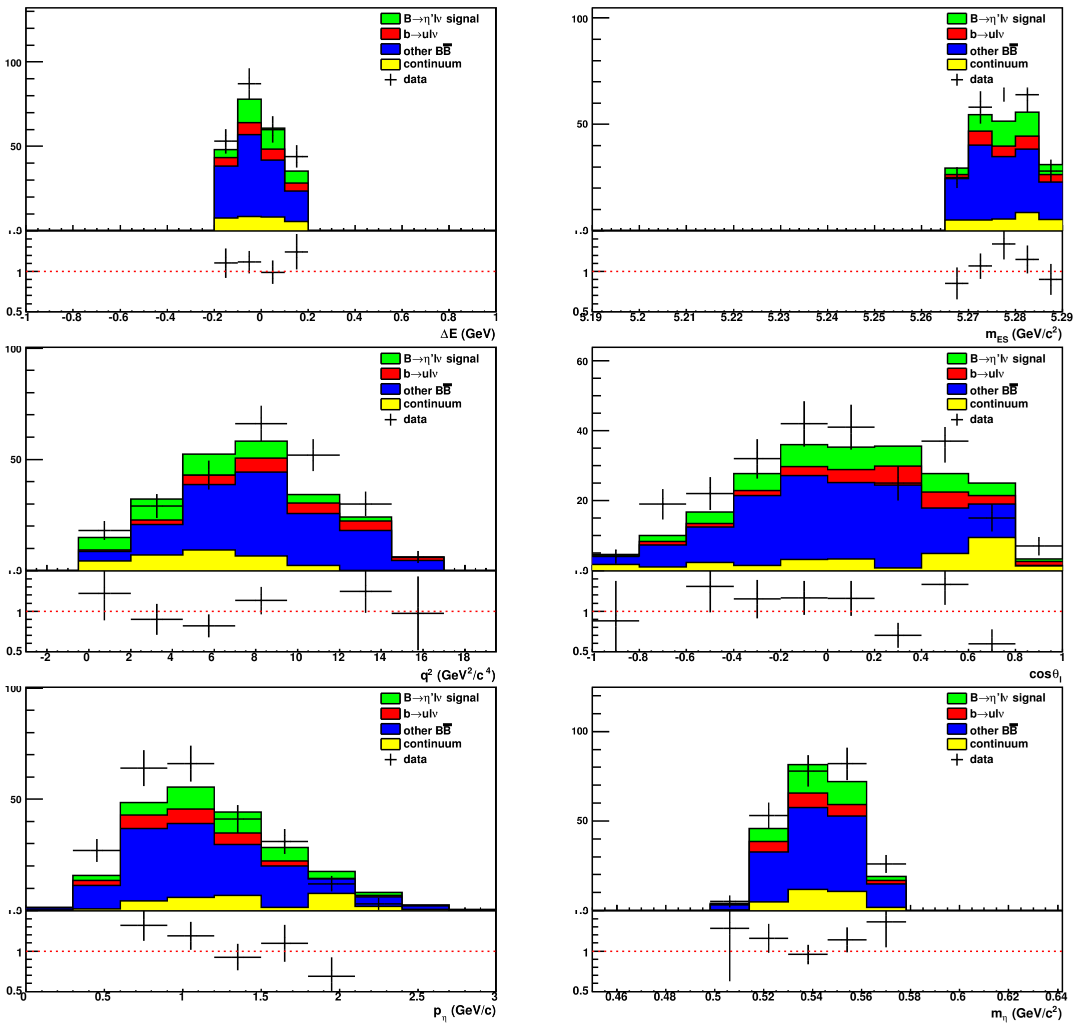

Figure 3.90 – Comparison of additional Y signal candidates related distributions obtained from the on-resonance data and MC simulation, both generated from the signal region of ΔE and m_{ES}, for $B^{+} \rightarrow \eta^{\prime}\ell^{+}\nu$ ($\gamma\gamma$ decay channel only), after applying all analysis cuts and MC simulation corrections.

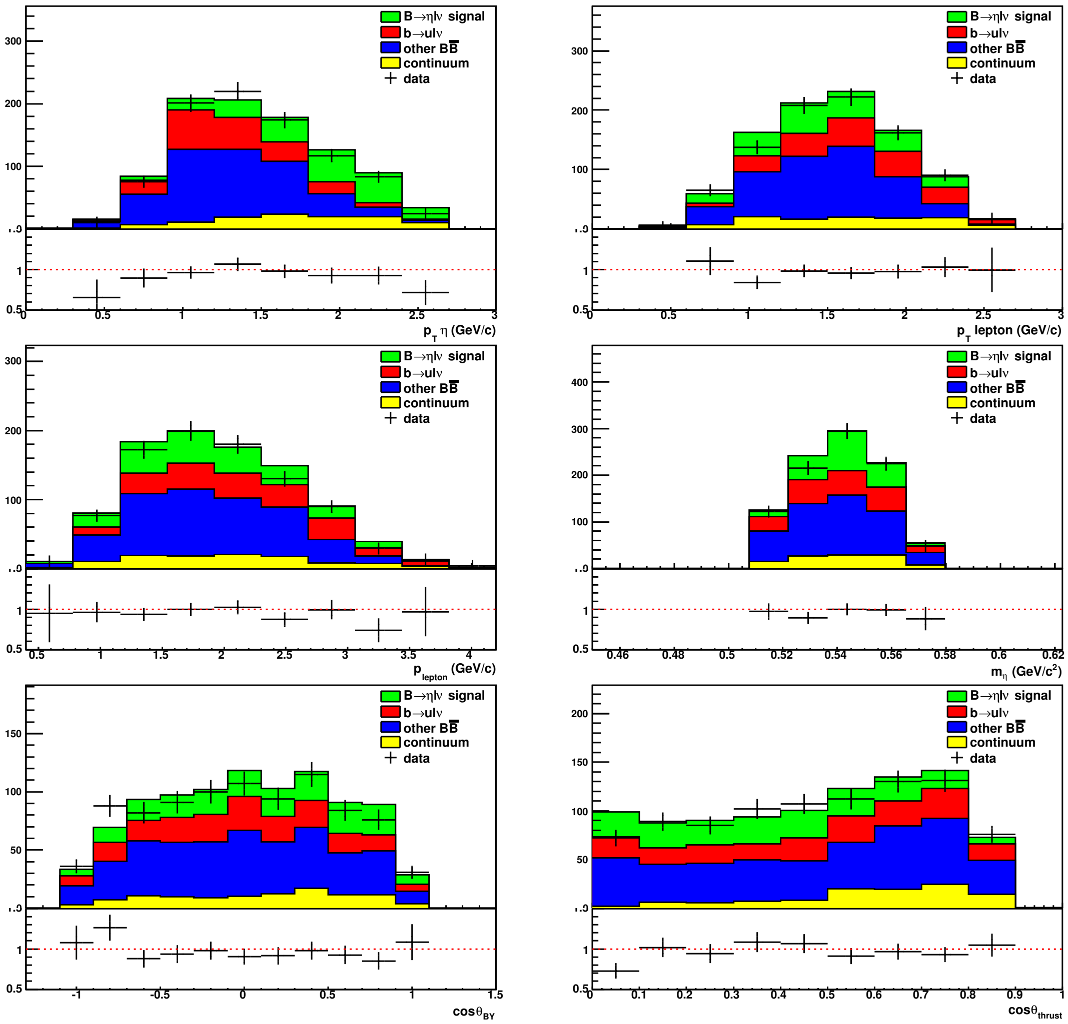

Figure 3.91 – Comparison of Y signal candidates related distributions obtained from the on-resonance data and MC simulation, both generated from the signal region of ΔE and m_{ES}, for $B^+ \to \eta\ell^+\nu(\gamma\gamma$ decay channel only), after applying all analysis cuts and MC simulation corrections.

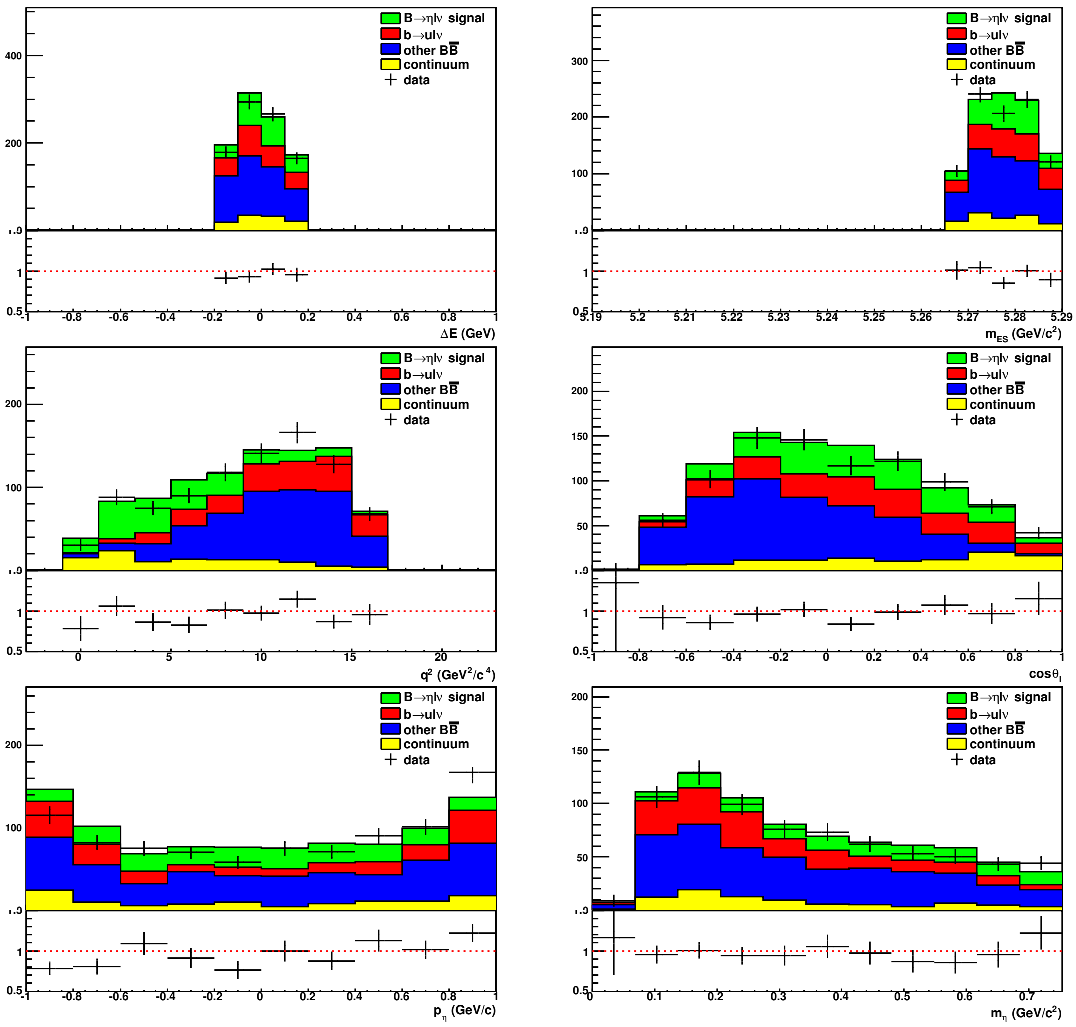

Figure 3.92 – Comparison of additional Y signal candidates related distributions obtained from the on-resonance data and MC simulation, both generated from the signal region of ΔE and m_{ES}, for $B^+ \to \eta\ell^+\nu$ ($\gamma\gamma$ decay channel only), after applying all analysis cuts and MC simulation corrections.

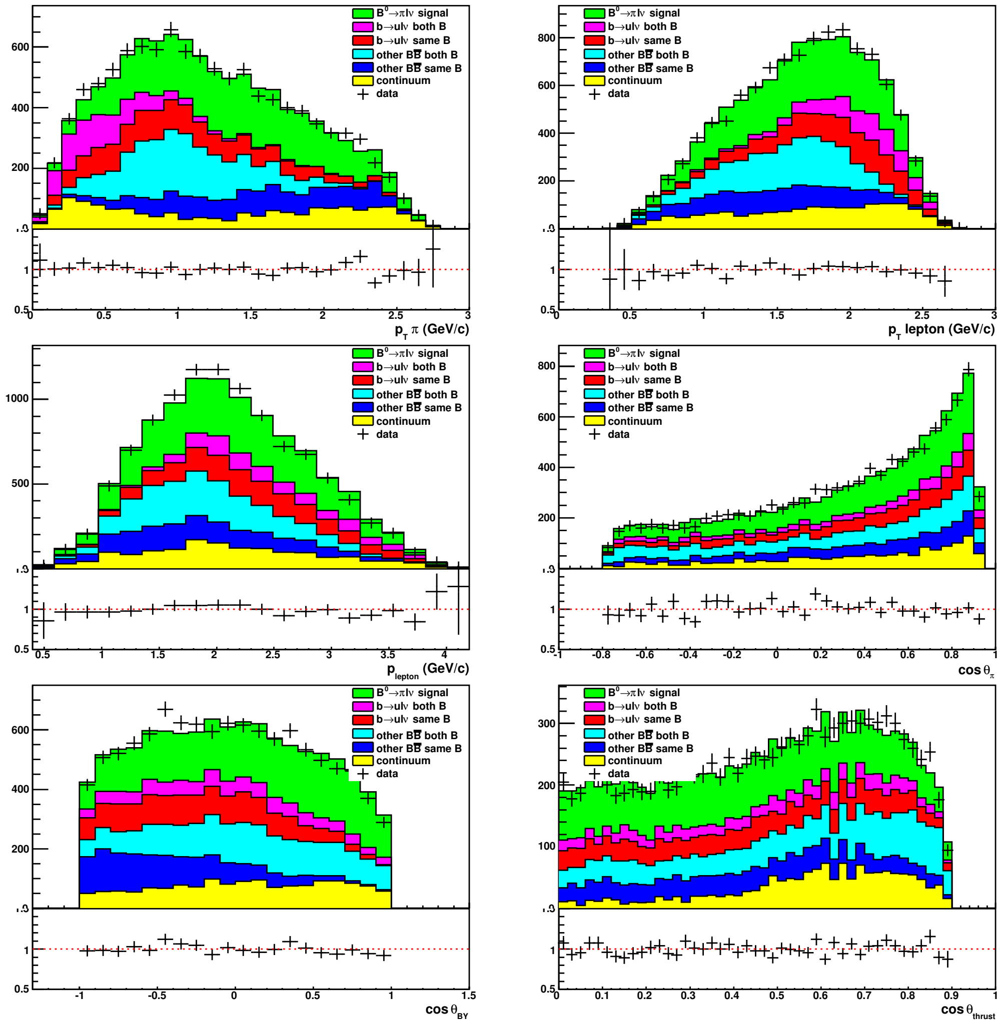

Figure 3.93 – Comparison of Υ signal candidates related distributions obtained from the on-resonance data and MC simulation, both generated from the signal region of ΔE and m_{ES}, for $B^0 \to \pi^- \ell^+ \nu$, after applying all analysis cuts and MC simulation corrections.

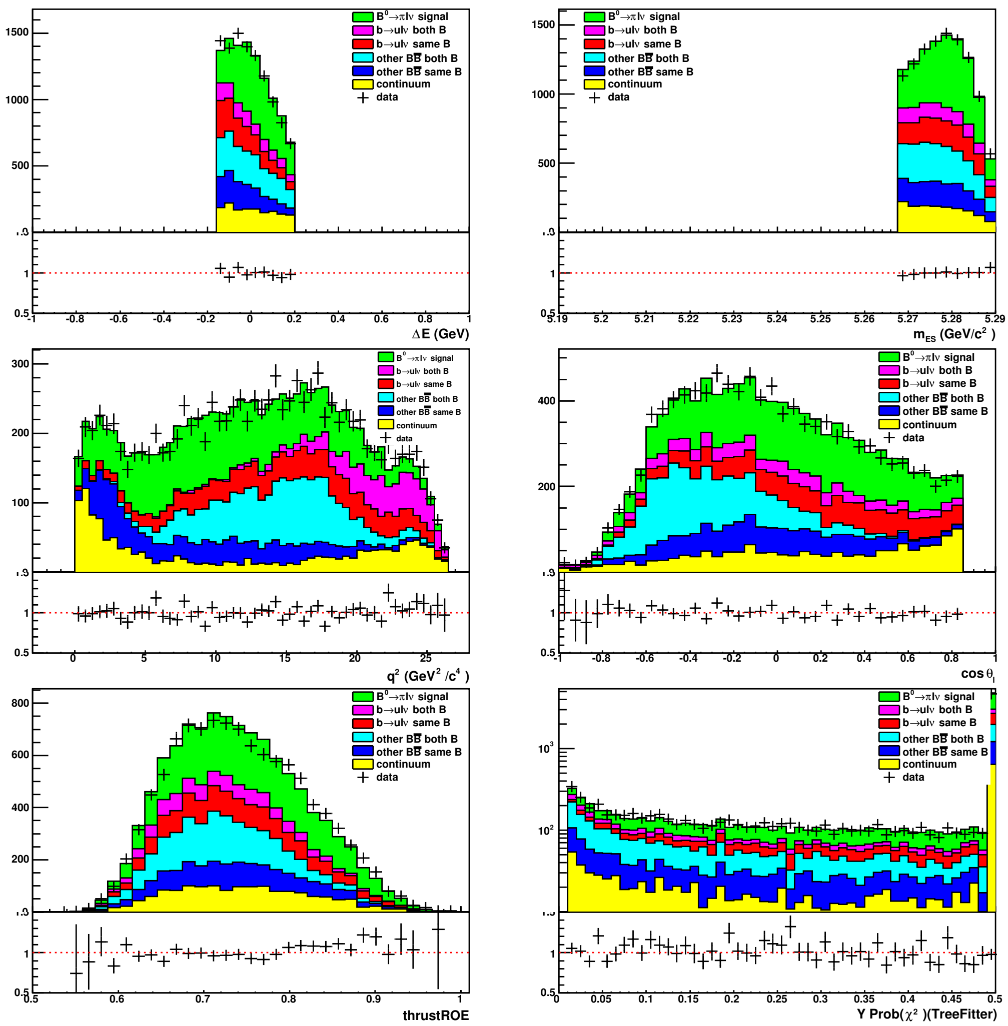

Figure 3.94 – Comparison of additional Y signal candidates related distributions obtained from the on-resonance data and MC simulation, both generated from the signal region of ΔE and m_{ES}, for $B^0 \to \pi^- \ell^+ \nu$, after applying all analysis cuts and MC simulation corrections.

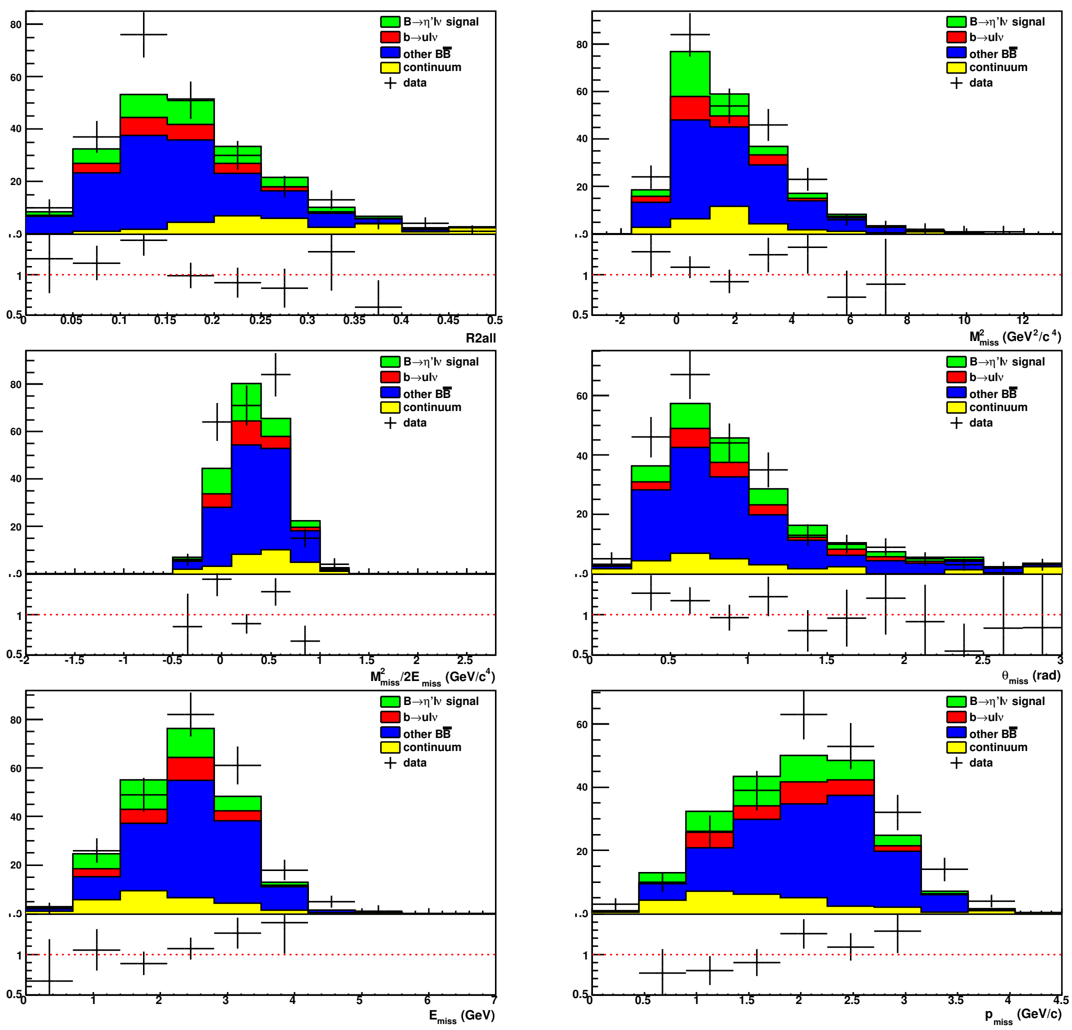

Figure 3.95 – Comparison of event variables' distributions obtained from the on-resonance data and MC simulation, both generated from the signal region of ΔE and m_{ES}, for $B^+ \to \eta^{'} \ell^+ \nu$ ($\gamma\gamma$ decay channel only), after applying all analysis cuts and MC simulation corrections.

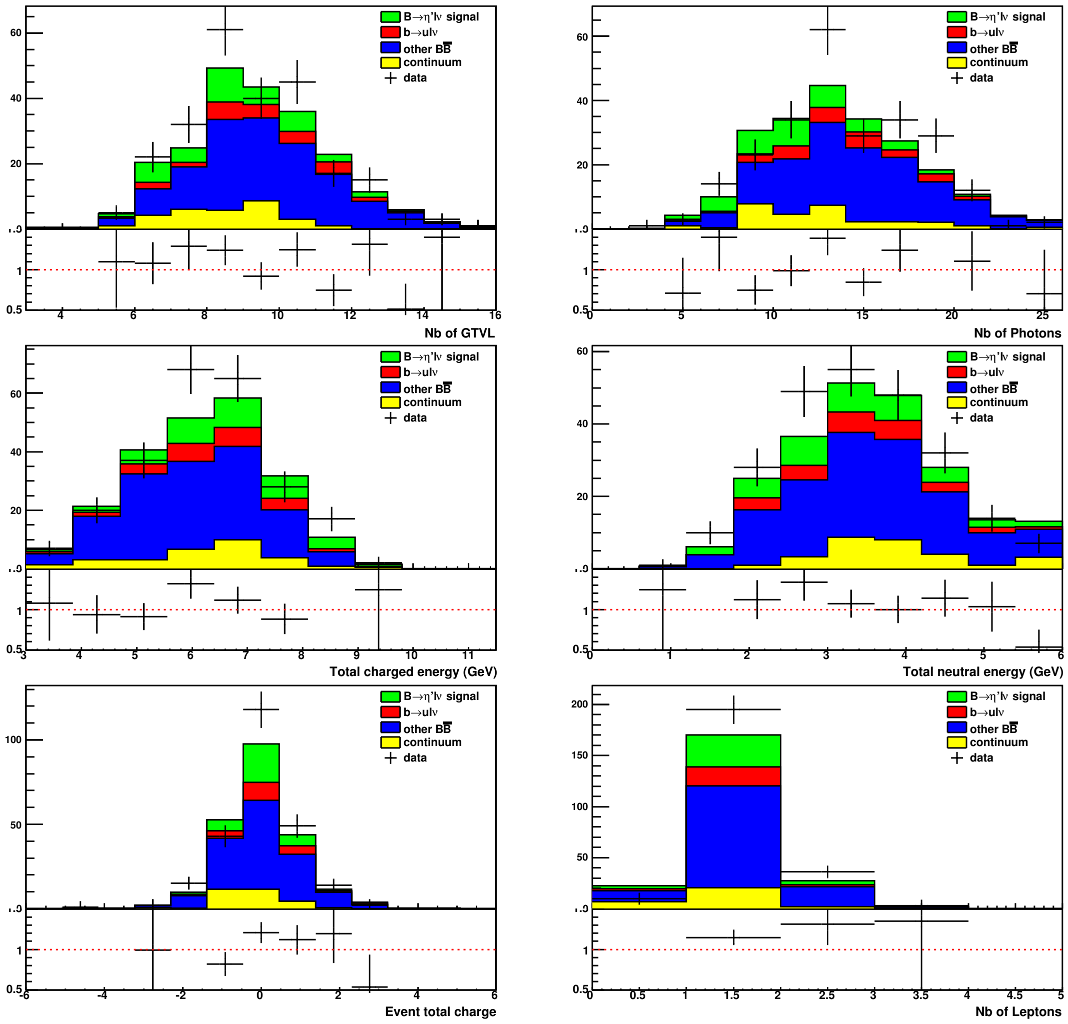

Figure 3.96 – Comparison of additional event variables' distributions obtained from the on-resonance data and MC simulation, both generated from the signal region of ΔE and m_{ES}, for $B^+ \to \eta' \ell^+ \nu$ ($\gamma\gamma$ decay channel only), after applying all analysis cuts and MC simulation corrections.

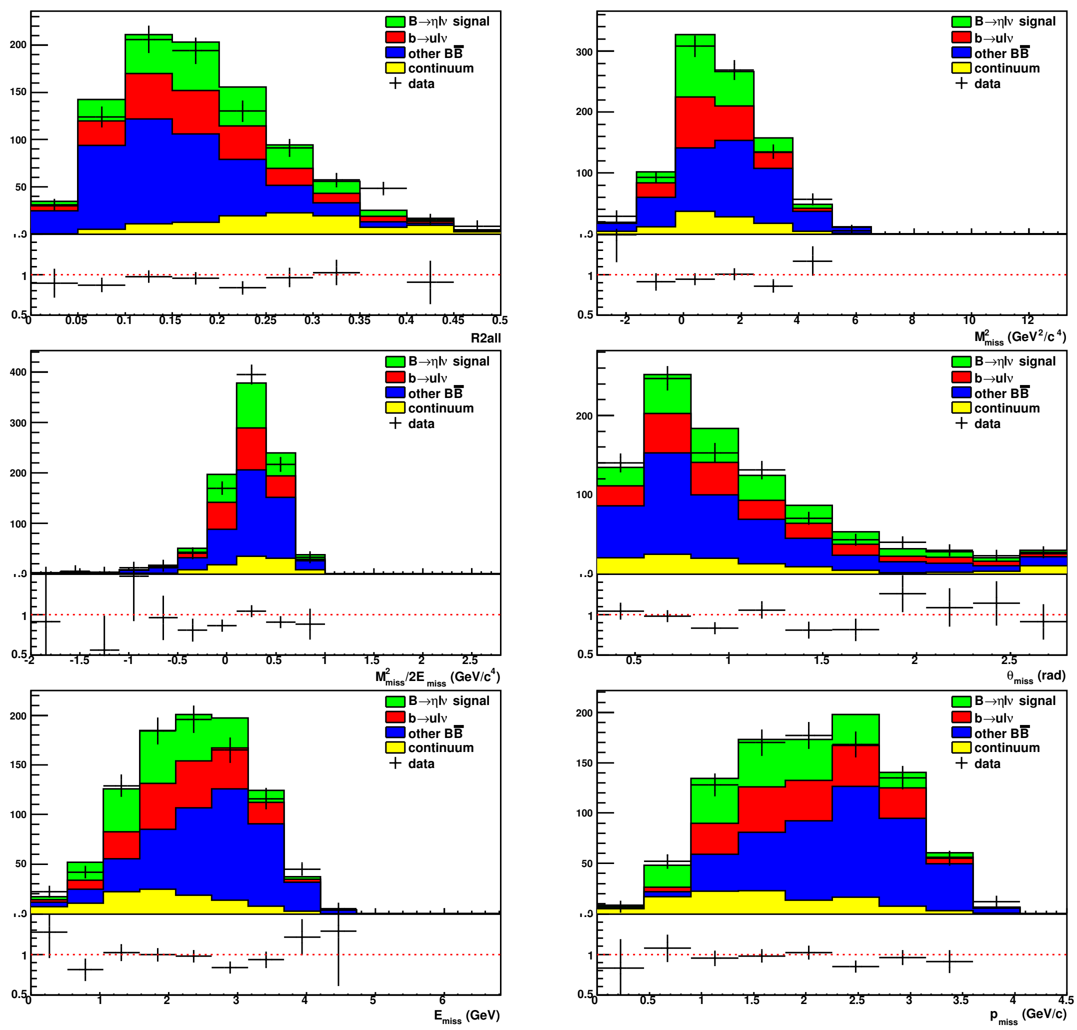

Figure 3.97 – Comparison of event variables' distributions obtained from the on-resonance data and MC simulation, both generated from the signal region of ΔE and m_{ES}, for $B^+ \to \eta\ell^+\nu$ ($\gamma\gamma$ decay channel only), after applying all analysis cuts and MC simulation corrections.

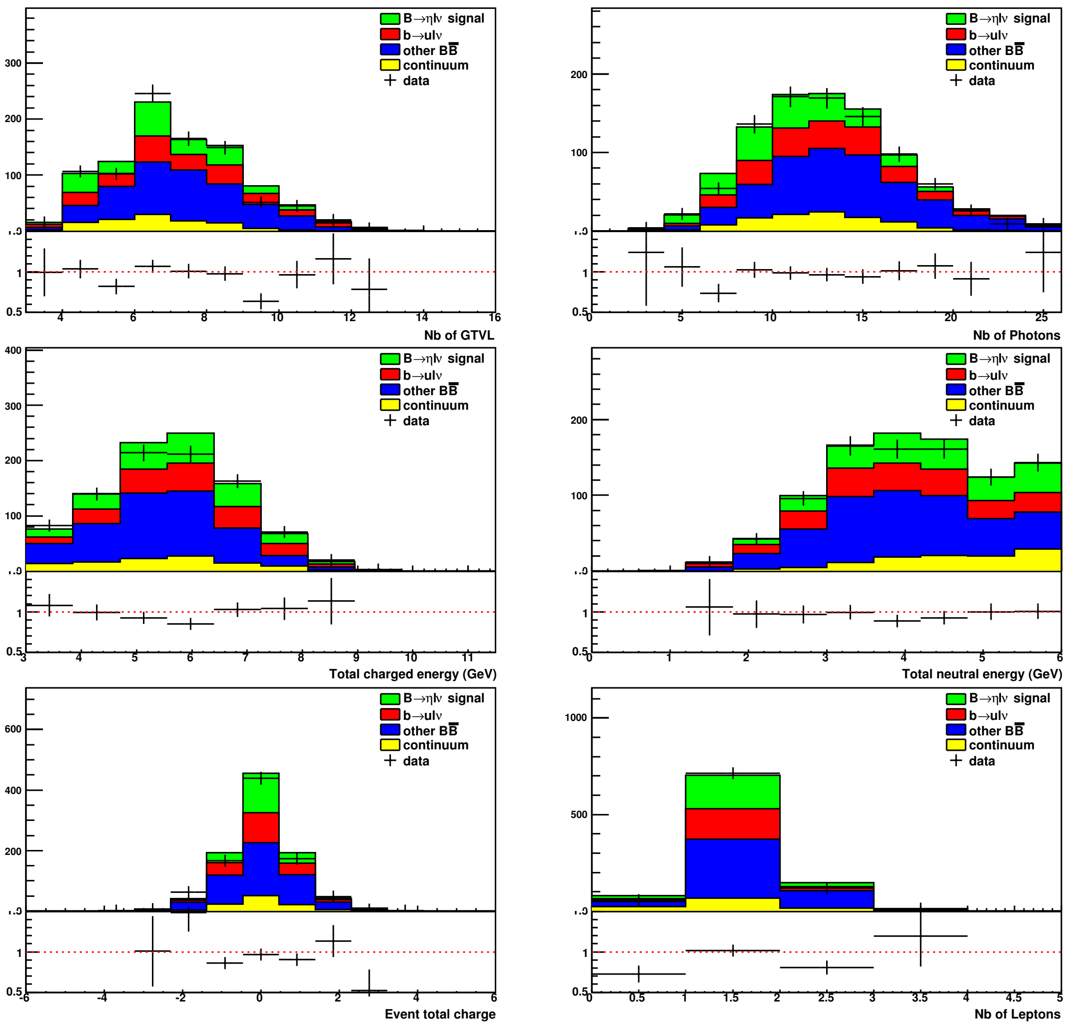

Figure 3.98 – Comparison of additional event variables' distributions obtained from the on-resonance data and MC simulation, both generated from the signal region of ΔE and m_{ES}, for $B^+ \to \eta \ell^+ \nu$ ($\gamma\gamma$ decay channel only), after applying all analysis cuts and MC simulation corrections.

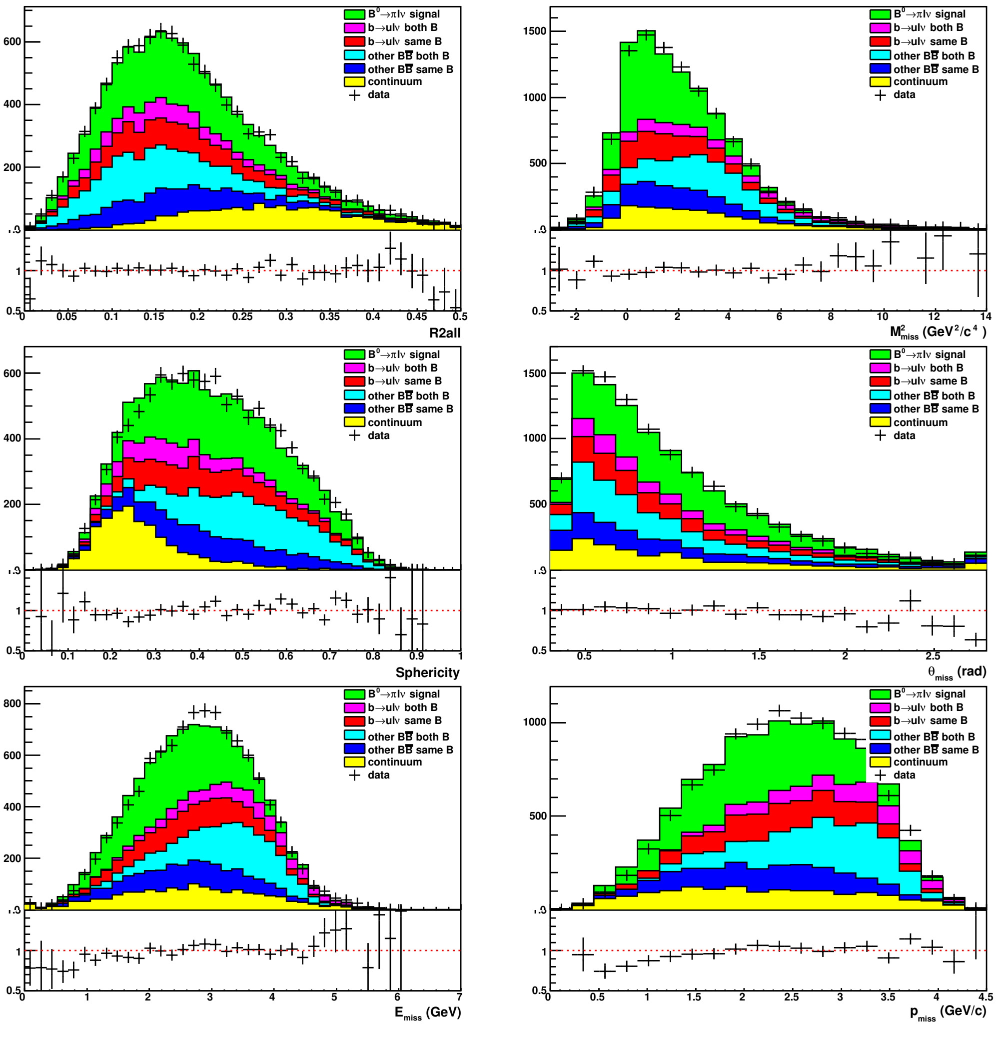

Figure 3.99 – Comparison of event variables' distributions obtained from the on-resonance data and MC simulation, both generated from the signal region of ΔE and m_{ES}, for $B^0 \to \pi^- \ell^+ \nu$, after applying all analysis cuts and MC simulation corrections.

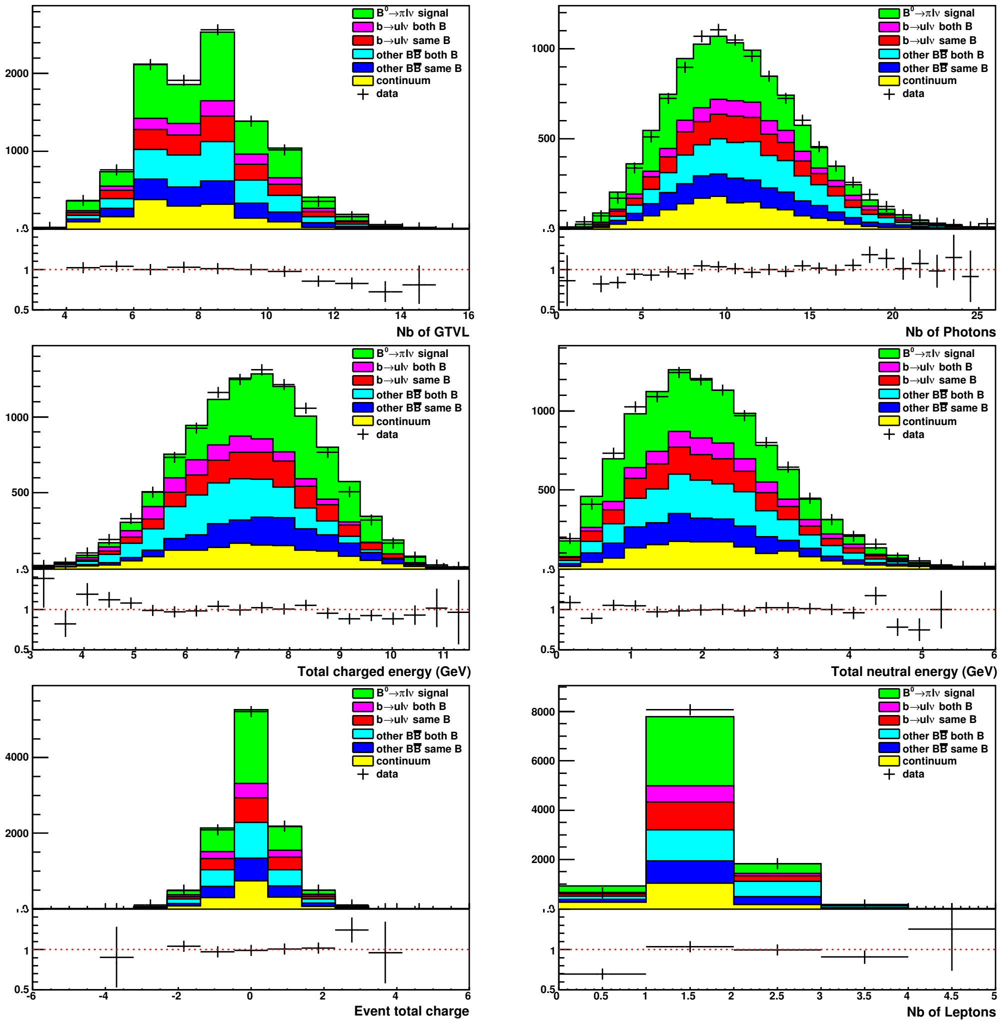

Figure 3.100 – Comparison of additional event variables' distributions obtained from the on-resonance data and MC simulation, both generated from the signal region of ΔE and m_{ES}, for $B^0 \to \pi^- \ell^+ \nu$, after applying all analysis cuts and MC simulation corrections.

3.9.2 Selection of q^2 binning configurations for the backgrounds in $B^0 \to \pi^- \ell^+ \nu$ decays

The three configurations discussed below are based on physics arguments. It is well known, as shown in Fig. 3.22, that the distributions for the $b \to u\ell\nu$ backgrounds are not the same as the backgrounds for other $B\bar{B}$. During our analysis, it was realized, as shown in Fig. 3.22, that the distributions for these backgrounds are also different depending on whether both meson and lepton come from the decay of the same B or when the lepton comes from one B decay and the meson from the other B decay. We must thus deal with at least 4 background categories to which we must of course add a category for the continuum background.

Now, although we do have some knowledge of Xulnu and Xclnu decays, that knowledge is far from precise. It is thus entirely justified to have at least 2 parameters for each category. This applies as well to the continuum background since even though we do have off-resonance data, this data is not sufficiently precise to allow us to fix it. In this latter case, two parameters are entirely justified as long as they remain within 1.5 sigma of the measured off-resonance data/continuum MC ratios, as indeed they do (scaling factors between 0.9 and 1.00, as given in Table 3.56, and a value of sigma of the order of 0.06, as shown in Fig. 3.101).

We can thus easily justify a configuration with 10 parameters. We also considered a configuration with 12 parameters (3 parameters each for the other $B\bar{B}$ same B and continuum backgrounds) for added flexibility. We also considered a configuration with 8 parameters where we reduced the number of parameters from two to one for the two background same B categories since these backgrounds may be somewhat better known than the backgrounds coming from the decay of both B.other. The results for the three configurations are given below where we analyzed the real data.

– 2 bins $b \to u\ell\nu$ same B and both B, 2 bins other $B\bar{B}$ both B, 3 bins each other $B\bar{B}$ same B and continuum, Fig. 3.102 :
  $BF = 1.415 \pm\ 0.052$, $\chi^2/ndof = 375.2/384$, $Prob(\chi^2) = 61.9\%$
  $|V_{ub}| \times 10^3 = 3.68$ (LCSR), 3.26 (HPQCD), 3.15 (FNAL)

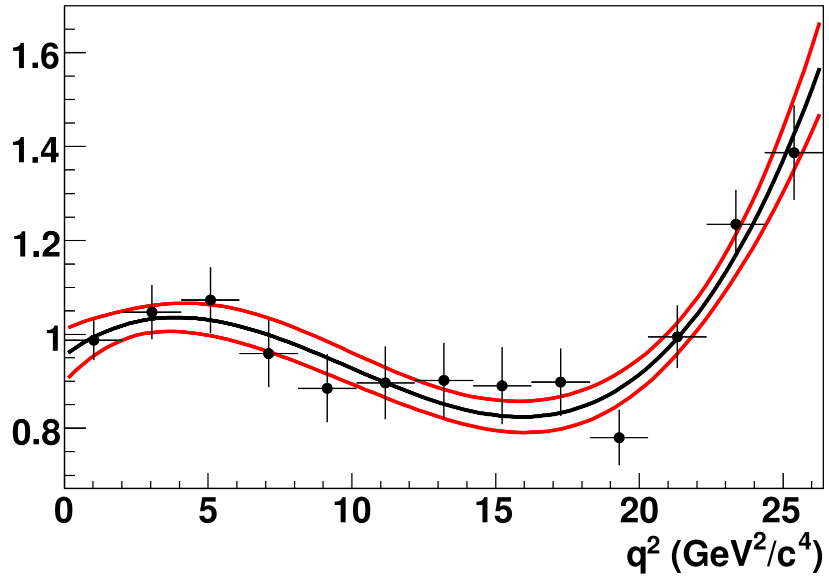

Figure 3.101 – Off-resonance Data/Continuum MC ratio of as a function of q^2 with $\pm$ 1 sigma curves shown in red. The black curve is the fit result to the ratios.

– 2 bins for each background category, Fig. 3.103 :

$BF = 1.423 \pm\ 0.050$, $\chi^2/ndof = 410.6/386$, $Prob(\chi^2) = 18.7\%$

$|V_{ub}| \times 10^3 =$ 3.69 (LCSR), 3.24 (HPQCD), 3.14 (FNAL)

– 1 bin $b \to u\ell\nu$ and other $B\bar{B}$ same B, 2 bins $b \to u\ell\nu$, other $B\bar{B}$ both B and continuum, Fig. 3.104 :

$BF = 1.409 \pm\ 0.048$, $\chi^2/ndof = 417.8/388$, $Prob(\chi^2) = 14.2\%$

$|V_{ub}| \times 10^3 =$ 3.68 (LCSR), 3.24 (HPQCD), 3.13 (FNAL)

As can be seen, all three results are entirely compatible with each other. The 10-parameter configuration yields the best value of χ^2 over the fit region. However, the 10- and 8-parameter configurations also yield reasonable values of χ^2. Since all three configurations considered yield essentially the same values of $|V_{ub}|$, we decided to select the 10-parameter configuration as a reasonable compromise between a very good value of χ^2 and a relatively small number of parameters.

Lack of statistics prevented us from probing different binning options for the $B^+ \to$

$\eta^{(')}\ell^+\nu$ decays. For these decays, the data for both B and same B backgrounds were combined into a single data set. The continuum was kept fixed for $B^+ \to \eta^{'}\ell^+\nu$ ($\gamma\gamma$ channel) and $B^+ \to \eta\ell^+\nu$ (3π channel) decays but was allowed to vary in 1 q^2 bin for $B^+ \to \eta\ell^+\nu$ ($\gamma\gamma$ channel) decays. The other $B\bar{B}$ background was varied in 1 q^2 bin in all three decay modes.

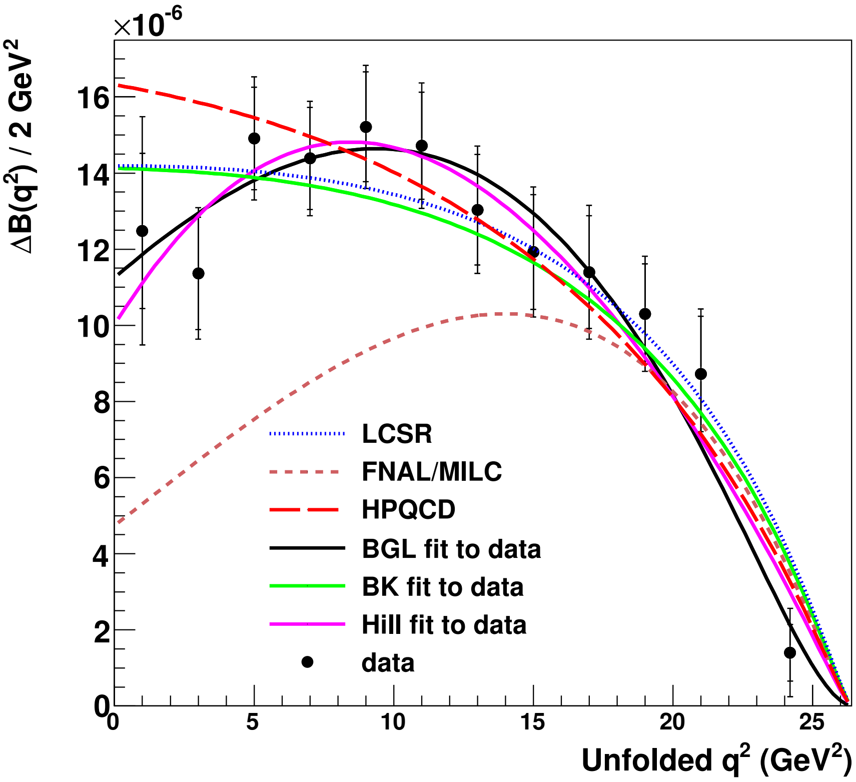

Figure 3.102 – Partial $\Delta\mathcal{B}(q^2)$ spectrum in 12 bins of q^2 for $B^0 \to \pi^- \ell^+ \nu$ decays using 12 backgound parameters. The smaller error bars are statistical only while the larger ones include systematic uncertainties. The solid black, green and pink curves show the results of the fit of the BGL, BK and Hill parametrizations to the data, respectively. The data are also compared to unquenched LQCD calculations (HPQCD and FNAL/MILC) [31, 32] and a LCSR calculation [55].

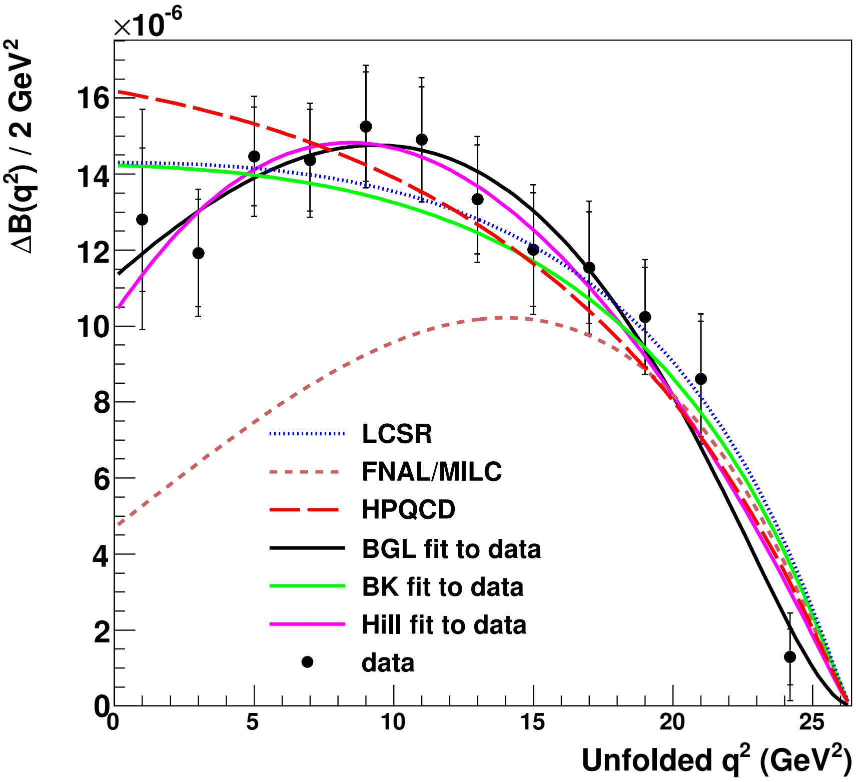

Figure 3.103 – Partial $\Delta\mathcal{B}(q^2)$ spectrum in 12 bins of q^2 for $B^0 \to \pi^- \ell^+ \nu$ decays using 10 backgound parameters. The smaller error bars are statistical only while the larger ones include systematic uncertainties. The solid black, green and pink curves show the results of the fit of the BGL, BK and Hill parametrizations to the data, respectively. The data are also compared to unquenched LQCD calculations (HPQCD and FNAL/MILC) [31, 32] and a LCSR calculation [55].

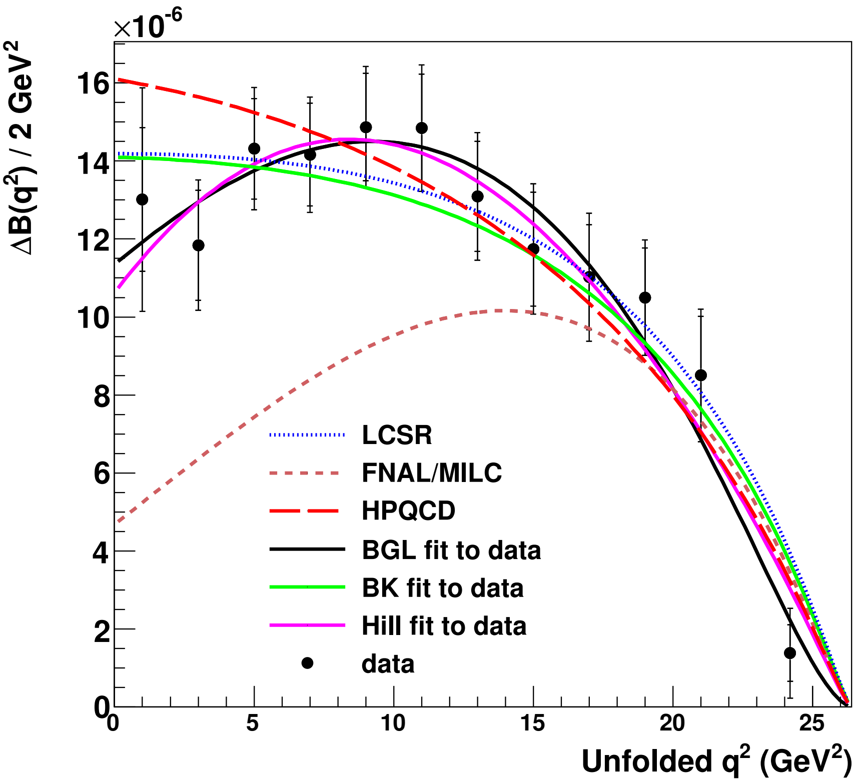

Figure 3.104 – Partial $\Delta\mathcal{B}(q^2)$ spectrum in 12 bins of q^2 for $B^0 \to \pi^- \ell^+ \nu$ decays using 8 backgound parameters. The smaller error bars are statistical only while the larger ones include systematic uncertainties. The solid black, green and pink curves show the results of the fit of the BGL, BK and Hill parametrizations to the data, respectively. The data are also compared to unquenched LQCD calculations (HPQCD and FNAL/MILC) [31, 32] and a LCSR calculation [55].

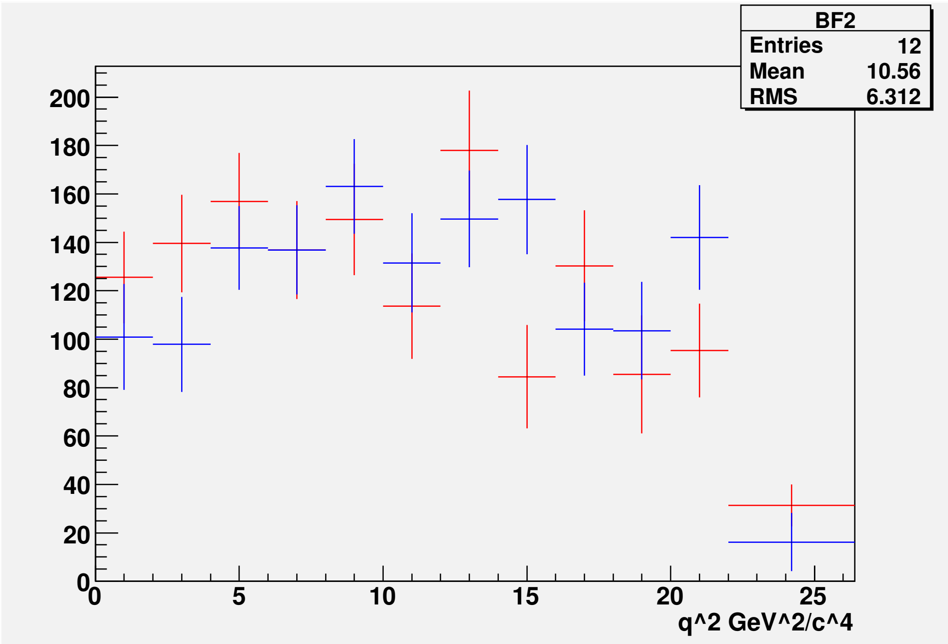

Figure 3.105 – Comparison of our $B^0 \to \pi^- \ell^+ \nu$ partial BFs (blue) with those from our previous analysis (red) for Runs 1-4 data.

3.9.3 Comparison of partial and total BFs values with those from our previous $B^0 \to \pi^- \ell^+ \nu$ analysis

The present value of BF=$1.44\pm$ 0.07 obtained for Runs 1-4 data, with the same background categories ($b \to u\ell\nu$, other $B\bar{B}$ and continuum) and the same q^2 binning (3 bins $b \to u\ell\nu$, 4 bins other $B\bar{B}$, each with a floating scaling factor and 1 bin fixed continuum) as in our previous analysis, is compatible with the previous result : BF=$1.46 \pm$ 0.07. In Fig. 3.105, we compare the values of the partial BF distribution over the full q^2 range with those obtained in our previous analysis. The agreement between the two shapes is acceptable. The slight difference between the BF values and the shapes arises from the fact that, in the present analysis, we used cuts optimized with Runs 1-6 data. When we use the same cuts as in our previous analysis, we obtain exactly the same value of BF=$1.46 \pm$ 0.08 for Runs 1-4 data.

3.9.4 BK fit comparison with our previous $B^0 \rightarrow \pi^- \ell^+ \nu$ analysis

We performed the Becirevic-Kaidalov (BK) fit to the partial BFs (without FSR). The value of $\alpha_{BK} = 0.50 \pm 0.05$ we obtain is in very good agreement with the value found in our previous anlalysis, $\alpha_{BK} = 0.52 \pm 0.06$. The fit (Fig. 3.73) with a value of $\chi^2 = 12.1/10$ is acceptable. More recent Hill and BGL parametrizations give much better fits, as shown in Fig. 3.73 and Table 74.

3.9.5 Results for electrons only or muons only in $B^0 \rightarrow \pi^- \ell^+ \nu$ decays

We extracted the total BF from a data set containing electrons only, muons only or both electrons and muons for Runs 1-6, for a given set of conditions. We obtain :

- For $B^0 \rightarrow \pi^- e^+ \nu$ decays : BF=$(1.50 \pm\ 0.06) \times 10^{-4}$
  For $B^0 \rightarrow \pi^- \mu^+ \nu$ decays : BF=$(1.46 \pm\ 0.08) \times 10^{-4}$
  For $B^0 \rightarrow \pi^- \ell^+ \nu$ decays : BF=$(1.47 \pm\ 0.05) \times 10^{-4}$
- For $B^+ \rightarrow \eta e^+ \nu$ decays : BF=$(0.40 \pm\ 0.07) \times 10^{-4}$
  For $B^+ \rightarrow \eta \mu^+ \nu$ decays : BF=$(0.30 \pm\ 0.07) \times 10^{-4}$
  For $B^+ \rightarrow \eta \ell^+ \nu$ decays : BF=$(0.37 \pm\ 0.05) \times 10^{-4}$
- For $B^+ \rightarrow \eta^{'} \ell^+ \nu$ decays : BF=$(0.23 \pm\ 0.07) \times 10^{-4}$

This test could not be carried out for $B^+ \rightarrow \eta^{'} \ell^+ \nu$ because of insufficient statistics for this channel.

It should be noted that the final values of the BFs are different from those above for the simple reason that the final set of conditions is not exactly the same as the one used in the present calculations. However, this does not detract from the fact that our results are similar regardless of the nature of the lepton involved.

3.9.6 Fit results in each of the ΔE-$m_{\rm ES}$ bins

In Figs. 3.106 and 3.107, we compare the MC distributions to the on-resonance data, before and after the fit, in each of the 34 ΔE-$m_{\rm ES}$ bins, for each bin of q^2 for the $B^0 \rightarrow \pi^- \ell^+ \nu$ decays. Similar results are obtained for $B^+ \rightarrow \eta \ell^+ \nu$ decays but are not shown in this document. There is a significant improvement in agreement between the data points and the MC predictions after the fit. To make it easier to see this effect, we also give the data/MC ratios, before and after the fit, in Figs. 3.108 and 3.109, respectively. These ratios are spread about the value of 1 after the fit, as expected when the fitting procedure works correctly. It is also apparent from these figures that nothing strange is happening in our analysis.

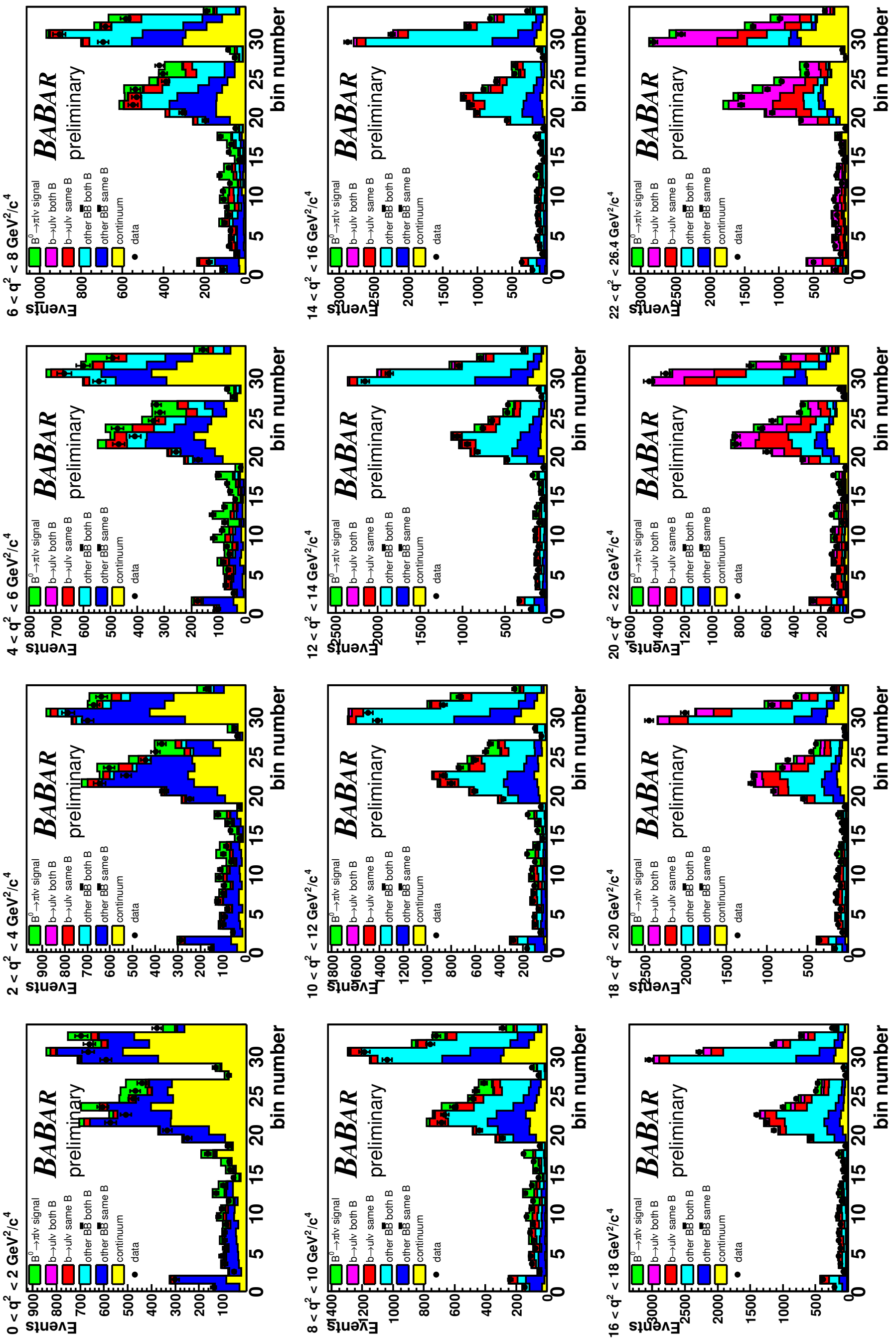

Figure 3.106 – Data and MC comparison in each of the 34 ΔE-$m_{\rm ES}$ bins for $B^0 \rightarrow \pi^-\ell^+\nu$ decays before the fit.

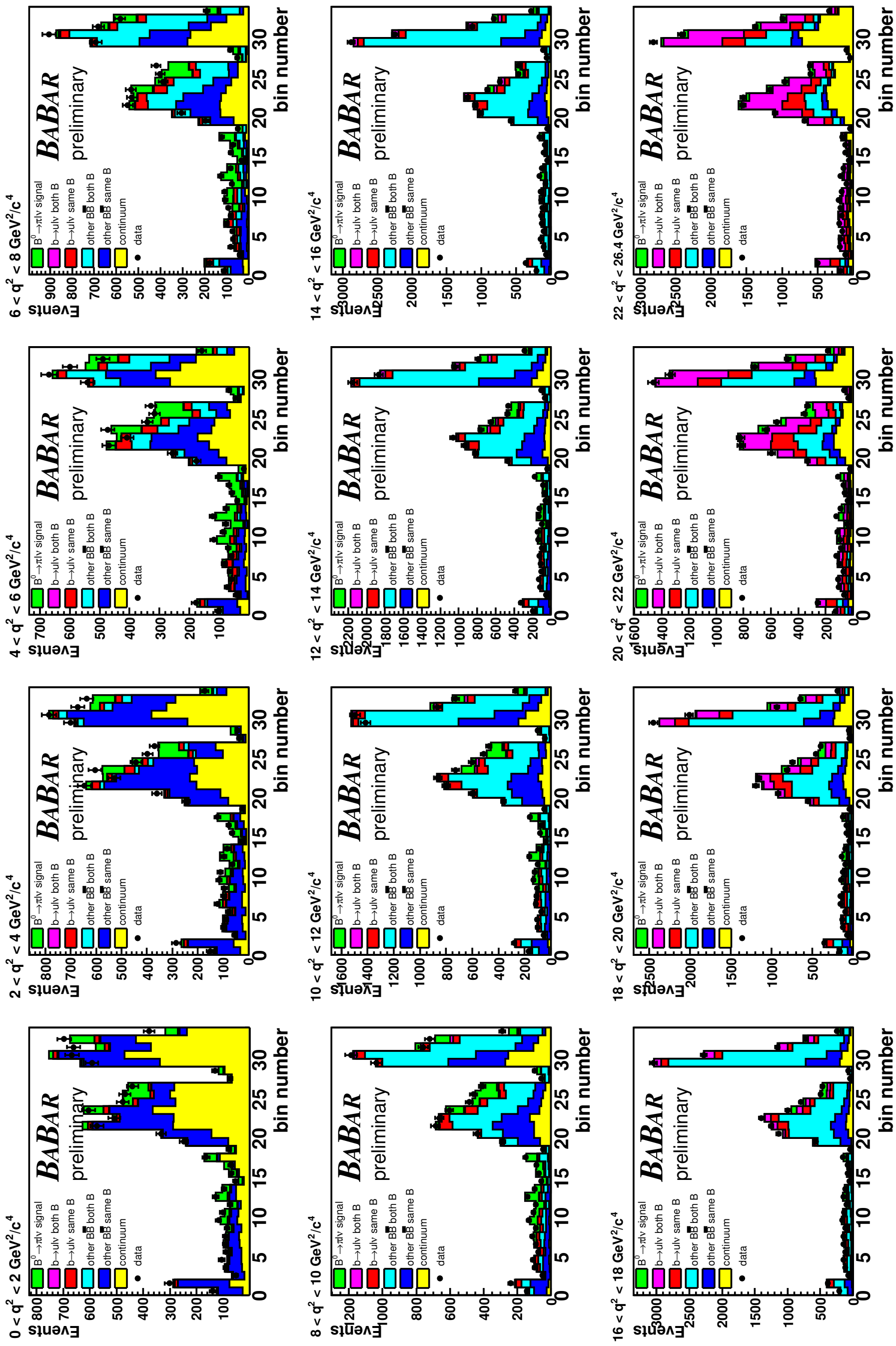

Figure 3.107 – Data and MC comparison in each of the 34 ΔE-m_{ES} bins for $B^0 \to \pi^-\ell^+\nu$ decays after the fit.

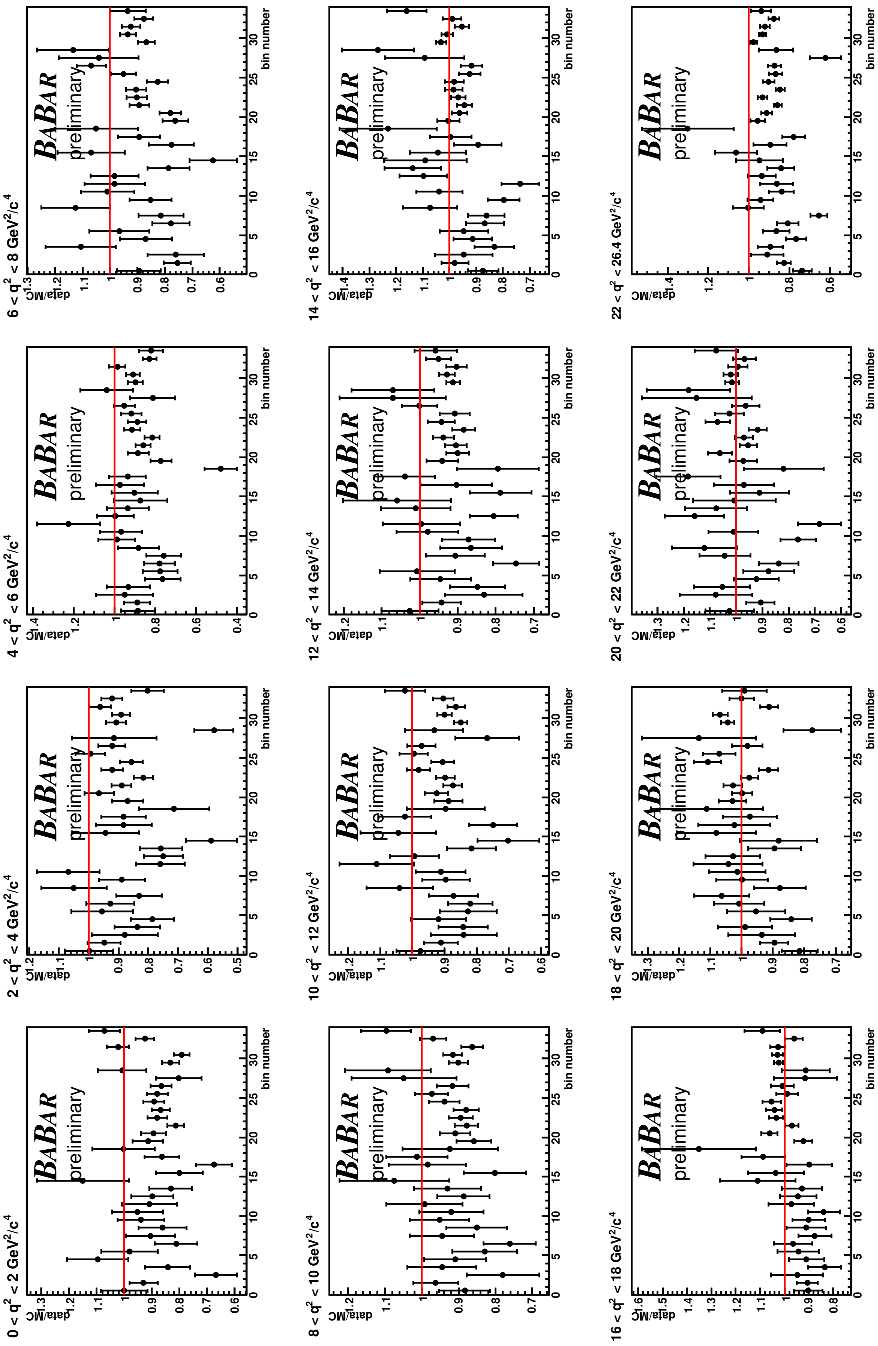

Figure 3.108 – Data/MC ratio in each of the 34 ΔE-m_{ES} bins for $B^0 \to \pi^- \ell^+ \nu$ decays before the fit.

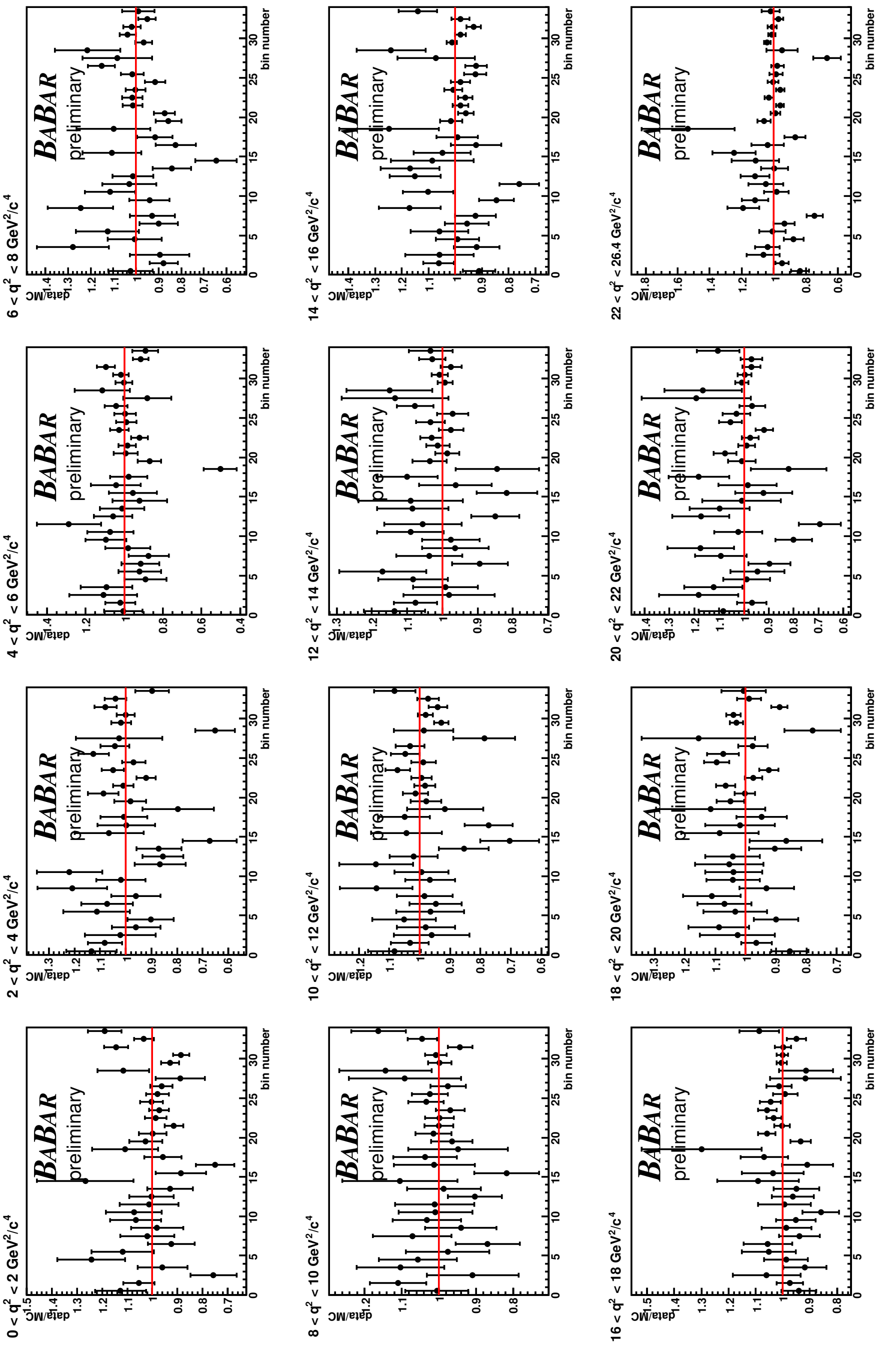

Figure 3.109 – Data/MC ratio in each of the 34 ΔE-$m_{\rm ES}$ bins for $B^0 \to \pi^- \ell^+ \nu$ decays after the fit.

3.10 Summary

Tableau 3.77 – Summary of the main results.

$\mathcal{B}(B^0 \to \pi^-\ell^+\nu) = (1.42 \pm 0.05_{stat} \pm 0.08_{syst}) \times 10^{-4}$
$\mathcal{B}(B^+ \to \eta\ell^+\nu) = (3.61 \pm 0.45_{stat} \pm 0.44_{syst}) \times 10^{-5}$
$\mathcal{B}(B^+ \to \eta^{'}\ell^+\nu) = (2.43 \pm 0.80_{stat} \pm 0.34_{syst}) \times 10^{-5}$
LCSR : $\lvert V_{ub}\rvert = \left(3.69 \pm 0.07_{stat} \pm 0.10_{syst}{}^{+0.54}_{-0.52}{}_{\mathrm{FF}}\right) \times 10^{-3}$
HPQCD : $\lvert V_{ub}\rvert = \left(3.24 \pm 0.13_{stat} \pm 0.16_{syst}{}^{+0.57}_{-0.37}{}_{\mathrm{FF}}\right) \times 10^{-3}$
FNAL : $\lvert V_{ub}\rvert = \left(3.14 \pm 0.12_{stat} \pm 0.16_{syst}{}^{+0.35}_{-0.29}{}_{\mathrm{FF}}\right) \times 10^{-3}$

We have measured the partial BFs of $B^+ \to \eta\ell^+\nu$ in 3 bins of q^2 and of $B^0 \to \pi^-\ell^+\nu$ in 12 bins of q^2. From these distributions, we extract the $f_+(q^2)$ shapes which are found to be compatible with all three theoretical predictions for the $B^0 \to \pi^-\ell^+\nu$ decays and with the LCSR calculation for the $B^+ \to \eta\ell^+\nu$ decays. The BGL parametrization fits our data well and allows us to obtain the value of $|V_{ub}f_+(0)|$.

The values of the partial BFs and their uncertainties in Table 3.61 together with the covariance matrices of the statistical and systematic uncertainties presented in Tables 3.72 and 3.73 allow the present data to be studied with different $f_+(q^2)$ parametrizations or compared to different QCD calculations. They also allow the use of our data in independent analyses that may lead to improved values of $|V_{ub}|$.

Our measured branching fractions of the three decays under study, summarized in Table 3.77, lead to a significant improvement in our knowledge of the composition of the inclusive charmless semileptonic decay rate. Our value of the total BF for $B^+ \to \eta^{'}\ell^+\nu$, with a significance of 2.7σ, is an order of magnitude smaller than the most recent CLEO result [35]. Our value of the total BF for $B^+ \to \eta\ell^+\nu$ supercedes a previous untagged BABAR result [78]. The ratio value of $\mathcal{B}(B^+ \to \eta^{'}\ell^+\nu)/\mathcal{B}(B^+ \to \eta\ell^+\nu) = 0.67 \pm 0.24_{stat} \pm 0.11_{syst}$ allows an important gluonic singlet contribution to the η' form factor. Our value of the total BF for $B^0 \to \pi^-\ell^+\nu$ is in very good agreement with previous BABAR results [39, 79] and has comparable precision to the present world average [24]. For $B^0 \to \pi^-\ell^+\nu$ decays, we obtain values of $|V_{ub}|$ for three different QCD calculations.

The three values are all acceptable according to our data and are consistent with the value measured in inclusive semileptonic decays : $|V_{ub}|$ = $\left(4.06 \pm 0.15_{exp}{}^{+0.25}_{-0.27}{}_{\mathrm{FF}}\right) \times 10^{-3}$ [24]. Furthermore, our results are also consistent with those of Ref. [79], a recent BABAR result based on an untagged analysis with an overlapping data set. At this time, we do not attempt to combine these highly correlated results. We defer this to a future paper.

[23] "CP violation and the CKM matrix", A. Höcker, Z. Ligeti, Ann. Rev. Nucl. Part. Sci. **56**, 501 (2006).

[24] Particle Data Group, C. Amsler *et al.*, Phys. Lett. **667**, 1 (2008).

[25] CKMfitter Group (J. Charles *et al.*), Eur. Phys. J. **C41**, 1-131 (2005). Updated results and plots available at : http ://ckmfitter.in2p3.fr.

[26] J.D. Richman and P.R. Burchat, Rev. Mod. Phys. **67**, 893 (1995).

[27] M. Kobayashi and T. Maskawa, Prog. Theor. Phys. **49**, 652 (1973).

[28] "$B \to \eta(')$ Form Factors in QCD", P. Ball and G. W. Jones, JHEP **08**, 025 (2007) [arXiv :hep-ph/0706.3628v2].

[29] D. Atwood and A. Soni, Phys. Lett. B **405**, 150 (1997) [arXiv :hep-ph/9704357] ;
A. L. Kagan and A. A. Petrov [arXiv :hep-ph/9707354] ;
M. R. Ahmady, E. Kou and A. Sugamoto, Phys. Rev. D **58**, 014015 (1998) [arXiv :hep-ph/9710509].

[30] "Reweighting of the form factors in exclusive $B \to X\ell\nu_\ell$ decays", D. Côté, BAD # 809 (2004).
D. Côté *et al.*, Eur. Phys. J. C **38**, 105 (2004).

[31] E. Gulez *et al.* (HPQCD Collaboration), Phys. Rev. **D73**, 074502 (2006).

[32] C. Bernard *et al.* (FNAL/MILC Collaboration), Phys. Rev. **D80**, 034026 (2009) ;R. Van de Water, private communication.

[33] Y. Y. Charng, T. Kurimoto and H. N. Li, Phys. Rev. D **74**, 074024 (2006) [arXiv :hep-ph/0304278] ;
Eur. Phys. J. C **30**, 367 (2003) [arXiv :hep-ph/0307092].

[34] J.P. Alexander *et al.* (CLEO collaboration), Phys. Rev. Lett. 77, 25 (1996).

[35] "Study of the q^2 dependence of $B \to \pi\ell\nu$ and $B \to \rho(\omega)\ell\nu$ decay and extraction of $|V_{ub}|$", S.B. Athar *et al* (CLEO collaboration), Phys. Rev. **D68**, 072003 (2003).

[36] "Study of $B \to \pi\ell\nu$ and $B \to \rho\ell\nu$ decays and determination of $|V_{ub}|$", B. Aubert *et al.* (BABAR Collaboration), Phys. Rev. **D72** 051102 (2005) ; "Measurement of Untagged Exclusive Charmless Semileptonic Decays $B \to \pi(\rho)\ell\nu$", A. Weinstein, J. Dingfelder, E. Elsen, M. Kelsey, V. Lüth, BAD # 531 (2005).

[37] B. Aubert *et al.* (BABAR Collaboration), Phys. Rev. Lett. **97**, 211801 (2006).

[38] "Measurements of branching fractions and q^2 distributions for $B \to \pi\ell\nu$ and $B \to \rho\ell\nu$ decays with $B \to D(^*)\ell\nu$ decay tagging", T. Hokuue *et al.* (Belle Collaboration), Phys. Lett. **B648**, 139 (2007).

[39] B. Aubert *et al.* (BABAR Collaboration), Phys. Rev. Lett. **98**, 091801 (2007).

[40] "Choice of Kinematic Variables in B Meson Reconstruction—Take 3", W. Ford, BAD # 53 (2000).

[41] "XSLBtoXulnuFilter : Exclusive semileptonic b $\to$ u skim", S. Brunet, D. Côté, M.G. Greene, BAD # 740 V8 (2005).

[42] "Measurement of the Number of Υ_{4S} Mesons Produced in Run 1 (B Counting)", C. Hearty, BAD # 134 (2001).

[43] http ://www.slac.stanford.edu/xorg/hfag/

[44] BABAR physics book.

[45] Prescription from BABAR's tau AWG.

[46] G.C. Fox and S. Wolfram, Phys. Rev. Lett. **41**, 1581 (1978).

[47] W. D. Hulsbergen, Nucl. Instrum. Meth. **A552**, 566 (2005).

[48] "Measurement of $B \to D^*$ Form Factors in the Semileptonic Decay $\bar{B}^0 \to D^{*+}\ell^-\bar{\nu}$", M.S. Gill, A. Snyder, BAD #943 V14 (2004).

[49] Private communication with Arthur E. Snyder.

[50] R. J. Barlow and C. Beeston, Comput. Phys. Commun. **77**, 219 (1993).

[51] "ROOT - An Object Oriented Data Analysis Framework", R. Brun and F. Rademakers, Nucl. Instrum. Meth. **A389**, 81-86 (1997).
Also see : http ://root.cern.ch/.

[52] D. Becirevic and A. B. Kaidalov, Phys. Lett. **B478**, 417 (2000).

[53] T. Becher and R. J. Hill, Phys. Lett. **B633**, 61 (2006).

[54] C. G. Boyd, B. Grinstein and R. F. Lebed, Phys. Rev. Lett. **74**, 4603 (1995). hep-ph/9412324 C. G. Boyd and M. J. Savage, Phys. Rev. D **56**, 303 (1997). hep-ph/9702300

[55] G. Duplancic, A. Khodjamirian, T. Mannel, B. Melic and N. Offen, JHEP **804**, 14 (2008) ; A. Khodjamirian, private communication.

[56] http ://www.slac.stanford.edu/BFROOT/www/Physics/Tools/generators/2004-update/btou_BR.gif

[57] D. Scora, N. Isgur, Phys. Rev. **D52** 2783 (1995).

[58] "$B_{d,s} \to \rho, \omega, K^*, \phi$ Decay Form Factors from Light-Cone Sum Rules Revisited", P. Ball, R. Zwicky, Phys. Rev. **D71** 014029 (2005).

[59] I.Caprini, L.Lellouch, M.Neubert, Nucl. Phys. **B530**, 153 (1998).

[60] B. Aubert *et al.* (BABAR Collaboration), Phys. Rev. **D74**, 092004 (2006).

[61] http ://www.slac.stanford.edu/BFROOT/www/Physics/Analysis/AWG/InclusiveSL/common/dominique_hybrid.html/hybrid_1.4.html

[62] http ://www.slac.stanford.edu/$\sim$lodovico/protected/vub/hybrid.html

[63] O.L. Buchmüller, H.U. Flächer, Phys. Rev. **D73**, 073008 (2006).

[64] http ://www.slac.stanford.edu/BFROOT/www/Physics/Tools/Pid/PidOnMc/pidonmc.html

[65] http ://www.slac.stanford.edu/BFROOT/www/Physics/TrackEfficTaskForce/TrackingTaskForce-2004.html

[66] http ://www.slac.stanford.edu/BFROOT/www/Physics/Analysis/AWG/Neutrals/validation/recipe22.html

[67] "K_S production spectra", W. Wulsin, J. Dingfelder, BAD #1642 (2009).

[68] "Study of K_L^0 efficiency and reconstruction using data samples", M. Bona, D. Côté, G. Cavoto, E. Di Marco, M. Pelliccioni, M. Pierini, BAD #1191 V3 (2006).

[69] GEANT4 Collaboration, S. Agostinelli *et al.*, Nucl. Instrum. Methods **A506**, 250 (2003).

[70] http ://www.slac.stanford.edu/∼tbrandt/pid/sys/pidsys.pdf

[71] http ://roofit.sourceforge.net/

[72] Private communication with R. Zwicky.
http ://babar-hn.slac.stanford.edu :
5090/HyperNews/get/semi_lept_decays/380.html

[73] E. Barberio and Z. Was, Comput. Phys. Commun. **79**, 291 (1994).

[74] E. Richter-Was *et al.*, Phys. Lett. **B303**, 163 (1993).

[75] A. Budkin, V. Golubev, V. Luth, Y. Skopven, BAD #755, v19 (2005).

[76] "Measurement of the $B^0 \to \pi^- \ell^+ \nu$ form-factor shape and branching fraction, and determination of $|V_{ub}|$ with a loose neutrino reconstruction technique", D. Côté, S. Brunet, M. Simard, P. Taras, B. Viaud, BAD #1313, v11 (2007).

[77] "How to evaluate the goodness of the fit ?", B. Viaud, http ://www.slac.stanford.edu/BFROOT/www/doc/BbrMeetingOrganizer/vol01/dev/ mtg000312/itm0001463/LooseNuReco.pdf, p. 9-13.

[78] B. Aubert *et al.*, Phys. Rev. **D79**, 052011 (2009).

[79] P. del Amo Sanchez *et al.* (BABAR Collaboration), arXiv :1005.3288, submitted to Phys. Rev. **D**.

CHAPITRE 4

ARTICLE PUBLIÉ DANS PHYSICAL REVIEW D : MEASUREMENT OF THE $B^0 \to \pi^- \ell^+ \nu$ AND $B^+ \to \eta^{(\prime)} \ell^+ \nu$ BRANCHING FRACTIONS, THE $B^0 \to \pi^- \ell^+ \nu$ AND $B^+ \to \eta \ell^+ \nu$ FORM-FACTOR SHAPES, AND DETERMINATION OF $|V_{UB}|$

P. del Amo Sanchez,[1] J. P. Lees,[1] V. Poireau,[1] E. Prencipe,[1] V. Tisserand,[1] J. Garra Tico,[2] E. Grauges,[2] M. Martinelli[ab],[3] D. A. Milanes,[3] A. Palano[ab],[3] M. Pappagallo[ab],[3] G. Eigen,[4] B. Stugu,[4] L. Sun,[4] D. N. Brown,[5] L. T. Kerth,[5] Yu. G. Kolomensky,[5] G. Lynch,[5] I. L. Osipenkov,[5] H. Koch,[6] T. Schroeder,[6] D. J. Asgeirsson,[7] C. Hearty,[7] T. S. Mattison,[7] J. A. McKenna,[7] A. Khan,[8] A. Randle-Conde,[8] V. E. Blinov,[9] A. R. Buzykaev,[9] V. P. Druzhinin,[9] V. B. Golubev,[9] E. A. Kravchenko,[9] A. P. Onuchin,[9] S. I. Serednyakov,[9] Yu. I. Skovpen,[9] E. P. Solodov,[9] K. Yu. Todyshev,[9] A. N. Yushkov,[9] M. Bondioli,[10] S. Curry,[10] D. Kirkby,[10] A. J. Lankford,[10] M. Mandelkern,[10] E. C. Martin,[10] D. P. Stoker,[10] H. Atmacan,[11] J. W. Gary,[11] F. Liu,[11] O. Long,[11] G. M. Vitug,[11] C. Campagnari,[12] T. M. Hong,[12] D. Kovalskyi,[12] J. D. Richman,[12] C. West,[12] A. M. Eisner,[13] C. A. Heusch,[13] J. Kroseberg,[13] W. S. Lockman,[13] A. J. Martinez,[13] T. Schalk,[13] B. A. Schumm,[13] A. Seiden,[13] L. O. Winstrom,[13] C. H. Cheng,[14] D. A. Doll,[14] B. Echenard,[14] D. G. Hitlin,[14] P. Ongmongkolkul,[14] F. C. Porter,[14] A. Y. Rakitin,[14] R. Andreassen,[15] M. S. Dubrovin,[15] G. Mancinelli,[15] B. T. Meadows,[15] M. D. Sokoloff,[15] P. C. Bloom,[16] W. T. Ford,[16] A. Gaz,[16] M. Nagel,[16] U. Nauenberg,[16] J. G. Smith,[16] S. R. Wagner,[16] R. Ayad,[17,*1] W. H. Toki,[17] H. Jasper,[18] T. M. Karbach,[18] A. Petzold,[18] B. Spaan,[18] M. J. Kobel,[19] K. R. Schubert,[19] R. Schwierz,[19] D. Bernard,[20] M. Verderi,[20] P. J. Clark,[21] S. Playfer,[21] J. E. Watson,[21] M. Andreotti[ab],[22] D. Bettoni[a],[22] C. Bozzi[a],[22] R. Calabrese[ab],[22] A. Cecchi[ab],[22] G. Cibinetto[ab],[22] E. Fioravanti[ab],[22] P. Franchini[ab],[22] E. Luppi[ab],[22] M. Munerato[ab],[22] M. Negrini[ab],[22] A. Petrella[ab],[22] L. Piemontese[a],[22] R. Baldini-Ferroli,[23] A. Calcaterra,[23] R. de Sangro,[23] G. Finocchiaro,[23] M. Nicolaci,[23] S. Pacetti,[23] P. Patteri,[23] I. M. Peruzzi,[23,*2] M. Piccolo,[23] M. Rama,[23] A. Zallo,[23] R. Contri[ab],[24] E. Guido[ab],[24]

M. Lo Vetere[ab],[24] M. R. Monge[ab],[24] S. Passaggio[a],[24] C. Patrignani[ab],[24] E. Robutti[a],[24]
S. Tosi[ab],[24] B. Bhuyan,[25] V. Prasad,[25] C. L. Lee,[26] M. Morii,[26] A. Adametz,[27]
J. Marks,[27] U. Uwer,[27] F. U. Bernlochner,[28] M. Ebert,[28] H. M. Lacker,[28] T. Lueck,[28]
A. Volk,[28] P. D. Dauncey,[29] M. Tibbetts,[29] P. K. Behera,[30] U. Mallik,[30] C. Chen,[31]
J. Cochran,[31] H. B. Crawley,[31] L. Dong,[31] W. T. Meyer,[31] S. Prell,[31] E. I. Rosenberg,[31]
A. E. Rubin,[31] A. V. Gritsan,[32] Z. J. Guo,[32] N. Arnaud,[33] M. Davier,[33] D. Derkach,[33]
J. Firmino da Costa,[33] G. Grosdidier,[33] F. Le Diberder,[33] A. M. Lutz,[33] B. Malaescu,[33]
A. Perez,[33] P. Roudeau,[33] M. H. Schune,[33] J. Serrano,[33] V. Sordini,[33,*3]A. Stocchi,[33]
L. Wang,[33] G. Wormser,[33] D. J. Lange,[34] D. M. Wright,[34] I. Bingham,[35]
C. A. Chavez,[35] J. P. Coleman,[35] J. R. Fry,[35] E. Gabathuler,[35] R. Gamet,[35]
D. E. Hutchcroft,[35] D. J. Payne,[35] C. Touramanis,[35] A. J. Bevan,[36] F. Di Lodovico,[36]
R. Sacco,[36] M. Sigamani,[36] G. Cowan,[37] S. Paramesvaran,[37] A. C. Wren,[37]
D. N. Brown,[38] C. L. Davis,[38] A. G. Denig,[39] M. Fritsch,[39] W. Gradl,[39] A. Hafner,[39]
K. E. Alwyn,[40] D. Bailey,[40] R. J. Barlow,[40] G. Jackson,[40] G. D. Lafferty,[40]
J. Anderson,[41] R. Cenci,[41] A. Jawahery,[41] D. A. Roberts,[41] G. Simi,[41] J. M. Tuggle,[41]
C. Dallapiccola,[42] E. Salvati,[42] R. Cowan,[43] D. Dujmic,[43] G. Sciolla,[43] M. Zhao,[43]
D. Lindemann,[44] P. M. Patel,[44] S. H. Robertson,[44] M. Schram,[44] P. Biassoni[ab],[45]
A. Lazzaro[ab],[45] V. Lombardo[a],[45] F. Palombo[ab],[45] S. Stracka[ab],[45] L. Cremaldi,[46]
R. Godang,[46,*4]R. Kroeger,[46] P. Sonnek,[46] D. J. Summers,[46] X. Nguyen,[47] M. Simard,[47]
P. Taras,[47] G. De Nardo[ab],[48] D. Monorchio[ab],[48] G. Onorato[ab],[48] C. Sciacca[ab],[48]
G. Raven,[49] H. L. Snoek,[49] C. P. Jessop,[50] K. J. Knoepfel,[50] J. M. LoSecco,[50]
W. F. Wang,[50] L. A. Corwin,[51] K. Honscheid,[51] R. Kass,[51] J. P. Morris,[51]
N. L. Blount,[52] J. Brau,[52] R. Frey,[52] O. Igonkina,[52] J. A. Kolb,[52] R. Rahmat,[52]
N. B. Sinev,[52] D. Strom,[52] J. Strube,[52] E. Torrence,[52] G. Castelli[ab],[53] E. Feltresi[ab],[53]
N. Gagliardi[ab],[53] M. Margoni[ab],[53] M. Morandin[a],[53] M. Posocco[a],[53] M. Rotondo[a],[53]
F. Simonetto[ab],[53] R. Stroili[ab],[53] E. Ben-Haim,[54] G. R. Bonneaud,[54] H. Briand,[54]
G. Calderini,[54] J. Chauveau,[54] O. Hamon,[54] Ph. Leruste,[54] G. Marchiori,[54] J. Ocariz,[54]
J. Prendki,[54] S. Sitt,[54] M. Biasini[ab],[55] E. Manoni[ab],[55] A. Rossi[ab],[55] C. Angelini[ab],[56]
G. Batignani[ab],[56] S. Bettarini[ab],[56] M. Carpinelli[ab],[56,*5]G. Casarosa[ab],[56] A. Cervelli[ab],[56]
F. Forti[ab],[56] M. A. Giorgi[ab],[56] A. Lusiani[ac],[56] N. Neri[ab],[56] E. Paoloni[ab],[56] G. Rizzo[ab],[56]

J. J. Walsh[a],[56] D. Lopes Pegna,[57] C. Lu,[57] J. Olsen,[57] A. J. S. Smith,[57] A. V. Telnov,[57] F. Anulli[a],[58] E. Baracchini[ab],[58] G. Cavoto[a],[58] R. Faccini[ab],[58] F. Ferrarotto[a],[58] F. Ferroni[ab],[58] M. Gaspero[ab],[58] L. Li Gioi[a],[58] M. A. Mazzoni[a],[58] G. Piredda[a],[58] F. Renga[ab],[58] T. Hartmann,[59] T. Leddig,[59] H. Schröder,[59] R. Waldi,[59] T. Adye,[60] B. Franek,[60] E. O. Olaiya,[60] F. F. Wilson,[60] S. Emery,[61] G. Hamel de Monchenault,[61] G. Vasseur,[61] Ch. Yèche,[61] M. Zito,[61] M. T. Allen,[62] D. Aston,[62] D. J. Bard,[62] R. Bartoldus,[62] J. F. Benitez,[62] C. Cartaro,[62] M. R. Convery,[62] J. Dorfan,[62] G. P. Dubois-Felsmann,[62] W. Dunwoodie,[62] R. C. Field,[62] M. Franco Sevilla,[62] B. G. Fulsom,[62] A. M. Gabareen,[62] M. T. Graham,[62] P. Grenier,[62] C. Hast,[62] W. R. Innes,[62] M. H. Kelsey,[62] H. Kim,[62] P. Kim,[62] M. L. Kocian,[62] D. W. G. S. Leith,[62] S. Li,[62] B. Lindquist,[62] S. Luitz,[62] H. L. Lynch,[62] D. B. MacFarlane,[62] H. Marsiske,[62] D. R. Muller,[62] H. Neal,[62] S. Nelson,[62] C. P. O'Grady,[62] I. Ofte,[62] M. Perl,[62] T. Pulliam,[62] B. N. Ratcliff,[62] A. Roodman,[62] A. A. Salnikov,[62] V. Santoro,[62] R. H. Schindler,[62] J. Schwiening,[62] A. Snyder,[62] D. Su,[62] M. K. Sullivan,[62] S. Sun,[62] K. Suzuki,[62] J. M. Thompson,[62] J. Va'vra,[62] A. P. Wagner,[62] M. Weaver,[62] W. J. Wisniewski,[62] M. Wittgen,[62] D. H. Wright,[62] H. W. Wulsin,[62] A. K. Yarritu,[62] C. C. Young,[62] V. Ziegler,[62] X. R. Chen,[63] W. Park,[63] M. V. Purohit,[63] R. M. White,[63] J. R. Wilson,[63] S. J. Sekula,[64] M. Bellis,[65] P. R. Burchat,[65] A. J. Edwards,[65] T. S. Miyashita,[65] S. Ahmed,[66] M. S. Alam,[66] J. A. Ernst,[66] B. Pan,[66] M. A. Saeed,[66] S. B. Zain,[66] N. Guttman,[67] A. Soffer,[67] P. Lund,[68] S. M. Spanier,[68] R. Eckmann,[69] J. L. Ritchie,[69] A. M. Ruland,[69] C. J. Schilling,[69] R. F. Schwitters,[69] B. C. Wray,[69] J. M. Izen,[70] X. C. Lou,[70] F. Bianchi[ab],[71] D. Gamba[ab],[71] M. Pelliccioni[ab],[71] M. Bomben[ab],[72] L. Lanceri[ab],[72] L. Vitale[ab],[72] N. Lopez-March,[73] F. Martinez-Vidal,[73] A. Oyanguren,[73] J. Albert,[74] Sw. Banerjee,[74] H. H. F. Choi,[74] K. Hamano,[74] G. J. King,[74] R. Kowalewski,[74] M. J. Lewczuk,[74] C. Lindsay,[74] I. M. Nugent,[74] J. M. Roney,[74] R. J. Sobie,[74] T. J. Gershon,[75] P. F. Harrison,[75] T. E. Latham,[75] E. M. T. Puccio,[75] H. R. Band,[76] S. Dasu,[76] K. T. Flood,[76] Y. Pan,[76] R. Prepost,[76] C. O. Vuosalo,[76] S. L. Wu.[76]

(The BABAR Collaboration)

[1]Laboratoire d'Annecy-le-Vieux de Physique des Particules (LAPP), Université de

Savoie, CNRS/IN2P3, F-74941 Annecy-Le-Vieux, France, [2]Universitat de Barcelona, Facultat de Fisica, Departament ECM, E-08028 Barcelona, Spain, [3]INFN Sezione di Bari[a] ; Dipartimento di Fisica, Università di Bari[b], I-70126 Bari, Italy, [4]University of Bergen, Institute of Physics, N-5007 Bergen, Norway, [5]Lawrence Berkeley National Laboratory and University of California, Berkeley, California 94720, USA, [6]Ruhr Universität Bochum, Institut für Experimentalphysik 1, D-44780 Bochum, Germany, [7]University of British Columbia, Vancouver, British Columbia, Canada V6T 1Z1, [8]Brunel University, Uxbridge, Middlesex UB8 3PH, United Kingdom, [9]Budker Institute of Nuclear Physics, Novosibirsk 630090, Russia, [10]University of California at Irvine, Irvine, California 92697, USA, [11]University of California at Riverside, Riverside, California 92521, USA, [12]University of California at Santa Barbara, Santa Barbara, California 93106, USA, [13]University of California at Santa Cruz, Institute for Particle Physics, Santa Cruz, California 95064, USA, [14]California Institute of Technology, Pasadena, California 91125, USA, [15]University of Cincinnati, Cincinnati, Ohio 45221, USA, [16]University of Colorado, Boulder, Colorado 80309, USA, [17]Colorado State University, Fort Collins, Colorado 80523, USA, [18]Technische Universität Dortmund, Fakultät Physik, D-44221 Dortmund, Germany, [19]Technische Universität Dresden, Institut für Kern- und Teilchenphysik, D-01062 Dresden, Germany, [20]Laboratoire Leprince-Ringuet, CNRS/IN2P3, Ecole Polytechnique, F-91128 Palaiseau, France, [21]University of Edinburgh, Edinburgh EH9 3JZ, United Kingdom, [22]INFN Sezione di Ferrara[a] ; Dipartimento di Fisica, Università di Ferrara[b], I-44100 Ferrara, Italy, [23]INFN Laboratori Nazionali di Frascati, I-00044 Frascati, Italy, [24]INFN Sezione di Genova[a] ; Dipartimento di Fisica, Università di Genova[b], I-16146 Genova, Italy, [25]Indian Institute of Technology Guwahati, Guwahati, Assam, 781 039, India, [26]Harvard University, Cambridge, Massachusetts 02138, USA, [27]Universität Heidelberg, Physikalisches Institut, Philosophenweg 12, D-69120 Heidelberg, Germany, [28]Humboldt-Universität zu Berlin, Institut für Physik, Newtonstr. 15, D-12489 Berlin, Germany, [29]Imperial College London, London, SW7 2AZ, United Kingdom, [30]University of Iowa, Iowa City, Iowa 52242, USA, [31]Iowa State University, Ames, Iowa 50011-3160, USA, [32]Johns Hopkins University, Baltimore, Maryland 21218, USA, [33]Laboratoire de l'Accélérateur Linéaire, IN2P3/CNRS et Université Paris-Sud 11, Centre Scientifique d'Orsay, B. P. 34, F-91898 Orsay Cedex, France, [34]Lawrence Livermore National Laboratory, Livermore, California 94550, USA, [35]University of Liverpool, Liverpool L69 7ZE, United Kingdom, [36]Queen Mary, University of London, London, E1 4NS, United Kingdom, [37]University of London, Royal Holloway and Bedford New College, Egham, Surrey TW20 0EX, United Kingdom, [38]University of Louisville, Louisville, Kentucky 40292, USA, [39]Johannes Gutenberg-Universität Mainz, Institut für Kernphysik, D-55099 Mainz, Germany, [40]University of Manchester, Manchester M13 9PL, United Kingdom, [41]University of Maryland, College Park, Maryland 20742, USA, [42]University of Massachusetts, Amherst, Massachusetts 01003, USA, [43]Massachusetts Institute of Technology, Laboratory for Nuclear Science, Cambridge, Massachusetts 02139, USA, [44]McGill University, Montréal, Québec, Canada H3A 2T8, [45]INFN Sezione di Milano[a] ; Dipartimento di Fisica, Università di Milano[b], I-20133 Milano, Italy, [46]University of Mississippi, University, Mississippi 38677, USA, [47]Université de Montréal, Physique des Particules, Montréal, Québec, Canada H3C 3J7, [48]INFN Sezione di Napoli[a] ; Dipartimento di Scienze Fisiche, Università di Napoli Federico II[b], I-80126 Napoli, Italy, [49]NIKHEF, National Institute for Nuclear Physics and High Energy Physics, NL-1009 DB Amsterdam, The Netherlands, [50]University of Notre Dame, Notre Dame, Indiana 46556, USA, [51]Ohio State University, Columbus, Ohio 43210, USA, [52]University of Oregon, Eugene, Oregon 97403, USA, [53]INFN Sezione di Padova[a] ; Dipartimento di Fisica, Università di Padova[b], I-35131 Padova, Italy, [54]Laboratoire de Physique Nucléaire et de Hautes Energies, IN2P3/CNRS, Université Pierre et Marie Curie-Paris6, Université Denis Diderot-Paris7, F-75252 Paris, France, [55]INFN Sezione di Perugia[a] ; Dipartimento di Fisica, Università di Perugia[b], I-06100 Perugia, Italy, [56]INFN Sezione di Pisa[a] ; Dipartimento di Fisica, Università di Pisa[b] ; Scuola Normale Superiore di Pisa[c], I-56127 Pisa, Italy, [57]Princeton University, Princeton, New Jersey 08544, USA, [58]INFN Sezione di Roma[a] ; Dipartimento di Fisica, Università di Roma La Sapienza[b], I-00185 Roma, Italy, [59]Universität Rostock, D-18051 Rostock, Germany, [60]Rutherford Appleton Laboratory, Chilton, Didcot, Oxon, OX11 0QX, United Kingdom, [61]CEA, Irfu, SPP, Centre de Saclay, F-91191

Gif-sur-Yvette, France, [62]SLAC National Accelerator Laboratory, Stanford, California 94309 USA, [63]University of South Carolina, Columbia, South Carolina 29208, USA, [64]Southern Methodist University, Dallas, Texas 75275, USA, [65]Stanford University, Stanford, California 94305-4060, USA, [66]State University of New York, Albany, New York 12222, USA, [67]Tel Aviv University, School of Physics and Astronomy, Tel Aviv, 69978, Israel, [68]University of Tennessee, Knoxville, Tennessee 37996, USA, [69]University of Texas at Austin, Austin, Texas 78712, USA, [70]University of Texas at Dallas, Richardson, Texas 75083, USA, [71]INFN Sezione di Torino[a] ; Dipartimento di Fisica Sperimentale, Università di Torino[b], I-10125 Torino, Italy, [72]INFN Sezione di Trieste[a] ; Dipartimento di Fisica, Università di Trieste[b], I-34127 Trieste, Italy, [73]IFIC, Universitat de Valencia-CSIC, E-46071 Valencia, Spain, [74]University of Victoria, Victoria, British Columbia, Canada V8W 3P6, [75]Department of Physics, University of Warwick, Coventry CV4 7AL, United Kingdom, [76]University of Wisconsin, Madison, Wisconsin 53706, USA, [*1]Now at Temple University, Philadelphia, Pennsylvania 19122, USA, [*2]Also with Università di Perugia, Dipartimento di Fisica, Perugia, Italy, [*3]Also with Università di Roma La Sapienza, I-00185 Roma, Italy, [*4]Now at University of South Alabama, Mobile, Alabama 36688, USA , [*5]Also with Università di Sassari, Sassari, Italy.

We report the results of a study of the exclusive charmless semileptonic decays, $B^+ \to \eta^{(\prime)}\ell^+\nu$ and $B^0 \to \pi^-\ell^+\nu$, undertaken with approximately 464 million $B\overline{B}$ pairs collected at the $\Upsilon(4S)$ resonance with the BABAR detector. The analysis uses events in which the signal B decays are reconstructed with a loose neutrino reconstruction technique. We obtain partial branching fractions for $B^+ \to \eta\ell^+\nu$ and $B^0 \to \pi^-\ell^+\nu$ decays in three and twelve bins of q^2, respectively, from which we extract the $f_+(q^2)$ form-factor shapes and the total branching fractions $\mathcal{B}(B^+ \to \eta\ell^+\nu) = (0.36 \pm 0.05_{stat} \pm 0.04_{syst}) \times 10^{-4}$ and $\mathcal{B}(B^0 \to \pi^-\ell^+\nu) = (1.42 \pm 0.05_{stat} \pm 0.08_{syst}) \times 10^{-4}$. We also measure $\mathcal{B}(B^+ \to \eta'\ell^+\nu) = (0.24 \pm 0.08_{stat} \pm 0.03_{syst}) \times 10^{-4}$. We obtain values for the magnitude of the CKM matrix element $|V_{ub}|$ using three different QCD calculations.

4.1 Introduction

A precise measurement of the CKM matrix [80] element $|V_{ub}|$ will constrain the description of weak interactions and CP violation in the Standard Model. The rate for exclusive charmless semileptonic decays involving a scalar meson is proportional to $|V_{ub}f_+(q^2)|^2$, where the form factor $f_+(q^2)$ depends on q^2, the square of the momentum transferred to the lepton-neutrino pair. Values of $f_+(q^2)$ are given by unquenched Lattice QCD (LQCD) calculations [81, 82], reliable only at large q^2 ($\gtrsim 16\ \mathrm{GeV}^2$), and by Light Cone Sum Rules (LCSR) calculations [83, 84], based on approximations only valid at small q^2 ($\lesssim 16\ \mathrm{GeV}^2$). The value of $|V_{ub}|$ can thus be determined by the measurement of partial branching fractions of charmless semileptonic B decays. Extraction of the $f_+(q^2)$ form-factor shapes from exclusive decays [85] such as $B^0 \to \pi^-\ell^+\nu$ [86] and $B^+ \to \eta^{(\prime)}\ell^+\nu$ may be used to test theoretical calculations [87]. The values of the branching fractions (BF) of the $B^+ \to \eta^{(\prime)}\ell^+\nu$ decays will also improve our knowledge of the composition of charmless semileptonic decays and help constrain the size of the gluonic singlet contribution to the form factors for these decays [84].

In this paper, we present measurements of the partial BFs $\Delta\mathcal{B}(B^+ \to \eta\ell^+\nu, q^2)$ and $\Delta\mathcal{B}(B^0 \to \pi^-\ell^+\nu, q^2)$ in 3 and 12 bins of q^2, respectively, as well as the total BFs for all three decay modes. Values of the total BFs were previously reported in Refs. [86, 88–91]. We use the values of $\Delta\mathcal{B}(q^2)$ for the $B^0 \to \pi^-\ell^+\nu$ mode with form-factor calculations [81–83] to obtain values of $|V_{ub}|$. Values of $|V_{ub}|$ have previously been extracted from $B^0 \to \pi^-\ell^+\nu$ measurements by CLEO [88], BABAR [86, 89, 92] and Belle [90]. A very recent measurement by BABAR [93] will be discussed in Section VI.

4.2 Data Sample and Simulation

We use a sample of 464 million $B\overline{B}$ pairs corresponding to an integrated luminosity of 422.6 fb^{-1} collected at the $\Upsilon(4S)$ resonance with the BABAR detector [94] at the PEP-II asymmetric-energy e^+e^- storage rings and a sample of 44 fb^{-1} collected approximately 40 MeV below the $\Upsilon(4S)$ resonance (denoted "off-resonance data"). Detailed Monte Carlo (MC) simulations are used to optimize the signal selections, to estimate the signal efficiencies, and to obtain the shapes of the signal and background distributions. MC samples are generated for $\Upsilon(4S) \to B\bar{B}$ events, $e^+e^- \to u\overline{u}/d\overline{d}/s\overline{s}/c\overline{c}/\tau^+\tau^-$ (continuum) events, and dedicated $B\bar{B}$ samples containing $B^0 \to \pi^-\ell^+\nu$ and $B^+ \to \eta^{(\prime)}\ell^+\nu$ signal decays. The signal MC events are produced with the FLATQ2 generator [95] and are reweighted to reproduce the $f_+(q^2, \alpha, c_B)$ Becirevic-Kaidalov (BK) parametrization [96], where the values of the shape and normalization parameters, α and c_B, are taken from Ref. [86]. The BABAR detector's acceptance and response are simulated using the GEANT4 package [94].

4.3 Event Reconstruction and Candidate Selection

We reconstruct the $B^0 \to \pi^-\ell^+\nu$ and $B^+ \to \eta^{(\prime)}\ell^+\nu$ decays. The η meson is reconstructed in the $\eta \to \gamma\gamma$ and $\eta \to \pi^+\pi^-\pi^0$ decay channels (combined BF of 62%) while the η' is reconstructed in the $\eta' \to \eta\pi^+\pi^-$ channel, followed by the $\eta \to \gamma\gamma$ decay (product BF of 17.5%) [97]. The $\eta' \to \rho^0\gamma$ decay channel suffers from large backgrounds and we do not consider it. We carry out an untagged analysis with a loose neutrino reconstruction technique [86], thereby obtaining a large candidate sample.

Event reconstruction with the BABAR detector is described in detail elsewhere [94]. Electrons (muons) are identified by their characteristic shower signatures in the electromagnetic calorimeter (muon detector), while charged hadrons are identified using the Cherenkov detector and dE/dx measurements in the drift chamber. The average electron (muon) reconstruction efficiency is 93% (70%), while its misidentification probability is $< 0.2\%$ ($< 1.5\%$). The neutrino four-momentum, $P_\nu = (|\vec{p}_{miss}|, \vec{p}_{miss})$, is inferred from the difference between the momentum of the colliding-beam particles $\vec{p}_{beams}$ and the vector sum of the momenta of all the particles detected in a single event $\vec{p}_{tot}$, such that $\vec{p}_{miss} = \vec{p}_{beams} - \vec{p}_{tot}$. To evaluate E_{tot}, the energy sum of all the particles, we assume zero mass for all neutrals since photons are difficult to disentangle from neutral hadrons and we take the mass given by the particle identification selectors for the charged particles. In this analysis, we calculate the momentum transfer as $q^2 = (P_B - P_{meson})^2$ instead of $q^2 = (P_\ell + P_\nu)^2$, where P_B, P_{meson} and P_ℓ are the four-momenta of the B

meson, of the π, η or η' meson, and of the lepton, respectively. With this choice, the value of $\tilde{q}^2$ is unaffected by any mis-reconstruction of the rest of the event. Here P_B has an effective value. To estimate this value, we first combine the lepton with a π, η or η' meson to form the so-called Y pseudo-particle. The angle, θ_{BY}, between the Y and B momenta in the $\Upsilon(4S)$ frame, can be determined by assuming $B \to Y\nu$. In this frame, the Y momentum, the B momentum and the angle θ_{BY} define a cone with the Y momentum as its axis and where the true B momentum lies somewhere on the surface of the cone. The B rest frame is thus known up to an azimuthal angle ϕ defined with respect to the Y momentum. The value of $\tilde{q}^2$ is then computed as the average of four $\tilde{q}^2$ values corresponding to four possible angles, ϕ, $\phi + \pi/2$, $\phi + \pi$, $\phi + 3\pi/2$ rad, where the angle ϕ is chosen randomly and where the four values of $\tilde{q}^2$ are weighted by the factor $\sin^2\theta_B$, θ_B being the angle between the B direction and the beam direction in the $\Upsilon(4S)$ frame [98]. We note that, θ_{BY} being a real angle, $|\cos\theta_{BY}| \leq 1$. We correct for the reconstruction effects on the q^2 resolution (0.51 GeV^2) by applying an unregularized unfolding algorithm to the measured q^2 spectra [99].

The candidate selections are optimized to maximize the ratio $S/\sqrt{(S+B)}$ in the MC simulation, where S is the number of signal events and B is the total number of background events. Continuum background is suppressed by requiring the ratio of second to zeroth Fox-Wolfram moments [100] to be smaller than 0.5. This background is further suppressed for $B^0 \to \pi^-\ell^+\nu$ by selections on the number of charged particle tracks and neutral calorimeter clusters [101] that reject radiative Bhabha and converted photon processes. We ensure that the momenta of the lepton and meson candidates are kinematically compatible with a real signal decay by requiring that a geometrical vertex fit of the two particles gives a χ^2 probability greater than 0.01 and that their angles in the laboratory frame be between 0.41 and 2.46 rad with respect to the e^--beam direction, the acceptance of the detector. To avoid $J/\psi \to \mu^+\mu^-$ decays, we reject $B^0 \to \pi^-\mu^+\nu$ candidates if the Y mass corresponds to the J/ψ mass. The electron (muon) tracks are required to have momenta greater than 0.5 (1.0) GeV in the laboratory frame to reduce misidentified leptons and secondary decays such as $D \to X\ell\nu$, J/ψ, τ and kaon decays. Furthermore, the momenta of the lepton and the meson are restricted to enhance signal over background. We require : for $B^0 \to \pi^-\ell^+\nu$ decays, $|\vec{p}^*_\ell| > 2.2$ GeV or $|\vec{p}^*_\pi| > 1.3$ GeV or $|\vec{p}^*_\ell| + |\vec{p}^*_\pi| > 2.8$ GeV ; for $B^+ \to \eta\ell^+\nu$ decays, $|\vec{p}^*_\ell| > 2.1$ GeV or $|\vec{p}^*_\eta| > 1.3$ GeV or $|\vec{p}^*_\ell| + |\vec{p}^*_\eta| > 2.8$ GeV ; and for $B^+ \to \eta^{'}\ell^+\nu$ decays, $|\vec{p}^*_\ell| > 2.0$ GeV or $|\vec{p}^*_{\eta'}| > 1.65$ GeV or $0.69 \times |\vec{p}^*_\ell| + |\vec{p}^*_{\eta'}| > 2.4$ GeV (all asterisked variables are in the center-of-mass frame). For the $B^+ \to \eta^{(')}\ell^+\nu$ decays, we restrict the reconstructed masses of the η' and η to lie in the intervals $0.92 < m_{\eta'} < 0.98$ GeV and $0.51 < m_\eta < 0.57$ GeV. For these decays, we also reject events with q^2 higher than 16 GeV^2, since the signal is dominated by background in that range. Most backgrounds are reduced by $\tilde{q}^2$-dependent selections on the angle ($\cos\theta_{thrust}$) between the thrust axes of the Y and of the rest of the event, on the polar angle (θ_{miss}) associated with $\vec{p}_{miss}$, on the invariant missing mass squared ($m^2_{miss} = E^2_{miss} - |\vec{p}_{miss}|^2$) divided by twice the missing energy ($E_{miss} = E_{beams} - E_{tot}$), and on the helicity angle ($\cos\theta_\ell$), the angle between the direction of the W boson (ℓ and ν combined) in the rest frame of the B meson, and the direction of the lepton in the rest frame of the W boson. The q^2 selections are shown in Fig. 4.1 and their effects illustrated in Fig. 4.2 for $B^0 \to \pi^-\ell^+\nu$ decays. In Fig. 4.2, a single vertical line indicates a fixed cut ; a set of two vertical lines represent a q^2-dependent cut. The position of the two lines correspond to the minimum and maximum values of the cut, as shown in Fig. 4.1. The functions describing the q^2 dependence are given in Tables 3.3-3.1 of the Appendix for the three decays under study. For $B^+ \to \eta\ell^+\nu$ decays, more background is rejected by requiring that $|\cos\theta_V| < 0.95$, where θ_V is the helicity angle of the η meson [95].

The kinematic variables $\Delta E = (P_B \cdot P_{beams} - s/2)/\sqrt{s}$ and $m_{ES} = \sqrt{(s/2 + \vec{p}_B \cdot \vec{p}_{beams})^2/E^2_{beams} - \vec{p}^2_B}$ are used in a two-dimensional extended maximum-likelihood fit [102] to separate signal from background. Here, $\sqrt{s}$ is the center-of-mass energy of the colliding particles and $P_B = P_{meson} + P_\ell + P_\nu$, in the laboratory frame. We only retain candidates with $|\Delta E| < 1.0$ GeV and $m_{ES} > 5.19$ GeV, thereby removing the region with large backgrounds from the fit. On average, fewer than 1.14 candidates is observed per event. For events with multiple candidates, only the candidate with the largest value of $\cos\theta_\ell$ is kept. The signal event reconstruction efficiency varies between 8.3% and 14.6% for $B^0 \to \pi^-\ell^+\nu$, and 1.4% and 2.6% for $B^+ \to \eta\ell^+\nu$ decays

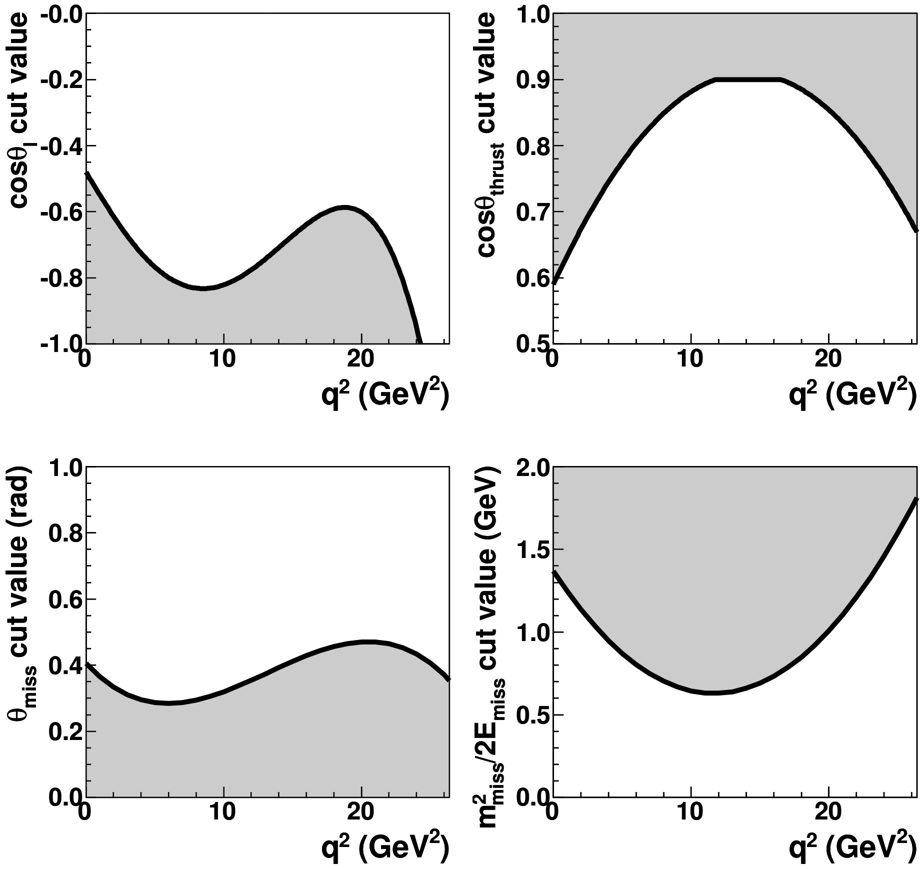

Figure 4.1 – Distributions of the selection values in the signal region for the q^2-dependent variables used in the analysis of $B^0 \rightarrow \pi^- \ell^+ \nu$ decays. The vertical axis represents the selection value for a given $\tilde{q}^2$ value. We reject an event when its value is in the shaded region.

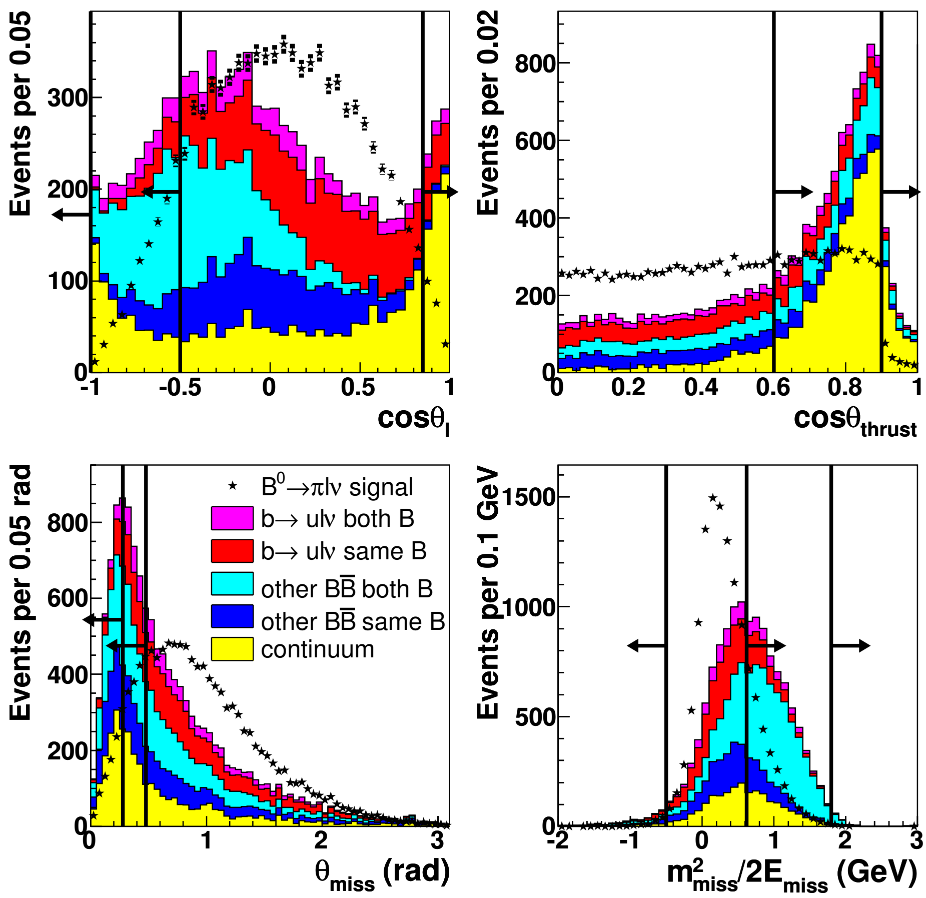

Figure 4.2 – (color online) Distributions in the signal region for the q^2-dependent selections used in the analysis of $B^0 \to \pi^- \ell^+ \nu$ decays. The arrows indicate the rejected regions. All the selections have been applied except for the one of interest. In each panel, the signal area is scaled to the area of the total background.

($\gamma\gamma$ channel), depending on q^2. It is 0.6% for both $B^+ \to \eta\ell^+\nu$ ($\pi^+\pi^-\pi^0$ channel) and $B^+ \to \eta^{'}\ell^+\nu$ decays.

4.4 Backgrounds and Signal Extraction

Backgrounds can be broadly grouped into three main categories : decays arising from $b \to u\ell\nu$ transitions (other than the signal), decays in other $B\bar{B}$ events (excluding $b \to u\ell\nu$) and decays in continuum events. For the $B^0 \to \pi^-\ell^+\nu$ mode only, in which there are many events, each of the first two categories is further split into a background category where the pion and the lepton come from the decay of the same B, and a background category where the pion and the lepton come from the decay of different B mesons.

Given the sufficient number of events for the $\pi\ell\nu$ decay mode, the data samples can be subdivided in 12 bins of $\tilde{q}^2$ for the signal and 2 bins for each of the five background categories. Two bins are used for each background category since the background q^2 spectra are not that well known and need to be adjusted in the fit when the number of events is sufficiently large to permit it. The q^2 ranges of the background binning for the $B^0 \to \pi^-\ell^+\nu$ decay are [0,18,26.4] GeV^2 for the $b \to u\ell\nu$ same B category, [0,22,26.4] GeV^2 for the $b \to u\ell\nu$ both B category, [0,10,26.4] GeV^2 for the other $B\bar{B}$ same B category, [0,14,26.4] GeV^2 for the other $B\bar{B}$ both B category and [0,22,26.4] GeV^2 for the continuum category. In each case, the q^2 ranges of the two bins are chosen to contain a similar number of events. All the signal and background events, in each q^2 bin, are fitted simultaneously. For the $\eta^{(\prime)}\ell\nu$ modes, a smaller number of events leads us to restrict the signal and each of the three background categories to a single q^2 bin except for the signal in the $\eta\ell\nu$ mode when $\eta \to \gamma\gamma$, which is investigated in 3 bins of $\tilde{q}^2$.

We use the ΔE-m_{ES} histograms, obtained from the MC simulation as two-dimensional probability density functions (PDFs), in our fit to the data to extract the yields of the signal and backgrounds as a function of $\tilde{q}^2$. As an initial estimate, the MC continuum background yield and q^2-dependent shape are first normalized to match the yield and q^2-dependent shape of the off-resonance data control sample. This results in a large sta-

Tableau 4.1 – Fitted yields in the full q^2 range for the signal and each background category, total number of MC and data events, and values of χ^2 for the fit region.

Decay mode	$\pi^-\ell^+\nu$	$\eta\ell^+\nu$	$\eta'\ell^+\nu$
Signal	11778 ± 435	888 ± 98	141 ± 46
$b \to u\ell\nu$	27793 ± 929	$2201(fixed)$	$204(fixed)$
Other $B\overline{B}$	80185 ± 963	17429 ± 247	2660 ± 82
Continuum	27790 ± 814	3435 ± 195	$517(fixed)$
MC events	147546 ± 467	23953 ± 183	3522 ± 68
Data events	147529 ± 384	23952 ± 155	3517 ± 59
χ^2/ndf	$411/386$	$56/52$	$19/17$

tistical uncertainty due to the small number of events in the off-peak data. To improve the statistical precision, the continuum background, initially normalized to the off-peak data, is allowed to vary in the fit to the data for the $\pi\ell\nu$ and $\eta\ell\nu(\gamma\gamma)$ modes where we have a large number of events. The fit result is compatible with the off-peak prediction within at most one standard deviation. Because of an insufficient number of events, the $b \to u\ell\nu$ background is fixed in the fit for the $\eta^{(\prime)}\ell\nu$ modes, and the continuum contribution is also fixed for the $\eta\ell\nu(3\pi)$ and $\eta'\ell\nu$ modes. Whenever a background is not varied in the fit, it is fixed to the MC prediction except for the continuum background which is fixed to its normalized yield and q^2-dependent shape using the off-resonanc data. The background parameters which are free in the fit require an adjustment of less than 10% with respect to the MC predictions. For illustration purposes only, we show in Fig. 4.3 ΔE and $m_{\rm ES}$ fit projections in the signal-enhanced region for $B^0 \to \pi^-\ell^+\nu$ decays in two ranges of q^2 corresponding to the sum of eight bins below and four bins above $\tilde{q}^2$ = 16 GeV^2, respectively. More detailed ΔE and $m_{\rm ES}$ fit projections in each $\tilde{q}^2$ bin are also shown in Figs. 3.71 and 3.72 of the Appendix for the $B^0 \to \pi^-\ell^+\nu$ decays. The data and the fit results are in good agreement. Fit projections for $B^+ \to \eta^{(\prime)}\ell^+\nu$, only available below $\tilde{q}^2$ = 16 GeV^2, are shown in Fig. 4.4. Table 4.1 gives the total fitted yields in the full q^2 range for the signal and each background category as well as the χ^2 values and degrees of freedom for the overall fit region. The yield values in the $B^+ \to \eta\ell^+\nu$ column are the result of the fit to the combined $\gamma\gamma$ and 3π modes.

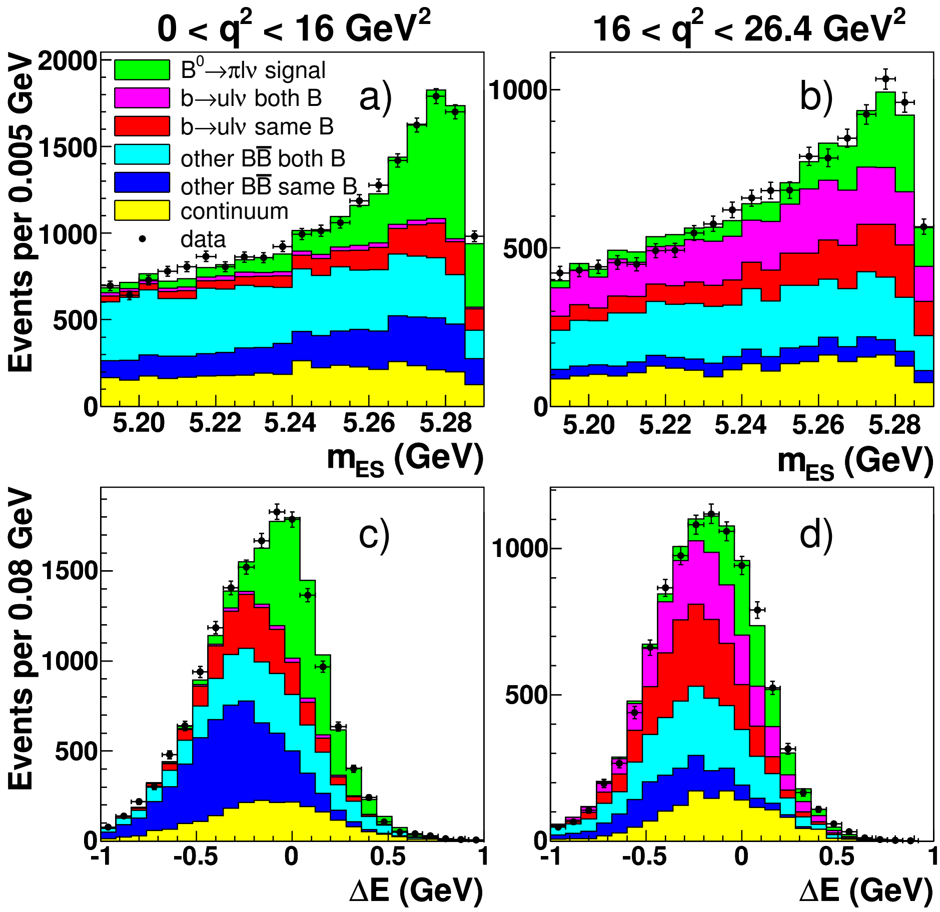

Figure 4.3 – (color online) Projections of the data and fit results for the $B^0 \to \pi^- \ell^+ \nu$ decays, in the signal-enhanced region : (a,b) m_{ES} with $-0.16 < \Delta E < 0.20$ GeV ; and (c,d) ΔE with $m_{\mathrm{ES}} > 5.268$ GeV. The distributions (a,c) and (b,d) are projections for $\tilde{q}^2 < 16$ GeV^2 and for $\tilde{q}^2 > 16$ GeV^2, respectively.

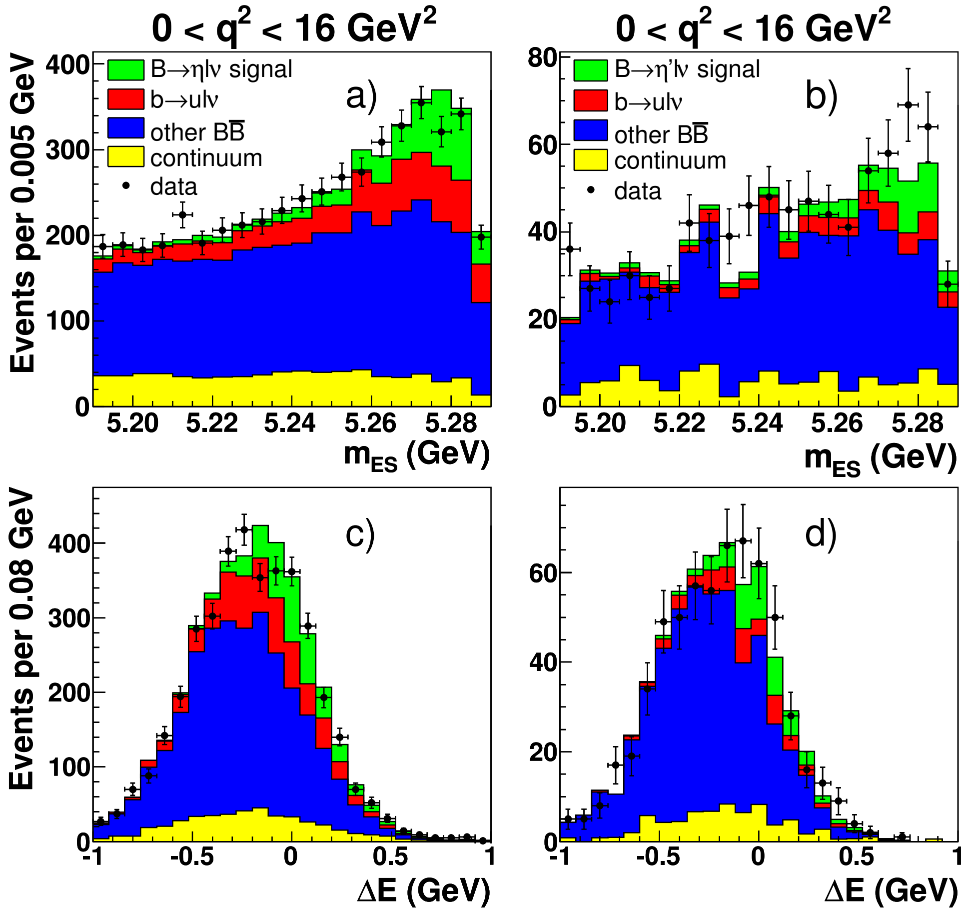

Figure 4.4 – (color online) Projections of the data and fit results for the $B^+ \to \eta^{(\prime)}\ell^+\nu$ decays, in the signal-enhanced region : (a,b) m_{ES} with $-0.16 < \Delta E < 0.20$ GeV ; and (c,d) ΔE with $m_{\mathrm{ES}} > 5.268$ GeV. The distributions (a,c) and (b,d) are projections for the $B^+ \to \eta\ell^+\nu$ and $B^+ \to \eta^{\prime}\ell^+\nu$ decays, respectively, both for $\tilde{q}^2 < 16$ GeV^2.

Tableau 4.2 – Values of signal yields, $\Delta\mathcal{B}(q^2)$ and their relative uncertainties (%) for $B^0 \to \pi^-\ell^+\nu$, $B^+ \to \eta\ell^+\nu$ and $B^+ \to \eta^{'}\ell^+\nu$ decays.

Decay mode	$\pi^-\ell^+\nu$				$\eta\ell^+\nu$	$\eta'\ell^+\nu$
q^2 range (GeV^2)	q^2<12	q^2<16	q^2>16	full q^2 range	q^2<16	q^2<16
Yield	6541.6	8422.1	3355.4	11777.6	887.9	141.0
BF (10^{-4})	0.83	1.09	0.33	1.42	0.36	0.24
Statistical error	3.9	3.7	7.6	3.5	12.5	32.8
Detector effects	3.1	3.5	6.1	4.0	8.0	8.8
Continuum bkg	0.9	0.8	1.0	0.7	0.3	7.1
$B \to X_u\ell\nu$ bkg	2.0	1.7	4.2	2.0	7.6	6.7
$B \to X_c\ell\nu$ bkg	0.6	0.7	1.8	1.0	1.2	2.6
Other effects	2.3	2.2	3.2	2.3	3.4	4.6
Total uncertainty	5.9	5.9	11.3	6.3	17.0	35.8

4.5 Systematic Uncertainties

Systematic uncertainties on the values of the partial branching fractions, $\Delta\mathcal{B}(q^2)$, and their correlations among the q^2 bins have been investigated. These uncertainties are estimated from the variations of the resulting partial BF values (or total BF values for $B^+ \to \eta^{'}\ell^+\nu$ decays) when the data are re-analyzed with different simulation parameters and reweightings. For each parameter, we use the full MC dataset to generate new ΔE-m_{ES} distributions ("MC event samples") by varying randomly only the parameter of interest over a complete ($> 3\sigma$) gaussian distribution whose standard deviation is given by the uncertainty on the specific parameter under investigation. One hundred such samples are generated for each parameter. Uncertainties due to B counting and final state radiation are estimated by generating only one sample. Each MC sample is analyzed the same way as real data to determine values of $\Delta\mathcal{B}(q^2)$ (or total BF values for $B^+ \to \eta^{'}\ell^+\nu$ decays). The contribution of the parameter to the systematic uncertainty is given by the RMS value of the distribution of these values over the one hundred samples.

The systematic uncertainties due to the imperfect description of the detector in the simulation are computed by using the uncertainties, determined from control samples, on the tracking efficiency of all charged particle tracks, on the particle identification efficiencies of signal candidate tracks, on the calorimeter efficiencies (varied separately for photons and K_L^0), on the energy deposited in the calorimeter by K_L^0 mesons as well as on their production spectrum. The reconstruction of these neutral particles affects the analysis through the neutrino reconstruction. The uncertainties due to the generator-level inputs to the simulation are given by the uncertainties in the BFs of the background processes $b \to u\ell\nu$ and $b \to c\ell\nu$, in the BFs of the secondary decays producing leptons [97], and in the BFs of the $\Upsilon(4S) \to B\overline{B}$ decays [87]. The $B \to X\ell\nu$ form factor uncertainties, where $X = (\pi, \rho, \omega, \eta^{(\prime)}, D, D^*)$, are given by recent calculations or measurements [97]. The uncertainties in the heavy quark parameters used in the simulation of non-resonant $b \to u\ell\nu$ events are given in Ref. [103]. We assign an uncertainty of 20% [104] to the final state radiation (FSR) corrections calculated by PHOTOS [105]. Finally, the uncertainties due to the modeling of the continuum are established by using the uncertainty in its $\tilde{q}^2$ distribution shape and, when the continuum background is fixed, the uncertainty in the total yield, both given by comparisons with the off-resonance data control sample.

The list of all the systematic uncertainties, as well as their values for the partial and total BFs, are given in Tables II.4 and II.5 of the Appendix. The item "Signal MC stat error" in these tables includes the systematic uncertainty due to the unfolding procedure. The correlation matrices obtained in the measurement of the partial BFs are presented in Tables 3.40, II.7 and II.8. A condensed version of all the uncertainties is given in Table 4.2 together with signal yields and partial BFs in selected $\tilde{q}^2$ ranges. The values given for the $B^+ \to \eta\ell^+\nu$ decays are those obtained from the fits to the distributions of the $\eta \to \gamma\gamma$ and $\eta \to \pi^+\pi^-\pi^0$ channels combined. The larger relative uncertainties occurring in bin 12 of Table II.4 are due to poorly reconstructed events, and to the small raw yield in that bin. The former arises from the presence of a large number of low momentum pions and a large background. This makes it difficult to select the right pion and results in a larger absolute uncertainty on the fitted yield. The small yield leads to a fairly large unfolding correction in this bin and thus to a considerably reduced unfolded yield. On the other hand, the unfolding process increases the absolute uncertainty only slightly. The reduced yield together with the larger absolute uncertainty lead to the larger relative uncertainties reported in the table.

4.6 Results

The partial BFs are calculated for $B^0 \rightarrow \pi^-\ell^+\nu$ and $B^+ \rightarrow \eta\ell^+\nu$ decays using the unfolded signal yields, the signal efficiencies given by the simulation and the BFs $\mathcal{B}(\Upsilon(4S) \rightarrow B^0\overline{B}^0) = 0.484 \pm 0.006$ and $\mathcal{B}(\Upsilon(4S) \rightarrow B^+B^-) = 0.516 \pm 0.006$ [87]. We obtain the total BFs :

$$\mathcal{B}(B^0 \rightarrow \pi^-\ell^+\nu) = (1.42 \pm 0.05_{stat} \pm 0.08_{syst}) \times 10^{-4},$$
$$\mathcal{B}(B^+ \rightarrow \eta\ell^+\nu) = (3.39 \pm 0.46_{stat} \pm 0.47_{syst}) \times 10^{-5} \text{ and}$$
$$\mathcal{B}(B^+ \rightarrow \eta^{'}\ell^+\nu) = (2.43 \pm 0.80_{stat} \pm 0.34_{syst}) \times 10^{-5}.$$

The BF value for $B^+ \rightarrow \eta^{'}\ell^+\nu$ has a significance of 3.2σ when we take into account only the statistical uncertainty [106]. Taking into account the effect of the systematic uncertainty which increases the total uncertainty by about 8% leads to a reduced significance of 3.0σ. The BF value, obtained from a fit to the combined $\gamma\gamma$ and 3π channels of the $B^+ \rightarrow \eta\ell^+\nu$ decays, is in good agreement with the weighted average of the total BFs obtained separately for the $\gamma\gamma$ and 3π channels. Consistent results are obtained when dividing the final data set into chronologically-ordered subsets, electron only and muon only subsets, modifying the q^2 or the ΔE and m_{ES} binnings, and varying the event selection requirements.

The experimental $\Delta\mathcal{B}(q^2)$ distributions are displayed in Fig. 4.5 for $B^0 \rightarrow \pi^-\ell^+\nu$ decays and in Fig. 4.6 for $B^+ \rightarrow \eta\ell^+\nu$ decays, together with theoretical predictions. To allow a direct comparison with the theoretical predictions, which do not include FSR effects, the experimental distributions in these figures have been obtained with the efficiency given by the ratio of q^2 unfolded events generated after all the cuts with a simulation which includes FSR to the total number of events generated before any cut and with no FSR effects i.e. with PHOTOS switched off. We obtain the $f_+(q^2)$ shape from a fit to these distributions. The χ^2 function minimized in the fit to the $f_+(q^2)$ shape uses the BGL parametrization [107] consisting of a two-parameter polynomial expansion. For the $B^0 \rightarrow \pi^-\ell^+\nu$ decays, the fit gives $a_1/a_0 = -0.63 \pm 0.29$ and $a_2/a_0 = -6.9 \pm 1.7$, with $P(\chi^2) = 92.1\%$ as well as a value of $|V_{ub}f_+(0)| = (8.6 \pm 0.3_{stat} \pm 0.3_{syst}) \times 10^{-4}$ from the fit extrapolated to $q^2 = 0$. This value can be used to predict rates of other decays such

Tableau 4.3 – Values of $|V_{ub}|$ derived from the form-factor calculations for the $B^0 \to \pi^- \ell^+ \nu$ decays. The three uncertainties on $|V_{ub}|$ are statistical, systematic and theoretical, respectively.

	q^2 (GeV^2)	$\Delta\mathcal{B}$ (10^{-4})	$\Delta\zeta$ (ps^{-1})	$\lvert V_{ub}\rvert$ (10^{-3})	$Prob(\chi^2)$
HPQCD [81]	> 16	$0.33 \pm 0.03 \pm 0.03$	2.02 ± 0.55	$3.28 \pm 0.13 \pm 0.15^{+0.57}_{-0.37}$	28.8%
FNAL [82]	> 16	$0.33 \pm 0.03 \pm 0.03$	$2.21^{+0.47}_{-0.42}$	$3.14 \pm 0.12 \pm 0.14^{+0.35}_{-0.29}$	17.4%
LCSR [83]	< 12	$0.84 \pm 0.03 \pm 0.04$	$4.00^{+1.01}_{-0.95}$	$3.70 \pm 0.07 \pm 0.08^{+0.54}_{-0.39}$	39.9%

as $B \to \pi\pi$ [108]. For completeness, we also show the fit to the BK parametrization [96], which gives $\alpha_{BK} = 0.52 \pm 0.04$, with $P(\chi^2) = 28.6\%$.

The q^2 distribution extracted from our data is compared in Fig. 4.5 to the shape of the form factors obtained from the three theoretical calculations listed in Table 4.3 : the one based on Light Cone Sum Rules [83] for $q^2 < 12\ \mathrm{GeV}^2$, and the two based on unquenched LQCD [81, 82] for $q^2 > 16\ \mathrm{GeV}^2$. We first normalize the form factor predictions to the experimental data by requiring the integrals of both to be the same over the $\tilde{q}^2$ ranges of validity given in Table 4.3 for each theoretical prediction. Considering only experimental uncertainties, we then calculate the χ^2 probabilities relative to the binned data result for various theoretical predictions. These are given in Table 4.3 for the $B^0 \to \pi^- \ell^+ \nu$ decays. All three calculations are compatible with the data. As shown in Fig. 4.6, an LCSR calculation [84] is compatible with the data for the $B^+ \to \eta \ell^+ \nu$ decays. It should be noted that the theoretical curves in Fig. 4.5 have been extrapolated over the full $\tilde{q}^2$ range based on a parametrization obtained over their $\tilde{q}^2$ ranges of validity. These extended ranges are only meant to illustrate a possible extension of the present theoretical calculations.

We extract a value of $|V_{ub}|$ from the $B^0 \to \pi^- \ell^+ \nu$ $\Delta\mathcal{B}(q^2)$ distributions using the relation : $|V_{ub}| = \sqrt{\Delta\mathcal{B}/(\tau_{B^0}\Delta\zeta)}$, where $\tau_{B^0} = 1.525 \pm 0.009$ ps [87] is the B^0 lifetime and $\Delta\zeta = \Gamma/|V_{ub}|^2$ is the normalized partial decay rate predicted by the form-factor calculations [81–83]. The quantities $\Delta\mathcal{B}$ and $\Delta\zeta$ are restricted to the $\tilde{q}^2$ ranges of validity given in Table 4.3. The values of $\Delta\zeta$ are independent of experimental data. The values of $|V_{ub}|$ given in Table 4.3 range from $(3.1 - 3.7) \times 10^{-3}$. A value of $|V_{ub}|$ could not be

Tableau 4.4 – Values of quantities of interest and their averages obtained in the study of $B^0 \to \pi^- \ell^+ \nu$ decays. The third uncertainty, given for the average values, is due to the form factor calculation. It is not shown for the individual determination of $|V_{ub}|$.

	Present work	Ref. [93]	Average
Total BF	$1.42 \pm 0.05 \pm 0.07$	$1.41 \pm 0.05 \pm 0.07$	$1.42 \pm 0.04 \pm 0.07$
$\lvert V_{ub}\rvert_{HPQCD} \times 10^3$	$3.28 \pm 0.13 \pm 0.15$	$3.21 \pm 0.13 \pm 0.12$	$3.23 \pm 0.09 \pm 0.13^{+0.57}_{-0.37}$
$\lvert V_{ub}\rvert_{FNAL} \times 10^3$	$3.14 \pm 0.12 \pm 0.14$	$3.07 \pm 0.11 \pm 0.11$	$3.09 \pm 0.08 \pm 0.12^{+0.35}_{-0.29}$
$\lvert V_{ub}\rvert_{LCSR} \times 10^3$	$3.70 \pm 0.07 \pm 0.08$	$3.78 \pm 0.08 \pm 0.10$	$3.72 \pm 0.05 \pm 0.09^{+0.54}_{-0.39}$
$\lvert V_{ub} f_+(0)\rvert \times 10^4$	$8.5 \pm 0.3 \pm 0.2$	$10.8 \pm 0.5 \pm 0.3$	$9.4 \pm 0.3 \pm 0.3$
BGL a_1/a_0	$-0.63 \pm 0.27 \pm 0.10$	$-0.82 \pm 0.23 \pm 0.17$	$-0.79 \pm 0.14 \pm 0.14$
BGL a_2/a_0	$-6.9 \pm 1.3 \pm 1.1$	$-1.1 \pm 1.6 \pm 0.9$	$-4.4 \pm 0.8 \pm 0.9$

obtained from the $B^+ \to \eta \ell^+ \nu$ decays because the required theoretical input, $\Delta\zeta$, is not yet available.

4.7 Combined BABAR results

At first glance, there appears to be a large overlap between the present analysis of the $B^0 \to \pi^- \ell^+ \nu$ data and that of another recent BABAR measurement [93]. However, there are significant differences between the two analyses. Considering the same fit region, we obtain 147529 selected events (signal or background) compared to 42516 such events in Ref. [93]. This difference can easily be explained by the fact that we use the full BABAR data set in the present analysis but not so in Ref. [93]. Furthermore, the use of the loose neutrino reconstruction technique in this work leads to a larger background. Only 140 events are found in common between the two data sets i.e. 0.3% overlap. The statistical uncertainties are thus expected to be uncorrelated between the two analyses. The event reconstruction and simulation are also somewhat different. For example, the values of q^2 are computed using different, although in principle equivalent, relations : here, $q^2 = (P_B - P_\pi)^2$ versus $q^2 = (P_\ell + P_\nu)^2$ in Ref. [93]. Nevertheless, almost all of the systematic uncertainties are expected to be highly correlated.

It is gratifying to note that, as shown in Table 4.4, the total BF as well as the values of $|V_{ub}|$ obtained in the two analyses are in good agreement with each other. The value of $|V_{ub}|$ quoted under Ref. [93] in Table 4.4 for the FNAL [82] theoretical prediction is obtained using the values of the partial BFs given in Ref. [93] for $q^2 > 16\ \mathrm{GeV}^2$. The similar numbers of signal events (11778 ± 435 here compared with 10604 ± 376 in Ref. [93] when the events from $B^+ \to \pi^0 \ell^+ \nu$ decays are also included) lead to similar statistical uncertainties in the two analyses.

It is possible to obtain a good approximation to the average of the present results and those of Ref. [93] obtained in the $B^0 \to \pi^- \ell^+ \nu$ decays by taking the statistical uncertainties to be uncorrelated and the systematic uncertainties to be fully correlated. The additional $|V_{ub}|$ value obtained in Ref. [93] with a combined fit to data and theoretical points is not included in the average values given in Table 4.4. We employ the above averaging procedure to determine the averages, and associated uncertainties, given in Table 4.4 for the total branching fraction and the values of $|V_{ub}|$.

This averaging method is not appropriate for the fitted BGL coefficients (a_1/a_0 and a_2/a_0) and the value of $|V_{ub} f_+(0)|$, since, as shown in Table 4.4, the two measurements of these quantities are only marginally compatible. Instead, we perform a new fit of the BGL parametrization to the combined partial branching fraction results from the two analyses, the twelve values obtained in this analysis and the six values from Ref. [93]. Here again, the statistical covariance matrices are uncorrelated and the systematic covariance matrices are fully correlated between the two data sets. The combined error matrix from the two analyses is used to perform the fit, with the result shown in Fig. 4.7 and a χ^2 probability $P(\chi^2) = 14.2\%$. When only the statistical covariance matrix is used, the χ^2 probability is reduced to 3.1%. We note that the discrepancy in the two analyses of the partial BFs at low values of q^2 does not lead to discrepancies in the resulting values of the total BF or $|V_{ub}|$, as is evident in Table 4.4. Finally, we do not attempt to average the partial branching fractions due to the different q^2 binning used in the two analyses.

4.8 Summary

In summary, we have measured the partial BFs of $B^+ \to \eta \ell^+ \nu$ decays in 3 bins of q^2 and of $B^0 \to \pi^- \ell^+ \nu$ decays in 12 bins of q^2. From these distributions, we extract the $f_+(q^2)$ shapes which are found to be compatible with all three theoretical predictions considered for the $B^0 \to \pi^-\ell^+\nu$ decays and with the LCSR calculation for the $B^+ \to \eta\ell^+\nu$ decays. The BGL parametrization fits our data well and allows us to obtain the value of $|V_{ub}f_+(0)|$. Our measured branching fractions of the three decays reported in this work lead to a significant improvement in our knowledge of the composition of the inclusive charmless semileptonic decay rate. Our value of the total BF for $B^+ \to \eta^{'}\ell^+\nu$ is an order of magnitude smaller than the most recent CLEO result [88]. Our value of the total BF for $B^+ \to \eta\ell^+\nu$ is consistent with a previous untagged BABAR result [91]. The value of the ratio $\mathcal{B}(B^+ \to \eta^{'}\ell^+\nu)/\mathcal{B}(B^+ \to \eta\ell^+\nu)$ = $0.67 \pm 0.24_{stat} \pm 0.11_{syst}$ allows an important gluonic singlet contribution to the η' form factor. The present value of the total BF for $B^0 \to \pi^-\ell^+\nu$ is in good agreement with a previous untagged BABAR measurement [86] as well as with a recent BABAR result [93]. It has comparable precision to the present world average [87]. For $B^0 \to \pi^-\ell^+\nu$ decays, we obtain values of $|V_{ub}|$ for three different QCD calculations. The results are in good agreement with those of Refs. [86, 93]. The three values are all acceptable according to the data. Two of these values [81, 83] are consistent, within large theoretical uncertainties, with the value measured in inclusive semileptonic B decays : $|V_{ub}|$ = $(4.27 \pm 0.38) \times 10^{-3}$ [87]. We also provide the average values of the total BF and of $|V_{ub}|$ obtained in the present work and those of Ref. [93]. We also give the values of $|V_{ub}f_+(0)|$, $a1/a0$ and $a2/a0$ obtained in a combined BGL fit to the two data sets.

We would like to thank A. Khodjamirian, A. Kronfeld and R. Van de Water for useful discussions concerning their form-factor calculations and for providing the values of $\Delta\zeta$ used in this work. We would also like to thank J. Dingfelder and B. Viaud for their numerous contributions to this analysis. We are grateful for the extraordinary contributions of our PEP-II colleagues in achieving the excellent luminosity and machine conditions that have made this work possible. The success of this project also relies critically on the expertise and dedication of the computing organizations that support BABAR. The collaborating institutions wish to thank SLAC for its support and the kind hospitality extended to them. This work is supported by the US Department of Energy and National Science Foundation, the Natural Sciences and Engineering Research Council (Canada), the Commissariat à l'Energie Atomique and Institut National de Physique Nucléaire et de Physique des Particules (France), the Bundesministerium für Bildung und Forschung and Deutsche Forschungsgemeinschaft (Germany), the Istituto Nazionale di Fisica Nucleare (Italy), the Foundation for Fundamental Research on Matter (The Netherlands), the Research Council of Norway, the Ministry of Education and Science of the Russian Federation, Ministerio de Ciencia e Innovación (Spain), and the Science and Technology Facilities Council (United Kingdom). Individuals have received support from the Marie-Curie IEF program (European Union), the A. P. Sloan Foundation (USA) and the Binational Science Foundation (USA-Israel).

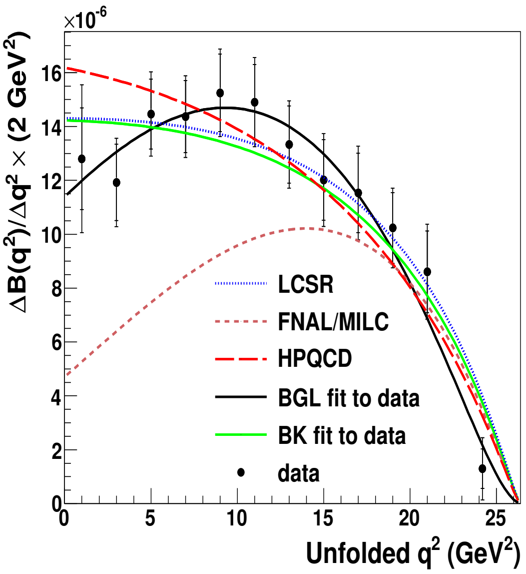

Figure 4.5 – (color online) Partial $\Delta\mathcal{B}(q^2)$ spectrum in 12 bins of q^2 for $B^0 \to \pi^-\ell^+\nu$ decays. The data points are placed in the middle of each bin whose width is defined in Table II.4.The smaller error bars are statistical only while the larger ones also include systematic uncertainties. The solid green and black curves show the result of the fit to the data of the BK [96] and BGL [107] parametrizations, respectively. The data are also compared to unquenched LQCD calculations (HPQCD [81], FNAL [82]) and an LCSR calculation [83].

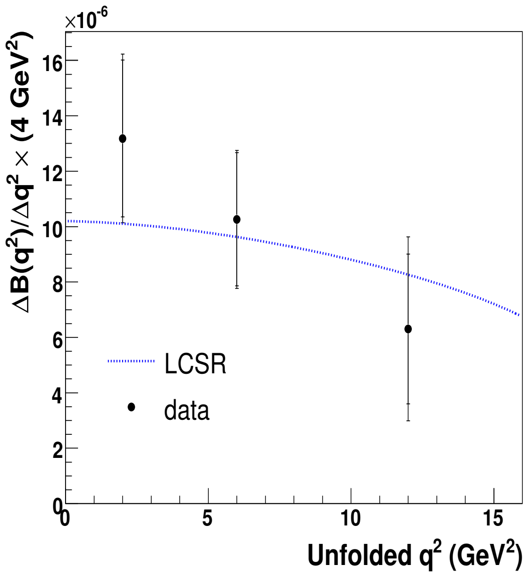

Figure 4.6 – (color online) Partial $\Delta\mathcal{B}(q^2)$ spectrum in 3 bins of q^2 for $B^+ \to \eta\ell^+\nu$ decays. The data points are placed in the middle of each bin whose width is defined in Table II.5. The smaller error bars are statistical only while the larger ones also include systematic uncertainties. The data are also compared to an LCSR calculation [84].

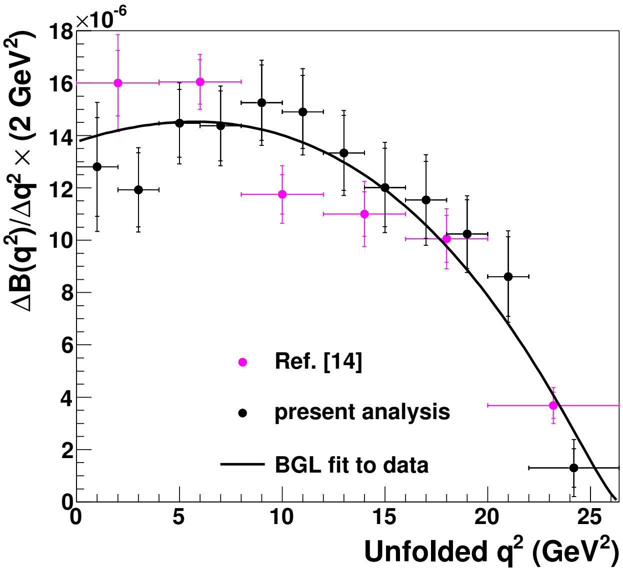

Figure 4.7 – (color online) Partial $\Delta\mathcal{B}(q^2)$ spectrum for $B^0 \rightarrow \pi^-\ell^+\nu$ decays, in 12 bins of q^2 for the present work and 6 bins of q^2 for Ref. [93]. The smaller error bars are statistical only while the larger ones also include systematic uncertainties. The solid black curve shows the result of the fit to the combined data for the two analyses using the BGL [107] parametrization.

[80] M. Kobayashi and T. Maskawa, Prog. Theor. Phys. **49**, 652 (1973).

[81] E. Gulez *et al.* (HPQCD Collaboration), Phys. Rev. **D73**, 074502 (2006) ; Erratum ibid. **D75**, 119906 (2007).

[82] C. Bernard *et al.* (FNAL/MILC Collaboration), Phys. Rev. **D80**, 034026 (2009) ; R. Van de Water, private communication.

[83] G. Duplancic *et al.*, JHEP **804**, 14 (2008) ; A. Khodjamirian, private communication.

[84] P. Ball and G. W. Jones, JHEP **08**, 025 (2007).

[85] Charge conjugate decays and $\ell = e$ or μ are implied throughout this paper.

[86] B. Aubert *et al.* (*BABAR* Collaboration), Phys. Rev. Lett. **98**, 091801 (2007).

[87] K. Nakamura *et al.* (Particle Data Group), Jour. of Phys. **G37**, 075021 (2010) ; see also "Determination of $|V_{cb}|$ and $|V_{ub}|$", ibidem.

[88] S. B. Athar *et al.* (CLEO Collaboration), Phys. Rev. **D68**, 072003 (2003) ; D. M. Asner *et al.* (CLEO Collaboration), Phys. Rev. **D76**, 012007 (2007) ; N. E. Adam *et al.* Phys. Rev. Lett. **99**, 041802 (2007).

[89] B. Aubert *et al.* (*BABAR* Collaboration), Phys. Rev. Lett. **97**, 211801 (2006).

[90] T. Hokuue *et al.* (Belle Collaboration), Phys. Lett. **B648**, 139 (2007).

[91] B. Aubert *et al.* (*BABAR* Collaboration), Phys. Rev. **D79**, 052011 (2009).

[92] B. Aubert *et al.* (*BABAR* Collaboration), Phys. Rev. Lett. **101**, 081801 (2008).

[93] P. del Amo Sanchez *et al.* (*BABAR* Collaboration), arXiv :1005.3288, accepted by Phys. Rev. **D**.

[94] B. Aubert *et al.* (*BABAR* Collaboration), Nucl. Instrum. Methods **A479**, 1 (2002).

[95] D. Côté *et al.*, Eur. Phys. J. C **38**, 105 (2004).

[96] D. Becirevic and A. B. Kaidalov, Phys. Lett. **B478**, 417 (2000).

[97] C. Amsler *et al.* (Particle Data Group), Phys. Lett. **B667**, 1 (2008).

[98] B. Aubert *et al.* (BABAR Collaboration), Phys. Rev. **D74**, 092004 (2006).

[99] G. Cowan, Statistical Data Analysis, Chap. 11, Oxford University Press (1998).

[100] G. C. Fox and S. Wolfram, Phys. Rev. Lett. **41**, 1581 (1978).

[101] B. Aubert *et al.* (BABAR Collaboration), Phys. Rev. **D67**, 031101 (2003).

[102] R.J. Barlow and C. Beeston, Comput. Phys. Commun. **77**, 219 (1993).

[103] O.L. Buchmüller, H.U. Flächer, Phys. Rev. **D73**, 073008 (2006).

[104] E. Richter-Was *et al.*, Phys. Lett. **B303**, 163 (1993).

[105] E. Barberio and Z. Was, Comput. Phys. Commun. **79**, 291 (1994).

[106] Y. Zhu, High Ener. Phys. Nucl. Phys. **30**, 331 (2006).

[107] C. G. Boyd and M. J. Savage, Phys. Rev. **D56**, 303 (1997).

[108] T. Becher and R. J. Hill, Phys. Lett. **B633**, 61 (2006).

[109] H. Ha *et al.* (Belle Collaboration), arXiv :1012.0090v3[hep.ex], submitted to PRD-RC (2010).

CONCLUSION

Les résultats qui ont été présentés dans cette thèse sont les rapports d'embranchement partiels et totaux des désintégrations semileptoniques $B^0 \to \pi^- \ell^+ \nu$, $B^+ \to \eta \ell^+ \nu$ et $B^+ \to \eta' \ell^+ \nu$, les formes spectrales de q^2 pour décrire les facteurs de forme $f_+(q^2)$ pour les modes $B^0 \to \pi^- \ell^+ \nu$ et $B^+ \to \eta \ell^+ \nu$, ainsi qu'une détermination de $|V_{ub}|$ extraite du mode $B^0 \to \pi^- \ell^+ \nu$. Cette valeur de $|V_{ub}|$ exclusive est importante pour restreindre davantage les paramètres du *Modèle Standard* et pour vérifier et démystifier l'écart de plus de 2σ entre les valeurs de $|V_{ub}|$ inclusives et exclusives actuelles.

Au Chapitre 1, nous avons vulgarisé les éléments théoriques nécessaires pour comprendre la nature et l'importance des résultats expérimentaux afin de mesurer les paramètres libres du *Modèle Standard*. En premier lieu, nous avons fait un survol du *Modèle Standard* qui tente de décrire le plus exactement possible les particules élémentaires et leurs interactions. Plus particulièrement, l'interaction faible fait intervenir une matrice de mélange entre les quarks électrofaibles et les quarks physiques que nous appellons la matrice CKM et qui contient quatre paramètres libres. De cette matrice découle les relations d'unitarité et le Triangle d'Unitarité, comportant entre autre l'élément V_{ub}. Par la suite, nous avons fait le lien qui existre entre V_{ub} et les rapports d'embranchement des désintégrations semileptoniques des mésons B, comme $B^0 \to \pi^- \ell^+ \nu$, par le biais de facteurs de formes de la CDQ devant être calculés théoriquement. Nous avons énuméré les raisons qui expliquent les difficultés entourant les différents calculs théoriques. Finalement, nous avons terminé par la paramétrisation des facteurs de forme par des fonctions analytiques qui peuvent être utilisées pour lisser les données expérimentales et ainsi obtenir le spectre de q^2 nécessaire pour extraire la valeur de $|V_{ub}|$.

Au Chapitre 2, nous avons décrit les accélérateurs et les détecteurs utilisés dans BABAR. Nous y avons détaillé l'accélerateur linéaire *Linac* et le collisionneur *PEP-II* pour expliquer l'origine des collisions $e^+ - e^-$. Nous avons vu également que le détecteur BABAR était composé des cinq détecteurs suivants : le détecteur de vertex au silicium

(SVT), la chambre à dérive (DCH), le détecteur de lumière Čerenkov à réflections internes (DIRC), le calorimètre électromagnétique (EMC) et le retour de flux magnétique instrumenté (IFR). Ensuite, nous avons expliqué l'importance d'avoir un système de déclenchement grandement rapide et efficace pour éliminer des millions d'événements de bruits de fond et ne conserver qu'une centaine d'événements intéressants par seconde. Finalement, nous avons défini les algorithmes de reconstruction des traces chargées permettant par la suite de définir des algorithmes d'identification des particules.

Au Chapitre 3, nous avons expliqué en détail, dans une note interne de la Collaboration *BABAR*, la méthode utilisée pour mesurer les rapports d'embranchement partiels et totaux, le spectre des facteurs de forme $f_+(q^2)$ et l'extraction de $|V_{ub}|$. Ce chapitre est le coeur de l'analyse et explique en profondeur la technique utilisée, l'optimisation des sélections d'événements, les résultats obtenus et leurs interprétations. Nous avons développé une technique de reconstruction relâchée du neutrino qui a été approuvée et utilisée lors de notre étude précédente sur le même sujet et qui a été publiée dans PRL (*Physical Review Letters*) [86]. Une particularité de cette technique est qu'elle calcule $q^2 = (P_B - P_{X_u})^2$ au lieu de $q^2 = (P_\ell + P_\nu)^2$, permetant ainsi d'éliminer les contraintes de reconstruction du neutrino. D'autres expériences, comme Belle, sont en train de publier leurs résultats en utilisant la même méthode. Cette analyse apporte toutefois des éléments nouveaux par rapport à l'analyse précédente en ce qui a trait aux désintégrations semileptoniques $B^0 \to \pi^-\ell^+\nu$. Mis à part le fait que nous utilisons environ deux fois plus de données expérimentales, nous avons séparé le bruit de fond en cinq catégories au lieu de trois et utilisé les derniers algorithmes de reconstruction des traces chargées plus performants. Ces innovations se sont traduites par une meilleure compréhension du bruit de fond, entrainant ainsi une diminution des incertitudes systématiques. Un ajout intéressant est l'utilisation de cette méthode pour mesurer les rapports d'embranchement sur d'autres modes de désintégrations semileptoniques comme $B^+ \to \eta\ell^+\nu$ et $B^+ \to \eta^{'}\ell^+\nu$. Cette technique s'est avérée aussi pertinente pour ces deux modes, mais le manque de statistique nous ont obligés à restreindre le bruit de fond encore à trois catégories. Dans tous les cas, nous avons commencé une analyse basée uniquement sur la simulation Monte Carlo et sur des échantillons de contrôle. De cette simulation et de ces échantillons, nous avons optimisé les sélections des événements pour éliminer le plus de bruit de fond possible et obtenu l'efficacité du signal en fonction de q^2. Une fois l'approbation obtenue du groupe semileptonique de BABAR, nous avons regardé les résultats des données expérimentales et ils étaient en accord avec la simulation Monte Carlo. Le nombre d'événements signaux obtenus par un lissage des données en fonction de q^2 furent déconvolué pour corriger les erreurs de reconstruction de la vraie valeur de q^2. Cette procédure nous a permis de mesurer les rapports d'embranchement partiels et totaux en utilisant l'efficacité du signal en fonction de la vraie valeur de q^2. En dernier lieu, nous avons comparé le spectre des facteurs de formes théoriques au spectre de q^2 expérimentale afin d'extraire des valeurs de $|V_{ub}|$ provenant des différents calculs théoriques. Il est important de mentionner que les résultats des rapports d'embranchement partiels et totaux obtenus par la technique de reconstruction relâchée du neutrino sont indépendants de toute hypothèse théorique.

Au Chapitre 4, nous avons exposé un article publié dans PRD (*Physical Review D*) qui résume en quelques pages tout le contenu du Chapitre 3. Cet article est en quelque sorte une mise-à-jour de notre précédent article publié dans PRL (*Physical Review Letters*) [86]. Les rapports d'embranchement partiels et les matrices de corrélations rendent possibles l'extraction de $|V_{ub}|$ par des calculs théoriques plus performants dans le futur.

En conclusion, nous avons mesuré les rapports d'embranchement partiels des interactions $B^0 \to \pi^-\ell^+\nu$ et $B^+ \to \eta\ell^+\nu$ en douze et trois intervalles de q^2, illustrés aux Figures 4.8 et 4.9, respectivement. À partir de ces distributions, nous avons mesuré le spectre du facteur de forme $f_+(q^2)$ qui est compatible avec les prédictions théoriques FNAL, HPQCD et LCSR pour le mode $B^0 \to \pi^-\ell^+\nu$ dans leurs intervalles de validité. Pour la première fois, le spectre du facteur de forme a été mesuré pour le mode $B^+ \to \eta\ell^+\nu$ et il est compatible avec le calcul théorique LCSR. Toutefois, les valeurs de $|V_{ub}|$ exclusives ne sont extraites que par le mode $B^0 \to \pi^-\ell^+\nu$ et sont montrées dans le Tableau 4.5 pour les trois calculs théoriques. De plus, nous montrons dans le même

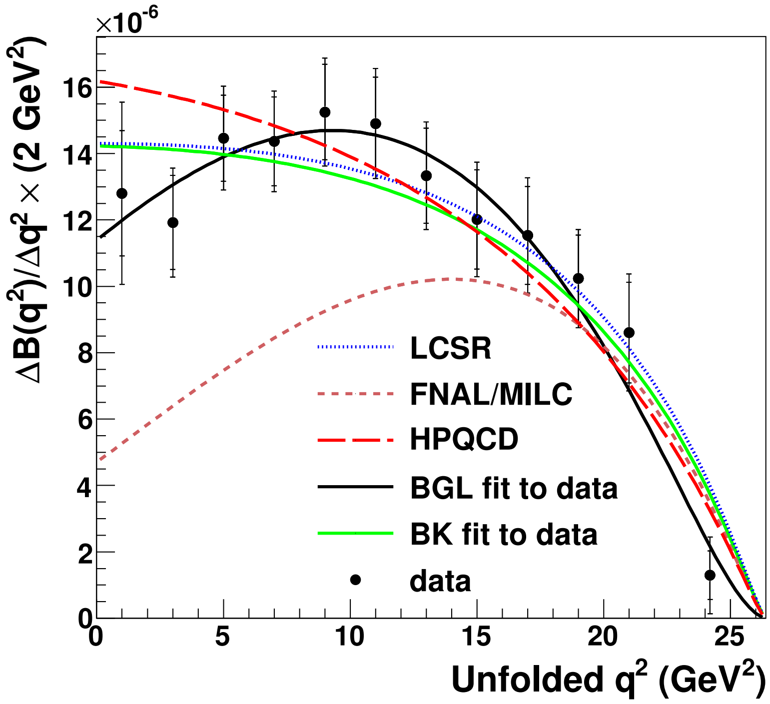

Figure 4.8 – Spectre des rapports d'embranchement partiels $\Delta\mathcal{B}(q^2)$ dans les douze intervalles de q^2 pour le mode $B^0 \to \pi^-\ell^+\nu$.

tableau les rapports d'embranchement totaux qui ont été calculés pour les trois modes $B^0 \to \pi^-\ell^+\nu$, $B^+ \to \eta\ell^+\nu$ et $B^+ \to \eta^{'}\ell^+\nu$, ainsi qu'une valeur de $|V_{ub}f_+(0)|$ pour le mode $B^0 \to \pi^-\ell^+\nu$ obtenue par un lissage des rapports d'embranchement partiels avec la paramétrisation BGL.

Ces résultats sont extrêmement précis. En effet, les mesures des rapports d'embranchement pour les modes $B^+ \to \eta\ell^+\nu$ et $B^+ \to \eta^{'}\ell^+\nu$ sont les plus précises à ce jour avec une incertitude de 17.8% et 35.8%, respectivement. Le rapport d'embranchement du mode $B^0 \to \pi^-\ell^+\nu$ a une incertitude de 6.7% et est comparable en précision avec une autre analyse de BABAR utilisant une méthode exclusive différente avec $q^2 = (P_\ell + P_\nu)^2$ et qui obtient $\mathcal{B}(B^0 \to \pi^-\ell^+\nu)$=$(1.41 \pm 0.05_{stat} \pm 0.07_{syst}) \times 10^{-4}$. Les valeurs de $|V_{ub}|$ et leurs incertitudes dominées par l'incertitude théorique sont également similaires. Le

Tableau 4.5 – Principaux résultats de cette thèse.

$\mathcal{B}(B^0 \to \pi^- \ell^+ \nu)$=$(1.42 \pm 0.05_{stat} \pm 0.08_{syst}) \times 10^{-4}$		
$\mathcal{B}(B^+ \to \eta \ell^+ \nu)$=$(0.36 \pm 0.05_{stat} \pm 0.04_{syst}) \times 10^{-4}$		
$\mathcal{B}(B^+ \to \eta^{'} \ell^+ \nu)$=$(0.24 \pm 0.08_{stat} \pm 0.03_{syst}) \times 10^{-4}$		
Paramétrisation	Valeur des paramètres	Prob(χ^2)
BGL [106]	$a_1/a_0 = -0.64 \pm 0.30$ $a_2/a_0 = -6.8 \pm 1.8$	92.2%
BK [96]	$\alpha_{BK} = 0.51 \pm 0.04$	39.6%
Calcul théorique	Valeur de $\|V_{ub}\|$ (10^{-3})	Prob(χ^2)
HPQCD [81]	$3.24 \pm 0.13_{stat} \pm 0.16_{syst}{}^{+0.57}_{-0.37}{}_{théo}$	30.1%
FNAL [82]	$3.14 \pm 0.12_{stat} \pm 0.16_{syst}{}^{+0.35}_{-0.29}{}_{théo}$	18.4%
LCSR [83]	$3.70 \pm 0.07_{stat} \pm 0.09_{syst}{}^{+0.54}_{-0.39}{}_{théo}$	47.0%
$\|V_{ub} f_+(0)\| = (8.6 \pm 0.3_{stat} \pm 0.3_{syst}) \times 10^{-4}$		

Tableau 4.6 – Comparaison de nos résultats avec des mesures précédentes.

rapports d'embranchement	méthodes	expériences
$\mathcal{B}(B^0 \to \pi^- \ell^+ \nu)$=$(1.42 \pm 0.05_{stat} \pm 0.08_{syst}) \times 10^{-4}$	**sans étiquette (neutrino relâché)**	BABAR
$\mathcal{B}(B^0 \to \pi^- \ell^+ \nu)$=$(1.46 \pm 0.07_{stat} \pm 0.08_{syst}) \times 10^{-4}$	sans étiquette (neutrino relâché)	BABAR [86]
$\mathcal{B}(B^0 \to \pi^- \ell^+ \nu)$=$(1.41 \pm 0.05_{stat} \pm 0.07_{syst}) \times 10^{-4}$	sans étiquette	BABAR [93]
$\mathcal{B}(B^0 \to \pi^- \ell^+ \nu)$=$(1.54 \pm 0.17_{stat} \pm 0.09_{syst}) \times 10^{-4}$	étiquette semileptonique	BABAR [92]
$\mathcal{B}(B^0 \to \pi^- \ell^+ \nu)$=$(1.38 \pm 0.19_{stat} \pm 0.14_{syst}) \times 10^{-4}$	étiquette semileptonique	Belle [90]
$\mathcal{B}(B^0 \to \pi^- \ell^+ \nu)$=$(1.37 \pm 0.15_{stat} \pm 0.11_{syst}) \times 10^{-4}$	sans étiquette	CLEO2 [88]
$\mathcal{B}(B^+ \to \eta \ell^+ \nu)$=$(0.36 \pm 0.05_{stat} \pm 0.04_{syst}) \times 10^{-4}$	**sans étiquette (neutrino relâché)**	BABAR
$\mathcal{B}(B^+ \to \eta \ell^+ \nu)$=$(0.31 \pm 0.06_{stat} \pm 0.08_{syst}) \times 10^{-4}$	sans étiquette (neutrino relâché)	BABAR [91]
$\mathcal{B}(B^+ \to \eta \ell^+ \nu)$=$(0.64 \pm 0.20_{stat} \pm 0.03_{syst}) \times 10^{-4}$	étiquette semileptonique	BABAR [92]
$\mathcal{B}(B^+ \to \eta^{'} \ell^+ \nu)$=$(0.24 \pm 0.08_{stat} \pm 0.03_{syst}) \times 10^{-4}$	**sans étiquette (neutrino relâché)**	BABAR
$\mathcal{B}(B^+ \to \eta^{'} \ell^+ \nu)$=$(0.04 \pm 0.22_{stat} \pm 0.05_{syst}) \times 10^{-4}$	étiquette semileptonique	BABAR [92]
$\mathcal{B}(B^+ \to \eta^{'} \ell^+ \nu)$=$(2.66 \pm 0.80_{stat} \pm 0.56_{syst}) \times 10^{-4}$	sans étiquette	CLEO2 [88]

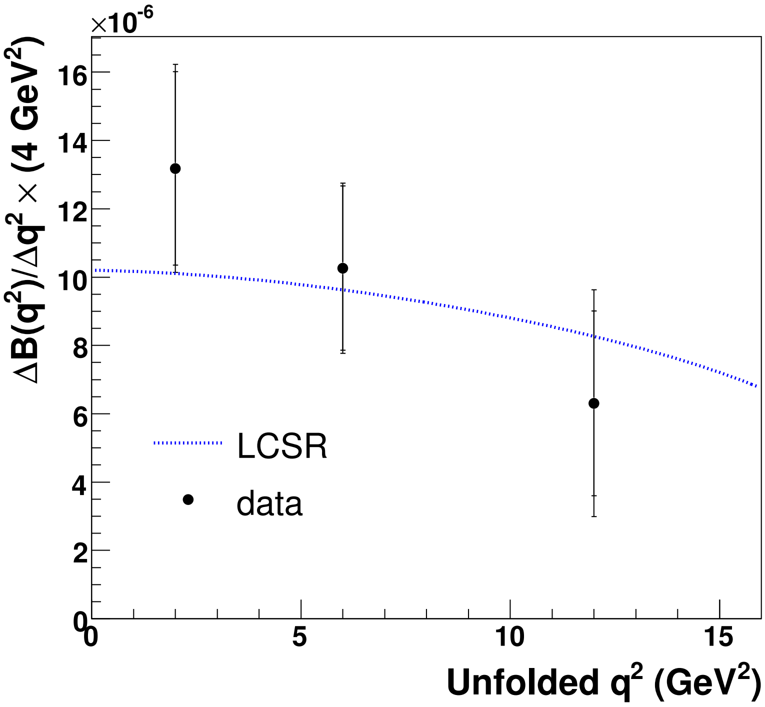

Figure 4.9 – Spectre des rapports d'embranchement partiels $\Delta\mathcal{B}(q^2)$ dans les trois intervalles de q^2 pour le mode $B^+ \to \eta\ell^+\nu$.

Tableau 4.6 montre les anciennes mesures des rapports d'embranchement de ces trois modes qui peuvent être comparées avec les nôtres.

Finalement, la mesure de $|V_{ub}|$ exclusive obtenue par le calcul théorique FNAL $|V_{ub}|_{FNAL} = (3.14^{+0.40}_{-0.35}) \times 10^{-3}$ possède toujours une légère tension avec la mesure inclusive dont la moyenne est $|V_{ub}|_{inclusif} = (4.27 \pm 0.38) \times 10^{-3}$. Une plus grande précision sur l'incertitude théorique est souhaitable, car elle pourra aider à élucider le mystère qui persiste entre les valeurs inclusives et exclusives de $|V_{ub}|$. Par ailleurs, la valeur de $|V_{ub}|$ indirecte obtenue après un lissage des paramètres de la matrice CKM est $|V_{ub}|_{indirecte} = (3.47^{+0.16}_{-0.12}) \times 10^{-3}$ et est en excellent accord avec nos résultats. Lorsque de nouveaux calculs théoriques seront disponibles, il sera possible de recalculer de nouvelles valeurs de $|V_{ub}|$ exclusives en utilisant les résultats présentés dans cette thèse. Il faudra attendre au moins dix ans avant d'obtenir une précision expérimentale significativement plus grande pour ces désintégrations avec les résultats des nouvelles expériences comme le *SuperB*. Une bonne partie du détecteur *BABAR* sera récupérée notament par le *SuperB* qui devrait atteindre des luminosités instantanées 100 fois supérieures à celle de l'expérience *BABAR*. Un mois de données enregistrées au *SuperB* sera équivalent à plus de huit ans de données enregistrées par *BABAR*. Ainsi, avec l'amélioration des calculs théoriques et expérimentales d'ici une dizaine d'années, il sera possible de vérifier plus précisément la validité du *Modèle Standard*. La chasse à la nouvelle physique est ouverte !

Annexe I

Annexe du Chapitre 3

I.1 Standard definitions and terminology

I.1.1 Charged Tracks Lists

The definitions of the charged tracks lists in release 22 have changed compared to the ones defined in release 18. The primary charged tracks list is *ChargedTracks* which corresponds to all candidates with a non-zero charge and with a pion mass hypothesis assigned. As listed in Table I.1, other lists, *GoodTracksVeryLoose* (GTVL), *GoodTracks-Loose* (GTL) and *GoodTracksTight* (GTT), are subsets of this list, based on the following selection criteria for each track :

- maximum distance of closest approach to the beam spot center in the xy direction ($DOCA_{xy}$)
- maximum distance of closest approach to the beam spot center in the z direction ($DOCA_z$), where the z direction is parallel to the beam direction.
- maximum momentum in LAB frame (p_{LAB})
- minimum transverse momentum (pt)

Criteria	GTVL	GTL & GTT
$DOCA_{xy}$ max.(cm)	1.5	1.5
$DOCA_z$ max.(cm)	2.5	2.5
p_{LAB} max.(GeV/c)	none	10
pt min.(GeV/c)	none	0.05

Tableau I.1 – Subset lists of the *ChargedTracks* list. In release 22 and after, the GTL and GTT lists was merged together to a single list. To avoid any confusion, we always use the terminology GTL and GTVL lists.

I.1.2 Neutral (Photons) Lists

The primary neutral list is *CalorNeutral* which corresponds to all bumps in the calorimeter not matched to a charged track and with a photon mass hypothesis assigned. As listed in Table I.2, other lists, *GoodPhotonLoose* (GPL), *GoodPhotonDefault* (GPD), are subsets of this list, based on the following selection criteria for a set of bumps in an event :

- minimum raw energy (E)
- maximum lateral moment (LAT)

Criteria	GPL	GPD
E min.(MeV)	30	100
LAT max.	0.8	0.8

Tableau I.2 – Subset lists of the *CalorNeutral* list

I.1.3 Neutrino reconstruction four-vectors

Three basic four-vectors are often used throughout this document.

- s is the four-momentum sum of the colliding e^+ and e^- beams, as provided by PEP-II, i.e. $\sqrt{s}$ is the center of mass energy available in an event ;
- P_{tot} is the four-momentum sum of all reconstructed GTVL tracks and CalorNeutral bumps, its energy component is referred to as E_{tot} ;
- P_{miss} is the missing momentum four-vector, defined as $P_{miss} \equiv (|\vec{p}_{miss}|, \vec{p}_{miss})$ with $\vec{p}_{miss} = \vec{s} - \vec{p}_{tot}$. By setting the P_{miss} energy to $|\vec{p}_{miss}|$, P_{miss} is massless by construction. This method gives a more accurate estimate of the signal neutrino four-vector than setting $E_{miss} = s_{energy} - E_{tot}$.

To reconstruct P_{tot} and the other full-event quantities, we use the CalorNeutral selection of EMC bumps instead of more stringent selections because our MC studies show that it yields more precise measurements of the $\mathcal{B}(B^+ \to \eta^{(\prime)}\ell^+\nu)$ and $f_+(q^2)$ shape parameters. With more stringent EMC selections (e.g. *à la* BAD 1111), too many real photons are rejected, which results in additional missing energy that is not coming from the signal neutrino. The consequences of using tight EMC bump selections are thus that the ΔE and m_{ES} shape differences between signal and background are not significant and the separation of the signal from the background becomes more difficult.

I.1.4 Terminology of semileptonic decays

The following terminology is used throughout this document to describe $B \to X_u \ell \nu$ decays, where $X_u = \pi$, η or η'.

- Y represents a fictive particle whose four-momenta is the vectorial sum of the X_u meson and the lepton four-momenta : $P_Y = P_{X_u} + P_\ell$, so that $B \to X_u \ell \nu$ could be written as $B \to Y \nu$;
- q^2 means either the true q^2 in its theoretical sense or the experimental unfolded q^2 which is in principle equivalent to the true q^2 ;
- $\tilde{q}^2$ means the reconstructed q^2. It differs from the true and unfolded q^2 because of experimental uncertainties.

I.1.5 Illustration of the effectiveness of the selected cuts

In this section, we show that each cut used is effective to discriminate between signal and background. In Figs. I.1 - I.4, we show the distributions for six of the main cuts used in the analysis of the $\pi \ell \nu$ decay mode : $cos\theta_{BY}$, $Y\ Prob(\chi^2)$, $cos\theta_\ell$, $cos\theta_{thrust}$, θ_{miss} and $M^2_{miss}/2E_{miss}$, with all the cuts used in the analysis applied except for the cut of interest (Figs. I.1, I.3) and with all the cuts applied, including the cut of interest (Figs. I.2, I.4). In Figs. I.5 - I.8, we show similar distributions for six of the main cuts used in the analysis of the $\eta \ell \nu$ mode : $cos\theta_V$, $Y\ Prob(\chi^2)$, $cos\theta_\ell$, $cos\theta_{thrust}$, θ_{miss} and $M^2_{miss}/2E_{miss}$.

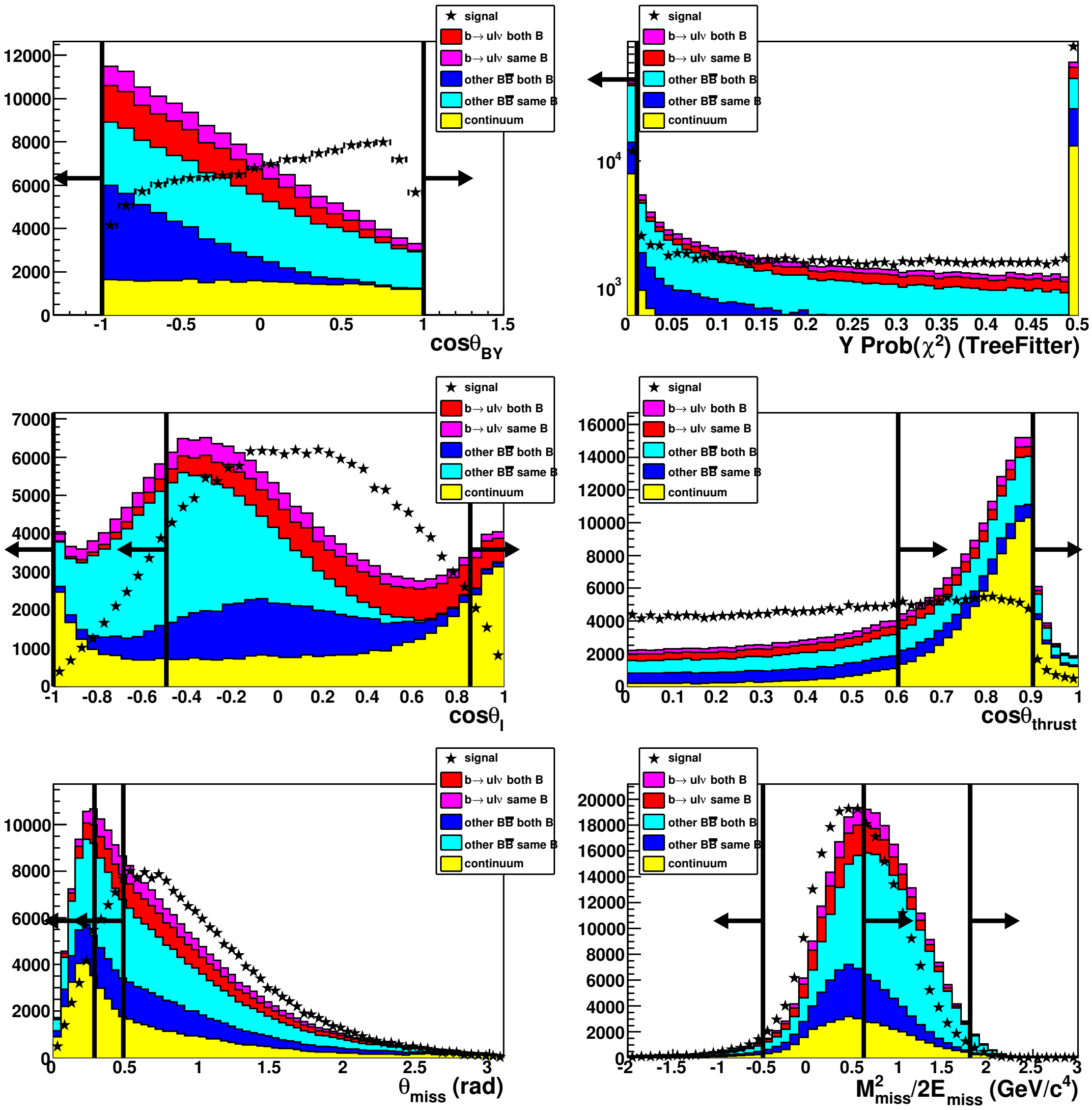

Figure I.1 – Distributions in the fit region for six of the main cuts used in the analysis of $B^0 \to \pi^- \ell^+ \nu$ decays. All the cuts have been applied except for the cut of interest. In each panel, the signal area is scaled to the area of the total background. The four bottom panels are the q^2-dependent cut variables.

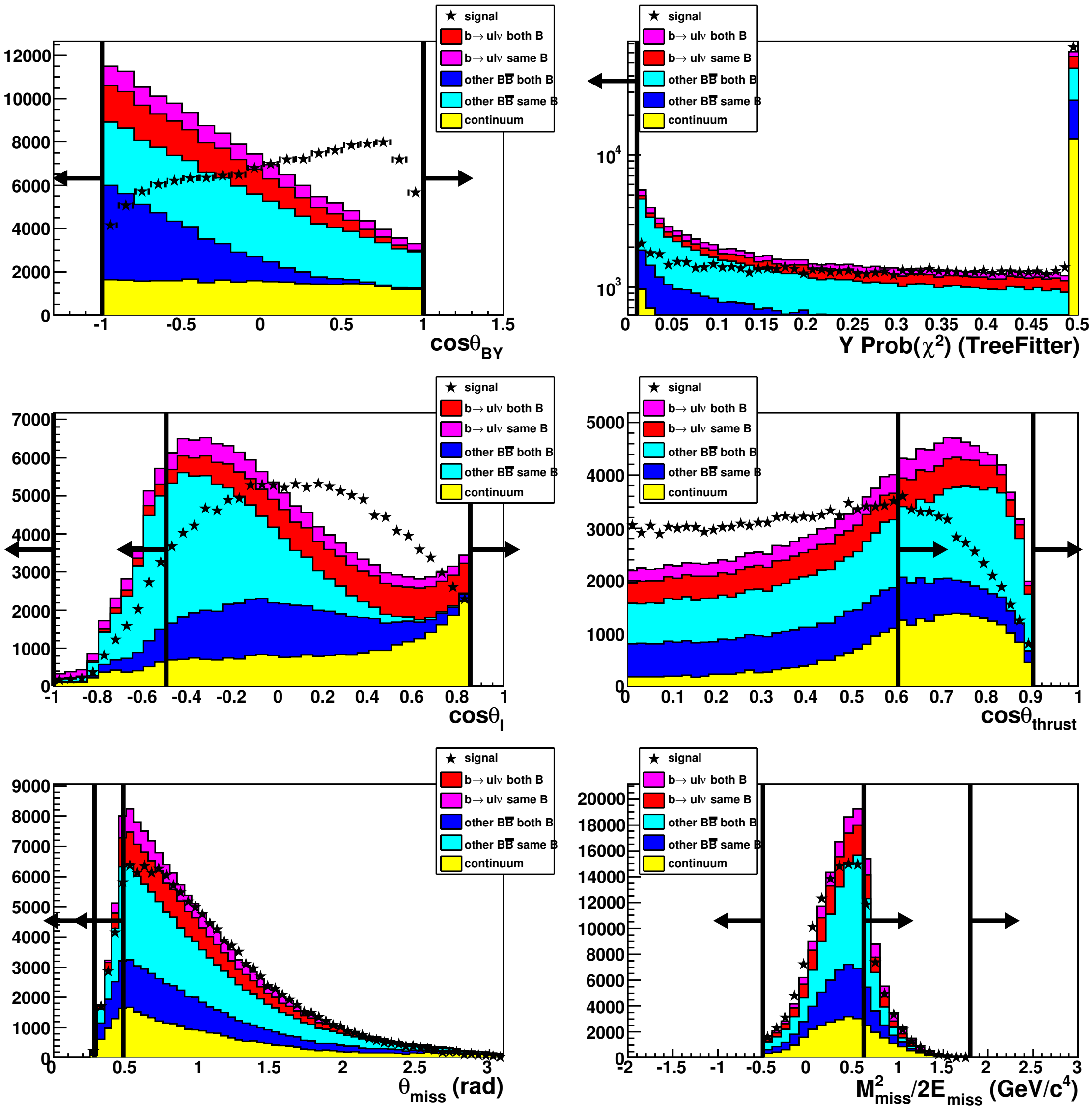

Figure I.2 – Distributions in the fit region for six of the main cuts used in the analysis of $B^0 \to \pi^- \ell^+ \nu$ decays. All the cuts have been applied including the cut of interest. In each panel, the signal area is scaled to the area of the total background. The four bottom panels are the q^2-dependent cut variables.

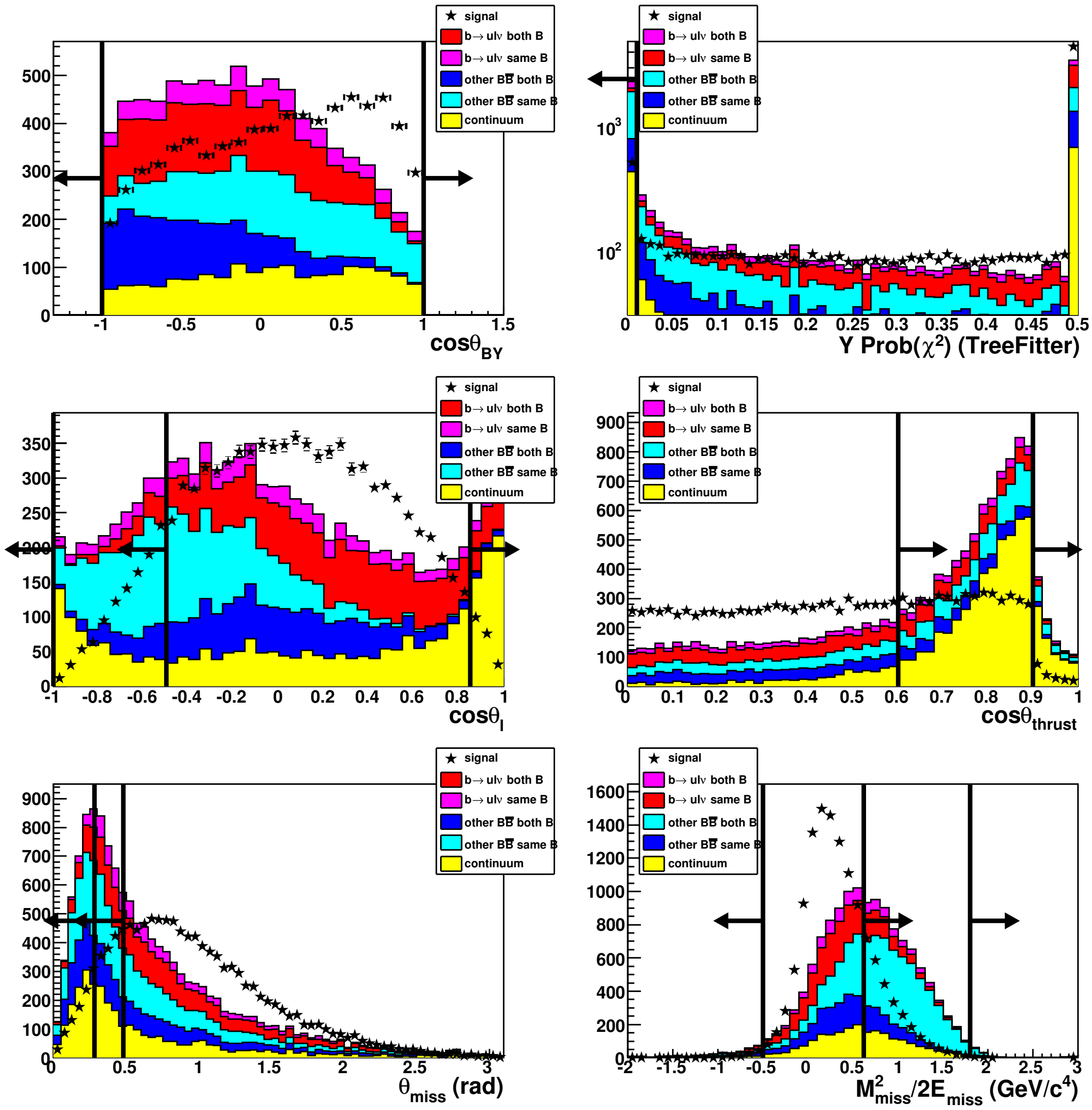

Figure I.3 – Distributions in the signal region for six of the main cuts used in the analysis of $B^0 \to \pi^- \ell^+ \nu$ decays. All the cuts have been applied except for the cut of interest. In each panel, the signal area is scaled to the area of the total background. The four bottom panels are the q^2-dependent cut variables.

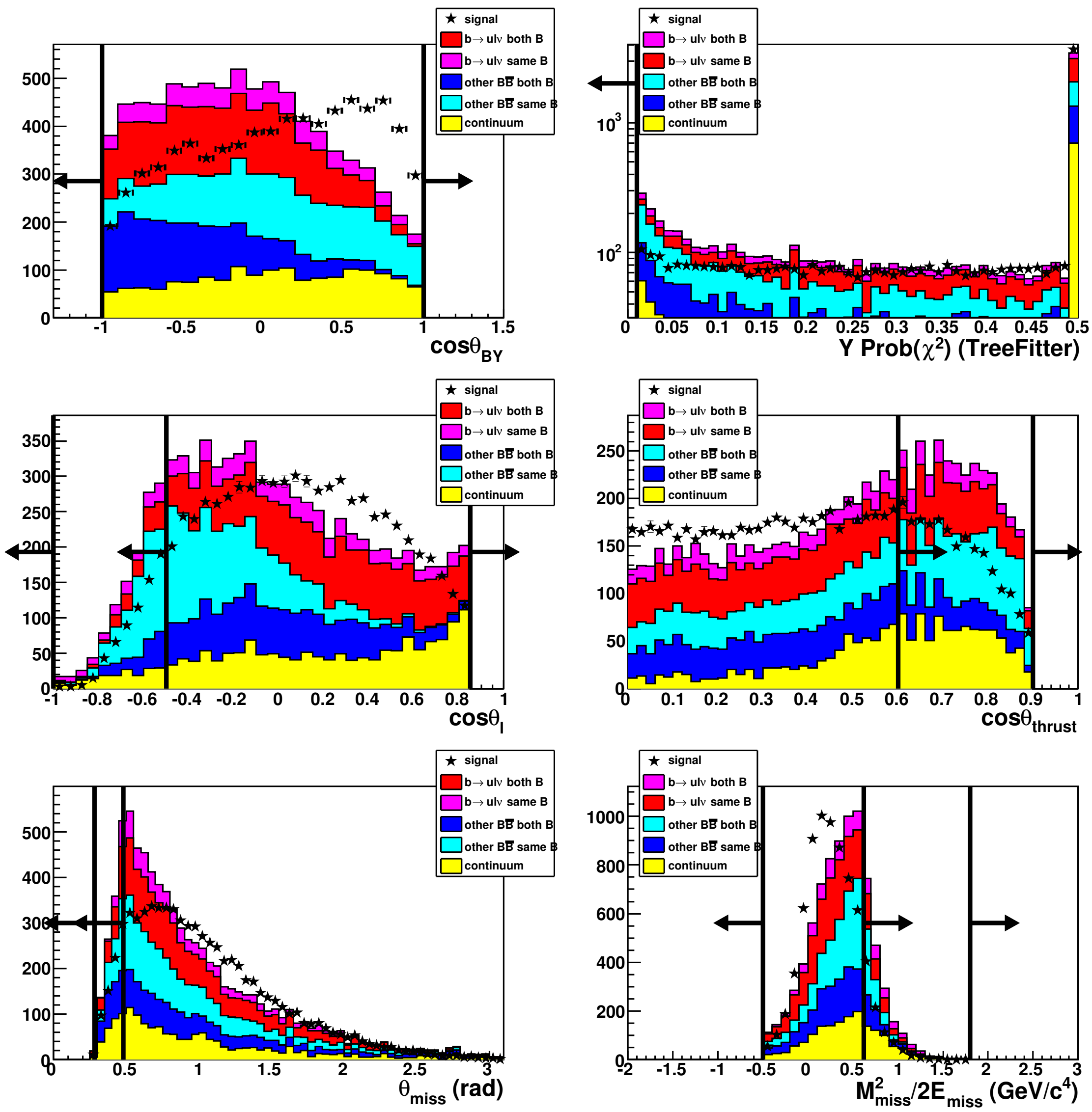

Figure I.4 – Distributions in the signal region for six of the main cuts used in the analysis of $B^0 \to \pi^- \ell^+ \nu$ decays. All the cuts have been applied including the cut of interest. In each panel, the signal area is scaled to the area of the total background. The four bottom panels are the q^2-dependent cut variables.

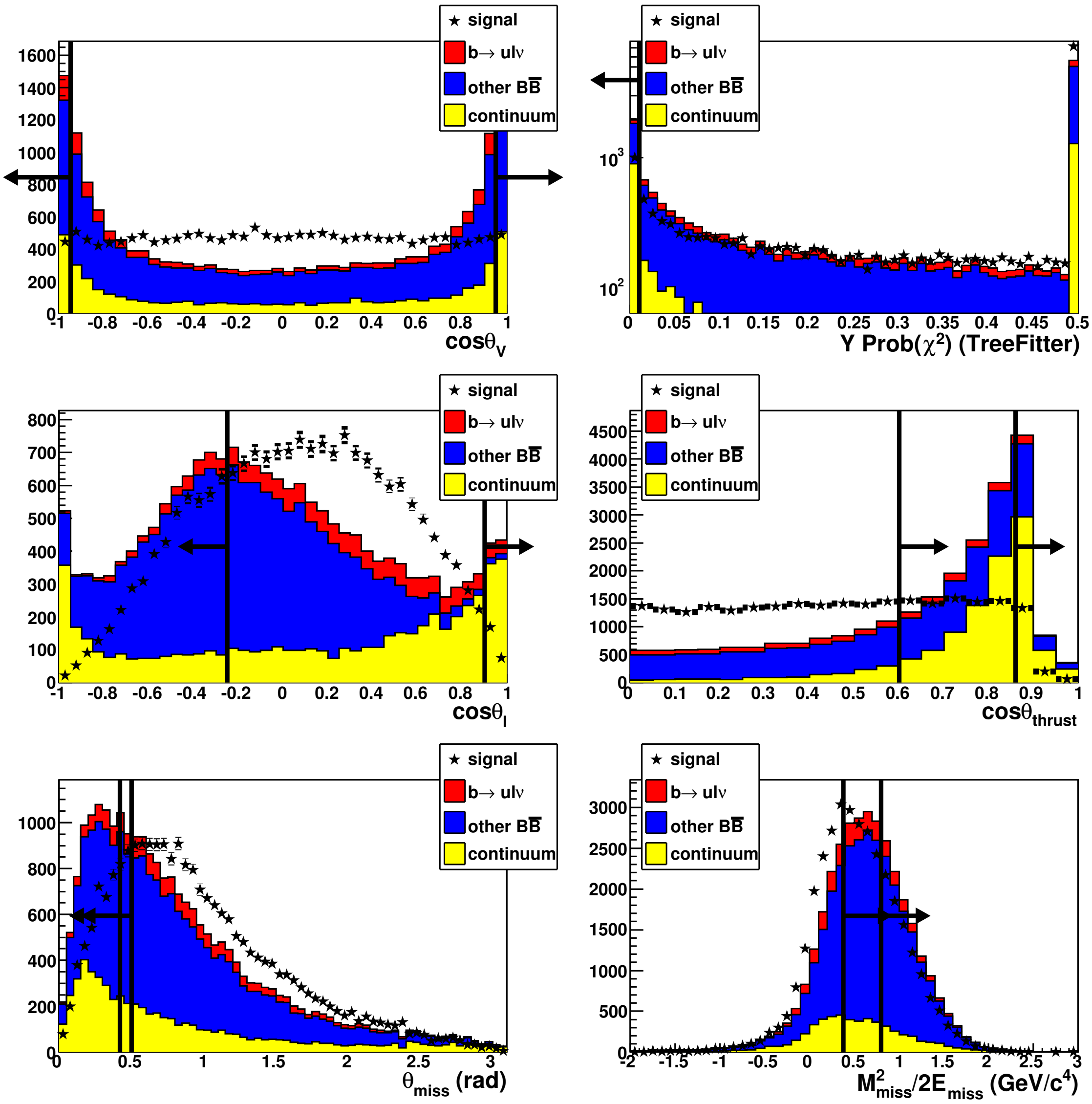

Figure I.5 – Distributions in the fit region for six of the main cuts used in the analysis of $B^+ \to \eta\ell^+\nu$ decays. All the cuts have been applied except for the cut of interest. In each panel, the signal area is scaled to the area of the total background. The four bottom panels are the q^2-dependent cut variables.

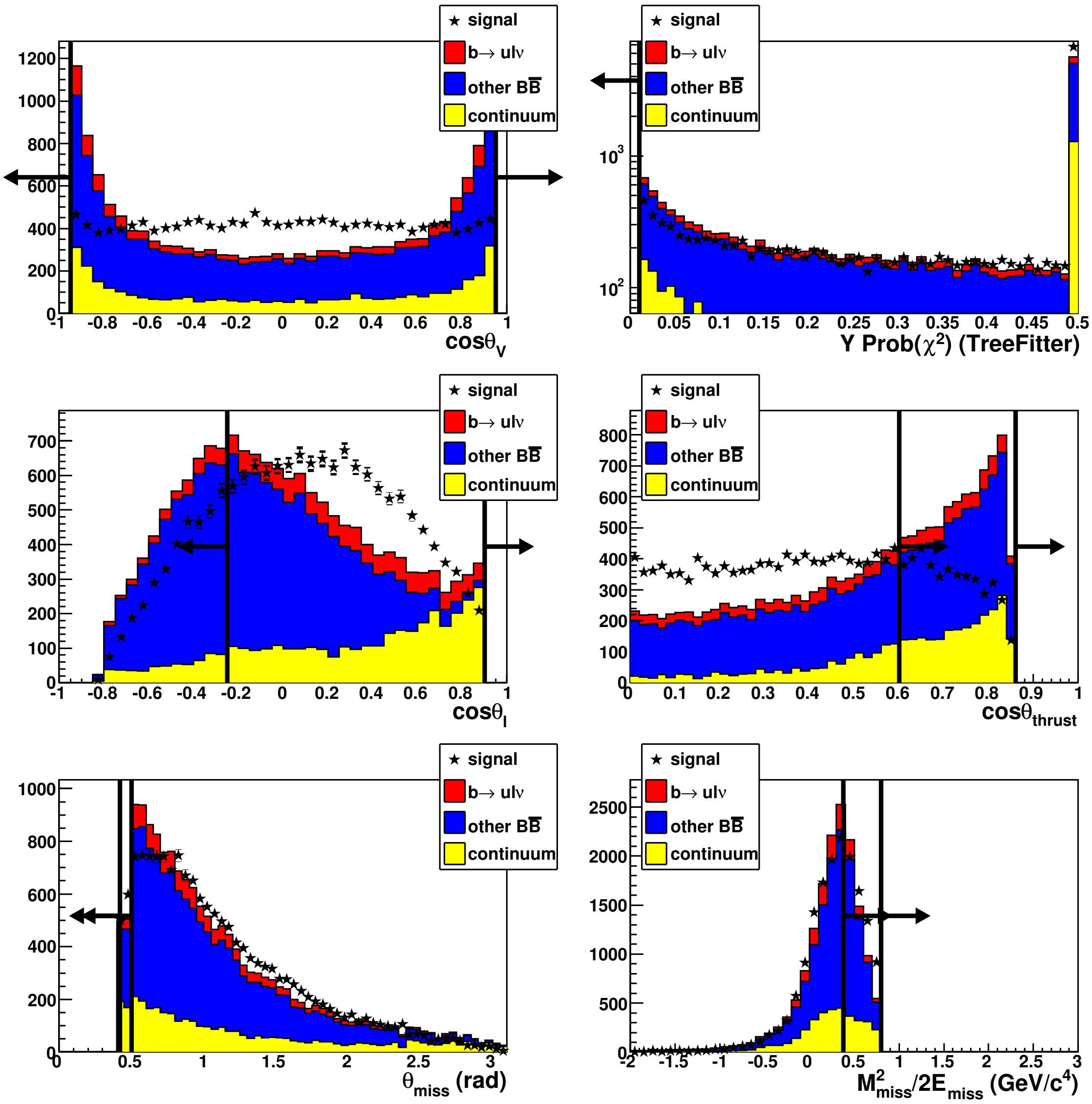

Figure I.6 – Distributions in the fit region for six of the main cuts used in the analysis of $B^+ \to \eta\ell^+\nu$ decays. All the cuts have been applied including the cut of interest. In each panel, the signal area is scaled to the area of the total background. The four bottom panels are the q^2-dependent cut variables.

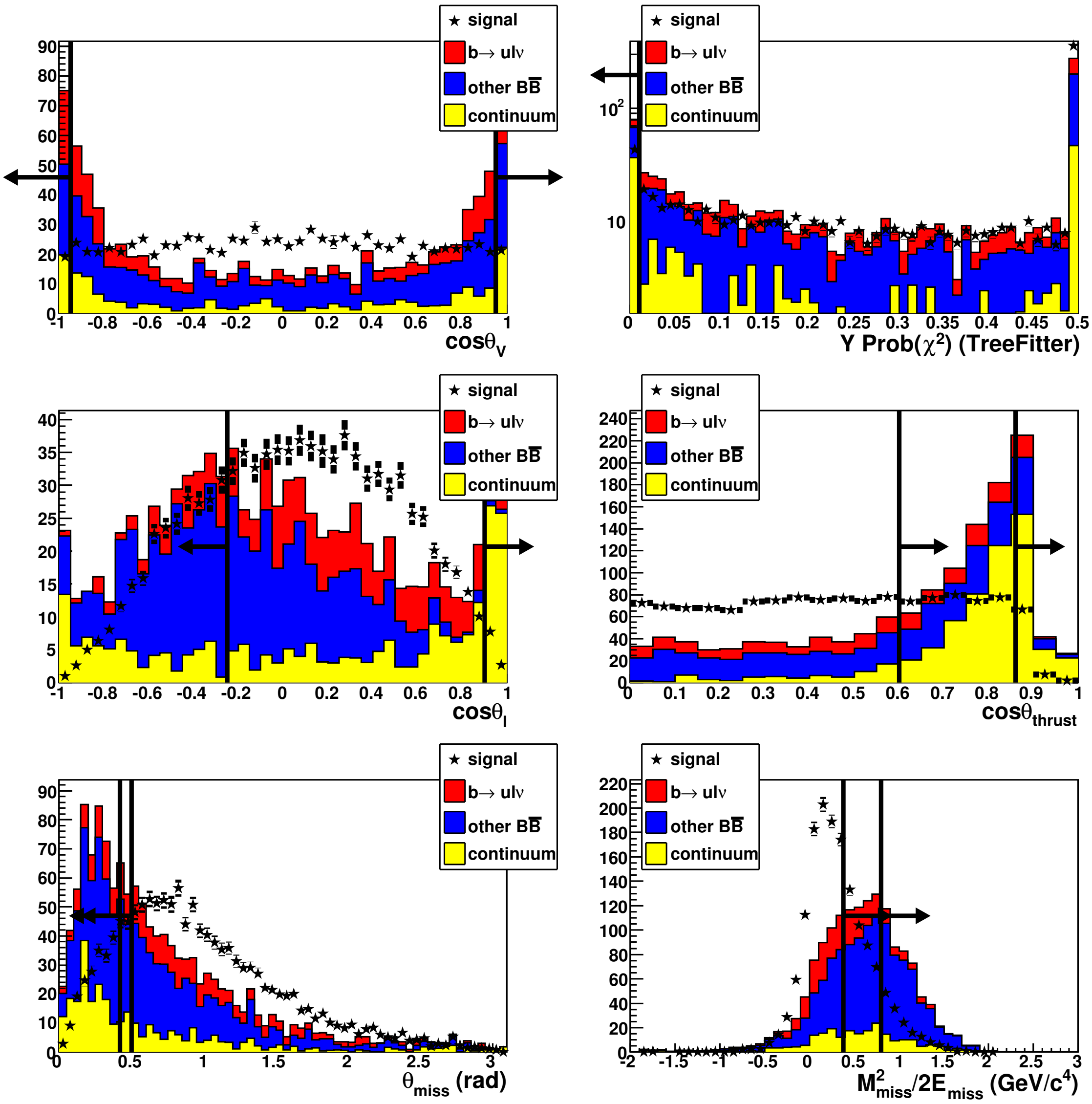

Figure I.7 – Distributions in the signal region for six of the main cuts used in the analysis of $B^+ \to \eta\ell^+\nu$ decays. All the cuts have been applied except for the cut of interest. In each panel, the signal area is scaled to the area of the total background. The four bottom panels are the q^2-dependent cut variables.

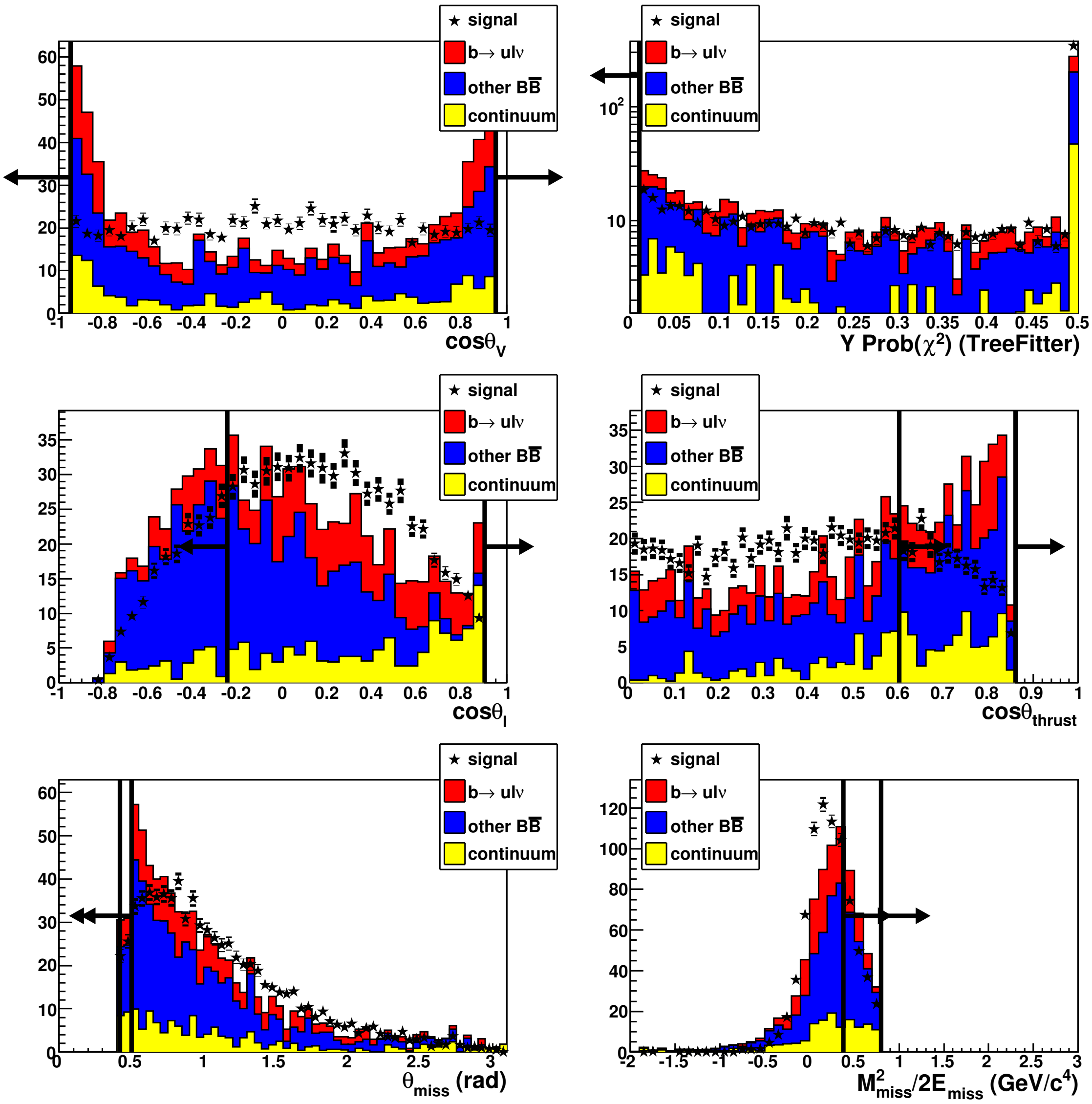

Figure I.8 – Distributions in the signal region for six of the main cuts used in the analysis of $B^+ \to \eta\ell^+\nu$ decays. All the cuts have been applied including the cut of interest. In each panel, the signal area is scaled to the area of the total background. The four bottom panels are the q^2-dependent cut variables.

Annexe II

Annexe du Chapitre 4

II.1 Appendix

In Tables II.1-II.3, we give the functions describing the q^2 dependence of the selections used to reduce the backgrounds in the three decays under study.

The list of all the systematic uncertainties, as well as their values for the partial and total BFs, are given in Tables II.4 and II.5 for the $B^0 \rightarrow \pi^- \ell^+ \nu$ and $B^+ \rightarrow \eta^{(\prime)} \ell^+ \nu$ decays, respectively. In Table II.4, we have one column for each bin of $\tilde{q}^2$, three columns for various ranges of $\tilde{q}^2$ as well as the last column for the global result. In row 1, “Fitted yield”, we give the raw fitted yield as number of events. In row 2, “Yield statistical error”, we give the statistical uncertainty in % for each fitted yield. In row 3, “Efficiency”, we give the efficiency in % attached to each yield. In row 4, “Eff. (Without FSR)”, we give the efficiency in %, modified to remove the FSR effect. In row 5, “Unfolded yield”, we give the yields from row 1 unfolded to give the true values of the yields in each bin, expressed as number of events. In row 6, “$\Delta\mathcal{B}$", we give the values of the partial BFs computed as usual using the true (unfolded) yields and the efficiencies with FSR. In row 7, “$\Delta\mathcal{B}$ (Without FSR)", we give the values of the partial BFs computed as usual using the true (unfolded) yields and the efficiencies modified to remove the FSR effect. In rows 8 - 39, we give the contributions in % to the relative systematic uncertainties for each value of $\Delta\mathcal{B}$ as a function of $\tilde{q}^2$. In row 40, “Signal MC statistical error”, we give the statistical uncertainty due to the number of MC signal events. In row 41, “Total systematic error”, we give the total systematic uncertainty in % for each value of $\Delta\mathcal{B}$, obtained as the sum in quadrature of all the systematic uncertainties in each column. In row 42, “Total statistical error”, we give the statistical uncertainty in % for each value of $\Delta\mathcal{B}$ obtained from propagating the statistical uncertainties on the raw fitted yields, following the unfolding process and taking into account the efficiencies. In row 43, “Total error”, we first give the total uncertainty in % for each value of $\Delta\mathcal{B}$,

Tableau II.1 – q^2-dependent selections used in $B^0 \to \pi^- \ell^+ \nu$ decays.

$\cos\theta_\ell < 0.85$ for all values of $\tilde{q}^2$
$\cos\theta_\ell > -0.0000167 * q^8 + 0.000462 * q^6 + 0.000656 * q^4 - 0.0701 * q^2 - 0.48$
$m^2_{miss}/2E_{miss} > -0.5\ \mathrm{GeV}$ for all values of $\tilde{q}^2$
$m^2_{miss}/2E_{miss} < 0.00544 * q^4 - 0.127 * q^2 + 1.37\ \mathrm{GeV}$
$\cos\theta_{thrust} < 0.9$ for all values of $\tilde{q}^2$
$\cos\theta_{thrust} < -0.00159 * q^4 + 0.0451 * q^2 + 0.59$
$\theta_{miss} > -0.000122 * q^6 + 0.00483 * q^4 - 0.0446 * q^2 + 0.405\ rad$
($\tilde{q}^2$ is given in units of GeV^2)

obtained as the sum in quadrature of the total systematic error and the total statistical error. We then give, in the last four columns, the total uncertainties in % for each range of $\tilde{q}^2$, obtained as the sum in quadrature of the total errors for the appropriate number of $\tilde{q}^2$ bins. A similar description applies to Table II.5.

In our analysis, we compute the covariance matrix for each source of uncertainty, and use these matrices to calculate the uncertainties on the total BFs. The correlation matrices for the total statistical and systematic uncertainties are given in Table II.6 for the $B^+ \to \eta\ell^+\nu$ yields and in Tables II.7 and II.8 for the $B^0 \to \pi^-\ell^+\nu$ yields, respectively. Finally, detailed ΔE and m_{ES} fit projections in each $\tilde{q}^2$ bin are also shown in Figs. II.1 and II.2, respectively, for the $B^0 \to \pi^-\ell^+\nu$ decays.

Tableau II.2 – q^2-dependent selections used in $B^+ \to \eta\ell^+\nu$ decays.

$\cos\theta_\ell < 0.9$ for all values of $\tilde{q}^2$
$\cos\theta_\ell > 0.00629 * q^4 - 0.119 * q^2 - 0.252$
$m^2_{miss}/2E_{miss} < 0.8$ GeV, $\tilde{q}^2 < 7.5$ GeV^2
$m^2_{miss}/2E_{miss} < -0.05 * q^2 + 1.175$ GeV, $7.5 < \tilde{q}^2 < 16.0$ GeV^2
$\cos\theta_{thrust} < 0.05 * q^2 + 0.6$, $\tilde{q}^2 < 5.0$ GeV^2
$\cos\theta_{thrust} < 0.85$, $5.0 < \tilde{q}^2 < 16.0$ GeV^2
$\cos\theta_{miss} < 0.92$, $\tilde{q}^2 < 11.0$ GeV^2
$\cos\theta_{miss} < 0.88$, $11.0 < \tilde{q}^2 < 16.0$ GeV^2
($\tilde{q}^2$ is given in units of GeV^2)

Tableau II.3 – q^2-dependent selections used in $B^+ \to \eta^{'}\ell^+\nu$ decays.

$m^2_{miss}/2E_{miss} > -0.3$ GeV for all values of $\tilde{q}^2$
$m^2_{miss}/2E_{miss} < 0.35 * q^2 + 0.325$ GeV, $\tilde{q}^2 < 2.5$ GeV^2
$m^2_{miss}/2E_{miss} < 1.2$ GeV, $2.5 < \tilde{q}^2 < 4.5$ GeV^2
$m^2_{miss}/2E_{miss} < -0.1 * q^2 + 1.65$ GeV, $\tilde{q}^2 > 4.5$ GeV^2
$\cos\theta_{thrust} < 0.05 * q^2 + 0.575$, $\tilde{q}^2 < 6.5$ GeV^2
$\cos\theta_{thrust} < 0.9$, $6.5 < \tilde{q}^2 < 12.5$ GeV^2
$\cos\theta_{thrust} < -0.05 * q^2 + 1.525$, $\tilde{q}^2 > 12.5$ GeV^2
$\theta_{miss} > -0.1 * q^2 + 0.45$ rad, $\tilde{q}^2 < 2.5$ GeV^2
$\theta_{miss} > 0.2\ rad$, $2.5 < \tilde{q}^2 < 5.5$ GeV^2
$\theta_{miss} > 0.05 * q^2 - 0.075$ rad, $\tilde{q}^2 > 5.5$ GeV^2
($\tilde{q}^2$ is given in units of GeV^2)

Tableau II.4 – $B^0 \to \pi^- \ell^+ \nu$ yields, efficiencies(%), $\Delta\mathcal{B}$ (10^{-7}) and their relative uncertainties (%). The $\Delta\mathcal{B}$ and efficiency values labelled “Without FSR” are modified to remove FSR effects. This procedure has no sigificant impact on the $\Delta\mathcal{B}$ values.

q^2 bins (GeV^2)	0-2	2-4	4-6	6-8	8-10	10-12	12-14	14-16	16-18	18-20	20-22	22-26.4	q^2<12	q^2<16	q^2>16	Total
Fitted yield	894.7	987.8	1177.1	1181.3	1178.6	1122.1	996.1	884.5	904.3	847.5	729.9	873.9	6541.6	8422.1	3355.4	11777.6
Yield statistical error	12.8	8.1	6.0	6.4	6.7	7.0	8.2	9.8	10.3	10.5	14.0	21.0	3.2	3.6	7.9	3.7
Efficiency	8.34	9.10	9.22	9.09	8.59	8.46	8.53	8.50	9.40	10.52	11.61	14.59	-	-	-	-
Eff. (Without FSR)	8.00	8.97	9.15	9.18	8.63	8.53	8.58	8.61	9.45	10.66	11.71	14.70	-	-	-	-
Unfolded yield	919.9	960.7	1189.6	1184.5	1182.9	1141.5	1027.3	929.2	979.5	979.9	905.8	376.7	6579.1	8535.7	3241.9	11777.6
$\Delta\mathcal{B}$	122.7	117.6	143.6	145.0	153.4	150.2	134.1	121.7	116.0	103.7	86.8	28.7	832.5	1088.3	335.3	1423.5
$\Delta\mathcal{B}$ (Without FSR)	128.0	119.2	144.6	143.7	152.5	149.0	133.3	120.1	115.3	102.3	86.1	28.5	837.1	1090.5	332.3	1422.8
Tracking efficiency	3.2	1.9	3.1	2.2	2.3	3.9	2.6	4.0	3.5	1.3	4.1	9.4	2.3	2.5	2.9	2.6
Photon efficiency	6.0	3.4	2.6	1.3	2.2	2.5	3.1	3.0	5.0	1.4	5.1	24.2	1.9	2.2	4.6	2.7
K_L^0 efficiency	0.9	0.3	0.6	0.3	0.5	0.4	0.5	0.8	0.6	0.4	1.7	6.8	0.3	0.3	1.0	0.4
K_L^0 production spectrum	1.0	0.6	1.0	0.6	1.1	1.0	0.6	2.7	1.7	1.0	2.0	8.3	0.7	0.9	1.9	1.1
K_L^0 energy	1.0	0.6	0.3	0.2	0.2	0.3	0.2	0.4	0.6	0.7	0.8	7.1	0.2	0.3	0.8	0.3
ℓ identification	4.0	1.0	1.2	1.3	0.6	0.6	1.6	1.0	0.9	1.6	0.7	4.9	0.3	0.5	1.1	0.6
π identification	0.5	0.2	0.2	0.2	0.2	0.2	0.2	0.3	0.3	0.3	0.3	5.5	0.2	0.2	0.7	0.3
Bremsstrahlung	0.6	0.3	0.1	0.2	0.2	0.2	0.2	0.3	0.3	0.3	0.3	5.3	0.2	0.2	0.7	0.3
$\tilde{q}^2$ continuum shape	7.9	1.6	0.9	0.3	0.7	0.3	1.1	0.3	0.7	1.1	1.2	5.4	0.9	0.8	1.0	0.7
$\mathcal{B}(B^+ \to \pi^0\ell^+\nu)$	0.5	0.1	0.1	0.1	0.1	0.1	0.2	0.3	0.3	0.3	0.4	7.1	0.2	0.2	0.8	0.3
$\mathcal{B}(B^0 \to \rho^-\ell^+\nu)$	0.5	0.3	0.1	0.1	0.2	0.1	0.2	0.3	0.3	0.3	0.5	10.1	0.2	0.2	0.9	0.3
$\mathcal{B}(B^+ \to \rho^0\ell^+\nu)$	0.7	0.2	0.1	0.1	0.2	0.2	0.2	0.3	0.4	0.3	0.3	7.3	0.2	0.2	0.8	0.3
$\mathcal{B}(B^+ \to \omega\ell^+\nu)$	0.5	0.1	0.1	0.1	0.1	0.1	0.2	0.3	0.3	0.4	0.3	8.2	0.2	0.2	0.9	0.3
$\mathcal{B}(B^+ \to \eta\ell^+\nu)$	0.5	0.1	0.1	0.1	0.1	0.1	0.2	0.3	0.3	0.3	0.2	5.5	0.2	0.2	0.7	0.3
$\mathcal{B}(B^+ \to \eta^{'}\ell^+\nu)$	0.5	0.1	0.1	0.1	0.1	0.1	0.2	0.3	0.3	0.3	0.3	5.4	0.2	0.2	0.7	0.3
Non resonant $b \to u\ell\nu$ BF	0.6	0.3	0.1	0.1	0.2	0.2	0.2	0.4	0.5	0.3	0.6	7.8	0.2	0.2	0.7	0.3
SF parameters	0.9	0.5	0.9	0.4	0.3	0.5	0.6	0.3	0.5	2.3	4.1	23.4	0.6	0.4	2.3	0.8
$B \to \rho\ell\nu$ FF	2.4	1.4	2.1	1.4	1.9	1.6	0.8	0.7	2.4	3.0	1.1	16.6	1.8	1.5	1.8	1.5
$B^0 \to \pi^-\ell^+\nu$ FF	0.5	0.1	0.1	0.1	0.1	0.1	0.2	0.3	0.3	0.3	0.3	7.5	0.2	0.2	0.9	0.3
Other scalar FF	1.1	0.3	0.5	0.5	0.4	0.3	0.3	0.7	1.7	2.1	2.0	8.7	0.4	0.3	0.6	0.3
$B \to \omega\ell\nu$ FF	0.6	0.1	0.1	0.1	0.1	0.1	0.2	0.3	0.5	0.6	0.6	18.1	0.2	0.2	1.8	0.5
$\mathcal{B}(B \to D\ell\nu)$	0.6	0.6	0.2	0.1	0.3	0.2	0.5	0.3	0.4	0.4	0.4	5.6	0.2	0.3	0.7	0.4
$\mathcal{B}(B \to D^*\ell\nu)$	0.7	0.3	0.2	0.3	0.4	0.3	0.3	0.5	0.4	0.3	0.5	5.7	0.3	0.3	0.7	0.4
$\mathcal{B}(B \to D^{**}\ell\nu)$	0.7	0.3	0.3	0.5	0.5	0.3	0.8	0.6	1.1	0.7	0.7	5.8	0.3	0.3	0.9	0.4
Non resonant $b \to c\ell\nu$ BF	0.6	0.2	0.2	0.1	0.2	0.2	0.2	0.5	0.3	0.3	0.3	5.6	0.2	0.2	0.7	0.3
$B \to D\ell\nu$ FF	0.5	0.2	0.3	0.1	0.2	0.1	0.2	0.4	0.4	0.3	0.4	5.7	0.2	0.2	0.7	0.3
$B \to D^*\ell\nu$ FF	0.6	0.2	0.2	0.4	0.2	1.0	0.6	1.9	0.4	0.7	1.1	6.9	0.2	0.3	1.0	0.5
$\Upsilon(4S) \to B^0\bar{B}^0$ BF	1.5	1.7	1.2	1.3	1.3	1.2	1.5	1.2	1.4	1.4	1.0	5.8	1.3	1.4	1.2	1.3
Secondary lepton	4.3	3.2	2.1	1.2	1.7	0.5	1.2	0.5	0.5	0.9	3.7	5.8	1.0	0.9	1.2	0.9
Final state radiation	0.3	1.3	0.8	2.2	0.3	1.4	1.2	1.3	1.4	1.6	0.8	3.4	1.0	1.1	1.5	1.2
B counting	1.1	1.1	1.1	1.1	1.1	1.1	1.1	1.1	1.1	1.1	1.1	1.1	1.1	1.1	1.1	1.1
Fit bias	0.1	0.3	0.4	0.1	0.1	0.4	0.4	0.7	0.1	1.0	2.0	30.8	0.2	0.0	1.8	0.4
Signal MC stat error	1.3	1.6	1.4	1.6	1.4	1.5	1.4	1.4	1.3	1.4	1.2	2.5	0.6	0.4	0.6	0.3
Total systematic error	12.9	6.4	6.0	4.9	5.0	5.9	5.6	7.0	7.8	6.3	10.0	61.6	4.4	4.6	8.3	5.2
Total statistical error	14.7	11.9	9.0	9.3	9.4	9.4	10.8	12.5	12.8	12.8	17.6	56.7	3.9	3.7	7.6	3.5
Total error	19.6	13.5	10.8	10.5	10.7	11.1	12.1	14.3	15.0	14.3	20.3	83.8	5.9	5.9	11.3	6.3

Tableau II.5 – $B^+ \to \eta^{(\prime)}\ell^+\nu$ yields, efficiencies(%), $\Delta\mathcal{B}$ (10^{-7}) and their relative uncertainties (%).

Decay mode	$\eta'\ell^+\nu$	$\eta\ell^+\nu$ (3π)	$\eta\ell^+\nu$ ($\gamma\gamma$)				$\eta\ell^+\nu$ (3π and $\gamma\gamma$ combined)			
q^2 bins (GeV^2)	Total	Total	0-4	4-8	8-16	Total	0-4	4-8	8-16	Total
Fitted yield	141.0	244.8	279.9	216.8	146.7	643.4	303.9	331.5	252.5	887.9
Yield statistical error	32.8	25.6	13.9	17.2	33.9	12.0	14.1	14.2	26.6	11.0
Efficiency	0.61	0.59	2.01	2.55	1.42	-	2.53	3.41	1.94	-
Unfolded yield	141.0	244.8	299.1	210.9	133.3	643.4	319.3	334.8	233.9	887.9
$\Delta\mathcal{B}$	242.5	431.5	155.3	86.3	97.7	339.3	131.8	102.6	126.2	360.6
Tracking efficiency	5.2	4.1	3.2	2.4	14.6	2.6	2.1	2.0	11.1	2.8
Photon efficiency	5.6	3.1	10.1	4.3	27.4	7.0	8.0	3.8	9.0	5.7
K_L^0 efficiency	2.5	0.7	8.6	2.9	27.2	3.2	1.0	0.5	2.2	0.6
K_L^0 production spectrum	2.7	1.4	4.7	1.5	16.2	2.5	0.8	0.5	2.3	1.0
K_L^0 energy	1.1	1.4	0.6	0.5	2.5	0.9	0.6	0.4	2.3	1.0
ℓ identification	2.0	1.8	0.1	2.7	3.9	1.8	0.2	1.9	3.4	1.8
π identification	0.6	0.5	-	-	-	-	0.1	0.2	0.5	0.3
Bremsstrahlung	0.5	0.2	1.6	2.7	22.2	8.0	0.3	0.7	12.3	4.2
Continuum yield	4.9	1.1	-	-	-	-	-	-	-	-
$\tilde{q}^2$ continuum shape	5.2	2.6	2.6	1.5	4.5	0.5	2.4	0.7	2.8	0.3
$\mathcal{B}(B^0 \to \pi^-\ell^+\nu)$	0.0	0.1	0.0	0.0	0.1	0.0	0.0	0.0	0.1	0.0
$\mathcal{B}(B^+ \to \pi^0\ell^+\nu)$	0.2	0.0	0.4	0.9	5.2	1.9	0.3	0.6	2.9	1.3
$\mathcal{B}(B^+ \to \eta^{(\prime)}\ell^+\nu)$	0.4	0.4	0.0	0.1	0.8	0.2	0.1	0.1	1.0	0.4
$\mathcal{B}(B^0 \to \rho^-\ell^+\nu)$	0.3	0.5	0.1	1.1	6.9	2.3	0.1	0.6	4.2	1.7
$\mathcal{B}(B^+ \to \rho^0\ell^+\nu)$	0.0	0.3	0.1	0.1	0.5	0.1	0.0	0.1	0.8	0.2
$\mathcal{B}(B^+ \to \omega\ell^+\nu)$	0.8	1.1	0.1	0.2	2.6	0.8	0.1	0.1	2.6	0.9
Non resonant $b \to u\ell\nu$ BF	2.3	3.5	0.4	0.9	9.5	3.1	0.5	0.6	8.6	3.4
η BF	3.1	1.2	0.5	0.7	0.7	0.6	0.5	0.6	0.7	0.5
SF parameters	4.3	6.3	1.4	2.7	16.8	6.1	1.5	2.5	14.3	6.2
$B \to \rho\ell\nu$ FF	0.1	0.7	0.1	2.3	1.7	0.9	0.1	1.5	0.9	0.5
$B^+ \to \eta^{(\prime)}\ell^+\nu$ FF	1.1	1.0	0.1	0.1	1.4	0.4	0.1	0.1	1.5	0.6
Other scalar FF	2.9	4.2	7.7	1.4	0.1	3.2	0.7	0.1	0.0	0.2
$B \to \omega\ell\nu$ FF	1.2	2.1	0.1	0.5	2.8	0.7	0.1	0.4	3.9	1.3
$\mathcal{B}(B \to D\ell\nu)$	1.6	0.7	0.3	0.7	0.6	0.3	0.3	0.7	0.7	0.4
$\mathcal{B}(B \to D^*\ell\nu)$	0.3	0.4	0.1	0.8	1.2	0.4	0.1	0.7	1.0	0.4
$\mathcal{B}(B \to D^{**}\ell\nu)$	2.0	1.2	0.6	0.9	2.5	0.7	0.6	0.7	2.6	0.9
Non resonant $b \to c\ell\nu$ BF	0.1	0.1	0.2	0.1	0.8	0.2	0.3	0.1	0.4	0.2
$B \to D\ell\nu$ FF	0.1	0.3	0.1	0.1	0.5	0.2	0.1	0.1	0.7	0.3
$B \to D^*\ell\nu$ FF	0.6	0.9	0.5	0.9	1.3	0.4	0.5	1.2	1.2	0.4
$\mathcal{B}(\Upsilon(4S) \to B^0B^0)$	1.1	1.2	1.4	1.1	0.9	1.2	1.4	1.2	1.0	1.2
Secondary lepton	4.2	5.0	1.3	0.7	9.1	2.1	1.2	1.6	9.3	3.0
B counting	1.1	1.1	1.1	1.1	1.1	1.1	1.1	1.1	1.1	1.1
Signal MC stat error	1.2	1.1	1.4	1.6	1.2	0.7	1.3	1.3	1.0	0.5
Total systematic error	14.3	12.4	17.0	8.7	55.4	14.1	9.3	6.6	28.7	11.6
Total statistical error	32.8	25.6	14.6	21.0	39.3	13.7	15.2	16.6	30.3	12.5
Total error	35.8	28.4	22.4	22.7	67.9	19.6	17.8	17.8	41.8	17.0

Tableau II.6 – Correlation matrix of the partial $\Delta\mathcal{B}(B^+ \to \eta\ell^+\nu, q^2)$ statistical and systematic uncertainties.

	statistical			systematic		
q^2 bins (GeV^2)	0-4	4-8	8-16	0-4	4-8	8-16
0-4	1.00	-0.08	0.00	1.00	0.36	0.05
4-8	-0.08	1.00	-0.06	0.36	1.00	0.29
8-16	0.00	-0.06	1.00	0.05	0.29	1.00

Tableau II.7 – Correlation matrix of the partial $\Delta\mathcal{B}(B^0 \to \pi^-\ell^+\nu, q^2)$ statistical uncertainties.

q^2 bins (GeV^2)	0-2	2-4	4-6	6-8	8-10	10-12	12-14	14-16	16-18	18-20	20-22	22-26.4
0-2	1.00	-0.16	0.17	0.02	-0.02	0.03	0.01	0.04	0.05	0.02	0.04	-0.00
2-4	-0.16	1.00	-0.32	0.11	0.00	-0.00	-0.01	0.01	0.01	-0.00	0.00	-0.00
4-6	0.17	-0.32	1.00	-0.30	0.15	0.02	0.06	0.06	0.07	0.00	0.01	0.01
6-8	0.02	0.11	-0.30	1.00	-0.22	0.13	0.07	0.06	0.07	0.00	0.00	0.02
8-10	-0.02	0.00	0.15	-0.22	1.00	-0.22	0.16	0.05	0.08	0.01	-0.00	0.02
10-12	0.03	-0.00	0.02	0.13	-0.22	1.00	-0.15	0.10	0.07	-0.01	0.02	0.00
12-14	0.01	-0.01	0.06	0.07	0.16	-0.15	1.00	-0.16	0.13	-0.01	0.05	-0.00
14-16	0.04	0.01	0.06	0.06	0.05	0.10	-0.16	1.00	-0.01	0.01	-0.02	-0.02
16-18	0.05	0.01	0.07	0.07	0.08	0.07	0.13	-0.01	1.00	-0.17	0.09	-0.08
18-20	0.02	-0.00	0.00	0.00	0.01	-0.01	-0.01	0.01	-0.17	1.00	0.05	-0.05
20-22	0.04	0.00	0.01	0.00	-0.00	0.02	0.05	-0.02	0.09	0.05	1.00	-0.35
22-26.4	-0.00	-0.00	0.01	0.02	0.02	0.00	-0.00	-0.02	-0.08	-0.05	-0.35	1.00

Tableau II.8 – Correlation matrix of the partial $\Delta\mathcal{B}(B^0 \to \pi^-\ell^+\nu, q^2)$ systematic uncertainties.

q^2 bins (GeV^2)	0-2	2-4	4-6	6-8	8-10	10-12	12-14	14-16	16-18	18-20	20-22	22-26.4
0-2	1.00	-0.45	0.37	0.30	0.59	0.47	0.54	0.38	0.39	0.03	0.44	0.34
2-4	-0.45	1.00	-0.24	0.03	-0.27	-0.09	-0.17	-0.19	-0.37	0.36	-0.37	-0.02
4-6	0.37	-0.24	1.00	0.78	0.83	0.76	0.67	0.68	0.52	0.31	0.71	0.42
6-8	0.30	0.03	0.78	1.00	0.71	0.74	0.65	0.63	0.46	0.47	0.53	0.32
8-10	0.59	-0.27	0.83	0.71	1.00	0.74	0.71	0.70	0.50	0.35	0.66	0.38
10-12	0.47	-0.09	0.76	0.74	0.74	1.00	0.74	0.80	0.61	0.36	0.61	0.38
12-14	0.54	-0.17	0.67	0.65	0.71	0.74	1.00	0.69	0.73	0.29	0.56	0.33
14-16	0.38	-0.19	0.68	0.63	0.70	0.80	0.69	1.00	0.71	0.34	0.65	0.36
16-18	0.39	-0.37	0.52	0.46	0.50	0.61	0.73	0.71	1.00	-0.03	0.62	0.22
18-20	0.03	0.36	0.31	0.47	0.35	0.36	0.29	0.34	-0.03	1.00	-0.02	0.18
20-22	0.44	-0.37	0.71	0.53	0.66	0.61	0.56	0.65	0.62	-0.02	1.00	0.52
22-26.4	0.34	-0.02	0.42	0.32	0.38	0.38	0.33	0.36	0.22	0.18	0.52	1.00

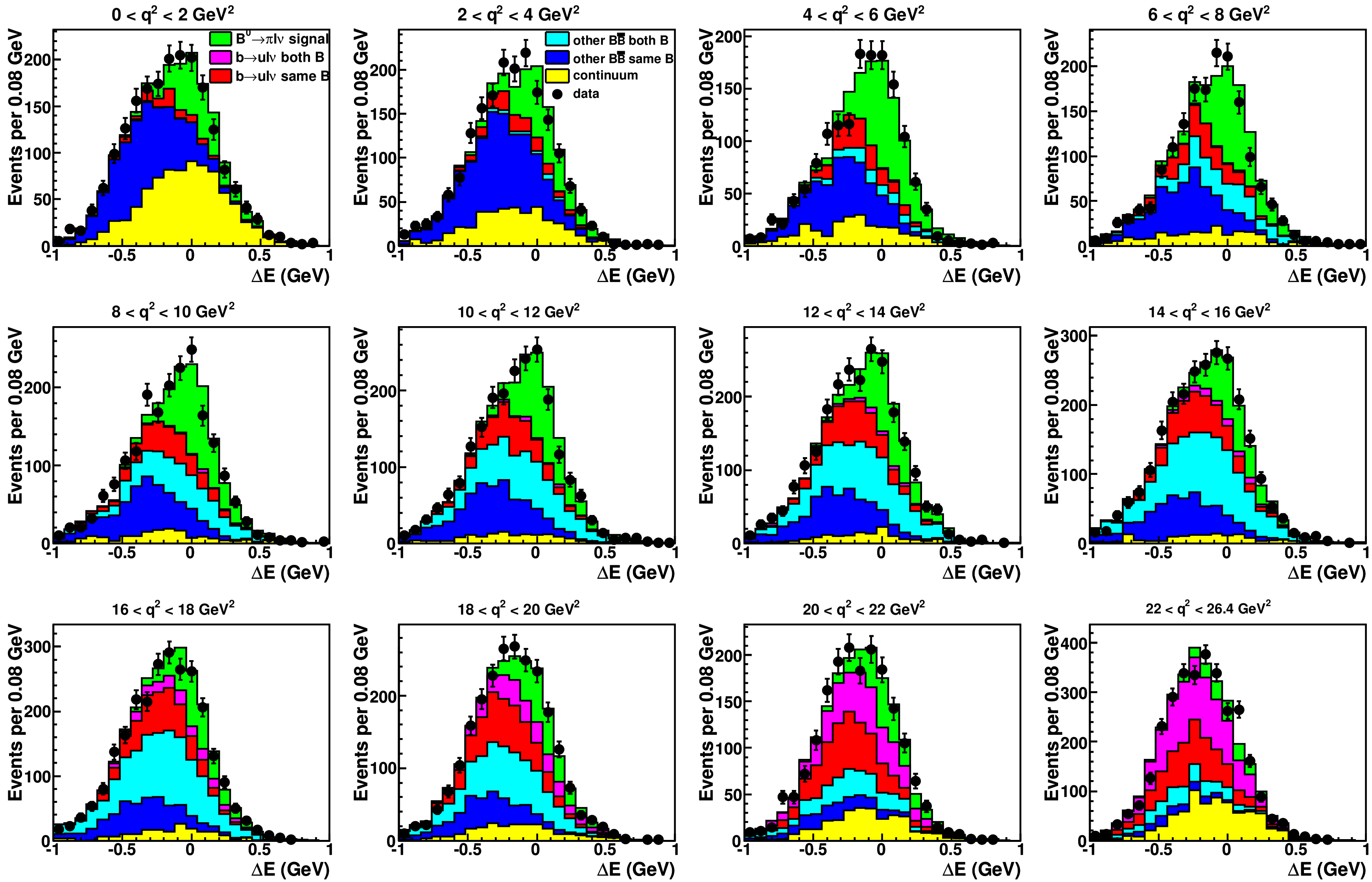

Figure II.1 – (color online) ΔE yield fit projections in the signal-enhanced region, with $m_{\rm ES} > 5.2675$ GeV, obtained in 12 q^2 bins from the fit to the experimental data for $B^0 \to \pi^- \ell^+ \nu$ decays. The fit was done using the full ΔE-$m_{\rm ES}$ fit region.

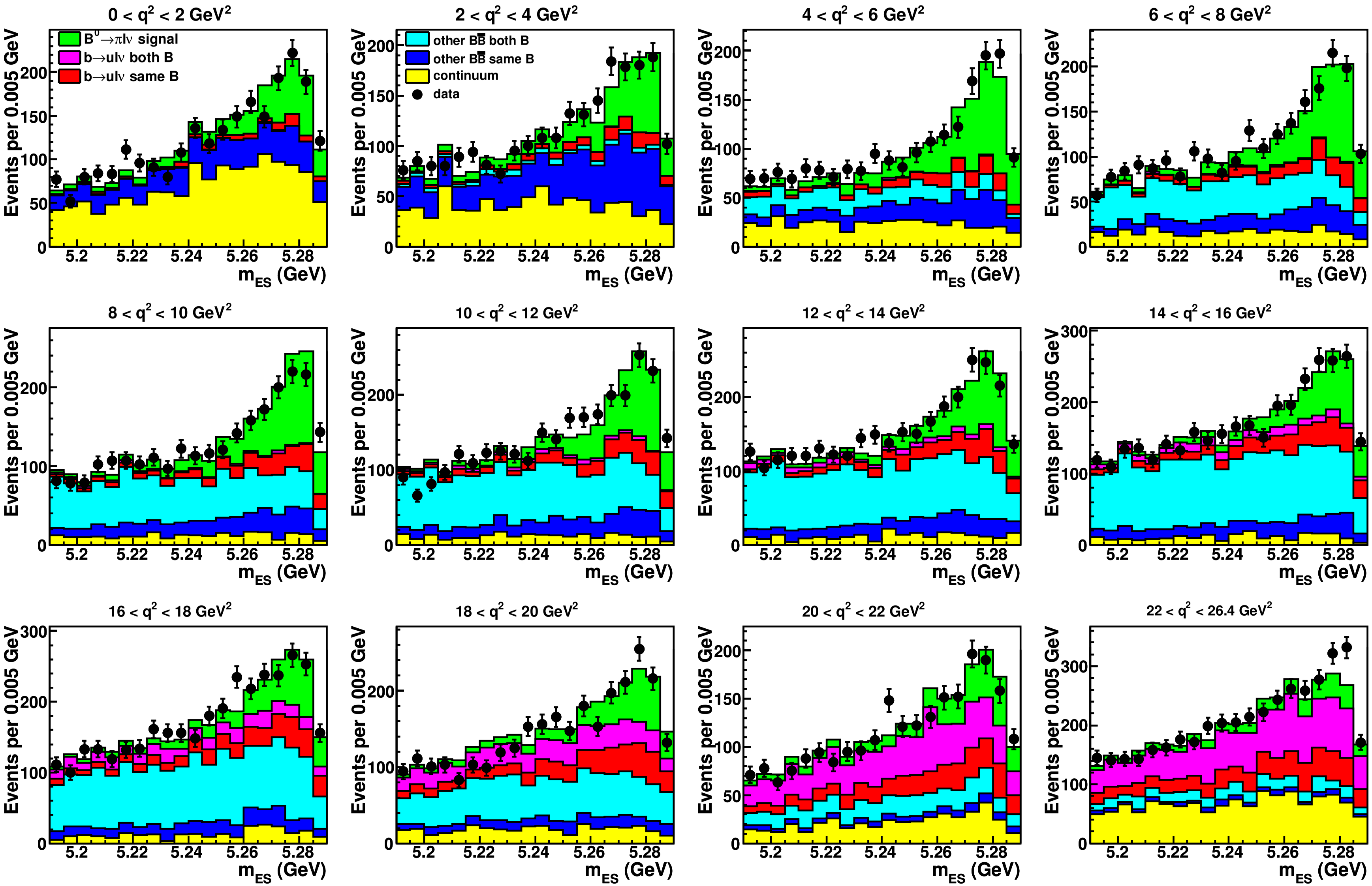

Figure II.2 – (color online) m_{ES} yield fit projections in the signal-enhanced region, with $-0.16 < \Delta E < 0.2$ GeV, obtained in 12 q^2 bins from the fit to the experimental data for $B^0 \to \pi^- \ell^+ \nu$ decays. The fit was done using the full ΔE-m_{ES} fit region.